

Konferenzbeiträge / Atti / Proceedings

Building Simulation Applications BSA 2019

4th IBPSA-Italy Conference
Bozen-Bolzano, 19th–21st June 2019

Edited by

**Giovanni Pernigotto, Francesco Patuzzi,
Alessandro Prada, Vincenzo Corrado, Andrea Gasparella**

bu,press

bozen
bolzano
university
press



Freie Universität Bozen
Libera Università di Bolzano
Università Lìdia de Bulsan

Konferenzbeiträge / Atti / Proceedings

Building Simulation Applications BSA 2019

4th IBPSA-Italy Conference
Bozen-Bolzano, 19th–21st June 2019

Edited by

**Giovanni Pernigotto, Francesco Patuzzi,
Alessandro Prada, Vincenzo Corrado, Andrea Gasparella**

bu,press

bozen
bolzano
university
press

Scientific committee

Ian Beausoleil-Morrison, Carleton University, Canada
Jan L.M. Hensen, Technische Universiteit Eindhoven, The Netherlands
Gregor P. Henze, University of Colorado Boulder, USA
Ardeshir Mahdavi, Technische Universität Wien, Austria
Athanasios Tzempelikos, Purdue University, USA
Reinhard Radermacher, University of Maryland, USA
Francesco Asdrubali, Università degli Studi Roma Tre, Italy
Paolo Baggio, Università degli Studi di Trento, Italy
Maurizio Cellura, Università degli Studi di Palermo, Italy
Cristina Cornaro, Università degli Studi di Tor Vergata, Italy
Vincenzo Corrado, Politecnico di Torino, Italy
Andrea Gasparella, Free University of Bozen-Bolzano, Italy
Livio Mazzarella, Politecnico di Milano, Italy
Adolfo Palombo, Università degli Studi di Napoli Federico II, Italy

Students Tutoring Scientific Committee

Fabian Ochs, Universität Innsbruck, Austria
Matthias Schuss, Technische Universität Wien, Austria
Alessia Arteconi, Università Politecnica delle Marche, Italy
Ilaria Ballarini, Politecnico di Torino, Italy
Annamaria Buonomano, Università degli Studi di Napoli Federico II, Italy
Marco Caniato, Free University of Bozen-Bolzano, Italy
Francesca Cappelletti, Università IUAV di Venezia, Italy
Gianpiero Evola, Università degli Studi di Catania, Italy
Francesco Patuzzi, Free University of Bozen-Bolzano, Italy
Giovanni Pernigotto, Free University of Bozen-Bolzano, Italy
Anna Laura Pisello, Università degli Studi di Perugia, Italy
Alessandro Prada, Università degli Studi di Trento, Italy

Organizing committee

Paolo Baggio, Università degli Studi di Trento, Italy
Marco Baratieri, Free University of Bozen-Bolzano, Italy
Marco Caniato, Free University of Bozen-Bolzano, Italy
Francesca Cappelletti, Università IUAV di Venezia, Italy
Vincenzo Corrado, Politecnico di Torino, Italy
Andrea Gasparella, Free University of Bozen-Bolzano, Italy
Norbert Klammsteiner, Energytech G.m.b.H./S.r.l -Bozen, Italy
Fabian Ochs, Universität Innsbruck, Austria
Francesco Patuzzi, Free University of Bozen-Bolzano, Italy
Giovanni Pernigotto, Free University of Bozen-Bolzano, Italy
Alessandro Prada, Università degli Studi di Trento, Italy
Fabio Viero, Manens – Tifs, Italy



This work—excluding the cover and the quotations—is licensed under the Creative Commons Attribution-ShareAlike 4.0 International License.

Cover design: DOC.bz

© 2020 by Bozen-Bolzano University Press

Free University of Bozen-Bolzano

All rights reserved

1st edition

www.unibz.it/universitypress

ISSN 2531-6702

ISBN 978-88-6046-176-6

Table of Contents

Preface.....	VII
The Impact of Occupancy-Related Input Data Uncertainty on the Distribution of Building Simulation Results <i>Christiane Berger, Elisa Primo, Dawid Wolosiuk, Vincenzo Corrado, Ardeshir Mahdavi</i>	1
New Tools for the Hygrothermal Assessment of Building Components: A Comparison of Different Methodologies <i>Carlotta Dolzani, Martina Demattio, Marco Larcher, Ulrich Klammsteiner, Ulrich Santa</i>	7
Evaluation of Energy Flexibility From Residential District Cooling <i>Alice Mugnini, Fabio Polonara, Alessia Arteconi</i>	15
Dynamic Characterization of Thermal Bridges in Historic Balconies in Palermo <i>Roberta Zarcone, Maurizio Brocato</i>	23
Multi-Stage Multi-Level Calibration of a School Building Energy Model <i>Ilaria Pittana, Alessandro Prada, Francesca Cappelletti, Andrea Gasparella</i>	29
Dynamic Modelling and Control System Optimization of a Reversible Air-to-Water Heat Pump with Heat Recovery for Domestic Hot Water Production <i>Matteo Dongellini, Luigi Belmonte, Gian Luca Morini</i>	37
Numerical Evaluation of Moisture Buffering Capacity of Different Inner Casing <i>Enrico Baschieri, Anne Friederike Goy</i>	47
A CitySim Urban Energy Simulation for the Development of Retrofit Scenarios for a Neighborhood in Bolzano, Italy <i>Fahad Haneef, Federico Battini, Giovanni Pernigotto, Andrea Gasparella</i>	59
Wind and Urban Spaces. Evaluation of a CFD Parametric Framework for Early-Stage Design <i>Viola Maffessanti</i>	67
Analysis of Two Shading Systems in a Glazed-Wall Physiotherapy Center in Bolzano, Italy <i>Luca Zaniboni, Giovanni Pernigotto, Andrea Gasparella</i>	77
Assessing Solar Radiation in the Urban Area of Bolzano, Italy, by Means of SEBE Simulations <i>Gianluca Pappaccogli, Giovanni Pernigotto, Alessandro Prada, Andrea Gasparella</i>	85
Numerical and Experimental Study on the Impact of Humidity on the Thermal Behavior of Insulated Timber Walls <i>Maja Danovska, Michele Libralato, Giovanni Pernigotto, Alessandra De Angelis, Onorio Saro, Paolo Baggio, Andrea Gasparella</i>	91
Sensitivity Analysis of SEBE Model Using Different Meteorological Input: A Case Study in Bolzano, Italy <i>Gianluca Pappaccogli, Giovanni Pernigotto, Alessandro Prada, Andrea Gasparella</i>	101
Numerical and Experimental Characterization of the Thermal Behavior of Complex Fenestrations Systems Under Dynamic Conditions <i>Ingrid Demanega, Giuseppe De Michele, Martin Hauer, Stefano Avesani, Giovanni Pernigotto, Andrea Gasparella</i>	109
Modelling the Sound Insulation of Mass Timber Floors Using the Finite Transfer Matrix Method <i>Federica Morandi, Marco Caniato, Olivier Robin, Luca Barbaresi, Andrea Gasparella, Patrice Masson, Nouredine Atalla</i>	117
Safety at Chimney-Roof Penetration: A Numerical Investigation <i>Manuela Neri, Leppanen Perttu, Mika Alanen, Davide Luscietti, Mariagrazia Pilotelli</i>	123
Building Energy Models with Morphological Urban-Scale Parameters: A Case Study in Turin <i>Ilaria Ballarini, Andrea Costantino, Domenico Dirutigliano, Roberto Boggetti, Fabio Fantozzi, Jérôme Kämpf, Guglielmina Mutani, Giacomo Salvadori, Valeria Todeschi</i> ..	131
Use of the ISO 12354 Standard for the Prediction of the Sound Insulation of Timber Buildings: Application to Three Case Studies <i>Francesca Di Nocco, Federica Morandi, Luca Barbaresi, Antonino Di Bella</i>	141

Testing the BIM-Ladybug Tools Interoperability: A Daylighting Simulation Workflow <i>Laura Pompei, Giulia Spiridigliozzi, Livio De Santoli, Cristina Cornaro, Fabio Bisegna</i>	149
An Attempt to Rank Italian Historical Opera Houses Based on Numerical Simulation <i>Giulia Fratoni, Anna Rovigatti, Massimo Garai</i>	157
Energy and Exergy Analysis of a HVAC System Having a Ground Source Heat Pump as Generation System <i>Paolo Valdiserri, Michael Lucchi, Marco Lorenzini</i>	165
Double-Layer Gypsum Panels: Prediction of the Sound Reduction Index Using the Transfer Matrix Method <i>Nicola Granzotto, Edoardo A. Piana</i>	173
Static vs Dynamic Hygrothermal Simulation for Cellulose-Based Insulation in Existing Walls: A Case Study Comparison <i>Matteo Bilardo, Fabrizio Giorgio, Enrico Fabrizio, Francesco Prizzon</i>	181
Design and Evaluation of Extreme Moisture Reference Years for Moisture-Related Risk Assessments <i>Michele Libralato, Giovanni Pernigotto, Alessandro Prada, Alessandra De Angelis, Onorio Saro, Andrea Gasparella</i>	191
Building Integrated Photovoltaic Thermal Collectors: Modelling and Experimental Investigation of Two Novel Cost-Effective Prototypes <i>Giovanni Barone, Annamaria Buonomano, Cesare Forzano, Adolfo Palombo</i>	201
A Psycho-Acoustical Experiment Using a Stereo Dipole for Spatial Impression of Music Signals <i>Benedetto Nastasi, Massimiliano Manfren, Francesca Merli</i>	213
On the Use of 3D Auralisation to Evaluate Room Acoustic Enhancement in Auditorium Restoration <i>Benedetto Nastasi, Massimiliano Manfren, Francesca Merli, Vincenzo Vodola</i>	223
Acoustic Comfort for Spaces Used by People with Cognitive Impairment: A Starting Point for the Application of Acoustic Event Detection and Sound Source Recognition Systems <i>Federica Bettarello, Marco Caniato, Giuseppina Scavuzzo, Andrea Gasparella</i>	231
Acoustics and Spatial Sound Distribution in the Theatre Comunale in Bologna, Italy <i>Massimiliano Manfren, Benedetto Nastasi, Francesca Merli, Vincenzo Vodola</i>	239
The Acoustic Simulation of Performing Area in the Auditorium: Some Examples in Italy <i>Vincenzo Vodola, Benedetto Nastasi, Massimiliano Manfren</i>	245
Acoustic Refurbishment on a Temporary Auditorium: BIM Design and Interventions Influences <i>Marco Caniato, Federica Bettarello, Matteo Bellè, Andrea Gasparella</i>	251
Control Strategies to Increase the Photovoltaic Self-Consumption for Air-Source Heat Pump Systems <i>Maria Pinamonti, Alessandro Prada, Paolo Baggio</i>	259
Sound Reduction Index of Clay Hollow Brick Walls <i>Nicola Granzotto, Edoardo Alessio Piana, Antonino Di Bella</i>	267
Prediction of the Acoustic and Thermal Performance of a Multilayer Partition <i>Manuela Neri, Mariagrazia Pilotelli, Edoardo A. Piana, Adriano M. Lezzi</i>	275
Implementing the Sustainable Energy (and Climate) Action Plans: Quasi-Steady State or Dynamic Modeling Approach <i>Concettina Marino, Antonino Nucara, Giorgia Peri, Matilde Pietrafesa, Gianfranco Rizzo, Gianluca Saccianoce</i>	283
Comparison Between the EN ISO 52016-1 Hourly Calculation Method and a Fully Detailed Dynamic Simulation <i>Giovanna De Luca, Mamak P. Tootkaboni, Ilaria Ballarini, Vincenzo Corrado</i>	291
On the Thermophysical Performance Optimization of Italian Schools of the 60s: A Case Study in Ostia (RM) <i>Francesco Asdrubali, Luca Evangelisti, Lucia Fontana, Claudia Guattari, Ilaria Montella, Pietro Prestininzi, Ginevra Salerno, Chiara Tonelli, Valeria Vitale</i>	299
On the Parasitic Heat Transfer Between Dwellings in the Case of Individual Heating: First Results by Simulation Across the EU <i>Viola Iaria, Carlo Mazzenga, Vincenzo A. Spena</i>	307
Analysis of the Surroundings Impact on the Building Energy Performance by Means of a BIM Analytical Model Coupled with Dynamic Simulation <i>Alessia Maiolatesi, Alessandro Prada, Fabio Luce, Giovanna Massari, Paolo Baggio</i>	315
Calibration of a UMI Simulation Model for a Neighborhood in Bolzano, Italy <i>Federico Battini, Giovanni Pernigotto, Andrea Gasparella</i>	323

Preface

Unlike the previous editions, the fourth Building Simulation Applications BSA 2019 Conference took place in June, from 19th to 21st, instead of during the winter period. For the biennial conference hosted by the Free University of Bozen-Bolzano, IBPSA Italy had to double its efforts, considering its concurrent commitment to the organization of Building Simulation 2019 in Rome.

Even so, BSA 2019 featured more than 60 participants and around 130 different authors, with a significant presence of delegates from abroad and, in particular, from Austria. A different review process was introduced, with the full paper submission and review following the conference. Based on this, only 40 out of the 54 works presented during the conference in two parallel sessions were accepted for inclusion in this proceedings book.

The initiatives for students and practitioners offered in the previous edition were renewed. As regards the former, new editions of the “Student School on Building Performance Simulation Applications” – this year dealing with indoor lighting simulation and building acoustics simulation – and the “Student Award” were organized. Similarly, the “IBPSA Italy Round Table for Designers and Practitioners” took place to discuss current trends, criticalities and the potential of the use of building simulations in professional activities.

Regarding the main topics analysed in the last edition of Building Simulation Applications, in addition to the analysis of building energy performance, particular attention was paid to hygro-thermal simulations of building components, the development of advanced controls for HVAC components – particularly, heat pumps, urban simulation and urban weather data – and the integration of BIM solutions in building design. A special and novel focus for the conference was acoustics, with three dedicated sessions and 15 presentations, ranging from simulations of acoustic comfort and room acoustics, to the acoustic behaviour of components and structures.

Interesting overviews of current trends and the development of building simulation tools and methods were offered in the two keynotes hosted

during the conference. Lori McElroy, current IBPSA President, spoke about “Building Performance Simulation – Future Trends and the Role of IBPSA”, and Vincenzo Corrado, former IBPSA Italy president, discussed recent developments in technical standards in his speech “Energy Performance Assessment of Buildings in a Legal Context: New Standards and National Trends”.

Finally, Ardeshir Mahdavi (Technische Universität Wien, Austria – Department of Building Physics and Building Ecology) offered a special lecture about building simulations to the PhD students present at the conference, titled “Some lateral thoughts on building performance simulation”, engaging all attendees in some critical reflexions on the uses and applications of building performance simulations.

With the success of the 2019 edition, six years after the first conference, BSA has been confirmed as a lively expression of the IBPSA national Building Simulation community, its commitment to research, its attention to practice, and its international connections.

Andrea Gasparella, Free University of Bozen-Bolzano

The Impact of Occupancy-Related Input Data Uncertainty on the Distribution of Building Simulation Results

Christiane Berger – TU Wien, Austria – christiane.berger@tuwien.ac.at

Elisa Primo – Politecnico di Torino, Italy – elisa.primo@polito.it

Dawid Wolosiuk – TU Wien, Austria – dawid.wolosiuk@tuwien.ac.at

Vincenzo Corrado – Politecnico di Torino, Italy – vincenzo.corrado@polito.it

Ardeshir Mahdavi – TU Wien, Austria – amahdavi@tuwien.ac.at

Abstract

In building performance simulation, fixed input assumptions lead to fixed computed values for building performance indicators. This has been suggested to be misleading, as it does not express the uncertainty of simulation-based performance predictions. A counter-argument to this position suggests that the empirical basis for the determination of the statistical uncertainty distribution of occupancy-related input assumptions is rather scant. Arbitrary assignment of uncertainty functions (distribution ranges and shapes) to input variables can indeed generate corresponding performance result distributions. However, this could be even more misleading than fixed values, as the resulting uncertainty impression is empirically ungrounded. To address this objection, it has been suggested that the computed uncertainty ranges for performance indicators may be, to a certain extent, resistant to the ranges and shapes of associated input data distributions and hence still useful. In the present contribution, we examine the above suggestion, namely the resilience of performance simulation output distribution to the assumed model input uncertainties. To this end, parametric simulations were conducted and processed to explore the implications of different input data assumptions for the values of computed performance indicator values for a sample building model.

1. Introduction

A common argument against the use of such fixed input assumptions for building performance simulation is the uncertainty challenge. Hence, so goes the criticism, the input data uncertainty is not manifest in the results, which can be misleading (Mechri, 2009; Tian et al., 2018; Li et al., 2019).

It has been suggested that replacing single value input data assumptions with distributions of input data variables is preferable. However, there is a paucity of empirical information on the uncertainty distributions of occupancy-related simulation model input data assumptions. It is of course possible to select – more or less arbitrarily – some distribution ranges and shapes of certain input variables to generate corresponding performance result distributions instead of single values. However, this approach could be even more misleading as the resulting uncertainty ranges are not empirically grounded (Mahdavi, 2015; Mahdavi & Tahmasebi, 2019).

The present paper examines the suggestion that computed uncertainty ranges for performance indicators may be at least partially resistant to the ranges and shapes of associated input data distributions. We explore the validity of this suggestion via systematic simulation runs applied to a case study building in Italy. This case study model is subjected to variation (i.e. different distribution shapes and ranges) of input data assumptions for the values of computed performance indicators.

2. Method

In order to explore the implications of occupancy-related input data assumptions (i.e. different distribution shapes and ranges) for the values of key performance indicator values, an illustrative case, namely a typical apartment in a residential building in Italy, was selected (Fig. 1). This building is located in the Italian climatic zone E (Milano, 2404 HDD). General information on the building is given in Table 1 including geometry-related variables (V_g : gross volume; $A_{f,net}$: net floor area; A_w : window area) and construction-related variables (U-values of external wall $U_{ext,wall}$, wall adjacent to unheated space $U_{wall,unheated}$, floor U_{floor} , and window U_{window}). Within this case study, the aforementioned assumption, namely the resilience of performance simulation output distribution in view of input data variation, is tested via systematic simulation applied to this apartment.

The building is modelled in EnergyPlus (EnergyPlus, 2019) and parametric simulation runs are expressed in RStudio (RStudio, 2019). First, we obtained fix-value simulation results for the base case (BC), whose simulation model likewise involved only fix values of input variables. Subsequently, we considered different distribution shapes and ranges and examined the effect of input variable distributions on the corresponding distributions of computed performance indicator values. In the present contribution, a number of generic input data variations, namely three normal distributions with three different widths (labelled as N_N , N_S , and N_W) (Fig. 2) as well as one left-skewed distribution (S_L) and one right-skewed distribution (S_R) (Fig. 3) are considered.

The study considers the following input variables: Heating temperature set-point (θ_{sp-h} in $^{\circ}\text{C}$), air change rates (ACH in h^{-1}), and internal gains (q_{int} in W.m^{-2}). The simulated performance indicator is the annual heating demand ($q_{a,h}$ in $\text{kWh.m}^{-2}.\text{a}^{-1}$). The response of simulated performance indicator to input variable assumptions are captured in two distinct sets of simulation runs. Whereas in the first set only one input variable's value is parametrically varied, in the second set the values of multiple input variables are varied simultaneously.

In the following, the results of both groups of variation are discussed in detail.

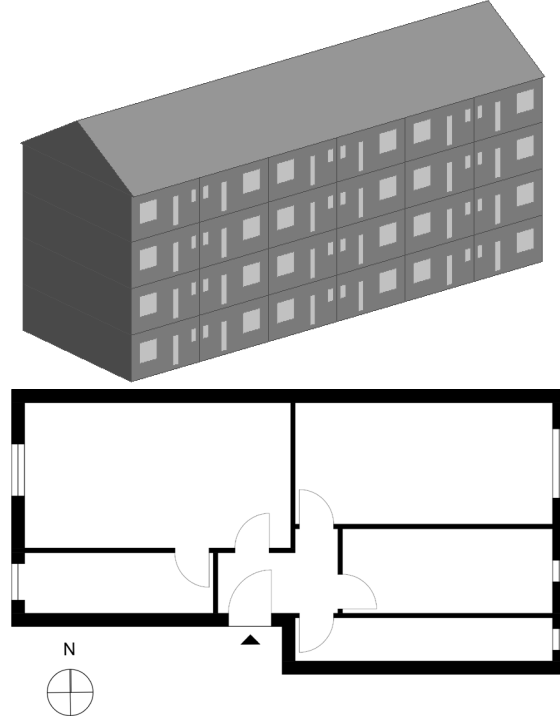


Fig. 1 – Case study building in Milan, Italy (Top: 3D model. Bottom: floor plan of the selected case study apartment)

Table 1 – Overview of case study apartment data

	Variable	Unit	Value
Geometry	V_g	m^3	259
	$A_{f,net}$	m^2	65
	A_w	m^2	7.96
Construction	$U_{ext,wall}$		0.26
	$U_{wall,unheated}$	$\text{W.m}^{-2}.\text{K}^{-1}$	0.56
	U_{floor}		1.34
	U_{window}		1.40

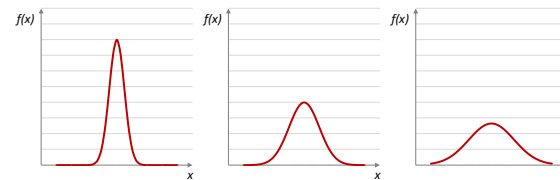


Fig. 2 – Narrow (N_N), standard (N_S), and wide (N_W) normal distribution

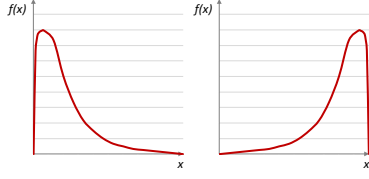


Fig. 3 – Right-skewed (S_R) and left-skewed (S_L) distribution

3. Results and Discussion

3.1 One-at-a-Time Variation of Model Input Variables

The first set of results concerns the response of the simulated performance indicator (i.e. annual heating demand) to one-at-a-time variation of the model input variables. The distribution of the values of one input variable (heating temperature set-point) is shaped according to the aforementioned distributions. Fig. 4 shows the resulting five different heating temperature set-point distributions.

A total of 100 simulations are performed to generate each of the five resulting distribution functions of the annual heating demand. The corresponding simulation results are shown in Fig. 5. Table 2 includes a number of basic statistical markers for both the distributions of the input variable value (namely the heating temperature set-point θ_{sp-h}) and the corresponding distributions of the computed building performance indicator values (heating demand $q_{a,h}$). These include the mean (μ), standard deviation (σ), and coefficient of variation (CV) for the five aforementioned distribution functions.

These results suggest that the value of a computed building performance indicator strongly depends on the assumed distribution of the input variable value. This means that the usability of a simulation-based generation of output distributions would be very limited, if no basis or reasoning is provided concerning the underlying input variable distribution assumptions.

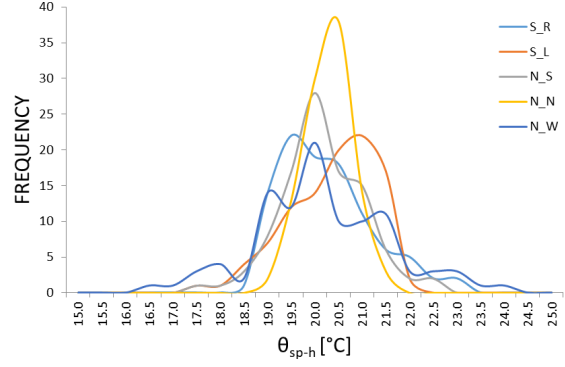


Fig. 4 – Assumed heating temperature set-point distributions toward computation of annual heating demand (see Fig. 5)

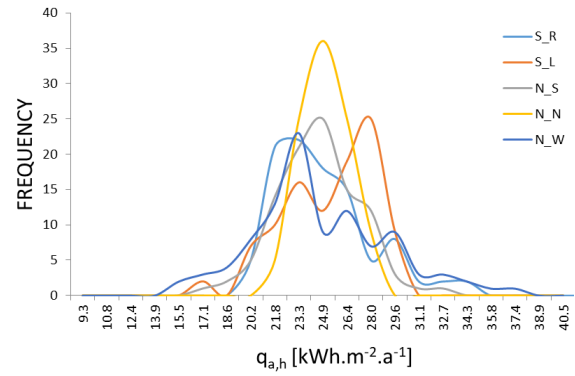


Fig. 5 – Computed annual heating demand distributions as a consequence of assumed input variable distributions (see Fig. 4)

Table 2 – Statistical data regarding the first set of simulation runs (consequences of assumed heating temperature set-point assumptions for computed distributions of annual heating demand)

	θ_{sp-h} [°C]			$q_{a,h}$ [kWh.m ² .a ⁻¹]		
	μ	σ	cv	μ	σ	cv
BC	20.00	-	-	24.15	-	-
N_S	19.89	0.89	4.46	23.86	2.74	11.48
N_N	20.02	0.50	2.52	24.24	1.57	6.50
N_W	19.91	1.40	7.05	24.00	4.39	18.29
S_R	19.99	0.98	4.88	24.19	3.10	12.81
S_L	20.12	0.94	4.66	24.59	2.89	11.75

3.2 Concurrent Manipulation of Multiple Input Variables

As mentioned previously, the second set of parametric simulations explore the response of simulation results to concurrent manipulation of multiple input variables in terms of distribution functions. To illustrate this point, Figs 6 and 7 show the concurrent parametric variation of two input variable values, namely heating temperature set-points [θ_{sp-h}] and air change rates [ACH]. Thereby, three different combinations of distribution functions are considered (Fig. 6):

- A. Right-skewed distribution of θ_{sp-h} and ACH
- B. Standard normal distribution of θ_{sp-h} and ACH
- C. Right-skewed distribution of ACH and left-skewed distribution of θ_{sp-h}

The set of input values for the heating temperature set-points [θ_{sp-h}] and air change rates [ACH] are generated according to the aforementioned three different combinations of distribution functions. A total of 100 simulations are performed to generate the resulting distribution functions for annual heating demand for each of the three combinations (see A, B, and C above).

Fig. 7 displays the resulting three different distributions of the computed heating demand of the aforementioned case study apartment.

According to the results of this second set of simulation runs, there is no evidence that arbitrary variations of input data distributions necessarily result in reproducible and consistent distributions of computed building performance indicator values.

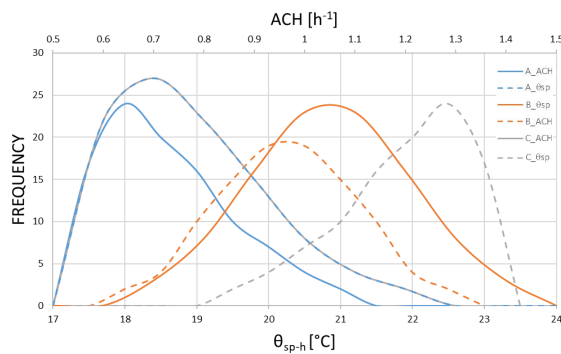


Fig. 6 – Selected distributions of input variables θ_{sp-h} and ACH toward computation of annual heating demand (see Fig. 7)

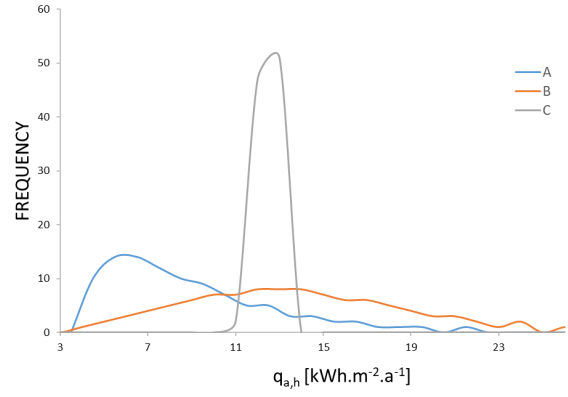


Fig. 7 – Computed distributions of annual heating demand as a consequence of assumed input variable distributions (see Fig.6)

To further pursue this point, we varied (concurrently and randomly) three different input data variables, namely the heating temperature set-point [θ_{sp-h}], the air change rate [ACH], and the internal gain [q_{int}] (see Figs 8 to 10 for the corresponding distributions).

For each of the three input variables (θ_{sp-h} , ACH, and q_{int}) the distribution functions are randomly selected. Subsequently, the values of each of the three input variables are randomly selected from a set of 100 values that constitute each of the distribution functions.

In total, 10000 simulations are performed to generate the distribution function of the annual heating demand. The resulting distribution of the computed overall annual heating demand is shown in Fig. 11. An overview of the statistical markers pertaining to distributions of the input variables and the distribution of the results is given in Table 3.

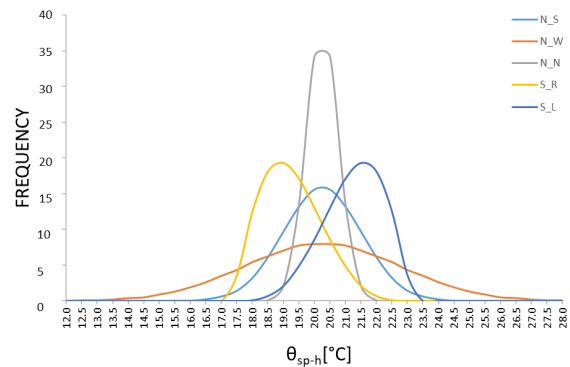


Fig. 8 – Selected distributions for heating temperature set-point [θ_{sp-h}] toward computation of annual heating demand (see Fig. 11)

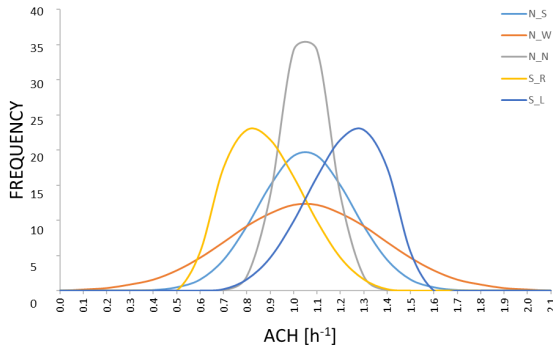


Fig. 9 – Selected distributions for air change rate [ACH] toward computation of annual heating demand (see Fig. 11)

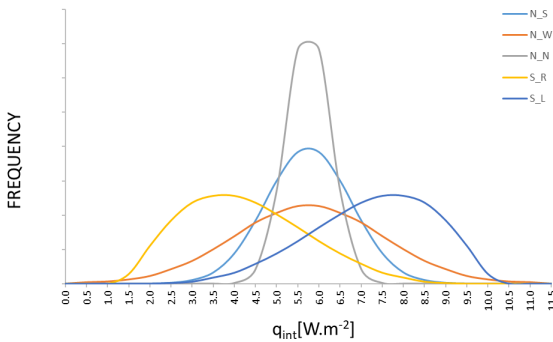


Fig. 10 – Selected distributions for internal gains [qint] toward computation of annual heating demand (see Fig. 11)

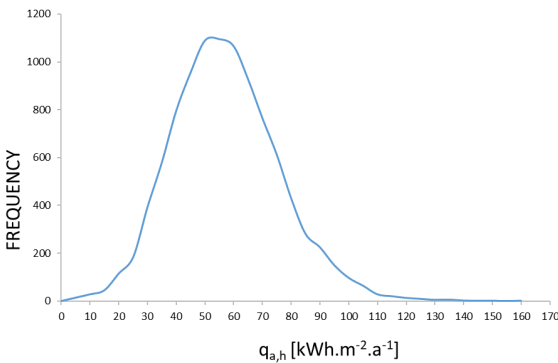


Fig. 11 – Computed distribution of annual heating demand as a consequence of assumed input variable distributions (see Figs. 8 to 10)

Table 3 – Statistical data regarding the assumed distributions of concurrently varied input variables (θ_{sp-h} , ACH, and qint) as well as the resulting distribution of the output variable ($q_{a,h}$)

	μ	σ	cv
θ_{sp-h}	20.00	1.50	0.08
ACH	1.00	0.24	0.24
qint	5.55	1.86	0.34
$q_{a,h}$	54.84	18.58	0.34

These last results imply that a fairly stable distribution of the simulated values of a performance indicator may emerge, if we conduct extensive Monte Carlo simulations involving both multiple input variables and multiple distribution shapes of those variables. For a given group of such variable sets and distributions sets, we may even be able to propose default uncertainty ranges. However, this approach would not resolve the problem stated at the outset. As long as the combination of input variable sets and corresponding distribution shapes involve arbitrary choices, the resulting output distributions and corresponding uncertainty ranges remain likewise arbitrary. Provision of standardized uncertainty ranges (for instance, standard deviations) for simulation results may be a possible option, assuming the availability of predefined input variable distribution shape catalogues. The question is, however, whether conducting an extensive set of parametric simulation runs is not a rather prohibitive expenditure of time and effort, given the fairly limited meaning and utility of the provided uncertainty information.

Acknowledgement

The treatment presented in this paper benefited from authors' participation in the IEA EBC Annex 79 and the related discussions.

References

- EnergyPlus 2019. <https://energyplus.net/> Accessed 20.06.2019
- Li, J., Z. Yu, F. Haghighat, and G. Zhang. 2019. "Development and improvement of occupant behavior models towards realistic building performance simulation: A review." *Sustainable Cities and Society* 50 (2019) 101685. doi.org/10.1016/j.scs.2019.101685.
- Mahdavi, A. 2015. "Common fallacies in representation of occupants in building performance simulation." In BSA2015 - Building Simulation Applications 2015 - 2nd IBPSA-Italy Conference, Bozen, Italy. Edited by IBPSA Italy. Paper-Nr. Keynote #3. Free University of Bolzano.

- Mahdavi, A., and F. Tahmasebi. 2019. "People in building performance simulation." In *Building Performance Simulation for Design and Operation*, edited by Hensen, J., and Lamberts, R., 117-145 New York: Routledge.
- Mechri, H. E. 2009. "Practical applications of uncertainty and sensitivity techniques on building energy analysis." PhD thesis. Politecnico di Torino.
- RStudio 2019. <https://rstudio.com/> Accessed 20.06.2019
- Tian, W., Y. Heo, P. de Wilde, Z. Li, D. Yan, C. S. Park, X. Feng, and G. Augenbroe. 2018. "A review of uncertainty analysis in building energy assessment." *Renewable and Sustainable Energy* 93 (2018) 285-301. doi.org/10.1016/j.rser.2018.05.029.

New Tools for the Hygrothermal Assessment of Building Components: A Comparison of Different Methodologies

Carlotta Dolzani – CasaClima Agency, Bolzano, Italy – carlotta.dolzani@agenziacasaclima.it

Martina Demattio – CasaClima Agency, Bolzano, Italy – martina.demattio@agenziacasaclima.it

Marco Larcher – EURAC Research, Bolzano, Italy – marco.larcher@eurac.edu

Ulrich Klammsteiner – CasaClima Agency, Bolzano, Italy – ulrich.klammsteiner@agenziacasaclima.it

Ulrich Santa – CasaClima Agency, Bolzano, Italy – ulrich.santa@agenziacasaclima.it

Abstract

This paper presents new tools for the hygrothermal assessment of building components. The first assessment method based on the Glaser approach is implemented on the existing software ProCasaClima, whereas the second method constitutes a new tool for the dynamic simulation of combined transport of heat and moisture in building components: ProCasaClima Hygrothermal. This latter tool is more advanced since it takes into account capillary liquid transport and moisture storage properties of materials. At the same time, ProCasaClima Hygrothermal aims to be user-friendly to maximize its diffusion among technicians. The two assessment methods will be presented and compared in the results through a case study represented by an external wall internally insulated and located in the climate of Bolzano/Bozen. A second analysis is carried out specifically on the Hygrothermal tool to compare the results obtained with two different climate files. The first uses the reference year data provided by the CTI while the second is based on climate data obtained from the software Meteonorm, once again on the city of Bolzano/Bozen, but also including data referring to the rain. Finally, it will be possible to evaluate the influence of this phenomenon on the risk of interstitial condensation for the specific case analysed. The studies presented in this paper are supported by the ERDF European project BuildDOP.

1. Introduction

The main reason behind the necessity of performing an hygrothermal assessment concerns the prevention of building pathologies, degradation of components and comfort issues.

The Italian building stock is rich in buildings requiring energy requalification interventions.

Based on the experience gained by CasaClima Agency on certified buildings, it is clear that some design solutions, which could be critical from the hygrothermal point of view, are often applied in the construction phase without performing the required hygrothermal evaluations in the design stage. This issue is due to the lack of simple and easily accessible evaluation tools as well as to the lack of knowledge of stakeholders involved in the design and construction process of buildings. In particular, the use of vapor barriers or moisture-variable vapor barriers for interior insulation in mixed constructions, common in the Alpine region, can lead to construction damage in the event of improper installation. Moreover, the application of the capillary active insulation system is often limited due to the absence of a user-friendly simulation tool that can predict properly their hygrothermal performances.

Thus, within the BuildDOP project (Agenzia per l'Energia Alto Adige – CasaClima, 2018), the CasaClima Agency with the support of Eurac Research has developed two tools for the hygrothermal analysis of building components: an assessment tool based on the Glaser methodology and a dynamical simulation tool, ProCasaClima Hygrothermal. The aim is to push the application of dynamic hygrothermal simulations, even in smaller renovation projects where interior insulation is frequently used and integrate them in the building certification process. The general objective of the implementation of these two hygrothermal assessment methods is to provide designers and

building consultants with all the tools needed to perform the verifications required in Appendix D of the CasaClima Technical Directive. This Appendix requires hygrothermal verification in two cases: internally insulated external walls and non-ventilated flat roofing (Agenzia per l'Energia Alto Adige – CasaClima, 2017).

This paper reports the development of the two different calculation approaches designated to the evaluation of interstitial condensation risk on building components i.e. a Glaser based method (EN ISO 13788) and a dynamic simulation tool (EN 15026). The results of the two calculation approaches are compared using a case study. Moreover, the dynamical simulation is performed in two different ways: including and neglecting the effect of driving rain on the building component. The aim is to evaluate the impact of this parameter on the simulation results in a typical Italian climate.

2. Implementation of the Standards

2.1 Glaser Method: UNI EN ISO 13788

The implementation of the above-described methodologies is carried out using the Excel GUI working environment.

Firstly, the Glaser method (EN ISO 13788) has been analysed and implemented step by step following the prescriptions of the standard. The input parameters for the computation are monthly average external conditions (UNI 10349-1) and hygrothermal properties of the materials constituting the building component to be verified.

In particular, in terms of the climate data, the following monthly parameters are necessary for the calculation: outdoor temperature, extreme relative humidity that allows us to obtain the vapour pressure, air temperature and indoor relative humidity. In addition, the properties of materials and products concern conductivity and thermal resistance, the water vapour resistance factor, the equivalent air thickness for the diffusion of water vapour, to which surface resistances are added ($R_{se} = 0,04 \text{ m}^2 \times \text{K/W}$ ed $R_{si} = 0,25 \text{ m}^2 \times \text{K/W}$). At each interface between materials, the partial vapor and

saturation pressures are computed and, comparing their values, it is possible to identify potential condensation interfaces. In case a condensation layer is identified, the vapour flow rates in that layer are calculated and consequently the amount of condensation or evaporation occurring. The calculation is carried out by means of a graphic monthly method, considering periods of accumulation and evaporation.

This tool has been integrated in the already existing software of the CasaClima Agency "Pro-CasaClima" in the sheets dedicated to the description of the construction elements. It is possible to select different humidity classes to be applied as indoor climatic conditions, following the prescriptions of the UNI EN ISO 13788 standard.

As output, the user gets an initial feedback on the presence or absence of interstitial condensation in the construction under monthly stationary conditions. In the case of absence, the component can be considered safe under the initial assumptions of absence of driving rain or, more generally, where the phenomena of the hygroscopic capacity of the materials, the transport of humidity to the liquid state and capillary ascent can be considered negligible. By contrast, in the case of presence of interstitial condensation in the component or if it is not possible to apply the stationary method due to the presence of the phenomena described above, the user will have to proceed with a more detailed simulation thorough a dynamic analysis by means of the new simulation tool ProCasaClima Hygrothermal. As the Glaser approach is a simplified method, it presents some limitations: only vapor diffusion is taken into account as a moisture transport mechanism, moisture storage properties of materials are neglected, average monthly climate data are considered and driving rain is completely neglected. It can therefore lead to substantial errors in the evaluation when other transport mechanisms are relevant or when the hygroscopic storage properties as well as the contribution of rain cannot be neglected.

2.2 ProCasaClima Hygrothermal: EN 15026

A more complex and accurate calculation technique is suggested by the EN 15026 standard which includes, unlike the previous procedure, the following aspects: 1. capillary liquid transport 2. hygroscopic storage properties of the material 3. modification of physical properties of materials according to the moisture content 4. hourly weather data 5. effect of radiation and eventually driving rain. The new software ProCasaClima Hygrothermal, developed in cooperation with Eurac Research, responds to these characteristics. The external solver of the tool is the same used in DELPHIN while the graphic interface, the selection of input and output parameters were developed to provide a user-friendly instrument for designers. This tool presents the advantage of combining the ease of use typical of any Excel file and the high level of performance which is featured in the most popular dynamic simulation software such as WUFI or DELPHIN. Above all, this new software is available to the user completely free of charge.

Several aspects have been considered to make the tool user friendly, such as the guided input of data through drop down menus, which helps the designers to select the correct parameters. The tool is currently able to simulate the combined transport of heat and moisture in 1D wall build-ups. Through the application to a case study, the types of data input and output that the new software proposes will be analysed and described in more detail.

3. Simulation

The selected case study construction is reported in the volume “Risanare l’esistente” by Cristina Benedetti and consists of an external wall internally insulated. Referring to Fig. 1, it is possible to recognize the outermost layer of lime cement mortar (3 cm) followed by 45 cm of stone masonry and another layer of mortar. Internally the element is insulated with 12 cm of wood fibre and finally 0.4 cm of internal lime plaster (Benedetti C., 2011).

Firstly, the wall is analysed according to the two

calculation methods to compare the results that they generate. Secondly, the focus is applied on the software ProCasaClima Hygrothermal and the same wall is simulated both using climate data that do not include rain and climate data that include rain.

These tests are carried out in the city of Bolzano (Italian climate zone E). The basic hygrothermal properties of the materials constituting the wall are reported in Table 1.

Table 1 – Fundamental hygrothermal properties of materials used for the hygrothermal assessment. The reported parameters are: bulk density (ρ), specific heat capacity (c_p), thermal conductivity (λ), vapor diffusion resistance factor (μ)

ID	Material	ρ [kg/m ³]	c_p [J/kg K]	λ [W/m K]	μ [-]
1	Lime Plaster (fine)	1600	850	0,70	7
2	Wood Fibre Insulation Board	168	1700	0,045	39
3	Lime cement mortar	1900	850	0,80	19
4	Sandstone Krenzheimer	2400	1000	2,00	248
5	Lime cement mortar	1900	850	0,80	19

3.1 UNI EN ISO 13788 Evaluation

The interstitial condensation assessment carried out in accordance with the standard UNI EN ISO 13788 is applied to the city of Bolzano using the monthly external climate data taken from the standard UNI 10349. As regards the indoor boundary conditions, these are deduced in accordance with the UNI EN ISO 13788 standard, considering the third humidity class (“Buildings with unknown occupation”) for maritime climates. However, the tool implemented in ProCasaClima gives the user the possibility to choose any of the 5 humidity classes for the verification.

3.2 ProCasaClima Hygrothermal Simulation

In this section the relevant input parameters for the simulation with the new software and the relative outputs are described through the application to the case study construction.

In ProCasaClima Hygrothermal materials can be chosen by the user from a rich database, which is

the same of the DELPHIN software. There is also the possibility for the user to customize his/her own materials starting from a material in the database and then changing its name and its main hygrothermal characteristics and then saving it in a user defined database. The component is graphically displayed with its own layers and the position of monitors, as reported in Fig. 1.



Fig. 1 – Graphical visualization of the layers constituting the building element and of the monitor position within the GUI of ProCasaClima Hygrothermal

Monitors provide detailed outputs for a specific position of the construction, considered to be particularly dangerous from the hygrothermal point of view by the user.

In terms of the climate data, ProCasaClima Hygrothermal has an internal database containing the data for all Italian provinces developed by the CTI (Murano et al., 2016). A temperature correction is subsequently applied to the climate data if the analysed construction has a different altitude with respect to the location included in the database. These data, processed in the form of TRYs according to the standard EN ISO 15927-4, include outdoor temperatures, relative humidity, global and diffuse radiation and wind speed all on an hourly basis. Alternatively, the user can import his own climate data in a .csv format, which can also be generated with the support of the software Meteororm. In this case, not only can the user select the province but also the exact GPS coordinates of his case study to best simulate local aspects such as the influence of the horizon on the climate. Unlike the previous case, in the latter it will be possible to obtain the precipitation data in the chosen site and see them graphically represented as illustrated in Fig. 2.

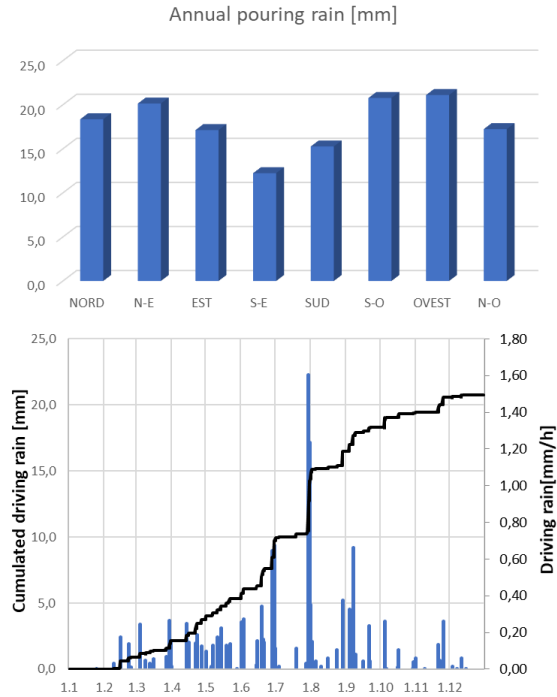


Fig. 2 – Graphs of the annual driving rain subdivided on the 8 orientations for the climate of Bolzano taken from Meteororm. Below: hourly and cumulated driving rain data for the west façade

The construction is simulated selecting the west orientation, since it represents the direction in which there is the greatest amount of driving rain during the year. This will maximize the influence of this parameter, for the evaluation of the impact of driving rain on the simulation.

The interior climate in ProCasaClima Hygrothermal is calculated on the basis of external temperature and relative humidity by means of two simplified adaptive interior climate models that are described in the standard EN 15026 and EN ISO 13788. The user has the possibility to select the classes provided by both standards, but for the simulation object of this paper the third class in maritime climate provided by EN ISO 13788 is chosen to have the same boundary conditions with respect to the simplified calculation method. This approach for calculating internal climate data leads to a variation of the internal temperature during the year in the range between 20 °C and 23.7 °C and relative humidity ranging from 43% to 71%.

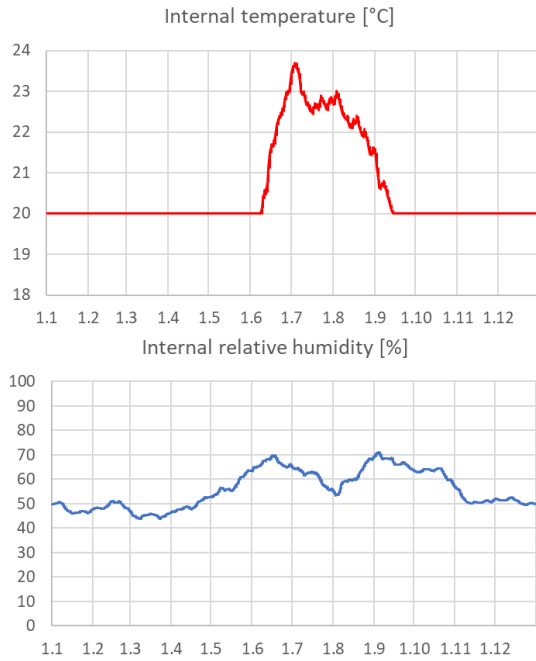


Fig. 3 – Trend of the internal temperature and relative humidity during the year calculated following the prescriptions of the standard EN ISO 13788

The heat and vapour transmission coefficients are set according to the EN ISO 6946 and EN 15026 standards according to the type of construction element analysed (external wall, roof). In particular, for the study conducted in this paper the heat conduction exchange coefficient is equal to $25 \text{ W/m}^2\text{K}$ ($R_{se} = 0.04 \text{ m}^2\text{K/W}$) while the vapour diffusion coefficient is $8.034 \times 10^{-8} \text{ s/m}$. For internal surfaces these parameters assume respectively the following values: $4 \text{ W/m}^2\text{K}$ ($R_{si} = 0.25 \text{ m}^2\text{K/W}$ (to take into account the presence of furniture) and $2.420 \times 10^{-8} \text{ s/m}$.

The starting month for the dynamic simulation is conventionally fixed at October, being the first month of heating for the climate zones most at risk of interstitial condensation, i.e. Italian climate zones E and F. A timeframe of at least 3 years of simulation is recommended in order to reduce the influence of the starting conditions set by default i.e. relative humidity equal to 80% and internal temperature of 20°C (Larcher et al., 2019). The driving rain coefficients consistent with the EN ISO 15927-3 standard are: roughness coefficient (1.01), topographic coefficient (1.00), obstruction coefficient (0.80), coefficient relative to the wall (0.40), splashing coefficient (0.70), total reduction coefficient (0.23).

4. Discussion and Result Analysis

The evaluation carried out in accordance with UNI EN ISO 13788 standard (Glaser method) presents a risk of interstitial condensation, even if limited. Two interfaces are involved: the one between the masonry and the internal plaster layer and the one between the plaster and the internal insulation. Globally, the period of condensation extends from November to March and then dries completely in spring. The maximum value of accumulated condensation occurs in the month of February and is equal to 64.7 g/m^2 . Even if it is not a particularly high value, it should be taken into account that the Glaser method states the simplifications mentioned in section 2.2, so it is appropriate to evaluate the same component with a more detailed calculation method that considers phenomena such as capillary liquid transport and hygroscopic storage properties.

The output types provided by ProCasaClima Hygrothermal are of a spatial and temporal nature, consisting of temperatures, relative humidity and moisture content for the different layers or monitor positions. In this section outputs provided by the software are analyzed, comparing the case in which the contribution of rain is taken into account (climate data generated with Meteonorm) to that in which precipitations are neglected (CTI typical meteorological years climate data).

The first result analyzed is the total moisture content accumulated in the all construction over the years. The simulation is carried out over a period of 3 years and the third-year trend is the one to be considered significant in order to assess the risk of interstitial condensation. Indeed, simulating a longer period of time, the curve of the third year would be repeated periodically in the following years.

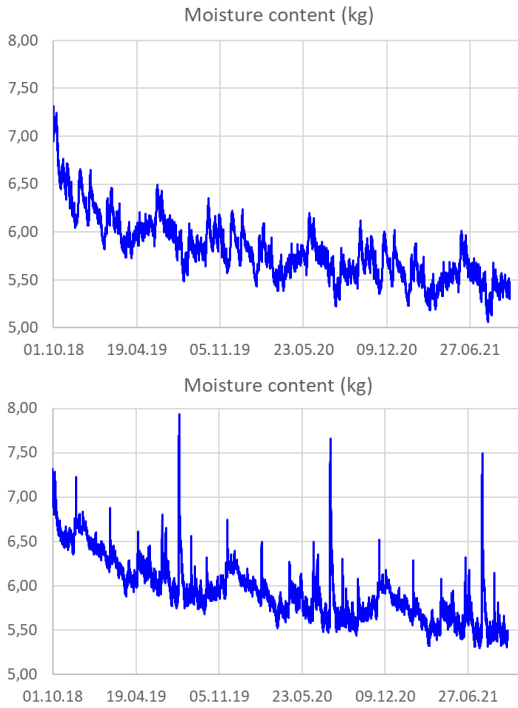


Fig. 4 – Trend of the moisture content in the constructive element during the 3 years of simulation taking into consideration in the upper graph the climate data of Bolzano provided by the CTI (no rain) and in the lower part the Meteonorm data

The results for the third year of simulation show a higher moisture content in the second case compared to the first with peaks during the rainy seasons up to 7.5 kg/m^2 of moisture in the structure while in the first case this parameter never exceeds the value of 6.2 kg/m^2 . However, the presence of driving rain introduces significant modifications of the total moisture content only for limited time frames during the most severe rain events. Far from these rain events the moisture accumulated in the construction is comparable in the two simulations. In addition, it can be observed that the overall decreasing trend of the total moisture content is the same in both simulations.

The next outputs are the spatial profiles of relative humidity in which the minimum, average and maximum values of this parameter are shown in the component for the third and last year of simulation. The interface with the highest value of relative humidity is the one between the internal plaster adjacent to the insulation and the masonry. For this reason, in this position a monitor is inserted, which makes it possible to analyze this specific part of the construction in more detail.

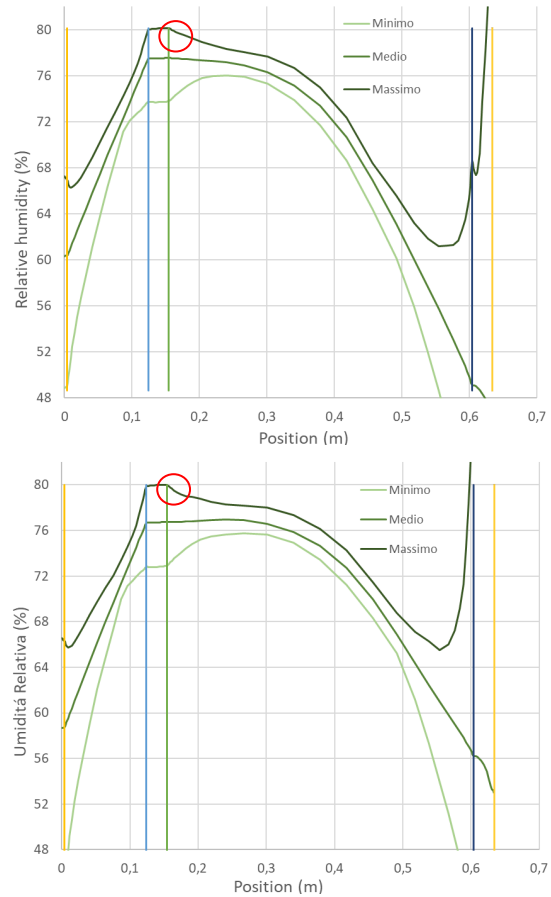


Fig. 5 – Spatial profiles representing the maximum, average and minimum value of relative humidity obtained in the last year of simulation in the element, once again comparing the situation starting with the climate data of Bolzano provided by the CTI (no rain) and in the lower part the Meteonorm data. The red circle contains the critical point of the element

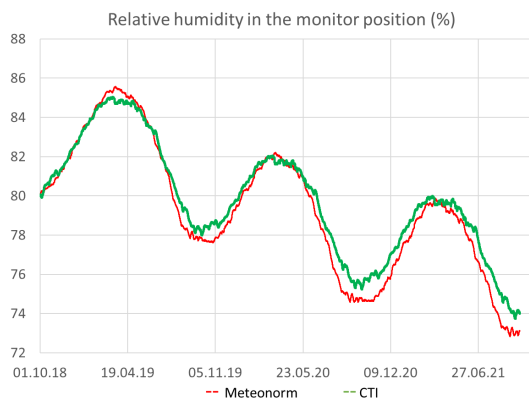


Fig. 6 – Trend of the relative humidity in the monitor position during the simulation period. The red line refers to the simulation performed with data containing rain contributes (Meteonorm). The green line refers to the simulation performed using CTI climate data

In the interface that divides the masonry from the existing interior plaster, the simulation results in a

temperature range varying from 3 °C to 30 °C and a relative humidity value from 74% to 85% in the case of external climatic data provided by the CTI and present in the climate data base of Pro-CasaClima Hygrothermal. A similar behavior is also found for the climatic data obtained from Meteonorm (that include rain) with a variation of temperatures from 2 to 31 °C and relative humidity ranging from 73% to 85%. No condensation occurs in the construction since the relative humidity is way below 95% which is considered the threshold where free water starts to be present in building materials (W.T.A. Merkblatt 6-5).

The output presented in Fig. 5 and Fig. 6 confirms that the impact of driving rain is very limited in this climate and for this construction. The effect of the driving rain is visible only for short time frames and only in the outer layers of the construction and therefore it does not lead to any modification when analyzing the formation of interstitial condensation.

5. Conclusion

This paper has presented the approach for the interstitial condensation verification implemented in the new generation of the CasaClima software in order to provide the user with simple and clear tools to meet the requirements of the CasaClima Technical Directive.

The main focus is on the new software Pro-CasaClima Hygrothermal, a tool for the hygro-thermal modelling of one-dimensional construction elements in dynamic regime. To highlight all the characteristics of the new tool, a case study has been applied, represented by an external wall in stone masonry insulated internally with 12 cm of wood fibre. Two different climatic datasets referring to the city of Bolzano are applied, one includes the effect of the driving rain and the other does not.

The risk of condensation in stationary conditions was also assessed, using the Glaser method, which was also implemented in the CasaClima software package. It can therefore be considered that three verifications were carried out globally on the same stratigraphy, comparing calculation methods and

different climatic conditions including or excluding rain. In all cases, the same interface was highlighted as the most critical, i.e. the one between the stone masonry and the existing interior plaster. The verification in stationary conditions shows a risk of formation of interstitial condensation with a maximum value of condensation accumulated in the month of February equal to 64,7 g/m². The other two simulations do not highlight this risk and do not differ with regard to the relative humidity value in the critical interface. It can be concluded that, in the specific case of the analysed wall and for the climate of Bolzano, the rain has a negligible impact on the results.

Future developments of the study will focus on the simulation of different constructions in different and more extreme climatic zones to verify the reliability of the trend recorded for the case study illustrated in this paper and located in Bolzano.

Acknowledgement

This work is carried out within the ERDF European project BuildDOP.

References

- Agenzia per l'Energia Alto Adige - CasaClima. 2018. "BuildDOP. Attività di progetto". Accessed September 13. <https://www.agenziacasaclima.it/it/progetti-di-ricerca/builddop/attivita-di-progetto-1797.html>
- Agenzia per l'Energia Alto Adige - CasaClima. 2017. *Direttiva Tecnica Nuovi edifici*.
- Benedetti, C. 2011. *Risanare l'esistente: Soluzioni per il comfort e l'efficienza energetica*. 1st ed. Bolzano: Bozen Bolzano University press.
- Ente italiano di Normazione. 2013. *Prestazione igrometrica dei componenti e degli elementi per edilizia – Temperatura superficiale interna per evitare l'umidità superficiale critica e la condensazione interstiziale – Metodi di calcolo (UNI EN ISO 13788)*.
- Ente Italiano di Normazione. 2016. *Riscaldamento e raffrescamento degli edifici - Dati climatici - Parte 1: Medie mensili per la valutazione della prestazione*

termo-energetica dell'edificio e metodi per ripartire l'irradianza solare nella frazione diretta e diffusa e per calcolare l'irradianza solare su di una superficie inclinata (UNI 10349-1).

European Committee for Standardisation. 2009. *Hygrothermal performance of buildings - Calculation and presentation of climatic data - Part 3: Calculation of a driving rain index for vertical surfaces from hourly wind and rain data (EN ISO 15927-3).*

European Committee for Standardisation. 2005. *Hygrothermal performance of buildings - Calculation and presentation of climatic data - Part 4: Hourly data for assessing the annual energy use for heating and cooling (EN ISO 15927-4).*

European Committee for Standardisation. 2007. *Building components and building elements - Thermal resistance and thermal transmittance - Calculation method (EN ISO 6946).*

European Committee for Standardisation. 2007. *Hygrothermal performance of building components*

and building elements - Assessment of moisture transfer by numerical simulation (EN 15026).

Larcher, M., A. Troi and M. Demattio. 2019. "A new tool for the hygrothermal simulation of building components: ProCasaClima Hygrothermal." *Proceedings from BS2019*, 2-4 September 2019.

Murano, G., V. Corrado and D. Dirutigliano. 2016. "The new Italian climatic data and their effect in the calculation of the energy performance of buildings." *Energy Procedia* 101, 153-160. doi: 10.1016/j.egypro.2016.11.020

W.T.A. Merkblatt 6-5. 2014. *Interior insulation according to WTA II: evaluation of internal insulation systems with numerical design methods*, Wissenschaftlich - Technische Arbeitsgemeinschaft für Bauwerkserhaltung und Denkmalpflege e.V., 2014.

Evaluation of Energy Flexibility From Residential District Cooling

Alice Mugnini – Università Politecnica delle Marche, Italy – a.mugnini@pm.univpm.it

Fabio Polonara – Università Politecnica delle Marche / Consiglio Nazionale delle Ricerche (CNR), Italy – f.polonara@univpm.it

Alessia Arteconi – Università Politecnica delle Marche, Italy – a.artecni@univpm.it

Abstract

Space cooling represents one of the fastest growing energy demands in buildings. Without any action to increase energy efficiency, this trend will be confirmed in the next decades, contributing significantly to the peak electricity demand growth. The need to increase both the energy efficiency and flexibility of the air conditioning (AC) sector is so urgent because of the strong penetration of renewable energy sources (RES) in the electricity generation mix.

District cooling (DC) systems are recognised as one of the best solutions to reach this goal. As the DC energy efficiency benefits are not questioned, the objective of this paper is to provide a qualitative evaluation of the potential of DC networks in terms of energy flexibility. By modelling a small residential neighbourhood to be satisfied with a given cooling power availability, the effect of the different DC thermal inertia levels (e.g. the pipelines network, the buildings envelope and a dedicated thermal energy storage device) is investigated by means of two qualitative flexibility indicators (the wasted cold energy and the overheating time). The analysis shows that a great potential of energy flexibility is contained in DC systems. In particular, a great thermal demand management potential can be obtained when the buildings envelope thermal inertia is activated properly.

1. Introduction

The United Nations Environment Programme (UN Environment, 2018) estimates that the energy consumption in the refrigeration, air conditioning (AC) and heat pump (HP) sectors is expected to surge by a factor of 33 by 2100. In particular, space cooling seems to be the fastest growing sector, having more than tripled, between 1990 and 2018, its energy demand (IEA, 2019). More than 1.6 billion air conditioning units are now in operation around the

world, making it the leading driver of new electricity demand in buildings (IEA, 2019).

Although the AC sector has in recent years reached high-performance levels (Carrier launched a new AC unit in early 2018 with a SEER of 12.3), the most widespread technologies among users are far from reaching such levels of performance. Moreover, a growing spread of localized AC technologies tends to increase the peak energy demand. Thus, the great impact of such energy demand on the overall electricity consumptions, combined with the increasing penetration of renewable energy sources (RES), whose generation is discontinuous and uncertain, make it necessary to plan strategies to improve the energy efficiency and flexibility of the AC sector, i.e. Demand Side Management (DSM) strategies.

District cooling (DC) is identified as a possible solution to fulfil this demand in a more efficient and flexible way (Connolly et al., 2012). The EU Energy Efficiency Directive (EED) has recognised DC systems as one of the important pillars for achieving the energy efficiency target (European Parliament, 2012), and the SETIS report identifies the DC technology as the best available technology (BAT) for the Cooling market in the EU (Garcia et al., 2012).

Many are the strengths of DC: (i) different cooling production systems can be combined (e.g. vapour compression chillers, absorption chillers, free cooling, ...) (Passerini et al., 2017), (ii) containing different levels of thermal inertia, it can make the AC sector, whose energy flexibility is low (Arteconi et al., 2019), more suitable for load management and (iii) it allows the implementation of thermal energy management strategies at district level.

There are many studies in the literature that prove the energy benefits of district heating networks, but not much can be found on DC. With this paper we

will provide a preliminary qualitative analysis of the energy flexibility that can be obtained from a small residential district cooling network. By means of a dynamic simulation model of a residential neighbourhood, the effect of the different thermal inertia levels available in the DC plant is investigated, in an attempt to maximize the use of available cooling energy while maintaining indoor thermal conditions of the users.

2. Methods

In DC systems the achievement of good environmental sustainability levels is closely linked to the flexibility of the network. The management of non-simultaneous energy demand with supply would be very difficult with low flexible systems. In this work the energy flexibility of cooling networks is defined as the ability of the overall DC to manage and uncouple its energy demand and supply.

In a DC system three levels of thermal inertia can be exploited (Vandermeulen et al., 2018): (i) the network, (ii) the buildings envelope thermal mass and (iii) the contribution of a dedicated device added to the DC plant, as a thermal energy storage (TES) system.

In this paper each of these contributions is evaluated by means of daily energy simulations (with a timestep of 10 minutes) of a hypothetical residential district realized in TRNSYS (Solar Energy Laboratory, 2012). The thermal inertia contributions are activated when there is a cooling demand but there is no more cooling availability on the supply side. Each thermal inertia contribution is activated as explained in the following.

The network contribution (i) is represented by the thermal energy carried by the fluid in the pipes. The fluid can satisfy the users requirements and warm up until a limit condition occurs (i.e. thermal balance with the ground temperature). The second thermal inertia contribution, the building inertia (ii), is activated with a control strategy on the users' temperature set-points. The building thermal mass is used as passive thermal storage with a pre-cooling of the living areas with programmed lowering of the users' indoor temperature. The last thermal inertia contribution (iii) is represented by a

sensible TES of different sizes.

In the analysis, a hypothetical daily profile of available cooling thermal power, which is assumed to be recovered from a technological process (e.g. natural gas regassification plants), is provided to the district as a cold flow rate available at a given supply temperature (further details are reported in Section 3). It is assumed that the cooling power profile is able to satisfy the average daily cold energy demand and the peak cooling power demand of the district (derived by the sizing procedure exposed in Section 3) but with a random time displacement between demand and supply curves (Fig. 1).

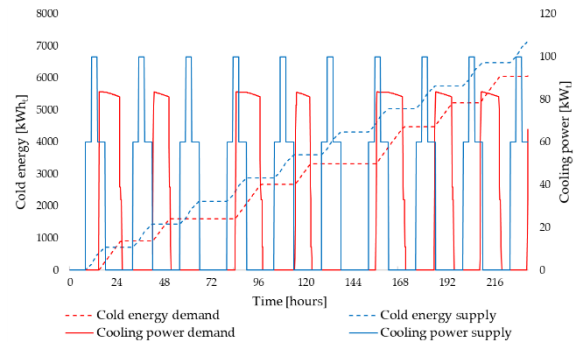


Fig. 1 – Daily cooling power and cumulative cold energy demand and supply for the residential district

Since the purpose of an optimal network management is the minimization of the wasted available cooling load, two qualitative indicators are calculated to assess the DC network flexibility potential.

1. The wasted cold energy, defined as the percentage of daily energy actually used compared to the given supply cooling energy availability.
2. The overheating time, defined as the hours per day in which the user comfort (comfort condition set at 26 °C) cannot be maintained.

These two indicators are obtained from the energy simulation results of the district described in the following section and they are calculated for the day in which the daily users cold demand is closer to the average cooling supply. In this way, the wasted cold energy is mainly due to a not effective use of the energy flexibility rather than to a difference between energy demand and supply. The results of the evaluation are shown and discussed in Section 5.

3. Case Study

In this work the DC flexibility potential of a small residential cooling network (14 users) is investigated. Users are located in Rome (41° 55' N, 12° 31' E) and modelled as modern single-family houses (SFH) (data for SFH built after 2006 derived from Tabula project (Corrado et al., 2014)). In Table 1, 2 and 3 the structure composition and the thermal properties of the materials (UNI, 2014a) of the external walls, roof and floor are reported.

Type 88 of TRNSYS is used to model each building which is composed of a single thermal zone with a simple lumped capacitance structure. Two parameters are required by Type 88 to define the building thermal inertia: the overall building loss coefficient and the building thermal capacitance.

As average value of the thermal transmittances of the different parts of the building envelope (calculated with values reported in Table 1, 2 and 3 (UNI, 2008)), the first parameter is equal to $0.38 \text{ W m}^{-2} \text{ K}^{-1}$. The second one is assumed to be 68.66 MJ/K . It is calculated according to the UNI EN ISO 13790 (UNI, 2008) considering the building structures described in Table 1, 2 and 3.

The single building is composed of two floors and has a living area of 160 m^2 (80 m^2 per floor). For each external wall, 8 % of window surface area rate is considered. Solar radiation is provided as internal gain to Type 88 according to the procedure reported in the Italian standard UNI TS 11300:1 (UNI, 2014b) with irradiation data contained in the weather file, obtained with Meteonorm V 5.0.13 (TESS, 2013). As far as the occupants' gains are concerned, 4 occupants are considered for each building and a corresponding internal gain of 110 W/person is introduced. Artificial lighting accounts for a power density of 5 W m^{-2} and it turns on if the total horizontal radiation is less than 120 W m^{-2} , while it turns off if radiation is greater than 200 W m^{-2} . The contribution of natural ventilation is introduced too, assuming air changes per hour equal to 0.5 h^{-1} .

The building cooling distribution system comprises fan coil units (FCU) modelled with Type 996. Cold water is supplied at a design temperature of 7°C , with a temperature difference between delivery and return of 5°C (Fig. 2 reports the TRNSYS model of the single user connected to the DC).

Table 1 – External Wall structure: materials listed from inside to outside with their thermal properties (density, thermal conductivity and heat capacity)

Material	s [m]	ρ [kg/m ³]	λ [W/(mK)]	c [J/(kgK)]
Internal plaster	0.02	1400	0.70	1000
Hollow bricks	0.08	800	0.40	1000
Thermal insulator	0.08	30	0.04	1250
Bricks	0.25	1800	0.72	1000
External Plaster	0.02	1800	0.90	1000

Table 2 – Roof structure: materials listed from inside to outside with their thermal properties (density, thermal conductivity and heat capacity)

Material	s [m]	ρ [kg/m ³]	λ [W/(mK)]	c [J/(kgK)]
Internal plaster	0.02	1400	0.70	1000
Bricks	0.20	1800	0.72	1000
Concrete	0.05	2400	1.91	1000
Thermal insulator	0.12	30	0.04	1250
Roof tiles	0.03	2000	1.00	800

Table 3 – Floor structure: materials listed from inside to outside with their thermal properties (density, thermal conductivity and heat capacity)

Material	s [m]	ρ [kg/m ³]	λ [W/(mK)]	c [J/(kgK)]
Floor	0.02	1700	1.47	1000
Concrete	0.05	2400	1.91	1000
Thermal insulator	0.10	30	0.04	1250
Concrete	0.10	2400	1.91	1000

For the plant sizing, the design peak cooling demand is evaluated by means of the Carrier-Pizzetti (Pizzetti, 2012) technical dynamic method. For Rome, with the outside design conditions suggested by the standard UNI/TR 10349-2 (UNI, 2016), a daily sensible thermal load of 6.3 kWt is calculated (comfort conditions are set to 26°C and 50% of relative humidity) with a latent contribution of about 2 kWt .

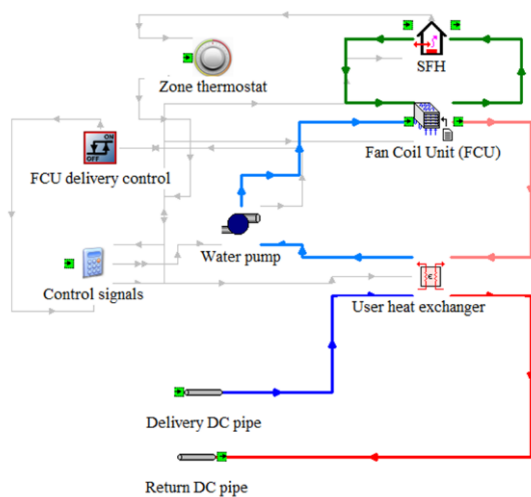


Fig. 2 – Single user model. Screen of TRNSYS Simulation Studio

The heat exchange between the FCU water circuit and the DC network is realized by means of a simple constant effectiveness heat exchanger (Type 91 in TRNSYS). It is a zero-capacitance sensible heat exchanger that requires the value of the effectiveness to calculate the actual heat exchanged compared to the maximum possible heat transfer (based on ϵ -NTU method). In our case a constant value of 30% is used for the heat exchanger effectiveness. This value is assessed so that the peak cooling power transfer among the water in the FCU circuit and the cold fluid in the DC pipes occurs at the design temperatures.

In Fig. 3 a scheme of the DC network is reported. A mixture of water and glycol is used as heat transfer fluid (Celsius SAS, 2019). In design conditions it is delivered at a temperature of $-10\text{ }^{\circ}\text{C}$, with a design temperature difference between supply and return of $5\text{ }^{\circ}\text{C}$. The pipes are modelled as underground pipes (ground temperature of $14\text{ }^{\circ}\text{C}$) with Type 31. Type 31 models the thermal behaviour of a fluid flow in a pipe using variable size segments of fluid. Thus, it is possible to take into consideration the effects of heat diffusion delay along pipes.

Referring to real pipes used for district heating and cooling systems (Aquatechnik Group, 2013), large thicknesses (26-28 cm) of thermal insulation based on polyurethane rigid foam (thermal conductivity of $0.027 \text{ W m}^{-1} \text{ K}^{-1}$) are considered to minimize the ground cooling energy losses. As far as the pipes' length is concerned, a distance between two close nodes (users) of 10 m is assumed for a total piping length of the district cooling of 200 m.

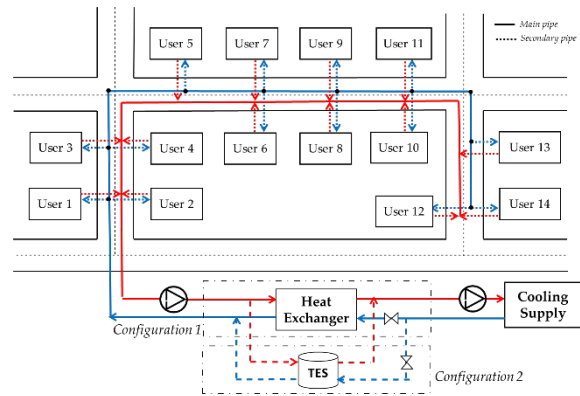


Fig. 3 – DC network plant scheme. Configuration 1: heat exchange between demand and supply realized with a heat exchanger. Configuration 2: heat exchange between cooling demand and supply realized with a TES

Two DC plant configurations, which differ on the interaction between the supply side and the demand side, are modelled (Fig. 3). In the first one (configuration 1) the heat exchange between the cooling demand and the supply is realized with a simple heat exchanger (Type 91). It is used to investigate the flexibility potential of the network and of the building envelope. The second configuration (configuration 2), by comparison, includes a TES on the demand side. It is a stratified cold-water tank, modelled through Type 4. In this case, the heat exchanger is not included and when there is cooling power availability, the heat transfer fluid enters directly into the cold side of the tank. Different sizes of the tank are tested. The sizes are varied in order to guarantee the users' design cooling load for variable periods of time. When the temperature difference between the inlet and outlet tank flow rates is below 2 °C, the TES is considered discharged.

4. Results and Discussion

In order to evaluate the energy flexibility potential of the residential DC system described in the previous section, the results of the DC daily energy simulations are analysed. The discussion focuses on a single representative summer day. It is chosen as the day in which the DC available cold energy is closer to the DC average daily cold energy demand (820 kWh_t). In this way the evaluation of the wasted cold energy is significative, since it represents the

amount of cooling demand that cannot be satisfied for the lack of flexibility of the system.

The first flexibility contribution that is investigated is that from the network. Fig. 4 reports the daily energy demand, supply and total heat exchanged by the heat exchanger on the supply side when the cooling power availability is directly combined with the cooling demand of the users (configuration 1).

As can be noticed in Fig. 4, the network flexibility contribution is low. At 7.00 pm, when there is no more cooling power availability, but users continue to ask for cooling, the network thermal inertia allows the demand to be satisfied for a very short time (about 25 minutes). The wasted cold energy is about 468 kWht (57 % of the total) with more than 4 hours of overheating (Table 4).

As far as the inertia of the buildings' envelope is concerned, a good flexibility performance can be observed. Fig. 5 shows the case in which the buildings envelope thermal inertia is activated for 1 hour (pre-cooling the buildings by lowering the internal temperature set-points by 1 °C) before the daily cooling demand occurs. In this case no overheating is measured and the wasted cold energy decreases to 337 kWht (41 %). Furthermore, different pre-cooling strategies to activate the buildings thermal mass are tested. The most interesting case can be noticed when the internal temperature set point is lowered during the early hours of the day (for 3 hours, from 8.00 am to 11.00 am) by all the users simultaneously. Indeed, during this period, there is no cooling demand, but cold supply energy is available. The wasted cold energy becomes 13 % without overheating. However, it is important to underline that this solution needs predictive control and more sophisticated management systems to be implemented.

Turning to the TES flexibility contribution evaluation, it is clear from the results that it is the means that allows a simpler and better decoupling in real-time of demand and supply. In Fig. 6, the cooling energy demand and the supply availability, when a 4500 litres cold water tank (1 hour of autonomy) is added to the demand side, is shown.

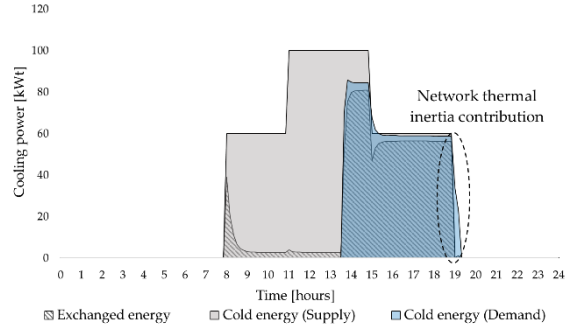


Fig. 4 – Daily cooling power demand, supply and heat exchanged in the case of DC system configuration 1. The dotted area represents the cold energy exchanged in the Heat Exchanger. The grey area is the free cooling daily availability. The blue area is the cooling energy demand of the district (all users)

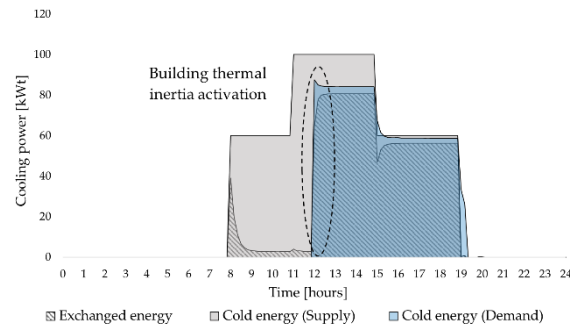


Fig. 5 – Daily cooling power demand, supply and heat exchanged in case of DC system configuration 1. Building envelope thermal inertia activation for 1 hour. The dotted area represents the cold energy exchanged in the Heat Exchanger. The grey area is the free cooling daily availability. The blue area is the cooling energy demand of the district (all users)

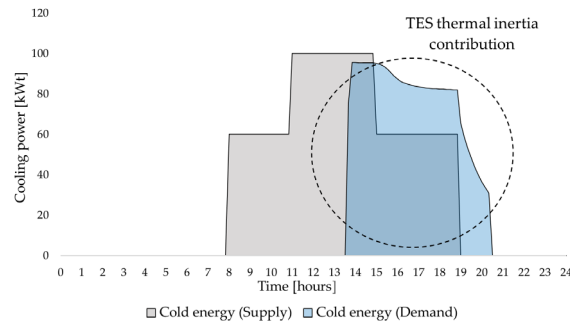


Fig. 6 – Daily cooling power demand and supply in the case of DC system configuration 2 with a 4500 litres TES (1 hour of autonomy). The grey area is the free cooling daily availability. The blue area is the cooling energy demand of the district (all users)

The thermal comfort can be maintained (overheating < 1%, Table 4) with 36% of wasted cooling energy (Table 4). Increasing the TES size, the energy flexibility performance increases as shown in Table 4. Practically without overheating (consistently less than 20 minutes), the wasted cold energy decreases, arriving at the minimum value when a

26000 litres TES (6 hours of autonomy) is used.

However, comparing the TES flexibility with the building thermal mass flexibility (Table 4), it is interesting to notice that, assuming it is possible to control the inside temperature set-points with appropriate predictive control strategies, the activation of the thermal inertia of the buildings can also guarantee good results. Indeed the building pre-cooling for 1 hour allows a similar flexibility as a 4500 litres TES, while a building pre-cooling for 3 hour offers the same flexibility as a 26000 litres TES (6 hours). It can therefore be concluded, even if a higher management complexity is required, a great flexibility potential is contained in the building envelope thermal mass. This result highlights how promoting the diffusion of smart buildings, whose energy demand could be managed by a district energy manager, can be a useful solution to optimize the energy sustainability and flexibility of the AC sector.

Table 4 – Qualitative indicators for the flexibility contributions analyzed. Wasted cold energy assessed as percentage of the average daily cold energy supply (820 kWh). Overheating hours as percentage of 24 hours

Flexibility contribution	Wasted cold energy [%]	Overheating time [%]
Network	57 %	18 %
Buildings (activation 1 hour)	41 %	0 %
Buildings (activation 3 hour)	13 %	0 %
TES 4500 litres (autonomy 1 hour)	36 %	<1 %
TES 9000 litres (autonomy 2 hours)	17 %	<1 %
TES 13000 litres (autonomy 3 hours)	19 %	<1 %
TES 26000 litres (autonomy 6 hours)	7 %	<1 %

5. Conclusion

The objective of this work is to provide a qualitative evaluation of the energy flexibility reserves that can be used in a residential district cooling system. The different thermal inertia assets of the network are investigated as flexibility providers and the main conclusions can be summarized in the following points: (i) as far as the network thermal inertia contribution is concerned, the pipelines provide a very small contribution: the cooling demand can be satisfied for less than 1 hour, when there is no cooling power availability. (ii) Assuming it is possible to control the inside temperature set-points of the users with appropriate predictive control strategies, the activation of the thermal inertia of the buildings, pre-cooling the buildings' thermal mass when the cooling supply is expected to be wasted, seems to have a great flexibility potential, comparable to the installation of a TES. (iii) A dedicated thermal inertia device is confirmed as the best means to decouple and manage in real-time energy supply and demand in the simplest way. In particular, the addition of a 26000 litres tank to the DC plant allows the best demand/supply balance with low discomfort levels.

Concluding, DC systems show benefits in terms of energy flexibility and environmental sustainability, since a good level of thermal inertia is present in the system. In this way it is possible to maintain the comfort of the users while maximizing the energy efficiency of the overall system.

In particular, the analysis highlights that investing in smart residential districts, managed by a district energy manager, could greatly increase both efficiency and flexibility of the AC sector.

Acknowledgement

This work has been supported by MIUR of Italy in the framework of PRIN2015 project: "Clean heating and cooling technologies for an energy efficient smart grid", Prot. 2015M8S2PA.

Nomenclature

AC	Air Conditioning
BAT	Best Available Technology
DC	District Cooling
DSM	Demand Side Management
EED	Energy Efficiency Directive
EU	European Union
FCU	Fan Coil Unit
HP	Heat Pump
RES	Renewable Energy Source
TES	Thermal Energy Storage

References

- Aquatechnik Group S.p.a.. 2013. *Pre-insulated piping system for the district heating & cooling (DHC)*.
- Arteconi, A., A. Mugnini, F. Polonara. 2019. "Energy flexible buildings: A methodology for rating the flexibility performance of buildings with electric heating and cooling systems." *Applied Energy*. 251, 113387. doi:<https://doi.org/10.1016/j.apenergy.2019.113387>.
- Celsius SAS, 2019. Accessed July 4. http://www.celsius-process.com/_it/strumenti.php
- Connolly, D., B. V. Mathiesen, P. A. Østergaard, B. Möller, S. Nielsen, H. Lund, U. Persson, D. Nilsson, S. Werner and D. Trier. 2012. "Heat Roadmap Europe 2050." *Study for the EU27*.
- Corrado, V., I. Ballarini and S. P. Corgnati. 2014. *Tabula Project: Building Typology Brochure-Italy*, 1-131.
- European Parliament (EU). 2012. "Directive 2012 of the European Parliament and of the council on energy efficiency (amending Directives 2009/125/EC and 2010/30/EU and repealing Directives 2004/8/EC and 2006/32/EC)." *Official Journal of the European Union*: L 315/1-L315-56.
- Garcia, N. P., K. Vatsopoulos A. K. Riekkola, L. A. P. Lopez and L. Olsen. 2012. JRC Scientific and Policy Reports: Best Available Technologies for the Heat and Cooling Market in the European Union. *SETIS Report (Strategic Energy Technologies Information System)*. Accessed July 4. <http://publications.jrc.ec.europa.eu/repository/bitstream/JRC72656/eur%2025407%20en%20-%20heat%20and%20cooling%20final%20report-%20online.pdf>
- International Energy Agency (IEA). 2019. *Cooling: Tracking Clean Energy Progress*. Accessed July 4. <https://www.iea.org/tcep/buildings/cooling/>
- Passerini, F., R. Sterling, M. Keane, K. Klobut and A. Costa. 2017. "Energy efficiency facets: Innovative district cooling systems." *The International Journal entrepreneurship and sustainability issues*. 4(3): 310-318. doi:10.9770/jesi.2017.4.3S(6)
- Pizzetti, C. 2012. *Condizionamento dell'aria e refrigerazione*, voll. 1 e 2.; Ambrosiana.
- Solar Energy Laboratory. 2012. *Trnsys 17. Using the Simulation Studio*. University Wisconsin-Madison 2, 1-29.
- TESS. 2013. *Trnsys 17- Weather Data*. Vol. 8, 1-79.
- UN Environment. 2018. *Annual Report*. Accessed July 4. <https://www.unenvironment.org/news-and-stories/story/un-environment-fights-cut-cooling-and-heating-emissions>
- UNI (Ente italiano di unificazione). 2008. *UNI EN ISO 13790. Energy performance of buildings. Calculation of energy use for space heating and cooling*.
- UNI (Ente italiano di unificazione). 2014a. *UNI/TR 11552. Opaque envelope components of buildings. Thermo-physical parameters*.
- UNI (Ente italiano di unificazione). 2014b. *UNI/TS 11300-1. Energy performance of buildings. Part 1: Evaluation of energy need for space heating and cooling*.
- UNI (Ente italiano di unificazione). 2016. *UNI/TR 10349-2. Heating and cooling of buildings - Climatic data - Part 2: Data for design load*.
- Vandermeulen, A., v. d. B. Heijde and L. Helsen. 2018. "Controlling District Heating and Cooling Networks to Unlock Flexibility: a Review." *Energy*, 151, 103-115. doi: <https://doi.org/10.1016/j.energy.2018.03.034>.

Dynamic Characterization of Thermal Bridges in Historic Balconies in Palermo

Roberta Zarcone – Université Paris-Est, France – zarconeroberta@gmail.com

Maurizio Brocato – Université Paris-Est, France – maurizio.brocato@paris-malaquais.archi.fr

Abstract

The improvement of the energy performance of a historic building entails a process of intervention that should take into account the historical, aesthetic, technical and material features. The first step of the retrofit process is an accurate knowledge of the thermal behaviour of historic building in order to preserve this heritage and reduce their impact on the environment. In terms of the thermal characterization of the construction elements of the traditional building in the Mediterranean region, the balconies constitute a disruptive element of the heat transfer by the envelope. Although there are many catalogues that collect typical actual constructive solutions with the corresponding thermal bridge values, the use of catalogues induces an error of 35% compared to physical reality. In this paper, we present a numerical method for the evaluation that takes into account the effects of thermal mass of thermal bridges in different historic balconies in the city of Palermo. We select typical construction details of balconies based on relevant literature on traditional architecture in Palermo. We present internal heat flow results and we compare them with the results of homogeneous envelope. Finally, we relate the results performed in dynamic and steady conditions.

1. Introduction

The improvement of the energy performance of a historic building entails a process of intervention that should take into account the historical, aesthetic, technical and material features (Genova, 2016).

The first step of the retrofit process is an accurate knowledge of the thermal behaviour of historic buildings in order to preserve this heritage and reduce its impact on the environment. In the last few decades, the need to reduce energy consumption in

the construction have led to finer analyses of the energy demand of buildings, taking into account time-varying parameters (Martin et al., 2011).

One of the first targets is therefore the reduction of energy losses by the envelope (Martin et al., 2012). Energy simulation software for buildings (BES) is providing an increasing number of results close to real energy demand with the implementation of dynamic analysis taking into account realistic conditions (Martin et al., 2011).

In terms of the thermal characterization of the construction elements of the traditional building in the Mediterranean region, the balconies constitute a disruptive element of the heat transfer by the envelope. In other words, they constitute thermal bridges (TB). Thermal bridges have a significant weight in the energy balance of a building (Citterio et al., 2008; Erhorn-Kluttig et al., 2009; Theodosiou et al., 2008).

A thermal bridge is a disruptive element of the heat transfer by the envelope, an area with more losses than the rest of the envelope. There might be two main causes for thermal bridge: one related to the geometry of the constructive node (presence of corners) and the other related to changes in materials or thermal resistances.

The need to facilitate the calculation of the effect of thermal bridges, simplified steady-state calculation methods have been developed in directives of different countries (Martin et al., 2011).

According to EN ISO 14683 (ISO 14683, 1999), there are different ways to calculate the TB heat transfer (Martin et al., 2012):

- Using the catalogues that collect the main technological solutions;
- Using a manual calculation for thermal bridges;
- Using a finite element method or a finite difference method.

In this paper, we present a dynamic finite element method taking into account the effects of thermal mass of TB for the evaluation of different kinds of historic balconies in the city of Palermo. We present results and we compare them with those of homogeneous envelope. Finally, we relate the results in two different types of balcony calculated in dynamic and steady conditions.

2. Method and Simulations

2.1 Method

In order to define the simulation, we consider a general transient thermal problem, on a domain Ω , governed by the equation of heat and Fourier's law:

$$\begin{cases} \rho c_p \frac{\partial T}{\partial t} + \text{div}(\underline{q}) = f \\ \underline{q} = -\lambda \text{grad}(T) \end{cases} \quad (1)$$

T is the temperature;
 q is heat flow;
 t is the time;
 f is the calorific heat capacity generated by a heat source;
 ρ is the density;
 c_p is heat capacity at constant pressure;
 λ is thermal conductivity.

The equation system (1) is complete with the initial state and the boundary conditions.

- Initial state;
- Imposed heat flow condition (adiabatic conditions in cut-off planes);
- Convective boundary conditions.

For this last condition, we consider the convective heat transfer, on a surface $\partial\Omega_c$, according to Newton's law:

$$q = h (T_{ext} - T) \quad (2)$$

T is the temperature on the convection surface $\partial\Omega_c$;
 q is convective heat flux passing through the convection surface (positive if the heat flux is directed into the system);
 h is the convective exchange coefficient;
 T_{ext} is the outside temperature.

The spatial discretization of this system of equations on a mesh of finite elements can be reduced to the following system of equations, to solve with different time steps:

$$\underline{\underline{C}} + \dot{T} + (\underline{\underline{K}} + \underline{\underline{H}})T = \underline{Q} + \underline{Q}_C \quad (3)$$

\underline{T} is temperatures at the nodes;
 \dot{T} is the time derivative of the temperatures at the nodes;
 \underline{Q} is the heat flux integrated into the nodes;
 $\underline{\underline{C}}$ is the capacity matrix;
 $\underline{\underline{K}}$ is the conductivity matrix;
 $\underline{\underline{H}}$ is the convection matrix;
 \underline{Q}_C is the term representing hTe .

2.2 Simulation in Steady-State

In steady state, an algorithm using the finite elements method is developed on Cast3m to solve Equation 3.

The boundary conditions are:

- a temperature difference of 20 K between inner and outer environments;
- a surface resistance equal to 0.13 m²K/W for inside and to 0.04 m²K/W for outside (according with ISO 6946).

2.3 Simulation in Dynamic State

In dynamic conditions, the external environmental parameters are characterized by significant variations over a period of 24 hours. To take into account these oscillations, the external temperature variations can be represented by a sinusoidal curve. According to Fig. 1, for a typical summer day in Palermo with a variation of +/- 15 K is used for the calculation.

Finally, we define heat flow conditions as a load that specifies the evolution of the convection outside temperature over time.

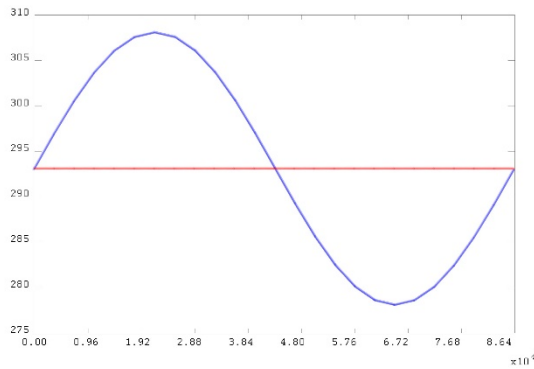


Fig. 1 – External temperature (blue curve) for a summer day and internal temperature (red curve)

2.4 Case Studies

In the Mediterranean region, climate and lifestyle have always favoured the construction of balconies, not only to provide enjoyment of the sun or protection from it, but also to have a direct relationship between the interior of the house and the street (Fatta, 2002). In spite of the differences in executive and formal qualities, there are two main types of balconies in Palermo: the first with stone consoles, which penetrate completely into the masonry. The second type is made of steel bars (Fig. 2).

Turning to the constructive solutions that will be compared, we consider two types of balconies, the first with a metallic I-beam and low thermal inertia and the other with *calcarenite* stone and high thermal inertia. We analyse the geometry, compositions and materials of these constructive solutions (Fatta, 2002). The thermal properties listed in Table 1, which define the constructive solutions of Fig. 3 are based on relevant literature on traditional architecture in Palermo (Genova, 2016).



Fig. 2 – The main types of balconies. Stone balcony (on the top), metallic balcony (on the bottom) (picture by Zarcone Roberta, 2017)

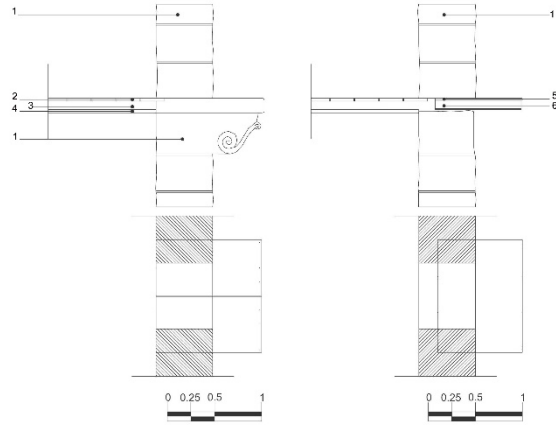


Fig. 3 – Setting up of: stone console (on the left) and metallic console (on the right)

Table 1 – Thermal properties of balcony constructive solution

Material	ρ [kg/m ³]	λ [W/mK]	c_p [J/kgK]
1. <i>Calcarenite</i> stone	1600	0.75	800
2. Floor tile	880	0.7	800
3. Mortar	1700	0.5	1000
4. Wood board	500	0.2	1600
5. Marble	2700	0.3	840
6. Metallic beam	27000	30	350

2.5 Results and Discussion

First, we compare the results of internal heat flow for each type of balcony with the homogeneous wall (HW) in dynamic state.

By plotting the results, we can note a difference between the heat flow in TB and in the HW (Fig. 4). For the balcony with metal console, as expected, the heat flow and the phase lag through the node are greater than on the homogeneous envelope. This is not always true for the balcony with a stone console. Indeed, the presence of the stone console increases the thickness and therefore the thermal inertia of the node; the effects of thermal bridge are reduced, due to the presence of a greater thickness of the stone. Table 2 shows numerical values of amplitude (absolute difference between the maximum or minimum interior heat flow from the average thermal flow) and phase lag (time that the outer thermal wave takes to penetrate inside the enclosure). Comparing these

results, it is possible to notice how the presence of the metal console reduces the phase lag compared to the homogeneous envelope by almost 5 hours. By comparison, the balcony with the stone console has a phase lag similar to that of the homogeneous envelope.

Secondly, we consider the internal heat flow in TB with standard methods, defined in steady state with an imposed temperature difference of 20 K, according with EN ISO 10211-2 (ISO 10211-2, 2007) (Fig. 5). We can note that the heat flux in the metallic balcony calculated in steady state is 1.5, higher than the stone one (Table 3). In dynamic conditions, the maximum heat flow is about 5.5 higher in the stone balcony than the metal one (Table 4). These results confirm that in the steady-state calculation, the assumptions made on the boundary conditions significantly affect the heat flow results. Not taking into account the temperature variation in time and therefore the thermal inertia of the nodes, the thermal flow gap in the two balconies is indeed considerably reduced compared to the real difference in thermal performance calculated in dynamic conditions.

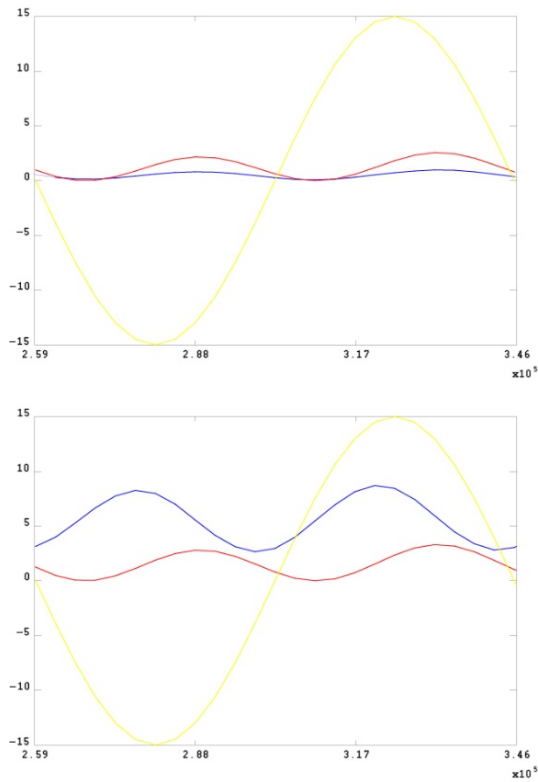


Fig. 4 – Comparison between heat flow on the node (blue curve), heat flow on the homogeneous part of the envelope (red curve) and temperature difference (yellow curve). Stone console (top) and metallic console (bottom)

Table 2 – Model's comparison of Q_{in} amplitude and phase lag in homogeneous wall

Constructive solutions	$A \left[\frac{W}{m^2} \right]$	$\varphi [h]$
1. Stone balcony	0.34	15.33
2. Metallic balcony	1.54	10.75
3. Homogeneous wall	1.25	15.55

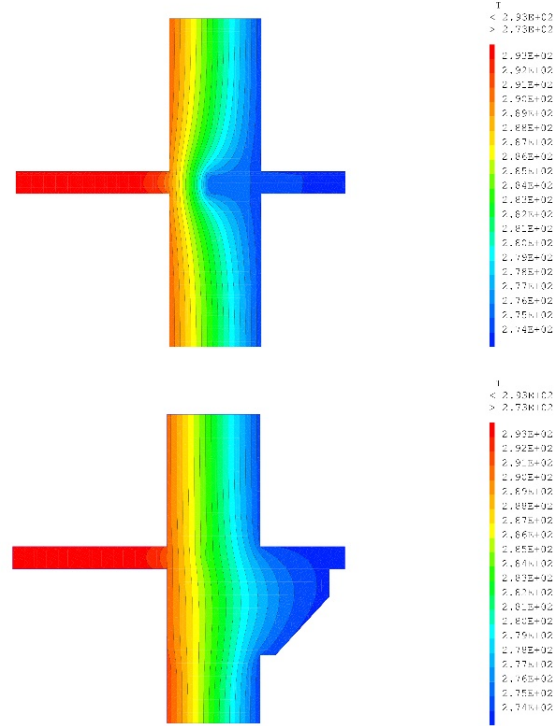


Fig. 5 – Temperature profile according to EN ISO 10211. Metal balcony (top), stone balcony (bottom)

Table 3 – Comparison between internal heat flow in steady model

Constructive solutions	$Q_{int} \left[\frac{W}{m^2} \right]$
Steady model	
1. Stone balcony	11.04
2. Metallic balcony	16.11

Table 4 – Comparison between internal heat flow in dynamic model

Constructive solutions	$Q_{int}^{max} \left[\frac{W}{m^2} \right]$
Dynamic model	
1. Stone balcony	1.57
2. Metallic balcony	8.96

3. Conclusion

In this paper, we presented the evaluation of thermal bridges on two typical traditional balconies in Palermo.

In the Mediterranean area, the use of stone in balconies leads to better thermal behaviours compared to metal balconies. In the case of the balcony with the stone console, we can disregard the influence of the presence of the balcony relative to a current part of the envelope. This means that with a calculation in steady state, it would be wrong to consider the balcony as a thermal bridge in the overall thermal balance of a building.

The dynamic calculations have shown that considering the inertia of the constructive component considerably reduces the effects of thermal bridge, by taking into account more correctly the real conditions.

The use of common catalogues can lead to 35% of errors, compared to physical reality. This error is due to different reasons: unreal dimensional and material characteristics of the node; calculation performed on steady state; boundary conditions not adapted to climatic area.

For an energetic intervention on the historic building, it seems necessary to conduct a phase of diagnosis of the constructive characteristics and its energetic behaviours with a fine approach of the thermal analysis.

References

- Citterio, M., M. Cocco and H. Erhorn-Kluttig. 2008. "Thermal bridges in the EBPB context: overview on MS approaches in regulations." *EPBD Buildings Platform*. 28-4: 64.
- Erhorn-Kluttig, H., and H. Erhorn. 2009. "Impact of thermal bridges on the energy performance of buildings." *Information Paper P148 of the EPBD Buildings Platform*.
- Fatta, G. 2002. *Il balcone nella tradizione costruttiva palermitana*. Palumbo, Palermo.
- Genova, E. 2016. *Il miglioramento energetico nel recupero degli edifici storici. Applicazione al patrimonio architettonico palermitano*. PhD thesis, Università degli Studi Di Palermo.
- ISO. 1999. *ISO 14683, Thermal Bridges in Building Construction, Linear thermal transmittance, Simplified Methods and Default Values*.
- ISO. 2007. *ISO 10211, Thermal Performance in Building Construction, Heat flows and surface temperatures, Detailed calculations*.
- Martin, K., A. Erkoreka, I. Flores, M. Odriozola and J.M. Sala. 2011. "Problems in the calculation of thermal bridges in dynamic conditions." *Energy and Buildings*. 43(2-3):529-535.
- Martin, K., C. Escudero, A. Erkoreka, I. Flores and J.M. Sala. 2012. "Equivalent wall method for dynamic characterisation of thermal bridges." *Energy and Buildings*. 55: 704-714.
- Theodosiou, T.G., and A.M. Papadopoulos. 2008. "The impact of thermal bridges on the energy demand of buildings with double brick wall constructions." *Energy and Buildings* 40 (11): 2083-2089.

Multi-Stage Multi-Level Calibration of a School Building Energy Model

Ilaria Pittana – University of Padova/Free University of Bozen-Bolzano, Italy – ilaria.pittana@phd.unipd.it

Alessandro Prada – University of Trento, Italy – alessandro.prada@unitn.it

Francesca Cappelletti – Iuav University of Venice, Italy – francesca.cappelletti@iuav.it

Andrea Gasparella – Free University of Bozen-Bolzano, Italy – andrea.gasparella@unibz.it

Abstract

The calibration of the building input parameters is the process aimed at minimizing the difference between actual and simulated performance. It is of paramount importance to implement a reliable model of an existing building, as this enables the study of its behaviour and the evaluation of improvement actions. However, when the number of unknown or uncertain parameters (such as thermo-physical properties of components and materials, infiltration and ventilation rates, internal thermal capacitances, system characteristics, etc.) is large, manual calibration methods require unacceptably long trial-and-error cycles and do not always ensure a significant improvement, as the complexity of the simulation increases. This paper explores the potential of calibrating an entire building simulation model by means of a stepwise approach and automated calibration of the model (optimization-based calibration). The approach is *multi-stage* since it considers different reference periods in order to calibrate different parameters, and *multi-level* as it starts from a room level, in order to apply the calibrated parameters to the entire building, and perform calibration to refine the estimation of the missing parameters. The described approach is shown to be effective in reducing the number of initial unknown inputs at each step as well as in validating the previous calibration results when moving to the multi-zone level. The application of the proposed calibration method to a case study aims at demonstrating the details of its implementation and its efficacy, using the available limited number of measurement sensors and short observation periods.

1. Introduction

In the last few decades, an increasing amount of research has focussed on the implementation and applications of building simulation procedures for

the definition and optimization of retrofitting strategies, for building operation or for the application of predictive methods for building system control in existing buildings (Tahmasebi and Mahdavi, 2013). Energy diagnoses of buildings require accurate simulation models to allow a reliable representation of the building and energy systems behaviour. To implementing a reliable building model, expensive and long-term monitoring of some building performance variables (e.g. energy consumption, air temperature, etc.) is generally required. A calibration process, by changing uncertain input parameters until the output matches measured values is often adopted to improve the agreement. However, when the complexity of the building is high, the number of descriptive parameters is typically too high to rely on a calibration method based on an iterative manual procedure. Such a procedure requires a time-consuming trial-and-error process (Yang et al., 2015) and potentially leads to results which are still far from reflecting the real building data. To simplify the problem, the calibration process can be divided into different steps in order to limit the number of model parameters calibrated at each step, considering their different impact in different reference periods. In addition, the monitoring phase can be less expensive by choosing a small representative portion of building to monitor and calibrate the values of some specific quantities to be extended to the whole-building model, thus leaving fewer parameters to calibrate when the whole building model is considered. This paper explores the potential of calibrating an entire building simulation model by means of a multi-stage and multi-level approach based on an automated process. The calibration was applied in a case study,

a school building located in the North-East of Italy, monitored from December 2012 to April 2014. The result is a multi-level calibration implemented through the automated discrepancy minimization of the simulated temperatures and the temperatures measured during short-term periods.

2. Methods

2.1 Calibration Method

The proposed calibration method is based on the monitoring of the air temperature of a limited part of a building, such as one or two reference rooms and all the surrounding rooms (i.e. monitored zones) in order to provide the required boundary conditions. The calibration phase is split into two main levels: (i) the calibration of a small part of the building (i.e. partial-building calibration) and (ii) the subsequent calibration of the whole-building model (i.e. whole-building calibration). To do this, a model of the reference rooms is set up to be calibrated. Inputs are not calibrated all together but the model is progressively calibrated during different periods of the year, adopting a multi-stage approach. These periods are chosen in order to avoid as much as possible any interference from different parameters and to be representative of different seasons and building operation in relation to people occupancy and the HVAC system mode (on/off). In each period, different sets of input parameters are consequently calibrated (e.g. physical characteristics of the building envelope and infiltration, heating system characteristics, shading level and ventilation rate due to occupants' presence and behaviour). The result is a multi-stage calibration of partial-building model. The calibrated parameters are extended to the whole-building model, and the remaining unknown quantities are calibrated, considering again the different periods already defined. The simulation output considered to calibrate the model is the air temperature of the reference rooms in the first level and the air temperature of all the monitored rooms in the second level. The calibration is performed according to an optimization-based approach (Tahmasebi et al., 2012; Tahmasebi and Mahdavi, 2013) aimed at the

simultaneous minimization of the differences between the simulated and monitored indoor air temperatures of the selected reference rooms in partial-building calibration and of all the monitored rooms in the whole-building calibration. In order to represent the cumulative differences between measured and simulated air temperatures, the cost function of the optimization-based calibration is defined using two statistical indexes, namely the Coefficient of Variation of the Root Mean Square Difference $CV(RMSD)$, and the regression coefficient R^2 (Equations 1 and 2):

$$CV(RMSD) = \frac{RMSD}{\bar{m}} \cdot 100 \quad (1)$$

with:

$$RMSD = \sqrt{\frac{\sum_{i=1}^n (m_i - s_i)^2}{n}} \quad (2)$$

where: m_i is the measured indoor air temperature; s_i is the simulated indoor air temperature; n is the number of the simulation time steps and \bar{m} is the measured mean temperature. The determination coefficient R^2 (Equation 3) is used for describing the proportion of the variance in measured data according with the model (Moriassi et al., 2007):

$$R^2 = \left(\frac{n \sum_i m_i \cdot s_i - \sum_i m_i \sum_i s_i}{\sqrt{(n \sum_i m_i^2 - (\sum_i m_i)^2) \cdot (n \sum_i s_i^2 - (\sum_i s_i)^2)}} \right)^2 \quad (3)$$

For calibration purposes, the minimization of the $CV(RMSD)$ was prioritised and different weighting factors were assigned to the statistical indexes. A cost function f (Equation 4) is defined for each monitored zone:

$$f = 0.7 \cdot CV(RMSD) + 0.3 \cdot (1 - R^2) \cdot (CV_{ini}(1 - R_{ini}^2)) \quad (4)$$

and the overall cost function f_{tot} is calculated as their summation. In Equation (4), CV_{ini} is the coefficient of variation of the RMSD of the initial model, and R_{ini}^2 is the coefficient of determination of the initial model. The parameters calibrated in one period are also adopted for the periods following. In the same way, those calibrated on the partial-building model (e.g. reference rooms) are extended to other similar zones where they can reliably be expected to be the same. In order to test and illustrate the above-mentioned methodology, a school building was calibrated in a case study. While the first level of this methodology (e.g. the partial calibration) has

already been implemented and described in some previous works (Penna et al., 2015a and 2015b), this paper focuses on the implementation of the second level (whole-building calibration). Two periods of the year have been considered to date, both without occupants: Period 1, characterized by no occupancy and system off, and Period 2, characterized by no occupancy inside and system on (Fig. 1). In order to test their effectiveness, the calibrated models in Period 1 and Period 2 were validated in other periods with the same characteristics, respectively unoccupied building, passive mode and unoccupied building, heating system on.

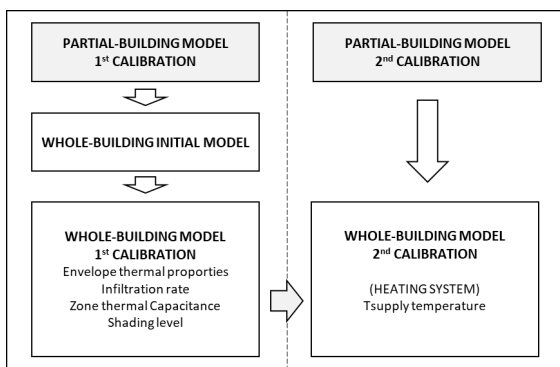


Fig. 1 – Scheme of the applied calibration procedure: from partial-building to the whole-building calibration. Period 1: non-occupied building, passive mode, Period 2: non-occupied building, system on

2.2 Monitoring of the Case Study

The building selected for testing the proposed method is a primary school located in Schio, a municipality in the North-East of Italy (Fig. 2). The building has three storeys: the basement and two upper floors, where the classrooms are. Two overlying classrooms located on the first (R1) and second floors (R2), were chosen as the reference rooms (Fig. 3) for the first level of the calibration, so the measuring instruments were located in those rooms and in the adjacent spaces (B1, B2, B3, B4, B5, B6 and B7) in order to also monitor the boundary conditions of the reference rooms. Measured air temperature was collected for 9 rooms in total (Fig. 3). The monitoring setup included data loggers to measure indoor air temperature (accuracy $\pm 0.35^{\circ}\text{C}$) and supply and return radiator pipe temperatures at small intervals (10 minutes). In the first level of this approach (Penna et al., 2015a and 2015b), i.e. the

partial-building calibration, also referred to as the ‘two-zone calibration’ in the following sections, the monitored temperatures of the spaces adjacent to the reference rooms had been used as boundary conditions. Moving to the second level, the so-called multi-zone or whole-building calibration, those boundary temperatures were used together with those of the reference rooms in the calibration process. A weather data file was created through the hourly weather recordings from the weather station of the municipality of Malo (10 km far away from school site).

2.3 Whole-Building Model Simulation and Calibration (Period 1)

The dynamic simulation model of the entire school was implemented with the simulation code TRNSYS v.17. A 3D geometrical model of the building was described using the TRNSYS plugin and Google Sketch-up v.8, while the building thermo-physical characteristics were set in TRNBuild. The model of the building was defined through the multi-zone building subroutine Type 56, using Simulation Studio, and ground temperature profile was modelled with the subroutine Type 77. A simulation time-step of 10 minutes was set.



Fig. 2 – Case study: San Benedetto Primary School (Italy)

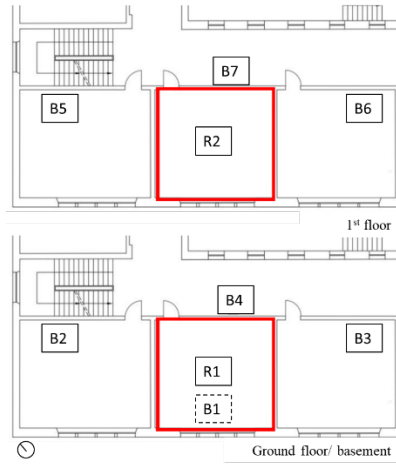


Fig. 3 – Monitoring of the case-study: sensors inside the 9 monitored rooms. Letters R and B before sensor numbering indicate respectively Reference room and Boundary room

Calibrated parameters from the partial-building (Table 1) model derived from the previous works (Penna et al., 2014, 2015a and 2015b) were used to construct the model of the entire school building. In detail, calibrated values of the thermal properties of the envelope (i), the infiltration rates (ii), the zone thermal capacitance, and the shading coefficients (iii) obtained from the two-zone calibration were extended to all the similar thermal zones (classrooms on the ground and first levels) in order to construct the whole-building multi-zone initial model (Table 1). Moreover, the multi-zone model requires a certain number of additional data that were not calibrated in the first level, namely the frame conductance and the glazing thickness of the single-glazing windows, the infiltration rate of the basement and the corridors, the thickness of the ground floor hollow slab and the shading coefficients. For all these quantities, tentative values were set in order to build the whole-building initial model (Table 3) and were calibrated further. For all calibration parameters, a variation range of $\pm 20\%$ of the initial value was determined for the calibration process. The parameters calibrated during Period 1, were extended further to the model for the calibration of the heating system operation during Period 2. The calibration was validated (Table 6) by simulating the building model in the period 20th August–1st September (unoccupied building, passive mode).

2.4 Whole-Building Model Simulation and Calibration (Period 2)

Calibration in Period 2 has the aim of calibrating the heating system characteristics and operation.

Table 1 – Input calibrated in the partial-building level for Period 1 (from 5th to 19th August) and extended to the whole building

Parameters	Calibrated value
Envelope thermal properties	
External Wall Brick	
• Conductivity λ [W/(m K)]	2.34
• Density ρ [kg/m ³]	1540
• External Solar Absorpt.	0.34
Internal Wall Brick	
• Conductivity λ [W/(m K)]	2.484
• Density ρ [kg/m ³]	2140
Internal floor Hollow Slab	
• Conductivity λ [W/(m K)]	1.8216
• Density ρ [kg/m ³]	1101
Roof Hollow Slab	
• Conductivity λ [W/(m K)]	2.54
• Density ρ [kg/m ³]	1387
• External Solar Absorpt.	0.58
Window 1	
• Frame Conductance U [W/(m ² K)]	4
• Transmittance * [W/(m ² K)]	1.57
Infiltration rate [ACH]	0.21
Air node thermal capacitance (mult. factor)*	17.55

The system was simulated through TRNSYS subroutines Types 869 and 362. The characteristics of the radiators calibrated during Period 2 in the two-zone calibration (Table 2), the heating system operation schedule and the radiators' supply temperature collected in the same period, were adopted for all radiators in the school in order to simulate the whole-building model. Two operation modes were determined: one during working days, based on a scheduled heating time and a climatic control of the water supply temperature, and a setback mode, when the building is unoccupied for a long period. During the scheduled heating time, the system is turned on from 6 am to 12 pm and a climatic adjustment of the radiator supply temperature, $T_{\text{supply},0}$, is assumed as in the following equations:

$$\text{If } T_{ext} < 10^{\circ}\text{C}; \quad T_{supply,0} = (a \cdot T_{ext} + b) \quad (5)$$

$$\text{If } T_{ext} > 10^{\circ}\text{C}; \quad T_{supply,0} = c \quad (6)$$

where T_{ext} is the outdoor air temperature and a , b , c are the multiplying coefficients of the supply temperature of the radiators. Outside the scheduled heating time, the heating system is switched on only when the indoor temperature falls below 14°C . For this period the supply temperature $T_{supply,0}$ assumes a constant value, d

$$\text{if } T_{indoor} < 14^{\circ}\text{C}; \quad T_{supply,0} = d \quad (7)$$

Moreover, a decremental factor is applied to $T_{supply,0}$ to take into account the thermal losses due to the distribution system, as follows:

$$T_{supply,1} = T_{supply,0} - \Delta T_1 \cdot (20 - T_{ext}) / (20 - T_{ext,0}) \quad (8)$$

$$T_{supply,2} = T_{supply,1} - \Delta T_2 \cdot (20 - T_{ext}) / (20 - T_{ext,0}) \quad (9)$$

where ΔT_1 and ΔT_2 are respectively the thermal loss between the basement and ground floor and between the basement and the first floor, calculated at a design external temperature ($T_{ext,0}$) equal to -10°C . Firstly, the whole-building initial model was built using the multiplying coefficients of the radiators a , b , c and d calibrated during the partial calibration while ΔT_1 and ΔT_2 were set as tentative values (Table 7). Secondly, a , b , c and d together with ΔT_1 and ΔT_2 were calibrated. For all coefficients, a variation range of $\pm 20\%$ of the tentative values was determined. The calibration was validated (Table 10) by simulating the building model in the period 4th–7th January (unoccupied building, passive mode).

3. Results

3.1 Whole-Building Initial Model and Calibrated Model (Period 1)

Table 3–6 report the standardized statistical indices RMSE, CV(RMSE) and R^2 of the partial-building calibrated model, the initial whole-building model, the whole-building calibrated model and the whole-building validated model in Period 1. Comparing the results of the whole-building initial model and those of the partial-building calibrated model, it can

be noticed that the air temperature of the two reference rooms is less accurately predicted by the whole-building model. The statistical indices of the two reference rooms (R1 and R2) are worse in the initial whole-building model: $\text{RMSD} = +31\%$, $\text{CV(RMSE)} = +29\%$, with the same $R^2 = 0.99$ for R1 and $\text{RMSD} = +22\%$, $\text{CV(RMSE)} = +20\%$, $R^2 = -1\%$ for R2). The same occurs comparing the partial-building calibrated model with the whole-building calibrated model $\text{RMSD} = +30\%$, $\text{CV(RMSE)} = +28\%$, $R^2 = -1\%$ for R1 and $\text{RMSD} = +21\%$, $\text{CV(RMSE)} = +19\%$, $R^2 = -2\%$ for R2), but globally, looking at the average values of the statistical indices calculated in all 9 monitored zones, the calibration leads to slight improvements in the initial whole-building model ($\text{RMSD}_{\text{avg}} = -11\%$, $\text{CV(RMSE)}_{\text{avg}} = -11\%$ with the same $R^2_{\text{avg}} = 0.99$). During the first validation period (from 20th August to 1st September), the statistical indices are slightly worse than those of the calibrated period ($\text{RMSD}_{\text{avg}} = +21\%$, $\text{CV(RMSE)}_{\text{avg}} = +31\%$, $R^2_{\text{avg}} = -1\%$). In Period 1 the CV(RMSE) related to the whole-building and the CV(RMSE) of the single rooms (Table 5–6) are inside the tolerance range of $\pm 30\%$ indicated by ASHRAE Guideline 14 (2002), in all the models (initial, calibrated and validated).

3.2 Whole-Building Model Simulation and Calibration (Period 2)

The standardized statistical indices RMSE, CV(RMSE) and R^2 of the partial-building calibration, the initial whole-building model, the calibrated model and the validated model in Period 2 are reported in (Table 7–10). Comparing the results of the whole-building initial model and those of the previous calibration of the partial-building model, it can be noticed that the air temperature of the two reference rooms is predicted with less accuracy by the whole-building model. The statistical indices of the two reference rooms (R1 and R2) are worse in the initial whole-building model ($\text{RMSE} = +51\%$, $\text{CV(RMSE)} = +51\%$, $R^2 = -6\%$ in the case of room R1 and $\text{RMSE} = +18\%$, $\text{CV(RMSE)} = +19\%$, $R^2 = -38\%$ for room R2). Calibration slightly improves the accuracy of the model when comparing the partial-building calibrated model with the whole-building calibrated model: it can be seen that the statistical indices of room R1 are worse in the whole-building

calibrated model (RMSD = +45 %, CV(RMSD) = +45 %, $R^2 = -9$ %), while for room R2 they are slightly better in the whole-building calibrated model (RMSD = -8 % and, CV(RMSD) = -9 %), except for R2 that is 22% worse.

Table 2 – Input calibrated during the partial-building model in Period 2: characteristics of the hydronic system set as constant in the whole-building model

Parameters	Values
Maximum Water Flow Rate [kg/h]	150
Nominal Power with $\Delta T = 60^\circ\text{C}$ [W]	2592
Radiator exponent	1.358
Radiator Thermal Capacitance [kJ/K]	134.5
Radiative Fraction (Nominal Conditions)	0.3

Table 3 – Input calibrated in the whole-building model during Period 1 (from 5th to 19th August)

Parameters	Initial value	Range value	Calibrated value
Basement floor Hollow			
• Slab thickness [m]	0.5	[0.4; 0.6]	0.4
Window (single glaze)			
• Frame Conductance U [W /m ² K]	7	[5.6; 8.4]	7
• Glaze thickness * [mm]	4	[4; 6]	4
Infiltration rate [ACH]			
• Basement (classrooms)	0.21	[0.15; 0.25]	0.21
• Ground floor (classrooms)	0.21	[0.15; 0.25]	0.21
• First floor (classrooms)	0.21	[0.15; 0.25]	0.21
• Basement (corridors)	0.21	[0.15; 0.50]	0.26
• Ground floor (corridors)	0.21	[0.15; 0.50]	0.46
• First floor (corridors)	0.21	[0.15; 0.50]	0.46
Shading coefficient			
• Basement	0.8	[0.45; 1]	0.81
• 1 st floor classroom (T18)	0.5	[0.25; 0.75]	0.43
Air node thermal capacitance (mult. factor)*			12
• Basement classrooms			
• Basement corridors	17.55	[1;20]	8.5
• Ground floor corridors			13
• First floor corridors			6.5

* The windows were evaluated as a discrete variable
 ** The Air node thermal capacitance is calculated as the product of indoor air capacitance and a multiplicative factor.

Table 4 – Statistical indices of Reference Room1 (R.1) and 2 (R.2) in Period 1 (from 5th to 19th August)

Model type	RMSD [°C]		CV(RMSD) [%]		R ²	
	R. 1	R. 2	R. 1	R. 2	R. 1	R. 2
Partial-building calibration	0.42	0.66	1.52	2.27	0.99	1.00
Whole-building initial model	0.61	0.84	2.15	2.84	0.99	0.99
Whole-building 1 st Calibration	0.60	0.83	2.12	2.80	0.98	0.98
1 st Validation	0.67	0.83	2.72	3.29	0.98	0.98

Table 5 – Statistical indices of all the 9 monitored rooms in Period 1 (from 5th to 19th August): Initial whole-building model and calibrated whole-building model

Whole-building initial model							
Thermal zone		RMSD [°C]		CV(RMSD) [%]		R ²	
		Init. Model	1 st Cal.	Init. Model	1 st Cal.	Init. Model	1 st Cal.
Basement	B1	0.47	0.27	1.81	1.05	0.96	0.97
	R1	0.61	0.60	2.15	2.12	0.99	0.98
Ground floor	B2	0.41	0.41	1.49	1.46	0.98	0.98
	B3	0.57	0.61	1.99	2.14	0.99	0.98
	B4	0.77	0.77	2.76	2.76	0.97	0.97
1 st floor	R2	0.84	0.83	2.84	2.80	0.99	0.98
	B5	0.42	0.38	1.46	1.33	0.99	0.99
	B6	0.56	0.50	1.88	1.66	0.97	0.97
	B7	0.50	0.29	1.68	0.97	0.98	0.98
	Average of the 9 zones	0.57	0.52	2.01	1.81	0.98	0.97

Table 6 – Statistical indices of all 9 monitored rooms: 1st validated model (from 20 August to 1st September)

Thermal zone		RMSD [°C]	CV(RMSD) [%]	R ²
Basement	B1	0.68	2.90	0.89
	R1	0.67	2.72	0.98
Ground floor	B2	0.29	1.21	0.99
	B3	0.91	3.65	0.98
	B4	0.44	1.80	0.97
1 st floor	R2	0.83	3.29	0.98
	B5	0.45	1.81	1.00
	B6	1.02	4.03	0.97
	B7	0.59	2.35	0.98
Average of the 9 zones		0.65	2.64	0.97

Looking at the average value of the statistical indices calculated in the 9 monitored zones, the calibration of the multiplying coefficients a , b , c , d and ΔT_1

and ΔT_2 is effective in determining the improvement of the simulation, leading to a decrease in the average statistical indices: $\text{RMSD}_{\text{avg}} = -16\%$, $\text{CV}(\text{RMSD})_{\text{avg}} = -17\%$, $\text{R}^2_{\text{avg}} = +3\%$ (Table 9). During the 2nd validation period (4th January-7th January), RMSD_{avg} and $\text{CV}(\text{RMSD})_{\text{avg}}$ are slightly worse than those of the calibrated model, while R^2_{avg} improves. Generally, looking at the whole-building performance, including in Period 2, the $\text{CV}(\text{RMSD})_{\text{avg}}$ and those of the single rooms are inside the tolerance of $\pm 30\%$ indicated by ASHRAE Guideline 14 (2002), in all the models (initial, calibrated and validated).

4. Conclusions

In this work a calibration methodology based on a “multi-stage multi-level approach” has been presented. The calibration phase is split into two main levels: (i) the calibration of a small part of the building (i.e. partial-building calibration) and (ii) the subsequent calibration of the whole-building model (i.e. whole-building calibration). The main advantages of this method are that it makes it possible (i) to extend inputs calibrated in the multi-stage calibration of a partial-building model in different periods to the entire building in order to build the whole-building initial model in the same periods and (ii) to use the measurements inside a small portion of a building during short periods (i.e.: short-term measurements in 9 rooms) to calibrate the whole building, avoiding any additional monitoring costs. This method was tested and validated in a real school building. The calibrated inputs of the partial-model of the school in Period 1 (non-occupied building, passive mode) and Period 2 (non-occupied building, heating system on) were extended to the model of the whole school building in order to build the whole-building initial model in the same periods and calibrate the residual unknown inputs. The application of this approach in this case study highlights the fact that the partial-building models calibrated in Period 1 (non-occupied building, passive mode) and Period 2 (non-occupied building, heating system on) are reliable approximations of the whole-building model in the same periods. In detail, the whole-building initial model in Period 1 was not

significantly improved by the whole-building calibration. On the one hand, this could mean that the new inputs chosen for the multi-level calibration were not relevant for improving the whole-building model; on the other hand, this could prove the effectiveness of the partial-building model calibration and the representativeness of the rooms chosen as a reference for the entire building. The results obtained in the whole-building initial model in Period 2 are somewhat worse, in terms of the statistical indices (RMSD_{avg} , $\text{CV}(\text{RMSD})_{\text{avg}}$ and R^2_{avg}), than those of the partial-building calibrated model in Period 2, and the whole-building calibration proved to be more effective than in Period 1 in enhancing the model. This reveals that the inputs chosen to calibrate in this period had an effect on enhancing the model.

Table 7 – Input calibrated during the Period 2 (from 24th December to 4th January): multiplying coefficients of the radiators’ supply temperature during Period 2

Parameters	Initial value	Range value	Calibrated value
a [-]	-1.108436	[-1.33; -0.89]	-0.908436
b [-]	60	[48; 72]	53.5
c [-]	54	[43.2; 64.8]	45
d [-]	22	[17.6; 27.192]	27
ΔT_1 [°C]	5	[3; 7]	7
ΔT_2 [°C]	10	[8; 10]	8

Table 8 – Statistical indices of Reference Room1 (R1) and 2 (R2) in Period 2 (from 24th December to 4th January)

Model type	RMSD [°C]		CV(RMSD) [%]		R ²	
	R1	R2	R1	R2	R1	R2
Partial-building calibration	0.37	0.92	2.39	6.13	0.92	0.93
Whole-building initial model	0.76	1.13	4.92	7.60	0.87	0.67
Whole-building 1st Calibration	0.43	0.81	2.76	5.48	0.87	0.68
1st Validation	0.41	0.82	2.68	5.52	0.88	0.70

A further development of this work will be to use the calibrated models in Period 1 and Period 2 in order to calibrate users’ behavior inside the building in Period 3 (occupied building, passive mode) and Period 4 (occupied building, active heating)

respectively. The inputs calibrated in the partial-building model (i.e. shading level and air change rates in the two reference rooms) will be extended to all similar thermal zones (classrooms on the ground and first levels) in order to construct the whole-building multi-zone initial model in the two periods. Following this, unknown inputs (i.e. shading level and air change rates of corridors and rooms located in the basement building) will be calibrated. Moreover, the calibration process can be extended to a further level by calibrating the whole-building model on the energy consumption for heating.

Table 9 – Statistical indices of all 9 monitored rooms in Period 2 (from 24th December to 4th January): Initial model vs calibrated model

Whole-building initial model							
Thermal zone		RMSD [°C]		CV(RMSD) [%]		R ²	
		Init. Model	1 st Cal.	Init. Model	1 st Cal.	Init. Model	1 st Cal.
Basement	B1	1.26	1.29	7.89	8.09	0.66	0.53
	R1	0.76	0.43	4.92	2.76	0.87	0.88
Ground floor	B2	1.05	0.83	7.31	5.77	0.76	0.69
	B3	1.07	0.75	6.94	4.85	0.84	0.84
	B4	1.06	0.92	6.92	5.98	0.64	0.60
	R2						
1 st floor	B5	1.13	0.81	7.60	5.48	0.67	0.68
	B6	1.30	1.16	8.73	7.78	0.56	0.49
	B7	1.34	1.05	9.36	7.34	0.68	0.65
Average of the 9 zones		1.17	0.97	7.77	6.47	0.61	0.58

Table 10 – Statistical indices of all the 9 monitored rooms: 2nd validated model (from 4th January to 7th January)

Thermal zone		RMSD [°C]		CV(RMSD) [%]		R ²
Basement	B1	0.45		2.96		0.92
	R1					
Ground floor	B2	0.65		4.40		0.90
	B3	1.21		8.80		0.89
	B4	1.02		6.92		0.92
1 st floor	R2	0.59		3.93		0.87
	B5					
	B6	0.72		4.96		0.88
	B7	1.16		8.50		0.66
Average of the 9 zones		1.02		7.11		0.84

Acknowledgement

This study has been funded by the project “Klimahouse and Energy Production” in the framework of the programmatic-financial agreement with the Autonomous Province of Bozen-Bolzano of Research Capacity Building.

References

- ASHRAE. 2002. *Guideline 14–2002, Measurement of Energy and Demand Savings*. American Society of Heating, Ventilating, and Air Conditioning Engineers. Atlanta, Georgia: ASHRAE.
- Moriasi D. N., D. N. Arnold, M. W. Van Liew, R. L. Bingner, R. D. Harmel and T. L. Veith. 2007. “Model evaluation guidelines for systematic quantification of accuracy in watershed simulations.” *Transactions of the ASABE* 50(3), 885–900.
- Penna, P., F. Cappelletti, A. Gasparella, F. Tahmasebi and A. Mahdavi. 2015a. “Multi-stage calibration of the simulation model of a school building through short-term monitoring.” *Journal of Information Technology in Construction* 20: 132–145.
- Penna, P., A. Prada, F. Cappelletti and A. Gasparella. 2015b. “Multi-objective optimization of Energy Efficiency Measures in existing buildings.” *Journal of information technology in construction* 20: 132–145. doi:10.1016/j.enbuild.2014.11.003.
- Yang Z., and B. Becerik-Gerber. 2015. “A model calibration framework for simultaneous multi-level building energy simulation.” *Applied Energy* 149: 415–431. doi:10.1016/j.apenergy.2015.03.048.
- Tahmasebi, F., R. Zach, M. Schuß and A. Mahdavi. 2012. “Simulation Model Calibration: An Optimization-Based Approach”. *Fourth German-Austrian IBPSA Conference*.
- Tahmasebi, F., and A. Mahdavi. 2013. “A Two-Stage Simulation Model Calibration Approach To Virtual Sensors For Building Performance Data.” *Proceedings of BS2013: 13th Conference of International Building Performance Simulation Association*.

Dynamic Modelling and Control System Optimization of a Reversible Air-to-Water Heat Pump with Heat Recovery for Domestic Hot Water Production

Matteo Dongellini – University of Bologna, Italy – matteo.dongellini@unibo.it

Luigi Belmonte – University of Bologna, Italy – luigi.belmonte@studio.unibo.it

Gian Luca Morini – University of Bologna, Italy – gianluca.morini3@unibo.it

Abstract

Even if the energy demand for space heating/cooling of near zero energy buildings (nZEBs) is continuously decreasing due to the improvement of the insulation level of building envelope components, the energy requirement for domestic hot water (DHW) production cannot be similarly reduced: for this reason, the weight of DHW energy consumptions on the overall building energy performance is becoming more and more significant for nZEBs. A reversible heat pump with recovery of the condensation heat (HPHR) is one way to obtain significant energy savings and respond to this increasing influence of DHW production with respect to the energy demand in residential buildings, since this kind of device is able to simultaneously satisfy the energy needs for DHW production and space cooling during the summer season. In order to improve the energy efficiency of a HPHR, the heat recovery operating mode should be maximized during the cooling season: for this reason, a detailed analysis of the heat pump control system is needed. Heat pump performance strongly depends on the values of control parameters, which are influenced by the system working conditions, such as DHW draw-off profile, building heating/cooling load and thermal storage size. In this paper, a detailed analysis of the annual energy performance of a HPHR system is obtained by means of TRNSYS 17: several simulations are carried out by varying the control algorithm, in order to achieve the best seasonal performance factor of the system. The results reported present a series of rules for the best setting of the heat pump control system parameters to HVAC designers and heat pump manufacturers and highlight how significant energy savings can be achieved with the adoption of a HPHR with respect to traditional systems based on a gas boiler or a conventional heat pump without heat recovery.

1. Introduction

In recent years, the efforts of public and private bodies have aimed to reduce the energy demand of buildings: recent studies have demonstrated that, worldwide, residential and commercial structures are responsible for about 40% of the gross energy production (Krzaczek et al., 2019). Furthermore, in the European Union (EU) the residential sector alone is responsible for about the 25% of the total energy demand (Karytsas et al., 2019). For these reasons and due to increasingly negative environmental impacts, new constructions in the EU are required to comply with the near Zero Energy Building (nZEB) requirements by 2020 (EU, 2010). If the residential sector is considered, space heating (SH) accounts for the majority of the overall energy demand, followed by space cooling (SC), cooking, lighting and Domestic Hot Water (DHW) production (Krzaczek et al., 2019); when only the heating energy consumption is taken into account, DHW preparation represented approximately 19% of the total energy need of European residential buildings in 2013 (Kitzberger et al., 2019). Furthermore, the relevance of DHW production is continuously increasing in nZEBs: as improvements in building thermal insulation are made, so space heating/cooling energy demand is reduced, but hot water demand cannot be similarly decreased. For this reason, the contribution of DHW energy consumption may reach 50% of the total energy need of this kind of buildings (Bertrand et al., 2017).

Heat pumps are considered a suitable solution to decrease the primary energy consumption of buildings: these devices represent an effective alternative to traditional systems, such as boilers and

electric resistances, for DHW production and SH. Furthermore, reversible units are able to provide all the energy services in a building with a single device. In addition, in the residential sector air-source heat pumps (ASHPs) are the most widespread solution, due to the huge availability of heat sources, considerable efficiency and low installation costs (Wu et al., 2018).

Different solutions are currently proposed by heat pump manufacturers for DHW preparation. In order to prepare high temperature DHW in centralized systems, state-of-the-art heat pump systems are typically equipped with a desuperheater, which is an additional heat exchanger installed between the compressor and the condenser of the unit (Hengel et al., 2016). Generally, with this kind of device the simultaneous production of hot water for SH at intermediate temperatures and for DHW at high temperatures is possible. A promising technology for DHW production is represented by CO₂ heat pumps (Trinchieri et al., 2016): CO₂ is a non-flammable, non-toxic fluid characterized by a null GWP, whose thermo-physical properties allow the achievement of high energy efficiency.

In addition, during a significant part of the summer season heating and cooling energy are simultaneously needed for DHW production and SC, respectively. Unfortunately, traditional reversible ASHPs reject condensation heat to the external heat sink (i.e. the outdoor air) during the cooling operating mode; this waste thermal energy could be recovered and used to prepare DHW when this dual energy demand is requested at the same time. In this paper, the dynamic model of a multi-function heat pump with recovery of the condensation heat (HPHR), able to simultaneously satisfy DHW production and cooling needs during summer, is presented. Several Authors (Byrne et al., 2009; Ghoubali et al., 2014; Naldi et al., 2015) have focussed their research on this kind of units and results have shown that significant energy savings can be achieved with respect to traditional heat pumps. In this work, the model of a reversible air-to-water HPHR, characterized by three heat exchangers (i.e. a fin-and-tube coil and two plate heat exchangers for refrigerant/air and refrigerant/water thermal exchange, respectively), is described. The model of the unit has been developed by means of

the software TRNSYS 17, and with the cooperation of a heat pump manufacturer, which provided the performance data for the possible operating modes of the unit. Several simulations were carried out by varying the control algorithm of the HPHR in order to evaluate the optimal control management of the heat pump and to achieve the best seasonal energy performance.

2. Methodology

2.1 Simulation Layout

The dynamic model of the HPHR was coupled to a reference residential building. Both the heat pump system and the building was set up within TRNSYS environment, with a holistic approach. The reference construction considered in this paper is a well-insulated, detached building described in Dongellini et al. (2019); a 3D view of the house is shown in Fig. 1.

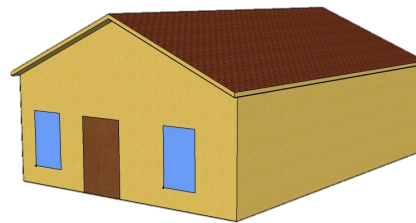


Fig. 1 – 3D view of the reference building

It is important to highlight that in this work the building heating/cooling load was modified with respect to that obtained in the work of Dongellini et al. (2019). The detached house was located in Palermo (lat. 38°6' North, long. 13°20' East, South of Italy); the thermal insulation of the building envelope had also increased: for example, the U-value of external walls had decreased to 0.34 W/m²K. In accordance with current Italian law, the heating period was fixed to four months (December 1st – March 31st), while the cooling period to six months (May 1st – October 31st). Furthermore, the energy demand for DHW production was evaluated in accordance with Italian Standard UNI/TS 11300-2 (UNI, 2014): according to the methodology reported by this Standard for the residential sector, the daily hot water need of the

reference building is equal to almost 120 litres. Furthermore, the hourly profile introduced by Standard UNI/TS 11300-4 (UNI, 2012) was used to define the hot water draw-off request: this is characterized by a smooth profile, with a maximum DHW draw-off equal to 16 l/h.

The whole dynamic model set up in this work is reported in Fig. 2. The behaviour of the heating system components was simulated by means of standard and TESS libraries elements. The storage tank for DHW production is a stratified vertical cylinder, divided into 5 vertical nodes with the same volume, characterized by a couple of inlet/outlet ports and an immersed coiled heat exchanger (Type 534 with HX). The tank is filled with technical water, heated by the heat pump, while the freshwater flows within the internal heat exchanger. Furthermore, the loss coefficient of the storage was set to 0.38 W/m²K.

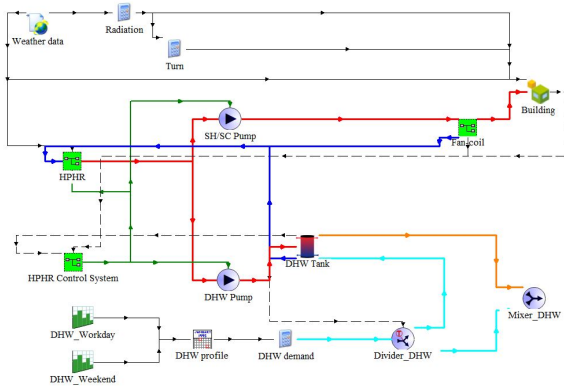


Fig. 2 – Layout of the developed TRNSYS model

Heating/cooling energy is delivered to the building by means of two-pipe three-speed fan-coils; four units were installed in the flat, one for each room, and they were sized on the basis of the zone cooling peak load. As will be seen later, the building cooling load is significantly larger than the heating required load. Fan-coil performance data at full and at partial load were provided by the manufacturer and were included within the External File schedule of Type 996.

2.2 HPHR Modelling

As reported in the Introduction of this paper, a HPHR is a device able to provide heating and cooling energy at the same time. In Fig. 3 the logical scheme of an air-to-water HPHR is shown.

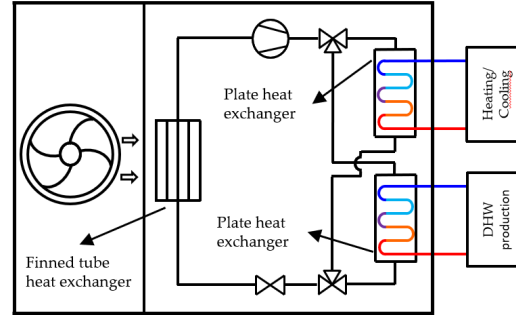


Fig. 3 – Logical scheme of an air-to-water HPHR

More specifically, a HPHR has three possible operating modes: heating mode (for SH or DHW production only), cooling mode (for SC only) and heat recovery mode (DHW production and SC at the same time). It is evident that this kind of device is equipped with three heat exchangers and a pair of three-way valves: depending on the unit operating mode the refrigerant fluid circuit varies and the heat pump performance changes. The heat exchange between the refrigerant and the external air occurs within the finned-tube coil, which operates as evaporator and condenser during heating and cooling working mode, respectively, while it is bypassed in heat recovery mode. On the other hand, the load side plate heat exchanger has the function producing hot (cold) water for space heating (cooling): for this reason, it is the condenser of the unit when only SH is needed and the evaporator during cooling and on heat recovery mode. Finally, the plate heat exchanger dedicated to DHW production is active only when hot water for sanitary use is needed (with or without a simultaneous request of SC): this element always operates as a condenser.

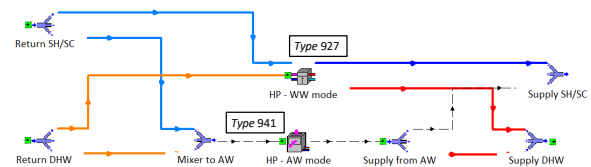


Fig. 4 – Dynamic model of the HPHR set up in TRNSYS

A Type which simulates the behaviour of a HPHR is not included within TRNSYS libraries. Consequently, an innovative subroutine was developed, in order to evaluate the performance of this kind of device. Generally, the HPHR considered in this work has two different operating modes: when heat recovery mode is possible, both the plate heat exchangers are active and the heat pump operates as a water-to-water unit; by comparison, during working modes in which only SH, SC and DHW production are needed the heat pump operates as a traditional air-to-water device. For this reason, the performance of the HPHR is calculated by means of standard Types 927 and 941 for water-to-water and air-to-water operating modes, respectively. In Fig. 4, the TRNSYS model of the HPHR developed in this work is shown: the heat pump control system, described in the following Section, selects the active Type based on the building loads.

2.3 Management of the System

The HPHR operating mode is defined by the management system according to different signals, depending on the season and the building loads.

In accordance with the standard heating/cooling periods reported in Section 2.1, SH mode is allowed only during the heating season, SC and heat recovery can be activated only during the cooling period while DHW production is potentially usable for the whole year.

On the other hand, the activation of the heat pump also depends on the effective load of the building. SH and SC working modes are, of course, activated when the conditioned zones need heating and cooling energy, respectively. In this case, the monitored variable used by the control system is the return water temperature $T_{w,in}$ (i.e. the temperature of the water entering the unit) and not the indoor air temperature directly, which is instead used by the fan-coil management system. The algorithm defined for SH is shown in Fig. 5(a); since the HPHR considered in this work is a single-stage device, the compressor has only two possible states: device switched on or switched off. For this reason, an on-off logic, characterized by a hysteresis cycle, is adopted: if the unit is switched off, it is activated when $T_{w,in}$ becomes lower than the

threshold value $T_{ON,SH}$. The heat pump is then switched off when $T_{w,in}$ rises above the other threshold value $T_{OFF,SH}$.

The management approach for SC, represented in Fig. 5(b), is based on a similar algorithm: in this case, if the HPHR is active it is switched off when $T_{w,in}$ is lower than the threshold value $T_{OFF,SC}$ and then it is reactivated as soon as $T_{w,in}$ becomes higher than the parameter $T_{ON,SC}$.

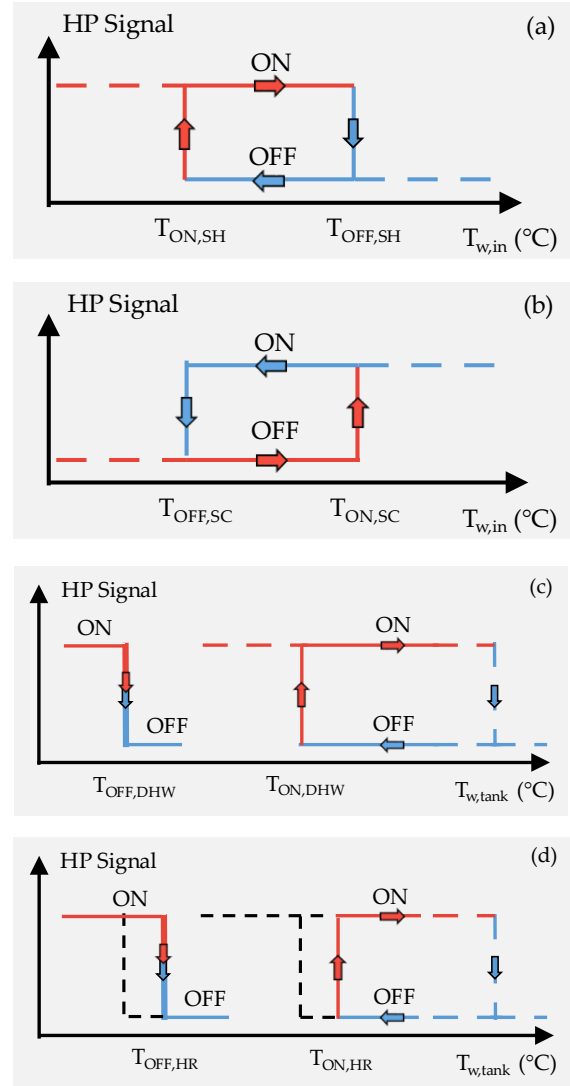


Fig. 5 – HPHR control algorithms for space heating (a), space cooling (b), DHW production (c), heat recovery (d)

In Fig. 5(c) the control logic for DHW production working mode is reported. The heat pump is controlled by monitoring the temperature of water within the storage tank at different heights ($T_{w,tank}$). More specifically, when the water temperature in

the upper part of the tank falls below the threshold $T_{ON,DHW}$ following a hot water draw-off, the HPHR is activated in DHW production mode, even if thermal energy for SH is required. This operating mode is active until the tank has completely heated up: when the temperature in the lower part of the storage exceeds the threshold value $T_{OFF,DHW}$, DHW production mode is disabled. It is important to highlight that the values of both parameters should be set to ensure a DHW temperature flowing out of the tank of above 40°C.

As discussed in previous sections, heat recovery mode is activated only following a simultaneous request for SC and DHW production. For this reason, HPHR operates in this mode if both services are needed (i.e. if $T_{w,in}$ is higher than $T_{ON,SC}$ and the DHW tank temperature decreases following a hot water draw-off); as will be further discussed in the following section, in order to extend the duration of heat recovery mode different values of the threshold parameters for the activation/deactivation of the tank heating (i.e. $T_{ON,DHW}$ and $T_{OFF,DHW}$) should be defined if cooling energy is required (with heat recovery potentially possible) or not. As shown in Fig. 5(d), both the threshold values are increased and are identified as $T_{ON,HR}$ and $T_{OFF,HR}$ during heat recovery mode. Different values in the threshold parameters for the management of DHW production and heat recovery modes were tested in order to investigate the potential decrease of the overall energy consumptions for SH, SC and DHW production along the year. In Section 3.1 the optimization of the HPHR control algorithm will be discussed and the optimal values of the unit control system will be shown.

2.4 HVAC system Characterization

The heat pump performance data for each possible operating mode (i.e. heating mode, cooling mode and heat recovery mode) were obtained from the unit technical datasheet and have been imported within TRNSYS through external files. It is important to stress that these data have been validated by the heat pump manufacturer by means of experimental measures conducted in a climatic chamber. In Fig. 6, a subset of the HPHR charac-

teristic curves is reported: more specifically, in Fig. 6(a) and Fig. 6(b) the unit performance data (i.e. heating/cooling capacity and COP/EER) are shown for different values of external air temperature and with the inlet water temperature fixed to 40°C for SH mode (Fig. 6(a)) and to 12°C for SC mode (Fig. 6(b)). The heat pump performance data during heat recovery mode are reported in Fig. 6(c): EER , heating and cooling capacity are shown as a function of the return water temperature.

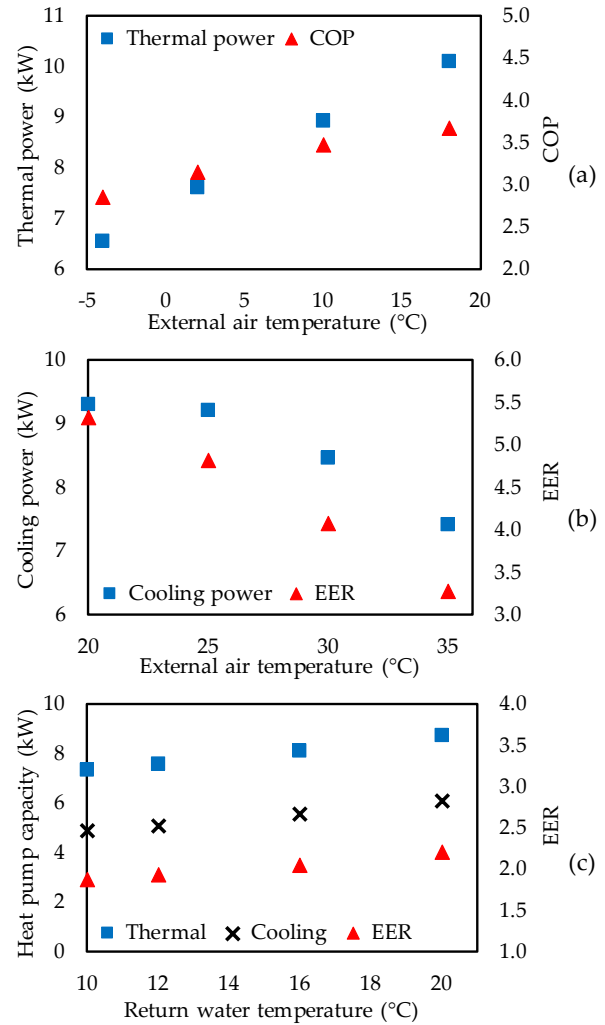


Fig. 6 – HPHR performance data for heating mode (a), cooling mode (b) and heat recovery mode (c)

3. Results and Discussion

The results of the simulations mainly relate to the seasonal energy performance of the HPHR during the cooling season and the percentage of DHW production energy need covered during heat

recovery mode: these results are reported in Table 1 for different settings of the heat pump control system.

3.1 Optimization of HPHR Control Logic

In a first series of simulations, the optimal values of the parameters introduced in Section 2 for the management of DHW production were assessed. Different settings of the control algorithm were considered: in Table 1 the main results obtained with the tested combinations ($T_{OFF,DHW} - T_{ON,DHW} / T_{OFF,HR} - T_{ON,HR}$) are reported. More specifically, the threshold values for the activation and deactivation of DHW production mode $T_{ON,DHW}$ and $T_{OFF,DHW}$ were varied within the range [35°C-42°C] and [43°C-45°C], respectively; on the other hand, the threshold values for heat recovery mode (i.e. $T_{ON,HR}$ and $T_{OFF,HR}$) were ranged between 40°C and 47°C and 43°C and 50°C, respectively.

With reference to the obtained results, the best setting of control system parameters ($T_{OFF,DHW}-T_{ON,DHW} / T_{OFF,HR}-T_{ON,HR}$) is (42°C-45°C / 47°C-50°C): for this combination, the Seasonal Performance Factor (SPF) of the heat pump during the summer season, which takes into account both SC and DHW production, increases by approximately 9% when compared to the reference case, characterized by no differentiation between the control algorithms for DHW and HR modes. This is a consequence of a twofold effect: first, the heat pump performance for SC slightly decreases, with a reduction of SPF of about 3%, while the heat pump seasonal performance for DHW production is enhanced by approximately 48%. In HR mode, the heat pump cooling performance is reduced with respect to SC mode, due to higher condensation temperatures, but free thermal energy is obtained for DHW preparation.

Table 1 – Energy performance of the HPHR system during the summer season for different settings of the management system

Control system setting ($T_{OFF,DHW} - T_{ON,DHW} / T_{OFF,HR} - T_{ON,HR}$)	Building service	Delivered energy (kWh)	Electric energy input (kWh)	Primary energy demand (kWh)	SPF	HR mode / DHW production (%)
40°C-43°C / 40°C-43°C	SC	3246	762	1905	4.25	0.18
	DHW	1525	388	969	3.93	
	Total	4771	1149	2874	4.15	
35°C-43°C / 40°C-43°C	SC	327	762	1906	4.25	0.05
	DHW	1517	368	918	4.13	
	Total	4764	1130	2824	4.23	
40°C-43°C / 42°C-45°C	SC	3246	762	1906	4.25	0.05
	DHW	1525	388	970	3.93	
	Total	4771	1150	2876	4.15	
40°C-43°C / 47°C-50°C	SC	3246	782	1955	4.15	24.85
	DHW	1530	295	739	5.18	
	Total	4775	1077	2694	4.43	
42°C-45°C / 47°C-50°C	SC	3247	793	1983	4.10	30.13
	DHW	1532	263	658	5.83	
	Total	4779	1056	2641	4.53	

Furthermore, it has been demonstrated that when SC is needed and, thus, HR mode is possible, the best energy performance can be achieved by increasing both threshold values $T_{ON,HR}$ and $T_{OFF,HR}$, in order to extend the duration of HR mode. With the reference configuration, the contribution of HR mode for DHW production energy need is negligible (lower than 1%, see Table 1); in comparison, by optimizing the system management almost 30% of the energy demand linked to hot water preparation is covered during HR working mode, with significant energy savings.

Finally, the annual energy performance of the HPHR for all building services (i.e. SH, SC and DHW production) was calculated and compared to that of traditional systems based on: i. a condensing gas boiler, for SH and DHW production, and an air-to-water chiller for SC; ii. a reversible air-to-water heat pump without condensation heat recovery. It is important to highlight that the seasonal generating efficiency of the boiler, η_s was fixed at 1.04, while chiller and heat pump were characterized by the same energy performance of the HPHR during heating, cooling and DHW production modes. Furthermore, the optimal setting of the HPHR control parameters, defined in the previous part of this paper, was considered.

In Table 2 the annual energy performance of the studied systems is shown: the seasonal efficiency η_s , the heating/cooling energy delivered to the building (E_{del}), the energy absorbed by the generating devices (E_{abs}) and the corresponding primary energy need (E_{pr}) are reported.

Results show that significant energy savings can be obtained with the adoption of a HPHR: the annual performance factor for this kind of system is 38% and 11% greater with respect to traditional systems based on two generators (i.e. a boiler and a chiller) or a heat pump without heat recovery, respectively. Moreover, more interesting results can be obtained if only the energy performance of the system for SC and DHW are taken into account: by using a HPHR the primary energy need linked to these services is reduced by 26%, if compared to the first system, and by 10% if compared to a traditional reversible heat pump. Finally, the results obtained in this work highlight that the primary energy demand for DHW production can

be dramatically reduced with the adoption of a HPHR characterized by optimized control management: in this case, the energy demand for DHW preparation is lowered by up to 70% and 46% with respect to the gas boiler and the conventional heat pump, respectively.

Table 2 – Annual energy performance for the simulated cases

Case	Service	E_{del} (kWh)	E_{abs} (kWh)	E_{pr} (kWh)	η_s
Boiler + chiller	SH	1677	1618	1637	1.04
	DHW	1741	1681	1693	1.04
	SC	4201	969	2397	1.79
	Total	7657	/	5727	1.36
HP without HR	SH	1676	487	1198	1.42
	DHW	1726	401	983	1.78
	SC	4201	969	2397	1.79
	Total	7641	1857	4577	1.69
HPHR	SH	1612	469	1154	1.42
	DHW	929	221	540	1.74
	SC	3650	823	2036	1.83
	HR (SC)	644	181	454	3.24
	HR (DHW)	825			
	Total	7660	1693	4185	1.87

4. Conclusion

In this work the dynamic model of a reversible air-to-water heat pump with condensation heat recovery (HPHR), able to simultaneously satisfy space cooling and DHW production needs, was developed by means of TRNSYS. Since this kind of heat pump is not included within the standard library of the software, an innovative dynamic model, able to calculate the energy performance of the unit in correspondence of all the possible working modes, was developed. The numerical results confirm that in order to increase the energy performance of the system, the period in which the heat pump operates in heat recovery mode (i.e. with the simultaneous production of DHW and cooling energy) must be expanded by optimizing the unit control management, which will vary according to the heat pump working mode (heating, cooling or heat recovery). The unit operating mode is defined by the temperature of the water stored in the stratified DHW tank,

measured at different heights: more specifically, when the water temperature in the upper part of the storage drops below a threshold value, the heat pump must be activated to charge the DHW tank; furthermore, the unit is deactivated when the temperature in the lower part of the storage exceeds a second threshold value. In order to extend the duration of heat recovery mode, the optimal values of the above-mentioned threshold temperatures were assessed and results show that these values depend on the HPHR working mode: when space cooling is needed and heat recovery mode is possible, both values should be increased to achieve the best energy performance. Moreover, the results obtained highlight how the annual energy performance of a HPHR is much higher (by up to 38%) with respect to those of traditional systems based on a gas boiler or a conventional heat pump without heat recovery, due to significant energy savings linked to heat recovery mode during the summer season.

The results outlined in this paper suggest a series of rules for the optimal setting of the heat pump control algorithm to HVAC designers and heat pump manufacturers: it has been demonstrated that by optimizing the management of the heat pump it becomes possible to extend the duration of the heat recovery mode of these kinds of units, thus increasing the overall energy performance of the system.

References

- Bertrand, A., A. Mastrucci, N. Schuler, R. Aggoune and F. Maréchal. 2017. "Characterisation of domestic hot water end-uses for integrated urban thermal energy assessment and optimisation". *Applied Energy* 186: 152-166. doi: 10.1016/j.apenergy.2016.02.107.
- Byrne, P., J. Miriel and Y. Lenat. 2009. "Design and simulation of a heat pump for simultaneous heating and cooling using HFC or CO₂ as a working fluid." *International Journal of Refrigeration* 32: 1711-1723. doi: 10.1016/j.ijrefrig.2009.05.008.
- Dongellini, M., A. Piazzzi, F. De Biagi and G. L. Morini. 2019. "The modelling of reverse defrosting cycles of air-to-water heat pumps with TRNSYS." *E3S Web of Conferences* 111: 01063. doi: 10.1051/e3sconf/201911101063.
- European Parliament. 2010. *Directive 2010/31/EC of the European Parliament and of the Council of 19 May 2010 on the energy performance of buildings*. Brussels, Belgium.
- Ghoubali, R., P. Byrne, J. Miriel and F. Bazantay. 2014. "Simulation study of a heat pump for simultaneous heating and cooling coupled to buildings." *Energy and Buildings* 72: 141-149. doi: 10.1016/j.enbuild.2013.12.047.
- Hengel, F., A. Heinz and R. Rieberer. 2016. "Performance analysis of a heat pump with desuperheater for residential buildings using different control and implementation strategies." *Applied Thermal Engineering* 105: 256-265. doi: 10.1016/j.applthermaleng.2016.05.110.
- Karytsas, S., O. Polyzou and C. Karytsas. 2019. "Factors affecting willingness to adopt and willingness to pay for a residential hybrid system that provides heating/cooling and domestic hot water." *Renewable Energy* 142: 591-603. doi: 10.1016/j.renene.2019.04.108.
- Kitzberger, T., D. Kilian, J. Kotik and T. Proll. 2019. "Comprehensive analysis of the performance and intrinsic energy losses of centralized Domestic Hot Water (DHW) systems in commercial (educational) buildings." *Energy and Buildings* 195: 126-138. doi: 10.1016/j.enbuild.2019.05.016.
- Krzaczek, M., J. Florczuk and J. Tejchman. 2019. "Improved energy management technique in pipe-embedded wall heating/cooling system in residential buildings." *Applied Energy* 254: 113711. doi: 10.1016/j.apenergy.2019.113711.
- Naldi, C., M. Dongellini and G. L. Morini. 2015. "Summer performances of reversible air-to-water heat pumps with heat recovery for domestic hot water production." *Energy Procedia* 78: 1117-1122. doi: 10.1016/j.egypro.2015.11.068.
- Trinchieri, R., N. Calabrese and P. Rovella. 2016. "Development and experimental analysis of CO₂ heat pump for DHW production." *Refrigeration Science and Technology* 1193-1200. doi: 10.18462/iir.gl.2016.1208.
- UNI. 2012. *UNI/TS 11300-4: Use of Renewable Energy and Other Generation Methods for Winter Air Conditioning and for Domestic Hot Water Production*. Milan, Italy.

- UNI. 2014. *UNI/TS 11300-2: Evaluation of Primary Energy Need and System Efficiencies for Space Heating, Domestic Hot Water Production, Ventilation and Lighting for Non-residential Buildings*. Milan, Italy.
- Wu, W., H. M. Skye and P. A. Domanski. 2018. "Selecting HVAC systems to achieve comfortable and cost-effective residential net-zero energy buildings." *Applied Energy* 212: 577-591. doi: 10.1016/j.apenergy.2017.12.046

Numerical Evaluation of Moisture Buffering Capacity of Different Inner Casing

Enrico Baschieri – Ecodesign s.r.l., Scandiano, Italy – baschieri@ecodesign.it

Anne Friederike Goy – Ecodesign s.r.l., Scandiano, Italy – goy@ecodesign.it

Abstract

How does the moisture buffering capacity of the inner casing vary, according to the degree of the relative humidity of the room? Can a "rule of thumb" be obtained from a numerical simulation of a case study? A numerical evaluation of a heavyweight building was run in order to estimate the different moisture buffering capacity of two different kinds of plasters. In this study, the environmental data of a room, calculated using a dynamic simulation, was integrated with the hygroscopic properties of the materials obtained from the archives of the software WUFI, in order to simulate the variation of the relative humidity of a room inside a nearly Zero Energy Building with a mechanical ventilation with heat recovery.

1. Introduction

The microclimate within a room is affected by several factors, such as the relative humidity, the heat sources, the ventilation and the presence of hygroscopic materials. As observed in the literature (e.g., Eckermann and Ziegert, 2006; Eshrar et al., 2015; Svennberg, 2006), the influence of the materials is manifested in the effects of thermal accumulation of the masses and in the effect of hygroscopic accumulation of porous materials overlooking the indoor air. The hygroscopic capacity of a room consists in the ability of the materials facing the internal air to moderate changes of the internal relative humidity. The moisture buffering function of internal casing is a passive system to reduce the fluctuations of indoor humidity. This humidity has a major influence on the internal comfort (Ronzino, 2014). With this study we have investigated the moisture buffering value of two different casings in order to estimate the effect of finishing materials on indoor relative humidity and, indirectly, on comfort.

2. Moisture Buffering Capacity

2.1 Hygroscopic Properties of Building Materials from UNI EN ISO 12571

2.1.1 Absorption as function of Relative Humidity

The moisture absorption and release of construction materials is strictly dependent on the relative humidity degree of the air inside a room (Fig. 1).

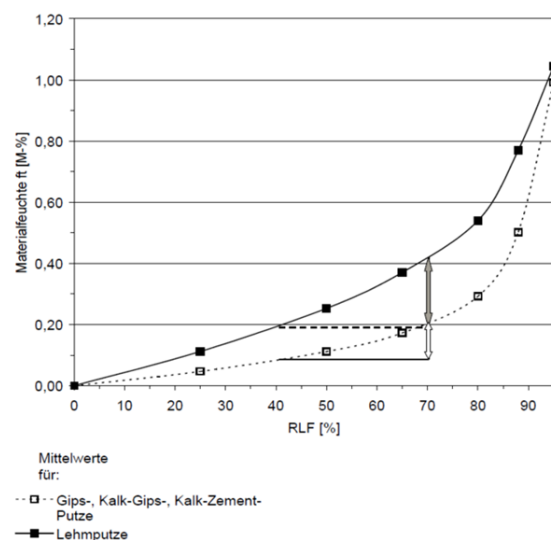


Fig. 1 – Absorption/Relative Humidity (UNI EN ISO 12571:2013)

2.1.2 Humidity absorption/release

The UNI EN ISO 12571:2013 reports the moisture absorption and release test curves of several materials. Fig. 2, for instance, depicts the experimental curves obtained for some materials, showing very different behaviours. In this case, experimental data were obtained in a test room, first increasing the relative humidity at a constant temperature from 50 to 80% and then, after 12 hours, reducing it to 50%.

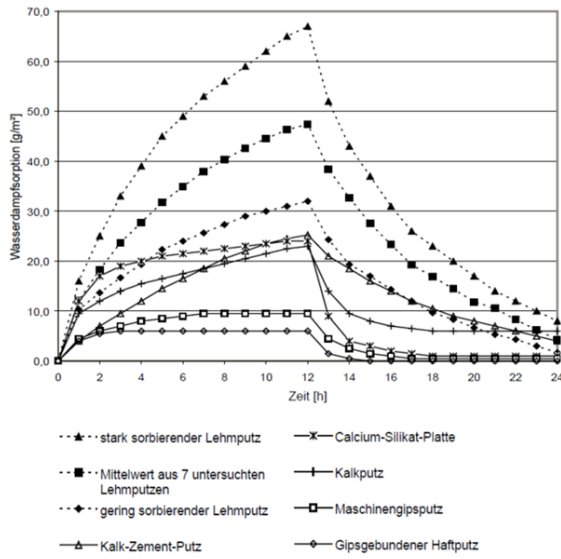


Fig. 2 – Humidity Absorption/Release (UNI EN ISO 12571:2013)

2.2 Ideal Moisture Buffer Value

The moisture buffering capacity is a property of materials, which can be described using the ideal Moisture Buffer Value. The MBV_{ideal} is defined as the exchange of moisture $g(t)$ normalized on the variation of RH of the surface ΔRH :

$$MBV_{ideal} \approx \frac{g(t)}{\Delta RH} = 0,00568 \times b_m \times \Delta p_v \times \sqrt{t_p} \quad \left[\frac{kg}{(m^2 \% UR)} \right] \quad (1)$$

Where:

- $g(t)$: Moisture flux [$kg / m^2 s$]
- ΔRH : Relative Humidity variation [%]
- b_m : Moisture effusivity [$\frac{kg}{m^2 Pa \sqrt{s}}$]
- Δp_s : Saturation vapour pressure variation [Pa]
- t_p : Period [s]

The ideal Moisture Buffer Value formula was taken from Carsten Rode et al. (2003, 2006).

2.3 Practical Moisture Buffer Value

The Moisture Buffer Value (MBV) indicates the amount of moisture that is absorbed or released by the material, per square meter of exchange surface, during a certain period of time when it is subject to

a specific variation of the RH of the indoor air, at a specific speed of the internal air. The MBV_{ideal} is derived from the hygroscopic properties of the material and is a property of the material itself, in contrast to the $MBV_{practical}$, which is experimentally measured, and includes also the effect of moisture resistance of the film-air surface, while the surface resistance is assumed to be equal to zero in the formula of the MBV_{ideal} .

Due to this simplification, the values of the calculated MBV of some materials are about three times larger than the measured values. The MBV estimates in a reliable way the moisture buffering capacity of building materials only when it is closely linked to the relative humidity rate of the room. For this reason, only one value of MBV is not enough to describe the moisture buffering capacity of building materials.

3. Case study

3.1 Indoor Environment

Starting from the results of the dynamic simulation of the environmental data of a sample room, run with the software Tas Engineering (ESDL, 2019), we investigated the moisture buffering capacity (MBV_{ideal}) of two different kinds of plasters (hydraulic lime plaster and clay plaster) in order to measure their ability to adjust the indoor relative humidity.

Our test room was a kitchen-dining room of 35.10 m², with 77.83 m² of plastered walls and ceiling, a net volume of 94.78 m³, with variable ventilation regime between day and night of 8.55 - 17.11 m³/h, equal to 0.09-0.18 ach, and an infiltration rate of about 0.06 ach at atmospheric pressure.

The indoor environment of our sample room is described in the following graphs.

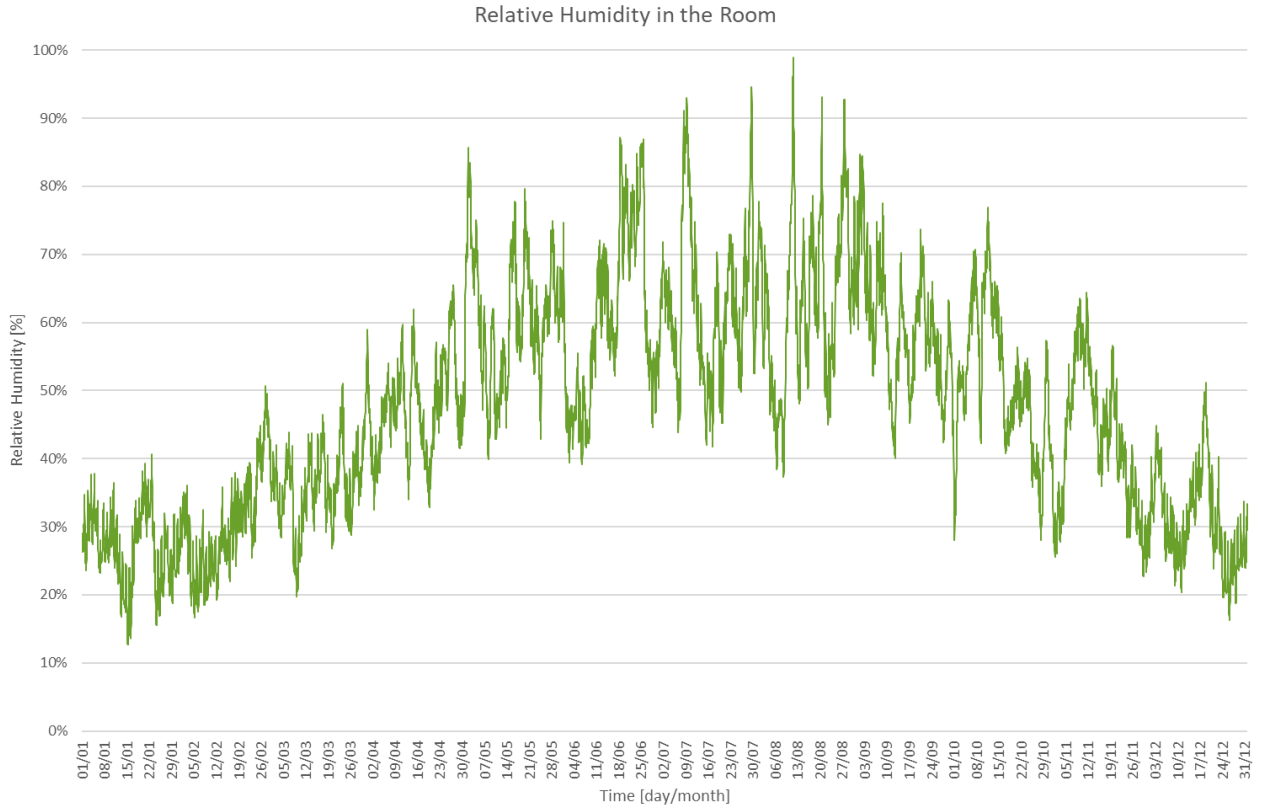


Fig. 3 – Relative Humidity of the room

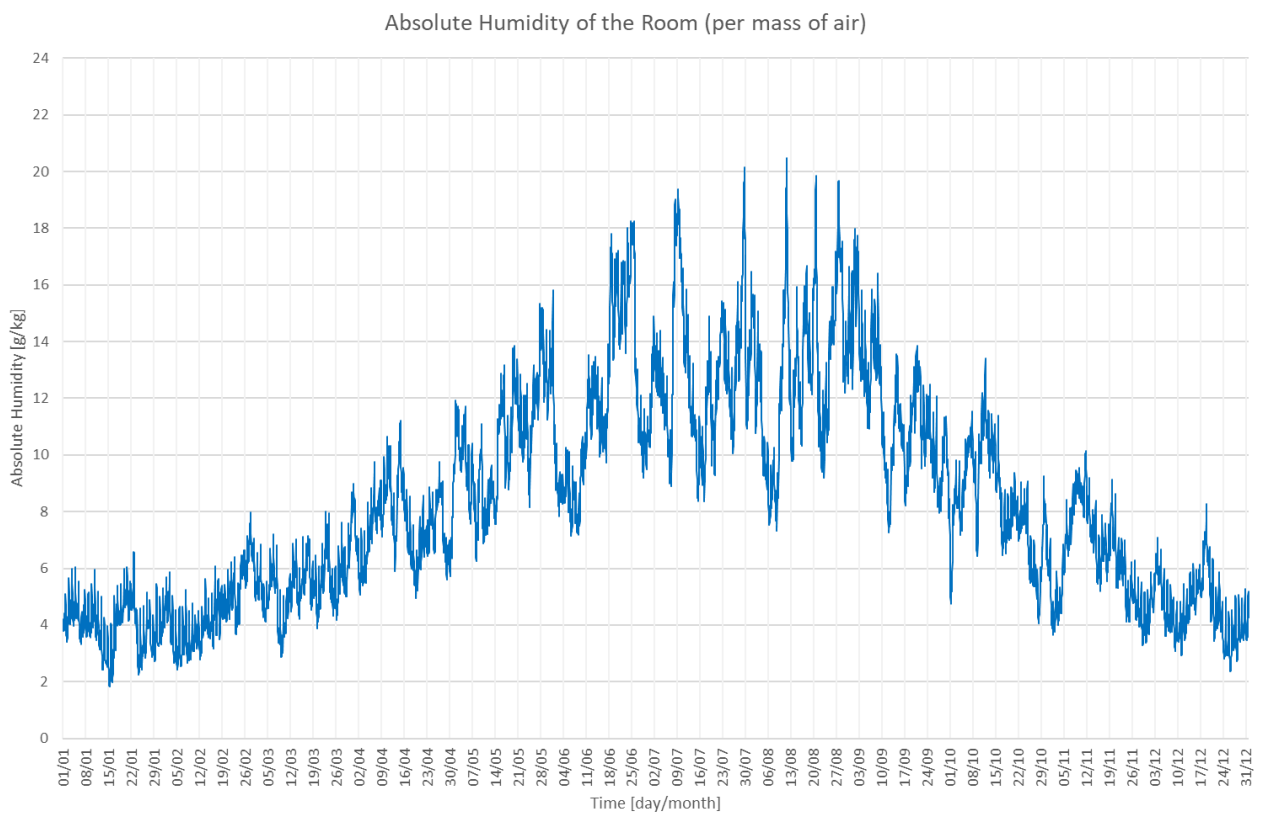


Fig. 4 – Absolute Humidity of the room (per mass of air)

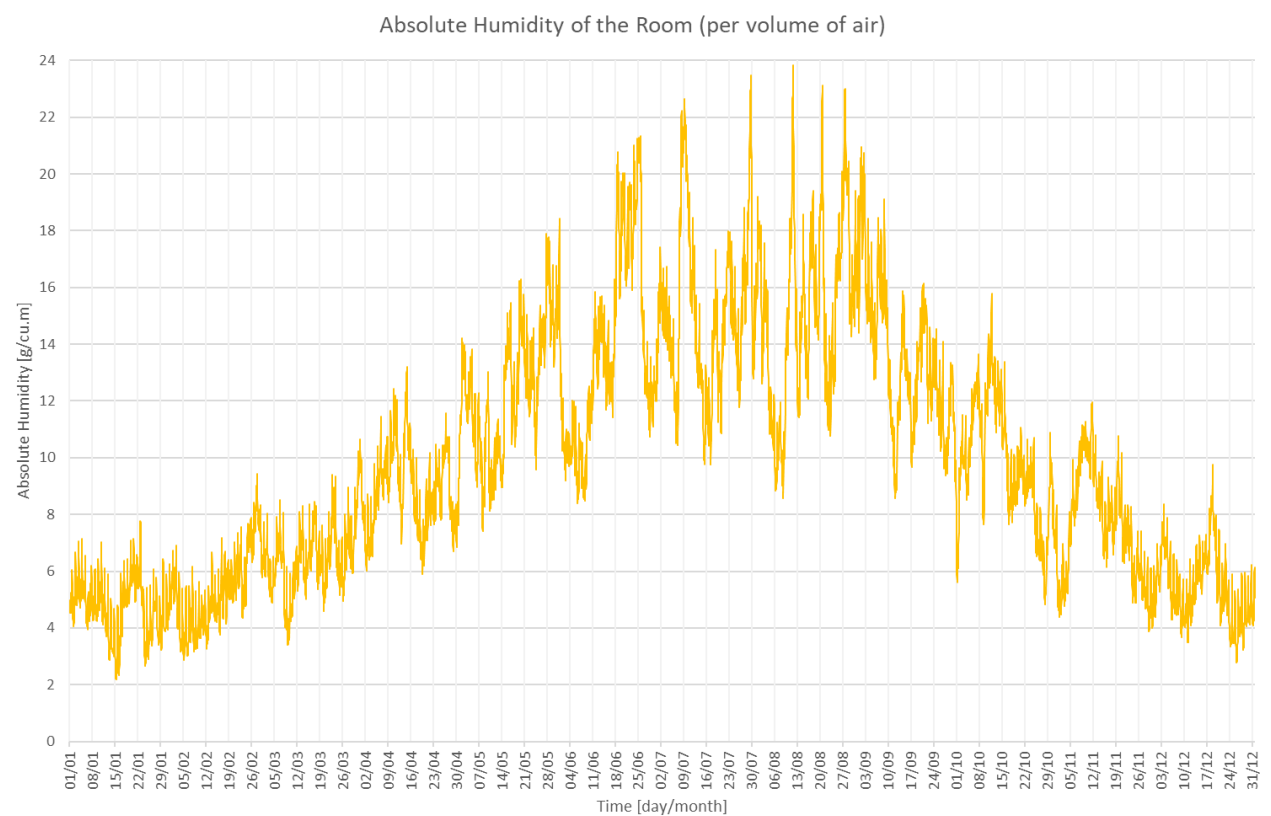


Fig. 5 – Absolute Humidity of the room (per volume of air)

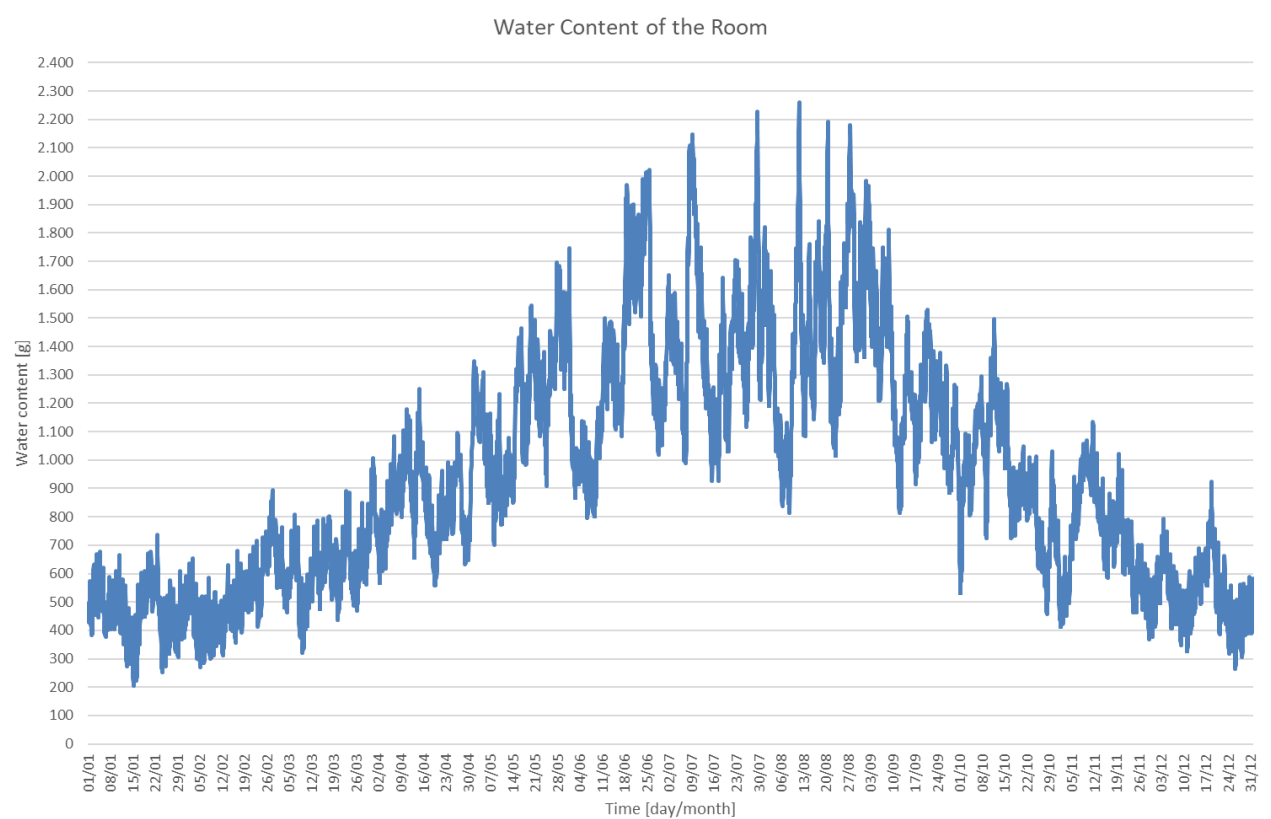


Fig. 6 – Moisture content of the room

3.2 Plaster Moisture Storage Functions

The experimental values of the original moisture storage curves, taken from the software WUFI, were streamlined between the given points to obtain a Moisture Buffering Capacity value for each tenth of percentage point of relative humidity, in order to have the same accuracy of the dynamic simulation data (Figs 7, 8, 9, 10).

The streamlined curves were used in Excel to calculate the MBV_{ideal} for each hour, taking in to account the relative humidity values and hourly variations calculated with the dynamic simulation.

Table 1 – Hydraulic lime plaster parameters from WUFI

Bulk density	kg/m ³	1830.0
Porosity	m ³ /m ³	0.27
Specific Heat Capacity, Dry	J/kgK	850.0
Thermal Conductivity, Dry, 10°C	W/mK	0.7
Water Vapour Diffusion Resistance Factor	-	19.99
Reference Water Content	kg/m ³	10.23
Free Water Saturation	kg/m ³	211.03
Water Absorption Coefficient	kg/m ² /s	0.067
Drying Factor	-	10
Moisture-dep. Thermal Cond. Supplement	%/M.-%	9.981
Typical Built-In Moisture	kg/m ³	211.03
Temp-dep. Thermal Cond. Supplement	W/mK ²	0.0002

Table 2 – Clay plaster parameters from WUFI

Bulk density	kg/m ³	1568.0
Porosity	m ³ /m ³	0.41
Specific Heat Capacity, Dry	J/kgK	488.0
Thermal Conductivity, Dry, 10 °C	W/mK	0.4837
Water Vapour Diffusion Resistance Factor	-	11.0
Reference Water Content	kg/m ³	39.0
Free Water Saturation	kg/m ³	375.0
Water Absorption Coefficient	kg/m ² /s	0.183
Drying Factor	-	10
Moisture-dep. Thermal Cond. Supplement	%/M.-%	8.0
Typical Built-In Moisture	kg/m ³	375.0
Temp-dep. Thermal Cond. Supplement	W/mK ²	0.0002

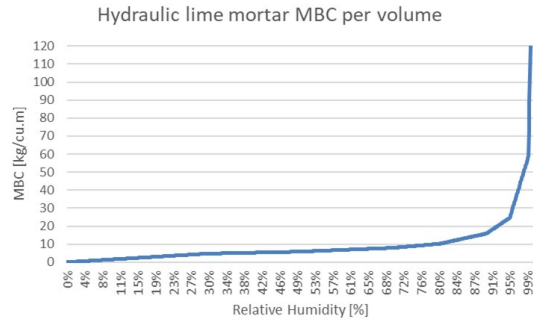


Fig. 7 – Moisture storage function of the hydraulic lime plaster

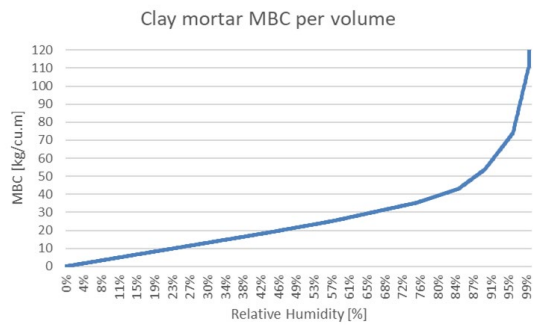


Fig. 8 – Moisture storage function of the clay plaster

The volumetric Moisture Buffering Capacity curves were used to derive the specific absorption curve, considering a plaster thickness of two centimeters.

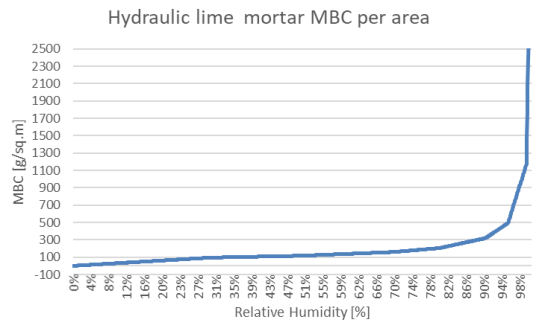


Fig. 9 – Moisture storage function of the hydraulic lime plaster per area

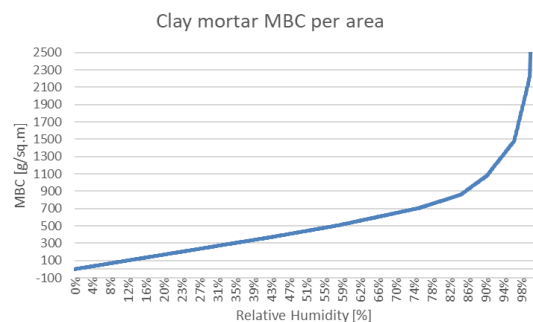


Fig. 10 – Moisture storage function of the clay plaster per area

3.3 Interaction Between Plaster and Relative Humidity

The moisture penetration depth in the plaster was calculated using the formula:

$$EMPD = \sqrt{\frac{\delta \times p_{s(\theta)} \times T}{\rho \xi \times \pi}} \quad (2)$$

Where:

- δ : Vapour permeability [kg/(m s Pa)]
- $p_{s(\theta)}$: Saturation vapour pressure [Pa]
- T : Period [s]
- ρ : Dry mass [kg/mc]
- ξ : Hygroscopic capacity [kg/kg]
- π : Pi [-]

The formula of the moisture penetration depth was taken from: Cunningham (2003). The moisture penetration depth in the hydraulic lime plaster varies between 2.3-2.7 mm, with a peak of 1.5-3.5 mm, depending on the relative humidity of the room (Fig. 11).

The moisture penetration depth in the clay plaster varies between 1.5-2.5 mm, because of the greater absorption capacity of the clay, which tends to slow down the penetration capacity (Fig. 12).

First of all, we investigated the specific absorption/release of the two materials. The specific moisture absorption/release of the hydraulic lime plaster was about ± 0.5 g/m² (Fig. 13). The specific moisture absorption/release of the clay plaster was about ± 1.5 g/m², three times bigger than the hydraulic lime plaster (Fig. 14).

Following this, we investigated the absolute moisture absorption/release of the two plasters, considering their extension in the envelope of the whole

room. We did not take in to account the MBD of other materials present in the room, such as wood floor, furniture, etc.

The hydraulic lime plaster was able to remove/add about 50 g of moisture from the room (Fig. 15).

The clay plaster was able to remove/add about 100-125 g of moisture from the room, about 2.0-2.5 times more than the hydraulic lime plaster (Fig. 16).

4. Mitigation Effects on the Room

Finally, we calculated the effect of this moisture absorption/release on the relative humidity of the room. The absorption/release effect was calculated taking in to account the variation of the relative humidity between two consecutive hours. A reduction of relative humidity in the room reduces the moisture absorption of the plaster (induces a moisture release), whereas an increase of relative humidity in the room stops the moisture release of the plaster (induces a moisture absorption).

4.1 Indoor Relative Humidity Variation

The indoor relative humidity variation changed with the two different kinds of plasters.

The hydraulic lime plaster was able to remove/add about 50 g of moisture from the room, varying the relative humidity by about $\pm 2-3\%$ (Fig. 17).

The clay plaster was able to remove/add about 100-120 g of moisture, varying the relative humidity of the room by about $\pm 8-10\%$ (Fig. 18).

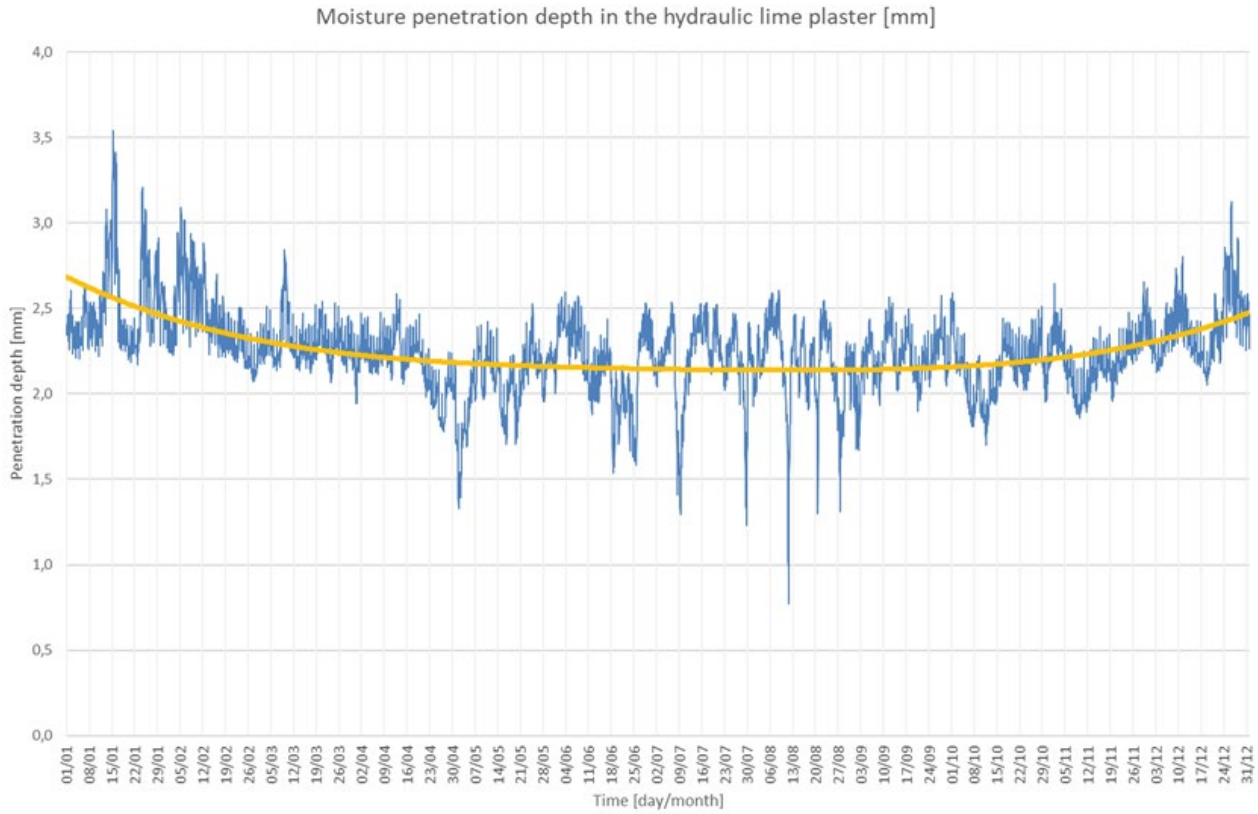


Fig. 11 – Moisture penetration depth in the hydraulic lime plaster

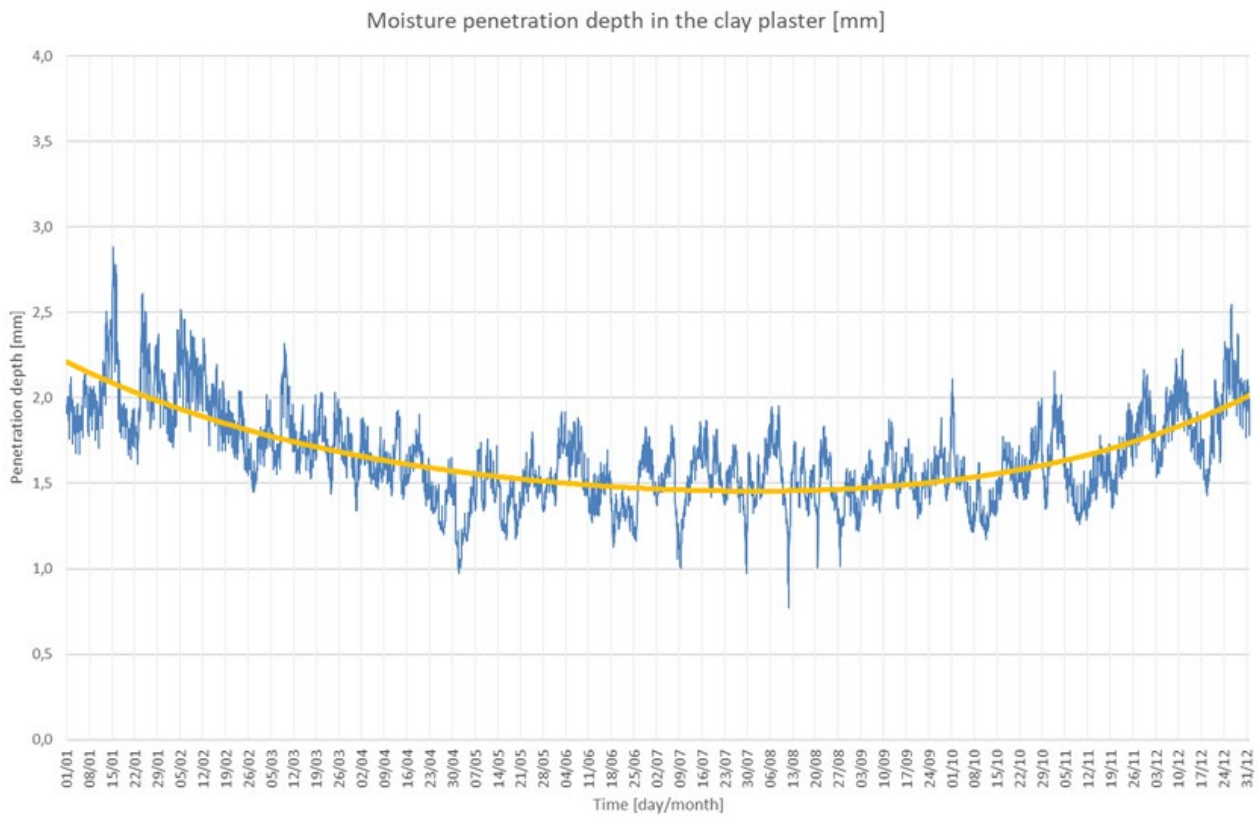


Fig. 12 – Moisture penetration depth in the clay plaster

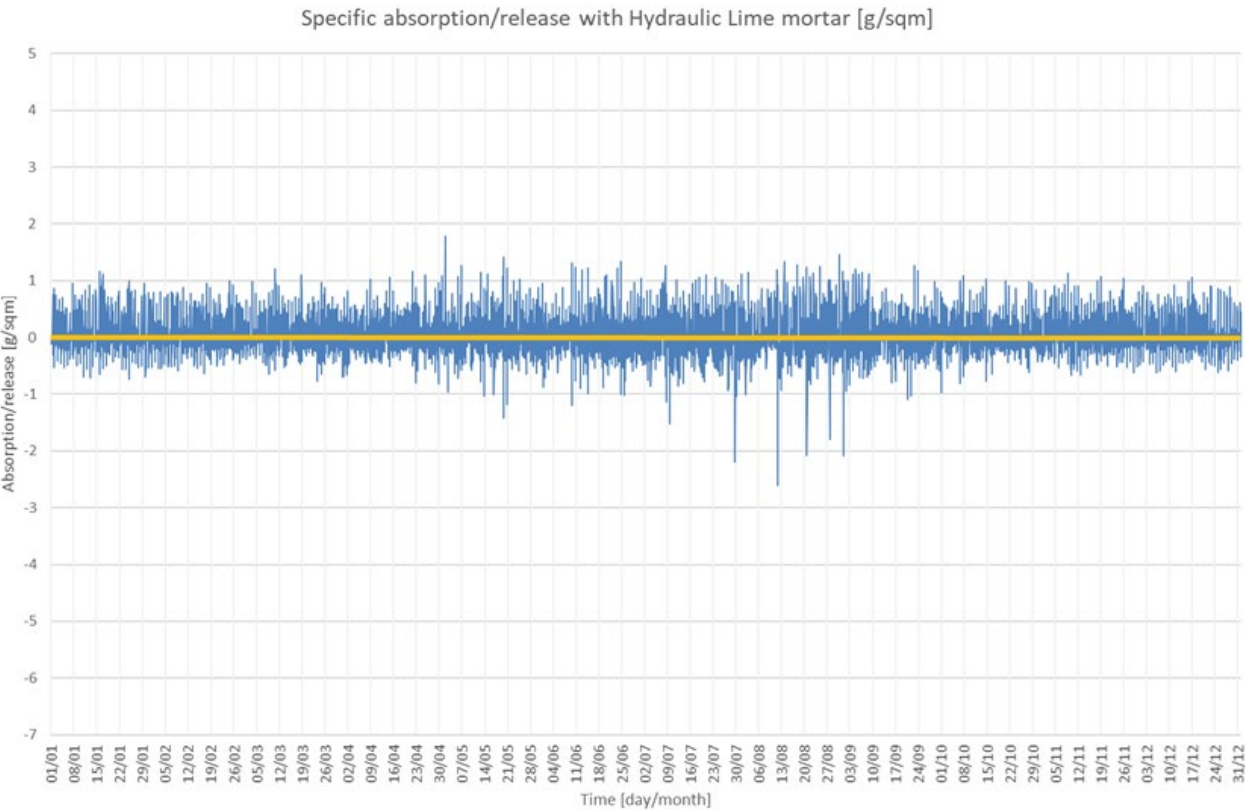


Fig. 13 – Specific absorption/release with Hydraulic Lime mortar

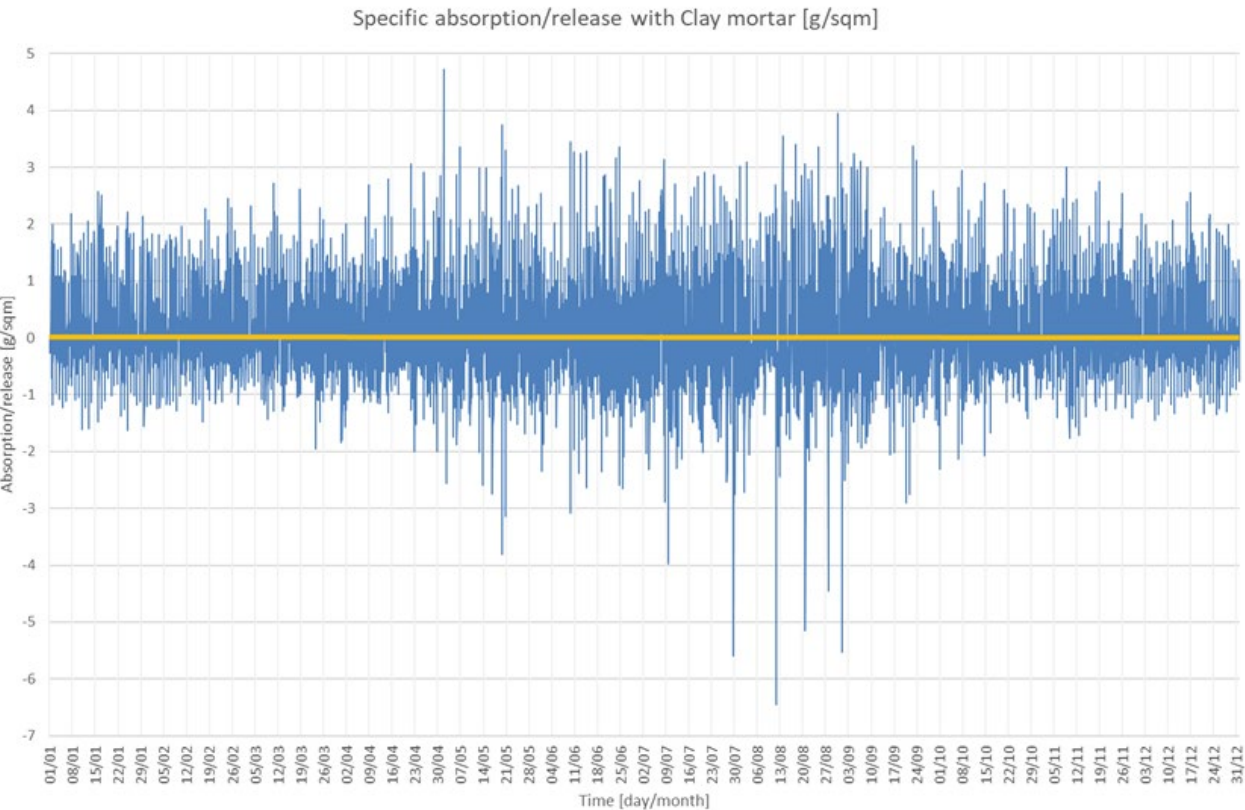


Fig. 14 – Specific absorption/release with Clay mortar

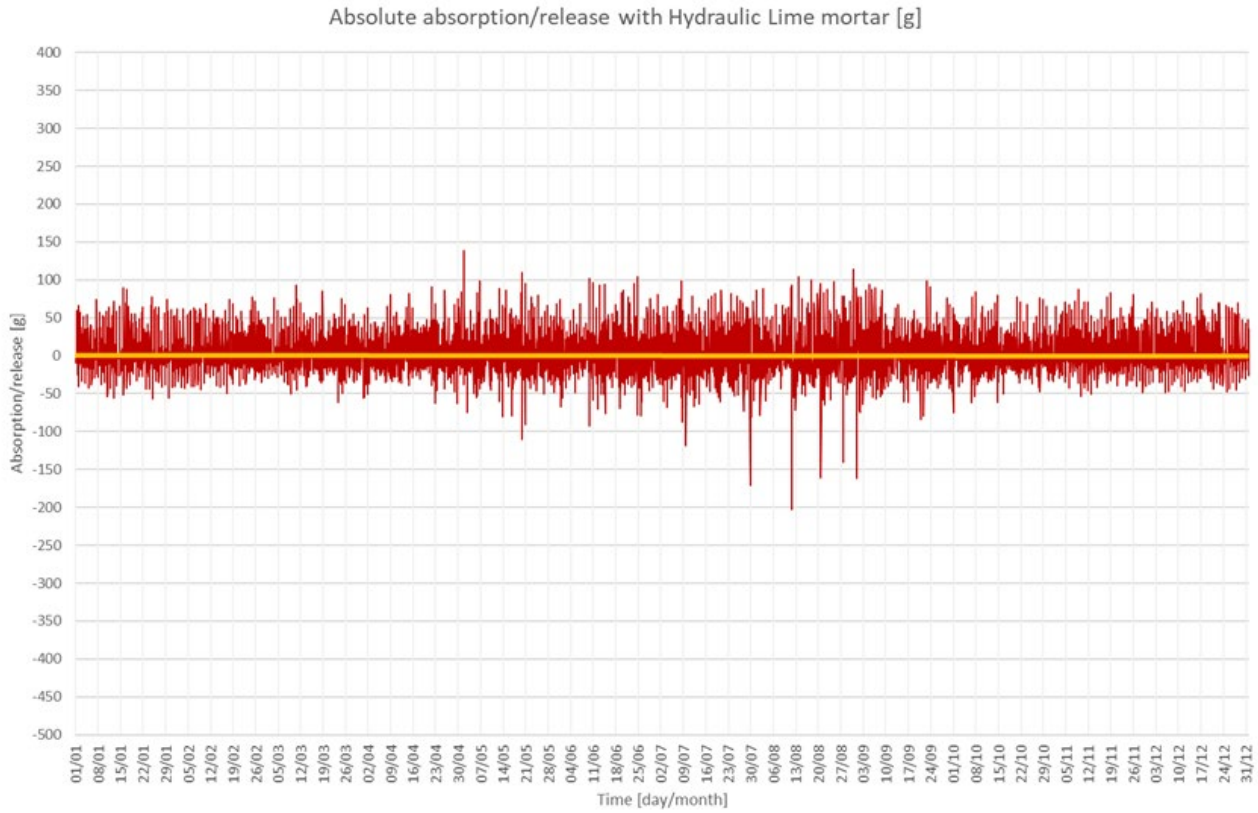


Fig. 15 – Absolute absorption/release with Hydraulic Lime mortar

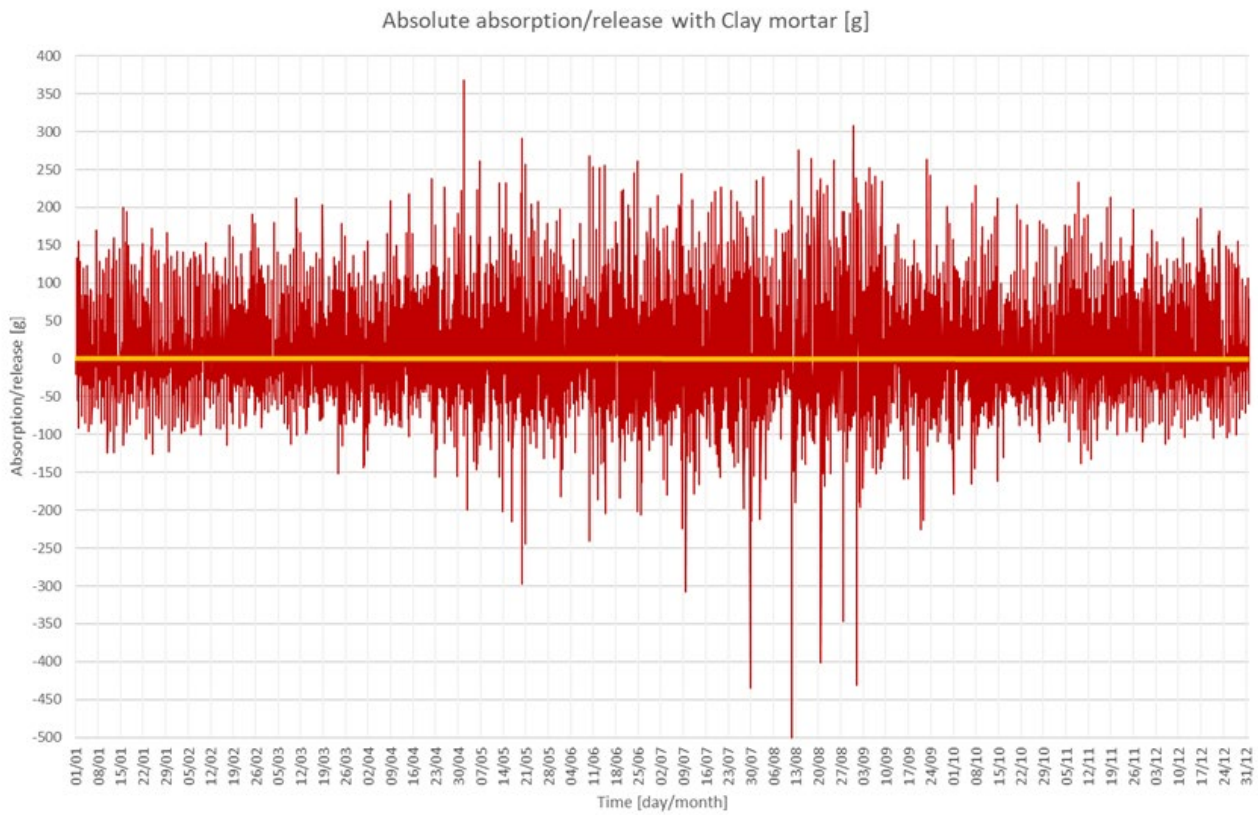


Fig. 16 – Absolute absorption/release with Clay mortar

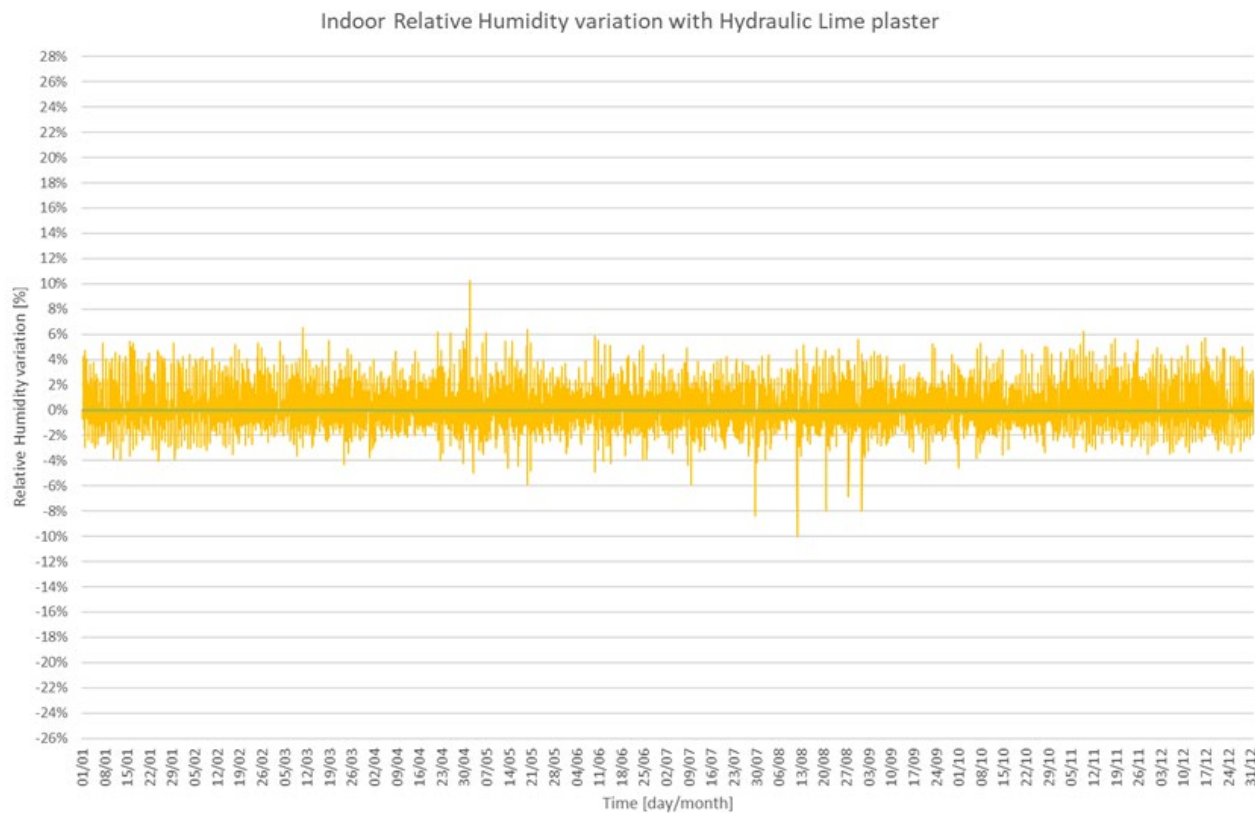


Fig. 17 – Indoor Relative Humidity with Hydraulic Lime plaster

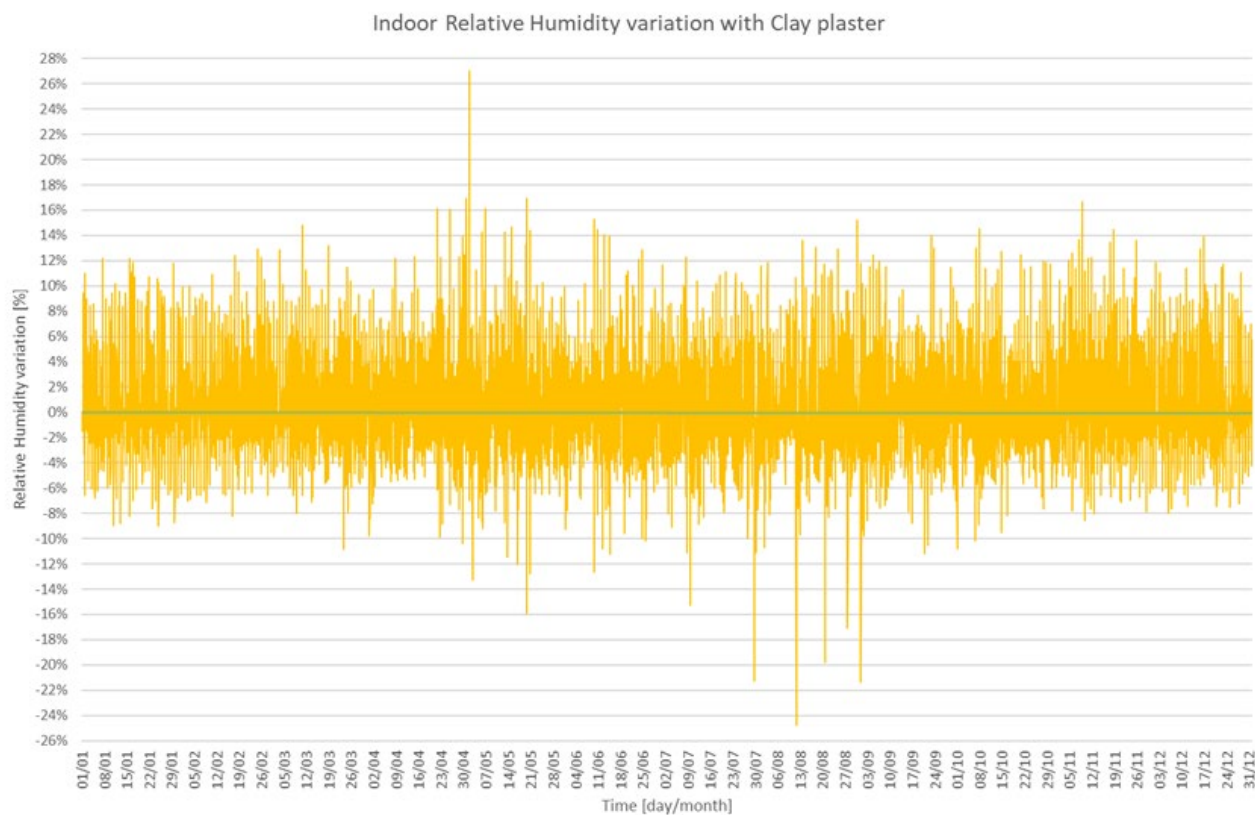


Fig. 18 – Indoor Relative Humidity with Clay plaster

5. Conclusions

The MBV is a parameter representative of the moisture buffering capacity of building materials, closely linked to the relative humidity rate of the internal air and to the analysed time period.

The moisture penetration depth, in the period of one hour, varies between 1 and 3.5 mm for both plasters, indicating the size of the reactive layer.

The Moisture Buffering Capacity of the finishing materials is able to correct the relative humidity of the room and can be used as passive strategy to adjust the interior relative humidity.

The moisture penetration depth is in the same order of measurement for both materials: 2.3-2.7 mm for the hydraulic lime plaster and 1.5-2.5 mm for the clay plaster.

The specific absorption/release is about $\pm 0.5 \text{ g/m}^2$ for the hydraulic lime plaster and 1.5 g/m^2 for the clay plaster.

The hydraulic lime plaster is able to remove/add about 50 g of moisture from the room, varying the relative humidity by about $\pm 2\text{-}3\%$.

The clay plaster is able to remove/add about 100-125 g of moisture, varying the relative humidity of the room by about $\pm 8\text{-}10\%$.

The Moisture Buffer Value (MBV) is a parameter indicative of the hygroscopic capacity of building materials. It is closely linked to the content of the internal relative humidity of the room and the period analysed.

The penetration depth of the moisture in the plaster, in the range of one hour, varies between 1 mm and 3-3.5 mm for both the layers of plaster, giving us the size of the reactive layer of the plaster.

The indoor relative humidity of the room varies considerably depending on the type of plaster analysed. The clay plaster is able to remove/add about 2.0-2.5 times more moisture than the hydraulic lime plaster and is able to vary the relative humidity of the room in the same proportion.

The moisture buffering capacity of clay plaster is suitable to be used as a passive strategy to mitigate the fluctuations of indoor relative humidity, in lightweight and in heavyweight buildings, in order to improve internal comfort.

References

- Cunningham, M.J. 2003. "The building volume with hygroscopic materials: an analytical study of a classical building physics problem." *Building and Environment* 38: 329-337.
- Eckermann, W., and C. Ziegert. 2006. *Auswirkung von Lehmbaumstoffen auf die Raumluftfeuchte*.
- EDSL Tas Engineering v.9.4.3. Accessed April 26, 2019, <http://www.edsl.net/>
- Eshrar, L., M. Lawrence, A. Shea and P. Walker. 2015. "Moisture buffer potential of experimental wall assemblies incorporating formulated hemp-lime." *Building and Environment* 93: 199-209.
- Rode, C., K. K. Hansen, T. Padfield, B. Time, T. Ojanen and J. Arfvidsson. 2003. *Workshop on Moisture Buffer Capacity - Summary Report*. Department of Civil Engineering, Technical University of Denmark.
- Rode, C., R. Peuhkuri, B. Time, K. Svennberg and T. Ojanen. 2006. "Moisture Buffer Value of Building Materials". *ASTM Symposium on Heat-Air-Moisture Transport: Measurements on Building Materials*, Toronto, April 23, 2006.
- Ronzino, A. 2014. "Influence of hygroscopic interior finishing on indoor comfort conditions". Doctoral thesis at Politecnico di Torino.
- Svennberg, K. 2006. "Moisture Buffering in the Indoor Environment". *Report TVBH-1016*. Building Physics LTH, Lund University.
- UNI. 2013. *UNI EN ISO 12571 - Hygrothermal performance of building materials and products -- Determination of hygroscopic sorption properties*. Milan, Italy: UNI.

A CitySim Urban Energy Simulation for the Development of Retrofit Scenarios for a Neighborhood in Bolzano, Italy

Fahad Haneef – Free University of Bozen-Bolzano, Italy – fahad.haneef@natec.unibz.it

Federico Battini – Free University of Bozen-Bolzano, Italy – federico.battini@natec.unibz.it

Giovanni Pernigotto – Free University of Bozen-Bolzano, Italy – giovanni.pernigotto@unibz.it

Andrea Gasparella – Free University of Bozen-Bolzano, Italy – andrea.gasparella@unibz.it

Abstract

The urban territory is responsible for a high percentage of natural resources depletion and waste generation. Population increases and cities expand, and thus energy demand climbs. Consequently, an efficient use of energy is becoming more and more crucial in order to promote both local and global sustainability. To achieve such a goal, the reduction of energy demand, the optimization of energy supply sources, and the increase of renewable energy share can facilitate the transition of urban areas into highly efficient and sustainable districts. In this framework, this study assesses to what extent typical building retrofit interventions can reduce energy consumption, enabling a transition towards a nearly Zero Energy District (*nZED*). A state-of-the-art urban simulation was developed with CitySim for part of the city of Bolzano, Italy, to evaluate the annual district energy uses and define possible efficiency measures (e.g., façade and roof insulation and substitution of windows). Achievable energy savings are analyzed and the most significant factors affecting the overall performance identified.

1. Introduction

Communities around the world are entering an age characterized by what some authors have labelled the “Fourth Industrial Revolution” (Rifkin, 2004), as society moves from fossil fuels – used since the “Second Industrial Revolution”, towards renewable energy generation and technologies to adopt in sustainable and smart communities. For communities around the world, energy needs are growing year after year, as population increases, cities expand, and energy demand climbs. The challenge of sup-

plying energy for increasing demand, while reducing carbon emissions, calls for more complex and new creative solutions (Clark, 2010).

Furthermore, there has been a rapid population shift from rural to urban areas. According to a recent UN report (UN, 2014), over 54 % of the total world population lives in cities and this is likely to increase to 66 % by 2050. As a result, cities, already responsible for approximately 70 % of the world’s fossil fuel emissions (Polly et al., 2016), are drastically expanding. Consequently, urban energy efficiency is crucial for promoting local and global sustainability (Aelenei et al., 2016; De Lieto Vollaro et al., 2014; Marique and Reiter, 2014).

Several case studies in the literature have explored the possibility of improving energy efficiency in buildings (Copiello, 2017). For instance, some authors have used data mining techniques to identify low-efficiency buildings (Zucker et al., 2014), analysed the efficacy of different energy policies (Lee et al., 2015), and discussed the energy saving potential from the renovation into net zero energy buildings (Konstantinou and Knaack, 2013; Luddeni et al., 2018). Other researchers have optimized existing and new building design and features (Afram et al., 2017; Evins, 2013; Gong et al., 2016), and investigated the effectiveness of smart energy management for buildings (Rocha et al., 2015), with different targets of energy consumption and renewable integration at district scale (Guen et al., 2018; Mohajeri et al., 2019). However, energy simulation tools and policies have mainly addressed individual buildings and smart energy systems. Hence, there is a need to expand energy performance assessment and energy efficiency actions from a building scale to urban scale, to help identify inefficient buildings

and the impact of the available retrofitting measures. The purpose of this case study is to analyse to what extent a set of energy efficiency measures can reduce the district energy consumption, facilitating the transition towards a nearly zero energy district, nZED. In this framework, a model of part of the city of Bolzano, Italy, was developed according to a state-of-the-art urban simulation. Annual district energy uses are analysed, with the aim of defining targeted energy policies with particular attention to façades, roof and windows renovation. The results allow the estimation of the achievable energy saving and the assessment of the most significant factors affecting the overall performance.

2. Method

2.1 Case Study and Input Data

The case study investigated in this research is located in the city of Bolzano (46° N, 11° E), in the North of Italy. The selected area is made up of 95 dwellings built during the period 1990-1995, all connected to the urban district heating network (Fig. 1).

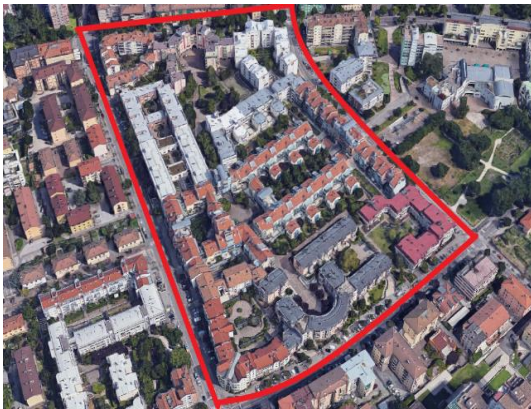


Fig. 1 – Google Map image of the selected district in Bolzano

Considering the way in which the 95 residential dwellings are connected and served by the district heating network, for the sake of simplicity they can be grouped into 11 main multi-zone buildings (named B1, B2, ..., B11 in this work).

The geometrical data relating to the district were available thanks to a GIS file containing detailed building footprints (Autonomous Province of Bozen-Bolzano, 2019) and a dataset of roof heights for the selected district developed by the authors. For about 2/3 of the sample of buildings in the district, it was possible to characterize in detail the thermal transmittances of the different building envelope components, by means of the energy certificates provided by the Klimahaus Agency, the local energy agency.

2.2 Modelling Approach

For modelling the buildings' space heating and cooling uses at an urban scale, the simulation code CitySim was selected. CitySim is a command-line integrated solver with a JAVA based graphical user interface, which includes integrated custom modules for modelling microclimatic effects, transient heat flow, plants and equipment, as well as occupants' presence and behaviour (Walter and Kämpf, 2015). In order to prepare the input quantities required by CitySim to run simulations, the approach described in Fig. 2 was implemented. After processing the geometrical data with QGIS, a 3D model was prepared with SketchUp and subdivided into different layers – each one dedicated to an individual category of envelope components such as walls, roofs and floors, and incorporated into the context geometry of surrounding buildings. In order to optimize the computational time needed for the simulation, the 11 multi-zone buildings in the district were aggregated into three groups considering the average thermal transmittances for the different types of components (Table 1).

Table 1 – Average thermal transmittances ($\text{W m}^{-2} \text{K}^{-1}$) of building components for the three groups

	Wall	Roof	Floor
Group1	0.60	0.32	0.39
Group2	0.64	0.24	0.46
Group3	0.52	0.35	0.43

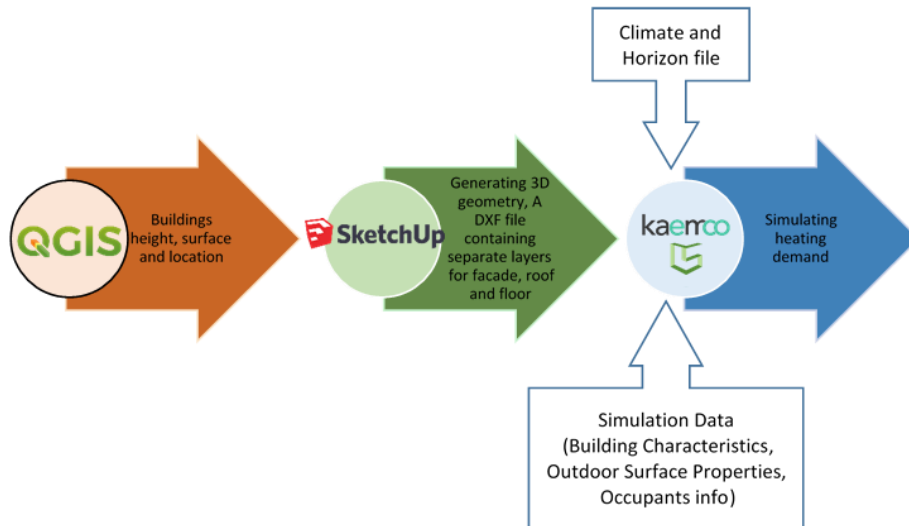


Fig. 2 – Flow chart of the developed methodology

2.3 Model Calibration

An initial CitySim model was developed with the input data collected from the building energy certificates, as well as some CitySim default values (Table 2). In order to check the representativeness of the model, four annual simulations were run using the hourly weather data collected at the meteorological station of Bolzano Hospital for the years 2012-2015, including air temperature and relative humidity, solar irradiation and wind speed data. Results were compared to the corresponding annual final energy uses provided by the Municipality of Bozen-Bolzano for each multi-zone building connected to the district heating network (B1, B2, ..., B11).

Since in a previous study (Battini et al., 2019) the same Bolzano district was modelled with the Urban Modelling Interface umi by MIT, and calibrated against the uses for the same period (2012-2015), a second CitySim simulation was run considering the parameters calibrated in umi as inputs.

After the assessment of the impact of the different parameters through a sensitivity analysis, a manual calibration was performed focusing on the most impactful inputs, i.e., ventilation rates and HVAC system efficiency; this is similar to the procedure adopted for the development of the umi model (Battini et al., 2019). The ventilation rates were varied in the range between 0.4 and 0.6 ACH, with a 0.05 ACH step, while the system efficiency between 0.82 and 0.88, with a 0.01 step, for a total of

30 combinations. The selection of ventilation rate and system efficiency minimizing the deviation between simulated and actual heating uses was done according to the k -fold cross validation method. Specifically, for each multi-zone building the root mean square difference RMSD was calculated over three out of the four available years, and the combination with the lowest RMSD value was selected and then validated against the fourth year. The procedure was repeated for all possible combinations of years and the most frequent pair of values of ventilation rate and system efficiency selected for each multi-zone building.

Table 1 – Citysim simulation initial inputs

$T_{min} = 20\text{ }^{\circ}\text{C}$; $T_{max} = 26\text{ }^{\circ}\text{C}$
Shading device 0
Cut-off irradiance: 1300 W m^{-2}
Windows U-value: $3.2\text{ W m}^{-2}\text{ K}^{-1}$
Windows SHGC: 0.75
Windows operable fraction: 100 %
Visible surface reflectance: 40 % roof, 70 % wall
Occupants: typical residential density: 25 m^2/person
Sensible heat: 75 W/person
Radiant part: 60 %
Latent heat: 45 W/person
HVAC system efficiency: 0.85

2.4 Development of the Retrofit Scenarios

As specified above, the energy efficiency measures discussed in this work relate to the building façade, roof or windows. In more detail, these are:

- façade insulation with an external polystyrene layer (thermal conductivity: $0.04 \text{ W m}^{-1} \text{ K}^{-1}$; density: 40 kg m^{-3} ; specific heat capacity: $1470 \text{ J kg}^{-1} \text{ K}^{-1}$) of 10 cm (minimum insulation) and 15 cm (high insulation);
- roof insulation with an external polystyrene layer of 10 cm (minimum insulation) and 15 cm (high insulation);
- substitution of windows with thermally efficient, double/triple glazing low/high SHGC (respectively, 0.35 or 0.6), with thermal transmittance equal to 1.2 and $0.6 \text{ W m}^{-2} \text{ K}^{-1}$, respectively.

As a whole, 15 scenarios were simulated, considering the typical year reported in EnergyPlus weather data as input (EnergyPlus, 2019):

- Case 0: current situation;
- Case 1: façade minimum insulation;
- Case 2: façade high insulation;
- Case 3: roof minimum insulation;
- Case 4: roof high insulation;
- Case 5: double glazing with high SHGC;
- Case 6: double glazing with low SHGC;
- Case 7: triple glazing with high SHGC;
- Case 8: triple glazing with low SHGC;

- Case 9: façade / roof minimum insulation;
- Case 10: façade / roof minimum insulation and double glazing with high SHGC;
- Case 11: façade / roof minimum insulation and double glazing with low SHGC;
- Case 12: façade / roof high insulation;
- Case 13: façade / roof high insulation and triple glazing with high SHGC;
- Case 14: façade / roof high insulation and triple glazing with low SHGC.

3. Results

The initial CitySim model provided results generally within 15% of actual measurements and a comparison with the actual annual energy uses for space heating showed these to be underestimates. As can be seen in Fig. 3 for the year 2014 and in Table 3, if calibrated umi parameters are used as input in CitySim, there is still a significant gap between simulated and actual consumption data, suggesting that a dedicated calibration is required for the CitySim model. Indeed, the highest accuracy is found after calibration through the k -fold cross validation. Calibrated values of system efficiency and ventilation rates according to the k -fold approach are reported in Table 4.

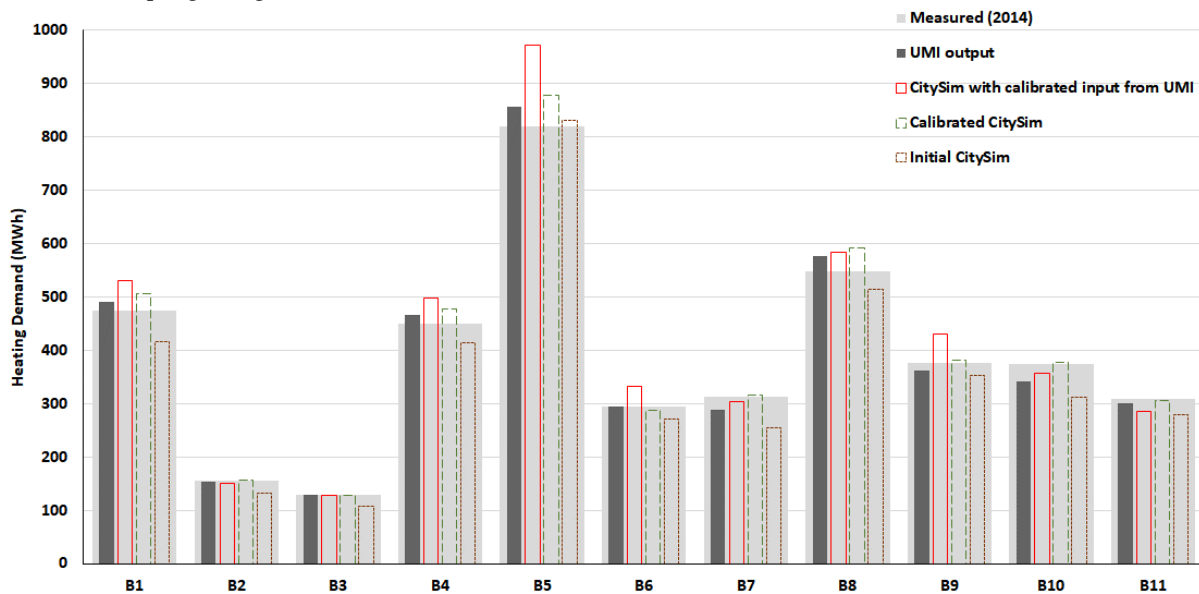


Fig. 3 – Annual energy uses for space heating for the 11 multi-zone buildings for the year 2014: comparison between actual consumption data, umi output, CitySim output using umi calibrated input, using the initial settings and after calibration

Table 3 – Percentage deviations of simulated CitySim annual heating demand using umi inputs or after CitySim calibration according to the *k*-fold approach

	2012		2013		2014		2015	
Building#	CitySim with umi inputs	Calibrated CitySim	CitySim with umi inputs	Calibrated CitySim	CitySim with umi inputs	Calibrated CitySim	CitySim with umi inputs	Calibrated CitySim
B1	3%	-2%	6%	1%	12%	7%	1%	-3%
B2	-2%	2%	-5%	-1%	-4%	1%	-7%	-2%
B3	3%	2%	5%	4%	-1%	-2%	-4%	-5%
B4	7%	2%	7%	2%	11%	6%	-3%	-7%
B5	14%	2%	14%	3%	18%	7%	3%	-8%
B6	35%	16%	12%	-4%	13%	-3%	3%	-12%
B7	5%	3%	8%	5%	4%	1%	-5%	-7%
B8	1%	9%	8%	17%	0%	8%	-5%	3%
B9	17%	3%	18%	4%	14%	1%	8%	-5%
B10	4%	3%	3%	2%	2%	1%	-4%	-5%
B11	-3%	5%	-7%	0%	-7%	-1%	-13%	-5%

Table 4 – Calibrated system efficiencies and ventilation rates according to the *k*-fold approach

Building #	System Efficiency (%)	Ventilation Rate (ACH)
B1	0.86	0.6
B2	0.88	0.6
B3	0.85	0.55
B4	0.87	0.55
B5	0.86	0.45
B6	0.87	0.45
B7	0.83	0.6
B8	0.85	0.55
B9	0.88	0.5
B10	0.86	0.6
B11	0.87	0.5

The 14 retrofit scenarios under consideration were simulated using the calibrated CitySim model and compared with the base case (Case 0), to assess the annual energy reduction that could be achieved by such refurbishments for each group of buildings. As highlighted by Fig. 4, the Case 13, i.e., high insulation of walls and roof (extra 15 cm insulation layer of polystyrene) and substitution of windows with triple glazing with high SHGC, would bring the largest energy savings, with a reduction of the calculated energy consumption to almost half of the

current value. It should be noted that significant improvements could also be achieved in Case 9 and Case 12, i.e. with the insulation of both walls and roof, either if 10 or 15 cm of polystyrene are chosen. Performance could be further enhanced only through interventions on the transparent components, preferring technological solution with high solar gain coefficients.

4. Discussion and Conclusion

In this work we modelled a neighborhood of the city of Bolzano, Italy, served by the local district heating network, in order to discuss the potential of urban building simulation for the definition of energy refurbishment strategies towards the transition into nearly zero energy districts nZEDs. Specifically, a CitySim model was developed and calibrated against a four-year set of annual energy consumptions for space heating. Calibration was performed first considering using calibrated inputs from a different urban simulation tool, umi, and then by means of a *k*-fold approach. Finally, 14 different intervention scenarios relating to the renovation of the building envelope (i.e., façades, roofs and windows) were analyzed and compared.

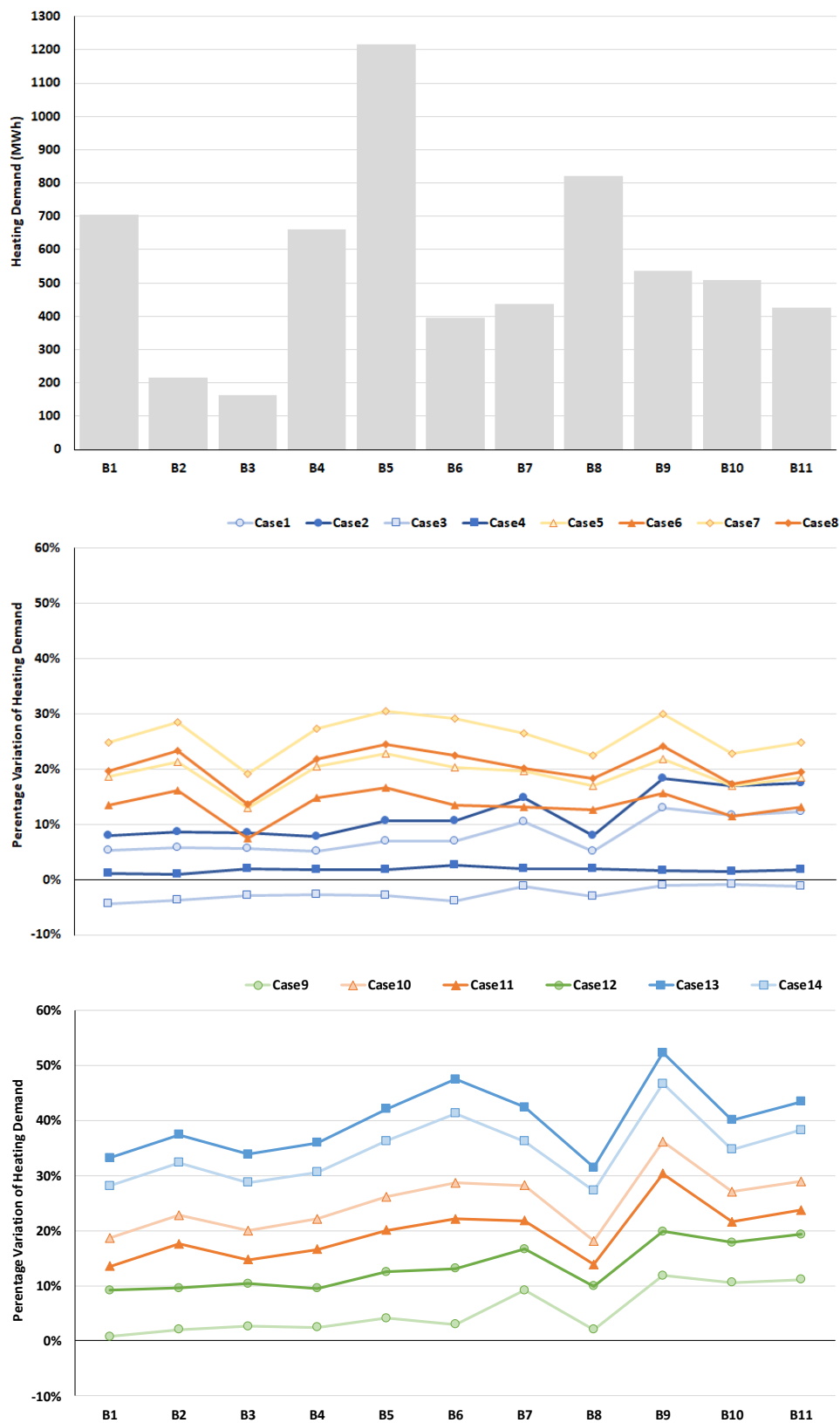


Fig. 4 – Annual space heating uses in the Case 0 (top) and percentage variations in the 14 retrofit scenarios (middle and bottom charts)

It was observed that the calibration of the urban model is not an easy task. In particular, it was noted that calibrated inputs from another tool, umi in this case, are not directly applicable to another, i.e. CitySim in this case. Furthermore, the application of average input values is also not sufficient to properly match the actual energy consumption data and it is necessary, at least, to work with aggregated groups of buildings. Finally, as observed in previous studies (Battini et al., 2019), the k -fold approach can be a useful method to apply when only a limited number of annual actual consumption data are available.

Regarding the retrofitting scenarios, since the district is made up of buildings constructed in the same period with similar technologies, no significant differences were found for the different groups and for all of them the largest saving potential is encountered when coupling the insulation of vertical walls and roofs with high performance glazing with high SHGC.

As a conclusion, although this example focused on only one portion of the city, it has been shown that it is possible to recognize the potential of urban modelling for defining targeted energy efficiency measures, enabling the identification of homogeneous groups and the optimization for each of the energy renovation solutions, maximizing in such a way the efficacy of the energy renovation strategy.

Acknowledgement

This study has been funded by the project “Klima-house and Energy Production” in the framework of the programmatic-financial agreement with the Autonomous Province of Bozen-Bolzano of Research Capacity Building.

The Authors would also like to thank the Klima-Haus Agency for providing access to the building energy certificates and to the Municipality of Bozen-Bolzano for the building energy consumption data.

References

- Aelenei, L., A. Ferreira, C.S. Monteiro, R. Gomes, H. Gonçalves, S. Camelo, and C. Silva. 2016. “Smart City: A Systematic Approach towards a Sustainable Urban Transformation.” *Energy Procedia* 91:970–79.
<https://doi.org/10.1016/j.egypro.2016.06.264>
- Afram, A., F. Janabi-Sharifi, A.S. Fung, and K. Raahemifar. 2017. “Artificial Neural Network (ANN) Based Model Predictive Control (MPC) and Optimization of HVAC Systems: A State of the Art Review and Case Study of a Residential HVAC System.” *Energy and Buildings* 141:96–113.
<https://doi.org/10.1016/j.enbuild.2017.02.012>
- Autonomous Province of Bozen-Bolzano. 2019. “Maps and WebGIS | Autonomous Province of Bolzano - South Tyrol.” Accessed September 9, 2019. <http://geoportale.retecivica.bz.it/maps-webgis-geobrowser.asp>
- Battini, F., G. Pernigotto, and A. Gasparella. 2019. “Calibration of a UMI simulation model for a neighborhood in Bolzano, Italy”. *Proceedings of Building Simulation Applications BSA 2019*, Bolzano, Italy: bu.press.
- Clark, W.W., ed. 2010. *Sustainable Communities*. New York, U.S.: Springer.
- Copiello, S. 2017. “Building Energy Efficiency: A Research Branch Made of Paradoxes.” *Renewable and Sustainable Energy Reviews* 69:1064–76.
<https://doi.org/10.1016/j.rser.2016.09.094>
- De Lieto Vollaro, R., L. Evangelisti, E. Carnielo, G. Battista, P. Gori, C. Guattari, and A. Fanchiotti. 2014. “An Integrated Approach for an Historical Buildings Energy Analysis in a Smart Cities Perspective.” *Energy Procedia* 45:372–78.
<https://doi.org/10.1016/j.egypro.2014.01.040>
- EnergyPlus. 2019. EnergyPlus Weather Data. Accessed in May, 2019. <https://energyplus.net/weather>
- Evins, R. 2013. “A Review of Computational Optimisation Methods Applied to Sustainable Building Design.” *Renewable and Sustainable Energy Reviews* 22:230–45.
<https://doi.org/10.1016/j.rser.2013.02.004>
- Gong, J., A. Kostro, A. Motamed, and A. Schueler. 2016. “Potential Advantages of a Multifunc-

- tional Complex Fenestration System with Embedded Micro-Mirrors in Daylighting." *Solar Energy* 139:412–25.
<https://doi.org/10.1016/j.solener.2016.10.012>
- Konstantinou, T, and U. Knaack. 2013. "An Approach to Integrate Energy Efficiency Upgrade into Refurbishment Design Process, Applied in Two Case-Study Buildings in Northern European Climate." *Energy and Buildings* 59:301–9.
<https://doi.org/10.1016/j.enbuild.2012.12.023>
- Le Guen, M., L. Mosca, A.T.D. Perera, S. Coccolo, N. Mohajeri, and J.-L. Scartezzini. 2018. "Improving the Energy Sustainability of a Swiss Village through Building Renovation and Renewable Energy Integration." *Energy and Buildings* 158:906–23.
<https://doi.org/10.1016/j.enbuild.2017.10.057>
- Lee, S., Y. Kim, and W.K. Chong. 2015. "A Statistical Analysis of Effectiveness of Energy Policy in the United States: Incentives vs. Regulations." *Procedia Engineering* 118:1282–87.
<https://doi.org/10.1016/j.proeng.2015.08.483>
- Luddeni, G, M. Krarti, G. Pernigotto, and A. Gasparella. 2018. "An Analysis Methodology for Large-Scale Deep Energy Retrofits of Existing Building Stocks: Case Study of the Italian Office Building." *Sustainable Cities and Society* 41:296–311. <https://doi.org/10.1016/j.scs.2018.05.038>
- Marique, A.-F., and S. Reiter. 2014. "A Simplified Framework to Assess the Feasibility of Zero-Energy at the Neighbourhood/Community Scale." *Energy and Buildings* 82:114–22. <https://doi.org/10.1016/j.enbuild.2014.07.006>
- Mohajeri, N., A.T.D. Perera, S. Coccolo, L. Mosca, M. Le Guen, and J.-L. Scartezzini. 2019. "Integrating Urban Form and Distributed Energy Systems: Assessment of Sustainable Development Scenarios for a Swiss Village to 2050." *Renewable Energy* 143:810–26.
<https://doi.org/10.1016/j.renene.2019.05.033>
- Polly, B., C. Kutscher, D. Macumber, M. Schott, S. Pless, B. Livingood, and O. Van Geet. 2016. "From Zero Energy Buildings to Zero Energy Districts." *American Council for an Energy Efficient Economy- 2016 Buildings Summer Study*.
- Rifkin, J. 2004. *The European Dream*. Oxford, U.K.: Polity.
- Rocha, P., A. Siddiqui, and M. Stadler. 2015. "Improving Energy Efficiency via Smart Building Energy Management Systems: A Comparison with Policy Measures." *Energy and Buildings* 88:203–13.
<https://doi.org/10.1016/j.enbuild.2014.11.077>
- Walter, E., and J.H. Kämpf. 2015. "A Verification of CitySim Results Using the BESTEST and Monitored Consumption Values." *Proceedings of the 2nd Building Simulation Applications Conference BSA 2015*, 215–22. Bolzano, Italy: bu.press.
- Zucker, G., J. Malinao, U. Habib, T. Leber, A. Preisler, and F. Judex. 2014. "Improving Energy Efficiency of Buildings Using Data Mining Technologies." In *23rd International Symposium on Industrial Electronics (ISIE)*, 2664–69. Istanbul, Turkey: IEEE.
<https://doi.org/10.1109/ISIE.2014.6865041>

Wind and Urban Spaces. Evaluation of a CFD Parametric Framework for Early-Stage Design

Viola Maffessanti – University College London, United Kingdom – viola.maffessanti.16@ucl.ac.uk

Abstract

Outdoor comfort and microclimate have recently garnered growing interest as important factors determining the success of urban open spaces. Increasing urban density, amongst the consequences of global urbanisation, is considered environmentally positive, but can also have a negative impact on outdoor comfort and on the Urban Heat Island (UHI). Wind plays an important role in alleviating UHI and ensuring comfortable outdoor conditions. However, accelerated winds around tall buildings can cause down-draughts, negatively affecting pedestrian comfort and safety. Monitoring airflow behaviours from the earliest design stages is crucial to adjusting the design accordingly. Expensive physical wind tunnels and sophisticated Computational Fluid Dynamics (CFD) are mainly the domain of wind engineers, while there is an overall lack of fast, intuitive, and yet accurate tools for non-specialists, such as urban designers and architects, particularly involved in the first design phases, to test several design options. Recently, CFD has been fully integrated within the user-friendly and fast-responsive Parametric Design platform, where several environmental simulations can be combined. The aim of this work is to evaluate CFD parametric tools from an *accuracy* and *speed* point of view, as a possible solution for non-specialist designers to simulate wind. A CFD parametric framework describing the systematic process to correctly perform airflow simulations with these tools was set-up and included best practice guidelines, a CFD parametric model construction and verification tests. Time was recorded across all simulations. Coupling CFD and parametric design proved positive, in terms of high accuracy and modelling time reduction, thanks to the automatization of some steps. However, the simulations required a long time and some CFD specialist knowledge, limiting the use by non-specialists. Improvements to this technology, computing time reduction strategies and future research were proposed.

1. Introduction

The progressive growth in global population since the 1950s has induced the phenomenon of urbanisation, which is predicted to rise to 68% by 2050 (UNDESA, 2018), with consequential urban expansion and densification (Rose et al., 2015). Environmentally, increasing density is considered positive compared to urban expansion, as it limits land exploitation and optimizes energy efficiency and infrastructures (Rakha et al., 2017; Rose et al., 2015). However, density also entails, among other things, worsening the outdoor air quality and the solar access of open spaces and buildings, and increases the Urban Heat Island (UHI) (Du et al., 2017), negatively affecting the quality of neighbourhoods and open spaces. It is therefore important to ensure comfortable outdoor environmental conditions within the urban context (Rakha et al., 2017) and considering wind from early design stages is fundamental to improving outdoor comfort and ensuring pedestrian safety. In hot climates, shaping urban developments to encourage airflow at pedestrian level strongly improves outdoor comfort (Du et al., 2017). On the other hand, especially in colder climates, high-rise buildings cause down-draughts at pedestrian level which can affect both pedestrian comfort and safety (Blocken et al., 2012).

However, the complexity of airflow phenomena has limited wind studies and simulations to the wind engineering discipline. Expensive physical wind tunnels and Computer Fluid Dynamics (CFD), a highly accurate but time consuming technology, require specialist knowledge (Blocken et al., 2012), and are usually used at later design stages. Early-stage design is characterised by testing several design options, and therefore fast environmental simulations are vital. Faster and easy-to-

use wind simulation software exist, for example, Autodesk Flow Design or ODS-studio, but compared to CFD software (Phoenix), they were found to be either very limited in their options of modelling and grid resolution, or difficult because they involved other software. Furthermore, although flow patterns were similar, their numerical accuracy was found to be very poor compared to CFD (Sousa et al., 2015). The CFD engine Phoenix (developed by CHAM) can be connected to the Rhinoceros 3D modelling platform through the plugin RhinoCFD, which is a useful starting point for neophytes. However, the Rhinoceros platform can run only a limited number of other environmental plugins and RhinoCFD does not allow iterative optimization processes. Furthermore, it is not a freely available software and its development depends on CHAM (Chronis et al., 2017). Overall, there is a lack of fast-responsive, easy-to-use, and accurate wind simulation tools, which can also be easily combined with other environmental plugins, and be used by non-specialist designers, such as architects and urban designers, to inform early-stage design, when main decisions are made and cannot be easily adjusted at later stages (Bottema, 1999).

A possible solution was recently offered by the integration of the Computational Fluid Dynamics (CFD) technology, which requires accurate inputs and modelling to be reliable, into the user-friendly and dynamic Parametric Design tools. These tools are particularly valid because they allow for real-time geometry modification and for optimisation. Parametric design is experiencing growing success among the design community, and also in relation to the wide range of open source environmental tools made available to a very diverse public of professionals (Sadeghipour Roudsari et al., 2013). However, very limited literature is currently available on CFD parametric tools. Mackey et al., 2017, studied the impact on a case-study of four main environmental factors defining outdoor comfort, including wind, simulated through Butterfly, a CFD parametric tool. In Chronis et al., 2017, Butterfly was technically compared to two other CFD tools (Rhino-CFD and Processing FFD), and defined as promising, but currently limited by its solver's complexity and by installation difficulties,

(Mackey, 2019) which are now mostly overcome.

The main aim of this work is therefore to assess how quickly, easily, and accurately, CFD wind analysis within the parametric modelling environment can be performed by non-specialist designers at early urban design stages. In order to do this, two main criteria are specifically focused on:

- *Accuracy*, in terms of the tool's ability to provide reliable and realistic results;
- *Speed*, intended both as short simulation time, fundamental during the iterative and dynamic design early-stages, and as learning time required by non-specialists.

To meet requirements for *accuracy*, a framework outlining the systematic process to correctly perform CFD parametric simulations was developed, and also represents the novelty of this work. Necessary *time* was evaluated throughout the process.

2. Methods and Simulation

The evaluation of this emerging technology was performed through four main steps:

- Review of CFD tools compatible with Grasshopper, parametric plugin of Rhinoceros (3D modelling software).
- Research of CFD Best Practice Guidelines (BPG's), to identify recommended inputs for CFD cases set-up.
- CFD parametric framework set-up, including initial inputs, CFD parametric model construction, and verification tests.
- Testing the framework using a case-study, including qualitative and quantitative results, CFD convergence and grid-independence tests, and time recording for each simulation.

2.1 CFD Parametric Tools Review

A limited number of plugins coupling CFD and parametric design (Grasshopper) were identified within literature. They were compared using the same criteria, (Table 1) where possible, to identify the tool for this work.

Table 1 – Comparison of CFD plugins for Grasshopper (GH)

Criteria	Ansys-CFX	FFD	Swift	Butterfly
Integration into GH	Script required (Python)	Plugin required	Yes	Yes
Speed	n/a	Faster than CFD	Slower than FFD	Slower than FFD
Accuracy	High	Lower	High	High
Cost	Not free	n/a	Free	Free
Customisation (language)	n/a	Yes (Programming)	Yes (C++)	Yes (Python, easier)
Learning material	n/a	n/a	Less	More

Butterfly was selected, based on the following considerations. Ansys-CFX requires an auto-run Python script (Chronis et al., 2017; Taleb and Musleh, 2015). Fast Fluid Dynamics requires an additional plugin and, despite being much faster than CFD, is inaccurate (Chronis et al., 2017). Swift (by ODS engineering) is fully integrated in Grasshopper, is freely available, and is based on OpenFOAM which is an established and accurate open source CFD engine. However, there are only few example files, a video, and an inactive forum (<https://www.ods-engineering.com/tools/ods-swift/>). Butterfly has similar characteristics to Swift, but is written and customisable in Python, an easier programming language. It also has few example files and videos but it does have an active and responsive forum and forms part of the Ladybug Tools, an extensive spectrum of environmental plugins (Chronis et al., 2017).

2.2 CFD Best Practice Guidelines (BPG)

To reduce CFD user errors, best practice guidelines were developed by groups of international researchers to properly set-up CFD simulations. Three different sources were compared due to their availability and recent date: European COST Action 732 (Franke et al., 2007), German Association of Engineers guidelines (VDI 3783 Part 9, 2005) and AIJ the Architecture Institute of Japan publication (Tominaga et al., 2008).

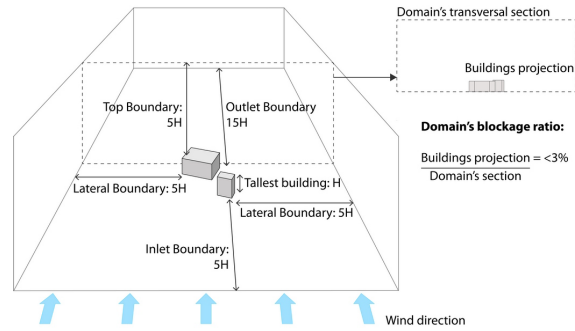


Fig. 1 – Selected domain's dimensions criteria

Criteria for this work were selected following a conservative approach (Fig. 1, Table 2) and used for setting-up the parametric model.

Table 2 – BPGs selected criteria for this work

BPG's Criteria	Selected Criteria
Mathematical Model	steady RANS
Turbulence Model	RNG k- ϵ
Blockage Ratio	<3% (priority on BPG's domain's dimensions)
Top Boundary	5H (H= tallest building's height)
Lateral Boundary	5H
Inlet Boundary	5H
Outlet Boundary	15H
Wind profile	Logarithmic Law
Min. grid resolution	Expansion ratio between 2 consecutive cells= max.1.3. Area of interest: min.10cells per building side and 10cells per volume cube root of volume.
Cells shape	Hexahedra
Refinement grid	Number of refined cells: 8 times the coarser one (2 per side); to test: min. 3 refinement levels
Probes extraction	At 1.75 m pedestrian height
Residuals reduction (CFD convergence)	Min. 5 orders of magnitude (Ferziger and Perić, 2002)

In the case-study, it was observed that using the guidelines' recommended factors, by which the tallest building height is multiplied to set all domain dimensions (Table 2: boundaries), the blockage ratio was greater than 3%, due to the blockage width resulting from the chosen wind direction. The 3% blockage ratio was therefore prioritised and the domain's dimensions were increased accordingly.

2.3 Parametric CFD Framework Definition

A CFD parametric framework was developed based on Butterfly's functionalities and BPG's, providing the necessary steps to perform a CFD parametric simulation (Fig. 2). The framework presents in grey the steps which can be parametrically set-up and in pink those which also belong to traditional CFD. It is horizontally divided in three parts: Initial inputs, CFD parametric model construction and Verification tests.

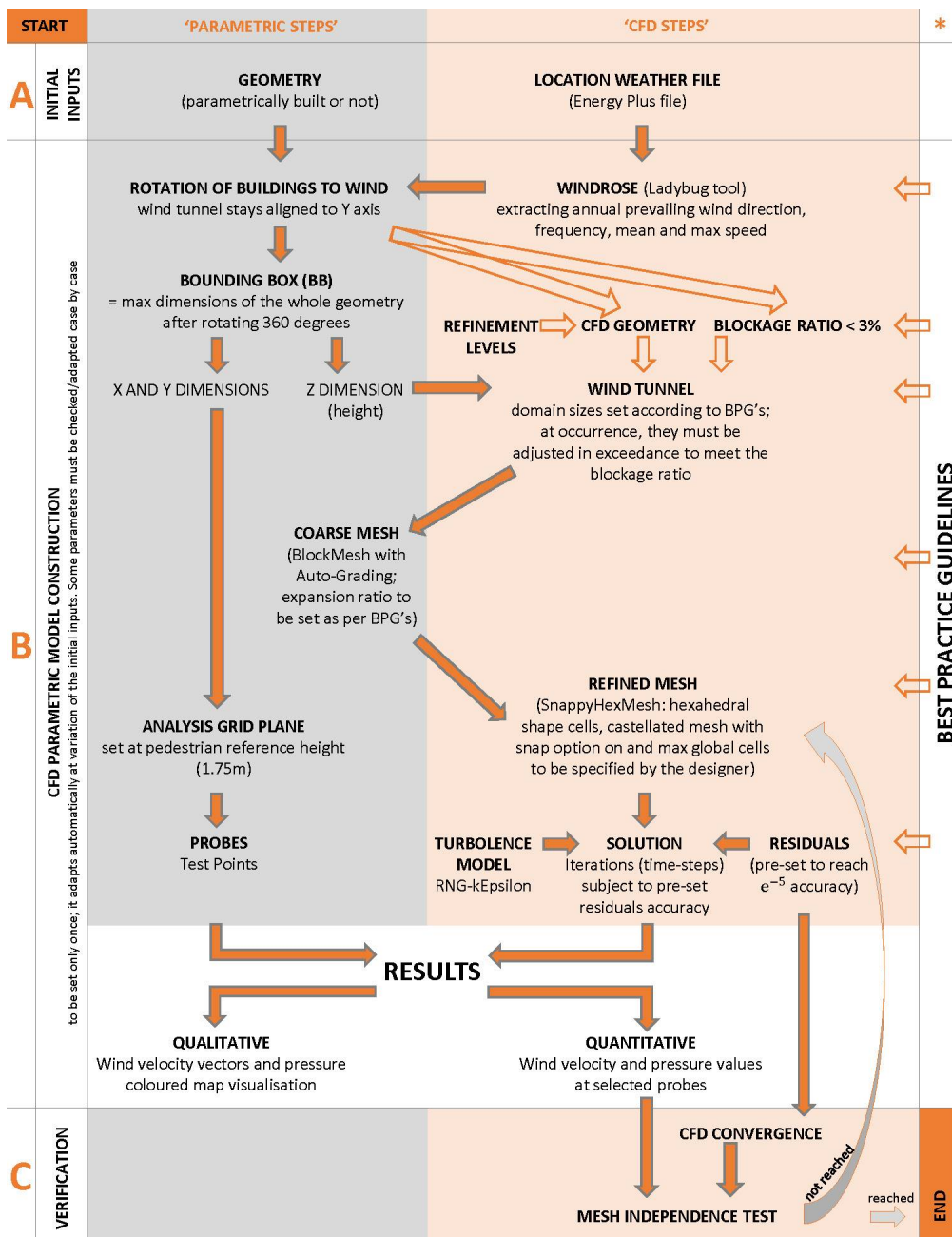


Fig. 2 – CFD Parametric framework

2.3.1 A: Initial inputs

To focus on the tool functionality, two small simplified buildings were used as a case study (Fig. 3)

(<https://github.com/ladybug-tools/butterfly-plus/tree/master/plugin/grasshopper/examplefiles>).

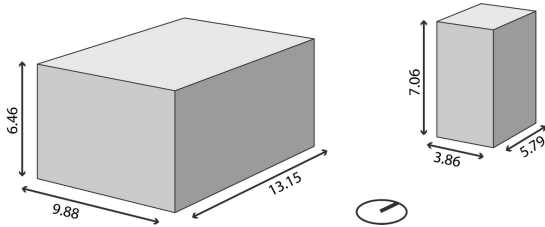


Fig. 3 – Case-study dimensions (meters) and orientation

Prevailing winds from London Gatwick Energy plus weather file were extracted with Ladybug component 'Windrose'. Average wind speed 3.45 m/s from 70 degrees direction was used.

2.3.2 B: CFD parametric model

A CFD model was built by combining existing Butterfly and Ladybug workflows, further parametrically tuned. The resulting model is a pre-set workflow, where the weather file and wind characteristics, geometry, and refined grid settings are the sole inputs to be updated for each case-study, while most functionalities automatically update. For example, the geometry is set to automatically rotate by the chosen wind direction angle (Fig. 4).

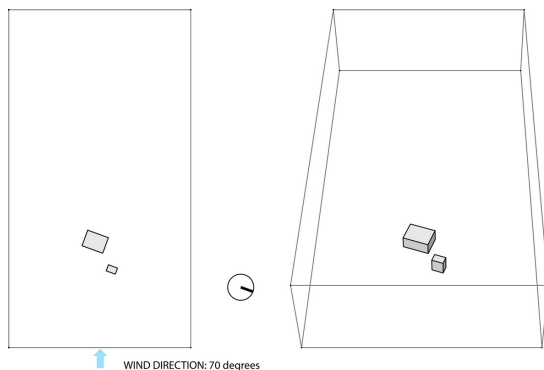


Fig. 4 – Automatic rotation of the geometry to the wind

Furthermore, the domain's dimensions, which depend on the height of the tallest building, are parametrically linked to it and automatically adjust

at height variation.

The recently implemented Autograding component parametrically generates the Openfoam coarse grid: denser (in this case-study: 1 m cell size) around the case-study and progressively less dense towards the domain's top and ends, following the set expansion ratio of 1.2 (Fig. 5).

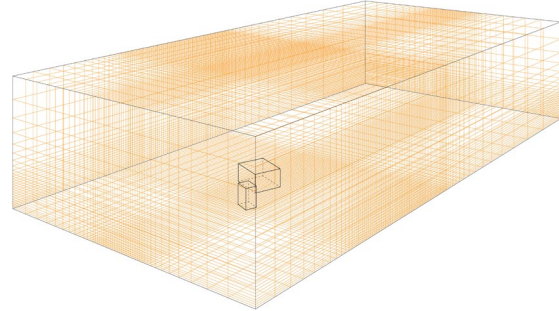


Fig. 5 – Coarse grid generated by the Autograding component

On the area of interest, Openfoam also requires the application of a refined hexahedral grid (SnappyHexMesh) which is, instead, case-specific. To define an appropriate grid refinement, six progressively finer grids were tested by setting the maximum global cells to 10 million, and by changing the BF 'refineLevels_' parameter in the "createBFGGeometry" component, using the values: (0,0), (1,1), (2,2), (3,3), (4,4) and (5,5) (Fig. 6), leaving all other parameters as "default". Consequentially, in each test, the number of global cells progressively increased with the grid refinement.

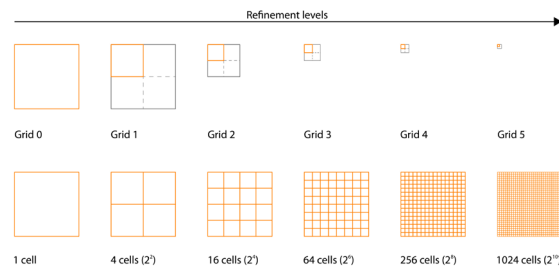


Fig. 6 - Refinement levels tested in the case-study

2.3.3 C: Verification tests

CFD solutions are only approximate to reality as they are based on the discretisation method. It is therefore crucial to perform verification tests to quantify uncertainty and ensure numerically accurate results (Roache, 1997). For each simulation, CFD convergence and grid independ-

ence tests were performed. The first are necessary to control the extent of iterative errors and ensure that each solution ran through enough iterations to achieve results close to reality. Logarithmic graphs of the residuals were plotted to verify convergence. Grid independence tests must be performed on at least three different grids to ensure that results only depend on boundary conditions and not on the grid refinement (Ferziger and Perić, 2002). Velocity and pressure values were extracted for each of the six grids tested in this work, and the error Root Mean Square (RMS) was calculated to estimate the discretisation error of each coarser grid compared to grid 5, the finest grid. Verification tests are key to determine each simulation's *accuracy*.

2.4 Framework Test on Case Study

The framework was tested in the case study, qualitative and quantitative results were extracted, and verification tests performed for each simulation. *Time* spent on meshing and solution processing was recorded to observe its variation with the increase in grid resolution. An appropriate grid refinement was then identified for this case study, which could reach the fastest solution without excessively compromising on accuracy.

3. Result Analysis and Discussion

The aim of this work was to assess CFD parametric tools for non-specialists at early design stage, focusing on *accuracy* and *speed*. A framework representing the correct simulation process was set up and tested on a case-study, and simulation time was recorded.

3.1 Result Analysis

Test results were used to evaluate the whole process from the point of view of *accuracy* and *speed*. In terms of *accuracy*, CFD parametric tools are interfaces of CFD engines, and therefore they also match their high accuracy. However, comparing quantitative and qualitative results of 6 different grids, it emerged that correctly setting-up and verifying simulations was important in order

to avoid compromising results. CFD convergence was achieved for the first 5 coarser grids, reaching the 5th order of magnitude (Table 2), meaning that the CFD solution process was complete and correctly representing reality. On the residuals graph of the most refined grid 5, pressure residual only reached a 4th order of magnitude, fluctuating horizontally after almost 8 simulation hours. To exclude the risk of divergence, the solution ran for a total of 17 hours and 39 minutes (3082 iterations), compared to 1.5 hours for grid 4 and 10 minutes for grid 0 (approximately 1250 iterations) (Fig. 7).

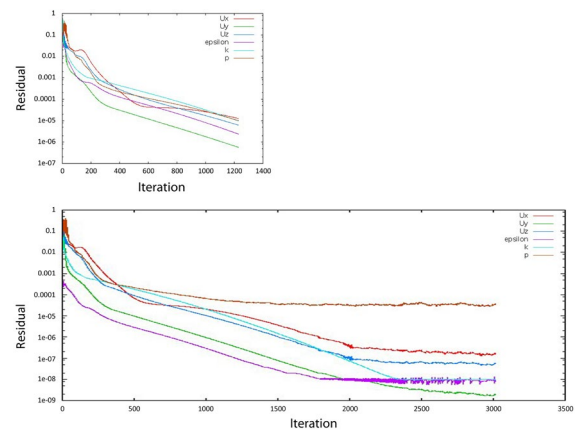


Fig. 7 – Residuals logarithmic graphs: grid 0, above, grid 5, below

Grid independence tests, calculating error RMS for each grid compared to the most refined, showed that the error progressively decreased with the increase in the grid's refinement (Fig. 8, 9, 10). Grid 4 was the coarsest grid maintaining an acceptable numerical error, and its results were therefore considered grid-independent.

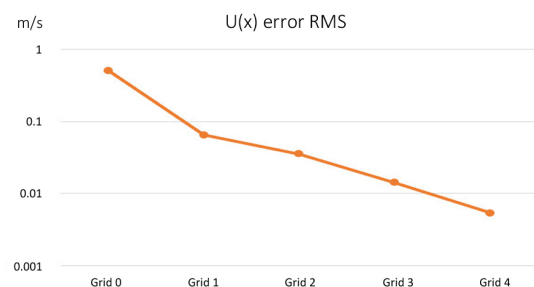


Fig. 8 – Error RMS graph: velocity U(x)

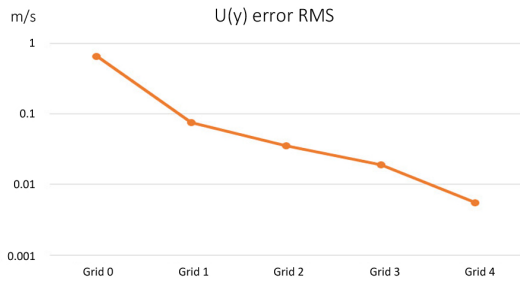


Fig. 9 – Error RMS graph: velocity U(y)

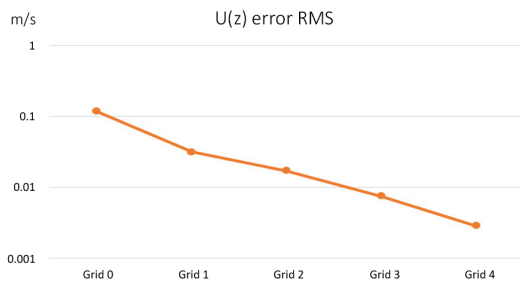


Fig. 10 – Error RMS graph: velocity U(z)

Differences across the six grids were also visually noticeable when comparing qualitative maps, particularly around the building corners and despite the low wind speed simulated (Fig. 11).

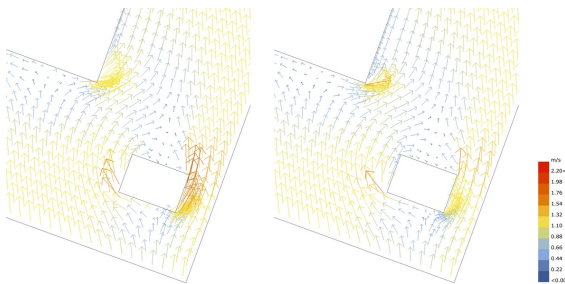


Fig. 11 – Velocity vectors: grid 0, left, and grid 5, right

Numerical and visual errors could be explained by observing the quality of the grids 0 and 5 applied on the modelled buildings (Fig. 12, in orange); grid 0 deformed the geometries of the buildings, particularly in the corners, confirming visually to be too coarse.

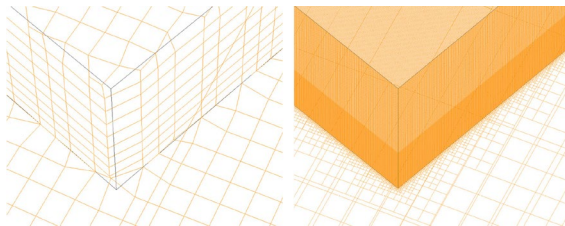


Fig. 12 – Refined grid: refinement level 0, left, and level 5, right

In terms of *speed*, modelling time was reduced thanks to parametric tool: once the framework is correctly set-up, it can be applied to several cases by only updating the inputs and tuning a few parameters. However, time required for both meshing and CFD solution exponentially increased with the grid refinement (Fig. 13).

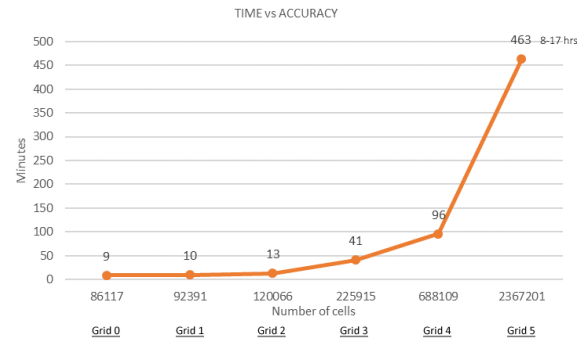


Fig. 13 – Time versus Accuracy diagram

Total time spent on performing the whole simulation was about 20 hours, which are a significant amount for a small case study and low wind speed. Grid 4 achieved reliable results in a reasonable time, and was consequently considered appropriate for this case study.

3.2 Discussion

Computational Fluid Dynamics is generally a time-consuming technology during modelling, meshing, running the solution and verification. The integration of CFD into the parametric design meant a considerable reduction of the initial modelling time, as once set-up the first time, the model can be re-used by only adjusting a small number of parameters. Furthermore, wind simulations can be included more easily in studies involving other environmental tools, for example for assessing outdoor comfort. However, considerable time was still required for accurate simulations, heavily affecting the use of these tools during early design stages, when simulation time should ideally not exceed a few minutes, particularly when testing design options, combining various environmental analyses or performing design optimization. Computational cost mainly depends on the speed of current computers for meshing and running the solution,

and on a long verification process, which, however, was demonstrated to be fundamental; using too coarse grids to speed-up the process may cause misleading results.

3.2.1 ‘Speed *versus* Accuracy’ dilemma: a matter of technological progress

Possible time-reduction strategies to overcome CFD bottlenecks were therefore investigated.

Reducing number of CFD simulations

For long annual hourly simulations, for instance, Ladybug tools developers suggest the use of so-called Wind Factors: only 36 simulations were run to cover the wind rose directions, and results divided by the correspondent weather file wind speed. For each direction, multiplying the wind factor by any meteorological wind speed, the local wind speed could be obtained without re-running CFD simulations each time. It was also noted that reducing the 36 simulations to only 2, the Universal Thermal Comfort Index (UTCI) results were very similar (Mackey et al., 2017). Further testing of this method may provide interesting results.

Adaptive grid refinement

An existing technology to identify the best grid refinement is the *adaptive grid refinement*, which predicts the wind pattern and refines the grid only where required (Kim and Boysan, 1999). This function is already available in Openfoam (Berce 2010; Karlsson, 2012), and could be implemented in CFD parametric tools using this engine.

Computational technologies

For this work’s case study, the same simulation ran for 1.5 hours on a laptop (Windows 10, 64 bit, 4 CPU, base speed: 2.0 GHz) and in 25 minutes on a desktop (Windows 10, 6 CPU; base speed: 3.7 GHz); computer speed and performance are crucial. Running simulations in parallel, meaning on more computer processors at the same time and combining results in post-processing (Greenshields, 2018), is a common function available both in Openfoam and Butterfly. The future of CFD technology greatly depends on High-Performance Computers, especially with parallel and hybrid computing architectures. Emerging technologies linked to quantum computing and advanced

3D memory are also promising (Slotnick et al., 2014). Artificial Intelligence (AI) was recently implemented for the creation of digital twins, which, through algorithms, can predict and reproduce virtual representations of airflow around buildings in real-time, with speeds 1000 greater than anything else currently available (Akselos, 2019). Finally, combining CFD with animation software using Langrarian Fluid (e.g. Autodesk Maya) or Eulerian approaches (e.g. SideFX Houdini) may greatly improve computational cost; however, meshing and results quality require further verification (Kaushik and Janssen, 2015).

3.2.2 Another type of ‘Speed *versus* Accuracy’ dilemma: a matter of purpose

Despite the reduced modelling time, substantial *time* and effort are required for running simulations and also for neophytes to sufficiently learn CFD, the parametric tool and its correct use. Indeed, the tool’s accuracy cannot be compromised; however, the *accuracy* of the results could be evaluated against reality by assessing an ‘acceptable error’ in relation to the purpose and scale of the simulation. Unlike other disciplines (e.g. aeronautical engineering) that require a high degree of accuracy, a greater error compared to reality may be tolerable in wind simulations for urban comfort. However, for early-stage design, although characterized by a simplified representation of urban context and architecture, wind simulation tools should be sufficiently accurate to correctly reproduce wind phenomena around and between buildings, and model turbulence, particularly in the presence of tall buildings, to provide correct indications for the design development. Consistent comparison of results of simpler and faster wind simulation tools with reality and CFD could verify these conditions and help define an acceptable error, leading to interesting findings on available technologies for non-specialists to consider wind as a driver of early-stage urban design.

4. Conclusion

This work aimed to evaluate CFD parametric tools for non-specialists to quickly, easily, and accurately simulate wind behaviour in early-stage urban design iterations. The necessary process to carry out simulations correctly and ensure accuracy of results was researched and a CFD parametric framework was set-up and tested. Although CFD parametric tools are equivalent in *accuracy* to their established CFD engines, the results demonstrated how their correct use is crucial. Regarding *speed*, CFD parametric tools can considerably reduce the modelling time and be integrated with other environmental plugins. However, significant time was still required to run simulations and perform verification tests, despite the small scale of the case study and low wind speed used. Existing simulation time reduction strategies, and ongoing and future developments of computer technology were explored. Finally, reflecting on the level of accuracy required for urban scale studies, further research could focus on faster and yet sufficiently accurate tools for designers to correctly simulate wind from the earliest stages of urban design.

Acknowledgement

A grateful acknowledgment to Dr. Dimitrios Rovas for his invaluable support. Thank you also to Fred Labbé, Theodore Galanos, Ladybug Tools Forum, Charles Collin, Sean Weston, David Avital, and to Astudio Architects: Directors Richard Hyams and Roger Bradshaw, and Manteer Bhambra.

References

- Akselos. 2019. "Technology". Accessed September 20, 2019. www.akselos.com/technology.
- Berce, A. 2010. "OpenFOAM Tutorial Anton Berce, Chalmers / Solid and Fluid Dynamics." *Fluid Dynamics* 1–24.
- Blocken, B., W. D. Janssen, and T. van Hooff. 2012. "CFD Simulation for Pedestrian Wind Comfort and Wind Safety in Urban Areas: General Decision Framework and Case Study for the Eindhoven University Campus." *Environmental Modelling and Software* 30: 15–34. doi: 10.1016/j.envsoft.2011.11.009.
- Bottema, M. 1999. "Towards Rules of Thumb for Wind Comfort and Air Quality." *Atmospheric Environment* 33 (24–25): 4009–17. doi: 10.1016/S1352-2310(99)00142-9.
- Chronis, A., A. Dubor, E. Cabay, and M. Sadeghipour Roudsari. 2017. "Integration of CFD in Computational Design - An Evaluation of the Current State of the Art Integration of CFD in Computational Design An Evaluation of the Current State of the Art." In *ECAADe 2017: Proceedings of the 35th International Conference on Education and Research in Computer Aided Architectural Design in Europe*.
- Du, Y., C. Ming Mak, K. Kwok, K.-T. Tse, T. Lee, Z. Ai, J. Liu, and J. Niu. 2017. "New Criteria for Assessing Low Wind Environment at Pedestrian Level in Hong Kong." *Building and Environment* 123: 23–36. doi: 10.1016/j.buildenv.2017.06.036.
- Ferziger, J. H., and M. Perić. 2002. *Computational Methods for Fluid Dynamics*. Berlin, Heidelberg: Springer Berlin Heidelberg. doi: 10.1007/978-3-642-56026-2.
- Franke, J., A. Hellsten, H. Schlünzen, and B. Carissimo. 2007. "Best Practice Guideline for the CFD Simulation of Flows in the Urban Environment." *COST Action*. Vol. 44.
- Greenshields, C. 2018. "OpenFOAM v6 User Guide: 3.4 Running Applications in Parallel." CFD Direct-The Architects of OpenFOAM. 2018. <https://cfd.direct/openfoam/user-guide/v6-running-applications-parallel/>
- Karlsson, J. 2012. "Implementing Anisotropic Adaptive Mesh Refinement in OpenFOAM."
- Kaushik, V., and P. Janssen. 2015. "Urban Wind Flow: Investigating the Use of Animation Software for Simulating Windflow around Buildings." *Real Time - Proceedings of the 33rd ECAADe Conference - Volume 1*:225–34.
- Kim, S.-E., and F. Boysan. 1999. "Application of CFD to Environmental Flows." *Journal of Wind Engineering and Industrial Aerodynamics* 81:145–58. doi: 10.1016/S0167-6105(99)00013-6.
- Mackey, C., T. Galanos, L. Norford, M. Sadeghipour Roudsari, and N. Sdn Bhd. 2017. "Wind, Sun, Surface Temperature, and Heat

- Island: Critical Variables for High-Resolution Outdoor Thermal Comfort." *Proceedings of Building Simulation 2017*: 985–93.
- Mackey, C. 2019. [www.github.com/ladybug-tools/butterfly/wiki/1.-blueCFD-Core-\(OpenFOAM\)-Installation](https://www.github.com/ladybug-tools/butterfly/wiki/1.-blueCFD-Core-(OpenFOAM)-Installation) (accessed September 21, 2019).
- Rakha, T. P. Zhand, and C. Reinhart. 2017. "A Framework for Outdoor Mean Radiant Temperature Simulation: Towards Spatially Resolved Thermal Comfort Mapping in Urban Spaces." *Proceedings of Building Simulation 2017*: 2414–20.
- Roache, P. J. 1997. "Quantification of Uncertainty in Computational Fluid Dynamics." *Annual Review of Fluid Mechanics* 29 (1):123–60. doi: 10.1146/annurev.fluid.29.1.123.
- Rose, C. M, E. Saratsis, S. Aldawood, T. Dogan, and C. Reinhart. 2015. "A Tangible Interface for Collaborative Urban Design for Energy Efficiency, Daylighting, and Walkability." *Proceedings of Building Simulation 2015*: 2691–98.
- Sadeghipour Roudsari, M., M. Pak, and A. Smith. 2013. "Ladybug: A Parametric Environmental Plugin for Grasshopper To Help Designers Create an Environmentally-Conscious Design." *Proceedings of Building Simulation 2013*: 3129–35.
- Slotnick, J., A. Khodadoust, J. Alonso, D. Darmofal, W. Gropp, E. Lurie, and D. Mavriplis. 2014. *CFD Vision 2030 Study: A Path to Revolutionary Computational Aerosciences*.
- Sousa, J. Pack Melo, R. A. Castro Moya, D. Prohasky, and C. E. Verzola Vaz. 2015. "Empirical Analysis of Three Wind Simulation Tools to Support Urban Planning in Early Stages of Design." *Anais Do XIX Congresso Da Sociedade Ibero-Americana de Gráfica Digital* 2015. doi: 10.5151/despro-sigradi2015-80189.
- Taleb, H., and M. A. Musleh. 2015. "Applying Urban Parametric Design Optimisation Processes to a Hot Climate: Case Study of the UAE." *Sustainable Cities and Society* 14: 236–53. doi: 10.1016/j.scs.2014.09.001.
- Tominaga, Y., A. Mochida, and R. Yoshie. 2008. "AIJ Guidelines for Practical Applications of CFD to Pedestrian Wind Environment around Buildings." *Journal of Wind Engineering and Industrial Aerodynamics* 96: 1749–61. doi: 10.1016/j.jweia.2008.02.058.
- UNDESA. 2018. *World Urbanization Prospects: The 2018 Revision*.
- VDI. 2005. *VDI 3783 Part 9, 2005. Environmental Meteorology— Prognostic Microscale Wind Field Models – Evaluation for Flow around Buildings and Obstacles*. Beuth Verlag, Berlin. doi: 10.1007/978-94-009-2939-5.

Analysis of Two Shading Systems in a Glazed-Wall Physiotherapy Center in Bolzano, Italy

Luca Zaniboni – Free University of Bozen-Bolzano, Italy – Luca.Zaniboni@unibz.it

Giovanni Pernigotto – Free University of Bozen-Bolzano, Italy – Giovanni.Pernigotto@unibz.it

Andrea Gasparella – Free University of Bozen-Bolzano, Italy – Andrea.Gasparella@unibz.it

Abstract

This work presents a study of a physiotherapy center located in the southern area of Bolzano, discussing its indoor visual comfort conditions, energy consumption for artificial lighting and daylight exploitation. Specifically, three South-West oriented physiotherapy cabins with large glazed façades were analyzed, using both measurements, in-situ subjective surveys, and simulations. First, illuminance measurements and visual comfort questionnaire responses were analyzed to detect possible issues related to the lighting system and the visual environment in the therapy cabins. Daysim models were then developed, compared with empirical data and deployed to assess advantages and drawbacks of the internal double layer roller shades. Finally, an alternative external venetian blinds system was proposed and studied.

1. Introduction

Maximization of daylight is fundamental for lighting energy saving. For this reason, as well as for architectural reasons, modern buildings often have large glazed façades. However, drawbacks of this design approach are an increased risk of glare and flash blindness, of building overheating due to solar gains, and of larger recourse to the installed cooling capacity. Furthermore, Hernández et al. (2017) remarked that also productivity is influenced by daylight.

To prevent these negative effects, proper shading systems and controls should be designed and operated. To do so, as observed by Bellia et al. (2014), indexes like the Daylight Autonomy DA and the Useful Daylight Illuminance UDI should be calculated, and the glare risk evaluated. Moreover, the integrated analysis on daylight, artificial

lighting system and shading devices is necessary to optimize both energy performance and occupants' comfort in the early design stage. The importance of reducing the number of shading operations was clarified by Xiong and Tzempelikos (2016). They developed a model-based algorithm for lighting and shading control, aiming to minimize lighting energy use while taking into account the three visual comfort criteria of DGP, vertical illuminance and work plane illuminance. A variable-control interval logic was developed and implemented in full-scale test offices, resulting in the reduction in the number of the shading operations without compromising their benefits, thus decreasing the disturbance of the occupants and increasing the equipment's lifespan. In this framework, simulation tools can be useful for the design of both lighting systems and daylight exploitation components. For instance, Freewan (2014) used IES/SunCast and Radiance simulations to study solar and daylight distribution on office surfaces during the year. Atzeri et al. (2014) used EnergyPlus to simulate different configurations of an open-space environment in Rome with outdoor and indoor shades. It was found out that the thermal comfort is always improved by the use of shades, but the energy demands can increase with some configurations: in particular, it does with internal devices, depending also on the orientation and the glazing type. Lau et al. (2016) simulated twenty office buildings in Kuala Lumpur, Malaysia, using IES VE to analyze the performances of different shading devices. Tuma and Ouahrani (2017) ran an EnergyPlus simulation, experimentally validated, in order to evaluate the annual energy savings achievable from the use of brise-soleil and venetian blinds on the south and north external façades of office spaces in Doha, Qatar. After a survey and in-situ

measurements, Maachi et al. (2019) used 3DSMax and Matlab to simulate and process the luminance level in collective housing.

Finally, when dealing with existing buildings, simulations can be combined not only with measurements but also with questionnaires to check the efficiency of existing shading devices and the need for intervention. For example, Day et al. (2019) collected physical data measurements and surveys to characterize the visual comfort perception in three large commercial office buildings, finding a relationship between daylight and perceived level of productivity and satisfaction.

In this work, a physiotherapy center located in the southern area of Bolzano, Italy, was investigated to evaluate the performance of the existing roller shading system, i.e. internal double layer roller shades. Objective and subjective assessments were performed by measuring illuminance in-situ and collecting the answers to questionnaires completed by the occupants during the period from July 2018 to April 2019. After detecting the main problems and advantages of the existing system installed, a Daysim model was developed and used to analyze an alternative venetian blinds system, by considering daylight exploitation, glare probability and solar gains.

2. Case Study

The study focuses on a physiotherapy center located on the fourth floor of a 2015 building in the southern area of Bolzano, Italy. The three rooms analyzed (namely Room 1, 2 and 3) were characterized by large glazed façades facing South-West, where static physiotherapy therapies are performed (Fig. 1). With respect to Rooms 1 and 2, with the external façade almost entirely glazed, in Room 3 the transparent portion is limited to about 25 %.

The shading system installed in the three rooms is a double layer (light and thick) internal roller shades system, with a visual transmittance of 0.3 and 0.05 respectively for the two layers (Fig. 2 left). Each one can be operated separately by the users through two switches. Dimmable lights with manual controls have been installed, with a total power of 84 W (Fig. 2 right).

The center opens from 8:00 am to 8:00 pm, with only one therapist and one patient in each cabin at a time. Typically, the patient lies on a therapy bed, with the operator standing on the side.

3. Methods

3.1 Visual Survey

First, a visual survey was conducted in the three rooms. Data regarding the geometry, the indoor surfaces, the windows and the shading devices, as well as the plants configuration and operating schemes were collected and analyzed. The technical datasheets delivered from the building's designer were the main source, integrated with in-situ measurements when necessary.



Fig. 1 – External view of the building and map of the physiotherapy center with the treatment cabins considered in this study highlighted



Fig. 2 – The double layer internal roller shades devices (left) and the lighting system installed in the three cabins (right)

3.2 Measurements and Questionnaires

Short-term measurements of illuminance on the therapy bed and on the desk were taken during the whole period of analysis, at different times of the day and the measurement was repeated with different configurations of lights and shadings systems. The following instruments were used:

1. a Delta Ohm h32.1 Thermal Microclimate data logger with an LP 471 PHOT illuminance probe with a resolution of 0.01 lx up to 199.99 lx, 0.1 lx

between 200 and 1999.99 lx, 1 lx between 2000 lx and 19999 lx and 10 lx until 199990 lx;

2. a Konika Minolta Illuminance Meter T-10A portable luxmeter with 1 lx resolution and maximum illuminance measurement of 299900 lx.

Questionnaires were developed based on ASHRAE Standard 55 (2017), EN ISO 7730:2005 and some previous work available in the literature (Azizpour et al., 2013; Hwang et al., 2007; Ricciardi and Buratti, 2009 and 2018; Skoog et al., 2005; Van Gaever et al., 2014; Verheyen et al., 2011). Lighting questions were included in an overall comfort questionnaire used in a previous study (Zaniboni et al., 2016). Two different sections in the questionnaires were developed to be completed respectively by physiotherapists and patients. The questionnaires included questions about date, time, general information about the respondent (i.e. age, weight, height, gender and health status) and the room where the therapy was performed. The questions regarding visual comfort comprised two 7-point scale questions about light and daylight satisfaction and a multiple-choice question regarding visual comfort problems, with the following options: glare, flash blindness, too low light, too high light, other and nothing. The questions needed to be answered by both occupants immediately before the therapy.

3.3 Simulation

Daylight simulations were performed considering the existing internal roller shades system and an alternative configuration with external venetian blinds, with 5 cm thick slats, 45° tilted, spaced 5 cm apart from each other and with a reflectance of 0.5. The simulations were run with Daysim, working with the Honeybee and Ladybug Grasshopper plugins of Rhinoceros (Figs 3 and 4). Occupancy, visible transmittance, and lighting power data from the visual survey were used as inputs. The reflectance of the opaque surfaces was estimated using the Radiance Color Pickler online tool (Jaloxa, 2009).

A maximum number of 5 ambient bounces was set for the rays in the simulation environment, in order to have a good balance between simulation accuracy and computational effort. The grid size was set to 0.25 m, at a height of 0.8 m from the floor, following

the suggestions of EN 12464-1:2011 for “Health care premises – Massage and radiotherapy”. The target illuminance was set equal to 300 lx, and a manual on/off switch set for lighting control.

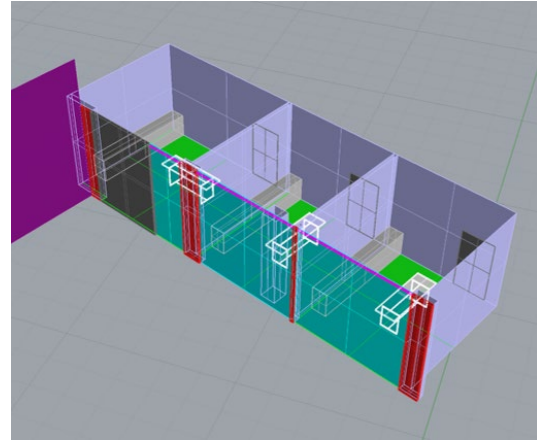


Fig. 3 – Rhinoceros geometrical model of the facility

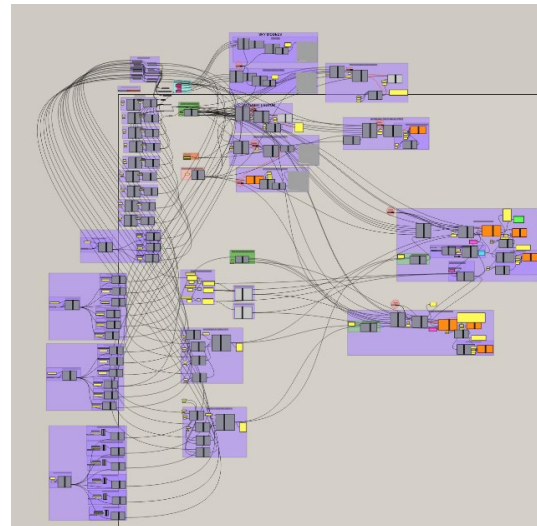
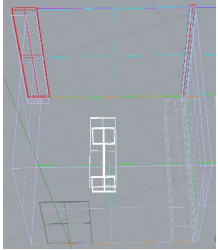
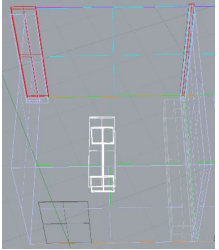
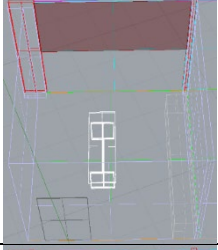
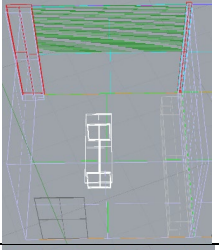
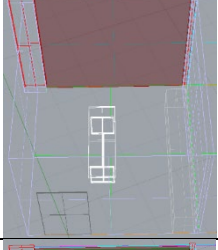
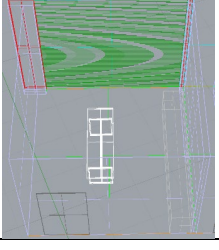
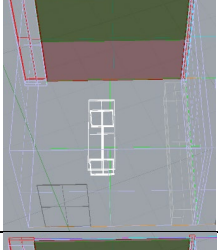
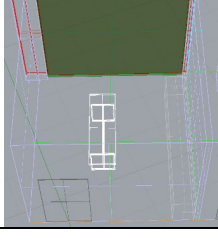


Fig. 4 – Honeybee Grasshopper model of the facility

The model was validated by comparing point-in-time measurements and simulations in the three cabins, using a weather file prepared with the global hourly horizontal irradiation data collected by the nearby meteorological station at Bolzano Hospital (Provincia Autonoma di Bolzano, 2019). After validation, annual simulations were run using the typical meteorological file included in EnergyPlus EPW weather file (EnergyPlus, 2019). Three types of outputs were obtained from annual simulations: (1) daylight availability on the work plane, expressed through daylight metrics and annual energy uses for lighting; (2) Daylight Glare Probability DGP, evaluated in the worst condition for the occupants

and considering different shading positions (Table 1); (3) total solar gains entering in the room with the two shading systems.

Table 1 – The different states considered with the two shading systems

	Roller Shades	Venetian Blinds
State 1		
State 2		
State 3		
State 4		
State 5		

Due to the different layouts of the three rooms, daylight availability and energy uses for indoor lighting were assessed, by considering the shading systems controlled by different lighting sensors: a control (Group 1) was adopted for Rooms 1 and 2 and a second one (Group 2) for Room 3 (Fig. 5 left). For

each, the shadings were lowered when the illuminance was larger than 2000 lx and raised when smaller than 300 lx at sensor's position. Considering that the patients lie on the beds looking at the doors, the risk of glare was considered higher for the therapist. Furthermore, the risk was found higher in Room 1 because it had the largest glazed area.

As a consequence, DGP analysis were performed for Room 1 with the subject looking at the window (Fig. 5 right). For similar reasons, the entering solar gains were assessed only in Room 1.

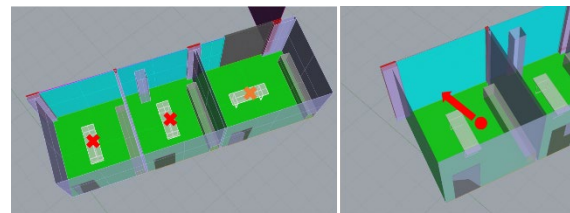


Fig. 5 – The position of the sensors in the three rooms (on the left): in color red the Group 1 sensors and in orange color the Group 2 one. On the right, the worst glare condition in the case-study for a therapist in Room 1

4. Results

In terms of the subjective assessment, 25 questionnaires were collected in the cabins during the analysis period. Occupants were very satisfied with the visual conditions, with 96% of therapists' and 88% of patients rating 7, the maximum satisfaction. Moreover, 96% and 92% of the answers, respectively by therapists and patients, reported a rating of 7, to the daylight satisfaction, while 100% and 88% stated that no visual comfort problems were present. The collected measurements showed that peaks over 2000 lx are present on the rooms' beds only when no shadings or just light shades are used. The objective assessment made it possible to check that the artificial lighting system is able to meet the EN 12464-1 requirements of 300 lx. Annual simulations with the current configuration confirmed that shading is almost not necessary in Room 3 (Control Group 2) and that, in the other two rooms (Control Group 1), the internal roller shades system is working well in preventing glare problems and also ensuring a good level of daylight. Nevertheless, the roller shades required 1054 movements to avoid the glare discomfort and do not prevent high solar gains during the summer period.

Simulations were subsequently repeated using venetian blinds as shading system. As shown in the DGP charts in Fig. 6, both systems are able to comply with the tolerance limit of 0.45 in the worst condition in Room 1, with few exceptions for the venetian blinds. Regarding the usage of the two shading systems (as shown in Figs 7 and 8 for the Control Group 1), it can be observed that the venetian blinds can ensure the same result as the roller shades but with only 693 movements during a typical year. Continuous daylight autonomy and Useful Daylight Illuminance (Table 2) showed that both systems ensure a high daylight exploitation. Values of Spatial Daylight Autonomy ($sDA_{300, 50\%}$) of 65.13 % and 67.02 % were obtained with roller shades and venetian blinds, respectively. Total annual power consumption for indoor lighting in Room 1 is 95.9 kWh_{el}/year for the current solution

and 84.8 kWh_{el}/year for the alternative solution (12 % less).

As regards the solar gains in Room 1, since the roller shades are installed inside, all solar gains enter the room. In contrast, external venetian blinds can prevent 2359.1 kWh and 3421.4 kWh thermal gains from being admitted into the thermal zones, during heating (15/10–15/04) and cooling (16/04–14/10) periods, respectively (Fig. 9). Although the reduction of solar gains in the heating period can increase the energy needs for space heating, their reduction in the cooling period can be beneficial and bring energy savings. Considering that the blocked gains are larger in the cooling period, advantages from savings in energy use for space cooling are expected to balance out the potential increase in energy use for space heating.

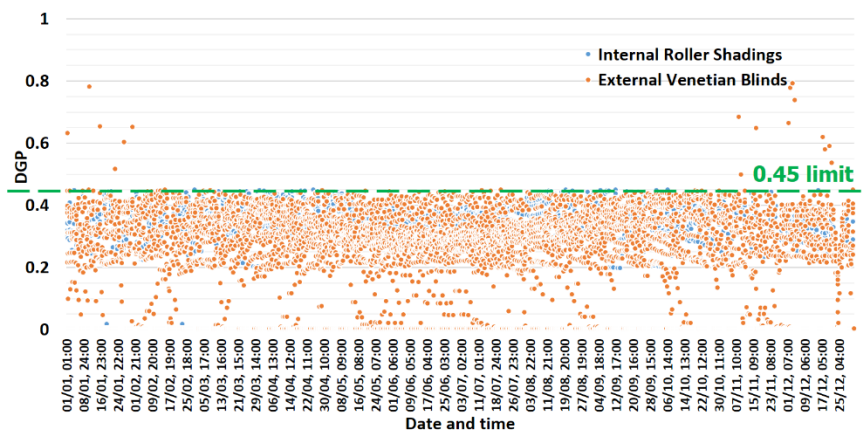


Fig. 6 – Daylight Glare Probability with the two systems

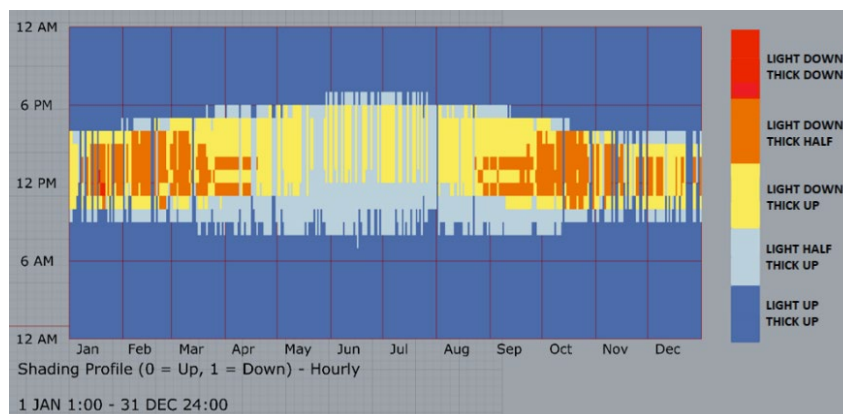


Fig. 7 – Shading states during the year with internal roller shades system

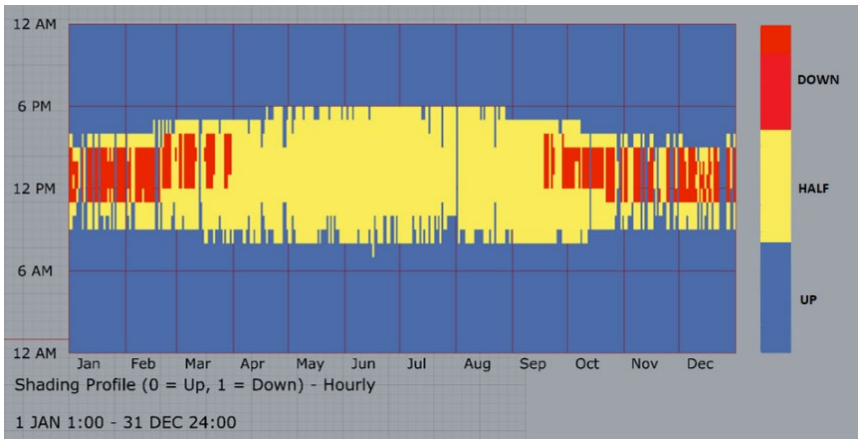


Fig. 8 – Shading states during the year with external venetian blinds

Table 2 – Continuous Daylight autonomy and Useful Daylight Illuminance with the current and the alternative solution

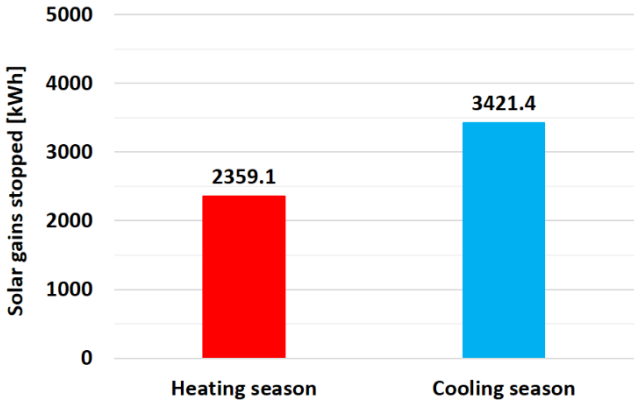
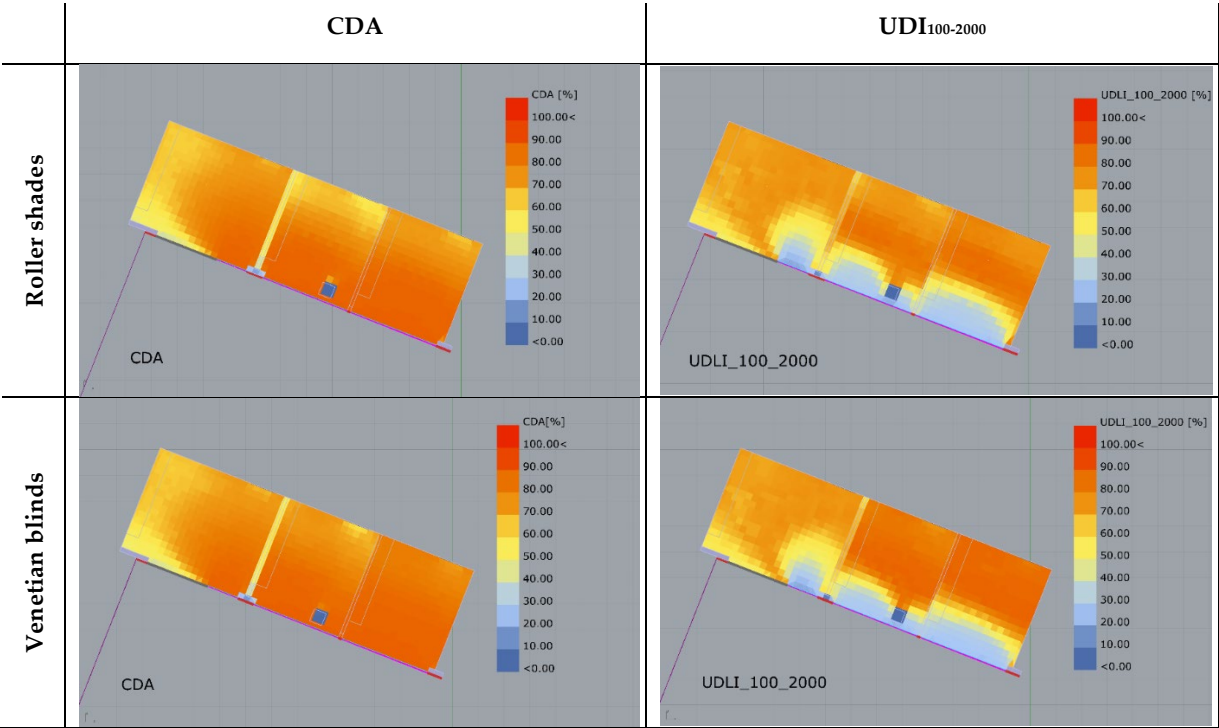


Fig. 9 – Solar gains blocked by the venetian blinds system in heating and cooling seasons in Room 1

5. Discussion and Conclusions

In this work, visual comfort and the lighting energy performance of a physiotherapy center in Bolzano, Italy, were analyzed through in-situ measurements, subjective surveys, and simulations. First, objective and subjective assessments were performed to see if the current internal double roller shades can prevent risks of glare and provide a good daylight exploitation. Then, an alternative shading system, i.e. external venetian blinds, was proposed to limit solar gains and reduce the lighting and cooling energy consumption. In order to perform a comparison, a model of the case-study was prepared using Rhinoceros and the Grasshopper plugins Ladybug and Honeybee, which couple the parametric working environment with Daysim. In particular, besides risk of glare and daylight, aspects related to shadings controls and movements and excess of solar gains in the therapy rooms were investigated.

It was observed that:

- In the current configuration, with a good managing of the shadings, there are no problems of glare. This is also confirmed by the measurements and the questionnaire survey, where both therapists and patients did not indicate the presence of glare or visual discomfort issues.
- Although both systems are effective in preventing visual discomfort, external venetian blinds are simpler to manage and allows a saving of 12 % of the energy consumption for indoor lighting in one of the rooms.
- Finally, the adoption of external venetian blinds can reduce the solar gains during summer and, thus, the load for space cooling as an additional benefit.

Acknowledgement

This study has been funded by the project “Klimahouse and Energy Production” in the framework of the programmatic-financial agreement with the Autonomous Province of Bozen-Bolzano of Research Capacity Building.

References

- American Society of Heating, Refrigerating, and Air-conditioning Engineers. 2017. *ASHRAE Standard 55: Thermal environmental conditions for human occupancy*. Atlanta, GA.
- Atzeri, A., F. Cappelletti and A. Gasparella. 2014. Internal versus external shading devices performance in office buildings. *Energy Procedia* 45: 463-472.
- Azizpour, S., S. Moghimi, E. Salleh, S. Mat, C.H. Lim, K. Sopian. 2013. “Thermal comfort assessment of large-scale hospitals in tropical climates: A case study of University Kebangsaan Malaysia Medical Centre (UKMMC).” *Energy and Buildings* 64: 317-322.
- Bellia, L., C. Marino, F. Minichiello and A. Pedace. 2014. “An overview on solar shading systems for buildings.” *Energy Procedia* 62: 309 – 317.
- Day, J.K., B. Futrell, R. Cox, N. Shelby and S. Ruiz. 2019. “Blinded by the light: Occupant perceptions and visual comfort assessments of three dynamic daylight control systems and shading strategies.” *Building and Environment* 154: 107-121.
- EnergyPlus. 2019. “Weather data”. EnergyPlus website (<https://energyplus.net/weather>), accessed on May 23 2019.
- European Committee for Standardisation (CEN). 2005. *EN ISO 7730:2005. Ergonomics of the thermal environment -- Analytical determination and interpretation of thermal comfort using calculation of the PMV and PPD indices and local thermal comfort criteria*. Brussels, Belgium.
- European Committee for Standardisation (CEN). 2011. *EN 12464-1:2011. Light and lighting - Lighting of work places - Part 1: Indoor work places*. Brussels, Belgium.
- Freewan, A.A.Y. 2014. “Impact of external shading devices on thermal and daylighting performance of offices in hot climate regions.” *Solar Energy* 102: 14-30.

- Hernández, F.F., J.M.C. Lòpez, J.M.P. Suárez, M.C.G. Muriano and S.C. Rueda. 2017. "Effects of louvers shading devices on visual comfort and energy demand of an office building. A case study." *Energy Procedia* 140: 207-216.
- Hwang, R.L., T.P. Lin, M.J. Cheng, J.H. Chien. 2007. "Patient thermal comfort requirement for hospital environments in Taiwan." *Building and Environment* 42: 2980-2987.
- Jaloxa. 2019. "Radiance Colour Pickler". Jaloxa website, accessed May 10 2019. http://www.jaloxa.eu/resources/radiance/colour_picker.shtml
- Lau, A.K.K., E. Salleh, C.H. Lim and M.Y. Sulaiman. 2016. "Potential of shading devices and glazing configurations on cooling energy savings for high-rise office buildings in hot-humid climates: The case of Malaysia." *International Journal of Sustainable Built Environment* 5: 387-399.
- Maachi, I.N., A. Mokhtari, M.E. Slimani. 2019. "The natural lighting for energy saving and visual comfort in collective housing: A case study in the Algerian building context." *Journal of Building Engineering* 24: 100760.
- Provincia Autonoma di Bolzano. 2019. "Servizi Web delle Misurazioni Meteo e Idrografiche". Accessed on May 20 2019. <http://dati.retecivica.bz.it/it/dataset/misure-meteo-e-idrografiche>
- Ricciardi, P., and C. Buratti. 2009. "Adaptive analysis of thermal comfort in university classrooms: Correlation between experimental data and mathematical models." *Building and Environment* 44: 674-687.
- Ricciardi, P., and C. Buratti. 2018. "Environmental quality of university classrooms: Subjective and objective evaluation of the thermal, acoustic, and lighting comfort conditions." *Building and Environment* 127: 23-36.
- Skoog, J., N. Fransson, L. Jagemar. 2005. "Thermal environment in Swedish hospitals: summer and winter measurements." *Energy and Buildings* 37: 872-877.
- Touma, A., and D. Ouahrani. 2017. "Shading and day-lighting controls energy savings in offices with fully-Glazed facades in hot climates." *Energy and Buildings* 151: 263-274.
- Van Gaever, R., V.A. Jacobs, M. Diltoer, L. Peeters, S. Valanduit. 2014. "Thermal comfort of the surgical staff in the operating room." *Building and Environment* 81: 37-41.
- Verheyen, J, N. Theys, L. Allonsius, F. Descamps. 2011. "Thermal comfort of patients: Objective and subjective measurements in patient rooms of a Belgian healthcare facility." *Building and Environment* 46: 1195-1204.
- Xiong, J., A. Tzempelikos. 2016. "Model-based shading and lighting controls considering visual comfort and energy use." *Solar Energy* 134: 416-428.
- Zaniboni, L., K. Kiesel, M. Schuß, G. Pernigotto, A. Gasparella, A. Mahdavi. 2016. "Indoor evaluation of a health care facility: a case study." 12th REHVA World Congress 2016 at Aalborg, May 22-25, 2016. Aalborg, DK.

Assessing Solar Radiation in the Urban Area of Bolzano, Italy, by Means of SEBE Simulations

Gianluca Pappaccogli – Free University of Bozen-Bolzano, Italy – gianluca.pappaccogli@unibz.it

Giovanni Pernigotto – Free University of Bozen-Bolzano, Italy – giovanni.pernigotto@unibz.it

Alessandro Prada – University of Trento, Italy – alessandro.prada@unitn.it

Andrea Gasparella – Free University of Bozen-Bolzano, Italy – andrea.gasparella@unibz.it

Abstract

Downward shortwave incoming irradiance plays a key role in urban areas, especially in those located in complex terrains. Accurate modelling of this weather variable is crucial for the characterization of physical processes, and in particular heat exchanges, occurring between buildings and the urban atmosphere. In this framework, the present research evaluated the capabilities of the Solar Energy on Building Envelopes (SEBE) model, which can be used to describe the urban geometry through 2D high-resolution DSMs and simulate total irradiation on buildings' façades. Specifically, this work focused on the urban area of Bolzano, a city located in the north-eastern Italian Alps in a basin where three valleys join, and assessed the SEBE output by comparison with the total daily irradiation on a vertical building façade for a six-month period (i.e. July-December 2018). Meteorological forcing for simulations was provided by the observed hourly data of shortwave radiation (i.e. global GHI and diffuse DHI horizontal, and direct normal DNI irradiance), collected at rooftop level in the urban area of Bolzano. The overall performance of the model was found to be accurate, both for different analysed periods and for daily climatic classification.

1. Introduction

The constant increase in energy demand has brought increasing attention to solar energy as an energy source which is available worldwide, especially in urban areas where other renewable energies are generally not present. Moreover, in a context of continuous urbanization, the study of solar radiation in the complex urban environment is becoming crucial in order to provide building simulation codes with robust and adequate inputs. Indeed,

the shaded/sunlit urban surface portions represent the dominant component of shortwave energy input in urban areas, especially during clear-sky conditions. However, the complex shadowing patterns led by different building distributions represent the main challenge in terms of computational effort needed to create urban models.

For this purpose, simplifying the assumptions of the three-dimensional geometry of urban fabric is required in agreement with the represented level. Accordingly, several urban parametrization schemes have been developed since the 2000s, with different levels of detail, such as the *slab* (Liu et al., 2006), *single-layer* (Kusaka et al., 2001) and *multi-layer* (Martilli et al., 2002; Masson et al., 2000) models, representing respectively 2D or 3D regular building volume arrays. In these schemes, the distribution and intensity of solar radiation reaching the different urban surfaces are computed by a simple shadow-casting algorithm in conjunction with a rotating, infinitely-long street canyon scheme (Lindberg et al., 2015a).

In recent years, several GIS-based tools have been developed using high-resolution digital surface models (DSMs) derived from LiDAR data, in order to estimate solar radiation for extensive urban areas, such as the Solar Energy on Building Envelopes – SEBE (Lindberg et al., 2015b). Accordingly, 3D geographical data of urban fabric make it possible to derive very high-resolution information about building structures, which are typically used in micro- to local scale modelling, providing realistic representations of specific building stocks.

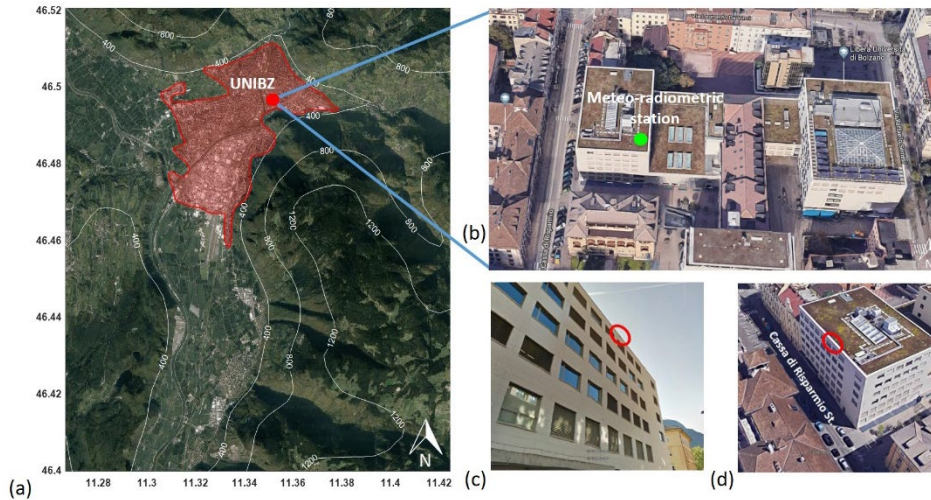


Fig. 1 – (a) The urban area of Bolzano (area shaded in red). Height contours (above sea level) are also presented, (b) The zoomed-in area represents the position of the meteo-radiometric station located on the rooftop of the Free University of Bozen-Bolzano, (c,d) Position of SPN1 sunshine pyranometer fixed on the vertical façade exposed to west at 25 a.g.l.

In this work, Solar Energy on Building Envelopes (SEBE) was used to estimate the shortwave irradiance on the ground, roofs and building walls throughout the urban core of the medium-sized (approximately 100,000 inhabitants) city of Bolzano. The city is located in a basin where three valleys in the north-eastern Italian Alps join (Fig. 1a). The climatic conditions in the city are closely related to the complex topography of the surrounding area, which influences in particular the flow field and solar radiation (Pappaccogli et al., 2018). It is therefore crucial to take into account the interactions between the surrounding orography, which generates a shadowing effect, and geometry of the urban fabric, which modifies the radiative balance within the urban environment (i.e., the share of direct and diffuse shortwave radiation). In the current research, observed horizontal solar radiation data were used as meteorological input for SEBE, and the computed solar radiation on a vertical building surface compared with measurements collected in a six-month period (i.e., July–December 2018).

2. Methods

2.1 Model Structure

SEBE uses digital surface models (DSMs) to calculate solar radiation, which consist of building and ground heights. In addition, two optional DSMs of

the same resolution and extent as the ground and building DSM can be used to represent 3D vegetation of trees and bushes (which are not considered in this case study). Specifically, the SEBE model computes the 'shadow volumes' by sequentially moving the raster DSM at the azimuth angle of the sun, reducing the height at each iteration based on the elevation angle of the sun (Ratti and Richens, 1999). For a detailed description of the shadow casting algorithm, see Ratti and Richens (2004), and Lindberg and Grimmond (2010).

Based on observed hourly meteorological data as input, the SEBE model uses the unobstructed three components of shortwave radiation: direct radiation perpendicular to the sun (DNI), horizontal diffuse (DHI) and global (GHI). As these variables are not commonly available (especially DNI and DHI), the model allows the calculation of the diffuse component from the global through the statistical model presented in Reindl et al. (1990), which can take into account the ambient air temperature (T_a) and relative humidity (RH) to improve the accuracy of the calculation. Accordingly, the direct shortwave radiation component (DNI) on a surface perpendicular to the sun rays is then estimated from DHI using the following equation:

$$I = (G - D) / \sin \eta \quad (1)$$

where η is the sun's altitude.

In order to avoid the hourly time step iteration, the meteorological data are pre-processed and redistributed into 145 patches of similar solid angles throughout the sky vault according to the well-known approach presented by Tregenza and Sharples (1993). The diffuse radiation component is redistributed for the patches based on the all-weather model of sky luminance developed by Perez et al. (1993).

The output of the SEBE model consists of the total irradiance for a roof pixel (R) on a DSM by summing the direct, diffuse and reflected radiation as follows

$$R = \sum_{i=1}^p [(I\omega S + DS + G(1 - S)\alpha)]_i \quad (2)$$

where p is the number of patches on the hemisphere, I is the incidence direct radiation, D is diffuse radiation, G is the global radiation originating from the i^{th} patch, α is the surface albedo and ω is the sun incidence angle. The first and second terms represent the direct and diffuse irradiance respectively, whereas the third term accounts for reflected irradiance (Lindberg et al., 2015b). S represents the shadow computed at each pixel:

$$S = S_b - (1 - S_v)(1 - \tau) \quad (3)$$

where S_b and S_v are respectively shadows from buildings and vegetation, and τ is the transmissivity of shortwave radiation through vegetation.

Finally, the reflection term at the wall pixels is only considered for half of the hemisphere, with the reflected part originating from the ground calculated as follows:

$$\text{Ground}_{\text{reflected}} = (G\alpha)/2 \quad (4)$$

For tilted roofs, the reflection from the ground is not considered, as it is negligible due to the small view factor from the tilted roofs to the ground (Lindberg et al., 2015b).

2.2 Model Setup

The SEBE model was evaluated by comparing simulated and observed vertical shortwave radiation

data on the building façade exposed to west and located in the core area of Bolzano, Italy (Fig. 1). The assessment was performed by considering a daily time step. Surface albedo was set to 0.15, which represents the typical value for urban surfaces (Oke, 1989).

2.3 Simulated Domain and Meteorological Input Data

A regular domain of approximately a 1 km² horizontal dimension with spatial resolution of 1 m (Fig. 2) was derived by the spatial average of digital surface models with 0.5 m resolution from the GeoCatalogo of the Autonomous Province of Bozen-Bolzano (<http://geocatalogo.retecivica.bz.it/geocatalog>). The fine resolution of DSM was able to represent different heights and orientations of the walls, and to take into account the slope of the roofs, when different building archetypes are analysed. Fig. 2 shows the building height distribution across the model domain, displaying input building information used in the SEBE model.

The observed solar radiation data provided by the meteorological station located at the Free University of Bozen-Bolzano on the flat rooftop of the E-building were used as input and boundary conditions for SEBE simulations (Fig. 1b). This station was installed at the Free University of Bozen-Bolzano in 2017, on the rooftop of the building of the University, in a position relatively free from external obstructions (above the rooftop level of the city). The measurements site is located in the city centre (Lat. +46°29.89' N; Lon. +11°20.98' E), which is representative of the climatic conditions of the basin, located away from the slopes of the surrounding mountains. Specifically, the measurements of the direct normal and diffuse horizontal solar radiation are carried out respectively by means of an EKO MS-56/pyrheliometer and a MS-802/pyranometer, fixed on a STR-22G EKO sun-tracker station, both for six months (i.e. from July to December 2018).

In this study, vegetation is excluded in the DSMs, as it is not present in the analysed street canyon.

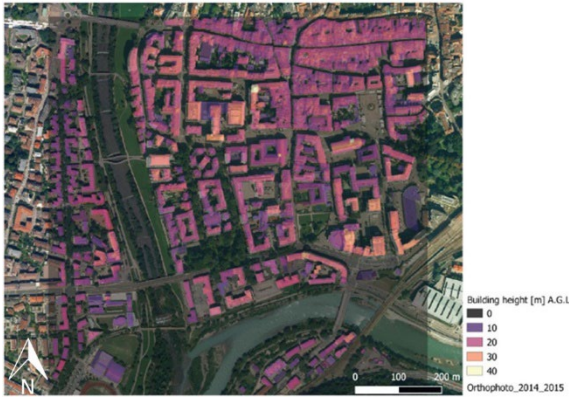


Fig. 2 – The study area in Bolzano (Italy), used for model evaluation, showing building height provided by *DSMs* (spatial resolution 1 m).

2.4 Field Observations

The SEBE model was evaluated for one point location placed on the building façade of the Free University of Bolzano, located in the urban core of the city (Fig. 1c, d). The façade borders a regular street canyon with an aspect ratio $H/W \sim 1.3$ (where H is the average building height and W is the average width of the street), which is delimited by multi-storey buildings with tilted rooftops.

In particular, a SPN1 pyranometer was installed on the external façade of the E-building of the Free University of Bozen-Bolzano at a height of 25 m a.g.l. (Fig. 1c, d). The façade is exposed to the west (azimuth angle $=270^\circ$) according to a surface analysis based on the DSM model. Data were collected between 5 July 2018 and 31 December 2018. Solar radiation on this vertical surface was saved at the acquisition sampling frequency of 1 minute, and later recalculated into hourly integrals by means of MATLAB® software, in order to match the time resolution needed for input data in the SEBE model. A total of 179 daily data points were used in the evaluation analysis.

3. Results

Using the meteorological data collected at the university building rooftop as input for SEBE, the observed and simulated daily vertical total irradiation were compared for the analysed period of July to December 2018.

In order to obtain a representative sky-type classification, the clearness index was computed using the Surface Solar Irradiance (SSI) provided by MSG Meteosat satellite data normalized by the corresponding extra-atmospheric irradiance according to Ineichen et al. (2009), as ground measurements in complex terrain are affected by the shadowing effect of surrounding orography. Accordingly, the average daily values of the clearness index are used to classify different weather conditions. To quantitatively validate the results of the model, the mean error (BIAS), the root-mean-square error (RMSE) and the coefficient of determination (R^2) were evaluated, quantifying the difference between the simulated and observed daily total irradiation on the building façade.

Fig. 3 reports the comparison between observed and simulated total daily irradiation (expressed as watthours per square meter) on the vertical surface, which are respectively correlated with the clearness index and daily climatic classification. As shown in Fig. 3a, the SEBE model performs well at the analysed location during different climatic conditions ($R^2 = 0.952$), showing a good estimation of the shortwave fluxes on the vertical wall in the street canyon. As can be noted, a slight overestimation of the modelled shortwave fluxes at the wall location occurs, with a BIAS of 31.83 Wh m^{-2} .

Focusing on the different climatic classes, no specific pattern can be observed. Specifically, an overestimation of the simulated total daily irradiation occurs during overcast sky conditions (BIAS = 134.4 W m^{-2}), which decreases during intermediate (BIAS = 125.4 W m^{-2}) and clear-sky (BIAS = 31.8 W m^{-2}) conditions. However, several significant underestimations occur during clear-sky conditions, which lead to an increase in RMSE (246.3 Wh m^{-2}), while no significant outliers are observed for intermediate and clear-sky conditions.

These errors are linked to the inexact partition between the global and diffuse radiation components during clear-sky conditions.

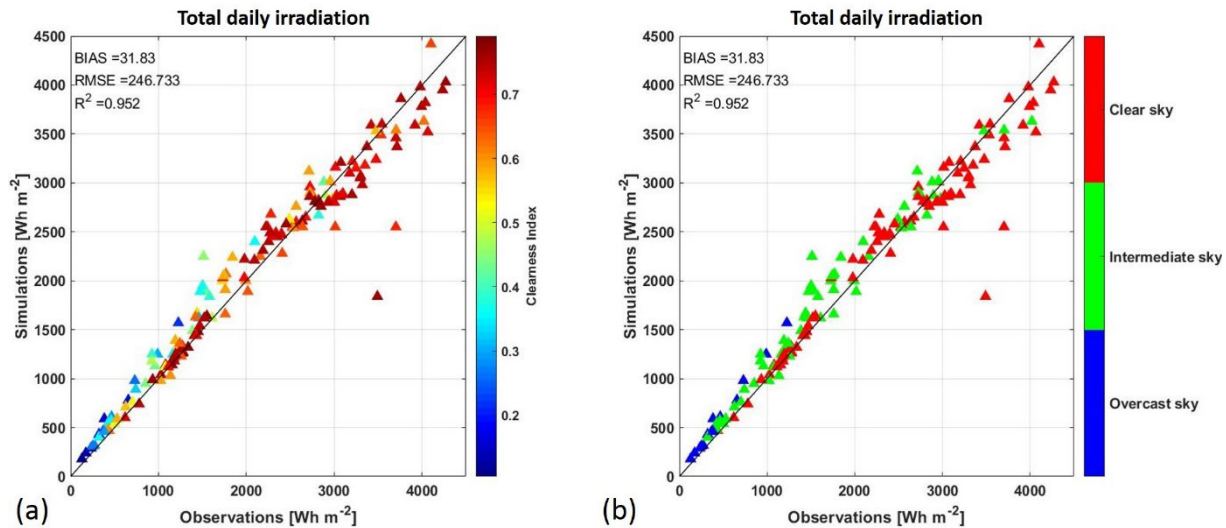


Fig. 3 – Scatter plots of observed and simulated total daily irradiation correlated to (a) clearness index, (b) daily sky-types classification, during the analyzed period (i.e., July–December 2018)

Finally, it should be remembered that the university building is located in the historical city centre, which is characterized by complex envelope structures (e.g., historical towers, balconies etc.), probably not perfectly described by the 1 m digital surface model.

4. Conclusions

A six-month daily simulation was carried out by means of the Solar Energy on Building Envelopes (SEBE) model, in order to study the distribution of solar radiation on roofs and building walls through the core area of the city of Bolzano, Italy. The urban geometry was accurately described using high-resolution 2D raster DSM, which makes it possible to compute 3D surface irradiation information through an extensive area up the city-centre scale. Observed hourly data on shortwave radiation provided by a meteorological station installed on a university building were used as hourly input data for SEBE simulations. The model was evaluated for a vertical façade exposed to west, in a street canyon of Bolzano.

The results highlight that the SEBE model accurately reproduces the downward shortwave fluxes for the different simulated periods (i.e. from July to December) and for daily classifications of sky types. Further developments are planned in order to test

the sensitivity of the SEBE model on different urban surfaces (such as tilted and flat roofs), using different meteorological input data (i.e. using only global horizontal radiation components provided by conventional weather stations or from satellites).

Acknowledgement

This study has been funded by the project “Klimahouse and Energy Production” in the framework of the programmatic-financial agreement with the Autonomous Province of Bozen-Bolzano of Research Capacity Building and by the internal project “Bolzano Solar Irradiance Monitoring Network-SOMNE” of the Free University of Bozen-Bolzano.

References

- Ineichen, P., Barroso, C. S., Geiger, B., Hollmann, R., A. Marsouin, and R. Mueller. 2009. “Satellite Application Facilities irradiance products: hourly time step comparison and validation over Europe.” *International Journal of Remote Sensing* Vol. 30, No. 21, 10, 5549-5571.
- Kusaka, H., Kondo, H., Y. Kikegawa, and F. Kimura. 2001. “A simple single-layer urban canopy model for atmospheric models: Comparison with multi-layer and slab models”. *Boundary-Layer Meteorology* 101(3): 329-358.

- Lindberg, F., and C.S.B. Grimmond. 2010. "Continuous sky view factor maps from high resolution urban digital elevation models." *Climate Research* 42, 177–183.
- Lindberg, F., C.S.B. Grimmond, and A. Martilli. 2015a. "Sunlit fractions on urban facets – Impact of spatial resolution and approach." *Urban Climate* 12: 65–84.
- Lindberg, F., Jonsson, P., T. Honjo, and D. Wästberg. 2015b. "Solar energy on building envelopes- 3d modelling in a 2d environment." *Solar Energy* 115: 369–378.
- Liu, Y., Chen, F., T. Warner, and J. Basara. 2006. "Verification of a mesoscale data-assimilation and forecasting system for the Oklahoma city area during the joint urban 2003 field project." *Journal of Applied Meteorology and Climatology* 45(7): 912–929.
- Martilli, A., A. Clappier, and M. W. Rotach. 2002. "An urban surface exchange parameterization for mesoscale models." *Boundary-Layer Meteorology* 104(2): 261–304.
- Masson, V. 2000. "A physically-based scheme for the urban energy budget in atmospheric models." *Boundary-Layer Meteorology* 94(3): 357–397.
- Oke, T. R., 1989. *Boundary Layer Climates*, second ed., Routledge London.
- Pappacogli, G., Giovannini, L., F. Cappelletti, and D. Zardi. 2018. "Challenges in the application of a WRF/Urban-TRNSYS model chain for estimating the cooling demand of buildings: A case study in Bolzano (Italy)." *Science and Technology for the Built Environment* 24:529–544.
- Perez, R., R. Seals, and J. Michalsky. 1993. "All-weather model for sky luminance distribution – preliminary configuration and validation." *Solar Energy* 50, 235–245.
- Ratti, C.F. and P. Richens. 1999. "Urban texture analysis with image processing techniques." In: Proc CAADFutures99, Atlanta, GA.
- Ratti, C.F. and P. Richens. 2004. "Raster analysis of urban form." *Environment and Planning B-Plann. Des.* 31, 297–309.
- Reindl, D.T., Beckman, W.A., and J.A. Duffie. 1990. "Diffuse fraction correlation." *Solar Energy* 45, 1–7.
- Tregenza, P., and S. Sharples. 1993. "Daylighting Algorithms." ETSUS, UK, 1350–1993.

Numerical and Experimental Study on the Impact of Humidity on the Thermal Behavior of Insulated Timber Walls

Maja Danovska – Free University of Bozen-Bolzano, Italy – maja.danovska@natec.unibz.it

Michele Libralato – University of Udine, Italy – libralato.michele.1@spes.uniud.it

Giovanni Pernigotto – Free University of Bozen-Bolzano, Italy – giovanni.pernigotto@unibz.it

Alessandra De Angelis – University of Udine, Italy – alessandra.deangelis@uniud.it

Onorio Saro – University of Udine, Italy – onorio.saro@uniud.it

Paolo Baggio – University of Trento, Italy – paolo.baggio@unitn.it

Andrea Gasparella – Free University of Bozen-Bolzano, Italy – andrea.gasparella@unibz.it

Abstract

The push towards a lower environmental impact of the building sector has led to the widespread adoption of renewable organic materials such as wood and other bio-based insulation materials. These materials are characterised by a solid matrix with voids that can be filled with moist air and water and in which complex heat and mass transfer occurs, influencing the global thermal properties. Indeed, due to different heat transfer mechanisms involved, the apparent thermal conductivity varies both with temperature and moisture content because of water thermal conductivity is higher than air. However, many Building Simulation programs (e.g., EnergyPlus and TRNSYS) still adopt constant thermal properties for simulating the heat transfer in buildings, causing inaccuracies in calculations of heat flux and thus, in the prediction of the energy consumption of a building. The aim of this work is therefore to analyse experimentally and numerically the impact of both moisture and temperature on the thermal behaviour of an insulated timber wall. An experimental activity was conducted at the Building Physics Laboratory at the Free University of Bozen-Bolzano on Cross-lam (XLAM) and wooden insulation specimens to measure thermal conductivity at different temperatures and moisture contents by means of a heat flux meter (i.e., HFM) and a climatic chamber. A 1D model for coupled heat and mass transfer across the studied wall was then developed and calibrated against the experimental data. Finally, by simulating with both nominal (10 °C and 23 °C reference temperature) and actual thermal conductivity, hourly heat fluxes and energies were compared, taking into consideration climatic files relating to the Italian peninsula.

1. Introduction

The need to reduce the environmental impact of the building sector has led to the adoption of bio-materials such as wood. Wood, alone or as a component in different insulation products, guarantees a low environmental impact while ensuring reasonably good insulating properties because of the porosity in its structure, in which solid, gaseous and liquid phases coexist, and complex and interacting heat and mass transfer mechanisms operate (Bomberg and Shirliffe, 1978; Künzle, 1995; Luikov, 1975; Rudtsch, 2000; Scheffler, 2008; Time, 1998).

Coupled heat and mass transfer influences the apparent thermal conductivity of materials, which is not a constant value measured at the reference conditions set by EN ISO 10456:2007 (CEN, 2007), and varies as a function of temperature and moisture content. Studies have shown how the thermal conductivity of wood and wood-based products increases with temperature and values can be 35 % higher than the reference value if the temperature is higher (Suleiman et al., 1999; Vololonorina et al., 2014). Similarly, thermal conductivity of a moist wood-based fibreboard can be from 12 % to 61 % higher than in dry conditions, depending on the temperature of the mean specimen (Troppová, 2015). This phenomenon is observed by Vololonorina et al. (2014) for other wood-based products. Furthermore, the specific heat of wood increases with both temperature and moisture content, as reported in the work of Radmanović et al. (2014).

This dynamic change in the properties of the material can cause inaccuracies in the output of many Building Simulation programs in which thermal conductivity is kept constant. For this reason, this work aims to evaluate to what extent the moisture-temperature dependent thermal conductivity influences heat transfer across real insulated timber walls with different thicknesses. The work includes an experimental and a numerical part, in Section 2.1 and 2.2, respectively. The former consists of measurements of thermal conductivity at different temperatures and moisture contents for XLAM specimens and wooden insulation panels, carried out in order to correlate thermal conductivity to thermo-hygrometric conditions. Consequently, a 1D heat and mass transfer model was developed for three insulated walls with different thicknesses and the mass transfer was calibrated against experimental data. In particular, the vapor resistance factor was tuned by comparing simulated results with data from the conditioning process, from 80 % RH/ 23 °C to 10 % RH/ 23 °C. Finally, annual simulations were performed using the thermal conductivity measured in nominal conditions (10 °C and 23 °C reference temperature) and using the thermal conductivity in the actual conditions (i.e. thermal conductivity obtained from the thermal conductivity function). The results of these simulations were compared in terms of hourly specific heat fluxes and for seasonal energy exchanges in 110 cities.

2. Methodology

2.1 Experimental Activity

The experimental activity was focused on finding a correlation between thermal conductivity and mean temperature and water vapour partial pressure. Thermal conductivity measurements were conducted on 4 XLAM specimens (0.2 x 0.2 x 0.05 m) and 2 wooden insulation panels made of wood shavings, with dimensions of 0.3 x 0.3 x 0.05 m. Thermal conductivity measurements were repeated at different temperatures from 10 to 50 °C with 5 °C steps and different moisture contents (Table 1) obtained in a climatic chamber. The

thermal conductivity was measured in the Building Physics Laboratory at the Free University of Bozen-Bolzano by means of a Netzsch HFM 436/3 Lambda™ (in compliance with ISO 8301:1991, EN 12664:2001 and EN 12667:2001). Samples had been previously pre-conditioned in an ATT Angelantoni DM340 climatic chamber, in accordance with EN ISO 12571:2013 (CEN, 2013). A drying process was carried out at 105 °C as suggested by EN ISO 12570:2000 (CEN, 2000). Conditioning processes are intermediate processes where the moisture content of the material is either increased or reduced in the climatic chamber; in particular, the term “drying” refers to the process of removal of water at a higher temperature.

2.2 Mathematical Model for Heat and Mass Transfer

A numerical 1D model of heat and mass transfer was developed to evaluate the impact of both moisture and temperature on the heat flux across insulated walls consisting of an XLAM and an insulation panel. The model was developed from scratch to allow for better control of its implementation. Thermal conduction (Fourier’s law) and surface convection (Newton’s law) were accounted for in the heat transfer, while Fickian vapor diffusion was assumed for the mass transfer process. The storage moisture capacity C_m adopted in the mass transfer model was calculated starting from the sorption isotherms determined experimentally for the insulation panel and from data found in the literature for the spruce (Fitzpatrick et al., 2013). The following heat (Equation 1) and mass (Equation 2) transfer equations were solved numerically by implementing a finite differences scheme.

$$\rho c (\partial T / \partial t) - \nabla \cdot (\lambda \nabla T) = 0 \quad (1)$$

$$C_m \rho (\partial p_v / \partial t) - \nabla \cdot (\delta_p \nabla p_v) = 0 \quad (2)$$

The main parameters of the materials (thermal conductivity and density) were measured or calculated, while others, like specific heat capacity c (1380 J kg⁻¹ K⁻¹ and 1281 J kg⁻¹ K⁻¹ for spruce and insulation, respectively) were taken from the literature. The vapor permeability δ_p for the XLAM was obtained after the calibration of the mass

transfer model against experimental data (Section 3.2), while for the insulation panel, water vapor permeability was taken from the literature (Labat et al., 2016).

2.3 Simulation Procedure

Three insulated walls with different thicknesses were modelled (20 cm XLAM and 5, 10, 15 cm external insulation, respectively) for a period of one year. Space and time discretisation were 0.01 m and 1 h in the period. Surface convective heat transfer coefficients for horizontal heat flux, i.e. $20 \text{ W m}^{-2} \text{ K}^{-1}$ for the external side and $2.5 \text{ W m}^{-2} \text{ K}^{-1}$ for the internal side, were adopted. Effects of incident solar irradiance and precipitations were neglected. For the sake of simplicity, internal boundary conditions were assumed to be constant and equal to $20 \text{ }^{\circ}\text{C}$, with 50 % relative humidity. On the external side, hourly data from the CTI database (<https://try.cti2000.it/>) for 110 Italian cities were considered. For all locations, simulations were run twice, and considered:

- nominal thermal conductivity, measured at both $10 \text{ }^{\circ}\text{C}$ and $23 \text{ }^{\circ}\text{C}$ in the low moisture content state, as suggested by the EN ISO 10456:2007 (CEN, 2007).
- actual thermal conductivity, in which linear correlations (Equations 3 and 4) in temperature and water vapor partial pressure were obtained from the experimental activity.

The analysed output variables were:

- linear percentage trend deviation between the specific heat fluxes, calculated in nominal and actual conditions obtained as the slope of the scatter plot of the two quantities.
- annual area-specific energy differences (expressed in watt-hour per square meter) for thermal losses, i.e. when the internal specific heat flux is directed towards the external, and positive thermal contributions, when it is directed towards the inside.

3. Results and Discussions

3.1 Experimental Investigation

Thermal conductivity for one representative specimen for both materials was measured at three different moisture contents MC (Table 1). The behaviour of the other tested samples, both for XLAM and for the insulation, was analogous. The low MC state and the high MC states shown in Table 1 were obtained in the climatic chamber by conditioning samples at the reported values of temperature and relative humidity, while the “as-is” condition is that of the sample in equilibrium with the laboratory humidity.

Table 1 – Moisture content values for the three different conditions for XLAM and the wooden insulation specimen (INS)

		XLAM	INS
State	Condition	MC (%)	MC (%)
Low MC	$23 \text{ }^{\circ}\text{C}/10 \text{ } \%$ RH	3.5	3.6
“As-is”	$20\text{-}26 \text{ }^{\circ}\text{C}/30\text{-}40 \text{ } \%$ RH	6.3	8.0
High MC	$23 \text{ }^{\circ}\text{C}/80 \text{ } \%$ RH	13.2	13.6

As regards the XLAM, the measured dry weight was 651.0 g. The high MC state was obtained after 43 days of conditioning in the climatic chamber, starting from the “as-is” state with a mass increase of 6 %, while the low MC state was obtained after 9 days in climatic chamber at $23 \text{ }^{\circ}\text{C}/10 \text{ } \%$, starting from the high MC state. The mass loss registered was of approximately 5 %. The drying process from the “as-is” state lasted 3 days and the registered mass loss was of 6 % with respect to the “as-is” condition.

As regards the insulation panel, the measured dry weight was 490.9 g. The duration of the conditioning processes and the drying was shorter because of the lower inertia of the material due to its structure. Indeed, the high MC state was

obtained after 16 days in climatic chamber, while the low MC state was obtained after 12 days. The drying process lasted 3 days, as for the XLAM.

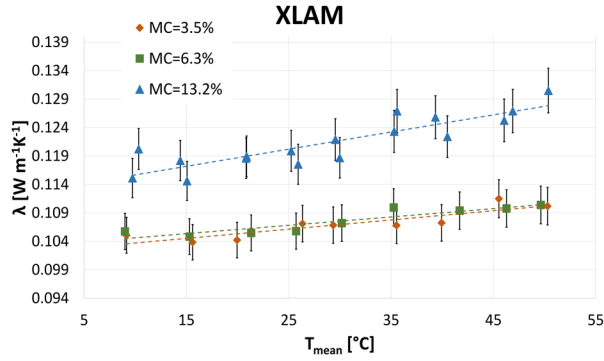


Fig. 1 – λ vs. T for the XLAM specimen at three different moisture conditions. Vertical bars represent the measurement uncertainty (3 %)

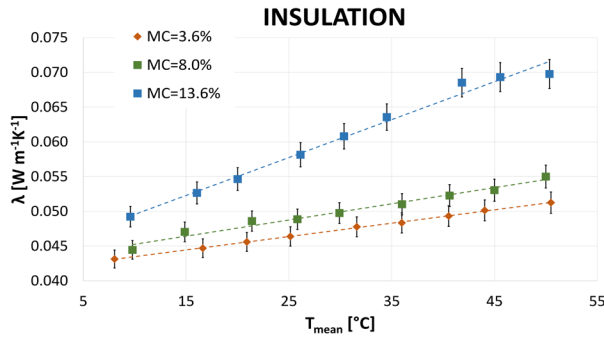


Fig. 2 – λ vs. T for the wooden insulation panel in three different moisture conditions. Vertical bars represent the measurement uncertainty (3 %).

Thermal conductivity λ of XLAM increased with temperature T in all the three cases, as expected (Fig. 1). The maximum difference obtained in the “as-is” state was equal to 11.3 %, by varying the temperature from 10 to 50 °C. By passing from the “as-is” to the high MC state, the obtained increase of thermal conductivity was 13.2 % at 23 °C. Thermal conductivity at the low MC state of 3.5 % had similar values to those in the “as-is” condition with 6.3 % MC (differences < 3 %), meaning that thermal conductivity had a strong non-linear behaviour. As regards the wooden insulation, the trends were analogous (Fig. 2), but the percentage increases were higher. At a reference temperature of 23 °C, the percentage increase from the lowest MC to the highest was 22.6 %. By considering only temperature variation, the maximum increase was 41.7 % with the highest MC, while at the lowest MC the increase was 18.8 %. These larger

differences were due to the lower value of thermal conductivity for the insulation than the wood. Nevertheless, the absolute increase was slightly higher for the insulation. Table 2 shows the calculated density and measured thermal conductivities used as input for the heat and mass transfer model. In particular, two values of nominal thermal conductivity were adopted: 10 °C and 23 °C, both in the low MC state.

Table 2 – Some input from the heat and mass transfer model obtained from the experimental activity

	XLAM		INS	
Density ρ	363		106.7	
Condition	Low MC/ 10 °C	Low MC/ 23 °C	Low MC/ 10 °C	Low MC/ 23 °C
λ	0.104	0.107	0.043	0.045

Equations 3 and 4 represent the obtained linear correlations between thermal conductivity ($\text{W m}^{-1} \text{K}^{-1}$) and temperature (°C) and water vapor partial pressure (Pa) for XLAM and insulation, respectively. The “as-is” data were neglected in the determination of the correlations because this state was not obtained in a controlled environment. The two following functions were adopted for simulations with actual conditions.

$$\lambda(T, p_v) = 0.099 + 2.125 \cdot 10^{-4} \cdot T + 7.380 \cdot 10^{-6} \cdot p_v \quad (3)$$

$$\lambda(T, p_v) = 0.034 + 3.694 \cdot 10^{-4} \cdot T + 6.760 \cdot 10^{-6} \cdot p_v \quad (4)$$

3.2 Mass Transfer Model Calibration

By using the conditioning data, the mass transfer model was calibrated for the XLAM in order to obtain the vapor resistance factor used in the mathematical model. In particular, the vapor resistance factor was tuned, by comparing simulated results with the process in the climatic chamber in which moisture content was reduced, i.e. from 23 °C/80 % to 23 °C/10 %, and by verifying that:

1. the simulated mass loss after 9 days is the same as the experimental mass loss (i.e., 34 g);
2. simulated and calculated mean fluxes correspond.

A value of 32 for the water vapor resistance factor μ was first obtained in the calibration stage by means of conditioning data from 23 °C/80 % to 23 °C/10 % and then checked against the experimental process which started from the “as-is” state to the high MC state (i.e., a mass increase of 46.5 g in 43 days). For the insulating material, no calibration process was performed because, firstly, the weighing time step suggested by the Standard EN ISO 12571:2013 (CEN, 2013) was too long for this material and furthermore, a higher precision balance would have been necessary and because the range of the μ -value in the literature for this kind of materials is narrow. For this reason, a value of 2 was chosen (Labat et al., 2016; Xing et al., 2018).

3.3 Average Percentage Impact

The overall effect of the actual thermal conductivity is to increase the heat flux and on average the deviation ranges from 3.8 to 4.8 %, considering the three different wall thicknesses (Fig. 3). Mean deviations were higher in the South than in the North because of the smaller magnitude of the flux (i.e. the smaller temperature difference between internal and external on average) in all the three configurations. With the lowest insulation thickness, the maximum mean deviation was 7.7 %, obtained in the southern climate of Reggio Calabria. By increasing the insulation thickness, mean deviations increased up to values of approximately 11 % in the South for Crotona. All the statistics related to the mean deviations are shown in Table 3.

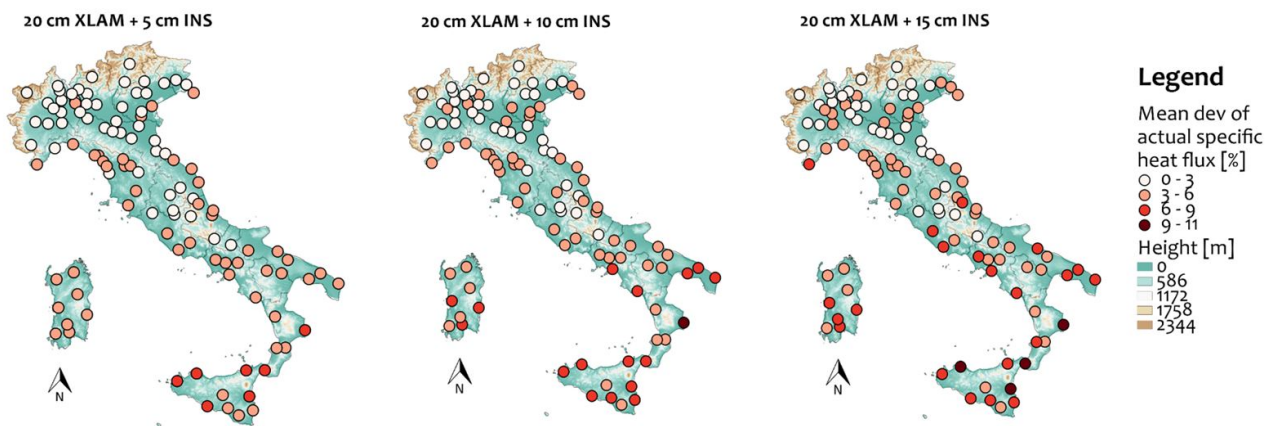


Fig. 3 – Percentage deviation (%) of the actual specific heat flux with respect to the nominal specific heat flux (at 10 °C) for each location in Italy and for the three configurations of the insulated wall

Table 3 – Statistics related to the mean deviation (%), the increase of positive and negative thermal losses (Wh m⁻²) for the three wall configurations. Nominal thermal conductivity at 10 °C

	20 cm XLAM + 5 cm INS			20 cm XLAM + 10 cm INS			20 cm XLAM + 15 cm INS		
	Mean deviation (%)	Increase in thermal loss (Wh m ⁻²)	Increase in thermal gain (Wh m ⁻²)	Mean deviation (%)	Increase in thermal loss (Wh m ⁻²)	Increase in thermal gain (Wh m ⁻²)	Mean deviation (%)	Increase in thermal loss (Wh m ⁻²)	Increase in thermal gain (Wh m ⁻²)
Average	3.8	558	340	4.4	475	315	4.8	417	276
Minimum	0.9	288	88	0.5	171	77	0.4	129	65
1 st quartile	2.6	501	247	2.8	414	229	3.0	359	201
Median	3.7	551	325	4.1	478	300	4.5	421	262
3 rd quartile	4.9	614	413	5.7	539	381	6.3	481	330
Maximum	7.7	872	707	9.5	764	661	10.6	665	593

Table 4 – Statistics related to the mean deviation (%), the increase of positive and negative thermal losses (Wh m⁻²) for the three wall configurations. Nominal thermal conductivity at 23 °C

	20 cm XLAM + 5 cm INS			20 cm XLAM + 10 cm INS			20 cm XLAM + 15 cm INS		
	Mean deviation (%)	Increase of thermal loss (Wh m ⁻²)	Increase of thermal gain (Wh m ⁻²)	Mean deviation (%)	Increase of thermal loss (Wh m ⁻²)	Increase of thermal gain (Wh m ⁻²)	Mean deviation (%)	Increase of thermal loss (Wh m ⁻²)	Increase of thermal gain (Wh m ⁻²)
Average	0.8	61	262	0.8	28	246	1.0	31	217
Minimum	-2.2	-424	65	-3.2	-474	57	-3.6	-427	49
1 st quartile	-0.4	-51	187	-0.8	-85	175	-0.9	-67	152
Median	0.7	81	248	0.5	46	231	0.7	46	203
3 rd quartile	1.9	187	315	2.2	159	295	2.5	149	257
Maximum	4.8	326	557	6.1	289	529	7.0	269	483

When considering a reference temperature of 23 °C for the nominal thermal conductivity, the values change considerably (Table 4) even if their distribution all over the peninsula is the same. In these conditions, locations where previously small positive mean deviations were registered are characterised by negative values, meaning that with the actual thermal conductivity the fluxes are smaller, so the wall performs better than in the nominal case. This unexpected behaviour was explained by the fact that in some locations the reference temperature of 23 °C was too high since the average external temperature was lower. This happens especially in colder locations (cities in the north and/or in mountainous areas).

3.4 Absolute Impact

By adopting a variable thermal conductivity, there is a general increase in thermal losses, on average from 417 to 558 Wh m⁻² for all the three configurations (Fig. 4). The maximum increase (872 Wh m⁻² higher than with the nominal conductivity) was registered for the less insulated wall in Oppido Lucano, a southern city at an altitude of approximately 700 m, with a low mean external temperature (i.e. 13 °C). By increasing the insulation layer, the heat fluxes towards the outside decrease, in

addition to the thermal losses. This is why with higher insulation thickness, the increase in thermal loss is lower. Moreover, thermal gains (towards the inside) increase all over the peninsula by considering a variable thermal conductivity (Fig. 5). On average, the increase is of approximately 340, 315 and 276 Wh m⁻² respectively for the three configurations with increasing insulation thickness. The maximum increase is for the less insulated wall, for the same reason, i.e. thermal losses. The maximum value is obtained for Taranto, a southern city, where the average external temperature and thus the inward heat flux are higher. With higher insulation thickness, the increase is clearly reduced since the magnitudes of thermal fluxes are lower. When the nominal thermal conductivity is evaluated at 23 °C, locations in which the thermal losses were already low, in this case, are characterised by negative values of variation in thermal losses as for the case of the mean deviations. This occurs because the reference wall temperature overestimates the actual conditions for those locations. For the thermal gains, no negative values are registered. This is because thermal gains usually occur when the external temperature is higher than 20 °C, thus, usually higher than the reference wall temperature.

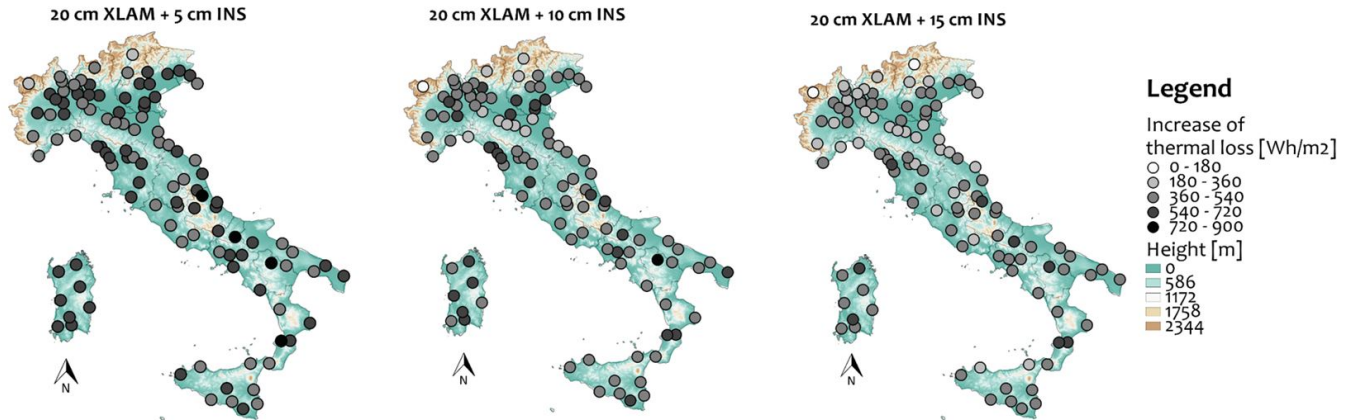


Fig. 4 – Increase in annual specific thermal losses (positive) calculated with variable thermal conductivity with respect to nominal thermal conductivity (at 10 °C) for the three configurations of the insulated wall (Wh m⁻²)

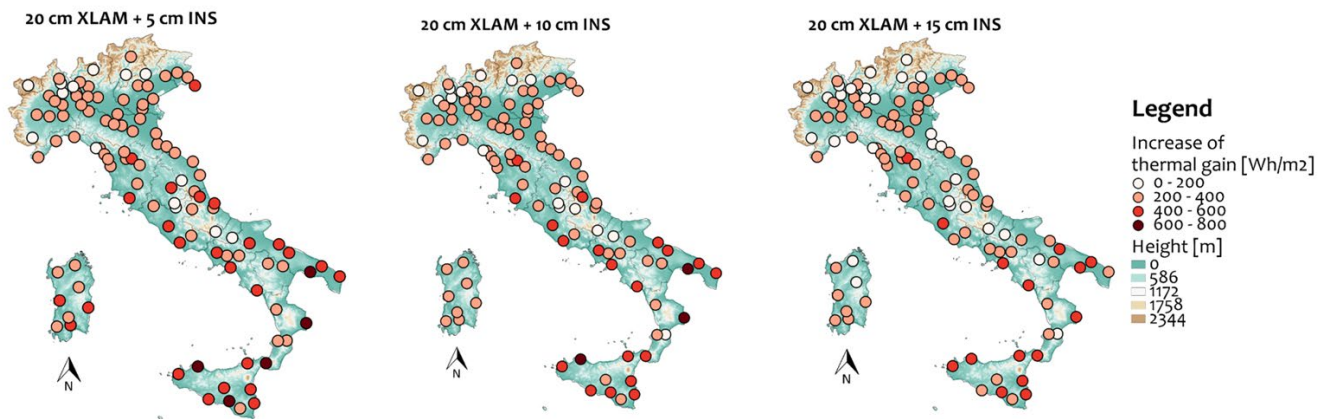


Fig. 5 – Increase in annual specific thermal gains (negative) calculated with variable thermal conductivity with respect to nominal thermal conductivity (at 10 °C) for the three configurations of the insulated wall (Wh m⁻²)

4. Conclusions

A numerical and experimental study on insulated timber walls was conducted in order to assess the impact of external temperature and water vapor partial pressure on thermal conductivity of wood and wood-based materials and subsequently on the specific heat flux across them. The focus was on both wood and wooden insulation, because of the higher sensitivity of wood to moisture variations than other building materials.

Thermal conductivity measurements were conducted at different temperatures and moisture contents for XLAM specimens and wooden insulation panels. From the experimental activity, thermal conductivity functions of the temperature and water vapor partial pressure were found for both materials. This allowed the implementation of a 1D

heat and mass transfer finite difference model. Unknown parameters were obtained either after calibration of the model against experimental data or from the literature. With this model, the thermal behaviour of three insulated wooden walls with a 20 cm XLAM layer and 5, 10 and 15 cm of insulation in 110 Italian locations was studied. Results of the experimental activity and of annual simulations with both nominal (10 °C and 23 °C reference temperature) and actual thermal conductivity for each location show that:

- Experimental thermal conductivity of XLAM and the wooden insulation panel increase both with temperature (+11 % for XLAM and +41 % for the insulation by varying the temperature from 10 to 50 °C) and moisture content (+13 % for XLAM and +22 % for the insulation by passing from “as-is” to the high MC state). The

higher percentage for the insulation is due to the smaller value of its thermal conductivity.

- When the heat flux is simulated by considering only the nominal thermal conductivity (at 10 °C) of the insulated walls, there is an underestimation of the heat flux throughout the Italian peninsula for each wall configuration (i.e. -11 % for the less insulated wall).
- The analysed locations show different trends, with northern climates characterized by a higher increase in thermal losses (up to 900 Wh m⁻²) and southern climates by a larger increase (of 800 Wh m⁻²) for all wall configurations.
- By increasing the external insulation thickness, differences among locations for both thermal losses and gains are less evident. This is because the specific heat flux decreases.
- It is fundamental to choose the proper reference temperature at which the nominal thermal conductivity is measured according to the climate. For example, in cold climates a reference temperature of 23 °C would be too high.
- Simulations with and without an insulation layer and the same boundary conditions show different results: without an insulation layer (i.e. with only 20 cm of XLAM), smaller percentage deviations and smaller increases in thermal losses and gains were obtained because the thermal performance (in terms of insulation power) of the wall is strongly influenced by the external insulation layer.

Further research in this area is planned and will include (i) the effects of temperature on mass diffusion; (ii) the effects of moisture content on specific heat; (iii) the phase change in the mass transfer model; and (iv) a better experimental characterisation in terms of both conditioning points in the climatic chamber and respective thermal conductivity measurements, in order to improve the fit for thermal conductivity data.

Acknowledgement

This research was funded by the project “Klima-house and Energy Production”, in the framework of the programmatic-financial agreement with the Autonomous Province of Bozen-Bolzano of Research Capacity Building.

Nomenclature

Symbols

c	specific heat capacity (J kg ⁻¹ K ⁻¹)
C_m	linear storage moisture capacity (kg kg ⁻¹ Pa ⁻¹)
∂	partial derivative
INS	insulation panel
λ	thermal conductivity (W m ⁻¹ K ⁻¹)
μ	vapor resistance factor (-)
MC	moisture content (% dry basis)
∇	gradient
p_v	water vapour partial pressure (Pa)
ρ	density (kg m ⁻³)
RH	relative humidity (%)
T	temperature (°C)
t	time (s)

References

- Bomberg, M. T., C. J. Shirlcliffe. 1978. “Influence of Moisture and Moisture Gradients on Heat Transfer through Porous Building Materials.” *Thermal transmission Measurements of Insulation, ASTM STP 660*, R.P. Tye, Ed., American Society for Testing and Materials pp. 211-233.
- CEN. 2000. *EN ISO 12570:2000. Hygrothermal performance of building materials and products- Determination of the moisture content by drying at elevated temperature*. Brussels, Belgium.
- CEN. 2007. *EN ISO 10456:2007. Building materials and products, Hygrothermal properties, Tabulated design values and procedures for determining declared and design thermal values*. Brussels, Belgium.
- CEN. 2013. *EN ISO 12571:2013. Hygrothermal performance of building materials and products- Determination of hygroscopic sorption properties*. Brussels, Belgium.

- Fitzpatrick, J. J., C. O'Sullivan, H. Boylan, O. Cribben, D. Costello, and K. Cronin. 2013. "Moisture sorption isotherm study of Sitka spruce, larch, willow and miscanthus chips and stems." *Journal of Biosystems Engineering* 115: 474–481. <https://doi.org/10.1016/j.biosystemseng.2013.05.004>
- Künzel, H.M. 1995. *Simultaneous Heat and Moisture Transport in Building components, One-and two-Dimensional Calculation Using Simple Parameters*. IRB-Verlag, Stuttgart.
- Labat, M., C. Magniont, N. Oudhof, and J-E. Aubert. 2016. "From the experimental characterization of the hygrothermal properties of straw-clay mixtures to the numerical assessment of their buffering potential." *Building and Environment* 97: 69-81. <https://doi.org/10.1016/j.buildenv.2015.12.004>
- Luikov, A.V. 1975. "Systems of differential equations of heat and mass transfer in capillary-porous bodies (review)." *International Journal of Heat and Mass Transfer* 18: 1–14. [https://doi.org/10.1016/0017-9310\(75\)90002-2](https://doi.org/10.1016/0017-9310(75)90002-2)
- Radmanović, K., I. Đukić, and S. Pervan. 2014. "Specific Heat Capacity of Wood." *Drona industrija* 65: 151-157. 10.5552/drind.2014.1333
- Rudtsch, S. 2000. "Thermal conductivity measurements for the separation of heat and mass diffusion in moist porous materials." *High temperature-high pressure* 32: 487–92. doi: 10.1068/htwu65
- Scheffler, G.A. 2008. "Validation of hygrothermal material modelling under consideration of the hysteresis of moisture storage." PhD thesis, Dresden University of Technology, Dresden, Germany.
- Suleiman, B.M, J. Larfeldt, B. Leckner, and M. Gustavsson. 1999. "Thermal conductivity and diffusivity of wood." *Wood Science and Technology* 33 (6): 468-473. doi:10.1007/s002260050130
- Time, B. 1998. „Hygroscopic moisture, transport in wood.“ Norwegian University of Science and Technology.
- Troppová, E., M. Svehlík, J. Tippner, and R. Wimmer. 2015. "Influence of Temperature and Moisture Content on the Thermal Conductivity of Wood-Based Fiberboards." *Materials and Structures* 40(12): 4077–83. <https://doi.org/10.1617/s11527-014-0467-4>
- Vololonorina, O., B. Perrin, and M. Coutand. 2014. "Characterization of hygrothermal properties of wood-based products – Impact of moisture content and temperature." *Construction and Building Materials* 63: 223-233. <https://doi.org/10.1016/j.conbuildmat.2014.04.014>
- Xing, Y., M. Brewer, H. El-Gharabawy, G. Griffith, and P. Jones. 2018. "Growing and testing mycelium bricks as building insulation materials." IOP Conf. Series: *Earth and Environmental Science* 121. doi :10.1088/1755-1315/121/2/022032

Sensitivity Analysis of SEBE Model Using Different Meteorological Input: A Case Study in Bolzano, Italy

Gianluca Pappaccogli – Free University of Bozen-Bolzano – gianluca.pappaccogli@unibz.it

Giovanni Pernigotto – Free University of Bozen-Bolzano – giovanni.pernigotto@unibz.it

Alessandro Prada – University of Trento – alessandro.prada@unitn.it

Andrea Gasparella – Free University of Bozen-Bolzano – andrea.gasparella@unibz.it

Abstract

In the present study, a sensitivity analysis was carried out in order to evaluate the performance of the Solar Energy on Building Envelopes (SEBE) model to different meteorological input data. The model was applied on a six-months period from July to December 2018. Geostationary satellite data provided by Meteosat MSG was first validated against measurements from permanent weather stations located both in the urban area of Bolzano and in the surrounding countryside. Subsequently, several SEBE simulations were performed in order to compare the outcomes obtained from satellite data against simulations fed by meteo-radiometric measurements. The validation of satellite data shows that global shortwave irradiance data provided by the Meteosat are representative of the solar radiation fluxes, even in a complex terrain. SEBE simulations fed by different meteorological input performed well at different comparison locations although showing slightly broad errors using satellite data as input.

1. Introduction

The importance of a reliable assessment of solar radiation in urban environment modelling is growing together with the spatial resolutions of models. Monitored meteorological parameters are essential to provide accurate boundary conditions as input for the models. Indeed, a growing number of weather stations are available in the complex urban environment, but each one provides data representative of a specific site morphology, encouraging their use for a limited area. Providing proper boundary conditions for urban modelling remains a difficult task, as they are usually derived from observations limited at a single-point, which negatively affects

model reliability, especially in complex terrains (Pappaccogli et al., 2018).

In this work, a case study for the urban area of Bolzano, Italy, was proposed in order to study the applicability of satellite data as available meteorological input for urban modelling in complex terrain. Furthermore, possible advantages led by satellite input data over weather stations were discussed as well, such as: (a) a better representation of short-wave flux in a 4-5-kilometer modelled grid; (b) the absence of potential biases due to the position of the weather station; (c) the availability of a regular pattern of input data at a global scale, which allows modelling where ground recordings are scarce.

As a first step, the images from Meteosat Second Generation (MSG) satellite were analysed to obtain hourly Surface Solar Irradiance (expressed as watts per square meter), which was first validated against global horizontal irradiance measurements from a network of ground weather stations located both in the urban and in the surrounding rural areas of Bolzano. Several simulations were then performed with the Solar Energy on the Building Envelopes (SEBE) model, in order to compare the outcomes obtained from satellite data against simulations fed by meteo-radiometric measurements. Finally, in order to test the performance of the SEBE model on different urban surfaces, such as roofs and walls, a validation was carried out on three different sites located in the urban area of Bolzano.

This work is organized as follows. The second section introduces the Meteosat satellite data and the spatial input used in the SEBE model, providing detailed information regarding the datasets and the methodologies used in this work, respectively. The

third section describes first the validation of the Meteosat satellite data by means of a comparison with data from a network of ground weather stations, and then the sensitivity analysis carried out to assess the impact of different input data on SEBE model results. Finally, the fourth section contains the discussion and conclusions.

2. Methods

2.1 Satellite Data

The hourly solar surface irradiance (SSI) data (Fig. 1) were derived from images obtained by geostationary Meteosat Second Generation (MSG) class meteorological satellites, operated by EUMETSAT. The images were obtained using the Spinning Enhanced Visible and Infrared Imager (SEVIRI) on-board instrument. The Meteosat satellites were placed in two geostationary locations: Meteosat-8 over Indian Ocean and Meteosat-11 in latitude-longitude 0°. The satellite data was remapped onto a 0.05° regular grid and expressed in watt per square meter. In particular, at the Bolzano latitude (i.e., 46.50 °N), the horizontal spatial resolution of each pixel is about 25 km².

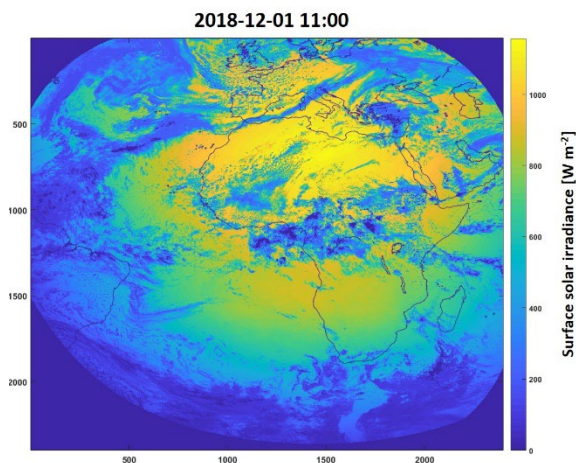


Fig. 1 – Example of Surface Solar Irradiance (SSI) from the Meteosat satellite data. The slot shown is 01 December 2018 at 11:00 UTM

In order to test the quality of the satellite data, Meteosat images were validated by a comparison with ground measurements, through an analysis of

the hourly irradiance values. Specifically, the satellite global horizontal irradiation GHI was compared against ground measurements at five convectional weather stations during a six-month period (i.e. July to December 2018), being representative of the annual declination variation. These meteorological stations provide measurements in both urban and rural areas, and belong to the network of conventional weather stations operated by the Provincial Agency for Environmental Protection (APPA), the Autonomous Province of Bolzano, as well as the meteo-radiometric station installed on the rooftop of the E-building of the Free University of Bozen-Bolzano. An overview of the weather stations selected for the aforementioned analysis is reported in Table 1.

Table 1 - List of selected weather stations for radiation measurements located close to the urban area of Bolzano used in the validation of the satellite-based radiation estimates.

ID Station	Position (°N, °E)	Altitude (m)	Location
AMBA	46.4993/11.3420	286	Rooftop/Urban
BOL	46.4977/11.3128	254	Suburban
BRO	46.4065/11.3111	226	Rural
SGEN	46.5304/11.3319	970	Rural
UNI	46.4981/11.3495	292	Rooftop/Urban

The validation results are reported in Section 3.1. Specifically, the hourly GHI estimates from MSG and the pyranometers at the five selected weather stations are compared, referring to all sky conditions that occurred during the entire 6-month dataset (i.e. July to December 2018). In order to quantitatively validate satellite data, the root-mean-square error (RMSE), mean error (BIAS) and the coefficient of determination (R^2) were evaluated, quantifying the difference between ground measured and satellite GHI. However, only values for a solar elevation $> 10^\circ$ were used in the analysis, as recommended by Ineichen et al. (2009).

Furthermore, a clearness-index was obtained using the solar radiation data provided by satellite images as they are not affected by the shadowing effect of surrounding orography in complex terrain measurements. Specifically, the Surface Solar Irradiance (SSI) provided by MSG Meteosat satellite data

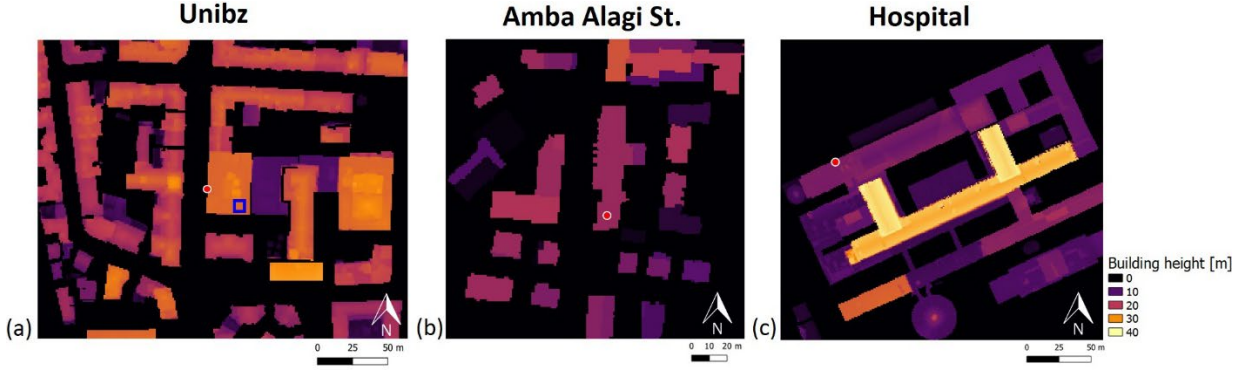


Fig. 2 - Digital surface model DSM with 1 m spatial horizontal resolution representing building heights at (a) university building ("Uni"); (b) Amba Alagi St. ("Amba") and (c) hospital ("Osp"). Observation points (red dots) and meteo-radiometric station ("UNI", blue square) are also shown

was normalized by the corresponding extra-atmospheric irradiance, as reported by Ineichen et al. (2009), as follows:

$$K_t = (SSI)/(SSI_{TOA}) \quad (1)$$

where SSI_{TOA} is the extra-atmospheric irradiance. In order to use the clearness index as a reliable sky condition descriptor, Perez et al. (1990) introduced a method to make the index independent of solar radiation angle:

$$K'_t = \frac{K_t}{\left\{1.031 \exp\left[\frac{-1.4}{(0.9+9.4/M)}\right] + 0.1\right\}} \quad (2)$$

where K'_t is the modified global or solar surface irradiance clearness index, M is the optical air mass as defined by Kasten (1980) and h is the solar elevation angle above the horizon expressed in degrees:

$$M = [\sin h + 0.15 (h + 3.885)^{-1.253}]^{-1} \quad (3)$$

Since the modified clearness index is relatively independent of the solar elevation angle, the three intervals were defined to characterize the three sky-types:

Clear sky conditions:	$0.65 < K'_t \leq 1.00$
Intermediate sky conditions:	$0.30 < K'_t \leq 0.65$
Overcast sky conditions:	$0.00 < K'_t \leq 0.30$

The sky-types classification is applied at the correlation analysis during the six-month analyzed period, which is reported in detail in Section 3.2.

2.2 Spatial Input Data

Three different locations were selected in order to validate the simulated SEBE output with radiometric ground observations. Specifically, Fig. 2a-c shows elements of the input surface information, such as the ground and building DSM, derived by the Geo-Catalogo of the Autonomous Province of Bolzano (<http://geocatalogo.retecivica.bz.it/geocatalog>). Two sets of data were used to derive the DSM: the LiDAR dataset was used to derive ground heights, whereas a high-detail 3D vector layer was used to define roof structures. As can be noted, only the area surrounding the comparison stations, which directly influences the measurements, has been modelled in order to reduce the computational effort of SEBE simulations.

The dimensions of the model domains are about one or two hundred meters on each side, with a horizontal spatial resolution of 1 m. The two weather stations referred to as Amba Alagi St., "Amba" and Hospital, "Osp", are both located on the building rooftops (Fig. 2b,c), characterized by a height of 17 m and 14 m, respectively, and record horizontal solar irradiation. By contrast, the University observation point ("Uni" in Fig. 2a) is located on the vertical façade of the E-building of the University Campus, at 25 m, and records vertical solar irradiation. Specifically, the validation instrument at the university site is a sunshine pyranometer SPN1, installed on a west-exposed vertical façade (Pappaccogli et al., 2019). "Uni" and "Amba" points are both located in the core of the city of Bolzano, in the dense neighbourhood of the city center, mainly characterized by midrise buildings (average heights of 13.6 m and 12.9 m, respectively), separated by

non-extensive and scattered green areas (urban fraction $\sim 70\%$). The station named “Osp”, instead, is located in the western part of the city in suburban area, where apple orchards and vineyards are contiguous to the urban area and fragmented only by sparse single-low buildings (Pappaccogli et al., 2018).

2.3 SEBE Simulations

As many simulations are involved in this work, each one adopting different sources and solar radiation components as meteorological input, a general overview of the SEBE simulations carried out is now presented. Since the analysis of the model results focuses on the comparison between observed and simulated daily solar irradiation at both wall and roof surfaces, for the purpose of readability, the names of the SEBE simulation report both the location used for comparison (“Uni”, “Amba” or “Osp”) and the source of meteorological input (Table 2). In particular, the source of meteorological input re indicated as “a” when the global horizontal irradiation GHI, the direct normal irradiation DNI, and the diffuse horizontal irradiation DHI measured by the meteorological station on the university E-building rooftop (referred to as “UNI”) are used; “b” when only the UNI GHI is employed; and “c” when the GHI provided by Meteosat satellite is considered.

Table 2 – Overview of the SEBE simulations with the respective analyzed building surface (left) and the meteorological input (top)

Daily global irradiation [Wh m ⁻²]	Source		
	UNI a	b	Meteosat c
Variables	GHI/DHI/DNI	GHI	GHI
Wall	Uni-a	Uni-b	Uni-c
Roof	Amba-a Osp-a	Amba-b Osp-b	Amba-c Osp-c

As reported by Lindberg et al. (2015), GHI, DNI and DHI are preferable to run SEBE but they are rarely available since conventional weather stations usually provide only GHI measurements. In this case, SEBE computes the diffuse component through the statistical model by Reindl et al. (1990), which considers air temperature and relative humidity to improve the accuracy of the calculations.

3. Results

3.1 Satellite Validation

Fig. 3 shows the scatter-plot for the hourly GHI estimates from MSG and the pyranometers at the five selected weather station reported in Table 1. The dots refer to all sky conditions which occurred during the entire 6-month dataset (i.e. July to December 2018). The two regression lines (red lines) represent the confidence intervals of $2 \times \text{RMSE}$.

As can be seen in Fig. 3, the satellite data compares well to ground observations throughout the analysed period (i.e. July to December 2018) and different weather conditions, which is confirmed by the correlation coefficient ($R^2 = 0.93$). No significant trend deviation can be observed, with a BIAS of about 9 W m^{-2} , and small relative errors ($\text{RMSE} = 66.4 \text{ W m}^{-2}$). However, the satellite data tend to overestimate and underestimate solar irradiance peaks, respectively, during summertime and wintertime, especially under clear-sky conditions. As expected, some errors occur during evening and morning transition periods, due to the coarse spatial resolution of the satellite data, which is stressed by the complex orography of the terrain. It is worth noting that the larger spread of the points placed below the value of around 400 W m^{-2} represents the GHI values both during the winter and overcast days, when the performance of satellite images is lower compared to clear-sky conditions. Moreover, it is worth highlighting that both errors and analysis results are similar to the findings of several studies in the literature (Federico et al., 2009; Kosmopoulos et al., 2015; Gomez et al., 2016).

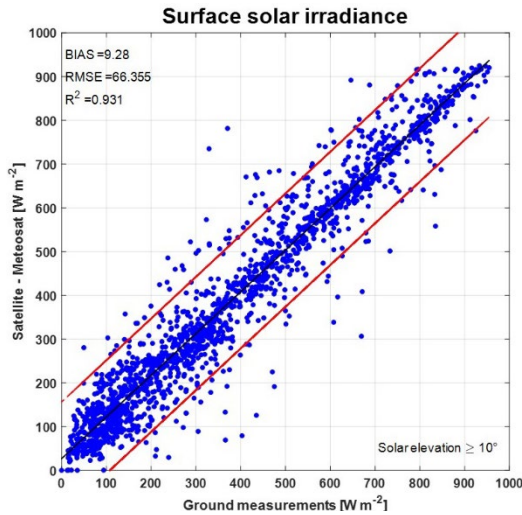


Fig. 3 – Satellite estimate of ground based measurement comparison for global horizontal irradiance (GHI) for all analyzed months (i.e. from July to December). Simple linear regression (black line), and confidence intervals of $2 \cdot \text{RMSE}$ (red lines)

3.2 SEBE Analysis

The analysis presented in this section (Figs 4 and 5) aims to evaluate the impact of the different meteorological input (i.e. three and one solar radiation components), provided by different sources (i.e., meteo-radiometric station and satellite), on the simulated daily surface irradiation on different building surfaces (i.e. roofs and walls). As in the satellite analysis, root-mean-square error (RMSE), mean error (BIAS) and the coefficient of determination (R^2) were evaluated (Table 3). Several scatter plots report the comparison between observed and simulated daily solar irradiation (expressed in wathours per square meter), distinguished respectively by the clearness-index (Fig. 4a-i) and sky-types classification (Fig. 5a-i).

Fig. 4a-c shows the comparison at the “Uni” site. The highest accuracy was found for simulations fed by “a” (UNI GHI/DNI/DHI) and “b” (UNI GHI) meteo-radiometric inputs, with a correlation coefficient R^2 of 0.95 and 0.96, respectively, while slightly lower accuracy was encountered in the case of “c” (Meteosat GHI) input ($R^2 = 0.88$). For the Amba Alagi St. site (Fig. 4d-f), very good agreement was registered for all simulations ($R^2 = 0.97$ -0.99), although a slight spread was detected for Amba-c simulation. Finally, the hospital site (Fig. 4g-i) displayed similar results for all different simulations ($R^2 = 0.96$). As can be noted, in the last site a slight overestimation occurred, especially during the summer period, as

confirmed by a BIAS of 385-490 Wh m^{-2} . These larger errors are probably due to the critical position of the weather station, installed close to small obstacles (such as the HVAC system cooling towers), which are not properly described by the 1 m DSMs. Furthermore, it is worth noting that the slight differences between Osp-c and other simulations (i.e., Osp-a and, Osp-b) are most likely related to the greater distance between the hospital site and the UNI meteo-radiometric station, which represents the source of meteorological input.

Table 3 – Mean errors (BIAS), root-mean-square errors (RMSE) and coefficient of determination (R^2) for daily solar irradiation compared with measurements at the three sites

	BIAS (Wh m^{-2})	RMSE	R^2
Uni-a	43.11	248.44	0.95
Uni-b	17.18	208.20	0.96
Uni-c	56.67	388.54	0.87
Amba-a	121.44	302.40	0.99
Amba-b	99.19	260.77	0.99
Amba-c	28.38	374.80	0.97
Osp-a	490.8	728.43	0.97
Osp-b	479.46	706.15	0.97
Osp-c	385.97	608.02	0.97

In order to evaluate the performance of the model during different types of sky conditions, similar analyses were carried out for the selected weather stations (Fig. 5a-i). Overall, a strong correlation between observed and simulated daily irradiation was registered for the three different sky-type classes in all sites. However, clear-sky conditions were characterized by wider spreads in all sites, while lower values were observed under overcast conditions.

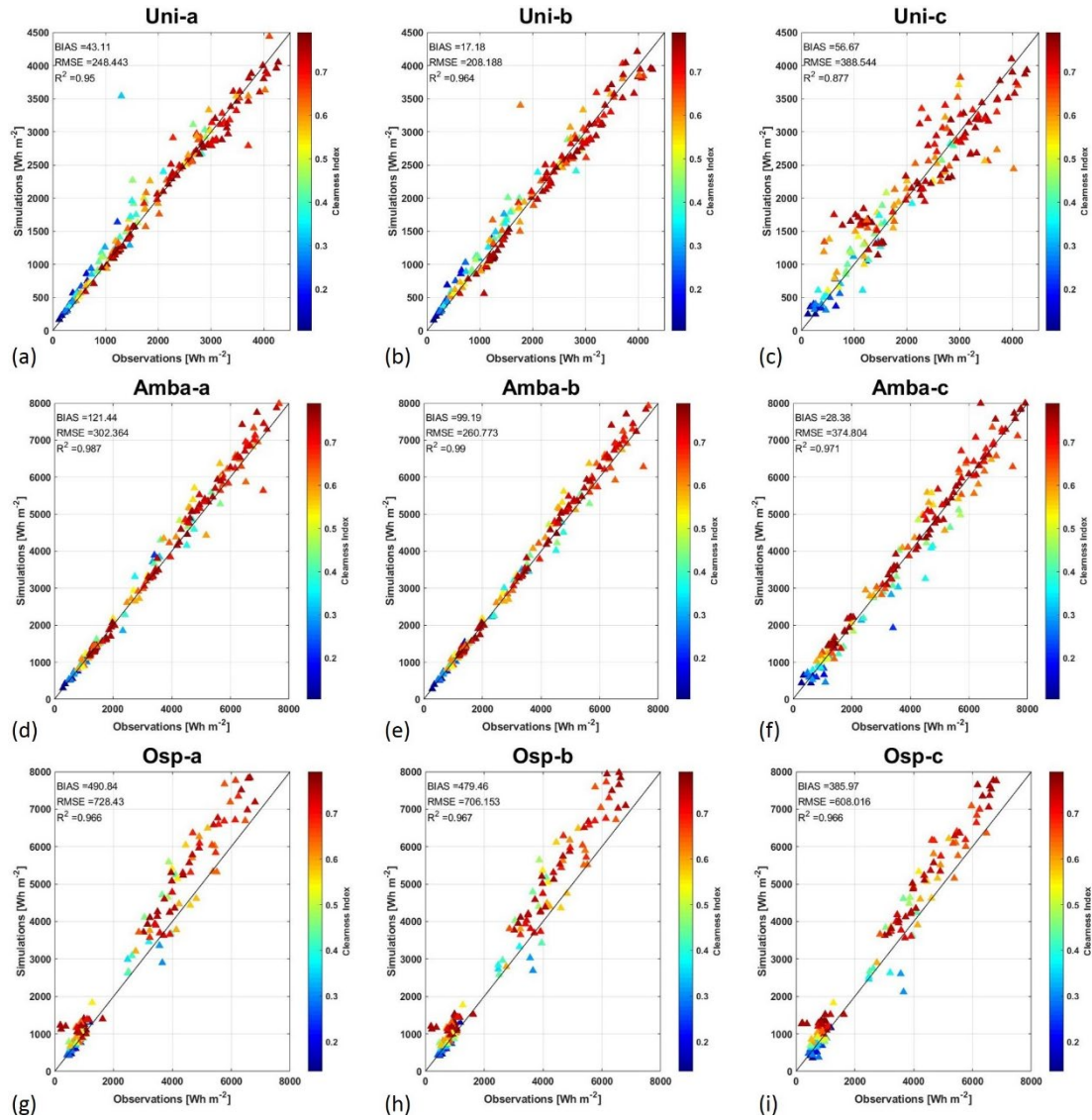


Fig. 4 – Scatter plot of observed and simulated total daily irradiation (Wh m^{-2}) correlated to clearness index during the analyzed period (i.e., July-December 2018) at (a-c) University; (d-f) Amba Alagi St., (g-i) Hospital location

4. Discussion and Conclusion

The results described in previous sections show that Meteosat satellite data, which provide the hourly Surface Solar Irradiance, are representative of the shortwave flux at urban scale, providing a regular input for modelled area even in a complex terrain. Indeed, the data used as boundary conditions in the SEBE model are able to describe the shortwave flux in a 4-5-kilometer grid, without affecting negatively the model reliability. However, ground measurements are still necessary in order to validate the relative satellite data according to weather station position.

In this respect, the global horizontal irradiance provided by Meteosat satellite images was compared with the ground measurements from a network of weather stations located close to the urban area of Bolzano. The satellite data were found in good agreement with the ground observations ($R^2 > 0.93$), throughout the analysed period (i.e. July to December 2018) and in different weather conditions. Nevertheless, satellite data tended to overestimate / underestimate solar irradiance peaks during summertime and wintertime, respectively, and especially under clear-sky conditions. Furthermore, some errors occurred during evening and morning transition periods, due to the coarse spatial resolution of satellite data.

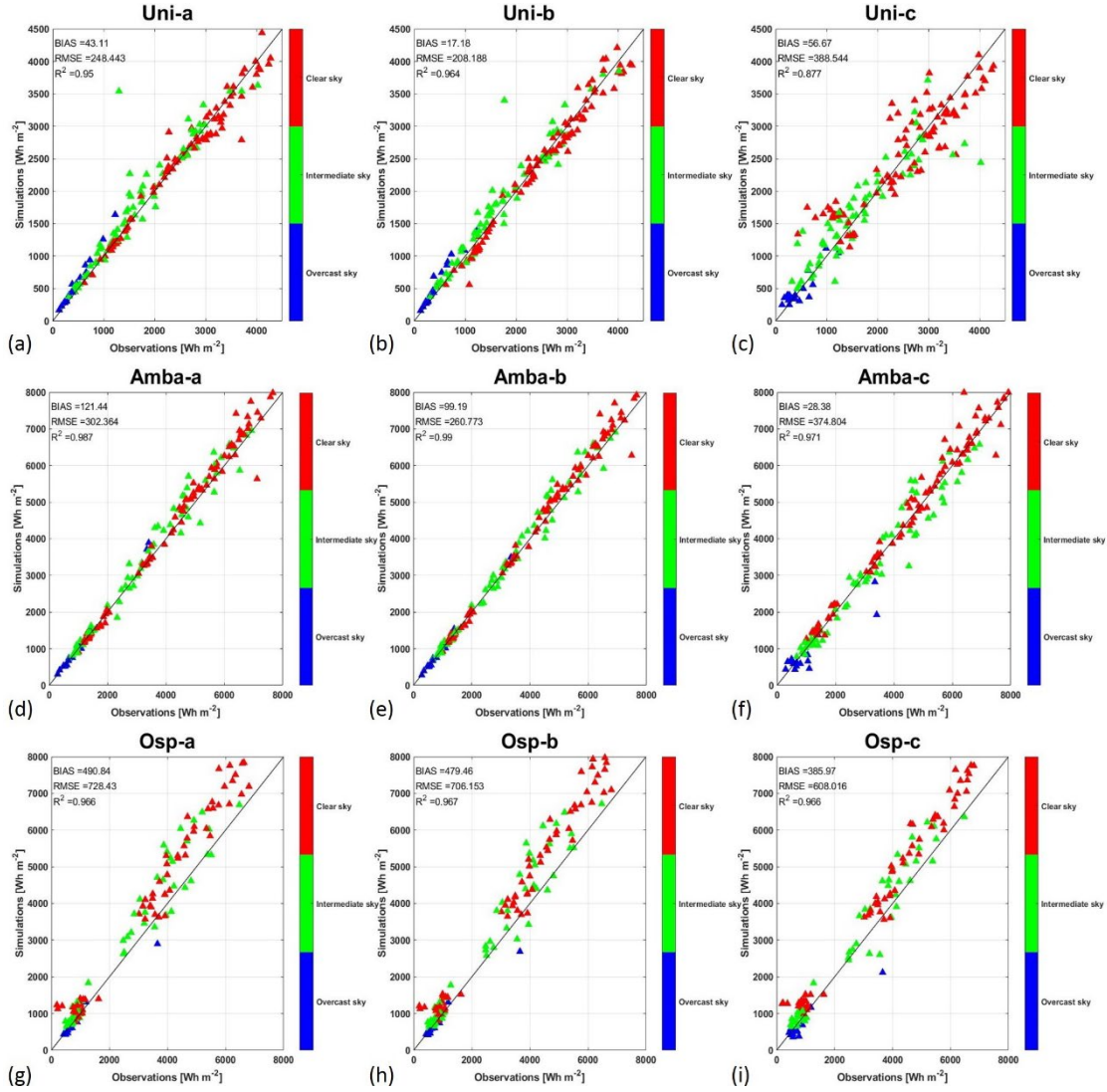


Fig. 5 – Scatter plot of observed and simulated total daily irradiation (Wh m⁻²) correlated to sky-types climatic classification during the analyzed period (i.e. July-December 2018) at (a-c) University; (d-f) Amba Alagi St., (g-i) Hospital location

As a whole, only a very slight overestimation occurred in the analysed six-months period, showing a BIAS and RMSE of 9 and 66.3 Wh m⁻², respectively. In terms of simulations, the sensitivity analysis highlighted that the different meteorological inputs have a small impact on the performance of the SEBE model. Indeed, good results were obtained for all studied sites, on both vertical and horizontal urban surfaces, with a correlation coefficient in the range of 0.88-0.99. In particular, the best approximation was obtained with the model fed by the global horizontal irradiation only, using the statistical model by Reindl et al. (1990) to calculate the diffuse radiation component.

Referring to the future developments, the assessment of the impact of input weather data will be further investigated by the coupling of SEBE output with Building Energy Simulation models.

Acknowledgement

This study has been funded by the project “Klima house and Energy Production” in the framework of the programmatic-financial agreement with the Autonomous Province of Bozen- Bolzano of Research Capacity Building and by the internal project “Bolzano Solar Irradiance Monitoring Network-SOMNE” of the Free University of Bozen-Bolzano.

References

- Gómez, I., V. Caselles, and M. J. Estrela. 2016. "Seasonal Characterization of Solar Radiation Estimates Obtained from a MSG-SEVIRI-Derived Dataset and a RAMS-Based Operational Forecasting System over the Western Mediterranean Coast." *Remote Sensing*, 8(1), 46.
- Ineichen, P., C. S. Barroso, B. Geiger, R. Hollmann, A. Marsouin, and R. Mueller. 2009. "Satellite Application Facilities irradiance products: hourly time step comparison and validation over Europe." *International Journal of Remote Sensing* Vol. 30, No. 21, 10, 5549–5571.
- Federico, S., R. C. Torcasio, P. Sanò, D. Casella, M. Campanelli, J. F. Meirink, P. Wang, S. Vergari, H. Diémoz, and S. Dietrich. 2009. "Comparison of hourly surface downwelling solar radiation estimated from MSG--SEVIRI and forecast by the RAMS model with pyranometers over Italy." *Atmospheric Measurement Techniques* 10: 2337–2352.
- Kasten, F. 1980. "A simple parameterization of two pyrheliometric formulae for determining the Linke turbidity factor." *Meteorologische Rundschau*, 33, 124–127.
- Kosmopoulos, P.G., S. Kazadzis, K. Lagouvardos, V., Kotroni, and A. Bais. 2015. "Solar energy prediction and verification using operational model forecasts and ground-based solar measurements." *Energy* 93, 1918–1930.
- Lindberg, F., P. Jonsson, T. Honjo, and D. Wästberg. 2015. "Solar energy on building envelopes- 3d modelling in a 2d environment." *Solar Energy* 115: 369–378.
- Pappaccogli, G., L. Giovannini, F. Cappelletti, and D. Zardi. 2018. "Challenges in the application of a WRF/Urban-TRNSYS model chain for estimating the cooling demand of buildings: A case study in Bolzano (Italy)." *Science and Technology for the Built Environment* 24:529–544.
- Pappaccogli, G., G. Pernigotto, A. Prada, A. Gasparella. 2019. "Assessing solar radiation in the urban area of Bolzano, Italy, by means of SEBE simulations." *Proceedings of Building Simulation Applications BSA 2019*, June 19-21 2019, Bolzano, Italy.
- Perez, R., P. Ineichen, R. Seals, and A. Zelenka. 1990. "Making full use of the clearness index for parametrizing hourly insolation conditions." *Solar Energy*. 45, 111–114.
- Reindl, D.T., W.A. Beckman, and J.A. Duffie. 1990. "Diffuse fraction correlation." *Solar Energy* 45, 1–7.

Numerical and Experimental Characterization of the Thermal Behavior of Complex Fenestrations Systems Under Dynamic Conditions

Ingrid Demanega – Eurac Research, Bozen-Bolzano, Italy – ingrid.demanega@eurac.edu

Giuseppe De Michele – Eurac Research, Bozen-Bolzano, Italy – giuseppe.demichale@eurac.edu

Martin Hauer – Bartenbach GmbH, Aldrans, Austria – martin.hauer@bartenbach.com

Stefano Avesani – Eurac Research, Bozen-Bolzano, Italy – stefano.avesani@eurac.edu

Giovanni Pernigotto – Free University of Bozen-Bolzano, Italy – giovanni.pernigotto@unibz.it

Andrea Gasparella – Free University of Bozen-Bolzano, Italy – andrea.gasparella@unibz.it

Abstract

Complex Fenestration Systems (CFS) with different types of shading devices are widely used to enhance the building envelope's energy efficiency and the occupants' visual and thermal comfort. These technologies are characterized, among other features, by advanced shading systems, with for example complex geometries and highly reflective surfaces, which introduce a performance dependence on the angle of incidence of solar radiation. This peculiarity has to be covered by adequate thermal and optical models. However, the current most widespread thermal models, based on the standard ISO 15099 and implemented in the main building energy simulation tools, have shown some restrictions in their applicability for CFS. In addition to this, professionals of the façade construction industry are interested in assessing the components' critical temperatures and the performance of the fenestration system under real dynamic operating conditions and in representative extreme conditions. In this framework, this study has investigated a new modelling approach for the thermal characterization of CFS under dynamic conditions by comparing simulation results with in-situ measurements of a triple-glazed window with integrated commercial blinds installed at the Free University of Bozen-Bolzano, Italy. The numerical assessment of the thermal behaviour of CFS was based on CFD simulations with the separately computed effect of solar radiation. The experimental characterization was performed with several instruments, such as conventional heat flux plates and a temperature-controlled in-situ measurement device to determine the undisturbed, transient heat flux through transparent components. From the comparison, a good correspondence between numerical and experimental results emerged and both approaches appraised the inertial effect of the fenestration system on the solar heat gain. Finally, it

was observed that accurate optical modelling, together with CFD simulation, made it possible to compute the solar absorption and its significant impact on the fluid flow in the cavity, the components' temperatures and the solar gains.

1. Introduction

Transparent components and shading devices, designed in an optimal way, are crucial to increase the building envelope's energy efficiency and the exploitation of natural lighting. In recent years, complex shading systems, which aim to enhance occupants' visual and thermal comfort while reducing the building energy consumption, have been introduced. *The term 'Complex Fenestration System' (CFS) refers to all window technologies, including solar and light scattering or reflecting components. Their optical and thermal properties are described using a complex dependence on the angle of incidence and wavelength of the solar radiation* (Kuhn et al., 2011). Examples of these technologies are daylight redirecting systems, venetian blinds with complex geometries and highly reflective surfaces and prismatic layers. Indeed, the dependence on the angle of incidence allows for an improved management of solar radiation (Konis and Selkowitz, 2017). However, due to their complex nature, adequate models to evaluate Complex Fenestration systems' thermal and optical behaviour are required. For the optical characterization of CFS, the available models, based on the Bidirectional Scattering Distribution Function (BSDF), have already reached a high level of accuracy and are

widely used to perform daylight analysis. The procedure for calculating the thermal performance of glazing and shading systems is described in the international standard ISO 15099 (ISO, 2003). The standard approach, implemented in the main simulation tools, has restrictions in the applicability of complex system geometries or particular types of coatings, such as highly reflective ones (Demanega et al., 2018). Indeed, the ISO 15099 considers standard blind geometries, such as solar screens or venetian blinds with flat geometries and refers to diffusely reflecting surfaces. Addressing these standard technologies, the computation of the convective heat transfer through the window cavities is performed with a pressure drop model and applied to a layer-by-layer approach. This assumes the shading device is a layer parallel to the glass pane and has certain opening characteristics. However, this assumption is not adequate in the case of venetian blinds or other particular types of shading devices with large openings (Hart et al., 2017). Furthermore, the standard algorithms do not account for the heat capacity and thus the thermal inertia of the fenestration system despite it being an important aspect when characterizing the window system under dynamic conditions. In addition, professionals in the construction industry claim it is necessary to assess the components' critical temperatures and the heat flow through CFS under real operating conditions. This study therefore aims to investigate a new modelling approach for the thermal characterization of CFS under dynamic conditions by comparing simulation results with in-situ measurements of a commercial system installed at the Free University of Bozen-Bolzano, Italy.

2. Simulation and Experiment

2.1 CFS Typology

The analyzed fenestration system was a commercial triple-glazed window composed of two sealed cavities and curved blinds with highly reflective surfaces integrated in the exterior cavity (Fig. 1). The thickness of the blinds was 0.2 mm, the width 15.9 mm and the pitch 12 mm. The analysis was done with a fixed slat inclination of 75° corresponding to

a closed position. The exterior and central glasses were float glasses, while the interior glass was laminated. The geometric and thermal parameters of the window system are listed in Tables 1 and 2. On face 3 (the exterior side of the central glass pane) and face 5 (the exterior side of the interior glass pane) a low-emissivity coating was placed with an emissivity of 0.037. Both cavities were filled with a gas mixture of 90 % argon and 10 % air. This fenestration system was mounted on the west façade of the Living Labs inside the Free University of Bozen-Bolzano.

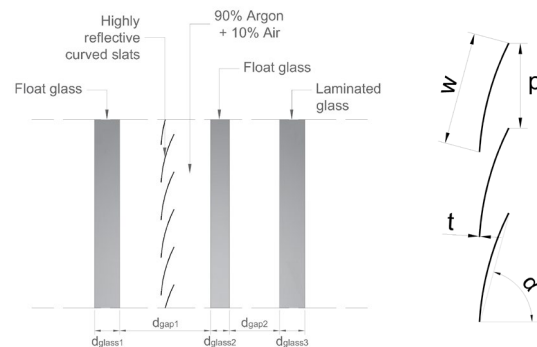


Fig. 1 – Layout of the Complex Fenestration System

Table 1 – CFS geometric parameters

Symbol	Parameter	Value
d_{glass1}	Glass 1 width	8 mm
d_{gap1}	Cavity 1 width	29 mm
d_{glass2}	Glass 2 width	6 mm
d_{gap2}	Cavity 2 width	16 mm
d_{glass3}	Glass 3 width	8.76 mm
w	Blind width	16 mm
t	Blind thickness	0.2 mm
p	Pitch	12 mm
α	Blind tilting	75°
H	Cavity height	0.9 m

Table 2 – CFS thermal parameters

Symbol	Unit	Cavity	Blind	Glass1/2	Glass3
λ	W/m/K	f(T)	100	1.0	0.757
c_p	J/kg/K	f(T)	900	820	820
ρ	kg/m ³	f(p,T)	2700	2500	2500
ε_f	-	-	0.150	0.037	0.037
ε_b	-	-	0.450	0.84	0.84

2.2 Modelling Approach

The thermal performance of the CFS is assessed by means of a new modelling approach, in which the fraction of absorbed solar radiation is calculated apart from the fluid flow and heat transfer and then included in a CFD simulation (Demanega et al., 2018). In this procedure solar radiation is treated with a detailed optical model based on ray tracing using the software Radiance (Ward, 1994); the resulting absorbed fraction of solar radiation is included in a comprehensive thermal modelling that couples heat transfer and fluid flow in a CFD simulation performed with the Finite Element (FE) software COMSOL Multiphysics. The simulation is done using time-dependent measured boundary conditions in terms of temperatures and solar irradiance. The computed heat flux is then compared with the in-situ measurements.

2.2.1 Solar radiation modeling

The optical modeling is required to compute the fraction of solar radiation absorbed by each solid element of the fenestration system. The highly reflective surface of the blinds and the curved geometry require a detailed modeling approach in order to appraise the angular dependent behavior. Thus, the analysis was carried out with the ray tracing software Radiance and a modified version of the Three-Phase Method (McNeil, 2014) that describes the way light passes through a fenestration system. Indeed, for this application, the scope was not the computation of the transmitted light but the absorbed radiation. The measured direct and diffuse horizontal irradiances were therefore used to generate the sky matrix to be coupled with the Bidirectional Scattering Distribution Function (BSDF) of the analyzed

fenestration system via the daylight matrix, which takes into consideration the real building and surrounding geometry in order to calculate the absorbed share of solar radiation for each time-step.

2.2.2 CFD and thermal modelling

The computation of the coupled heat transfer and fluid flow was done with a CFD simulation using the software COMSOL Multiphysics. Some assumptions for this application were made. In particular, the real geometry was reduced to a vertical section (2D domain). This simplification is justified by the studies performed by Pasut and De Carli (2012) with the conclusion that modeling the entire 3D geometry of the fenestration system, instead of a 2D one, does not provide a substantial improvement in the results, considering the required additional effort. The fluid was considered as incompressible and the buoyancy driven flow was solved with the Boussinesq approximation (Versteeg and Malalasekera, 2005). Due to the low Grashof number ($Gr \approx 10e4$), which measures the ratio of the buoyancy to viscous forces (Equation 1), the fluid flow was considered laminar (Schlegel, 2015).

$$Gr = \frac{g \beta \rho^2 \Delta T L^3}{\mu^2} \quad (1)$$

The long-wave radiation exchange between the solid elements of the CFS was computed with the radiosity method, the so-called surface-to-surface method (van Eck et al., 2016), which depended on the temperature of the single parts, the view factors and the emissivity of the surfaces. For the CFD simulation an adequate mesh was created: a structured quad mesh was used for the solid domains, while a free triangular grid was applied to the fluid domain. Furthermore, the mesh was refined near the boundaries to guarantee a smooth transition from the non-zero fluid velocity to the zero velocity on the surface. To evaluate the mesh quality and guarantee that the solution is independent from the grid size, a mesh sensitivity analysis was carried out: considering the U-value (thermal transmittance) as control parameter, the mesh was refined until no further significant improvement in the U-value result was reached. The final mesh is shown in Figs 2 and 3. The total number of elements amounts to 56 281.

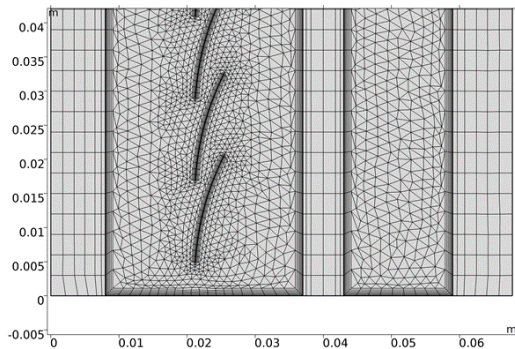


Fig. 2 – Final mesh of the Complex Fenestration System

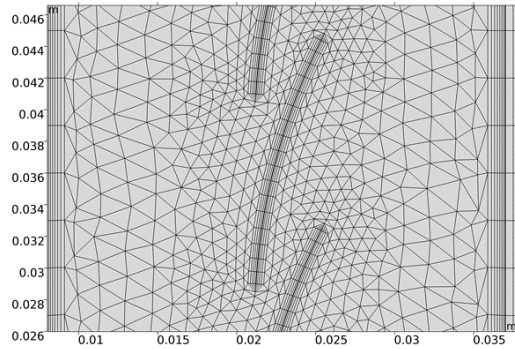


Fig. 3 – Final mesh around the blinds of the CFS

For the CFD simulation the boundary conditions in terms of measured internal and external surface temperatures were assigned, in addition to the pre-calculated solar absorption that was set up as heat source. The boundary conditions were measured during a sunny clear sky day in February 2018 from 9 am to 6 pm and assigned to the CFD model with a time-step of 300 s.

The conjugate heat transfer and fluid flow simulation was run with a time-dependent study and using a fully coupled solver. The simulation of each time-step was considered converged if the relative residuals of the continuity, momentum and energy equations were less than $10e-3$.

From the CFD simulation a temperature, pressure and velocity distribution over the fenestration system and for all the time-steps resulted. This made it possible to compute the total heat fluxes on all the grid points of the room-side face of the CFS. An integration of the heat flux over the total height of the interior glazing, except for the top and bottom extremes which had an extension of 10 % of the total height, was done. This made it possible to reproduce a similar condition as the measurement in which the heat flux was measured mainly at the center of the glazing, thus it did not account for the border effects.

2.3 In-Situ Measurements

In-situ measurements of the CFS installed on the west façade of the Living Labs of the Free University of Bozen-Bolzano were performed during a period of two weeks in February 2018. After analysing the experimental data, a sunny clear sky day was selected for the comparison with the CFD simulation. Different parameters were measured in order to characterize the thermal behaviour of the window system: internal and external air temperature near the façade, internal and external glazing surface temperature in different positions, total heat flux on the internal side, global and diffuse horizontal irradiance outside and total vertical irradiance on the façade.

For all the temperature measurements T-type thermocouples were used and their output voltage was read by a Datataker DT80 datalogger equipped with an internal reference. Those mounted on the exterior glazing surface were shielded from direct solar radiation using a silver tape to prevent the thermocouple from being heated up by direct irradiance. On the internal side, it was not necessary to shield the thermocouples since the closed position of the blinds prevented direct solar radiation hitting them. The total heat flux on the internal glazing surface was measured in two ways: conventional heat flux plates Hukseflux HFP01 and a temperature-controlled measurement device to determine the undisturbed, transient heat flux through transparent components (Hauer, 2017). This novel in-situ heat flux device (Fig. 4) measures the heat flow by means of a heat flux plate that is fixed slightly detached on the inner glazing surface via cupping vessels. In contrast to standard heat flux plates, this apparatus is continuously cooled through temperature-controlled Peltier elements, which prevent overheating of the device resulting from solar absorption, and therefore misleading measurement results.

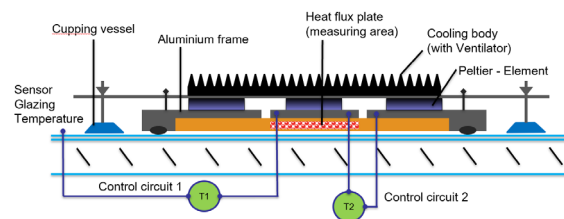


Fig. 4 – Section view of the in-situ heat flux device (Hauer, 2017)

The global and diffuse horizontal irradiance was measured with two Kipp&Zonen CMP11 thermopile pyranometers. With the use of the sole pyranometer placed on a horizontal surface, the global horizontal irradiance was measured, while to record the amount of diffuse irradiance a pyranometer with a solar tracker was used. In addition to the horizontal pyranometers, a Delta-T Devices SPN1 Sunshine Pyranometer was installed vertically on the external side of the west façade to evaluate the time-shift between the incident solar radiation and the measured heat flux on the internal side.

Fig. 5 shows all the measurement instruments installed on the analyzed fenestration system and Table 3 reports the instrument specifications.

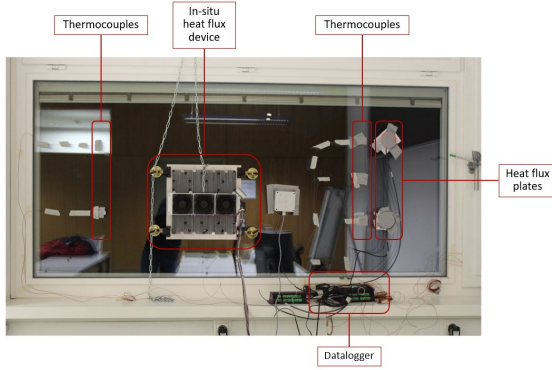


Fig. 5 – Measurement setup for the CFS

Table 3 – Instrument specifications

Parameter	Instrument	Accuracy
Temperature	T-type Thermocouple	$\pm 0.3\text{ }^{\circ}\text{C}$ ($k = 2$)
Heat flux	Hukseflux HFP01 Heat flux plate	$\pm 3\%$ ($k = 2$)
Heat flux	In-situ heat flux device	$< \pm 10\%$
Horizontal irradiance	Kipp&Zonen CMP11 Pyranometer	$\pm 2\%$ Daily total
Vertical irradiance	Delta-T Devices SPN1 Sunshine Pyranometer	$\pm 8\% \pm 10\text{ W/m}^2$ Individ. readings

3. Results and Discussion

The measurements on the fenestration systems provided several data and the inside and outside surface and air temperatures for a sunny clear sky day

were compared. Fig. 6 shows the trend of the external air temperature near the façade and the external surface temperatures measured at two different heights. During the day, the surface temperature is affected by a significant variation, starting from $1.0\text{ }^{\circ}\text{C}$ in the morning and reaching $36.8\text{ }^{\circ}\text{C}$ in the afternoon. In contrast, on the internal side the variation over the day is not so large due to the thermal insulation and inertia of the fenestration system and the controlled internal air temperature (Fig. 7).

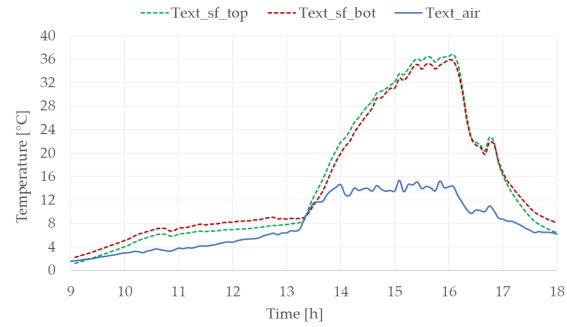


Fig. 6 – External air and surface temperatures for the CFS

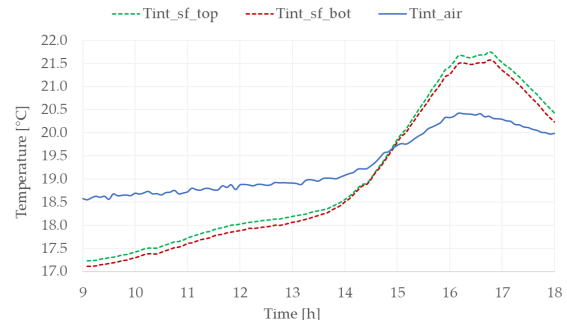


Fig. 7 – Internal air and surface temperatures for the CFS

A comparison between the total heat flux on the room-side face measured with the two types of instruments and the simulated heat flux was performed in order to characterize the thermal behaviour of the CFS under dynamic conditions and to validate the simulation against the measurement approaches (Figs 8 and 9). From this comparison, a good correspondence between simulated and measured heat flux emerged. In particular, during the period in which the system is heated up by direct solar radiation the correspondence was very good although the simulated values showed some steep fluctuations, which could be due to numerical errors. However, in the morning, when the façade is not affected by direct solar radiation, the simulated

heat flux had the same trend as the measured heat flux but it was underestimated. It can be noted that this difference decreased over the course of the morning, hence it could be a result of the fact that the simulation was initialized with the boundary conditions measured at the first instance of the comparison (i.e. 9 am) and did not consider the period before.

The peak heat flux resulting from the simulation amounted to 13.7 W/m², while the heat flux plates measured a peak value of 12.9 W/m² and the in-situ heat flux device of 11.0 W/m². The largest divergence between measurement results was recorded after sunset: in this time frame, an offset of up to 4 W/m² between the values measured by the two devices occurred. This deviation could be caused by a combination of a number of effects, such as the different response time to temperature variations of the two instruments. Indeed, the in-situ heat flux device showed a very fast reaction due to the Peltier coolers. In this period, the calculated heat flux was closer to the one measured by the heat flux plates. Beyond this, it is interesting to note that both the numerical model and in-situ measurements perceived the inertial effect of the glazing unit, which caused a time-shift of around one hour between the instance of the peak irradiance and that of maximum solar gain.

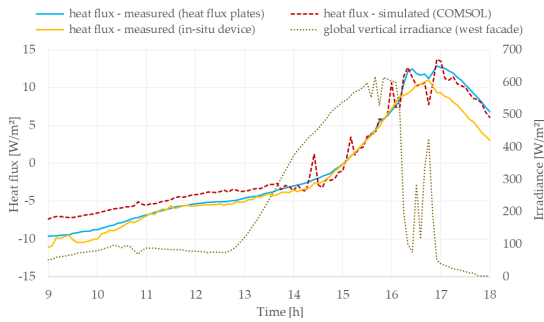


Fig. 8 – Comparison of simulated and measured heat flux through the CFS

Fig. 10 shows the relative deviations between the numerical and experimental results: in the case of positive – entering – heat flux, the relative deviations for the heat flux plates were mostly within 10 %, while they were around 20 %, in some instances even higher, in the case of the in-situ heat flux device due to the deviation of the results after sun-set.

In this period, the in-situ device underestimated the solar gains compared to the heat flux plates and the simulation results. Analysing the negative – exiting – heat flux, the relative deviation was mainly within 20 % for low heat fluxes and around 20 % for higher values.

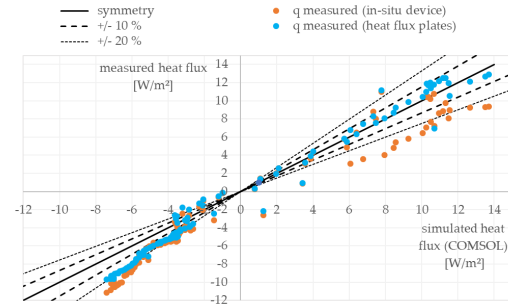


Fig. 9 – Deviations between simulated and measured heat flux

The discrepancy between simulated and measured data can be described through the RMSE (Root Mean Square Error) and MAE (Mean Absolute Error) defined as:

$$RMSE = \sqrt{\frac{\sum_{i=1}^n (q_{meas,i} - q_{sim,i})^2}{n}} \quad (2)$$

$$MAE = \frac{\sum_{i=1}^n |q_{meas,i} - q_{sim,i}|}{n} \quad (3)$$

The resulting mean errors RMSE and MAE for the in-situ heat flux device and the heat flux plates are reported in Table 4.

Table 4 – Comparison of simulation and measurement results

	RMSE [W/m ²]	MAE [W/m ²]
Simulation vs measurements (in-situ device)	2.16	1.81
Simulation vs measurements (heat flux plates)	1.45	1.24

From the RMSE and the MAE a good correspondence between numerical and experimental results emerged. However, these indicators confirmed a better correspondence of the simulation results with the heat flux plate measurements than the in-situ heat flux device for this configuration of glazing system and blind inclination. It should be noted that

the closed position of the blinds prevented direct solar radiation from reaching the measurement devices and overheating them. When there were different – more open – blind positions, the heat flux plates can become overheated and disturbed by the absorption of direct solar radiation. This was avoided with the in-situ heat flux device, mounted slightly detached from the glazing and cooled by temperature-controlled Peltier elements.

In addition to the heat flux, the comprehensive modelling of heat transfer and fluid flow coupled with the effect of solar radiation makes it possible to account for the components' temperatures that can be reached inside the sealed cavity. The absorption of solar radiation on the blinds and the glass panes significantly increases their temperature. The closed cavity does not enhance the heat dissipation, thereby inducing the filling gas temperature to rise. For this glazing configuration, the blinds in the upper part of the cavity can reach temperatures of around 50 °C, even in winter conditions with a maximum external air temperature of 15 °C.

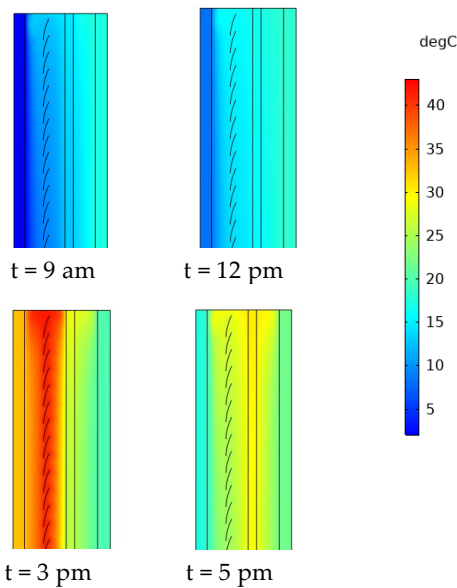


Fig. 10 – Temperature distribution within the CFS at different times

4. Conclusion

The results discussed show that the coupling of CFD simulations with the separately computed effect of solar radiation is a valid modelling approach for assessing the thermal performance of Complex Fenes-

tration Systems under dynamic conditions. This modelling approach could be appropriate for a detailed analysis of fenestration systems in order to assess specific properties, for instance secondary heat fluxes, maximum temperatures of certain components of the glazing unit or fluid flow rates in the cavity. From the numerical modelling of CFS, it emerged that the solar absorption has a significant impact on the fluid flow in the cavity, the solar heat gains and the temperatures of the components. Thus, in addition to a CFD-based approach that considers the effect of the fluid flow, an accurate optical modelling is essential to appreciate the glazing and shading complexity. Furthermore, the numerical and experimental characterization of the thermal behaviour of CFS under dynamic conditions provided evidence of the inertial effect of fenestration systems causing a time-shift of around one hour between the instance of the peak irradiance and that of maximum solar gain of the room.

For this glazing configuration with blinds in a closed position, numerical results in terms of heat fluxes are confirmed by experimental measurements, using both conventional heat flux plates and a temperature controlled in-situ heat flux measurement device.

Further analysis will be done in order to validate the modelling approach for different blind positions and apply it to naturally ventilated cavities. In this case, the fluid flow within the cavities is expected to have an even greater impact on the overall heat transfer and thus the performance of the fenestration system.

Acknowledgement

This study has been developed in the framework of the research activities of the project FACEcamp n. ITAT1039, funded by European Regional Development Fund and Interreg ITA AUT programme and by the project Klimahouse and Energy Production in the framework of the programmatic-financial agreement with the Autonomous Province of Bozen-Bolzano of Research Capacity Building of the Free University of Bozen-Bolzano.

Nomenclature

Symbols

G_r	Grashof number (-)
g	Gravitational acceleration (m/s ²)
β	Volume expansivity (1/K), $\beta=1/T$ for ideal gases
ρ	Density (kg/m ³)
ΔT	Temperature difference (K)
L	Characteristic length (m)
μ	Dynamic viscosity (Ns/m ²)
$q_{meas,i}$	Measured heat flux at timestep i (W/m ²)
$q_{sim,i}$	Simulated heat flux at timestep i (W/m ²)

References

- Demanega, I., G. De Michele, G. Pernigotto, S. Avesani, F. Babich, A. Gasparella. 2018. "CFD and ray tracing to evaluate the thermal performance of Complex Fenestration Systems." *Proceedings of the 2018 Building Simulation and Optimization Conference in Cambridge*, 460-466.
- Hart, R., H. Goudey, D. C. Curcija. 2017. "Experimental validation and model development for thermal transmittances of porous window screens and horizontal louvred blind systems." *Journal of Building Performance Simulation* 11(2), 1–15.
- Hauer, M. 2017. "Model Development and Validation for an Integrative Thermal and Daylight Evaluation of Complex Fenestration Systems in Building Performance Simulations". PhD Dissertation, Universität Innsbruck. Institut für Konstruktion und Materialwissenschaften, AB Energieeffizientes Bauen.
- ISO. 2003. *ISO 15099:2003: "Thermal performance of windows, doors and shading devices — Detailed calculations"*.
- Konis, K., S. Selkowitz. 2017. *Effective daylighting with high-performance facades: emerging design practices*. Springer.
- Kuhn, T. E., S. Herkel, F. Frontini, P. Strachan, G. Kokogiannakis. 2011. "Solar control: A general method for modelling of solar gains through complex facades in building simulation programs." *Energy and Buildings* 43, 19–27.
- McNeil, A. 2014. "The Three-Phase Method for Simulating Complex Fenestration with Radiance". LBNL.
<https://www.radiance-online.org/learning/tutorials/Tutorial-ThreePhaseMethod.pdf>
- Pasut, W., M. De Carli. 2012. "Evaluation of various CFD modelling strategies in predicting airflow and temperature in a naturally ventilated double skin façade." *Applied Thermal Engineering* 37, 267–274.
- Schlegel, F. 2015. "Using the Boussinesq Approximation for Natural Convection." COMSOL Blog. Accessed 2019 Sep 19.
<https://www.comsol.com/blogs/using-the-boussinesq-approximation-for-natural-convection/>
- Van Eck, R. 2016. "Surface to Surface Radiation Benchmarks." *Proceedings of the 2016 COMSOL Conference in Munich*, 1-6.
- Versteeg, H. K., W. Malalasekera. 2005. *An introduction to computational fluid dynamics: the finite volume method*. Harlow: Pearson/Prentice Hall.
- Ward, G. 1994. "The RADIANCE Lighting Simulation and Rendering System." *Proceedings of the 21st annual conference on Computer graphics and interactive techniques*, 459-472.

Modelling the Sound Insulation of Mass Timber Floors Using the Finite Transfer Matrix Method

Federica Morandi – Free University of Bozen-Bolzano, Italy – federica.morandi@unibz.it

Marco Caniato – Free University of Bozen-Bolzano, Italy – marco.caniato@unibz.it

Olivier Robin – Université de Sherbrooke, Canada – olivier.robin@usherbrooke.ca

Luca Barbaresi – University of Bologna, Italy – luca.barbaresi@unibo.it

Andrea Gasparella – Free University of Bozen-Bolzano, Italy – andrea.gasparella@unibz.it

Patrice Masson – Université de Sherbrooke, Canada – patrice.masson@usherbrooke.ca

Nouredine Atalla – Université de Sherbrooke, Canada – nouredine.atalla@usherbrooke.ca

Abstract

Cross Laminated Timber (CLT) technology has revolutionized the use of timber in construction in just 20 years. However, the development of mid- and high-rise CLT buildings has raised concerns about the sound insulation provided by these structural elements and about the reliability of simulation tools and models which are currently used. The mechanical characteristics of mass timber elements do not allow simplifications such as infinite out-of-plane stiffness, diffuseness of the vibrational field and perfectly elastic behavior upon impact, to mention a few, which are commonly assumed for traditional structures. The availability of modeling/simulation tools (and the relative input data) that provide accurate predictions of airborne and structure-borne sound insulation is therefore a current and relevant topic. This work presents an investigation into the input parameters to use for modelling CLT elements using the Finite Transfer Matrix Method (FTMM). The results of laboratory measurements on two CLT floors are compared to results obtained using two FTMM-based software packages in a three-step procedure. First, measurements were performed on two timber floor solutions. Following this, two operators working with different FTMM-based software packages performed blind simulations, based upon the information shared on the materials' characteristics. Finally, the input data were modified in order to return the best fit to the experimental data. The aim of the work is twofold: (1) to verify the degree of accuracy of the software and (2) following a reverse-engineering process, to retrieve the properties of the materials that need to be modelled through equivalent physical dimensions. The results for the bare CLT floor show that using dynamic E value for the plate modelling returns slightly

more accurate results. Conversely, the question of modelling of a complete floor, including a floating floor, deserves greater attention, as modelling the resilient underlay using static values of dynamic stiffness can alter the results to a great extent.

1. Introduction

Cross Laminated Timber is an engineered wood product made of layers of wood planks, which are glued crosswise to form a monolithic element. Its development in recent years has provided the opportunity for timber construction to enter the sector of mid- and high-rise buildings (Albee et al., 2018; Muszynski et al., 2017). The renewed attention to the characterization of the sound insulation of timber elements stems from this diffusion of multi-unit residential buildings and the consequent need for the fulfilment of the acoustic requirements according to national regulations.

Wood exhibits a strongly anisotropic behaviour but CLT elements are usually modelled as orthotropic plates due to the above-mentioned fabrication process. CLT is furthermore characterized by low structural damping and large out-of-plane bending stiffness in relation to the low density. Several hypotheses that underlie acoustic modelling of traditional building elements, such as concrete slabs or brick walls, are not verified for CLT elements. For example, the infinite out-of-plane stiffness hypothesis does not hold, and therefore the modelling of additional linings and floating floors requires cus-

tom adaptation terms and reference curves (Di Bella et al., 2016; Schoenwald et al., 2013). Moreover, when evaluating the response to impact excitation, one must consider that no elastic rebound can be assumed on timber elements.

These considerations emphasize the need to control the input data of any simulation tool for modelling CLT elements. In this scenario, the aim of this paper is to identify the optimal input parameters for acoustic modelling of CLT elements through the comparison of experimental measurements to the results of the modelling performed with two TMM-based software packages.

2. Methodology

The study is based on a three-step procedure. First, measurements of the sound insulation of two different CLT-based floor configurations were carried out under controlled laboratory conditions. Second, information concerning the materials used for the tests was provided to two operators, using two different software packages implementing FTMM. This method was preferred to other tools such as Finite Element Method or analytical methods for ease of implementation and for reduced computational time.

The operators performed ‘blind’ simulations, i.e. without having access to the results of the measurements. The results of the simulations were collected and compared to the measured data. Third, a strategy for the optimization of the modelling was addressed. The optimized input values were used to run additional simulations and compared to (i) the input data chosen and (ii) the different results provided by the two software packages.

2.1 Measurements

The airborne and impact sound insulation measurements were conducted at the Laboratory of Applied Acoustics at the University of Bologna. CLT floors were mounted and tested in the acoustic chambers with suppressed flanking transmission, according to the ISO 10140 standard. For the purpose of this study, the sound insulation relative to two different construction stages are analysed:

- A. bare CLT floor;
- B. complete structure including: CLT, polyethylene sheet, wet subfloor, resilient interlayer, sand and cement screed.

The availability of measured data at additional intermediate stages provided the opportunity to evaluate the contribution of each layer separately. The description of the materials is reported in Table 1; for each layer, t is the thickness, ρ is the mass density and s' the dynamic stiffness.

Table 1 – Characteristics of materials shared with the two operators

Material	Floor A	Floor B
CLT	$t = 0.16 \text{ m}$ $\rho = 420 \text{ kg/m}^3$	$t = 0.16 \text{ m}$ $\rho = 420 \text{ kg/m}^3$
PE sheet	No	Yes
Subfloor	-	$t = 0.12 \text{ m}$ $\rho = 500 \text{ kg/m}^3$ *
Resilient underlay	-	$t = 0.01 \text{ m}$ $s' = 12.5 \text{ MN/m}^3$ * $\rho = 80 \text{ kg/m}^3$
Floating floor	-	$t = 0.05 \text{ m}$ $\rho = 1950 \text{ kg/m}^3$ *

* The dynamic stiffness of the resilient underlay and the density of all cast-in screeds were measured at the Laboratory of Applied Acoustics and Structural Engineering at the University of Bologna.

Additional information was provided on the mechanical characteristics of CLT, such as out-of-plane E and G moduli as declared in the datasheet. The structural loss factor η was estimated from measurements of the structural reverberation time. The information provided was deemed representative of the average data available to practitioners.

2.2 Blind Simulations

The two operators were asked to perform blind simulations of the two floors, based upon the information provided and making assumptions on the missing information. At this stage, relevant differences had already been found in the approaches of the two operators. Table 2 reports a comparison of the choices performed.

Table 2 – Modelling assumptions chosen by the two operators for the blind simulation phase

Element	OP 1	OP 2
CLT	Viscoelastic, isotropic FTMM Static value of E $\nu = 0.3$ η as given	General laminate, 5 layers FTMM Static value of E $\nu = 0.01$ $\eta = 0.01$ ⁽³⁾
Resilient interlayer	E = 0.125 MPa $\nu = 0.41$ ⁽¹⁾ $\eta = 0.2$ ⁽²⁾	E = 2300 MPa ⁽⁴⁾ $\nu = 0.08$ ⁽⁵⁾ $\eta = 0.49$ ⁽⁶⁾

¹ G. Neville Greaves, Poisson's ratio over two centuries: challenging hypotheses, Notes Rec R Soc Lond. 2013 Mar 20; 67(1): 37–58

² A. Schiavi, Improvement of impact sound insulation: A constitutive model for floating floors, Applied Acoustics Volume 129, 1 January 2018, Pages 64-71

^{3,4,5,6} Hard rubber, from the Isotropic Elastic Material Library, Nova software, <https://www.mecanum.com/nova?lang=en>

The main differences are found for the modelling of the CLT element and the resilient underlay.

OP1 modelled CLT as a viscoelastic, isotropic material; this choice was influenced by previous experience in CLT modelling. Conversely, OP2 modelled CLT as a general laminate composed of 5 layers, having the thickness described in the technical datasheet. Both operators used finite size windowing and attributed to the CLT the static value of E that was provided in the datasheet. The assumption on the value of Poisson's ratio ν was different: OP1 picked the classical value of wood, while OP2 opted for an extremely low value to match the relation between the given E and G moduli, at the expense of a loss in physical meaning. For the structural loss factor η , OP1 picked the actual measured value (slightly dependent on frequency, but realistically approximated to a value of around 0.02), while OP2 picked the proposed fixed value of 0.01 (a hard rubber material was arbitrarily chosen from the existing materials library).

The resilient underlay was also characterized differently. OP1 assumed a Young's modulus of 0.125 MPa, calculated from the value of dynamic stiffness provided, and assumed damping and Poisson's ratio typical of similar materials present in the software library. OP2 also picked a resilient material from an existing library, but the elastic modulus was estimated as 2.3 GPa – indicating that the material is not used for building acoustics applications. It should be noted that the two operators had different backgrounds in acoustics: OP1 mainly works on building acoustics, while OP2 works on aerospace applications.

The results of the simulations performed with these input parameters are presented in Fig. 1.

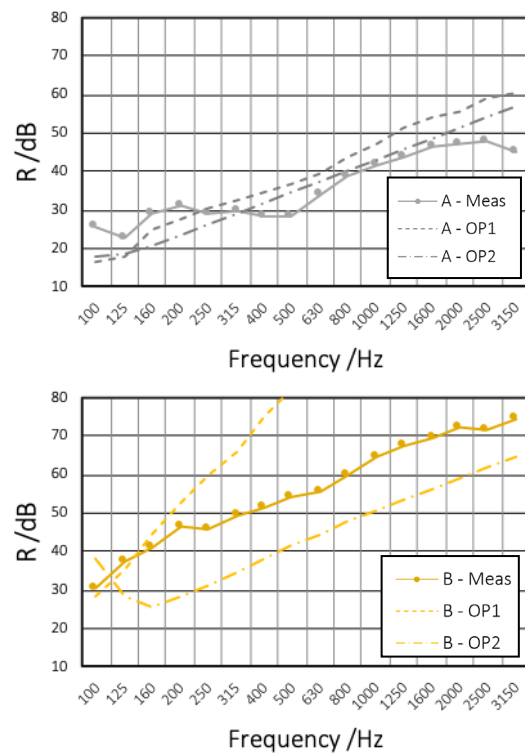


Fig. 1 – Sound reduction index R: measurements vs simulations. Top: configuration A, bare floor. Bottom: configuration B, complete floor. Measurements are represented using markers; the dashed line corresponds to OP1 while the dash-dot line corresponds to OP2

The results of the blind simulations are reported in Fig. 1. For the bare floor (configuration A), the frequency-averaged absolute difference between measurements and simulations is 6.6 dB for OP1 and 4.7 dB for OP2, suggesting that, besides software differences, the modelling of CLT as a lami-

nate provides a better estimate of the transmission coefficient. In case of the complete floor, the absolute difference between measurement and simulation results reach much larger values: 26.0 dB for OP1 and 12.6 dB for OP2.

The differences between simulations performed by the two operators are mostly related to the different input parameters chosen for the resilient underlay. The simulation performed by OP1, which uses values that closely match the actual characteristics of the resilient underlay, leads to a large discrepancy in results of the measurements.

2.3 Optimization Approach

The optimization process followed two approaches: on the one hand, objective optimization based upon mechanical characteristics of the materials and on the other hand, a ‘differential’ approach that seeks optimization across the available data.

2.3.1 Dynamic Young’s modulus for CLT

If one considers CLT as a viscoelastic material, then its mechanical characteristics will be affected by the driving frequency; the higher the frequency of excitation, the more stiff the material will behave. The apparent frequency-dependent Young’s modulus E can be calculated from Kirchhoff’s theory of wave propagation in thin plates, starting from the dispersion relations (Santoni et al., 2017):

$$E(f) = \frac{12\rho c_b^4(f)(1 - \nu^2)}{h^2\omega^2} \quad [Pa] \quad (1)$$

Where ρ is mass density, c_b is the bending waves velocity, ν is Poisson’s ratio, h is the thickness of the considered slab and ω is the angular frequency. The bending waves velocity of the CLT plate under test had been previously measured on the two main symmetry directions and averaged to compensate for the orthotropy of the plate. In this application, these previous results were used to calculate the dynamic E modulus.

The thin plate hypothesis underlying Kirchhoff’s theory implies a relevant simplification in the estimate of E . This happens because, starting from a cut-off frequency, the dispersion curves are affected by the predominance of shear waves, and this effect is not considered for thin plates. Therefore,

the E modulus is forced to compensate for this ill-posed model of wave propagation, assuming values that, at high frequencies, might not be physically meaningful (Rindel, 1994).

2.3.2 Dynamic Young’s modulus for the resilient underlay

The resilient underlay can be modelled using frequency-dependent values. The measurement procedure for dynamic stiffness, reported in the standard EN 29052-1, determines the measurand at the resonance frequency of a system consisting of a 200 kg/m² plate resting on a resilient layer, which lies on an inertial base. When the measurements are conducted using an electrodynamic shaker, the force injected by the shaker is measured with an impedance head and tests are repeated for different input amplitudes, the final values being read as an extrapolation of the measured data at null frequency. Approximately speaking, the dynamic stiffness expressed as a single number only describes the behavior of the material at the resonant frequency of the above-described system. For the results presented in this paper, it will be noted that simulations carried out using a single number match reasonably well to the results of the measurements at very low frequencies, i.e. where the behavior of the resilient material is well described by the testing methodology described above.

The dynamic values used thereafter were retrieved using a simplified scheme, in which the difference between the measurement on the bare floor and on the complete floor is attributed to the frequency-dependent mechanical properties of the resilient interlayer (Caniato et al., 2019). The input data for all other materials are assumed according to the values provided.

The standard EN ISO 12354-2:2017 provides a simplified equation to estimate the reduction of the impact sound pressure level ΔL of floating floors made of sand/cement, compared with a bare structure:

$$\Delta L = 30 \log \frac{f}{f_0} \quad [dB] \quad (2)$$

where f (Hz) are the one-third octave band centre frequencies and f_0 (Hz) is the resonance frequency

of the spring-mass system describing the floating floor:

$$f_0 = 160 \sqrt{\frac{s'}{m'}} \quad [\text{Hz}] \quad (3)$$

Where s' represents the dynamic stiffness of the resilient interlayer, expressed in MN/m^3 , and m' the mass per unit area of the floating floor, in kg/m^2 .

Since the sound insulation improvement ΔL was measured (as the difference between configuration A and B, see Section 2.2), it is possible to deduce the frequency-dependent value of s' from Equations 2 and 3. It is important to notice that the obtained value is not merely representative of the behavior of the resilient underlay, but also accounts for the global response of the floating floor.

3. Results and Discussion

The dynamic values of the elastic modulus of CLT and of the resilient interlayer were used as new inputs for the FTMM software and the updated outputs were compared to measurement results. Since the measured loss factor was almost constant in frequency, a constant value of 0.02 was considered and a Poisson's ratio of 0.3 was assumed. The results of the previous and optimized simulation for the bare floor are presented in Fig. 2, together with the experimental results.

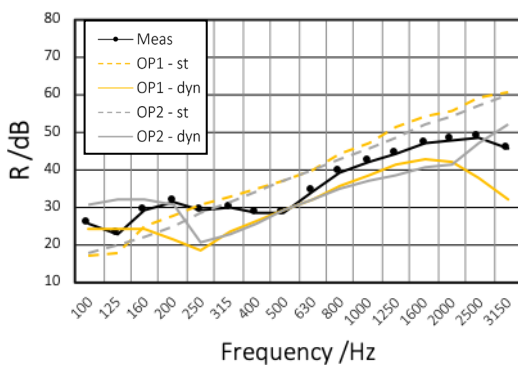


Fig. 2 – Measurements vs optimized simulations of the bare CLT floor (OP1). Measurements are represented with a continuous black line with markers, simulations with static values are represented in grey while dynamic values are presented in yellow

The results show a substantial improvement in the fit of the measured data in the frequency range above the critical frequency. For OP1, the frequen-

cy-averaged absolute error decreases from 6.6 to 5.2 dB. The difference is not relevant *per se*, but it is clear from Fig. 2 that the metric chosen is strongly affected by the behaviour of sound insulation at specific frequencies.

For the complete floor, the combinations proposed are the following:

- static E_{CLT} and static E_{RES}
- static E_{CLT} and dynamic E_{RES}
- dynamic E_{CLT} and static E_{RES}
- dynamic E_{CLT} and dynamic E_{RES}

The results presented by OP1 are presented in Fig. 3.

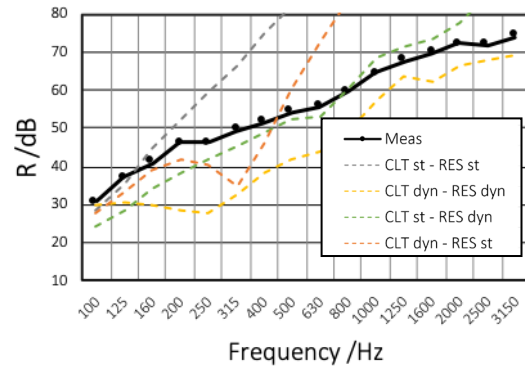


Fig. 3 – Measurement vs optimized simulations of the complete floor (OP1). Measurements are represented with a continuous black line with markers, while combinations of static/dynamic values of E for the CLT and the resilient interlayer are represented as colored dashed lines

The results that emerge from this analysis show that the most accurate analysis is achieved through modelling the CLT floor using a single static value of Young's modulus for the CLT part and dynamic values of E for the resilient interlayer. This emphasizes the need for further research on the characterization of these materials.

It should be noted that the dynamic E modulus of CLT was derived from measurements of the bending wave velocity performed on that same plate, which can be generally considered valid for all CLT panels characterized by that thickness and layer composition. Conversely, the determination of the apparent dynamic stiffness of the resilient underlay is based upon the measurements of impact sound insulation, subsequently used to estimate airborne sound insulation for one specific case. Therefore, it will be possible to draw conclusions using this approach only after analysing sev-

eral experimental tests performed on the resilient underlay with different floor configurations, and through the simulation of both impact and airborne sound insulation.

4. Conclusion

This paper has explored the influence of input parameters for the modelling of Cross Laminated Timber floors using the Finite Transfer Matrix Method. The investigation was conducted by asking two independent operators to perform simulations on a CLT floor that had previously been characterized in laboratory conditions. A first series of blind simulations (without having access to the experimental measures) was performed based on the assumed characteristics of the materials and a small number of assumptions made by each operator. These preliminary results provided a satisfactory agreement between measurement and simulation results for the bare CLT floor, while the complete floor simulations returned largely biased results. The optimization of the simulations was carried out through the introduction of dynamic values of the E modulus and of the dynamic stiffness of the material, leading to a significant reduction in absolute error between simulation and measurements.

Future work will address the joint effect of the floor modelling on airborne and impact sound insulation in order to provide a reliable characterization of the frequency-dependent mechanical properties of the resilient underlay.

References

- Albee, R., L. Muszynski, R. Hansen, C. Knowles, P. Larasatie, and J. Guerrero. 2018. "Recent developments in global cross-laminated timber (CLT) market." *Proceeding of the World Conference on Timber Engineering*, Seoul, South Korea, August 2018.
- Atalla, N., F. Sgard, and C. Kafui-Amedin. 2006. "On the modelling of sound radiation from poroelastic materials." *The Journal of the Acoustical Society of America* 120(4):1990–1996.
- Caniato, M., P. Bonfiglio, F. Bettarello, and A. Gasparella. 2019. "Innovative approach in acoustic simulation of timber walls." *Proceedings of the 16th International Conference of IBPSA - Building Simulation 2019*, Rome, Italy, September 2019.
- CEN. 2017. *EN ISO 12354-2:2017. Building acoustics – estimation of acoustic performance of buildings from the performance of elements – part 2: impact sound insulation between rooms*. Brussels, Belgium: CEN.
- CEN. 1989. *EN 29052-1:1989. Acoustics – Method for the determination of dynamic stiffness – Part 1: Materials used under floating floors in dwellings*. Geneva, Switzerland: ISO.
- Di Bella, A., N. Granzotto, and L. Barbaresi. 2016. "Analysis of acoustical behaviour of bare cross laminated timber floors for the evaluation of the improvement of impact sound insulation." *Proceedings of Meetings of Acoustics* 28:015016.
- ISO. 2010. *ISO 10140-1:2010. Acoustics – Laboratory measurement of sound insulation of building elements – Part 1: Application rules for specific products*.
- Muszynski, L., E. Hansen, S. Fernando, G. Schwartzmann, J. Jasmin Rainer. 2017. "Insights into the Global Cross Laminated Timber Industry." *BioProducts Business* 2(8):77–2.
- Rindel, J. 1994. "Dispersion and absorption of structure-borne sound in acoustically thick plates." *Applied Acoustics* 41 (2): 97–111.
- Santoni, A., S. Schoenwald, B. Van Damme, and P. Fausti. 2017. "Determination of the elastic and stiffness characteristics of cross-laminated timber plates from flexural wave velocity measurements." *Journal of Sound and Vibration* 400: 387–401.
- Schoenwald, S., B. Zeitler, I. Sabourin, F. King. 2013. "Sound insulation performance of Cross Laminated Timber Building Systems." *Proceedings of Internoise 2013*, Innsbruck, Austria.

Safety at Chimney-Roof Penetration: A Numerical Investigation

Manuela Neri – University of Brescia, Italy – manuela.neri@unibs.it

Leppänen Perttu – FirePro Palokatko Oy, Finland – perttu.leppanen@firepropalokatko.fi

Mika Alanen – Tampere University, Finland – mika.alanen@tuni.fi

Davide Luscietti – University of Brescia, Italy – davide.luscietti@unibs.it

Mariagrazia Pilotelli – University of Brescia, Italy – mariagrazia.pilotelli@unibs.it

Abstract

Chimneys convey exhaust gas produced in heat generators to the external ambient. To do this, they cross building elements such as floors and roofs, which can be made of flammable materials such as wood, wood fiber, cellulose, etc. This represents a dangerous condition that can lead to the overheating of the structure and, consequently, to possible fires. In recent years, numerous roof fires have occurred in Europe due to the presence of a chimney, and some of these have also involved certified chimneys. The aim of the certification procedure is the determination of the distance between chimney and flammable structures to avoid fires. This paper describes an investigation performed to understand the causes of the high number of fires and to propose solutions to the roof fires problem. The study was carried out numerically and experimentally, and consisted of three steps. Firstly, the chimney certification procedure was investigated to highlight possible weaknesses. Then, by means of a 2D and a 3D numerical models, the variables affecting heat transfer at chimney-roof penetration were identified. Finally, solutions and prescriptions to prevent roof fires are proposed. The solutions consist of a set of tables for checking chimney installations, and a universal device to be installed between chimney and roof to prevent the overheating of the latter, also in very critical conditions represented by soot fires, and installations in very thick and insulating roofs.

1. Introduction

In recent years, numerous roof fires have occurred in Europe due to the presence of a chimney, and some of these have also involved certified chimneys (Buffo and Dadone, 2007; Dadone, 2009; International Partnership for the Investigation of Fires Explosion, 2015; Ministry of the Environment

of Finland, 2011). Chimney certification is regulated by the EN 1859 standard (CEN, 2009), which prescribes two tests to determine the safety distance between chimney and flammable structures: the Heat Stress Test (HST) reproduces the normal use condition of chimneys, while the Thermal Shock Test (TST) reproduces the soot fire condition. In both tests, the chimney must be installed in a test structure made of two walls at a right angle, with two roofs positioned at different heights. The roofs are made of an insulating layer between two wooden layers. The thickness (S) and the thermal resistance (R) are 132 mm and 3.04 m²K/W for the upper roof, and 232 mm and 5.90 m²K/W for the lower roof. Despite the tests are aimed to test the worst conditions, the increasing attention to energy efficiency requires thicker and more insulating roofs (Manfren et al., 2019). The tests consist of feeding the chimney with gas at a predetermined temperature (T_{ch}) and then measuring the temperature at chimney-roof penetration. The maximum temperatures (T_{max}) measured on the test structure must be compared with two limit temperatures (85 °C for HST, and 100 °C for TST). If the limit temperatures are not exceeded, the chimney is certified and a label is applied to it. An example of such a label is EN1856-1-T600-N1-D-V2-L50050-G20. From the thermal point of view, the main information reported in the label is T600, which is the class temperature of the chimney (the maximum temperature of the exhaust gas), and G20, which represents the minimum distance (in millimetres) allowable between the chimney and flammable materials. Even though in real installations the clearance between chimney and roof must be sealed to avoid the entering of atmospheric agents, no information is report-

ed on the label on how the chimney should be sealed. This paper describes the steps that have led to an understanding of the heat transfer at chimney–roof penetration and to solutions for preventing roof fires. The data reported here were presented in several papers (Leppänen et al., 2015; Leppänen et al., 2017a; Neri et al., 2015a and 2015b; Neri et al., 2016; Neri and Pilotelli, 2018 and 2019), and the aim of this article is to describe the entire research body.

In addition to the above-mentioned research, a number of additional studies have been carried out. Kererekes (2018) outlined a test of a newly developed composite material for chimneys, while Leppänen and Malaska (2019) investigated the smouldering combustion of mineral wool. The effect of the design flue gas temperature has been investigated (Leppänen et al., 2015; Leppänen et al., 2017b), and the thermal performance of an innovative three-layer chimney was investigated by Drozdol (2020). Studies in the literature have also investigated aspects related to heat generators and emissions. For example, Polonini et al. (2018, 2019a, 2019b and 2019c) showed that the exhaust gas temperature for a pellet stove between 7 kW and 11 kW is normally around 190 °C and 230 °C. In non-optimal burning conditions, the formation of soot can be up to 5 times more than in optimal burning conditions.

2. Method and Results

The investigation that led to the comprehension of heat transfer at chimney roof–penetration consisted of several steps. Firstly, the chimney certification procedure was analysed to highlight possible weaknesses. Since heat transfer at chimney–roof penetration depends on many variables, a numerical approach was necessary. For this, 2D and 3D numerical models were defined to estimate the steady temperature of a roof near a chimney. The numerical approach made it possible to analyse a wider range of configurations. Subsequently, the numerical results were analysed statistically to assess the influence of each variable on the maximum roof temperature. Regression models to estimate the maximum roof temperature were identified by means of the DoE (Design of the Experiments) technique. Since the regression models use several coefficients and variables, they were translated into tables, with

which it is possible to check whether an installation is safe. Finally, a device for reducing the temperature at the chimney–roof penetration was defined.

2.1 Analysis of the EN 1859 Standard

Firstly, the chimneys certification procedure described in the EN 1859 (CEN, 2009) standard was analysed to understand whether it represents the most critical chimney operating conditions. The main aspects analysed were the position of the chimney in the roof, the exhaust gas temperature measurement point, the clearance sealing mode, the characteristics of the roof, and the initial test conditions. Even though in real installations chimneys are installed completely surrounded by a roof, in the TST and the HST tests, the chimney to be certified is installed in a test structure made of two walls at a right angle, with two roofs positioned at different heights. Since the limited horizontal thickness of the walls represents a thermal bridge, the roof temperature measured in the certification procedure may be lower than that measured in real installations. According to the standard (EN1859:2009), the exhaust gas temperature (T_{ch}) must be measured in the vicinity of the heat generator. Fig. 1 shows the exhaust gas temperature measured near the exhaust gas generator as prescribed by the standard (EN1859:2009), and at the chimney–roof penetration. It can be seen that in the vicinity of the chimney–roof penetration, the exhaust gas temperature (T_{ch}) can be much lower because of heat losses along the chimney flue. The difference in temperature can be up to 150 °C.

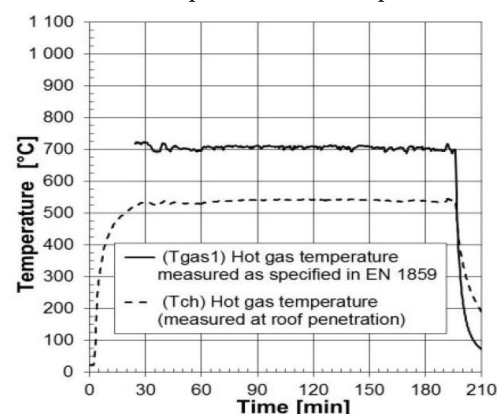


Fig. 1 – Comparison between exhaust gas temperature measured in the vicinity of the heat generator, and that measured in the vicinity of the chimney–roof penetration in the HST

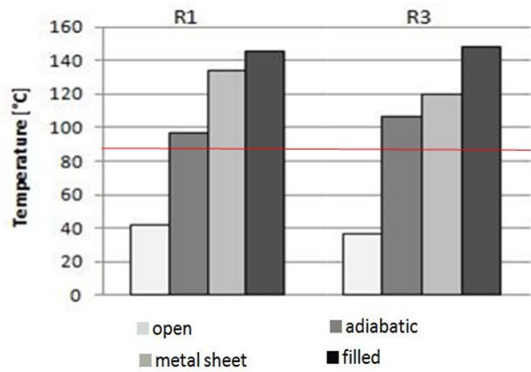


Fig. 2 – Maximum roof temperature obtained by varying the clearance sealing mode. The red line represents the limit temperature prescribed by the EN 1859 (EN1859:2009) standard for the HST. Results were obtained experimentally

In the TST and the HST, depending on the prescriptions provided by the chimney producer, the chimney can be installed in contact with or spaced from flammable materials. Consequently, the clearance between chimney and roof can be sealed or left open. If the clearance is left open, air can circulate and cool the roof; otherwise, the cooling process is limited. Despite these two possible conditions, no information is specified on the chimney label about the clearance sealing mode in the certification tests. To investigate the importance of this information, in an experimental campaign the clearance was sealed in different ways in order to reproduce possible real conditions. More precisely, the clearance was either left open, sealed with metal sheets, sealed with insulating panels, or filled with insulating materials. Leaving the clearance open allows complete air circulation. Sealing the clearance blocks the air between chimney and roof, but metal sheets allow heat transfer between the air trapped in the clearance and ambient, while the insulating panels reduce it. The tests were performed for two roofs, labelled R1 and R3. Roof R1 is the thickest roof prescribed by the standard (EN1859:2009), and roof R3 is 450 mm thick and its thermal resistance is 8.34 m²K/W. Fig. 2 shows the roof temperature measured experimentally in the different conditions. It can be seen that if the clearance is left open, the roof temperature is much lower than 85 °C, but if the clearance is closed or filled the roof temperature can be 110 °C higher.

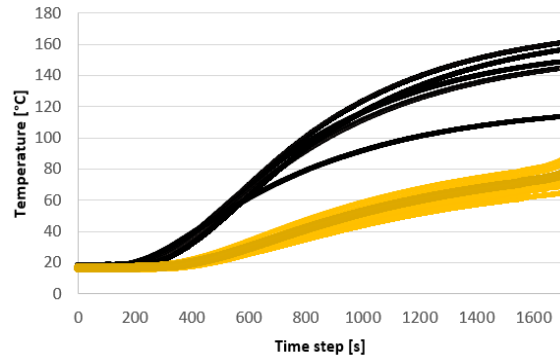


Fig. 3 – Roof temperature measured in the corner test structure prescribed by the standard (EN 1859:2009) and in the axial-symmetric test structure where the chimney is completely surrounded by a roof

By considering the roof thickness (S) and thermal resistance (R), it emerges that for real roofs they can be greater than those in the certification procedure, especially in energy-saving buildings. However, real roofs can be made of more layers and of different characteristics (EN 1859:2009). The investigation also analysed the influence of the position of the chimney in the roof. Fig. 3 compares the temperature measured when the chimney was installed at the centre of a roof (black lines), and in a corner test structure (yellow lines). It can be seen that the roof temperature strongly depends on the chimney position in the roof and the difference in temperature can be up to 80 °C: if the chimney is completely surrounded by the roof, the temperature is greater because the horizontal thickness of the roof reduces the heat transfer towards the ambient.

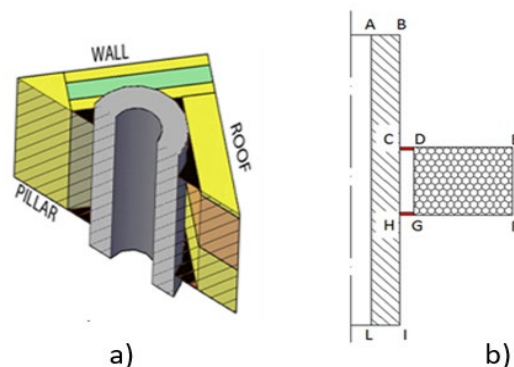


Fig. 4 – The 3D numerical model a) and the 2D numerical model b) used to investigate the influence of the variables

Another aspect relates to the initial TST condition. In the certification procedure, the TST is performed at ambient temperature, but real soot fires may

occur immediately after the heat generator is activated, or after a certain period of operation. In the case of the latter situation, the roof temperature (T_{max}) may be much higher than the ambient temperature. Consequently, the TST condition is insufficiently strict.

2.1.1 Numerical models to estimate the temperature at chimney–roof penetration

Since heat transfer at chimney–roof penetration depends on several variables, an extensive experimental campaign was not possible because the tests prescribed by the standard (EN 1859:2009) are expensive and time consuming. For this reason, the 3D and the 2D numerical models in Fig. 4 were defined to investigate heat transfer at chimney–roof penetration (Neri et al., 2015a). The 3D numerical model represents the certification procedure conditions where the chimney is installed near two walls at a right angle, while the 2D numerical model represents real installation conditions where the chimney is completely surrounded by a roof. The numerical models estimate the steady roof temperature correctly and in favor of safety. In the majority of cases, the calculated temperature is higher than the actual roof temperature because in the models air infiltration through the material is completely excluded. By comparing numerical and experimental results, it was shown that in the certification procedure the steady temperature is often not achieved because tests are stopped earlier (when the increase in the roof temperature is lower than $2^{\circ}\text{C}/30$ minutes). To estimate the steady temperature from the temperature-time curves obtained experimentally, the *Heating Curve Model* has been proposed (Neri et al., 2015a). This model makes it possible to calculate the steady temperature by performing shorter experimental tests. By means of the 2D and the 3D numerical models, the variables affecting heat transfer at chimney–roof penetration and their influence were investigated. The following variables were considered: roof thickness (S), roof thermal resistance (R), clearance sealing mode, distance between chimney and roof (G), position of roof layers (the influence of the position of the wooden and insulating layers), chimney thickness (S_{ch}), chimney thermal re-

sistance (R_{ch}), position of chimney layers, and exhaust gas temperature (T_{ch}). The range of each variable was identified and numerical simulations performed to assess the roof temperature variation. For example, to investigate the influence of the position of roof layers, numerical simulations were performed by considering two roofs of the same thickness (S) and thermal resistance (R) made of an insulating and a wooden layer and the position of the layers was changed. Fig. 5 shows the maximum roof temperature depending on the position of the wooden layer and for several clearance widths (G).

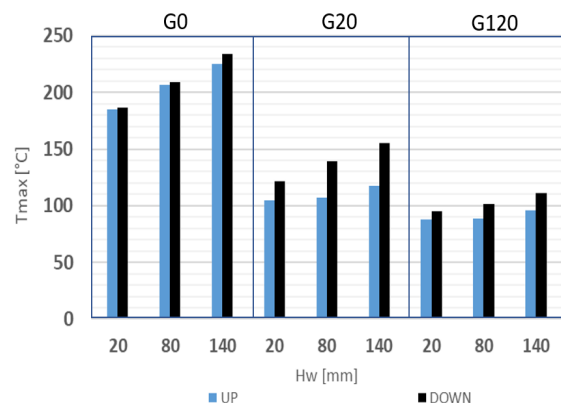


Fig. 5 – Maximum roof temperature for a roof made of a wooden layer and an insulating layer for different clearance widths (G) and different thicknesses (H_w) and positions of the wooden layer

2.2 Tables for Checking Chimney Installations

The maximum roof temperatures (T_{max}) obtained numerically were analysed statistically in Neri et al. (2017) by means of the DoE technique (Montgomery, 2002; Montgomery et al., 2003). The DoE is usually used to design experimental campaigns but, in this case, was used to determine the weight of each variable. The result of the statistical analysis is a set of regression models for calculating the roof maximum temperature (T_{max}). To obtain accurate regression models, it was necessary to analyse different types of roofs separately and, consequently, many regression models were found. Three chimney–roof configurations were considered, specifically: roofs made of a wooden layer above an insulating layer, roofs made of an insulating layer above a wooden layer, and roofs with a wooden layer between two insulating layers. Only

the case with clearance sealed adiabatically was considered. Since the regression models can be a source of errors, they are presented in the form of a table in Figure 6: the characteristics of the roof are reported on the left side hand, and the characteristics of the chimney are reported at the top. Consulting the table by selecting the characteristics of the roof and of the chimney identifies a box: a green box represents a safe installation, while a white box represents an unsafe installation. For a given chimney-roof configuration, if a white box is identified, a more insulated chimney can be chosen or the distance between chimney and roof (G) can be increased. For example, let us consider exhaust gas at 400°C , a roof made of a wooden layer and an insulating layer. The insulating layer is 60 mm thick (H_i) and the thermal conductivity is equal to 0.055 W/mK . The wooden layer is 20 mm thick (H_w). The chimney installer can choose among chimneys made of a material of thermal conductivity (λ_c) equal to 0.04 W/mK of different thickness, and these must be installed at 20 mm from flammable materials (G). From Fig. 6, it can be seen that the chimney installers cannot choose a chimney that is 50 mm thick (S_c) because the related box is white. By comparison, a chimney that is 70 mm thick can be installed safely because the related box is green.

T400			Sc		50			70						
G	Hw	Hi	$\lambda_i \backslash \lambda_c$	0.03	0.04	0.06	0.03	0.04	0.05	0.06	0.07	0.08	0.11	
20	20	60	0.03											
			0.055											
			0.08											
		140	0.03											
			0.055											
			0.08											
	80	220	0.03											
		0.055												
		0.08												
		60	0.03											
		0.055												
		0.08												
20	60	0.03												
		0.055												
		0.08												
	140	0.03												
		0.055												
		0.08												
220	0.03													
	0.055													
	0.08													

Fig. 6 – Table for checking chimney installations. T400 is the temperature class of the chimney, G is the distance between roof and chimney, H_w and H_i are the thickness of the wooden and the insulating layers respectively. λ_i and λ_c are the thermal conductivity of the insulating layer of the roof and of the chimney

2.3 Device For Limiting the Temperature at the Chimney–Roof Penetration (CEIL Device)

In order to limit the roof temperature even in very critical operating conditions, a device to be installed between the chimney and roof was designed (Neri and Pilotelli, 2019; Neri et al., 2020). The device must be installed as shown in Fig. 7b) and it is made of insulating and conductive elements: the insulating elements limit the heat flux towards the roof, whereas the conductive elements dissipate the heat in the surrounding. The difference between standard insulation and the effect of the device is shown in Fig. 7: the conductive elements act as cooling fins. The shape of the conductive elements, which guarantee a lower roof temperature, were investigated numerically as shown in Fig. 8.

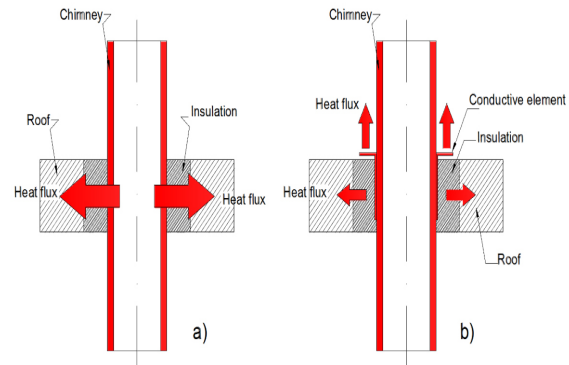


Fig. 7 – Representation of the heat flux with only insulation in the clearance a), and with the device in the clearance b)

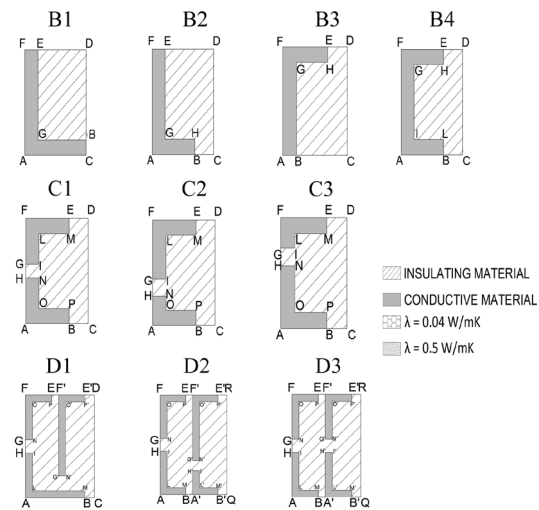


Fig. 8 – Configurations considered in the numerical analysis to design the device to limit the roof temperature

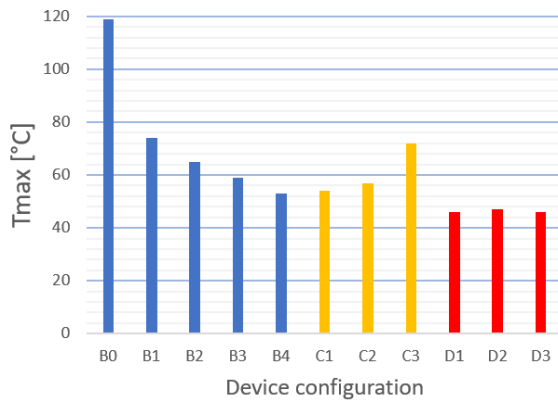


Fig. 9 – Maximum roof temperatures estimated for different device configurations. The device configurations are shown in Fig. 8. The configuration identified with B0 is made of insulating material only.

In the numerical simulations the horizontal thickness of the device was set at 100 mm. The thermal conductivity of the insulating layer was set equal at 0.04 W/mK and the thermal conductivity of the conductive at 15 W/mK, which is a value representative of steel. Firstly, the influence of a conductive element in the insulating layer between chimney and roof was assessed (configurations B1, B2, B3 and B4). A way to reduce thermal bridges between the indoor and the external ambient was investigated by considering configurations (C1, C2 and C3). Next, it was investigated how to further reduce the roof temperature by adding more insulating elements (D1, D2 and D3). The roof temperatures obtained numerically for the different configurations of the device are shown in Fig. 9. Results were verified experimentally (Neri et. al, 2020).

3. Discussion

From the results and discussions in the previous sections, it emerges that the certification procedure does not reproduce the worst chimney operating conditions. This may be one of the causes of the high number of roof fires to have occurred in Europe. This discrepancy is due to several factors, such as the position of the chimney in the test structure, the clearance sealing mode, and the exhaust gas temperature measurement point. Because of this, modifications to the certification procedure have been proposed (Leppänen et al., 2017a and 2017b). Since the exhaust gas temperature at chim-

ney–roof penetration can be lower than the temperature measured in the vicinity of the heat generator (Fig. 1), the related thermocouples should be installed in the vicinity of the roof. In this way, it is possible to regulate the exhaust gas temperature with more precision. This guarantees the prescribed exhaust gas temperature at chimney–roof penetration, where flammable material temperatures are measured. As can be seen in Fig. 2, the clearance sealing mode strongly affects the roof temperature, and as a consequence the sealing type should be specified in the label applied to certified chimneys. In this way, chimney installers can install the chimney as it was installed in the certification procedure. As shown in Fig. 3, the chimney should be installed so that it is completely surrounded by a roof in order to limit the dissipation of heat through the walls of the test structure. Fig. 5 shows that the maximum roof temperature depends on the characteristics of the roof, and this means that the roof of the test structure should be similar to that in which the chimney will be installed. For this reason, it is necessary to specify the characteristics of the roof in the label applied to certified chimneys. To reproduce the most critical chimney operating conditions, the TST must be performed immediately after the HST. If in the HST and in the TST it is not possible to achieve the steady condition, the final temperature should be estimated by means of the *Heating Curve Model*. In this way, it is possible to calculate the actual maximum roof temperature.

To check chimney installations, a set of tables have been proposed. They can be used in the design phase but also for checking existing chimney installations any time there are doubts about their safety. So far, only the configuration with clearance sealed adiabatically has been considered, but further studies could extend the analysis to other clearance sealing modes and also to the configurations with chimneys in contact with flammable materials.

Finally, a device to be installed between chimney and roof was proposed. The device is made of insulating and conductive elements. In Fig. 9, it can be seen that the presence of a conductive element leads to a lower roof temperature compared to that of a configuration with only insulating material

(B0). The shape and the number of the conductive elements affect the roof temperature: the higher the number of conductive elements, the lower the roof temperature. The higher the number of wings of the conductive element, the lower the roof temperature (B4). To limit thermal bridges through the device, the conductive element can be made of an upper and a lower parts spaced by several millimetres. However, the shape of the conductive elements affects the roof temperature: among configurations C1, C2 and C3, the lowest roof temperature was obtained for configuration C2, characterized by parts of the same size. By comparing the roof temperature obtained with only insulating material (B0) and with the final version of the device (D3), it can be seen that the final version of the device determines a temperature that is 70°C lower, despite the fact that the distance between chimney and roof is unchanged.

4. Conclusions

This paper has shown the main steps of a numerical and experimental study that has led to the understanding of heat transfer at chimney–roof penetration. First of all, it has been shown that the certification procedure does not reproduce the worst chimney operating conditions. Since information from the certification procedure does not guarantee safe installations, tools for checking chimney installations have been proposed to help chimney installers. A set of tables to check whether a chimney can be installed in a given roof safely has been proposed. For very critical operating conditions, such as soot fires and very thick roofs, a device for limiting the roof temperature was designed. The latter limits the roof temperature even in very critical chimney operating conditions, that is, even during soot fire events. By following the proposed recommendation the risk of roof fires can be reduced significantly.

References

- Buffo, S., and P. N. Dadone. 2007. "Studio Statistico Vigili Del Fuoco di Brescia Sulle Cause dell'Incendio Tetto". Vigili del Fuoco di Brescia.
- Dadone, P. N. 2009. "Analisi 00. Casi Verificatisi sul Territorio della Provincia di Brescia e Statistica delle Cause Incendi Tetto e Canne Fumarie", *Incendi tetto e Canne Fumarie Conference proceedings*, Brescia.
- Drozdol, K. 2020. "Experimental fire testing of an innovative three-layer chimney for residential buildings." *Journal of Building Engineering* 28. doi: 10.1016/j.job.2019.101019
- CEN. 2009. *EN 1859:2009+A1:2013 "Chimneys test methods"*. Brussels, Belgium.
- International Partnership for the Investigation of Fires Explosions and Other Major Incidents. Accessed 21 July 2015. www.burgoynes.com.
- Kererekes, Z., E. Lublóy, B. Elek and A. Restás. 2018. "Standard fire testing of chimney linings from composite materials." *Journal of Building Engineering* 19: 530-538. doi: 10.1016/j.job.2018.05.030
- Leppänen, P., T. Inha and M. Pentti. 2015. "An experimental study on the effect of design flue gas temperature on the fire safety of chimneys." *Fire Technology* 51:847-86. doi: 10.1007/s10694-014-0415-4
- Leppänen, P., M. Neri, D. Lusciatti, S. Bani, M. Pentti and M. Pilotelli. 2017a. "Comparison between European chimney test results and actual installations." *Journal of Fire Sciences*, 35 (1): 62-79. doi:10.1177/0734904116680222
- Leppänen, P., M. Malaska, T. Inha and M. Pentti. 2017b. "Experimental study on fire safety of chimneys in real use and actual site conditions" *Journal of Building Engineering* 14: 41-54. doi:10.1016/j.job.2017.09.014
- Leppänen, P., and M. Malaska. 2019. "Experimental Study on the Smouldering Combustion of Mineral Wool Insulation in Chimney Penetrations." *Fire Technology*. doi: 10.1007/s10694-019-00849-1
- Manfren, M., B. Nastasi, E. Piana, and L. Tronchin. 2019. "On the Link between Energy Performance of Building and Thermal Comfort: An Example." *AIP Conference Proceedings*, 2123:020066. Beirut, Lebanon: American Institute of Physics Inc., 2019. <https://doi.org/10.1063/1.5116993>

- Ministry of the Environment of Finland. 2011. "Finnish Concern on Fire Safety Risk Due to CE Marking of Appliances Fired by Solid Fuel and Chimney Products".
- Montgomery, Douglas. 2002. *Design and Analysis of Experiments*. 5th Edition. John Wiley and Sons.
- Montgomery, Douglas, and George Runger. 2003. *Applied Statistical and Probability for Engineers*. 3th Edition. John Wiley and Sons.
- Neri, M., P. Leppänen, S. Bani, M. Pentti and M. Pilotelli. 2015a. "Experimental and Computational Study of the Temperatures Field Around a Chimney Roof Penetration." *Fire Technology*. doi:10.1007/s10694-015-0540-8
- Neri, M., D. Luscietti, S. Bani, A. Fiorentino and M. Pilotelli. 2015b. "Analysis of the temperatures measured in very thick and insulating roofs in the vicinity of a chimney." *Journal of Physics: Conference Series* 655(1). doi: 10.1088/1742-6596/655/1/012019
- Neri, M., D. Luscietti, A. Fiorentino, and M. Pilotelli. 2016. "Experimental Analysis of Chimneys in Wooden Roofs." *Fire Technology*. doi: 10.1007/s10694-015-0525-7.
- Neri, M., D. Luscietti, A. Fiorentino, and M. Pilotelli. 2017. "Statistical Approach to Estimate the Temperature in Chimney Roof Penetration" *Fire Technology* 54(2): 395-417. doi: 10.1007/s10694-017-0689-4
- Neri, M., and M. Pilotelli. 2018. "Data on temperature-time curves measured at chimney-roof penetration." *Data in Brief* 20: 306-315. doi:10.1016/j.dib.2018.08.017
- Neri, M., and M. Pilotelli. 2019. "Device for Limiting the Temperature at Chimney-Roof Penetration in Very Critical Chimney Operating Conditions." *Fire Technology*. doi: 10.1007/s10694-019-00837-5
- Neri, M., P. Leppänen, M. Alanen, D. Luscietti, S. Bani, and M. Pilotelli. 2020. "Effects of the coupling of insulating and conductive materials to limit the temperature at chimney-roof penetration." *Fire Technology*. doi: 10.1007/s10694-020-00947-5
- Polonini, L. F., D. Petrocelli, S. P. Parmigiani and A. M. Lezzi. 2018. "Experimental study of PM emissions from wood pellet stoves with innovative burning pots." *EUBCE 2018*, Copenhagen.
- Polonini, L. F., D. Petrocelli, S. P. Parmigiani and A. M. Lezzi. 2019a. "Pm – O₂ correlation in combustion processes in pellet stoves and boilers." *European Biomass Conference and Exhibition Proceedings*: 497-503.
- Polonini, L. F., D. Petrocelli, S. P. Parmigiani and A. M. Lezzi. 2019b. "Experimental study of PM emissions from wood pellet stoves with an innovative burning pot." *Journal of Physics: Conference Series*. doi:10.1088/1742-6596/1224/1/012018
- Polonini, L. F., D. Petrocelli, S. Parmigiani, and A. M. Lezzi. 2019c. "Influence on CO and PM emissions of an innovative burner pot for pellet stoves: an experimental study." *Energies*. doi: 10.3390/en12040590

Building Energy Models with Morphological Urban-Scale Parameters: A Case Study in Turin

Roberto Boghetti – University of Pisa, Italy – roberto.boghetti@studenti.unipi.it

Fabio Fantozzi – University of Pisa, Italy – fabio.fantozzi@unipi.it

Jérôme Kämpf – Idiap Research Institute, Switzerland – jerome.kaempf@idiap.ch

Guglielmina Mutani – Politecnico di Torino, Italy – guglielmina.mutani@polito.it

Giacomo Salvadori – University of Pisa, Italy – giacomo.salvadori@unipi.it

Valeria Todeschi – Politecnico di Torino, Italy – valeria.todeschi@polito.it

Abstract

With a growing awareness around the importance of the optimization of building efficiency, being able to make accurate predictions of building energy demand is an invaluable asset for practitioners and designers. For this reason, it is important to continually improve existing models as well as introduce new methods that can help reduce the so-called energy performance gap, which separates predicted from actual consumption values. This is particularly true for urban scale simulations, where even small scenes can be very complex and carry the necessity of finding a reasonable balance between precision and computational efforts. The scope of this work is to present two different models that make use of morphological urban-scale parameters to improve their performances, taking into account the interactions between buildings and their surroundings. In order to do this, two neighbourhoods in the city of Turin (IT) were taken as case studies. The buildings studied present similar characteristics but are inserted in a different urban context. Several urban parameters were extracted using a GIS tool and used as input, alongside the building-scale features, for two different models: i) a bottom-up engineering approach that evaluates the energy balance of residential buildings and introduces some variables at block-of-buildings scale, ii) a machine learning approach based on the bootstrap aggregating (bagging) algorithm, which takes the same parameters used by the previous model as inputs and makes an estimation of the hourly energy consumption of each building. The main results obtained confirm that the urban context strongly influences the energy performance of buildings located in high built-up areas, and that introducing simple morphological urban-scale parameters in the models to take these effects into account can improve their performance while having a very low impact on the computational efforts.

1. Introduction

One of the key challenges of our century is to alleviate human pressure on the environment and particularly to slow down the climate change that greenhouse gas emissions are accelerating (Verbeke and Audenaert, 2018). The buildings sector accounts for a large share of the total energy-related CO₂ emissions - around 28% in 2018 - and it will therefore play a central role in the clean energy transition (IEA, 2019). In particular, the reduction of energy consumption in buildings, together with the transition to renewable energies, could be one of the main drivers of this turnaround (Mutani and Todeschi, 2018). An important step to achieve this goal is to develop robust models that allow us to make reliable estimates of the energy demand of buildings, which can be used as a base for planning the city of tomorrow (Streicher et al., 2019). However, building these models at urban scale is a complex task, as the energy consumption depends on several factors at different scales, such as the dynamic interaction between the outdoor climate and the specific characteristics of the building's surroundings, the thermal characteristics of its envelope elements and technical systems (Caruso et al., 2013; Palme et al., 2017; Perera et al., 2018). In this work, two energy models for residential buildings that take into account morphological urban-scale parameters are presented, evaluated and discussed. Comparable studies include (Hedegaard et al., 2019; Mutani and Todeschi, 2019; Nageler et al., 2017; Sola et al., 2018) for energy models and (Amasyali and El-Gohary, 2018; Boghetti et al., 2019) for data-driven ones.

2. Materials and Methods

This section describes two different approaches to create building energy models at neighborhood scale. The first is a bottom-up engineering model (hourly thermal balance), while the second one is a data-driven model based on the Bagging algorithm. Fig. 1 indicates the input data and the procedure used to compare the models.

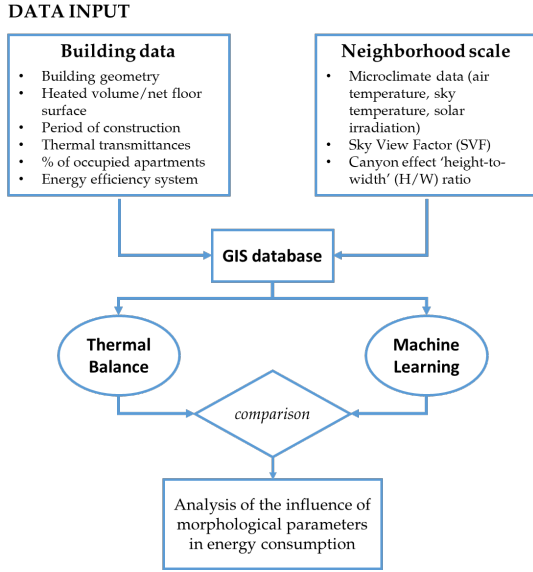


Fig. 1 – Flowchart of energy models comparison

2.1 Bottom-Up Engineering Model

Starting from previous research (Mutani et al., 2019), a bottom-up engineering hourly energy balance model for residential buildings was created. To evaluate the energy balance of buildings in a built-up urban context, the ISO 52016-1:2017 and ISO 52017-1:2017 standards were used, and the equations were implemented to consider only the data available at neighborhood scale and some morphological urban-scale parameters. The urban parameters used to create the model and to evaluate how the urban form affects the thermal energy consumption in buildings were: the canyon effect, which was quantified using the 'height-to-width' (H/W) ratio, this parameter is able to describe the typical urban microclimate around the buildings; the obstructions, the solar exposition and the thermal were evaluated with the H/W ratio and the Sky View Factor (SVF), which measures the visible portion of the sky from a given location (Middelà et al., 2018); the climate and

microclimate conditions were downloaded from the nearest weather station.

This section presents an engineering method based on energy balances with hourly time step by considering the main components of a building: the envelope, the glazing and the inside part of a building with the internal structures, the furniture and the air. An iterative procedure makes it possible to calculate the hourly temperatures of the three thermodynamic systems (Fig. 2). In this work, the following assumptions were adopted:

- the temperatures of the thermodynamic systems are uniform;
- heat conduction through the buildings elements is one-dimensional;
- thermal bridges are neglected;
- latent components of influx or out flux of moisture and the heat flow rates for humidification and dehumidification were neglected.

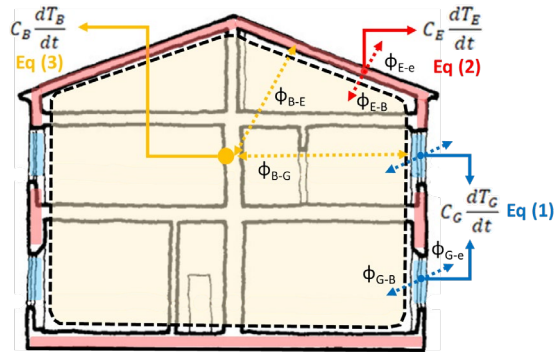


Fig. 2 – The three thermodynamic systems of the engineering dynamic model: B = internal structures, furniture and air; E = opaque envelope; G = glass

2.1.1 Thermal balance of the glasses

The hourly temperature of the glasses (G) of a building were obtained with the balance of the thermal flows between the glasses and the building (B) and the glasses and the outdoor environment (e) (Eq. 1).

$$C_G \frac{dT_G}{dt} = \sum \alpha_G \cdot I \cdot F \cdot A_G - \sum \frac{A_G}{\frac{1}{2} \cdot R_G + R_{se}} \cdot (T_G - T_{ae}) - \sum \frac{A_G}{\frac{1}{2} \cdot R_G + R_{si}} \cdot (T_G - T_B) - \phi_r \quad (1)$$

The term on the left side of Equation 1 describes how the energy stored in windows glasses changes with the time. The terms on the right side of the equation describe the absorption of solar irradiance

(I) and the heat fluxes for transmission between the glasses and the building and between the glasses and the external environment. For every hour, a coefficient is calculated to define the percentage of sunny surfaces as a function of the height of the sun and of the urban canyon height to distance ratio H/W (Mutani et al., 2019). The remaining terms, listed below, refer to:

- the heat flows by transmission between the glasses and the external environment:

$$\sum \frac{A_G}{\frac{1}{2} \cdot R_G + R_{se}} \cdot (T_G - T_{ae})$$

- the heat flows by transmission between the glasses and the internal building quota:

$$\sum \frac{A_G}{\frac{1}{2} \cdot R_G + R_{si}} \cdot (T_G - T_B)$$

The thermal capacity of the glasses C_G was calculated by considering the specific heat and the mass of the glasses.

2.1.2 Thermal balance of the envelope

The thermal balance of the heat flows for the building envelope was calculated using Equation 2.

$$C_E \frac{dT_E}{dt} = \sum \alpha_E \cdot I \cdot F \cdot A_E - \sum \frac{A_E}{\frac{1}{2} \cdot R_E + R_{se}} \cdot (T_E - T_{ae}) - \sum \frac{A_E}{\frac{1}{2} \cdot R_E + R_{si}} \cdot (T_E - T_B) - \phi_r \quad (2)$$

Similarly to Equation 1, the term on the left side describes how the energy stored in the envelope changes with the time; the terms on the left side describe the absorption of solar irradiance, the heat flow by transmission to the building and the external environment and the extra heat flow ϕ_r due to thermal radiation to the sky from the envelope. The ϕ_r depends on the shading reduction factor for the external obstructions F_{sh} and it was calculated with the SVF (Mutani et al., 2019; Mutani and Todeschi, under revision).

2.1.3 Thermal balance of the building

The thermal balance of the heat flows of the internal building components was calculated using Equation 3:

$$C_B \frac{dT_B}{dt} = \phi_H + \phi_I + \sum \tau_G \cdot I \cdot F \cdot A_G - \sum \frac{A_E}{\frac{1}{2} \cdot R_E + R_{si}} \cdot (T_B - T_E) - \sum \frac{A_G}{\frac{1}{2} \cdot R_G + R_{si}} \cdot (T_B - T_G) - c_a \cdot m_a \cdot (T_{B,ai} - T_{ae}) \quad (3)$$

The term on the left side of the Equation 3 describes how the energy stored inside the building changes with the time. On the right side, the first two terms i) ϕ_H and ii) ϕ_I described respectively i) the heat flow released by the heating system, which can be calculated by multiplying the energy supplied to the heating system for the system efficiency η_H (Mutani and Todeschi, under review) and ii) the heat flow rate due to internal heat sources that, for residential buildings, depends on the useful heated floor area and the average floor area per dwelling. The third term describes the solar transmission through the transparent elements with the F reduction factor calculated likewise in Equations 1 and 2. The last terms describe the heat flow rates by transmission and ventilation. For the internal heat gains and heat flow for ventilation, the hourly profiles that characterize the users' behavior in the Italian Standard UNI/TS 11300-1:2014 were utilized.

2.2 Bagging Model

The second model uses a machine learning approach based on the bootstrap aggregating (bagging) algorithm (Breiman, 1996) applied to a decision tree regressor. This method was chosen over other possible regression techniques as it provided better and more consistent results on the available data. The bagging algorithm works by sampling the data with replacement, running the prediction method(s) on the samples and finally aggregating the results by averaging the outputs. The decision tree regressor, on the other hand, is a simple learning algorithm that creates a set of binary rules to calculate the target value. The model was trained using real hourly consumption data from buildings of the two neighbourhoods that are not in the input database. As the output of a similar model is dependent on the decision trees that are generated for the bagging algorithm, the results given in this paper are averaged over the outputs of different instances of the model.

2.2.1 Model creation

The model was created using Scikit-learn (Pedregosa et al., 2011) and follows a standard workflow for machine learning applications. In the first phase, the data from the full database was pre-processed. Cat-

egorical features were converted into numerical data and the values of the whole database were scaled. While scaling is not necessary when using the decision tree regressor, it allows for efficient comparison of the results with those of other algorithms within the same script. The evaluated sample is then split from the training set as explained in Section 3.2. Once the data was processed, a first model was created and its performance evaluated. At this point, a backward feature elimination was performed in order to reduce the number of variables by eliminating those that were negatively affecting the performances of the algorithm. This dimensionality reduction method works by excluding one feature at a time and evaluating how the removal affects the performance of the model. If the precision improves, the feature is removed. The process continues iteratively until no variable can be dropped without a negative effect on the performances of the model. Morphological urban-scale parameters were not included in this step as the evaluation of their importance will be carried out subsequently. At the end of this process the resulting model was finally evaluated, and as an acceptable level of precision was reached no further improvements were made.

3. Case Study

Turin is located in the north-western part of Italy, in a continental temperate climate. In Turin there are about 60,000 heated buildings, nearly 45,000 of which are residential. These are mainly large and compact condominiums, and 80% of them were built before 1970 (Amasyali and El-Gohary, 2018; Hedegaard et al., 2019; Middela et al., 2018). In order to evaluate the influence of urban morphology on the consumption of buildings, two neighbourhoods –with similar building characteristics but different urban contexts– are taken as case studies. In the *Einaudi* (E) neighbourhood the buildings have a H/W average value of 0.56 and SVF of 0.63; while in the *Sacchi* (S) area these urban parameters have higher values, 0.64 and 0.76, respectively (Figs 3 and 4).

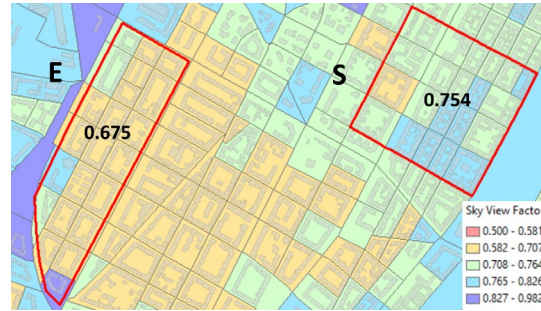


Fig. 3 – Sky View Factor (SVF) calculated with the use of GIS tool, Relief Visualization Toolbox, and the DSM

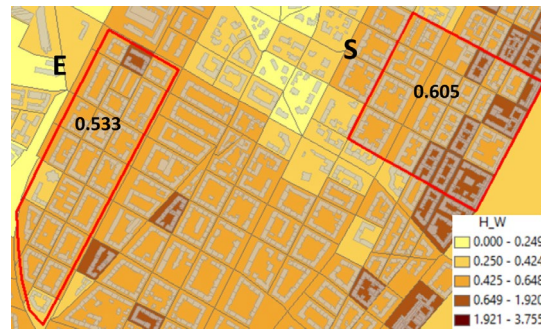


Fig. 4 – The canyon effect H/W calculated with the use of building characteristics at census section scale

3.1 Data Collection

The urban scale data as well as the geographic information were elaborated with the support of a Geographic Information System (GIS) tool, and a georeferenced database was created using the data presented below:

- *Building data* elaborated using: the Municipal Technical Map¹; the Territorial Database of the Region²; and the socio-economic data (ISTAT census database³).
- *Microclimate data* elaborated using *Politecnico* weather station measurements (heating degree days, air temperature, relative humidity, direct solar radiation).
- *Morphological urban-scale parameters* elaborated using *building data*, Satellite Images (Landsat 7 and 8) with a precision of 30 meters available from the USGS website; and the Digital Surface Model (DSM) of Turin with a precision of 5 meters provided by Piedmont Region.
- *Energy consumption data* were provided by the district heating IREN Company of Turin. The

1 <http://geoportale.comune.torino.it/web/>

2 <http://www.geoportale.piemonte.it/cms/>

3 <http://datiopen.istat.it/>

hourly space heating energy consumption refer to the season 2014-15.

3.2 Sampling

Among the available data, a representative sample of buildings was chosen as case study and used as a testing set for both models. The main reasons for using only a subset of the whole database were to save enough buildings to train the machine learning model and to reduce the high computational times of the bottom-up approach. The sampling was carried out on a random basis. Outliers, however, were excluded from the population beforehand in order to avoid errors correlated with the lack of variety in the training data, which would not have been meaningful for the evaluation of morphological urban-scale parameters. Figs 5 and 6 show the distribution of the values for the SVF and H/W ratio of the sample compared with those of the full database.

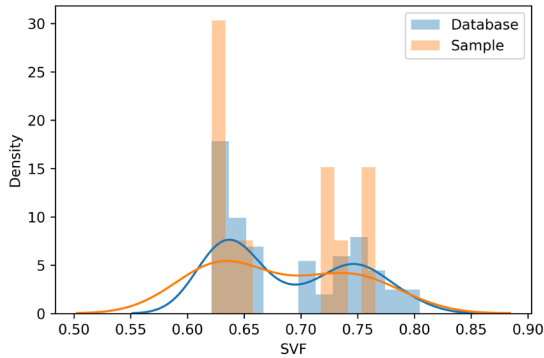


Fig. 5 – Distribution of the Sky View Factor values within the full database (in blue) and the sample (in orange)

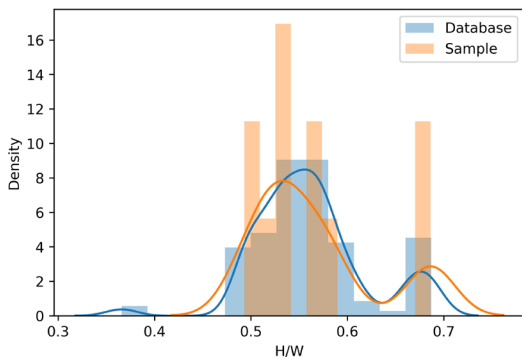


Fig. 6 – Distribution of the Canyon Effect (H/W) values within the full database (in blue) and the sample (in orange)

An overview of the distribution of these parameters in the sample can be found in Table 1, along with the period of construction, the S/V ratio and the thermal transmittances of the buildings.

Table 1 – Characteristics of a selected buildings in the *Einaudi* and *Sacchi* neighborhoods

IDbz	Period	S/V	U _E	U _G	U _g	U _r	H/W	SVF
E-129	19 - 45	0.280	1.35	4.75	0.79	1.76	0.589	0.627
E-132	46 - 60	0.290	1.18	4.4	0.615	1.35	0.569	0.621
E-187	46 - 60	0.286	1.18	4.4	0.615	1.35	0.522	0.650
E-202	61 - 70	0.285	1.13	4.9	0.65	1.49	0.569	0.621
E-227	61 - 70	0.413	1.13	4.9	0.65	1.49	0.589	0.627
S-46	19 - 45	0.344	1.35	4.75	0.79	1.76	0.533	0.722
S-202	19 - 45	0.336	1.35	4.75	0.79	1.76	0.675	0.747
S-262	19 - 45	0.346	1.35	4.75	0.79	1.76	0.600	0.782
S-268	46 - 60	0.404	1.18	4.4	0.615	1.35	0.686	0.765
S-97	61 - 70	0.323	1.13	4.9	0.65	1.49	0.686	0.765

4. Results and Discussion

In this section, the performances of the two models are compared and discussed, along with the improvements that urban parameters have brought in each case. From this work it emerges that urban parameters have a positive impact on the precision of both tested models: the solar exposure and heat exchanges with the external environment significantly influence energy consumption. In particular, in favourable conditions, with high values of SVF and good orientation, energy consumption is lower than in unfavourable conditions (low values of SVF and orientation). Moreover, the shape of the building is fundamental in its heat exchange, and the canyon effect H/W was used to describe the built environment compactness and the type of the surrounding open spaces. In terms of the two models, the following sections detail the results. In general, using a machine learning approach leads to better performances in terms of time and precision. On the other hand, its reliance on the availability of a comprehensive dataset for the training phase makes it less flexible and undermines its performances on heavily heterogeneous case studies.

4.1 Bottom-Up Engineering Model

This section reports the results obtained from the application of the hourly thermal balance model. To present the results, some buildings were selected based on the period of construction, the characteristics of urban context and the type of adjacent street, the consumption of buildings located on a large tree-lined street are influenced by this position (Amasyali and El-Gohary, 2018). In particular, the following figures refer to a number of buildings

located in the *Einaudi* area, distinguishing different periods of construction. Figure 7 shows an example of measured and calculated monthly space heating consumption of a residential building built in 1919-45.

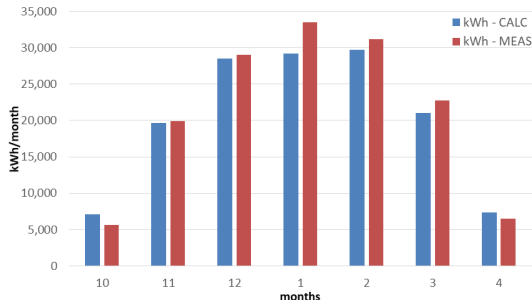


Fig. 7 – Monthly energy consumption for the season 2014-15: building 'E-129', bottom-up model

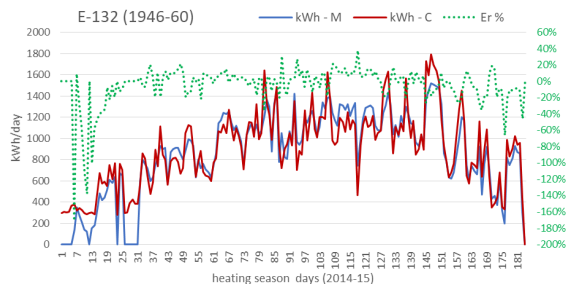


Fig. 8 – Daily consumption and relative error (E_r): building 'E-132', bottom-up model

Figure 8 describes the daily trends for the 2014-15 season of measured and calculated consumption and the daily relative error (E_r). The data refer to the building 'E-132' built in 1946-60. In general, the daily value of E_r varies between $\pm 20\%$. Figure 9 shows the cumulative frequency of the 'E-227' building (period 1961-70). It is possible to observe that the model is quite accurate (the greatest inaccuracy occurs in the months of October and April due to the imprecision of measured data at the beginning and the end of the heating season).

In future research, by improving the model with the introduction of other urban parameters (for example, considering the presence of vegetation), it will be possible to optimize the trend of energy consumption (high and low values). Considering the results obtained from the comparison between the *Einaudi* and *Sacchi* neighbourhoods (Fig. 10), it is possible to confirm that the canyon effect is very important in the simulation of energy consumption because it creates a microclimate around buildings by increasing the air temperature and, consequent-

ly a lower consumption will occur. Figure 10 shows that when H/W decreases, the SVF increases and therefore the consumption also increases. Furthermore, the canyon effect and the extra flow are more significant than the solar gains in an urban environment (Mutani et al., 2019).

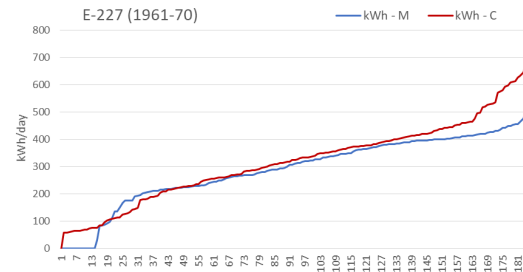


Fig. 9 – Cumulative curves: 'E-227', bottom-up model

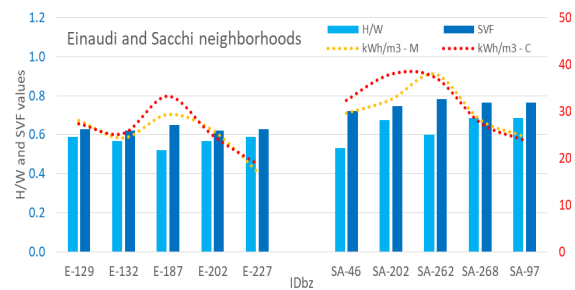


Fig. 10 – Comparison between energy consumption (measured and calculated) and urban parameters for buildings located in *Einaudi* and *Sacchi* neighborhoods

4.2 Bagging Model

With a MAPE of 14.12 % and a R^2 of 0.71, the data-driven model showed good precision on the sample. It was able to reproduce the hourly energy profiles of the buildings with an acceptable degree of error despite the low number of available observations compared to the complexity of the problem. A first comparison with the previous model is given in Figure 11, where the monthly energy demand of building 'E-129' is estimated again. The estimations of the bagging algorithm in this case were slightly more precise, and the tendency was to underestimate the energy consumption, as opposed to the bottom-up model where the errors were mostly on the positive side.

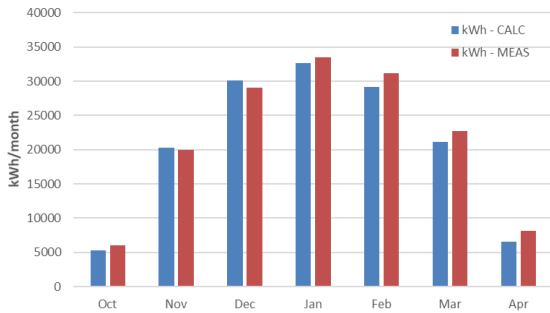


Fig. 11 – Monthly energy consumption for the season 2014-15: building 'E-129', bagging model

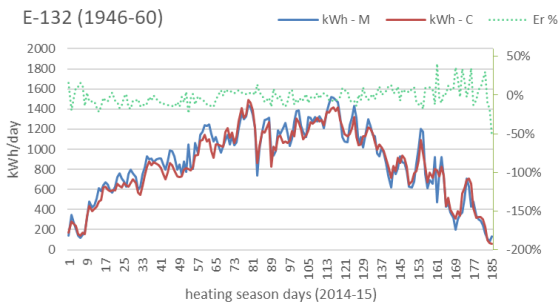


Fig. 12 – Daily consumption and relative error (E_r): building 'E-132', bagging model

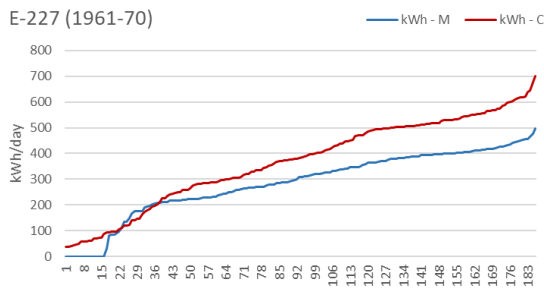


Fig. 13 – Cumulative curves: 'E-227', bagging model

With respect to daily energy demand, Figure 12 shows the performances of the model on building 'E-132'. Again, the error is generally contained within +20% and -20%, which is in line with literature values given the lack of information needed to characterize the human behavior. Both models were therefore able to output a good estimation without notable discrepancies with the real values. Similar to what happened with monthly values, the daily charts show that the two models tend to respectively overestimate and underestimate the real energy consumption.

As previously done with the bottom-up model, Figure 13 finally shows the cumulative frequency of the 'E-227' building. Again, the highest inaccuracy occurred in the months of October and April. While the total error at the end of the heating sea-

son was similar for the two models, their short-term behaviours were very different. The bagging algorithm accumulated its error gradually, as opposed to the bottom-up model where the error spiked to its final value mostly during the last month.

Table 2 – Comparison between results of two building energy models

ID _{bz}	Bottom-up model				Bagging model			
	E_r	$ E_r $	Calc.	Meas.	E_r	$ E_r $	Calc.	Meas.
	%		kWh/m ³ /y		%		kWh/m ³ /y	
E-129	1	17	27.99	27.30	-11	9	24.89	27.30
E-132	-6	15	24.26	25.23	0	0	25.38	25.23
E-187	-13	17	29.26	33.18	-10	14	28.57	33.18
E-202	-1	19	25.91	24.85	0	13	28.12	24.85
E-227	-7	20	17.07	18.74	19	30	24.36	18.74
S-46	-5	17	29.57	32.28	-6	6	30.48	32.28
S-202	-15	24	32.44	37.87	12	13	40.76	37.87
S-262	2	19	37.87	37.15	-12	16	31.19	37.15
S-268	3	17	28.16	27.52	2	2	28.18	27.52
S-97	4	16	24.54	23.75	16	25	29.65	23.75

4.3 Energy Models Comparison

An overview of the performances of the two models is given in Table 2. Overall, both models showed good performances and their errors were in line with the typical values of the energy performance gap. The precision of the data driven model, however, was less stable, ranging from an absolute error of 30% to less than 1% depending on the building. This behavior is possibly due to the lack of representative buildings of all kinds in the training set, which is a common problem of this approach.

5. Conclusions

Improving the precision of urban-scale energy simulations is an important step to achieve a more efficient use of energy resources. In this work, two simple energy models, which make use of morphological urban-scale parameters in order to take into account the effect of building-to-building interactions, were presented and studied.

The two models were i) a bottom-up engineering approach, ii) a machine learning approach based on the bootstrap aggregating (bagging) algorithm. Both models were able to estimate the hourly consumption of buildings with a low error compared to the expected performance gap that characterize

the problem. The precision of the bagging model, however, was more dependent on the building's characteristics: this behaviour is caused by the lack of representative datapoints in the training set. This reliance on having a good amount of comprehensive data, and the resulting poor generalizability of the model, are the main weaknesses of this approach. On the other hand, the bottom-up model requires longer times and human efforts to produce the output, while also lacking flexibility if one or more building features are missing.

Future work will aim at lessening the weaknesses of both models, for example by smoothing the workflow of the first model and by gathering more data for the second one; and at introducing more morphological parameters as well as properly studying their importance and their impact on the two models.

Nomenclature

A	area
c	specific heat capacity
C	thermal capacity
F	reduction factor
H/W	canyon height-to-distance ratio
ID	identification code
I	solar irradiance
m	mass-related
R	thermal resistance
S/V	surface-to-volume ratio
SVF	sky view factor
t	time
T	temperature
U	thermal transmittance
V	volume
τ	total solar energy transmittance
α	solar radiation absorption coefficient
η	system efficiency
Φ	heat flow rate, thermal power

Subscripts

a	air
B	building
bz	building zone
e	external
E	opaque envelope
G	glass
H	Heating
I	internal heat gains
i	internal
p	opaque
r	radiative (extra flux)
s	surface
sh	shading

References

- Amasyali, K., and N. M. El-Gohary. 2018. "A review of data-driven building energy consumption prediction studies." *Renewable and Sustainable Energy Reviews* 81: 1192-1205. doi: 10.1016/j.rser.2017.04.095
- Boghetti, R., F. Fantozzi, J. H. Kämpf, and G. Salvadori. 2019. "Understanding the performance gap: a machine learning approach on residential buildings in Turin, Italy." *JPCS* 1343 (1).
- Breiman, L. 1996. "Bagging predictors." *Machine learning* 24(2): 123-140. doi: 10.1007/BF00058655.
- Caruso, G., F. Fantozzi, F. Leccese. 2013 "Optimal theoretical building form to minimize direct solar irradiation." *Solar Energy* 97: 128-137. doi: 10.1016/j.solener.2013.08.010
- IEA. 2019. "Perspectives for the Clean Energy Transition. The Critical Role of Buildings." www.iea.org/publications/reports/PerspectivesfortheCleanEnergyTransition/.
- Hedegaard, R. E., M. H. Kristensen, T. H. Pedersen, A. Brun, S. Petersen. 2019. "Bottom-up modeling methodology for urban-scale analysis of residential space heating demand response." *Applied Energy* 242 :181-204. doi: 10.1016/J.APENERGY.2019.03.063
- Middela, A., J. Lukaszcyk, R. Maciejewski, M. Demuzere, and M. Roth. 2018. "Sky View Factor footprints for urban climate modeling." *Urban Climate* 25: 120-134. doi: 10.1016/j.uclim.2018.05.004
- Mutani, G., and V. Todeschi. 2018. "Energy Resilience, Vulnerability and Risk in Urban Spaces." *Journal of Sustainable Development of Energy, Water and Environment Systems* 6(4): 694-709. doi: 10.13044/j.sdewes.d6.0203
- Mutani, G., and V. Todeschi. 2019. "An Urban Energy Atlas and Engineering Model for Resilient Cities." *International Journal of Heat and Technology* 37(4): 936-947. doi: 10.18280/ijht.37.4.02
- Mutani, G., and V. Todeschi. under revision. "Building Energy Modeling at Neighborhood Scale." *Energy Efficiency*.
- Mutani, G., V. Todeschi, G. Grisolia, and L. Lucia. 2019. "Introduction to Constructal Law

- Analysis for a Simplified Hourly Energy Balance Model of Residential Buildings at District Scale." *TI-IJES* 6(1): 13–20. doi: 10.18280/ti-ijes.630102
- Nageler, P., G. Zahrer, R. Heimrath, T. Mach, F. Mauthner, I. Leusbrock, H. Schranzhofer, and C. Hochenauer. 2017. "Novel validated method for GIS based automated dynamic urban building energy simulations." *Energy* 139: 142–154. doi: 10.1016/j.energy.2017.07.151
- Palme, M., L. Inostroza, G. Villacreses, A. Lobato-Cordero, and C. Carrasco. 2017. "From urban climate to energy consumption. Enhancing building performance simulation by including the urban heat island effect." *Energy and Buildings* 145: 107–120. doi: 10.1016/j.enbuild.2017.03.069
- Pedregosa et al. 2011. "Scikit-learn: Machine Learning in Python." *JMLR* 12: 2825–2830.
- Perera, A. T. D., S. Coccolo, J. L. Scartezzini, and D. Mauree. 2018. "Quantifying the impact of urban climate by extending the boundaries of urban energy system modeling." *Applied Energy* 222: 847–860. doi: 10.1016/j.apenergy.2018.04.004
- Sola, A., C. Corchero, J. Salom, and M. Sanmarti. 2018. "Simulation tools to build urban-scale energy models: A review." *Energies* 11(12): 3269. doi: 10.3390/en11123269
- Streicher, K. N., P. Padey, D. Parra, M. C. Bürer, S. Schneider, and M. K. Patel. 2019. "Analysis of space heating demand in the Swiss residential building stock: Element-based bottom-up model of archetype buildings." *Energy and Buildings* 184: 300–322. doi: 10.1016/j.enbuild.2018.12.011
- Verbeke, S., and A. Audenaert. 2018. "Thermal inertia in buildings: A review of impacts across climate and building use." *Renewable and Sustainable Energy Reviews* 82: 2300–2318. doi: 10.1016/j.rser.2017.08.083

Use of the ISO 12354 Standard for the Prediction of the Sound Insulation of Timber Buildings: Application to Three Case Studies

Francesca Di Nocco – University of Bologna, Italy – francesca.dinocco2@unibo.it

Federica Morandi – Free University of Bozen-Bolzano, Italy – federica.morandi@unibz.it

Luca Barbaresi – University of Bologna, Italy – luca.barbaresi@unibo.it

Antonino Di Bella – University of Padova, Italy – antonino.dibella@unipd.it

Abstract

The ISO 12354 standards provide a method for modelling the sound insulation of building elements using the performance of the single elements as a starting point. The revision of the ISO 12354 Part 1 and 2 standard makes it possible to model timber buildings. In particular, the standards provide prediction formulas for estimating the vibration reduction index (K_{ij}) of heavy and light weight junctions and CLT junctions. The aim of this research is to study the dependence of the ISO 12354 output values on the input data fed to the model, in the specific case of timber buildings. The prediction tools were applied to three different timber buildings on which sound insulation and flanking transmission measurements were carried out on site. Different input data were used: laboratory and in situ measured values of airborne sound insulation, impact sound insulation and flanking transmission. The calculated values are compared with in situ acoustic tests of airborne sound insulation and impact sound insulation. The results show that the blind application of the ISO 12354 model can provide results that differ significantly from the measured on-site values; considerations are drawn concerning the availability of input data and the resonant transmission.

1. Introduction

The series of ISO 12354 standards provides a SEA-based method for modelling the sound insulation of building elements, starting from the characterization of the performance of the single elements. In particular, Parts 1 and 2 provide estimates of the apparent sound reduction index and the apparent impact sound insulation through the evaluation of the flanking transmission paths.

Timber buildings represent a relevant share in the market of new constructions (Caniato and Gasparella, 2019). Be it mass timber construction or timber frames, the prediction tools that have been successfully applied to traditional heavy construction have been found to be inadequate when applied blindly to timber structures. This is due to several factors; first, all the data relative to the “deltas” that have been previously measured on heavy elements cannot be directly used for timber elements, which are characterised by different mass and stiffness. The modelling of the flanking transmission also deserves attention, particularly for mixed structures. This work therefore discusses the application of the ISO 12354 model to timber buildings, with the aim of highlighting which precautions should be used when approaching the calculation of these structures. Acoustic tests of airborne sound insulation and impact sound insulation were conducted on site in three case studies. The descriptions of the construction details were used to generate the input data of the model. Whenever possible, the input data were retrieved from laboratory measurements taken by the University of Bologna and the University of Padova, concerning the sound insulation and flanking transmission measurements.

The results of the application of the model to the case studies are presented and discussed, along with some general remarks.

2. Research Method

This work has focused on implementation and verification of the new CEN calculation model for the estimation of acoustic performance of buildings, according to the recent revision of the series of ISO 12354 standards. The main innovations introduced concern: (i) the new classification of structures, currently divided into “type A” and “type B” structures, (ii) the introduction of new methods to calculate and consider only the resonant transmission for the lateral elements and (iii) the new methods for calculating the lateral transmission for Cross Laminated Timber (CLT) and timber frame structures. In general, an overall improvement was made to the calculation model, but the application of the model to three different case studies has highlighted some unresolved criticalities. The calculation model was implemented on software using the Visual Basic for Excel programming language and preliminarily calibrated on the examples given in the appendix to ISO 12354.

The case studies are three different wooden buildings, in which detailed measurements were carried out, in accordance with the ISO 16283 standards, during intermediate construction stages and after the completion of the works. In the three cases, the study was conducted on the sound insulation of the floor, which made it possible to simulate both the airborne sound insulation and the impact sound insulation. In particular, the three case studies are:

- A. timber frame building in Rimini: CLT floor 180 mm and lightweight multi-layer walls with internal layer in gypsum board;
- B. CLT building in Graz: CLT floor 160 mm and CLT walls 100 mm with multi-layer coverings;
- C. CLT building in Bologna: CLT floor 180 mm and CLT walls 120 mm with multi-layer coverings.

One of the main difficulties encountered was the scarce availability of input data for airborne and impact sound insulation of the single partitions. Input data were partially retrieved from laboratory measurements carried out on floors (University of Bologna) and on walls (University of Padova) (Di Bella et al. 2016, 2018) as recommended by the legislation. When these data were not available, a commercial software was used to simulate the partition.

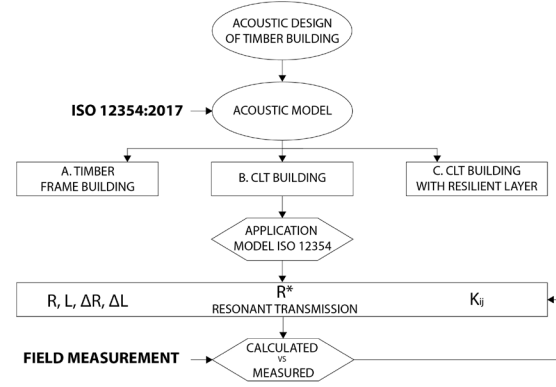


Fig. 1 – Flow chart of research method applied

3. The ISO 12354 Model

3.1 Apparent Sound Reduction Index R'

The apparent sound reduction index R' is determined through the logarithmic summation of all direct and flanking transmission terms through Equation 1.

$$R' = -10 \lg \left(10^{-\frac{R_{D,d}}{10}} + \sum_{j=1}^n 10^{-\frac{R_{ij}}{10}} \right) \quad (1)$$

The contribution of the direct transmission is given by the sum of the sound reduction index of the separating element $R_{s,situ}$ and of the contribution of additional layers $\Delta R_{D,situ}$ and $\Delta R_{d,situ}$ as in Equation 2.

$$R_{D,d} = R_{s,situ} + \Delta R_{D,situ} + \Delta R_{d,situ} \quad (2)$$

For each transmission path, the respective sound reduction index can be calculated according to Equation 3:

$$R_{ij} = \frac{R_{i,situ} + R_{j,situ}}{2} + \Delta R_{i,situ} + \Delta R_{j,situ} + \overline{D_{v,ij,situ}} + 10 \lg \frac{S_s}{\sqrt{S_i S_j}} \quad (3)$$

where $R_{i(j),situ}$ is the sound reduction index of element i (j), $\Delta R_{i(j),situ}$ is the increase of sound reduction index of element i (j) due to additional linings, $\overline{D_{v,ij,situ}}$ is the average insulation of vibration in the junction between elements i and j , S_s is the surface of the separating element, S_i is the surface of element i in the source room, S_j is the surface of element j in the receiving room.

3.2 Normalized Impact Sound Insulation L'_n

Similarly, the prediction of the normalised impact sound insulation L'_n can be expressed as:

$$L'_n = 10 \lg \left(10^{\frac{L_{n,d}}{10}} + \sum_{j=1}^n 10^{\frac{L_{n,ij}}{10}} \right) \quad (4)$$

where the contribution of direct transmission $L_{n,d}$ is given by the summation of the normalised impact sound insulation of the separating element $L_{n,situ}$, of the attenuation due to the presence of a floating floor ΔL_{situ} and the attenuation due to the presence of additional linings on the side of the receiving room (counter ceiling) $\Delta L_{d,situ}$, as in Equation 5.

$$L_{n,d} = L_{n,situ} - \Delta L_{situ} - \Delta L_{d,situ} \quad (5)$$

For each flanking transmission path, the normalised impact sound insulation can be calculated using the formulation in Equation 6.

$$L_{n,ij} = L_{n,situ} - \Delta L_{situ} + \frac{R_{i,situ} - R_{j,situ}}{2} - \Delta R_{j,situ} - \overline{D_{v,ij,situ}} - 10 \lg \sqrt{\frac{S_i}{S_j}} \quad (6)$$

3.3 Flanking Transmission

The flanking transmission was evaluated in three different ways: the K_{ij} provided by the ISO 12354 were used, considering the presence of the resilient interlayer, the K_{ij} values measured in situ and in a test facility. The values of K_{ij} , calculated according to the formulas contained in the annex F of the ISO 12354-1 standard, do not include the presence of different types of fastening systems or resilient layers (Morandi et al., 2018). In order to estimate the contribution of the resilient interlayer, the corrective term Δl - described for the rigid junctions as in annex E - was used (Rabold, 2017).

3.4 Structural reverberation time

For *in situ* correction the structural reverberation time was calculated with Equation 7:

$$T_s = \frac{2,2}{f \eta_{tot}} \quad (7)$$

where the total loss factor is:

$$\eta_{tot} = \eta_{int} + \frac{2\rho_0 c_0 \sigma}{2\pi f m'} + \frac{c_0}{\pi^2 S \sqrt{f f_c}} \sum_{k=1}^4 l_k \alpha_k \quad (8)$$

The internal loss factor of the CLT elements is > 0.03 (Schoenwald et al., 2013) and the α_k depend on the structural elements connected at the perimeter.

4. Case Studies

In the following paragraphs the three case studies are shown. Airborne and impact sound insulation tests were conducted in accordance with ISO 16283-1 and ISO 16283-2, respectively. Moreover, the flanking transmission of the CLT junctions were measured in an area of the construction site that was still under construction (not for case C).

In the discussion of the results, these three measurements will be combined to optimise the modelling of the partition under study.

4.1 A. Timber Frame Building in Rimini

The first building, located in Rimini (Italy), is made with light-weight timber frame walls and CLT floors. The floating floor is made by a dry solution with gravel and concrete fiber board.

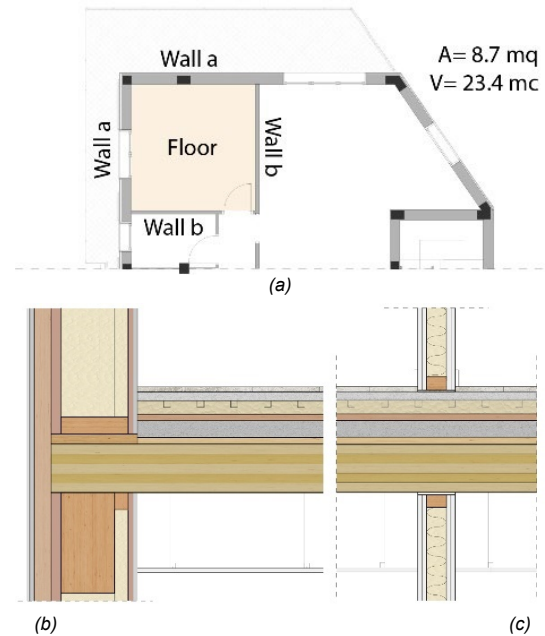


Fig. 2 – Distribution of the elements in the plan (a) and construction details: external wall type a – floor (b) and internal wall type b – floor (c)

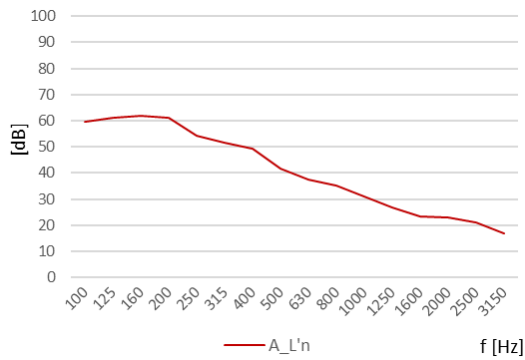


Fig. 3 – In situ impact sound measured in case A

4.2 B. CLT building in Bologna

The second building, located in Bologna (Italy), is a CLT structure. The floating floor is made by a wet solution with cement and a resilient interlayer. The interior lining is fiber gypsum board and mineral wool. The exterior lining is plaster and mineral wool.

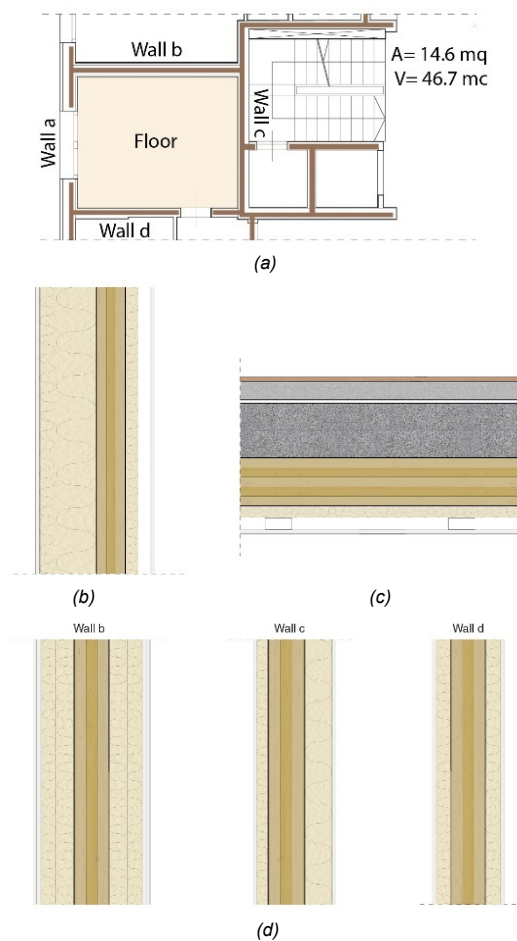


Fig. 4 – Distribution of the elements in the plan (a) and construction elements: external wall type a (b), separating floor (c) and internal wall (d)

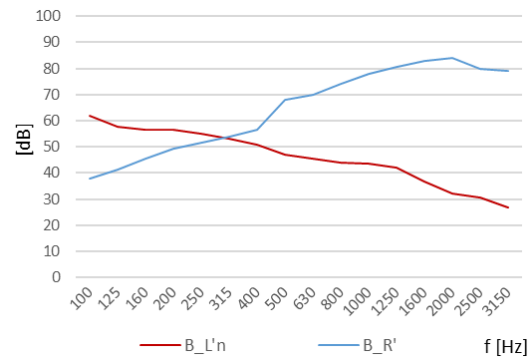


Fig. 5 – In situ sound reduction index and impact sound measured in case B

4.3 C. CLT building with resilient layer in Graz

The third building, located in Graz (Austria), is a CLT structure. The floating floor is made by a wet solution with cement and mineral wool. External walls are made with finishing, 140 mm mineral wool, CLT, 40 mm acoustic layer, 25 mm double fire-resistant gypsum board. The internal wall is a double wall with double fire-resistant gypsum board, CLT, 25 mm double fire-resistant gypsum board.

The resilient interlayer was placed between the floor and the upper wall.

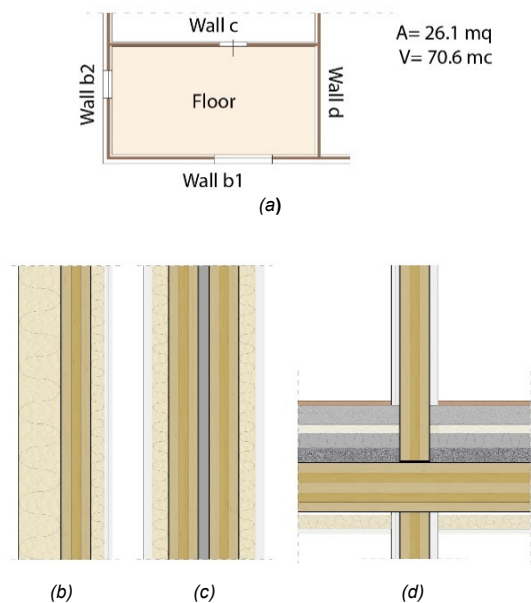


Fig. 6 – Distribution of the elements in the plan (a) and construction elements: external wall type b (b), internal wall type d (c) and detail internal wall type c - floor (d)

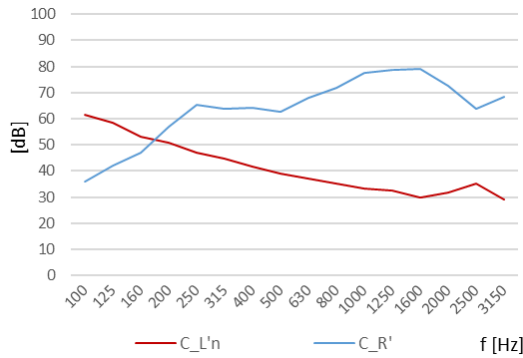


Fig. 7 – In situ sound reduction index and impact sound measured in case C

5. Application of the ISO Calculation Model

For each of the input floors described in Chapter 4, the apparent sound reduction index and impact sound modelled in accordance with the ISO 12354 standard are presented. All results are compared with in situ measurements.

5.1 Case A

In case A, 5 different calculation variables were evaluated:

- the data inputs are from laboratory measurements of similar solutions (label: ISO 12354);
- ΔL_n , ΔR are from measurements on site (label: ISO 12354_Var. 1);
- the application of transmission resonant R^* for each flanking path transmission (label: ISO 12354_Var. 2);
- the K_{ij} values are calculated with empirical formulas for CLT junctions (Annex E) (label: ISO 12354_Var. 3);
- the K_{ij} values retrieved from measurements on site (label: ISO 12354_Var. 4).

In Figs. 8 and 9, the importance of data input for L'_n and the effect of K_{ij} are shown.

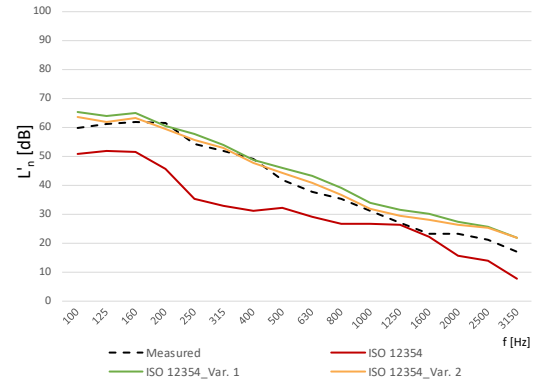


Fig. 8 – Comparison between impact sound measured and calculated values in case A: data input

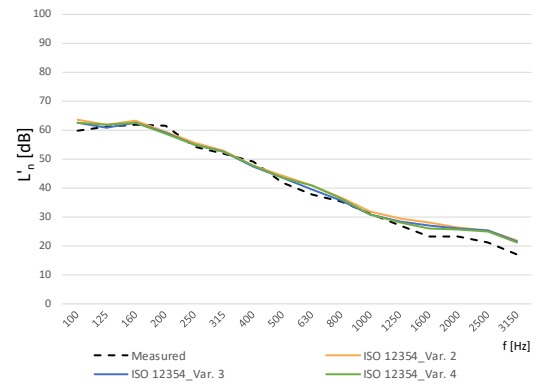


Fig. 9 – Comparison between impact sound measured and calculated values in case A: flanking transmission

5.2 Case B

In case B, 3 different calculation variables were evaluated:

- the data inputs are from simulations using commercial software (label: ISO 12354_Var.1);
- ΔL_n , ΔR are from laboratory measurements of similar solutions (label: ISO 12354_Var. 2);
- the K_{ij} values are measured in accordance with ISO 10848 (label: ISO 12354_Var. 3).

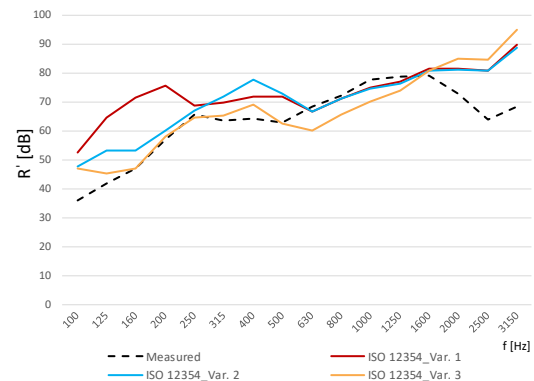


Fig. 10 – Comparison between sound insulation index measured and calculated values in case B

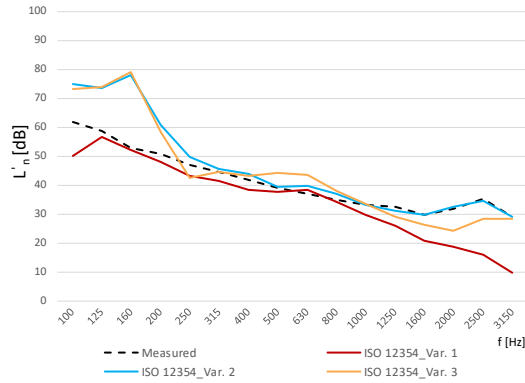


Fig. 11 – Comparison between impact sound measured and calculated values in case B

In ISO 12354_Var. 3 the measured values are used because the ISO Standard empirical formulas are not available.

5.3 Case C

In case C, 4 different calculation variables were evaluated:

- the K_{ij} values are calculated in accordance with ISO 12354, without resilient interlayer (label: ISO 12354);
- the K_{ij} values are calculated in accordance with ISO 12354, considering the presence of resilient interlayer (Annex E) (label: ISO 12354_Var.1);
- the K_{ij} values are measured in accordance with ISO 10848 (label: ISO 12354_Var.2);
- the K_{ij} values are calculated in accordance with ISO 12354, considering the T_s of internal lining of the elements (label: ISO 12354_Var.3);
- the K_{ij} values are correct in relation to the areas of the elements (label: ISO 12354_Var.).

In this case, the importance of flanking transmission data is evaluated. As in case B, there are no provisional formulas for the junction between the panels in CLT.

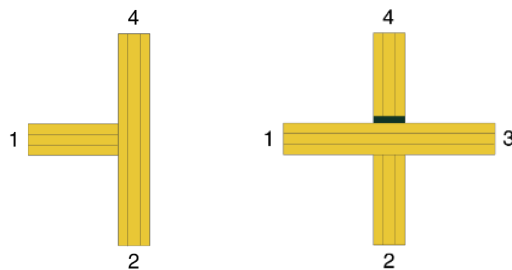


Fig. 12 – Arrangement of the panels: on the left "T" junction in case B, on the right "X" junction in case C. The black strip represents the resilient interlayer

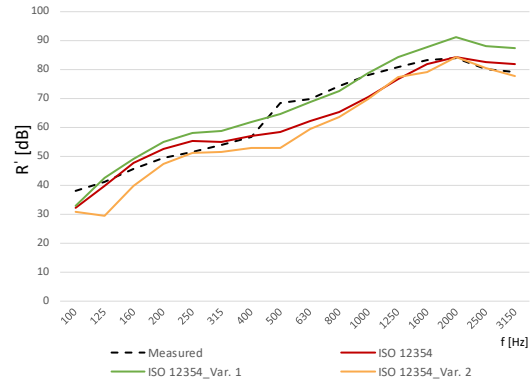


Fig. 13 – Comparison between sound insulation index measured and calculated values in case C: K_{ij} values are calculated and measured

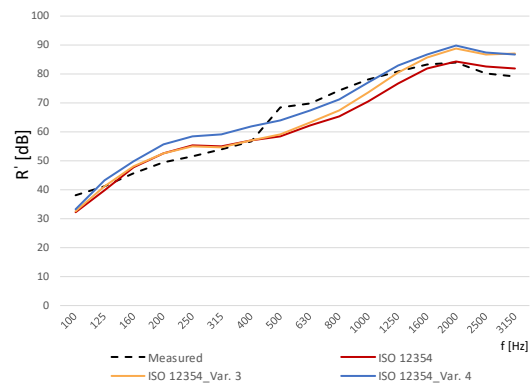


Fig. 14 – Comparison between sound insulation index measured and calculated values in case C: K_{ij} values are calculated and correct with T_s and areas of the elements

6. Results

The comparison between the three case studies showed with a good agreement that there are some precautions that should be considered when modelling timber buildings. The availability of data for the input of the model is extremely relevant. The same partitions modelled with commercial software and with experimental measurements provide different results, which strongly affect the final benchmarking. When possible, a direct reference to laboratory measurements should be made.

The K_{ij} values used as input also have a strong influence on the results. In particular, formulas provided in the ISO standard for CLT elements were shown to give very different results from the measured values, but when using the measured value in the ISO 12354 model, the simulations carried out with the ISO value fit better the experimental results.

The modelling of mixed junctions is critical because there is no reference on how to deal with the evaluation of the vibration reduction index (or normalized direction-averaged vibration level difference) and few experimental data are publicly available to the authors' knowledge.

The impact sound insulation is less affected by the flanking transmission paths compared to the airborne sound insulation; to evaluate the correctness of the modelling procedure, it is safer to rely on the airborne excitation.

The correction for resonant transmission should not be applied to CLT elements, while the modelling of the mixed junction needs this compensation to provide a good fitting with the experimental results. This outcome is consistent with recent literature on the mass timber elements.

7. Conclusion

The aim of this contribution is to use the detailed method provided by the series of ISO 12354 standards to model timber buildings in order to highlight the precautions that should be adopted and the need for future research. Three case studies, characterised by similar mass timber structures, which changed slightly from case to case, were analysed, and the effect of each modelling choice on the overall performance of the model was discussed. The availability of measured data is still the main point that needs to be addressed jointly by the scientific community, together with an insight on the modelling of the vibration reduction indices.

Acknowledgement

The measurement campaign was sponsored by Rothoblaas and Stora Enso. The authors thank the Ecotecsistemi, Fantoni SPA and Kulmer Bau GesmbH.

References

- Caniato, M., and A. Gasparella. 2019. "Discriminating People's Attitude towards Building Physical Features in Sustainable and Conventional Buildings." *Energies* 12(8), 1429.
- Di Bella, A., N. Granzotto, L. Barbaresi. 2016. "Analysis of acoustic behavior of bare CLT floors for the evaluation of impact sound insulation improvement." *Proc. Mtgs. Acoust.* 2016, 015016 (28).
doi: <https://doi.org/10.1121/2.0000420>
- Di Bella, A., N. Granzotto, G. Quartaruolo, A. Speranza and F. Morandi. 2018. "Analysis of airborne sound re-duction index of bare CLT walls." *Proc. of WCTE 2018 - World Conference on Timber Engineering*, Seoul, Rep. of Korea, 20–23 August, (2018).
- ISO. 2006. *ISO 10848-1:2006. Acoustics – Laboratory measurement of the flanking transmission of airborne and impact sound between adjoining rooms- Part 1: Frame document.*
- ISO. 2014. *ISO 16283-1:2014 Acoustics - Field measurement of sound insulation in buildings and of building elements - Part 1: Airborne sound insulation.*
- ISO. 2017a. *ISO 12354-1:2017. Building Acoustics – Estimation of acoustic performance in buildings from the performance of elements - Part 1, Airborne sound insulation between rooms.*
- ISO. 2017b. *ISO 12354-2:2017. Building Acoustics – Estimation of acoustic performance in buildings from the performance of elements - Part 2, Impact sound insulation between rooms.*
- ISO. 2017c. *ISO 10848-4:2017. Acoustics – Laboratory and field measurement of flanking transmission for airborne, impact and building service equipment sound between adjoining rooms. Part 4: Application to junctions with at least one Type A element.*
- ISO. 2018. *ISO 16283-2:2018 Acoustics - Field measurement of sound insulation in buildings and of building elements - Part 2: Impact sound insulation.*
- Morandi, F., S. De Cesaris, M. Garai, L. Barbaresi. 2018. "Measurement of flanking transmission for the characterisation and classification of cross laminated timber junctions." *Applied Acoustics* 141: 213-222.
- Rabold, A. 2017. „Mehrgeschosser in Massivholzbauweise - Schalltechnische Planung und Ausführung.“ *Bauphysikertreffen 2017*, Hochschule für Technik Stuttgart, 2017.
- Schoenwald, S., B. Zeitler, I. Sabourin and F. King. 2013. "Sound insulation performance of Cross Laminated Timber Building Systems." *Proc. of Internoise 2013*, Innsbruck, 2013.

Testing the BIM-Ladybug Tools Interoperability: A Daylighting Simulation Workflow

Laura Pompei – Sapienza University of Rome, Italy – laura.pompei@uniroma1.it

Giulia Spiridigliozzi – Sapienza University of Rome, Italy – giulia.spiridigliozzi@uniroma1.it

Livio De Santoli – Sapienza University of Rome, Italy – livio.desantoli@uniroma1.it

Cristina Cornaro – University of Rome Tor Vergata, Italy – cornaro@uniroma2.it

Fabio Bisegna – Sapienza University of Rome, Italy – fabio.bisegna@uniroma1.it

Abstract

While a considerable number of studies on Building Information Modelling (BIM) have been conducted in recent years, this area of research has long been considered important in the building sector, with particular concerns about Energy Design. In this regard, the work proposes an automated early design workflow to evaluate the building daylighting performance during the first design stages. Thanks to the potential use of interchange files and visual coding tools, such as Grasshopper, it is possible to implement the parametric design concepts, thus automating complex tasks. Specifically, in the analysed workflow, environmental algorithms and simulations are integrated to achieve reliable results with the minimum error percentage in data loss. The main finding concerns the BIM applications to perform daylighting design by the use of Ladybug tools from the Autodesk Revit export.

1. Introduction

Thanks to the new technologies in design, simulation and construction phase, it is possible to achieve energy-efficient solutions (De Santoli et al., 2017; Mancini et al., 2017). Nowadays, wide development studies are underway for BIM application in energy and daylighting performance. In this framework, the BIM-BEM (Building Energy Modelling) interoperability has been widely investigated (Kamel and Memari, 2019, Spiridigliozzi et al., 2019a, 2019b). BIM allows to have a central database, where data is not fragmented, thereby avoiding the traditional analysis limitations (Yujie et al., 2017). As reported in the literature (Dong et al., 2007; Ivanova et al., 2015; Kamel and Memari,

2019), numerical simulation and BIM integration are based on manual steps and exporting errors, providing fragmentation of data. The exchange file provides material properties, thermal zone data, limited data for the HVAC system and the site's information (Ivanova et al., 2015; Kamel and Memari, 2019). This research analyses and summarizes which objects are successfully transferred by the gbXML export and which suffer a transmission loss on the base of three export types. Following this preliminary study, the successfully exported data are implemented for the annual daylight simulations. Some researchers have suggested using middleware tools to improve the file export gap from BIM to BEM (Gigliarelli et al., 2017). Based on this, Salakij et al. 2016 developed an energy simulation tool using Matlab, which was able to read gbXML files. Ladan (2018) provides an overview of four programs specializing in energy and daylighting simulations by the gbXML file transmission. In this framework, the presented research aim is to define a methodology that allows information transfer from an architectural software (Autodesk Revit) to Ladybug tools, an environmental/energy open source, by the gbXML data format. In particular, this study focuses on the use of Honeybee, supplied by Ladybug tools, which support users to obtain environmental design by providing daylight simulations using RADIANCE engines. This open-source tool connects to Grasshopper/Rhino visual scripting, making it possible to graphically display the imported geometries. Finally, a calculation of different annual daylighting metrics is performed. The purpose of this paper is to explain the workflow, detailing the different model export set, and

reporting the data exchange limitations for daylighting simulation. Energy and environmental simulation results will be pursued in future work.

2. Methodology

The role of daylight is a well-known field and has become an essential resource for energy-saving and people's health (Halonen et al., 2010; Jenkins and Newborough, 2007). Accordingly, it is useful to support a properly designed daylighting environ-

ment, allowing users to obtain reliable results from the gbXML exchange file. In this study, both analysed tools were designed as parametric software, Revit Autodesk for the model configuration, and Grasshopper/Honeybee for the lighting simulation. To test and validate this methodology, a simplified model was utilized in accordance with the BEST-EST CASE ASHRAE 140 reference. Specifically, four base cases (900-930) with high mass were considered. The methodology description in Fig. 1 is reported in the following sections.

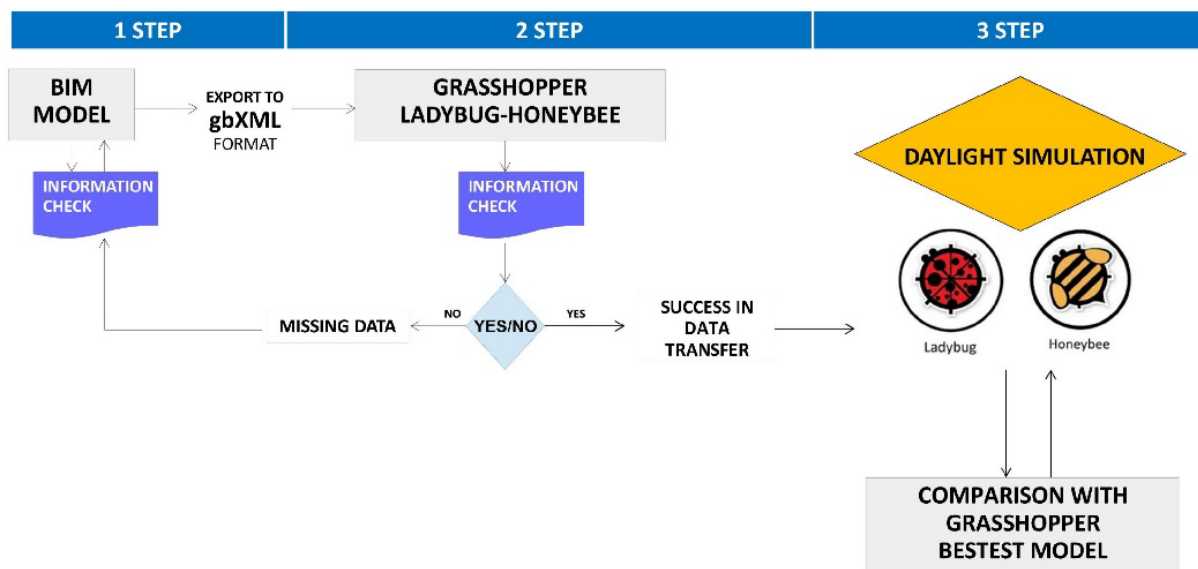


Fig.1 – Workflow applied to BESTEST

2.1 Workflow Description

1. The first step was to create the testing model (BESTEST) in the BIM software Revit, including all its geometric, spatial and thermal characteristics. This part played a fundamental role in the subsequent passages since an incorrect modelling criterion inevitably turns into an incorrect information transfer. Once the 3D model was complete, the analytical surfaces and the thermal zones of the energy model were identified. To correctly export a gbXML file, the first step is choosing between the energy setting or room/space volume; then set the building type, the project phase and the analytic construction. The Structural Function of the main elements (Internal or External) was correctly set for all vertical and horizontal objects. Honeybee needs

that information to run the daylighting simulation. Finally, the construction type is the last information to check before exporting the 3D model into Honeybee. Only for windows, is it not automated and requires users to create it manually. Once the model was correctly set, three-model export possibilities were investigated: the room export, the space export and the energy model export. The three export processes were analysed and were then compared to identify the correct methodology.

2. In the second step, the model was correctly exported and imported into the computational design environment. A new component added to Honeybee tool makes it possible to import gbXML files. During this step, all the information from the gbXML file is checked and if some is lost, the procedure is repeated from the

first step. Thanks to the verified data-transfer, it was possible to obtain reliable and fast preliminary results, which were completely in line with the conceptual design stage.

3. The third step consisted of running the daylight simulation in the Honeybee tool. Annual daylighting simulations (DA and sDA) were carried out for each case. Finally, the daylight results of BESTEST imported were compared with the one modelled directly with Rhinoceros/Grasshopper.

2.2 Export Set Types Description

In this section, an explanation of all tested exportation types is reported. The first one is the Room export set type, which implies the room's creation inside Revit. It is the easier gbXML export because few parameters are considered, such as: the export complexity (Simple/Complex), the detailed Elements (yes/no), the project phase (Existing/New Construction) and the building envelope (Use Function Parameter). In this case, the thermal zone properties were not considered. Subsequently, the space export set type implies a creation of spaces in the model. The Revit space includes all the thermal information such as the thermal zone properties, thermal load, systems, occupancy and lighting. In this case, further parameters were considered in addition to the previous ones, such as the building service (HVAC), the schematic types (if necessary) and the building infiltration class. Finally, the Energy Model export is the most complete gbXML export which consists of a separate energy model generation. In this case, the building type, the operating schedule, the HVAC Systems and the outdoor air information were also set. Only this export type needs the energy model creation inside Revit. Subsequently, the three export types were compared once imported into Honeybee. The criteria were mainly dictated by the potential error of the daylight simulation. The information was verified by identifying the data transmission loss inside the Honeybee tool.

2.3 Annual Daylight Simulation Setting

Two annual daylight simulations were carried out for each BESTEST, in order to test the imported files: the Daylight Autonomy (DA) and the Spatial Daylight Autonomy (sDA), using the time-varying illuminances derived from the Rome Ciampino climate file, during the typical 'working year' (i.e. between the hours 09:00–17:00). According to the definition of the Association Suisse des Electriciens and the work of Reinhart et al. 2006, the DA at a point in a building is defined as the percentage of occupied hours per year, when the minimum illuminance level can be guaranteed by daylight factor alone. The sDA, instead, measures the percentage of floor area that receives an established illuminance target for at least 50% of the annual occupied hours. For this study, the authors set an illuminance level of 300 lx (useful for normal activities). A grid of 165 points was used as the workplane, with a height of 0.8 m. The distance between consecutive points was 0.5 m, in all directions, in order to provide accurate results.

2.4 Case Study Description

The buildings chosen for testing the interoperability issues are the BESTEST Case 900-930 of ANSI/ASHRAE Standard 140-2004, as shown in Fig. 2. For the simulation analysis, the four case studies are located in Rome. The models have a single thermal zone without internal partition 8 m x 6 m, and two south-facing windows 2 m x 3 m for the cases 900-910, and east/west facing for the cases 920-930. Case study 910 differs from 900 because of the presence of a 1-meter horizontal overhang on the south wall at the roof level, while case 930 includes shade overhangs and shade fins around the east and west windows. The thermal and physical characteristics of the BESTEST construction elements are summarized in Tables 1 and 2. Once in the Honeybee tool, the EPW Rome Ciampino climate file was considered with a latitude of 41°48.0384' N and a longitude of 12°36.0948' E.

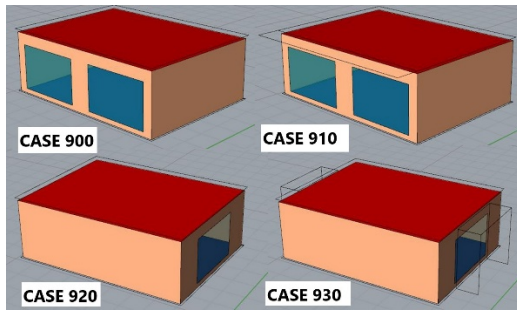


Fig. 2 – BESTEST Case 900-910-920-930

Table 1 – Construction elements properties

Wall Construction U=0.512 (W/m²-K)	Concrete Block 0.1 m Foam Insulation 0.0615 m Wood Siding 0.009 m
Floor Construction U=0.039 (W/m²-K)	Concrete Slab 0.08 m Insulation 1.007 m
Roof Construction U= 0.318 (W/m²-K)	Plasterboard 0.010 m Fiberglass Quilt 0.1118 m Roof Deck 0.019 m

Table 2 – Windows Construction properties (double glazing)

Double glazing U=0.94 (W/m²-K)	Glass thickness 0.003 m Air gap thickness 0.013 m
--	--

3. Results

3.1 Export Results

In this section, the three export results are discussed. Table 3 shows a summary report which lists the export types on the left, and the investigated characteristics on the top. The first one, the room export, worked properly, and no errors were found after the transmission process. Geometry and material properties were correctly imported, while space name, thermal load, and space thermal

properties were ignored due to the examined set. No errors were also found for the Space export after the transmission process: the geometry and material properties, the thermal load, and the space thermal properties were correctly imported. Finally, the last Energy model export type showed one error during the transmission process reported as: "2 surfaces have missing constructions, default construction will be used". In this case, no error justification was found, but it was possible to investigate the missing data integration once in the honeybee tool. Following the two missing surfaces replacement, this export type also worked correctly. Moreover, space and room exported work by integrating the window elements into the building envelope, as shown in Fig. 3(a), while the energy model export created a single closed envelope with windows attached over the wall surfaces, as can be seen in Fig. 3(b). However, this difference is only graphical since both these representations give the same simulation results. In our case, to run the daylighting simulation, the room export was considered. The choice was based on the data requirement for the daylight simulation. In this case, the building's thermal and infiltration data derived from the other two export types were not necessary.

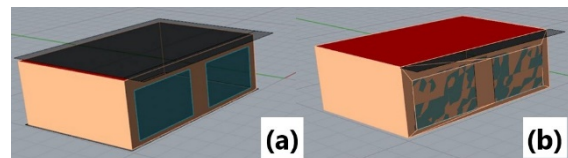


Fig. 3 – Space and room exports (a), Energy model export (b)

Table 3 – Report of the export type comparison

Export type	Case	Orientation	Site Location	Weather Data	Wall Geometry	Window Geometry	Floor Geometry	Roof Geometry	Shading	Shading Properties	Thermal properties	Material Name	Construction Type	Spaces Name	Spaces thermal properties	Thermal Loads
ROOM	900	✓	✓	X	✓	✓	✓	✓	-	-	✓	✓	✓	-	-	-
	910	✓	✓	X	✓	✓	✓	✓	X	X	✓	✓	✓	-	-	-
	920	✓	✓	X	✓	✓	✓	✓	-	-	✓	✓	✓	-	-	-
	930	✓	✓	X	✓	✓	✓	✓	X	X	✓	✓	✓	-	-	-
SPACE	900	✓	✓	X	✓	✓	✓	✓	-	-	✓	✓	✓	✓	✓	✓
	910	✓	✓	X	✓	✓	✓	✓	X	X	✓	✓	✓	✓	✓	✓
	920	✓	✓	X	✓	✓	✓	✓	-	-	✓	✓	✓	✓	✓	✓
	930	✓	✓	X	✓	✓	✓	✓	X	X	✓	✓	✓	✓	✓	✓
ENERGY	900	✓	✓	X	✓	✓	✓	✓	-	-	✓	✓	X	✓	✓	✓
	910	✓	✓	X	✓	✓	✓	✓	X	X	✓	✓	X	✓	✓	✓
	920	✓	✓	X	✓	✓	✓	✓	-	-	✓	✓	X	✓	✓	✓
	930	✓	✓	X	✓	✓	✓	✓	X	X	✓	✓	X	✓	✓	✓

Legend: ✓ Correct import - Not provided X Import error

3.2 Annual Daylighting Results

3.2.1 BESTEST 900: imported and modelled

The Annual Daylighting Autonomy (DA) and Spatial Daylighting Autonomy (sDA) were calculated for the BESTEST 900 (modelled and imported) with a threshold of 300 lx. Fig. 4 shows the Daylighting Autonomy results for each point inside the room.

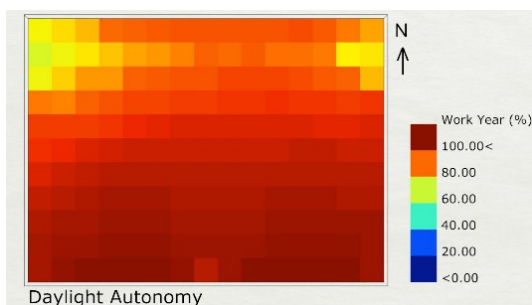


Fig. 4 – Case 900 imported: DA (300 lx) results

Reading from the false colour maps, DA is achieved more than 85% of the working year in the vicinity of the South facade. The lower results instead are located further away from the glazing facade. The large number of results were processed and summarized by the use of statistical indicators (Table 4).

Table 4 – Case 900: DA (300 lx) results

Statistical Indicators	Value (%)
Median	93
Maximum	100
Minimum	62
First Quartile	83
Third Quartile	97

It can be noted that the Median value is 93%, therefore some points registered high DA values, particularly those located near the window (at a distance of 1 m). The sDA simulation provided a value of 100%, highlighting the fact that the 300 lx level is guaranteed for at least 50% of the annual occupied hours. Moreover, case 900 was created by the 3D tool Rhinoceros to obtain reliable results which are useful for the validation of the model imported. Table 5 reports the DA results for case 900 modelled and as can be seen, the Minimum value decreased from 62% to 49%.

Table 5 – Case 900 modelled: DA (300 lx) results

Statistical Indicators	Value (%)
Median	92
Maximum	100
Minimum	49
First Quartile	82
Third Quartile	97

There are therefore some points (3 points) that registered lower values in respect to the case imported, as highlighted by the Median result. However, the global trend of the modelled results is comparable with the case 900 imported. The sDA simulation gives a value of 99.39%, which is compatible with the 900 sDA result.

3.2.2 BESTEST 910: imported and modelled
Daylighting results (e.g. DA and sDA) for case 910 achieved equal value compared to case 900 (see Table 4). Therefore, the comparison with the model created inside Rhinoceros assumed an essential role. Table 6 below summarizes DA results for the BESTEST 910 modelled and some differences can be seen with respect to the imported case. In general, the results are somewhat different compared to Table 4: in this case the values decrease, as can be expected due to the presence of the overhang (Table 6).

Table 6 – Case 910 modelled: DA (300 lx) results

Statistical Indicators	Value (%)
Median	91
Maximum	99
Minimum	42
First Quartile	81
Third Quartile	96

Consequently, BESTEST 910 imported seems to unrecognize the shading geometry, providing daylighting results equal to the case without the overhang. In addition, the sDA simulation obtained a value of 97.58%, lower than the imported gbXML case.

3.2.3 BESTEST 920: imported and modelled

Fig. 5 shows the DA distribution for the BESTEST 920 with 300 lx.

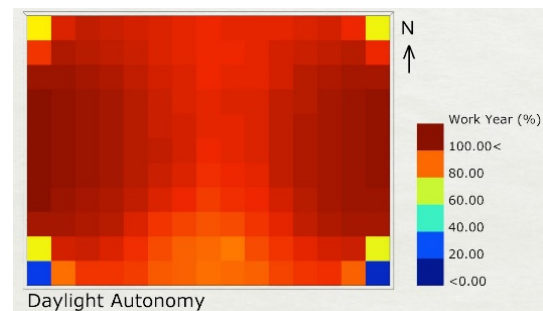


Fig. 5 – Case 920 imported: DA (300 lx) results

Reading from Fig. 5, high DA values are distributed near the glazing facades; conversely, the lower results are located at the corners of the room. The final results are also reported in the table below.

Table 7 – Case 920 imported: DA (300 lx) simulation results

Statistical Indicators	Value (%)
Median	92
Maximum	100
Minimum	7
First Quartile	89
Third Quartile	97

As shown in Table 7, the Minimum value is 7%, and was found in the vicinity of the room corners. Some points achieved the maximum values of 100% and the Median was 92%. In terms of the sDA, the measured value is 98.79%. Results related to the case modelled are reported in Table 8, which shows a few differences compared to Table 7.

Table 8 – Case 920 modelled: DA (300 lx) results

Statistical Indicators	Value (%)
Median	91
Maximum	100
Minimum	6
First Quartile	88
Third Quartile	96

As the BESTEST 900, the 920 is well recognized in its entirety by the simulation tool, providing reliable results. The Median value is lower due to the decrease in the Minimum value from 7% to 6%.

However, those differences are negligible. The value of sDA is 97.68%.

3.2.4 BESTEST 930: imported and modelled

Finally, Table 9 report DA results for the BESTEST 930 with the illuminance levels of 300 lx. The results of this case are not reported as figures due to the small difference between the values that cannot be highlighted through the qualitative images.

Table 9 – Case 930 imported: DA (300 lx) results

Statistical Indicators	Value (%)
Median	92
Maximum	100
Minimum	12
First Quartile	89
Third Quartile	97

The Minimum value is 12%, the Maximum is 100% and the Median is 92%. Moreover, the sDA simulation achieved a value of 98.79%. Table 10 also shows the DA results of this case modelled with the 3D tool.

Table 10 – Case 930 modelled: DA (300 lx) results

Statistical Indicators	Value (%)
Median	88
Maximum	99
Minimum	0
First Quartile	82
Third Quartile	94

The results from the statistical indicators were lower compared to the results from case 930 imported, particularly the Median and the Minimum. The DA trend is generally reduced due to the overhangs above the windows. Moreover, the sDA value of 92.73% underlines those differences with the case imported. In summary, these comparisons were useful for the results validation, highlighting that the shading element is not correctly imported through the gbXML file.

4. Conclusion

The role of BIM is widely recognized in terms of central data for management and exchanges files with other users in the building sectors. Moreover, the interoperability between BIM and the energy model is still underway, due to the different technical languages and information types. In this framework, the research proposes a methodology workflow that can help designers to evaluate the daylighting comfort during the first design stage, thanks to the BIM and Building Energy Modelling (BEM) interoperability. As far as the results are concerned, in general, the three export types work correctly inside the energy tools, due to the proper setting explained in the methodology section. The Room and Space export file has no errors during the importing process. The Energy Model imported is not influenced by the aforementioned warning error related to a specific surface, since it is only a different type of 3D geometrical mass. Some information has to be set inside the Honeybee tool, such as the EPW climate file and the window properties. It is then possible to run the annual daylighting simulations (DA and sDA). Moreover, the authors validated the daylighting results by comparing them to the BESTEST modelled directly into the 3D software. Due to this comparison, cases 900 and 920 are correctly imported and analysed inside the daylight tool.

On the other hand, BESTEST 910 and 930, the shading cases, did not provide reliable results and Honeybee is not able to recognize the imported overhang geometry. Consequently, the exchange information of the shading element requires further analysis in order to overcome this issue.

In conclusion, the authors note that this is the first step in the application of BIM and BEM interoperability for the daylight analysis. Future developments will investigate more complex case studies to test and verify this methodology by implementing other comfort and energy analysis.

Acknowledgement

This research has been carried out thanks to the “Renovation of existing buildings in NZEB vision (nearly Zero Energy Buildings)” Project of National Interest (Progetto di Ricerca di Interesse Nazionale - PRIN) funded by the Italian Ministry of Education, Universities and Research (MIUR).

References

- Association Suisse des Electriciens. 1989. *Swiss Norm SN 418911. Éclairage intérieur par la lumière du jour*. Zurich, Switzerland: Association Suisse Des Electriciens.
- De Santoli, L., F. Mancini, C. Clemente, and S. Lucci. 2017. “Energy and technological refurbishment of the School of Architecture Valle Giulia, Rome.” *Energy Procedia* 133: 382-391.
- Dong, B., K. P. Lam, Y. C. Huang, and G. M. Dobbs. 2007. “A comparative study of the IFC and gbXML informational infrastructures for data exchange in computational design support environments.” *Building Simulation* 2007.
- Gigliarelli, E., F. Calcerano, M. Calvano, F. Ruperto, M. Sacco, and L. Cessari. 2017. “Integrated numerical analysis and Building Information Modeling for Cultural Heritage”, *Building Simulation Applications* 2017.
- Halonen, L., E. Tetri, and P. Bhusal. 2010. *Guidebook on energy efficient electric lighting for buildings*. Espoo, Finland: Aalto University School of Science and Technology.
- Ivanova, I., K. Kiesel, and A. Mahdavi. 2015. “BIM-generated data models for EnergyPlus: A comparison of gbXML and IFC Formats.” *Building Simulation Applications* 2015.
- Jenkins, D., and M. Newborough. 2007. “An approach for estimating the carbon emissions associated with office lighting with a daylight contribution.” *Applied Energy* 84: 608-622. DOI: 10.1016/j.apenergy.2007.02.002
- Kamel, E. and A. M. Memari. 2019. “Review of BIM's application in energy simulation: Tools, issues, and Solutions.” *Automation in Construction* 97: 164–180. DOI: 10.1016/j.autcon.2018.11.008
- Ladan, G. 2018. “Daylight and energy simulation workflow in performance-based building simulation tools.” *Building Performance Analysis Conference and SimBuild*.
- Mancini, F., G. L. Basso, and L. D. Santoli. 2017. “Energy Use in Residential Buildings: Characterisation for Identifying Flexible Loads by Means of a Questionnaire Survey.” *Energies* 12(11), 2055. DOI: 10.3390/en12112055
- Reinhart, C. F., J. Mardaljevic, Z. Rogers. 2006. “Dynamic daylight performance metrics for sustainable building design.” *Leukos* 3(1):7–31. doi.org/10.1582/LEUKOS.2006.03.01.001
- Salakij, S., N. Yu, S. Paolucci, and P. Antsaklis. 2016. “Model-Based Predictive Control for building energy management. I: Energy modeling and optimal control.” *Energy and Buildings*, 133: 345-358. DOI: 10.1016/j.enbuild.2016.09.044
- Spiridigliozzi, G., L. D. Santoli, C. Cornaro, G. L. Basso, and S. Barati. 2019a. “BIM Tools Interoperability For Designing Energy-Efficient Buildings.” *AIP Conference proceedings*.
- Spiridigliozzi, G., L. Pompei, C. Cornaro, L. D. Santoli, and F. Bisegna. 2019b. “BIM-BEM support tools for early stages of zero-energy building design.” *IOP Conference Series Materials Science and Engineering*.
- Yujie, L., W. Zhilei, C. Ruidong, and L. Yongkui. 2017. “Building Information Modeling (BIM) for green buildings: A critical review and future directions.” *Automation in construction* 83: 134–148.

An Attempt to Rank Italian Historical Opera Houses Based on Numerical Simulation

Giulia Fratoni – University of Bologna, Italy – giulia.fratoni2@unibo.it

Anna Rovigatti – Atkins Global, United Kingdom – anna.rovigatti@atkinsglobal.com

Massimo Garai – University of Bologna, Italy – massimo.garai@unibo.it

Abstract

Due to the complexity of the acoustic field in articulated closed spaces, architectural acoustics is often approached as a reverse-engineering problem: criteria, reference values and analysis methods are extrapolated by comparing results from measurements in a set of case studies. Considering the methods and the results of previous works on Italian historical theatres, the present study shows the results of geometrical acoustic (GA) numerical simulations with the aim to attempt a ranking based on the subjective preference theory. The models were calibrated using several room criteria that had been previously measured in the framework of a measurement campaign performed in Italian theatres. The cluster chosen is intended to represent an adequate sample of case studies relative to different capacities and different design approaches, which were first developed in the seventeenth century.

1. Introduction

The theatres investigated in this study represent an adequate sample of case studies relative to the different design approaches of Italian Historical Opera Houses (D'Orazio and Nannini, 2019). These theatres shared the political events related to the foundation of the Kingdom of Italy (1861) and World War II, during which most of them were severely damaged, sacked and used as warehouses, public toilets, cellars or field hospitals. In the twenties, some of these theatres were equipped with an orchestra pit, whose construction changed the role of the proscenium arch. In particular, in many cases the stage was moved backward (D'Orazio et al., 2019) and as a consequence the

proscenium arch could no longer provide the typical strong early reflection on the audience.

A synthesis of the architectural features of these theatres can be found in Table 1. By using existing categories (Prodi et al., 2015), it is possible to distinguish between large (DUS, BOL) and mid-sized theatres (ALI, BON). See also Fig. 1.

Table 1 – Architectural features of the theatres analysed

ID	V_{fly} (m ³)	V_{hall} (m ³)	Shape	N
BOL	19900	5500	Bell	999
BON	11630	3130	Horse-shoe	798
ALI	5300	3360	Horse-shoe	835
DUS	2800	7400	Modern	999

2. Acoustic Criteria for Opera Houses

The acoustic quality of an opera house is described using measurable quantities that are the scientific expressions of precise subjective judgements. Over the years, several scholars have investigated the relation between objective parameters and individual perceptions of sound in an enclosed space. However, different approaches to the issue and difficulties found in dissimilar evaluations have not made it possible to achieve a single method. All that has been established until now is a series of measurable room criteria, some of which are still debated by experts while others are officially defined by standards (ISO 3382-1, 2009).

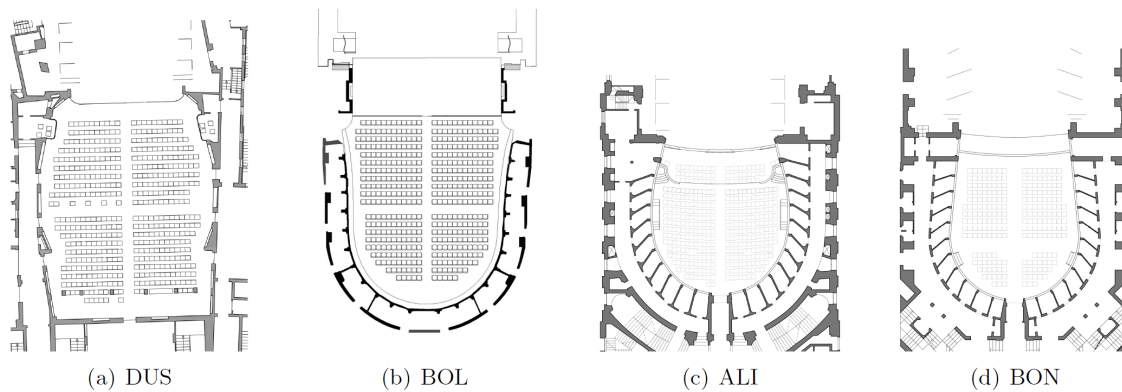


Fig. 1 – Plans of the main halls of the investigated theatres

All the indicators on which the present study is based are briefly described and commented on hereafter in relation to Italian Opera Houses. The most evident characteristic we perceive inside a hall is the reverberation, a parameter that intuitively indicates how long a sound persists in the space. For the first century of architectural acoustics (which dates back to Sabine's work) it has represented the main, if not the only, measurable descriptor used to qualify the acoustic behaviour of an enclosure.

Dealing with the subjective perception of reverberation, the Early Decay Time EDT plays a key role. During an “aria”, for instance, it is unlikely that a listener has the time to hear the whole decrease of a single note sound energy, so fast notes follow one another. In a few words, new acoustic phenomena mask the late reflections of sounds previously emitted, thus we are able to perceive only the beginning of the decay curve.

Clarity (C) is one of the parameters that describe the “balance between early and late arriving energy” (ISO, 2009) in a room. The integration time is assumed as 80 ms for music (C_{80}) and the integration extreme $t = 0$ represents the direct sound arrival time. A threshold of 50 ms was shown to be more suitable for mid-sized Italian opera houses (De Cesaris et al., 2015).

Sound strength (G) is a descriptor that quantifies the sound energy distribution in the hall; it indicates how much the hall naturally amplifies sounds (ISO, 2009). Sound strength index is one of the most important parameters to analyse and qualify the acoustics of the auditorium and the behaviour

of the coupled volumes (D’Orazio et al., 2017; Garai et al., 2016).

In ISO 3382-1 (2009) besides the mentioned monaural coefficients, a binaural index is also defined: the Inter-Aural Cross Correlation (IACC). The most general form of IACC is provided with $t_1 = 0$ and $t_2 = 1$, i.e. with a time comparable with reverberation time. Moreover, the IACC can be found out both for early energy (IACC_E with $t_1 = 0$ ms and $t_2 = 80$ ms) and for the reverberant field (IACC_L with $t_1 = 80$ ms and t_2 greater than reverberation time of the hall surveyed). Rather than the IACC coefficient, an alternative parameter is usually preferred: the Binaural Quality Index (BQI), defined as: $BQI = 1 - IACC_{E,3}$ where subscript E stands for early (integration's extremes $t_1 = 0$ ms and $t_2 = 80$ ms) and subscript 3 indicates that value has been averaged over the central octave bands (500-1000-2000 Hz).

Other objective acoustic criteria are used in the present paper. The Bass Ratio (BR) is defined as the ratio of the reverberation time at 125 Hz and 250 Hz to the reverberation time at 500 and 1000 Hz, usually evaluated in occupied condition (BR_{occ}). The Initial Time Delay Gap (ITDG) is the time difference between the direct sound and the first reflection. The Lateral Fraction (LF) is the ratio of the early energy measured with a figure-of-eight microphone ($t_1 = 5$ ms, $t_2 = 80$ ms) and the early energy measured with an omnidirectional microphone ($t_1 = 0$ s, $t_2 = 80$ ms). Subjective LF is expressed through the Lateral Fraction Cosine (LFC). Finally, the Surface Diffusivity Index (SDI) is defined as an average value of diffusivity of all surfaces in a room.

3. Calibration

The theatres were investigated using monoaural and binaural techniques in an unoccupied state, according to ISO 3382 (ISO, 2009).

The IRs were measured using a custom high-SPL dodecahedron (D’Orazio et al., 2016a) as sound source. IRs were acquired using ESS test signals (Guidorzi et al., 2015) and postprocessed in order to extract ISO 3382 criteria.

In each theatre, the number and type of curtains were noted. The curtains were set for a standard performance of a medium-sized orchestra following the requirements of the minimum amount of absorptive material on the stage, suggested in the Charter of Ferrara (Pompoli and Prodi, 2000), of 500 m².

The measurement campaign was characterised by a large number of measurements. In the stalls, IRs measurements were performed at all seats for several source positions: two on the stage, one on the fore-stage, one in the centre-stage, two in the orchestra pit, one in the covered part, one in the open part of the pit – at a height of 1.2 m. In each box, measurements were performed placing the microphone in the front position. In the gallery, measurements were taken in correspondence to the seats in the boxes, with some slight differences depending on the setting of the gallery. The height of the microphone was kept at 1.2 m. Over 50,000 IRs were processed: a more complete overview of this survey was presented in (Garai et al., 2015a).

The theatres were 3D modelled starting from architectural surveys (ALI, DUS, BON) or laser scanning (BOL only (Bitelli et al., 2017)). Numerical models were then calibrated by assigning material properties in each octave band, from 63 Hz to 8 kHz, following an iterative process (ODEON, 2010). The absorption coefficients were found in reference datasets (Cox and D’Antonio, 2009; Vorländer, 2007); the scattering coefficients take into account geometry of complex surfaces and receiver-surface distances (Shtrepi and Astolfi, 2015; Shtrepi, 2019). Values of both parameters were adjusted in order to fit the measured values (Postma and Katz, 2016).

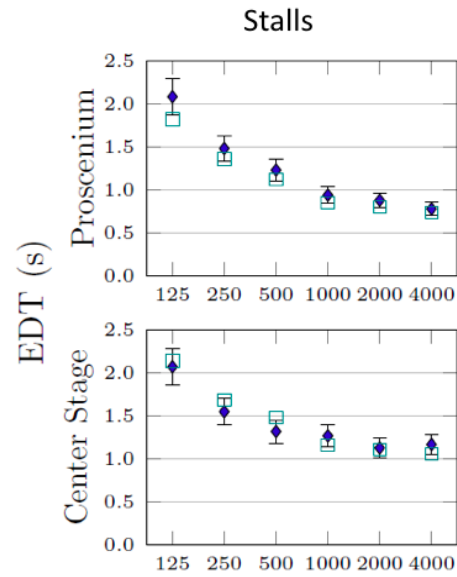


Fig. 2 – Calibration of ALI theatre, considering two source positions and three receivers areas (only stalls are displayed here). Comparison between measured and simulated values is provided in octave bands; error bars refer to 2 times the JND

The iterative process involved EDT and C_{80} criteria: for each sound source, the simulation results were averaged for each group of receivers, respectively: stalls, boxes and gallery. The calibration process was concluded when the differences in each octave were within 2 JNDs, which were, respectively, 10% for EDTs and 2 dB for C_{80} . An example of calibration results for EDT in the ALI theatre is shown in Fig. 2.

According to state-of-the-art practice (Lokki and Pätynen, 2009), simulations were carried out in hybrid mode, combining the mirror source method and ray-tracing techniques and setting a transmission order of 2. In other words, the first two simulated reflections preserve the phase information, which may be useful when the numerical models are used to auralise anechoic signals (D’Orazio et al., 2016b).

Fig. 3 shows how each layer influences the equivalent acoustic absorption area. The incidence of four layers covers the whole absorption: plaster (which involves all the surfaces covered by plaster), wood (the wooden stage), drapes (curtains and scenarios in the fly tower), and seats. Air absorption is negligible at low and mid frequencies.

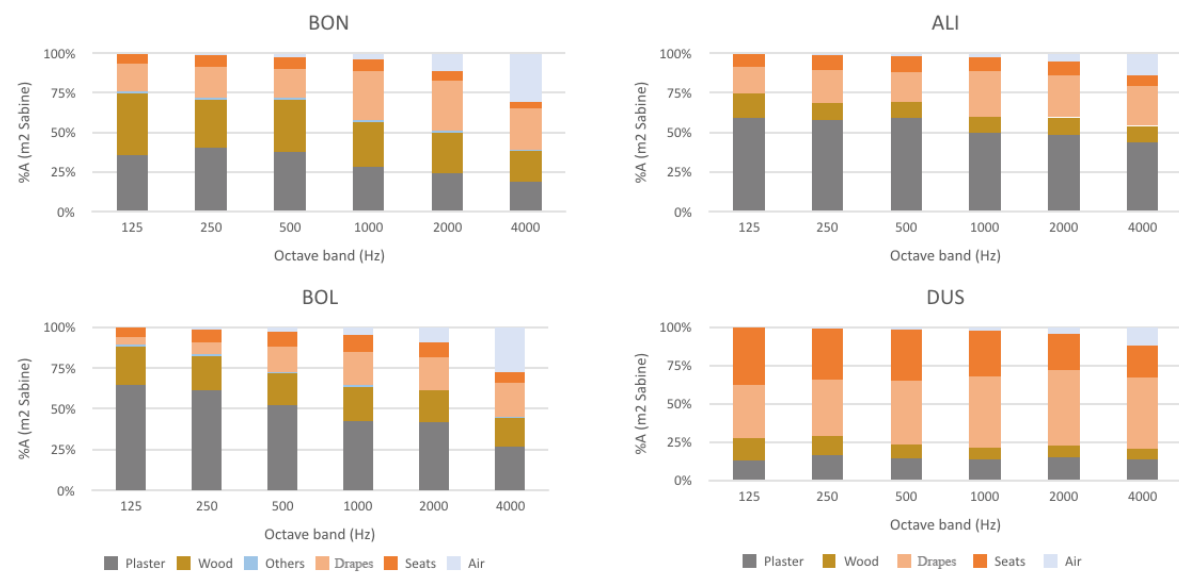
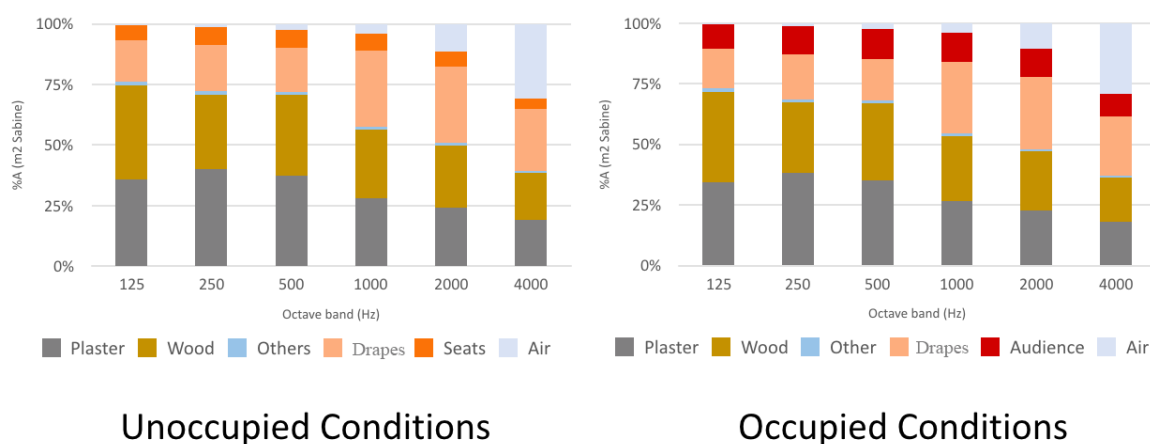


Fig. 3 – Percentage of equivalent absorption area of each layer in unoccupied conditions



Unoccupied Conditions

Occupied Conditions

Fig. 4– Percentage of equivalent absorption area of each layer in BON in unoccupied and occupied conditions

There was a significant difference between modern (DUS) and historical theatres (ALI, BON, BOL), concerning the weight of the seats and the plaster. The acoustic absorption of DUS is mainly characterised by chairs and drapes: it means that the acoustic behaviour depends on the mounting of scenarios, more than the occupied/unoccupied conditions. Indeed, the absorption of the upholstered chairs may be comparable to the absorption of the occupancy. Conversely, in the historical theatres, the plaster and the wood characterise the acoustic absorption of the theatres.

In each theatre the plaster coefficient was set differently depending on the materials on which the plaster was fixed: wood (as the case of ALI and BON), masonry (BOL) or concrete (DUS). Finally, the wooden stage may play a relevant role if the stage is large as the case of BON. Indeed, wooden layers may be absorbent at low frequencies due to the resonances of light parts (D'Orazio et al., 2018; Fratoni et al., 2019; Garai et al., 2015b). It can be noted that opera houses are coupled volumes, so the absorption of the fly tower does not necessarily influence the main hall (Garai et al., 2016).

4. Listener Absorption

Listener absorption may influence the reverberation time values of the hall (Beranek, 2006). Furthermore, frequency behaviour of listener absorption differs from the materials one, so the reverberation times may also change in frequency.

Absorption coefficients of the theatre layers should consider the orchestra occupancies too (Jeon et al., 2015, 2018). In an opera house the orchestra is placed in the pit, so the absorption of the musicians also influences the acoustic coupling between the pit and the hall.

Fig. 5 shows the differences between the equivalent absorption areas of BON theatre, respectively, in unoccupied and occupied conditions. It should be noted that in the historical theatres (BON, BOL, ALI), the audience absorption influences the octave bands between 125 and 8000 Hz, while in the modern theatres (DUS) the absorption of chairs is quite similar to that of listeners. Consequently, BR_{occ} values of the historical theatres span from 1.1 to 1.3, while $BR_{occ} = 1.5$ in DUS (see Table 2).

5. Ranking

Subjective preference theory dates back to the 1970's from studies on European Concert Halls (Schroeder et al., 1974), and has since been improved by Ando (Ando, 2015). Methods and results of the subjective preference are related to concert hall and music signals. Beranek (2003) extended Ando's subjective preference for concert halls, taking into account EDT at mid frequencies instead of T_{30} , BQI as a description of the cross correlation of early reflections, BR and SDI (Sound Diffusion Index). To go to the opera, or generally to stay in a theatre, is an experience which involves visual, musical, and literary experiences. Cirillo et al. (2011) adapted the Ando-Beranek approach to Italian opera houses, also taking into account the Balance (B) for the opera. A synthesis of preference models is shown in Table 3, considering the case of a soloist voice as signal source (D'Orazio et al., 2011; D'Orazio and Garai, 2017).

Table 2 – Reverberation time and bass ratio values of the theatres under study

ID	$T_{30,M,unocc}$ (s)	BR_{occ} (-)
BOL	1.53	1.1
BON	1.77	1.3
ALI	1.37	1.3
DUS	1.32	1.5

Table 3 – Criteria and preferred values of subjective preference theories. A $\tau_e = 20$ ms was assumed for opera singers. The reverberant-to-direct ratio was defined according to (Ando, 1983)

Criterion	Ando 2015	Beranek 2003	Cirillo et al. 2011
Listening level (dB)	Bin. Level ≈ 79	$G_{mid} > 1$	$G_{mid} 1 \div 8$
Spatiality (-)	IACC lowest	BQI 0.7	BQI > 0.7
Reverberation (s)	T_{30} $23\tau_{e,min}$	EDT 2.5	EDT $1.4 \div 1.6$
Intimacy (ms)	ITDG (1- $\log A$) $\tau_{e,min}$	ITDG 20	ITDG < 20
Clarity (dB)	-	-	$C_{50} 1 \div 5$
Warmness (-)	-	$BR_{occ} 1.1 \div 1.2$	BR $1.05 \div 1.25$
Diffusivity (-)	-	SDI 1	SDI 1

For the purpose of this analysis, the positions of the virtual sound source were chosen similarly on the proscenium in all the theatres under study: on the longitudinal axis of the stage at 1 m from the edge. Figs 5 and 6 show the maps of simulated values of four criteria involved in the subjective preference models in the stalls of two theatres:

- G for natural gain of the hall;
- EDT for subjective reverberation;
- LFC_{80} for spatiality;
- C_{80} for clarity and early-to-late ratio.

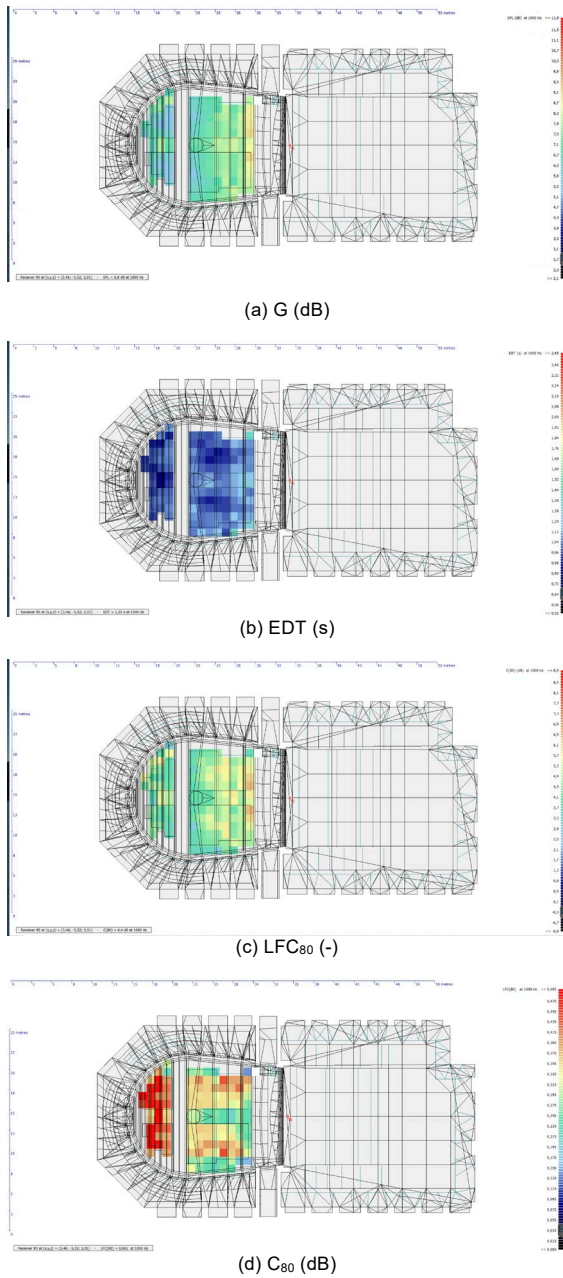


Fig. 5 – Maps of the distribution of G (dB), EDT (s), LFC₈₀ (-) and C₈₀ (dB) in the stalls area of the BON theatre. Sound source on the stage, at 1m from proscenium border

Stage acoustics was not taken into account in this work: an analysis of two halls (ALI, BON) was shown in a previous study (D’Orazio et al., 2015). Taking into account the subjective models and the simulation results, a preliminary ranking of the three historical opera houses is shown in Table 4. The DUS theatre, being a modern one, is not shown in this table.

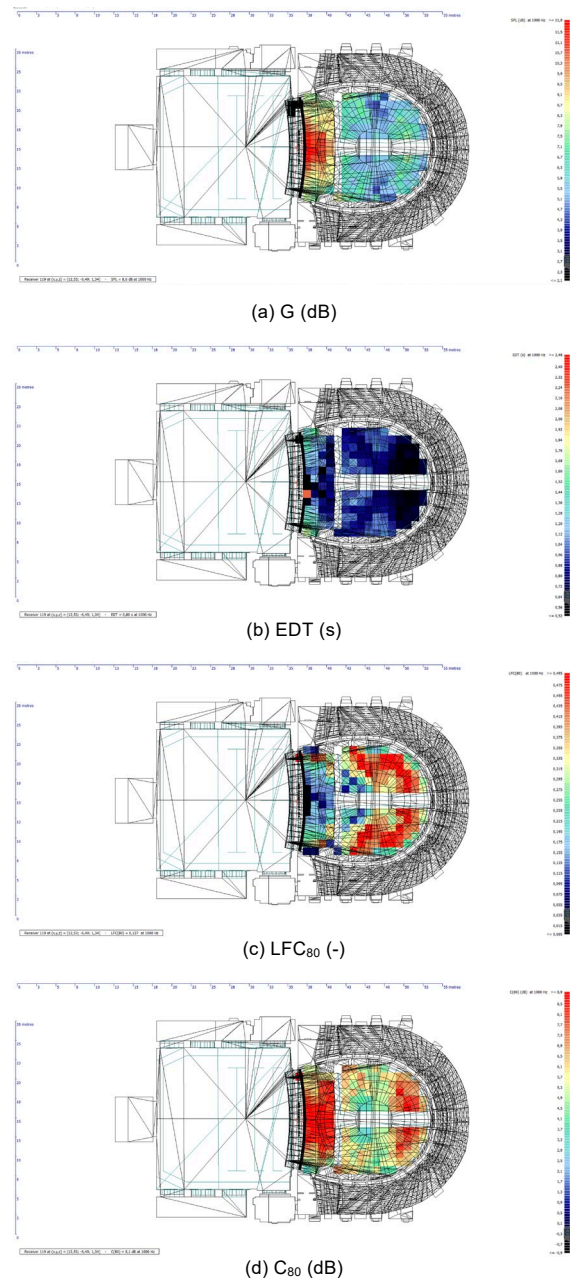


Fig. 6 – Maps of the distribution of G (dB), EDT (s), LFC₈₀ (-) and C₈₀ (dB) in the stalls area of the ALI theatre. Sound source on the stage, at 1m from proscenium border

6. Conclusion

A detailed measurement campaign was carried out in three historical opera houses and one modern theatre. ISO 3382 monaural criteria were used in order to calibrate numerical models, which were used to extract room criteria in occupied conditions. Criteria in both conditions (unoccupied and occupied) were used in subjective preference models previously proposed by scholars. Results show

pros and cons of each theatre, making it possible to validate the perceived acoustic quality of theatre under study when they are used for opera.

Table 4 – Quality classes (from D to A+) of the three historical opera houses studied

ID	Ando/Beranek	Cirillo	pros	cons
BOL	A	B	IACC	
BON	B	A	EDT	
ALI	B	B		Low G

References

- Ando, Y. 1983. "Calculation of Subjective Preference at Each Seat in a Concert Hall." *J. Acoust. Soc. Am.* 74(3): 873-887.
- Ando, Y. 2015. *Opera house acoustics based on subjective preference theory*. Springer.
- Beranek, L. L. 2003. "Subjective rank-orderings and acoustical measurements for fifty-eight concert halls." *Acta Acustica United with Acustica* 89:494-508.
- Beranek, L. L. 2006. "Analysis of Sabine and Eyring equations and their application to concert hall audience and chair absorption." *J. Acoust. Soc. Am.* 120(3):1399-1410.
- Bitelli, G., M. Dellapasqua, V. A. Girelli, E. Sanchini, M. A. Tini. 2017. "3d geomatics techniques for an integrated approach to cultural heritage knowledge: the case of San Michele in Acerboli's church in Santarcangelo di Romagna." *Proceedings of 1st International Conference on Geomatics and Restoration: Conservation of Cultural Heritage in the Digital Era, GeoRes* 2017.
- Cirillo, E., M. Dell'Alba, F. Martellotta. 2011. "Caratterizzazione acustica dei teatri storici di Puglia." *Proceedings of the 38th National Congress on Acoustics*, Rimini, Italy.
- Cox, T. J., P. D'Antonio. 2009. *Acoustic Absorbers and Diffusers. Theory, Design and Application*. CRC Press.
- D'Orazio, D., S. De Cesaris, M. Garai. 2011. "A comparison of methods to compute the "effective duration" of the autocorrelation function and an alternative proposal." *J. Acoust. Soc. Am.* 130(4):1954-1961.
- D'Orazio, D., S. De Cesaris, L. Guerra, A. Tovo, M. Garai. 2015. "Objective musician's criteria in Italian historical Theatres." *Proceedings of the 22nd International Congress of Sound and Vibrations*, Florence, Italy.
- D'Orazio, D., S. De Cesaris, P. Guidorzi, L. Barbaresi, M. Garai, R. Magalotti. 2016a. "Room acoustic measurements using a high-SPL dodecahedron." *Proceedings of the 140th Audio Engineering Society Convention (AES)*, Paris, France.
- D'Orazio, D., S. De Cesaris, M. Garai. 2016b. "Recordings of Italian opera orchestra and soloists in a silent room." *Proc. of Meetings on Acoustics* 28, 015014.
- D'Orazio, D., G. Fratoni, M. Garai. 2017. "Acoustics of a chamber hall inside a former church by means of sound energy distribution." *Journal Canadian Acoustic Association* 45(4):7-16.
- D'Orazio, D., M. Garai. 2017. "The autocorrelation-based analysis as a tool of sound perception in a reverberant field." *Rivista di Estetica* 66(3):133-147.
- D'Orazio, D., S. De Cesaris, F. Morandi, M. Garai. 2018. "The aesthetics of the Bayreuth Festspielhaus explained by means of acoustic measurements and simulations." *J. Cult. Herit.* 34:151-158.
- D'Orazio, D., A. Rovigatti, M. Garai. 2019. "The Proscenium of Opera Houses as a Disappeared Intangible Heritage: A Virtual Reconstruction of the 1840s Original Design of the Alighieri Theatre in Ravenna." *Acoustics* 1(3):694-710.
- D'Orazio, D., S. Nannini. 2019. "Towards Italian Opera Houses: A Review of Acoustic Design in Pre-Sabine Scholars." *Acoustics* 1:252-280.
- De Cesaris, S., F. Morandi, L. Loreti, D. D'Orazio, M. Garai. 2015. "Notes about the early to late transition in Italian theatres." *Proceedings of ICSV22*, Florence, Italy.
- Fratoni, G., D. D'Orazio, L. Barbaresi. 2019. "Acoustic comfort in a worship space made of cross-laminated timber." *Building Acoustics* 26(2):121-138.
- Garai, M., F. Morandi, D. D'Orazio, S. De Cesaris, L. Loreti. 2015a. "Acoustic measurements in

- eleven Italian opera houses: correlations between room criteria and considerations on the local evolution of a typology." *Build. Environ.* 94:900-912.
- Garai, M., K. Ito, D. D'Orazio, S. De Cesaris, F. Morandi. 2015b. "The acoustics of Bayreuth Festspielhaus." *Proceedings of the 22nd International Congress of Sound and Vibrations*, Florence.
- Garai, M., S. De Cesaris, F. Morandi, D. D'Orazio. 2016. "Sound energy distribution in Italian opera houses." *Proceedings of Meetings on Acoustics* 22ICA 28(1):15-19.
- Guidorzi, P., L. Barbaresi, D. D'Orazio, M. Garai. 2015. "Impulse responses measured with MLS or Swept-Sine signals applied to architectural acoustics: an in-depth analysis of the two methods and some case studies of measurements inside theaters." *Energy Procedia* 78:1611-1616.
- ISO. 2009. *ISO 3382-1. 2009. Acoustics - Measurement of room acoustic parameters. Part 1: Performance spaces.*
- Jeon, J.Y., J.H. Kim, J.K. Ryu. 2015. "The effects of stage absorption on reverberation times in opera house seating areas." *J. Acoust. Soc. Am.* 137(3):1099-1107.
- Jeon, J.Y., H.S. Jang, H.I. Jo. 2018. "Acoustic evaluation of orchestra occupancies in concert halls: Effect of sound absorption by orchestra members on audience acoustics." *Build. Environ.* 143(1):349-357.
- Lokki, T., J. Pätynen. 2009. "Applying anechoic recordings in auralization." *Proceedings of the EAA Symposium on Auralization*, Espoo, Finland.
- ODEON Room Acoustics Software, v.12, 2010.
- Pompoli, R., N. Prodi. 2000. "Guidelines for acoustical measurements inside historical opera houses: procedures and validation." *J. Sound Vib.* 232:281-301.
- Postma, B. N. J., B. F. G. Katz. 2016. "Perceptive and objective evaluation of calibrated room acoustic simulation auralizations." *J. Acoust. Soc. Am.* 140, 4326.
- Prodi, N., R. Pompoli, F. Martellotta, S. Sato. 2015. "Acoustics of Italian Historical Opera Houses." *J. Acoust. Soc. Am.* 138(2):769-781.
- Schroeder, M.R., D. Gottlob, K. F. Siebrasse. 1974. "Comparative study of European concert halls: correlation of subjective preference with geometric and acoustic parameters." *J. Acoust. Soc. Am.* 56:1195-1201.
- Shtrepi, L., A. Astolfi. 2015. "Objective and perceptual assessment of the scattered sound field in a simulated concert hall." *J. Acoust. Soc. Am.* 138, 1485.
- Shtrepi, L. 2019. "Investigation on the diffusive surface modeling detail in geometrical acoustics based simulations." *J. Acoust. Soc. Am.* 145, EL215.
- Vorländer, M. 2007. *Auralization: Fundamentals of Acoustics, Modelling, Simulation, Algorithms and Acoustic Virtual Reality*. Springer.

Energy and Exergy Analysis of a HVAC System Having a Ground Source Heat Pump as Generation System

Paolo Valdiserri – University of Bologna, Italy – paolo.valdiserri@unibo.it

Michael Lucchi – University of Bologna, Italy – michael.lucchi2@unibo.it

Marco Lorenzini – University of Bologna, Italy – marco.lorenzini@unibo.it

Abstract

This study reports on a dynamic simulation of the annual performance of a HVAC system consisting of a ground coupled heat pump (GCHP), which has which has a ground heat exchanger with horizontal pipes for winter and summer seasons. The simulations are performed by employing the software Trnsys. The HVAC system is connected to a thermal storage tank containing warm water in winter and cold water in summer, which serves a single-family dwelling located in the city of Rome, Italy. A first- and second-law analysis of the yearly performance of the entire system and of the single components was carried out, highlighting the components with the lowest exergy efficiency.

1. Introduction

In the European Union, the energy consumption in the building sector has reached 40% of yearly energy demand and contributes to around 36% of CO₂ emissions. To reduce these figures, EU member States are required to take actions that are compliant with the Energy Performance of Buildings Directive. Different strategies have been adopted by the single member states to reduce this energy consumption and to improve the energy efficiency in buildings. Among these are increasing the insulation thickness of the building envelope (Loreti et al., 2016), employing more efficient HVAC systems and using renewable energies (Valdiserri, 2018).

As far as the use of renewables are concerned, it is worth mentioning that in 2009 and 2018 the European Parliament identified aero-thermal, geothermal and hydrothermal energy as renewable energy source (RES). Ground-coupled heat pump (GCHP) systems for heating and cooling of new and existing

buildings satisfy both the demand of primary energy saving and the goal of the directive on renewable energy. As the soil can provide a higher temperature for heating and a lower temperature for cooling than the external air does, ground-coupled heat pumps usually reach higher COPs and EERs than those using outdoor air as a heat reservoir. Vertical and horizontal ground heat exchangers (Sarbu and Sebarchievici, 2014), GHEs, are usually connected with heat pumps: the single-pipe horizontal configuration is the easiest and cheapest to install, although it requires that a large plot of land be available close to the building served. Horizontal GHEs consist of a series of parallel pipe arrangements laid out in trenches dug approximately 1-2 metres below ground surface (Sanaye and Niroomand, 2010). Due to the low installation depth, horizontal GHEs are more affected by ambient temperature variations than vertical probes, so they require a more accurate design (Lucchi et al., 2017).

All the studies cited above focus on quantitative energy consumption without accounting for its quality. This is only possible through a second law approach, which can be implemented through an exergy analysis. Several studies suggest that the combination of low-temperature heating systems, with low-exergy sources, such as GCHP (e.g. Evola et al., 2018) are a profitable strategy for energy saving in buildings. In order to carry out an appropriate exergy analysis of an unsteady energy process, the definition of a dead state is of paramount importance. In cases such as the one studied here, where outdoor thermodynamic variables (temperature in particular) change over the day and over the seasons, there is no definition agreed upon by the whole scientific community (Serova and Brodianski,

2004). Some authors use the average outdoor temperature in the heating and cooling seasons as the reference temperature, whilst others (Zhou and Gong, 2013) calculated the exergy flow rate considering as dead state the hourly outdoor temperature. In this study the latter approach, i.e. a time-dependent dead state temperature, was adopted, as discussed below.

The aim of this work is to numerically evaluate the performance of a HVAC system consisting of a ground-coupled heat pump (GCHP) with horizontal GHE and both hot- and cold-water storage tanks for year-round operation. Simulations were run for a typical year for a single-family detached house around Rome, Italy. Data are presented on a monthly basis and for the whole year. The model was developed in the dynamic environment of Trnsys® 17 Simulation Studio (Klein et al., 2017). The energy analysis was conducted both in terms of first and second law of thermodynamics and the results for a typical year are discussed.

2. The Case Investigated

The building chosen for the simulation is a detached house located in Rome. It is a two-storied building with only the ground floor conditioned, with a living room, a kitchen, two bedrooms and a bathroom. The building was set-up in Sketchup® (Fig. 1).

The net surface area is 68.0 m², whereas the total area, including walls is 83.4 m². The net volume of the house to be conditioned is 183.8 m³, and the envelope through which heat is exchanged with the ambient is 276.6 m². In terms of the thermal characteristics of the building envelope, the external walls have a thermal transmittance of 0.38 Wm⁻²K⁻¹ whilst the value of the overall heat transfer coefficient value of the horizontal partitions is $U=0.42$ Wm⁻²K⁻¹. All the windows have double-pane glasses with a uniform thermal transmittance of 1.12 Wm⁻²K⁻¹.

All the conditioned rooms are heated and refrigerated by fan-coils except the bathroom, which is heated – in winter only – by a radiator. The water which feeds the fan coils, and in winter the radiator, is stored in a tank, which acts as buffer system to dampen temperature oscillations due to sudden

changes in outdoor conditions and to cover peak loads that might occur.

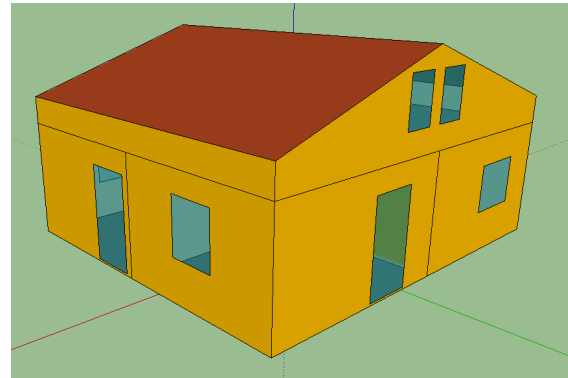


Fig. 1 – Sketch of the building

One water tank, which is shown as two different tanks in the representation in Fig. 2 and in the simulation, contains hot water in winter (HWT) and refrigerated water in summer (CWT). The water tank has a volume of 0.5 m³ and is connected to the heat pump.

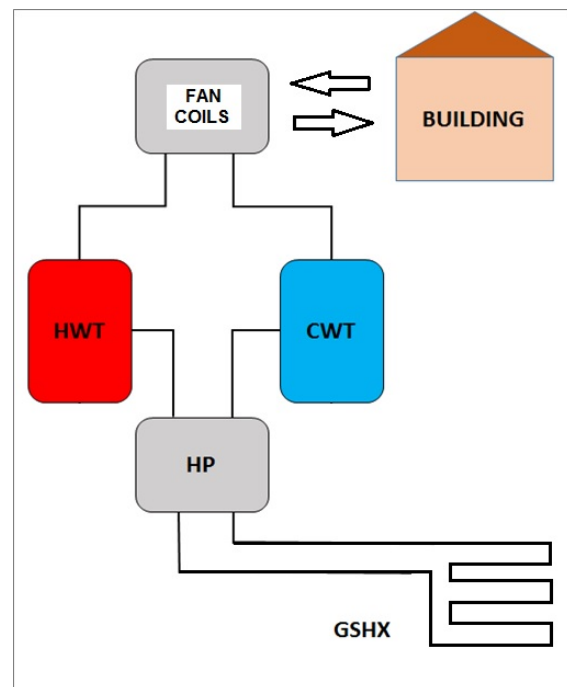


Fig. 2 – Representation of the HVAC system

The heat pump exchanges thermal energy with the ground by means of a horizontal GHE, where a mixture of water and glycol circulates. The geothermal field consists of 5 loops, each 100 m long, of high-density polyethylene pipes 32 mm in diameter

and 2.9 mm thick. The pipes are buried 1.5 m below the surface and are connected in parallel. The wheel-base between the pipes is 0.4 m and the total surface area occupied by the geothermal field is about 180 m².

The nominal cooling power of the heat pump is 1.8 kW with nominal energy efficiency ratio EER=4.5, when the temperature of the fluid at the evaporator is in the 15-10 °C range and the temperature of the fluid at the condenser lies in the 30-35 °C interval; the nominal heating power is 2.4 kW with a coefficient of performance COP=4.0, when the temperatures of the fluid at the evaporator is between 12 and 7 °C and the fluid at the condenser is at 40-45 °C. To better replicate the machine's actual behaviour, the EER and COP curves were deduced from the manufacturer's data.

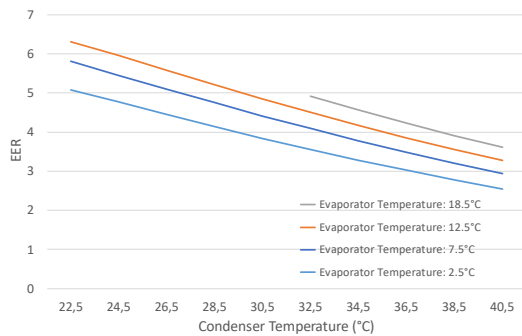


Fig. 3 – EER curves for the heat pump

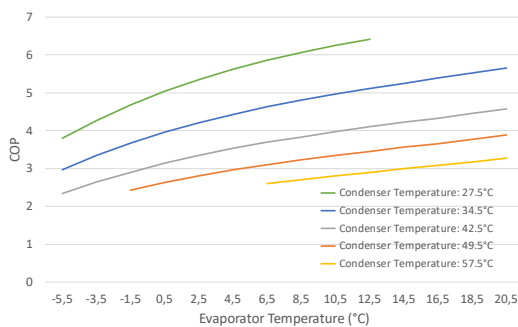


Fig. 4 – COP curves for the heat pump

Fig. 3 shows EER curves versus condenser mean temperature ($\Delta T=5$ K) for different values of the evaporator mean temperature ($\Delta T=5$ K), whilst COP values versus evaporator mean temperature for fixed condenser mean temperatures are plotted in Fig. 4 for the working ranges of interest.

The temperature set points of water feeding the fan coils are 42.5 °C in winter and 8.5 °C in summer, as-

suming a dead band of ± 2.5 °C (summer) and ± 1.5 °C (winter) for temperature control purposes.

Three different hydraulic circuits are inserted in the model: one to connect the heat pump to the GSHX, another between the HP and the water tank and the last circuit connects the water tank to the fan coils inside the building. The inlet temperature of each component is time dependent, whilst the circuits mass flow rates, when the pumps are switched on, are set at a constant value. The electric power required by the fan coils ranges between 20 and 50 watts, depending on the fan velocity. Two levels of temperature control are employed. The first is at the water tank, as described above, and the second in each single room.

During winter, the temperature in each room of the building is set at 20 °C (bathroom 22°C), whilst in summer it is at 26 °C, except the bathroom where cooling is not required. Weather data for the city of Rome were obtained from the Meteonorm database, included in the Trnsys® package.

The simulations were run at time steps of 5 minutes over the whole year, spanning both the heating and cooling seasons. The most significant data obtained and the quantities derived from them are discussed in the following section.

3. Analysis and Discussion of the Results

The COP and EER of the GCHP, both defined as the ratio between the energy exchanged with the water tank and the electrical energy supplied to the heat pump were computed over the corresponding seasons.

Fig. 5 shows the COP of the GCHP from the month of November until the end of March.

It is clear that the COP dropped from 4.6-5.2 at the beginning of the winter season to 3.8-4.4 in the month of January. This was due to the temperature depletion of the ground and, of course, to the harsher external conditions. It remained on this range until the middle of March and rose during the last days of the heating season. A similar behaviour can be observed analysing the energy efficiency ratio during the summer season. Fig. 6 shows the EER of the GCHP for three most important months in the

summer. In the beginning, the EER stayed in the range of 4.1-4.4, then it dropped down to 3.0-3.4 at the end of the summer season. In this case, the lowest values obtained were for the month of August, when outdoor temperatures were at their highest, and the ground had experienced a continuous temperature increase owing to contributions from both the GHE and solar radiation.

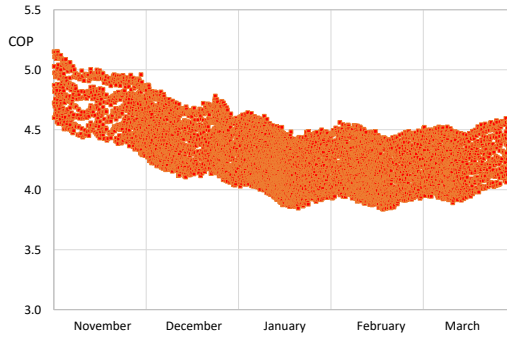


Fig. 5 – Winter season COP for the GCHP

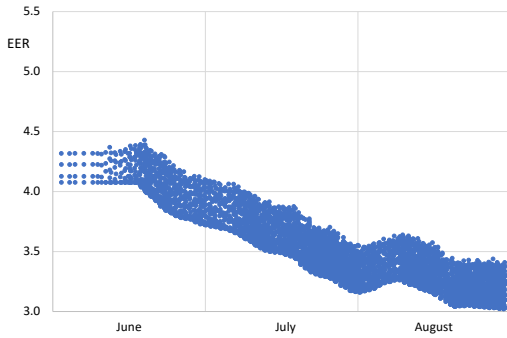


Fig. 6 – Summer season EER for the GCHP

Further, the heating monthly performance factor (HMPF) of the whole HVAC-Building system (adaption from Dincer, 2017) was calculated on a monthly basis as:

$$\text{HMPF} = \frac{Q_{bu}}{W_{el}} \quad (1)$$

Where Q_{bu} (J) is the energy delivered in a month to the rooms of the building by the HVAC to keep the desired set-point conditions and W_{el} (J) is the electric energy consumption during the same period, considering both the GSHP and all auxiliaries (fans, pumps, etc.).

Monthly Energy Efficiency Ratio (MEER, again, adapted from Dincer, 2017) is computed in the same way as the HMPF, albeit for the summer months, as shown in Equation (2):

$$\text{MEER} = \frac{Q_{bu}}{W_{el}} \quad (2)$$

Both HMPF and MEER define the behaviour of the HVAC-Building assembly in terms of first-law analysis, and the results are shown in Fig. 7.

The heating and cooling system coupled with the GCHP exhibits an excellent control of temperature and high-performance parameters (HMPF and MEER), as shown in Fig. 7.

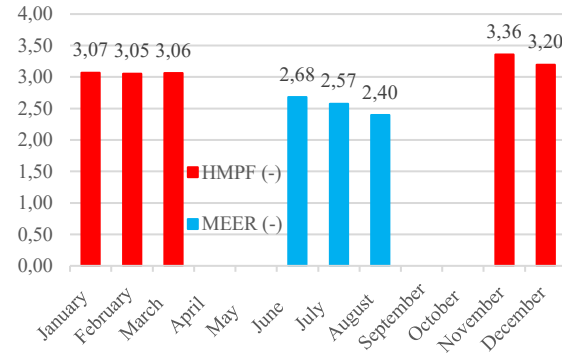


Fig. 7 – HMPF (red) and MEER (blue) for the combined system

The HMPF of the whole system from the month of November until the end of March decreased from 3.36 at the beginning of the winter season to 3.07 in the month of January. At the beginning of the summer season the MEER averaged 2.68; it then decreased to 2.40 at the end of the summer season. Although both HMPF and SEER could be shown and analysed in their evolution during some typical winter and summer days, this would be of little significance, and would in fact be misleading, because the disturbances (variable outdoor conditions and thermal loads) and system response are decoupled thanks to the presence of water storage tanks. Indeed, their purpose is to offer a thermal energy buffer to increase the efficiency of the system, possibly using advanced control strategies (D'Ettorre et al., 2019).

An exergy analysis has also been carried out both at system and component level. For the whole system the overall exergy efficiency ζ has been calculated for each month as:

$$\zeta = \frac{Ex_{bu}}{W_{el}} \quad (3)$$

Where Ex_{bu} is the total exergy in joule delivered to the building in a month and obtained as the summation of the amount of exergy delivered to the room

in the building. Its value was computed as:

$$\sum_{i=1}^n Q_{r,i} \cdot \left(1 - \frac{T_0}{T_{r,i}}\right) = \sum_{i=1}^n Q_{r,i} \cdot \eta_c \left(\frac{T_0}{T_{r,i}}\right) \quad (4)$$

In Equation (4), $Q_{r,i}$ is the energy delivered to the i -th room, which is at temperature $T_{r,i}$ (K), and T_0 (K) is the temperature of the dead state, which corresponds to the outdoor temperature, η_c is the Carnot factor, and n is the number of rooms.

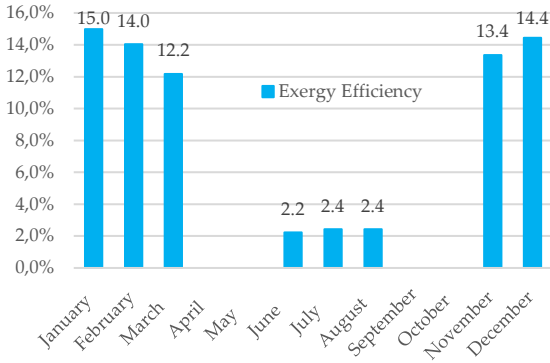


Fig. 8 – Monthly overall exergy efficiency (%) for the system

The reference temperature is chosen as time-dependent on the account of it also being the disturbance to the thermal system (HVAC-building), which therefore determines its behaviour over time and also represents the instant thermodynamic condition at which no useful work may be extracted from any system interacting with the environment. Choosing a fixed state, i.e. the minimum value recorded over each season, would be of no technical significance, since the temperature difference would amount to a few kelvins, and furthermore, the instant energy demands of the building are not dictated by such harsh conditions. If comparison between the exergy performance of the present system and another (e.g. an air-source heat pump) is desired, the same outdoor temperature history should be adopted for both cases, which is consistent with the present choice and makes any issues related to an 'absolute state', such as that given by some reference temperature a moot point. The results are shown in Fig. 8.

The results of the monthly exergy efficiency align with those expected for this kind of system (Verda et al., 2016); it is, however, interesting to note that the highest efficiencies during winter heating were obtained for the coldest months (December and January). This trend was also replicated for the sum-

mer, when August is the month with the best performance. It can be noted how exergy efficiency had a maximum (around 15%) in the middle of the winter season (January). Indeed, in this period the heating demand of the building and the Carnot efficiency associated with the heat transferred to the rooms reached their peak. The use of the ground as a heat source makes it possible to better exploit the energy resource in the coldest days. During the summer, the exergy efficiency dropped to values significantly lower than those obtained in winter: in particular, it lies between 2.2% and 2.4%. This is due to the very low values of the Carnot efficiency; during this time, the temperature of the rooms (which is kept at a set-point value of 26 °C) was close to T_0 , and the Carnot efficiency therefore dropped to very low values approaching zero.

This behavior can be explained by observing the amount of exergy extracted from the ground by the GHEs, Ex_g (J), which is calculated on a monthly basis using Equation (5):

$$Ex_{gd} = \sum_{j=1}^n \dot{m}_{w,gd,j} \cdot \left(h_{w,gd,o} - h_{w,gd,i} - T_0 \cdot c \cdot \ln \left(\frac{T_{w,gd,o}}{T_{w,gd,i}} \right) \right) \Delta \tau \quad (5)$$

Where \dot{m}_w is the water mass flowrate (kg s^{-1}) through the GHE over the time interval $\Delta \tau$ (s), c is the specific thermal capacity ($\text{kJ kg}^{-1} \text{K}^{-1}$), n is the number of time intervals over the period considered, $h_{w,o}$ and $h_{w,i}$ the outlet and inlet specific enthalpies (kJ kg^{-1}) of the water, and $T_{w,o}$ and $T_{w,i}$ (K) the outlet and inlet temperatures, respectively. The results are plotted in Fig. 9: it is evident that the maximum amount of exergy yield is obtained in the month with extremes of either heat or cold.

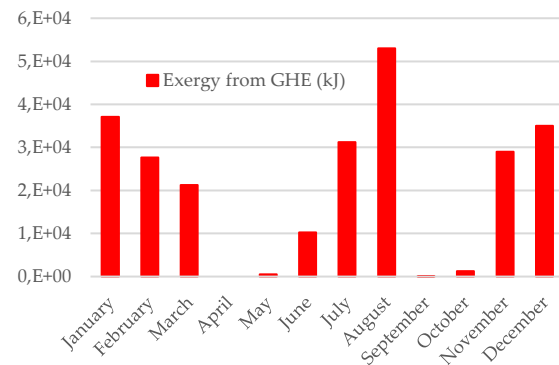


Fig. 9 – Monthly exergy extraction from GHE

Despite the amount of exergy extracted from the ground, the GHE is the component with the lowest exergy efficiency, which is similar to that of the whole system, as shown in Fig. 10.

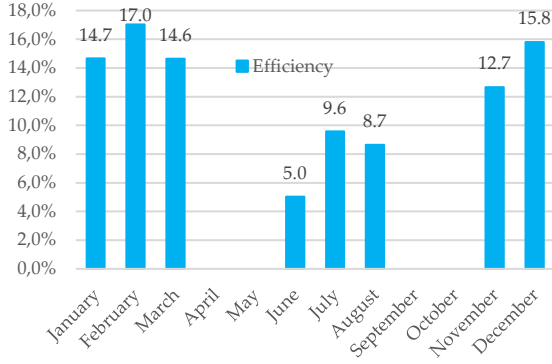


Fig. 10 – Monthly efficiency (%) for GHE

The explanation for this behaviour is to be sought in the way the exergy efficiency is defined for the component, Equation (6):

$$\zeta_{GH} = \frac{Q_{gh} \cdot \eta_c \left(\frac{T_0}{T_{lm,gh}} \right)}{Q_{gh} \cdot \eta_c \left(\frac{T_0}{T_g} \right)} = \frac{T_{lm,gh} - T_0}{T_g - T_0} \frac{T_g}{T_{lm,gh}} \quad (6)$$

$T_{lm,gh}$ (K) is the log-mean temperature difference between outlet and inlet of the GHE, whilst T_g (K), is the ground temperature, which should be uniform. The second rate in Equation (6) is close to unity, but the first is very small most of the time, hence the limited exergy efficiency.

The heat pump, on the other hand, has a different behaviour. In particular, its exergy efficiency is calculated as:

$$\zeta_{HP} = \frac{Ex_{ld}}{W_{el,hp} + Ex_{gh}} \quad (7)$$

Where Ex_{ld} (J) is the exergy that the heat pump supplies to the two storage tanks, Ex_{gh} (J) is the exergy which the pump receives from the ground through the heat exchanger and $W_{el,hp}$ (J) is the energy required to power the heat pump. The two contributions are obtained from Equations (8) and (9):

$$Ex_{ld} = \sum_{j=1}^n \dot{m}_{w,ld,j} \cdot \left(h_{w,ld,o} - h_{w,ld,i} - T_0 \cdot c \cdot \ln \left(\frac{T_{w,ld,o}}{T_{w,ld,i}} \right) \right) \Delta \tau \quad (8)$$

and

$$Ex_{gh} = \sum_{j=1}^n \dot{m}_{w,gh,j} \cdot \left(h_{w,gh,o} - h_{w,gh,i} - T_0 \cdot c \cdot \ln \left(\frac{T_{w,gh,o}}{T_{w,gh,i}} \right) \right) \Delta \tau \quad (9)$$

The symbols are analogous to those in Equation (5), but it must be remarked that if $\dot{m}_{w,gh,j}$ is the same as $\dot{m}_{w,gd,j}$, this is not the case for the values of the enthalpies nor of the water temperatures appearing in Equation (5) and in Equation (9), respectively.

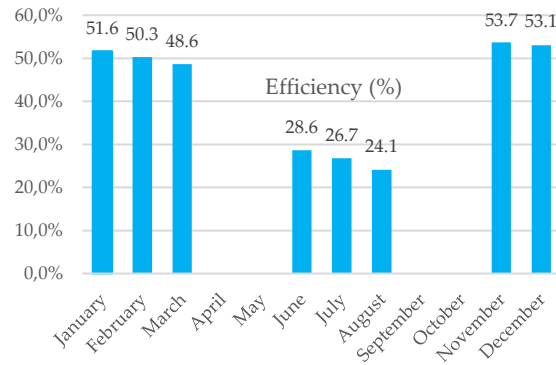


Fig. 11 – Monthly exergy efficiency (%) for the heat pump

The monthly exergy efficiencies for the heat pump are shown in Fig. 11. It can be noted that the trend is constantly diminishing, which hints at a steady decrease in the potential of the ground to supply exergy. This is due to the constant thermal depletion of the ground (which is progressively cooled in winter and heated in summer); this trend is enhanced by the type of GHE loops, which are laid less than 2 metres below the ground level and are therefore more influenced by thermal losses/gains from ambient temperature and radiation. It must also be noted, however, that this is an intrinsic characteristic of the model adopted to simulate the ground temperature, T_{gd} (K), (Kusuda et al., 1965).

The yearly exergy efficiency for one of the bedrooms, which is representative of the behaviour of the other rooms too, is shown in Fig. 12.

The efficiency is calculated as:

$$\zeta_{HP} = \frac{Ex_r}{W_{el,hp} + \Delta Ex_{fc}} \quad (10)$$

Ex_r (J) is similar to Ex_{bu} in Equation (3), but refers to a single room, $W_{el,hp}$ (J) is the electric energy to power the fan coils and ΔEx_{fc} is the exergy variation of the water flow between inlet and outlet of the fan coil.

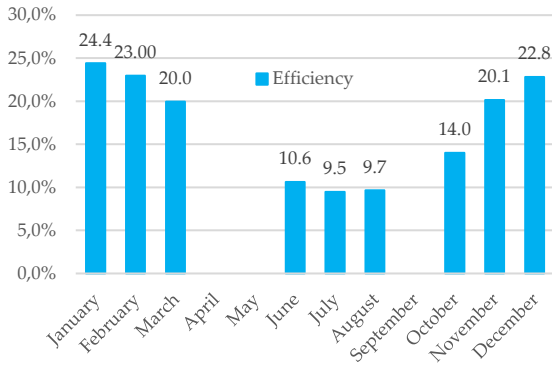


Fig. 12 – Monthly exergy efficiency (%) for one bedroom

ΔEx_{fc} is computed as per Equation (11), with the symbols denoting the same quantities as in Equations (8) and (9), except that they refer to the water flowing through the fan coils.

$$\Delta Ex_{fc} = \sum_{j=1}^n \dot{m}_{w,fc,j} \cdot \left(h_{w,fc,o} - h_{w,fc,i} - T_0 \cdot c \cdot \ln \left(\frac{T_{w,fc,o}}{T_{w,fc,i}} \right) \right) \Delta \tau \quad (11)$$

The maximum exergy efficiency is for the coldest months, both in winter (December to February) and in summer (June). In this case, the electric demand of the fan coils is likely to determine this trend.

4. Conclusions

This work presents a first- and second-law analysis of the yearly performance of a HVAC system coupled with a ground-source heat pump, used to control the temperature in a single-family dwelling located in Rome.

The results showed excellent energy performance of the system both in the cooling and heating periods. Exergy efficiencies are markedly lower during the summer owing to the lower Carnot efficiencies. The analysis at component level also highlighted the GSHX to be the least-efficient component.

Future developments of the research include a comparison, for the same building, between the HVAC system presented here (GSHP) and different kinds of generation systems such as a traditional gas-fired boiler or an air source heat pump.

Nomenclature

Symbols

c	Specific capacity ($\text{kJ kg}^{-1} \text{K}^{-1}$)
COP	Coefficient of performance (-)
EER	Energy efficiency ratio (-)
h	Specific enthalpy (kJ kg^{-1})
HMPF	Heating Monthly Performance Factor (-)
\dot{m}	Mass flowrate (kg s^{-1})
Q	Thermal energy (J)
SEER	Season Energy Efficiency Ratio (-)
T	Temperature (K)
U	Overall heat transfer coefficient ($\text{W m}^{-2} \text{K}^{-1}$)
W	Work (J)
$\Delta \tau$	Time interval (s)
η	Carnot factor (-)
ζ	Exergy efficiency (-)

Subscripts/Superscripts

bu	building
el	electric
fc	fan coil
gd	ground
gh	ground heat exchanger
HP	Heat pump
i	inlet
ld	load
lm	log-mean
o	outlet
r	room
w	water
0	ambient (dead state)

References

- D'Ettorre, F., P. Conti, E. Schito, D. Testi. 2019. "Model predictive control of a hybrid heat pump system and impact of the prediction horizon on cost-saving potential and optimal storage capacity." *Applied Thermal Engineering* 148: 524-535.
- Dincer, I. 2017. *Refrigeration Systems and Applications*. John Wiley & Sons.
- European Parliament and of the Council. 2009. "Directive 2009/28/EC of the European Parliament and of the Council of 23 April 2009 on the promotion of the use of energy from renewable sources and amending and subsequently repealing Directives 2001/77/EC and 2003/30/EC." *Official Journal of the European Union*.
- European Parliament and of the Council. 2018. "Directive (EU) 2018/844 of the European Parliament and of the Council of 30 May 2018 amending Directive 2010/31/EU on the Energy Performance of buildings and Directive 2012/27/EU on Energy Efficiency." *Official Journal of the European Union* 19.6.2018.
- European Parliament and Council. 2018. "Directive (EU) 2018/2001 of the European Parliament and of the Council of 11 December 2018 on the promotion of the use of energy from renewable sources." *Official Journal of the European Union*.
- Evola, G., V. Costanzo, L. Marletta. 2018. "Exergy Analysis of Energy Systems in Buildings." *Buildings* 8(12), 180.
- Klein, S.A., et al. 2010. *TRNSYS Version 17*. Madison, U.S.A.: Solar Energy Laboratory, University of Wisconsin-Madison.
- Kusuda, T., P.R. Achenbach. 1965. "Earth Temperature and Thermal Diffusivity at Selected Stations in the United States." *ASHRAE Transaction* 71(1): 61-75.
- Loreti, L., P. Valdiserri, M. Garai, 2016. "Dynamic Simulation on Energy Performance of a School." *Energy Procedia* 101: 1026-1033.
- Lucchi, M., M. Lorenzini, P. Valdiserri. 2017. "Energy performance of a ventilation system for a block of apartments with a ground source heat pump as generation system." *Journal of Physics: Conference Series* 796(1).
- Sanaye, S., B. Niroomand. 2010. "Horizontal ground coupled heat pump: Thermal-economic modeling and optimization." *Energy Conversion and Management* 51: 2600-2612.
- Sarbu, I., C. Sebarchievici. 2014. "General review of ground-source heat pump systems for heating and cooling of buildings." *Energy and Buildings* 70: 441-454.
- Serova, E. N., V. M. Brodianski. 2004 "The concept "environment" in exergy analysis. Some special cases." *Energy* 29: 2397-2401.
- Valdiserri, P. 2018. "Evaluation and control of thermal losses and solar fraction in a hot water solar system." *International Journal of Low Carbon Technologies* 13: 260-265.
- Verda, V., S. Cosentino, S. Lo Russo, A. Sciacovelli. 2016. "Second law analysis of horizontal geothermal heat pump systems." *Energy and Buildings* 124: 236-240.
- Zhou, Y., G. Gong. 2013. "Exergy analysis of the building heating and cooling system from the power plant to the building envelop with hourly variable reference state." *Energy and Buildings* 56: 94-99.

Double-Layer Gypsum Panels: Prediction of the Sound Reduction Index Using the Transfer Matrix Method

Nicola Granzotto – University of Brescia, Italy – nicola.granzotto@unibs.it

Edoardo A. Piana – University of Brescia, Italy – edoardo.piana@unibs.it

Abstract

Gypsum board walls are widely used in buildings today. A possible way to considerably increase the sound insulation performances of such light-weight walls is to apply a double or triple layer of screwed boards separated from each other. The separation between the boards prevents the decrease of the critical frequency towards lower values, while retaining the improvement of the sound insulation performances provided by the double layer. In this paper the loss of acoustic insulation performances due to the thin air layer between the coupled boards is studied and a modelling technique based on the transfer matrix method is used to simulate the acoustic behaviour of the resulting structure. The simulations are compared with laboratory measurements carried out according to the ISO 10140 series standards, and the transfer matrix approach is found to be suitable to describe the problem, provided that a modified model for the air gap between the boards is used.

1. Introduction

The early application of gypsum-based walls as construction materials dates back to the first half of the twentieth century in the US, and since then it has been continuously developed due to the unique characteristics of this material: low cost, good workability, relatively low weight and quick laying. The issuance of strict regulations regarding thermal and acoustic quality has further increased the preference for these materials in different sectors, especially the building construction, as they are particularly suitable to the tailored optimisation that new technologies require nowadays. A typical optimisation problem in building construction demands that both thermal and acoustic requirements are met: a complex task (Di Bella et al., 2015) in which an improve-

ment in either aspect does not necessarily imply the improvement in the other (Bettarello et al., 2010; Caniato et al., 2015; Caniato et al., 2019; Caniato et al., 2020; Di Bella et al., 2014). Therefore, the availability of simple tools to quickly and reliably predict the acoustic behaviour of the partition is of a certain importance.

Many authors have studied the sound insulation behaviour of lightweight walls made of gypsum board, gypsum fibreboards and wood panels featuring an air gap filled with mineral or glass wool. Abd El Gawad Saif and Seddek (2010) experimentally evaluated the sound insulation performances of different gypsum board-based partitions and investigated the influence of several factors on the resulting sound transmission class. Uris et al. (2002) studied the influence of the number and spacing of point connections due to screws on the sound reduction index of lightweight partitions. It was found that the screw spacing is more important in double-leaf walls than in uncoupled double walls due to structural transmission through the frame. Kim et al. (2010) identified several factors that influence the sound insulation performance of gypsum-board walls, such as the method used in attaching gypsum boards, the addition of a further board, the installation of sound absorbing material, the curing time of the plaster and the type of studs used. Roozen et al. (2015) found indeed that even the tightening level of the studs can considerably affect the insulation properties.

In terms of mathematical models, one of the best-known analytical approaches derives from Cremer's classic theory (1942), and is applicable to homogeneous plates. The introduction of a frequency-dependent bending stiffness by Nilsson (1990) also allows the approach to be extended to complex structures, such as sandwich panels, whose

bending stiffness can be measured experimentally and fed as input to the model (Nilsson and Nilsson, 2002). This method is used by Piana et al. (2014), and Piana et al. (2017) to determine the transmission loss of dry-wall panels displaying orthotropic and sandwich-like features, showing good agreement with standardised measurement results. Another possible approach is provided by the transfer matrix method (TMM), which is particularly suitable to model multi-layer structures. The modelling consists in two steps: representing each layer with a transfer matrix, whose structure depends on the material, and composing the matrices to form the overall transfer matrix that relates the input and output acoustic states (Vigran, 2008).

When two identical gypsum walls are screwed (but not glued) together, and separated by a thin air gap, in the case of a diffuse sound field, the resulting structure exhibits a doubled mass per unit area but the critical frequency is still that of a single-layer structure. This aspect leads to an increase in the performance of the double-layer solution with respect to a single-layer solution of equal mass. On the other hand, some issues in the modelling of the sound insulation behaviour arise if a narrow air gap is left between the two gypsum panels as is the practice. This paper examines the sound insulation performances of double-layered gypsum board walls with different thicknesses by investigating the influence of a thin layer of air between the two plates through the transfer matrix method. In the following section, the transfer matrix method is presented with reference to the case at hand. Section 3 describes the panels used for the evaluation in terms of geometry and measured sound reduction indices, which the model results are compared to in Section 4. Finally, the conclusions are drawn and possible future developments are identified.

2. Double-Layer Gypsum Board Model

2.1 Transfer Matrix Method

The transfer matrix method (TMM) for multilayer acoustical systems allows wave motion in a single direction (Vigran, 2008). For this reason, the structure must be “thin”, in that its thickness must be

small enough with respect to the wavelength for the wave motion inside the structure to be negligible. In this hypothesis, each i -th layer of the multilayer structure (see Fig. 1) can be represented by a 2-by-2 matrix describing the relationship between the inlet and outlet acoustical quantities – typically, pressure p and particle velocity u :

$$\begin{bmatrix} p_{i-1} \\ u_{i-1} \end{bmatrix} = \begin{bmatrix} T_{i,11} & T_{i,12} \\ T_{i,21} & T_{i,22} \end{bmatrix} \begin{bmatrix} p_i \\ u_i \end{bmatrix} = \mathbf{T}_i \begin{bmatrix} p_i \\ u_i \end{bmatrix} \quad (1)$$

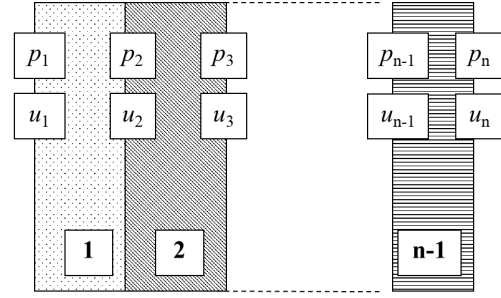


Fig. 1 – Multilayer structure

The elements of the matrix depend on the characteristics of the layer. For a fluid layer such as air, the fundamental quantities the transfer matrix depends on are the wavenumber in the fluid, k , or the propagation coefficient $\Gamma = jk$, and the characteristic impedance Z_c . Assuming oblique incidence at angle θ with respect to the normal, the transfer matrix of a porous layer can be written as

$$\mathbf{T}_{\text{fluid}} = \begin{bmatrix} \cosh(\Gamma d \cdot \cos(\theta)) & \frac{Z_c \sinh(\Gamma d \cdot \cos(\theta))}{\cos(\theta)} \\ \frac{\sinh(\Gamma d \cdot \cos(\theta))}{Z_c} \cos(\theta) & \cosh(\Gamma d \cdot \cos(\theta)) \end{bmatrix} \quad (2)$$

where d is the thickness of the layer. A similar formulation also holds for porous layers, provided that the porosity is accounted for in the anti-diagonal terms.

The transfer matrix for a thin panel, such as a gypsum board, basically depends on the wall impedance of the element, Z_p , defined as the ratio between the sound pressure difference across the layer and the velocity. If the velocity is assumed to be equal on both sides of the panel, the transfer matrix can be written as

$$\mathbf{T}_{\text{panel}} = \begin{bmatrix} 1 & Z_p \\ 0 & 1 \end{bmatrix} \quad (3)$$

The matrices for the individual layers can subsequently be multiplied to obtain the matrix describing the full multilayer structure:

$$\mathbf{T} = \mathbf{T}_1 \cdot \mathbf{T}_2 \cdot \dots \cdot \mathbf{T}_n \quad (4)$$

The transmission coefficient τ can be obtained from the overall transfer matrix:

$$\tau = \frac{2 \exp(jk_0 d_{\text{tot}})}{T_{11} + \frac{T_{12}}{\rho_0 c_0} + \rho_0 c_0 T_{21} + T_{22}} \quad (5)$$

and the sound reduction index is $R = 10 \log_{10} (1/\tau)$.

2.2 Modelling the Layers

In modelling the air layer, one must consider that using Equation (2) is suitable for large cavities whose effect can be seen in the audible frequency range. This effect causes the presence of a resonance frequency due to the mass-spring-mass system. Above this resonance frequency, a typical 12 dB/octave slope can be observed. When two gypsum boards are connected together, the air gap is so thin, compressed and damped that the only effect is the introduction of a flow resistivity to the air trying to flow through the space between the vibrating boards. For this reason, instead of modelling the gap between the panels as an air layer, it was modelled as a small cavity filled with a porous material with low-air-flow-resistivity. If the frame of the porous layer can be considered as motionless, a simplified model for the porous layer can be applied. The porous layer is then modelled as an equivalent fluid. The losses in the air gap were taken into account by introducing a flow resistivity r and a complex propagation coefficient Γ_c and a complex characteristic impedance Z_c are calculated. A Delany-Bazley-like model for porous materials was used to calculate the two characterising parameters (Mechel, 2008):

$$Z_c = Z_0 \left[1 + a \left(\frac{\rho_0 f}{r} \right)^{-b} - j c \left(\frac{\rho_0 f}{r} \right)^{-d} \right] \quad (6)$$

$$\Gamma_c = \frac{\omega}{c_0} \left[a' \left(\frac{\rho_0 f}{r} \right)^{-b'} + j \left(1 + c' \left(\frac{\rho_0 f}{r} \right)^{-d'} \right) \right] \quad (7)$$

An air flow resistivity of 2000 (Pa s/m²) and a thickness of 1 mm were considered. As a first approximation the following values were considered for the model parameters: $a=b=a'=b'=c'=d'=0$ and $c=d=1$. In terms of the gypsum board layers, only the wall impedance Z_p needs to be modelled. This can be done through Cremer's theory for homogeneous

panels:

$$Z_p = j\omega\mu \left[1 - (1 + j\eta) \left(\frac{f}{f_c} \right)^2 \sin^4(\theta) \right] \quad (8)$$

Here, μ is the mass per unit area of the panel, η is the loss factor of the structure, and f_c is the critical frequency, which depends on the bending stiffness D through the expression

$$f_c = \frac{c^2}{2\pi} \sqrt{\frac{\mu}{D}} \quad (9)$$

D being the bending stiffness of the panel. Here, the physical characteristics of the gypsum board were obtained through an inverse analysis starting from the measured mass per unit area of the panels. The modulus of elasticity and the loss factor can be derived by technical datasheet of the material and by dedicated measurements, where available. As an alternative, meaningful indications can also be obtained by measured sound reduction index curves.

3. Experimental Analysis

3.1 ISO 10140 Measurements

In order to validate the predictions provided by the model, gypsum board pairs with three different thicknesses were screwed together and some ad hoc measurements on the three structures were carried out in sound transmission suites following the procedure of ISO 10140 international standard series. In particular, the standard requires that a diffuse sound fields is established in two adjacent rooms. Through measurements of the sound pressure level and of the sound absorption characteristics of the receiving room, the sound reduction index R can be determined as:

$$R = L_1 - L_2 + 10 \log_{10} \left(\frac{S}{A} \right) \quad (10)$$

where A is the equivalent absorption area in the receiving room calculated as:

$$A = 0.16 \frac{V}{t_r} \quad (11)$$

and t_r is the reverberation time of the receiving room.

3.2 Description of the Panels

This paper investigates the sound reduction index of gypsum board panels which have a thickness of 9.5 mm, 12.5 mm and 15 mm, mounted as a single or double layer and fastened together by using 20 screws (4 columns \times 5 rows) on the panel surface (Table 1).

Table 1 – Gypsum board characteristics

Thickness (mm)	μ (kg/m ²)	ρ (kg/m ³)
9.5	6.9	730
12.5	9.0	721
15	12.5	833

The sound reduction index of the different panels was determined on 1700 mm \times 1090 mm specimens (Fig. 2). In order to avoid sound leakage through the sides of the specimens fitted into the wall dividing the two rooms, a sealant (Perennator TX 2001 S) was used to close the air gap between the frame and the plate. The sound pressure levels in the emitting and receiving rooms were measured by using a L&D 824 sound level meter and subsequently space-averaged. The reverberation time of the receiving room was measured using the interruption of stationary pink noise technique.



Fig. 2 – Installation of the panel according to ISO 10140

The results of the theoretical model were compared with sound reduction index measurements performed in sound transmission rooms according to the ISO 10140 series standards.

Figs 3, 4 and 5 show the comparison between the results of the simulations and the predictions carried out by using the transfer matrix method for the 9.5 mm, the 12.5 mm and the 15 mm double-panel gypsum boards:

- 1) Cremer model for single panel;
- 2) Cremer model for double layer of panels;
- 3) TMM model with air layer, modelled as a porous layer;
- 4) laboratory measurement.

The measurements showed that the critical frequencies of the tested structures with 9.5 mm, 12.5 mm and 15 mm boards are 4000 Hz, 3150 Hz and 2500 Hz, respectively.

From the simulation for a single gypsum board performed with Cremer's theory, it can be observed that the critical frequency of two identical layers spaced by a thin air gap is indeed the same as that of a single board, whereas the critical frequency of a monolithic double thickness layer would have been lower.

The transfer matrix model appears to predict correctly both the position in frequency of the coincidence dip and the values of sound reduction index around and above the critical frequency. This indicates that the loss factor has been modelled correctly, which is also confirmed by the slope that the sound reduction index curve features beyond the critical frequency.

It is important to note that if a classic transfer matrix approach for the air layer between the panels is used, a considerable underestimation of the performance around the cavity resonance frequency is obtained.

Below 400 Hz, the agreement of the simulations with the measured values becomes poor. This is due to the fact that, in the gypsum board transfer matrix, the wall impedance Z_p has been estimated through Cremer's theory, which is valid for infinite panels. The discrepancy between the curves is therefore due to the modal behaviour of the actual panel and to the so-called "baffle effect".

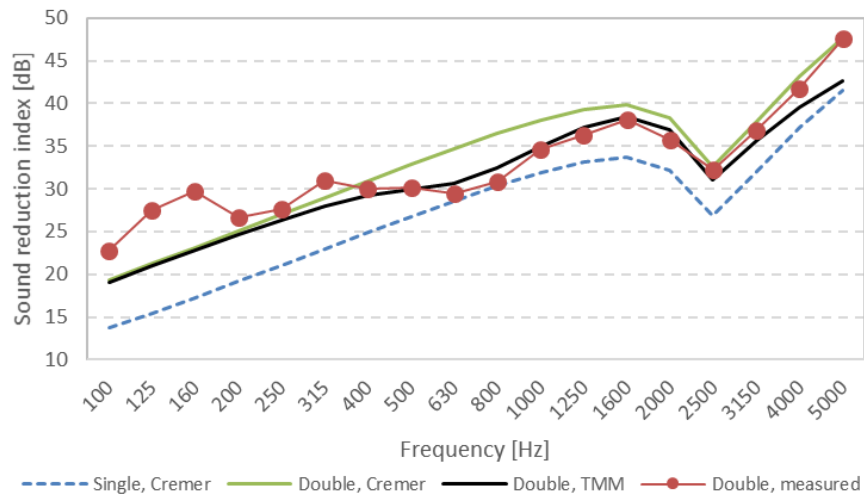


Fig. 3 – Double gypsum board 9.5 mm + 9.5 mm model comparison

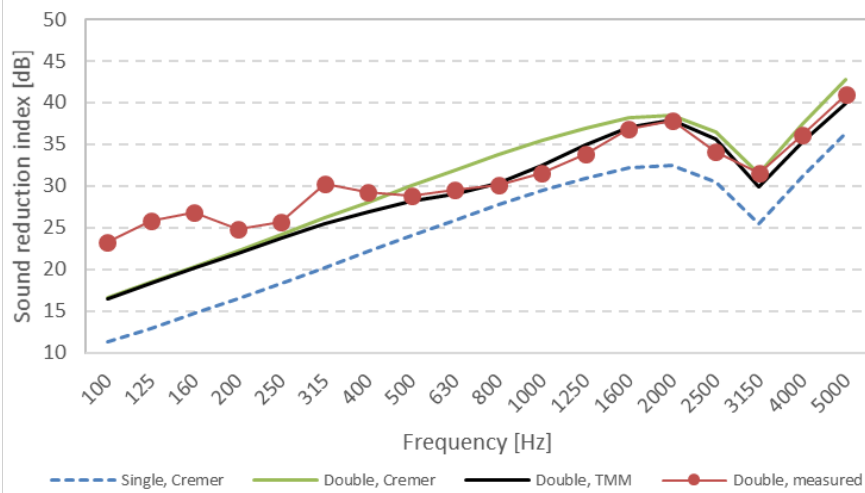


Fig. 4 – Double gypsum board 12.5 mm + 12.5 mm model comparison

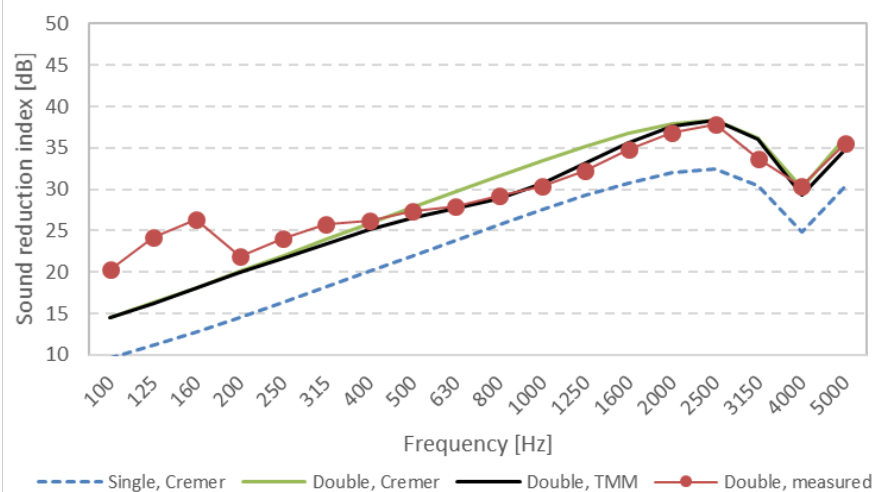


Fig. 5 – Double gypsum board 15 mm + 15 mm model comparison

4. Conclusion

This paper has studied the acoustic insulation performance of double layer gypsum board panels separated by a thin air gap. The multilayer acoustic structure was modelled with the transfer matrix method. In particular, the thin air layer was represented as a porous layer with very low flow resistivity, whereas the transfer matrix of the gypsum panel was built by using Cremer's theory for infinite homogeneous plates. The results of the simulations were compared with measurements in sound transmission suites. The modelling technique proved to be suitable to estimate correctly some fundamental elements of the acoustic behaviour of the structure, such as the maintenance of the same critical frequency as the single gypsum layer, the values of the sound reduction index and the slope of the curve at and above the coincidence region. At low frequencies, where the modal behaviour of the structure dominates, a discrepancy is observed between simulations and measurements, arguably due to the finite size of the tested panel with respect to the infinite panel theory used to estimate the wall impedance in the panel's transfer matrix.

Nomenclature

Symbols

τ	sound transmission coefficient (-)
W	sound power (W)
R	sound reduction index (dB)
L	mean equivalent sound pressure level (dB)
S	surface of the specimen
A	equivalent absorption area of the receiving room (m ²)
V	volume of the receiving room (m ³)
t_r	mean reverberation time of the receiving room (s)
μ	mass per unit area (kg/m ²)
t	thickness of the panel (m)
ρ	density (kg/m ³)
E	Young's modulus (GPa)
ν	Poisson's modulus
η	loss factor
f	frequency (Hz)

f_c	critical frequency (Hz)
T	transfer matrix
L	thickness of the air layer (m)
L_a	thickness of the porous layer (m)
θ	angle of incidence in air (rad)
θ_a	angle of incidence in a porous layer (rad)
Z_p	impedance of single gypsum-panel (Pa s m ⁻¹)
Z_a	impedance of porous layer (Pa s m ⁻¹)
Γ_a	porous complex propagation coefficient (m ⁻¹)
Z_0	impedance of air (Pa s m ⁻¹)
Γ_0	air complex propagation coefficient (m ⁻¹)
k_0	wave number (m ⁻¹)
ω	angular velocity (rad/s)
D	bending stiffness (m ⁻¹)
σ	air flow resistivity (Pa s/m ²)

Subscripts/Superscripts

1	transmitting room
2	receiving room
w	weighted value

References

- Abd El Gawad Saif, M., and H. S. Seddek. 2010. "The Sound Transmission Class for Different Constructions of Gypsum Board." *17th International Congress on Sound and Vibration 2: 867–77*. Cairo, Egypt, 18–22 July.
- Bettarello, F., P. Fausti, V. Baccan, M. Caniato. 2010. "Impact sound pressure level performances of basic beam floor structures." *Building Acoustics* 17(4): 305-316.
<https://doi.org/10.1260/1351-010X.17.4.305>
- Caniato, M., F. Bettarello, L. Marsich, A. Ferluga, O. Sbaizero, C. Schmid. 2015. "Time-depending performance of resilient layers under floating floors." *Construction and Building Materials*. 102. DOI: 10.1016/j.conbuildmat.2015.10.176
- Caniato, M., O. Kyaw, G. D'Amore, J. Kaspar, A. Gasparella. 2020. "Sound absorption performance of sustainable foam materials: Application of analytical and numerical tools for the optimization of forecasting models." *Applied*

- Acoustics* 161.
<https://doi.org/10.1016/j.apacoust.2019.107166>
- Caniato, M., F. Bettarello, C. Schmid, P. Fausti. 2019. "The use of numerical models on service equipment noise prediction in heavyweight and lightweight timber buildings." *Building Acoustics* 2(1): 35–55. <https://doi.org/10.1177/1351010X18794523>
- Cremer, L. 1942. "Theorie der Schalldämmung dünner Wände bei schrägem Einfall." *Akustische Zeitschrift* 7 (3): 81–104.
- Di Bella, A., N. Granzotto, H. Elarga, G. Semprini, L. Barbaresi, and C. Marinosci. 2015. "Balancing of Thermal and Acoustic Insulation Performances in Building Envelope Design." *Proceedings of INTER-NOISE 2015 - 44th International Congress and Exposition on Noise Control Engineering*. San Francisco, United States. 9–12 August.
- Di Bella, A., N. Granzotto, and C. Pavarin. 2014. "Comparative Analysis of Thermal and Acoustic Performance of Building Elements." *Proceedings of 7th Forum Acusticum*. Krakow, Poland. 7–12 September.
- Kim, K.-W., H.-J. Choi, and K.-S. Yang. 2010. "Sound Insulation Performance of Gypsum-Board Walls." *39th International Congress on Noise Control Engineering 2010, INTER-NOISE 2010*, 1: 555–64. 13–16 June.
- Mechel, F. P. 2008. *Formulas of Acoustics*. 2 ed. Oxford Oxfordshire; New York: Springer Nature.
- Nilsson, A. C. 1990. "Wave Propagation in and Sound Transmission through Sandwich Plates." *Journal of Sound and Vibration* 138 (1): 73–94. [https://doi.org/10.1016/0022-460X\(90\)90705-5](https://doi.org/10.1016/0022-460X(90)90705-5)
- Nilsson, E., and A. C. Nilsson. 2002. "Prediction and Measurement of Some Dynamic Properties of Sandwich Structures with Honeycomb and Foam Cores." *Journal of Sound and Vibration* 251 (3): 409–30. <https://doi.org/10.1006/jsvi.2001.4007>
- Piana, E. A., N. Granzotto, and A. Di Bella. 2017. "Sound Reduction Index of Dry-Wall Materials: Experimental Comparison of Model Predictions and Transmission Room Measurements." *24th International Congress on Sound and Vibration, ICSV 2017*. London, UK. 23–27 July.
- Piana, E. A., P. Milani, and N. Granzotto. 2014. "Simple Method to Determine the Transmission Loss of Gypsum Panels." *21st International Congress on Sound and Vibration 2014, ICSV 2014*, 5: 3700–3706. Beijing, China. 13–17 July.
- Roozen, N. B., H. Muellner, L. Labelle, M. Rychtáriková, and C. Glorieux. 2015. "Influence of Panel Fastening on the Acoustic Performance of Light-Weight Building Elements: Study by Sound Transmission and Laser Scanning Vibrometry." *Journal of Sound and Vibration* 346 (1): 100–116. <https://doi.org/10.1016/j.jsv.2015.02.027>
- Uris, A., J. Sinisterra, J. M. Bravo, J. Llinares, and H. Estelles. 2002. "Influence of Screw Spacings on Sound Reduction Index in Lightweight Partitions." *Applied Acoustics* 63 (7): 813–18. [https://doi.org/10.1016/S0003-682X\(01\)00072-X](https://doi.org/10.1016/S0003-682X(01)00072-X)
- Vigran, T. E. 2008. *Building Acoustics*. London; New York: Taylor & Francis.

Static vs Dynamic Hygrothermal Simulation for Cellulose-Based Insulation in Existing Walls: A Case Study Comparison

Matteo Bilardo – Politecnico di Torino, Italy – matteo.bilardo@polito.it

Fabrizio Giorgio – Politecnico di Torino, Italy – fabrizio.giorgio@polito.it

Enrico Fabrizio – Politecnico di Torino, Italy – enrico.fabrizio@polito.it

Francesco Prizzon – Politecnico di Torino, Italy – francesco.prizzon@polito.it

Abstract

When dealing with energy-saving topics, it is increasingly common to focus on the efficiency of existing systems, rather than adopting new ones. In the specific case of the building envelope this practice is supported by the difficulty in completely replacing opaque components of the envelope, such as external walls or roofs. This work involves the renovation of a cavity wall, with the aim of improving its energy performance. A traditional cavity wall has been modified by blowing a bio-based insulating material obtained from cellulose flakes inside the air cavity gap. Although an operation of this type leads to a significant increase in thermal performance of the wall, it is not equally obvious that it is effective in terms of humidity and vapor condensation. The purpose of this work is to evaluate the effect of the blowing process on the hygrometric performance of the opaque component to ensure correct compliance with the performance parameters established by Italian legislation in terms of vapor transmission and condensation phenomena. In order to study the hygrometric behaviour, a numerical model of the construction was developed and simulated. The simulation involved two different regulatory approaches, which were compared: a first calculation was carried out in steady-state conditions, according to the UNI EN ISO 13788 standard (ISO, 2012). Afterwards, a dynamic simulation following the UNI EN 15026 standard was performed (CEN, 2007). The results obtained by both the methods were analysed and compared. The results demonstrate that by adopting the calculation procedure in steady-state conditions, the phenomenon of interstitial condensation occurs. A different result is obtained by applying the calculation method in dynamic regime, according to which the vapor would not condense inside the structure.

1. Introduction

The fact that the construction sector is one of the main contributors to global energy consumption is now an established reality. Energy consumption of the European building stock is related to heating and cooling requirements, necessary to maintain an appropriate level of thermal comfort and IAQ within the living spaces (BPIE, 2015) and to climate scenarios (Bilardo et al., 2019). However, it is clear that the largest share of energy consumption in buildings does not come from new buildings, since they are subjected to an accurate design process from the energy point of view (Bourdeau et al., 2019). For this reason, when it comes to energy efficiency, it is of primary importance to consider the existing buildings' stock, responsible for higher energy utilization, with a consequent higher environmental impact.

The energy retrofit of the existing buildings therefore appears as a tool with great potential to achieve the objectives set out by the European commission (Cortiços, 2019). One possible way to improve the energy efficiency of an existing building is by considering an envelope retrofit. The renovation of the envelope aims to reduce the heat transfer of the envelope components in order to minimize energy needs and guarantee better thermal comfort of the indoor environment. This category of energy retrofit solution can sometimes be intrusive, modifying the external morphology of a building's façades by applying external insulation, or in interior spaces when applying insulating layers on the internal surfaces of the walls (Bottino-Leone et al., 2019).

Another possible solution is represented by the application of insulating materials inside the existing

walls with an air gap. This construction type, typical of the 1960s-1970s in the Italian building stock, is very widespread and represents an attractive opportunity for energy efficiency improvements. The application of insulating materials inside an air gap is also advantageous from the point of view of the impact on the building envelope since it does not modify the external surface nor the internal volume. One of the most adopted techniques of interspace insulation is the injection of insulation material using a special nozzle. In this way the insulating material is arranged homogeneously in the volume occupied by the air, decreasing the U-value of the wall and improving the overall thermal performance of the envelope. Among the insulating materials used for this type of application, organic products are of particular interest. This is firstly because they have a low thermal conductivity value, comparable with classical insulating material, and secondly because they are often produced from regenerated industrial waste materials, thus feeding the processes of sustainable circular economy. Although obtaining excellent results in terms of thermal insulation and reduction of energy consumption, organic insulating materials often face some difficulties in hygrometric verification and moisture transport (Cascione et al., 2017). According to the current Italian legislation (established by the DM 26/06/2015), the absence of mould formation and the absence of interstitial condensation phenomena must be verified in the heat transfer surfaces with outside boundary conditions. These verifications must be carried out in accordance with the current technical regulation, represented by the UNI EN ISO 13788 standard (ISO, 2012). However, this standard reports a simplified calculation method in steady-state conditions, which tends to overestimate the risk of interstitial condensation due to diffusion phenomena only, and does not consider other physical phenomena that affect constructions, including the transport of moisture by capillarity or the hygroscopic capacity of the material. To provide a more accurate determination of the hygrometric behaviour of a building construction, a more detailed analysis, based on dynamic properties of the envelope, is therefore required. A dynamic calculation method to describe the phenomena of moisture transport in a building construction is reported in the UNI EN 15026 standard (CEN, 2007). This standard, although not cited by the Italian legislation,

provides the tools for a more accurate calculation of the hygrometric behaviour, sometimes leading to different results when compared to the steady-state conditions.

In the present work, the application of cellulose flakes in the air gap of an existing wall is examined (Lopez Hurtado et al., 2016). Through specific simulation tools, the hygrometric behaviour of the wall is discussed first in steady-state conditions (adopting UNI EN ISO 13788) and then in a dynamic condition (adopting UNI EN 15026). The study refers to a typical existing wall on which this type of energy retrofit must be applied. From the results that were produced, the adoption of stationary methods for hygrothermal verification is questioned.

2. Methodology

This work presents a detailed analysis of the hygrometric behaviour of a cavity wall subjected to an energy retrofit intervention by blowing flakes of cellulose within the air gap. The purpose of this analysis is to verify the hygrometric behaviour of the case study construction by comparing a stationary calculation method with a dynamic simulation method. The methodology used to fulfil the purpose of the research is divided into three main parts, addressed in this work:

- 1) Characterization and specific modelling of the case study construction;
- 2) Hygrometric verification in steady-state conditions, in accordance with UNI EN ISO 13788;
- 3) Hygrometric verification in dynamic calculation conditions, in accordance with UNI EN 15026.

The objective of the analysis is the verification of the absence of risk of superficial and interstitial condensation as well as mould formation, in compliance with the current Italian legislation represented by the DM 26/06/2015. The reference weather conditions used for the simulation are those of Turin, a city in northern Italy with a humid subtropical climate.

The following calculation software tools were used to support the verification carried out:

- TerMus-G for steady-state conditions;
- WUFI® for dynamic simulation.

2.1 The Regulatory Issue

One of the problems that led to the development of this work is of a regulatory nature. The current Italian regulation scenario, defined by DM 26/06/2015, makes it necessary to design external construction where there is neither mould formation nor interstitial condensation. This results in a regulatory framework that is very restrictive and disadvantageous for natural-based material, such as cellulose flakes. Furthermore, the current legislation provides for the verification of the hygro-metric performances through the UNI EN ISO 13788 standard, using a steady-state approach. This evaluation is therefore very limiting and often the results it produces are not reliable. However, more accurate methods can be used to evaluate the hygro-metric behaviour of opaque elements, such as the evaluation of moisture transfer by numerical simulation described by the UNI EN 15026 standard.

2.2 Methodology for Stationary Calculation

The steady-state calculation method based on the UNI EN ISO 13788 standard consists of evaluating the trend of the vapour pressure and the saturation pressure inside the construction layers. A tool used to visualize these trends is the Glaser diagram. This graph, used to check the surface and interstitial condensation in the wall, is evaluated monthly with average boundary conditions, established by the legislation for each climatic location. Similarly, the conditions of the internal environment must also be known. The legislation proposes 5 types of internal environments, depending on the internal vapour production. To be consistent in the use of the weather data applied in the two simulation approaches, the same dataset was taken into consideration. The weather data used for the simulation come directly from the WUFI® software database and were developed by the Swiss institute TBZ (<https://tbz.ch>). Since the only national standard describing hourly weather data (UNI 10349) is not complete in terms of rain load, wind direction and speed, it was necessary to use hourly meteorological data developed by third parties. Table 1 summarizes the external and internal weather conditions adopted for the evaluation of the Glaser diagram in stationary conditions. For the

steady-state evaluation, average monthly values of temperature and relative humidity were extracted from the hourly dataset.

Table 1 – Monthly weather boundary conditions

	External		Internal	
	T [°C]	φ [%]	T [°C]	φ [%]
Jan	1.8	73.0	20.0	56.0
Feb	3.9	73.5	20.0	55.1
Mar	8.1	77.3	20.0	45.4
Apr	11.9	66.2	20.0	47.1
May	16.0	74.7	18.0	66.4
Jun	19.5	74.6	21.1	68.1
Jul	23.0	76.7	23.3	64.2
Aug	22.0	75.1	22.6	71.3
Sep	18.2	81.4	18.8	71.5
Oct	12.4	88.6	20.0	63.3
Nov	6.3	72.7	20.0	58.8
Dec	2.6	73.7	20.0	57.1

2.3 Methodology for Calculation in Dynamic Regime

The dynamic calculation method has hourly time-varying boundary conditions. The weather conditions include both the meteorological conditions of the chosen location and a hygro-thermal profile within the building. Hourly temperature and relative humidity have been likewise considered to set the internal conditions. Based on the calculation method proposed by the UNI EN 15026 standard, the internal air temperature is derived from the trend of the external temperature through the application of a linear function. The calculation of the internal temperature, however, respects some limits: it is kept constant at 20 °C when the external temperature drops below 10 °C - by heating - and does not exceed 25 °C when the outside temperature exceeds 20 °C - by cooling. With a similar linear correspondence, UNI EN 15026 also defines the dynamic trend of internal relative humidity, which however has been increased by 5% compared to the calculation value.

The dynamic simulation was performed over a period of two years, with a simulation step of 1 hour. A simulation period of two years was preferred over a single year since hygro-metric phenomena develop with longer times and usually follow seasonal trends. The adopted calculation profile made it possible to use the first simulation year to calibrate the model and generate realistic values of inputs for the second simulated year, which was the only one considered

for the analysis of the results presented in this paper. The simulation of the model involved both the resolution of the heat transport and conservation equations (Equation 1 and 2) and the moisture transport calculation (Equation 3), which considers the capillary transport phenomena, the latent heat involved in the gas-liquid phase transition (temperature function) and all the hygrometric functions presented in Section 3.2.

$$(c_m \cdot \rho_m + c_w \cdot w) \cdot \frac{\partial T}{\partial t} = - \frac{\partial (q_{\text{sens}} + q_{\text{lat}})}{\partial x} \quad (1)$$

$$q_{\text{sens}} = -\lambda(w) \cdot \frac{\partial T}{\partial x} \quad (2)$$

$$g_v = \frac{1}{\mu(c_\phi)} \delta_0 \frac{\partial p_v}{\partial x} \quad (3)$$

The results obtained from the simulation consist of the hourly trend of temperature and relative humidity, as well as the verification of condensation phenomena. To take the most critical case into consideration, the orientation of the wall was fixed to the North direction. Fig. 1 summarizes the physical phenomena taken into consideration by the models used in the two calculation methods applied to the case study in this work.

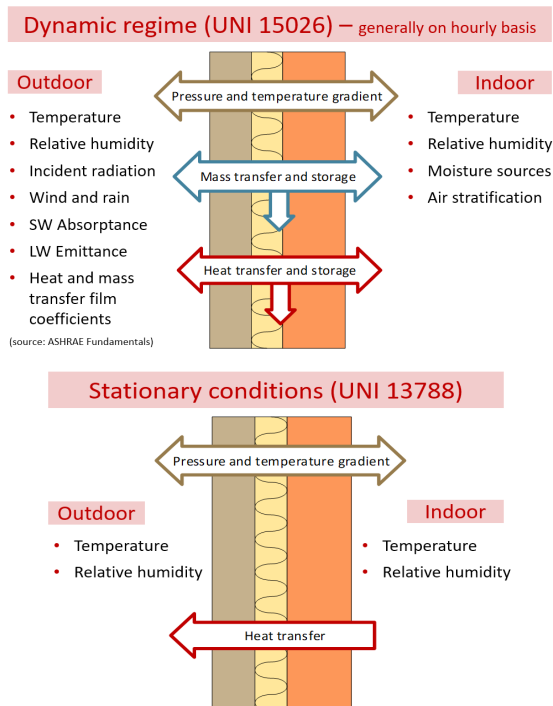


Fig. 1 – Dynamic vs stationary boundary conditions

3. Case Study Construction

The analysed construction is composed of the following elements, listed from the outer to the inner layer:

- 1) Exterior plaster (0.015 m)
- 2) Perforated brick (0.12 m)
- 3) Air gap filled with injected cellulose (0.19 m)
- 4) Perforated brick (0.08 m)
- 5) Interior plaster (0.015 m)

The insulating material used to increase the performance of the building envelope is natural cellulose, applied in the air gap of the structure through a blowing process. In order to make the numerical analysis as similar as possible to the real case, the flakes of cellulose produced by NESOCELL® s.r.l. were used as the reference product. The manufacturer provided the technical characteristics of the product to allow a detailed characterization of the model. The analysis presented in this document is therefore specific and related only to this case study. Given the variable nature of the phenomena connected to it (weather conditions, thickness of the layers, construction elements, etc.), this analysis cannot be fully applied to similar building constructions.

3.1 Thermophysical Properties of Materials

The thermophysical parameters of the cavity wall were derived from the technical standard UNI/TR 11552:2014, depending on the elements used and the typical year in which this type of construction was frequently realized (1960s–1970s). Table 2 collects the thermophysical parameters of each layer.

Table 2 - Thermophysical parameters

Layer	Material	s	ρ	C	λ	R
1	Exterior plaster	1.5	1800	1000	0.9	-
2	Perforated brick	12	800	1000	0.4	0.31
3	Air gap	19	1.25	1008	-	0.18
4	Perforated brick	8	800	1000	0.4	0.2
5	Interior plaster	1.5	1400	1000	0.7	-

After an initial comparison with the original wall, the air layer was replaced in the model by the layer of cellulose flakes, whose thermophysical properties are collected in Table 3.

Table 3 - Thermophysical parameters for the cellulose flakes

Layer	Material	s	ρ	C	λ	R
3_new	Cellulose	19	55	2150	0.038	-

3.2 Characterization of the Hygrometric Properties of Materials

For the modelling of the hygrometric behaviour of the materials in lack of certified or experimental data, materials with the same thermophysical characteristics as those defined in the previous paragraph were identified within the WUFI® database. The hygrometric characterization of cellulose flakes was instead the result of an experimental phase conducted in a laboratory environment and provided by the manufacturer (Table 4). The additional thermo-hygrometric parameters of the materials are:

- Porosity ϵ [m^3/m^3]
- Vapor diffusion resistance factor μ [-]
- Reference moisture content w_{80} [kg/m^3]
- Free water saturation w_f [kg/m^3]
- Moisture absorption coefficient A [$\text{kg}/(\text{m}^2\text{s}^{0.5})$]

Table 4 - Hygrometric properties of the construction layers

Layer	Material	ϵ	μ	w_{80}	w_f	A
1	Exterior plaster	0.24	19	45	210	0.017
2	Perforated brick	0.6	15	13	193	-
3_new	Cellulose	0.93	1.2	6.6	494	0.56
4	Perforated brick	0.6	15	13	193	-
5	Interior plaster	0.3	7	40	204	0.016

In addition to these parameters, in order to evaluate the thermo-hygrometric performance of the construction dynamically, it was necessary to define the following correlation curves:

- a) Thermal conductivity vs temperature
- b) Thermal conductivity vs moisture content;
- c) Free water transport coefficient vs moisture content;
- d) Vapor diffusion resistance factor vs relative humidity;
- e) Moisture vs relative humidity.

Every single material was characterized by these parameters. For the sake of brevity, Fig. 2 shows the curves a), b) and c) for the cellulose flakes only.

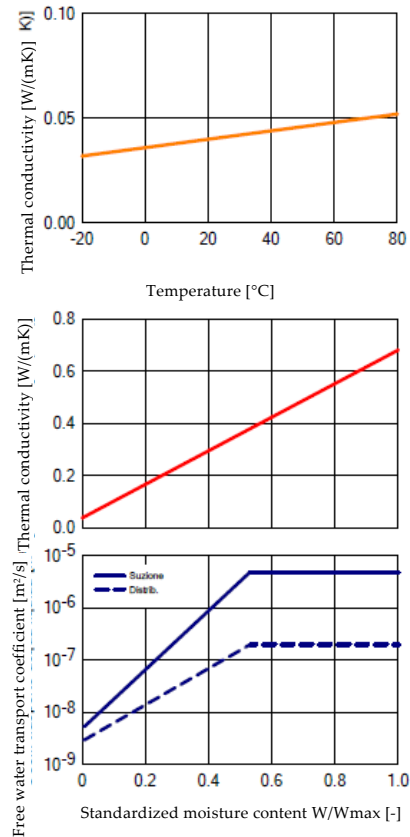


Fig. 2 - Dynamic hygrometric functions used for the numerical model for the cellulose flakes

4. Simulation Results and Discussion

In this section, the results of the calculations and simulations are presented and commented. A preliminary evaluation was carried out on the initial cavity wall before it was subjected to the energy retrofit process. Fig. 3 shows the Glaser diagram for the cavity wall. This result follows the UNI EN ISO 13788 standard and it was carried out during the critical month of January. The result in steady-state conditions confirms the absence of condensation phenomena. The relative pressure never reaches the saturation pressure value, even if very close values are reached at the critical interface between the air gap and the external perforated brick layer.

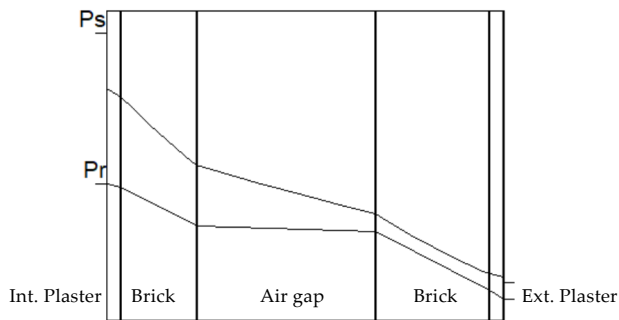


Fig. 3 – Glaser diagram evaluated in steady-state conditions for the cavity wall

4.1 Hygrometric Behavior of Retrofitted Wall (Steady-State Conditions)

The same analysis in steady-state conditions was conducted for the retrofitted wall, where the air gap was filled with cellulose flakes. As can be seen from Fig. 4, the trend of the saturation pressure p_s becomes lower than the relative pressure p_r (evaluated in the absence of interstitial condensation) at the interface between the cellulose and the external perforated brick. This phenomenon, described by the Glaser diagram in the figure, leads to the risk of interstitial condensation at the interface between the two elements.

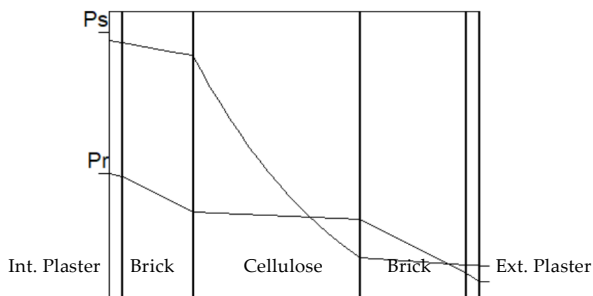


Fig. 4 – Glaser diagram evaluated in steady-state conditions for the retrofitted wall

The results of the analysis, conducted in the critical month of January, demonstrated the limits of the steady-state verification defined by the UNI EN ISO 13788 standard, because of which the construction of the case study is subjected to interstitial condensation. The annual amount of vapor condensed inside the wall was 466 kg/m². Although this result

does not support the adoption of retrofitting solutions with bio-based materials of this type, the application of real cellulose flakes in cavity walls leads to different results. Indeed, in real cases of retrofit involving cellulose flakes being blown into a wall, the interstitial condensation phenomenon does not occur, leaving the wall dry and with regular hygro-thermal performance (Nicolajsen, 2005). This discrepancy between real applications and design calculations brings to light the obvious limitations of the calculation of hygrometric performance in steady-state conditions, based on simplified calculation methods that generally lead to precautionary results.

4.2 Hygrometric Behavior of the Retrofitted Wall (by Dynamic Simulation)

A more detailed modeling of the same construction and of the elements in each of the layer made it possible to simulate the case study in a dynamic calculation regime, as proposed by the UNI EN 15026 standard. Through the dynamic simulation, the hygrometric conditions of the wall were computed hour by hour. After simulating the thermo-hygrometric behavior of the construction for 2 consecutive years (for the North-facing wall scenario), the set of curves of the values assumed by the temperature [°C], by the relative humidity [%] and by the moisture content of the wall [kg/m³] are shown in Fig. 5. Focusing on the temperature trend, the effectiveness of thermal insulation performed by the NESO-CELL® cellulose flakes considerably attenuates the variation of the external temperature. As can be seen from the annual variation in relative humidity, 100% is never reached inside the wall, a value that corresponds to the vapor condensation. Values corresponding to 100% relative humidity only occur close to the external surface of the wall and are due to its interaction with the external rain load, set by the weather conditions adopted for the simulation.

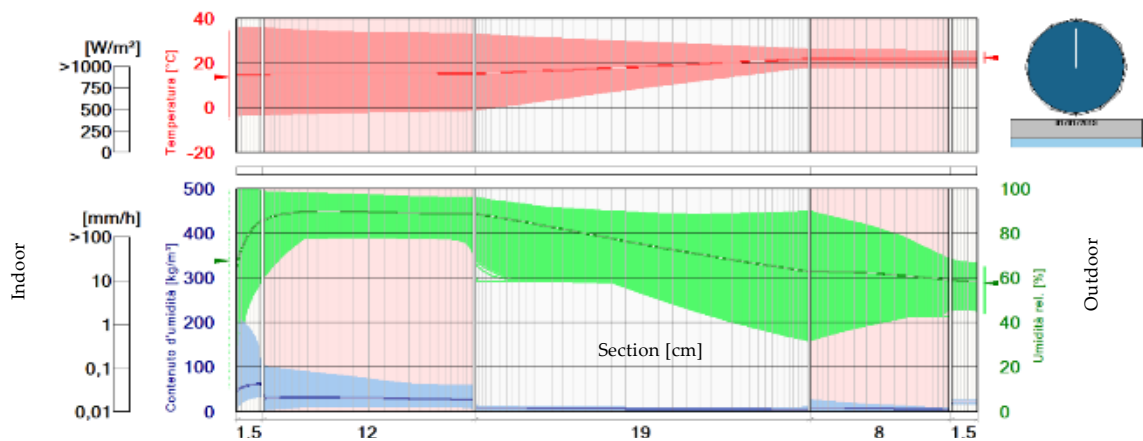


Fig. 5 – Set of curves of the temperature (red), relative humidity (green) and moisture content (blue) trends within the construction layers during the dynamic simulation period (second year only)

Moreover, in terms of moisture content, represented by the blue band and expressed in kg/m^3 , the cellulose flakes have excellent characteristics, maintaining very limited values compared to common insulating materials. To better understand the hygrometric behavior of the cellulose flakes, a punctual analysis of the simulation results was carried out, taking into consideration the critical interface between the cellulose layer and the external perforated brick, where vapor condensation was reached by calculation in steady-state conditions. In addition to the more critical scenario of the North-facing wall, the more favorable scenario of the South-facing wall was also taken into consideration. Fig. 6 reports the trend of relative humidity during the 2-year simulation period for the North (red) and South (green) simulated directions at the critical interface (cellulose – external brick). The results obtained, in contrast to the steady-state verification, show that the construction of the case study presents no risk of interstitial condensation, with values below 95% in the worst-case scenario.

Analysing the relative humidity distribution during the simulated period shown in Fig. 7, it can be seen that the seasonal effect of the RH value is clear when the wall faces North. In contrast, for a south-facing wall, the hygrometric performances, in addition to being better, are also more constant during the year. A different result occurs for the interface temperature, which is not as sensitive to the orientation as the relative humidity. The simulation results of the two scenarios are comparable without any substantial difference (Fig. 8).



Fig. 6 – Relative humidity trend on the cellulose - external perforated brick interface. Results from 2-year dynamic simulation

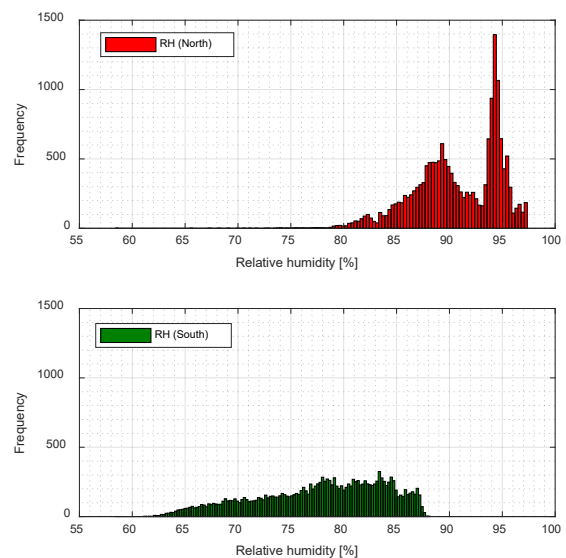


Fig. 7 – Relative humidity frequency for a north-facing wall (red) and a south-facing wall (green)

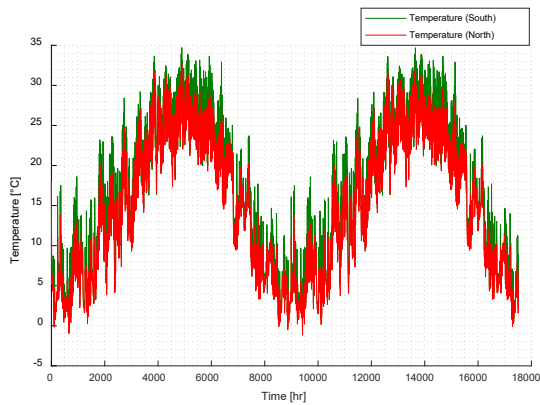


Fig. 8 – Temperature trend on the cellulose - external perforated brick interface. Results from 2-year dynamic simulation

5. Conclusion

The hygrometric analysis carried out using the two calculation methods proposed by the current technical standards has demonstrated the limits of the steady-state verification and the need to adapt the current legislation to the most advanced dynamic calculation. The two calculation methods presented were applied to a real case study and led to different results. The analysis presented in this paper showed the accuracy of dynamic calculation methods in describing the hygrometric behaviour of the case study wall. The adoption of the calculation method proposed by UNI EN 15026 is therefore decisive in the detailed characterization of specific walls, especially with organic materials. In particular, the case study analysed, which investigated the use of cellulose flakes inside a cavity wall, demonstrated how different calculation approaches can lead to contrasting solutions.

Acknowledgement

The authors would like to acknowledge the company NESOCELL s.r.l. for having provided the cellulose flakes adopted in this study.

Nomenclature

Symbols

T	Temperature ($^{\circ}\text{C}$)
RH	Relative humidity (%)
I	Solar radiation (kWh/m^2)
ρ	Density (kg/m^3)
c	Specific heat ($\text{J/kg}^{\circ}\text{C}$)
q	Heat (J)
t	Time (s)
g	Mass flow rate (kg/s)
λ	Thermal conductivity ($\text{W/m}^{\circ}\text{C}$)
x	Distance (m)
δ	Vapour permeability (kg/msPa)
w	Water content (kg/m^3)
s	Thickness (m)
C	Heat capacity ($\text{J/}^{\circ}\text{C}$)
R	Thermal resistance ($\text{W/m}^2^{\circ}\text{C}$)
ε	Porosity (m^3/m^3)

Subscripts/Superscripts

sens	Sensible
lat	Latent
v	Vapour
w	Water

References

- Bilardo, M., M. Ferrara, E. Fabrizio. 2019. "Resilient optimal design of multi-family buildings in future climate scenarios." *E3S Web Conf.* 111, 06006. <https://doi.org/10.1051/e3sconf/201911106006>
- Bottino-Leone, D., M. Larcher, D. Herrera-Avellanosa, F. Haas, A. Troi. 2019. "Evaluation of natural-based internal insulation systems in historic buildings through a holistic approach." *Energy*. <https://doi.org/10.1016/j.energy.2019.05.139>
- Bourdeau, M., X. Zhai, E. qiang, Nefzaoui, X. Guo, P. Chatellier. 2019. "Modeling and forecasting building energy consumption: A review of data-driven techniques." *Sustain. Cities Soc.* <https://doi.org/10.1016/j.scs.2019.101533>
- BPIE. 2015. *Indoor air quality, thermal comfort and daylight. Analysis of residential building regulations in eight EU member states.* Buildings Performance Institute Europe.

- Cascione, V., E. Marra, D. Zirkelbach, S. Liuzzi, P. Stefanizzi. 2017. "Hygrothermal analysis of technical solutions for insulating the opaque building envelope." *Energy Procedia*. <https://doi.org/10.1016/j.egypro.2017.08.141>
- CEN – European Committee for Standardization. 2007. *EN 15026 Hygrothermal performance of building components and building elements - Assessment of moisture transfer by numerical simulation*.
- Cortiços, N.D. 2019. "Renovation tool to improve building stock performance — Higher education context." *Sustain. Cities Soc.* <https://doi.org/10.1016/j.scs.2018.11.043>
- ISO - International Standard Organization. 2012. *ISO 13788:2012 Hygrothermal performance of building components and building elements - Internal surface temperature to avoid critical surface humidity and interstitial condensation - Calculation methods*.
- Lopez Hurtado, P., A. Rouilly, V. Vandenbossche, C. Raynaud. 2016. "A review on the properties of cellulose fibre insulation." *Build. Environ.* 96: 170–177. <https://doi.org/10.1016/j.buildenv.2015.09.031>.
- Nicolajsen, A. 2005. "Thermal transmittance of a cellulose loose-fill insulation material." *Build. Environ.* 40: 907–914. <https://doi.org/10.1016/j.buildenv.2004.08.025>

Design and Evaluation of Extreme Moisture Reference Years for Moisture-Related Risk Assessments

Michele Libralato – University of Udine, Italy – libralato.michele.1@spes.uniud.it

Giovanni Pernigotto – Free University of Bozen-Bolzano, Italy – giovanni.pernigotto@unibz.it

Alessandro Prada – University of Trento, Italy – alessandro.prada@unitn.it

Alessandra De Angelis – University of Udine, Italy – alessandra.deangelis@uniud.it

Onorio Saro – University of Udine, Italy – onorio.saro@uniud.it

Andrea Gasparella – Free University of Bozen-Bolzano, Italy – andrea.gasparella@unibz.it

Abstract

The risk analysis of moisture-related damages can potentially be carried out with the use of heat and moisture transfer simulations. These models require weather files as boundary conditions but, for most locations, the only weather files available are Typical Reference Years, for instance the TRY_{EN} defined in accordance with EN ISO 15927-4:2005. These reference years do not provide the critical conditions that should be used in risk assessments. In this work, two procedures to define Extreme Moisture Reference Years (ERY_{m1} and ERY_{m2}) are presented. ERY_{m1} and ERY_{m2} are designed to generate critical weather files to be used in simulations for the assessment of moisture related risks. The presented procedures are structure-independent and suitable for risk assessments that involve high air moisture content and low air temperature values. In order to assess the capabilities of ERY_m , five types of walls with different materials are simulated, considering three Italian climates (those of Gemona del Friuli, of Legnaro and of Trento) and four wall orientations (North, East, South, West). The results of simulations with ERY_{m1} and ERY_{m2} as weather files showed higher wall moisture contents and interstitial moisture accumulation risks than those with TRY_{EN} . This suggests that ERY_m could be used as a valid alternative to the TRY_{EN} in decision making frameworks and legislations that cannot include the *ad hoc* definition of a weather file for each structure, exposure and location.

1. Introduction

The boundary conditions of building energy simulations are usually defined using reference year weather files, which are meant to represent typical

meteorological years, excluding extreme events. When it is required by legislation or for an evaluation framework to perform a risk analysis involving extreme events, such weather files should not be taken into consideration. For this reason the standard EN ISO 13788:2012 (CEN, 2012), describing the Glaser method procedure, prescribes the use of the mean monthly temperature values likely to occur once every 10 years and, if the only available weather file is a representative year, it recommends subtracting 2 K from the external air temperatures during the heating period and adding 2 K during the cooling period.

The Glaser method, even with strong limitations, is considered by designers to be generally conservative, even though that is not always true (Libralato et al., 2019a), and is still used as risk assessment method for interstitial moisture accumulation. However, when the limitations of the Glaser method are met, the advanced approach of the standard EN 15026:2007 (CEN, 2007) should be used. This method can also be used for other risk assessment procedures, dependent on the moisture content of the materials (for example, the corrosion risk of metal inclusions, wood decay or freeze-thaw damage). According to the standard EN 15026:2007, the weather files should be chosen based on the nature of the problem that is being investigated. The evaluation of a damage risk requires a reference weather file with extreme conditions, to allow for a conservative design of the analyzed structure. By comparison, using a representative year, for example the Test Reference Year TRY_{EN} presented in the standard EN ISO 15927-4:2005 (CEN, 2005) provides

a reference year representative of the typical weather of location under consideration. The EN 15026:2007 suggests to use the “Moisture Design Reference Year”, a weather file that allows to design building envelopes that reach failure at an acceptable rate, for example once every ten years. Such a reference year should be selected among the years measured in a multi-year period according to the problem under investigation. The standard provides three examples:

- For **low temperature problems**, the year with the mean temperature closest to the 10th percentile value of the distribution of the annual mean temperatures should be used;
- For **high temperature problems**, the reference year should be that with a mean temperature closest to the 90th percentile value of the distribution of the annual mean temperatures;
- For **rain penetration problems**, the reference year should have an annual rainfall value closest to the 90th percentile of annual rainfall values.

The problem of the choice of this weather year is related to the fact that the results of the risk analysis are strongly dependent on the building structure, the materials and the type of risk considered. In each location, each structure could reach failure in different years. To overcome this problem, a weather selection method was proposed by Kalamees and Vinha (2004), based on the saturation deficit parameter which is not structure-dependent. A more recent structure-dependent approach was presented by Zhou et al. (2016), who adopted a Climate Index for a preliminary selection of three weather years, which were used to run risk assessment simulations and, subsequently, to complete the design-year identification.

Other structure-independent approaches were presented by Libralato et al. (2018 and 2019b) with methodologies based on Murano et al. (2018), derived from the Finkelstein-Schafer statistic (Finkelstein and Schafer, 1971). The produced Moisture Reference Years used to perform interstitial moisture accumulation analysis on walls made of different materials obtained risk values that were more conservative than the ones obtained with the Typical Meteorological Years.

In this work, following the procedure proposed by Pernigotto et al. (2019a, 2019b) for the development

of Extreme Reference Years ERY , two extreme moisture reference years, ERY_{m1} and ERY_{m2} , are proposed for the assessment of moisture-related risks. The approach is based on the method outlined in EN ISO 15927-4:2005 and uses the Finkelstein-Schafer statistics for the generation of reference years, which are built as a series of 12 months from a multi-year series of at least 10 years. Instead of looking for typicality and using all EN ISO 15927-4:2005-recommended weather variables (i.e. dry-bulb air temperature, relative humidity, global horizontal irradiance and wind speed), the statistics are exploited to identify those candidate months in the multi-year series characterized by anomalous trends and to focus only on air temperature and air humidity. Specifically, those months described by lower temperatures and higher air humidity ratios were targeted for inclusion in the ERY_m .

2. Method

The multi-year weather records from three locations in Northern Italy are considered:

- Gemona del Friuli (Udine, Friuli-Venezia Giulia; also referred to in figures as “Gemona” for brevity), provided by ARPA FVG (OSMER) - series from 2000 to 2018;
- Legnaro (Padova, Veneto), provided by ARPA Veneto - series from 2008 to 2018;
- Trento (Trentino-Alto Adige/Südtirol), provided by the Autonomous Province of Trento (IASMA Fondazione Edmund Mach) - series from 1986 to 2014.

The multi-year weather data was analyzed and checked for errors and outliers following the procedure adopted in previous works (Pernigotto et al., 2014; Antonacci and Todeschini, 2013), in compliance with the WMO Guide (WMO, 2008).

2.1 Extreme Reference Years Generation

The EN ISO 15927-4:2005 method and new approaches presented in this paper were applied for the generation of the TRY_{EN} , ERY_{m1} and ERY_{m2} weather files for the three weather stations. These generation procedures are statistical criteria to select the most or least representative months in the

multi-year weather record. The TRY_{EN} generation method considers dry-bulb air temperature, relative humidity, and solar irradiance as primary variables, and wind speed as a secondary variable. It is designed to obtain a reference year that is intended to be the most representative of the full multi-year series. The ERY_{m1} was obtained with a similar procedure but considering only the dry-bulb air temperature and the humidity ratio as primary variables. The selected months were the least representative of the multi-year weather record with a monthly mean air humidity ratio higher than the multi-year weather record mean for the considered month (for example, the mean humidity ratio of all the months of January). The same procedure was followed for the ERY_{m2} , considering as primary variable the humidity ratio. For the generation of the ERY_m from the multi-year series, the following procedure was used. A general variable p is used to describe the procedure.

1. The daily means \underline{p} are calculated for the primary climatic parameter p (for example dry-bulb air temperature or humidity ratio) for the whole multi-year.
2. The cumulative distribution function $\Phi(p, m, i)$ of the daily means \underline{p} over the whole multi-year series for each day i of a selected calendar month m , for each p must be defined sorting the means \underline{p} from the smallest to the greatest. The index i represents the order number of a day in the multi-year, from 1 to N (total number of days in the multi-year). The function Φ is obtained from the ranking $K(\underline{p}, m, i)$ of the i^{th} day:

$$\Phi(p, m, i) = \frac{K(i)}{N+1} \quad (1)$$

3. The cumulative distribution function $F(p, y, m, i)$ is calculated for the daily means within each calendar month m of each year y . $J(p, y, m, i)$ is the rank order of the i^{th} day obtained by ordering the daily means \underline{p} within the calendar month m and the year y :

$$F(p, y, m, i) = \frac{J(p, y, m, i)}{n+1} \quad (2)$$

where n is the number of days of the m calendar month under consideration.

4. The Finkelstein-Shafer statistic is calculated for each climatic parameter p and each calendar month m and year y in the multi-year series as:

$$F_S(p, y, m) = \sum_{i=1}^n |F(p, y, m, i) - \Phi(p, m, i)| \quad (3)$$

5. One climatic parameter p at a time is considered for each calendar month m , and sorted by increasing $F_S(p, y, m)$ values. For each of these, the ranks R are calculated and summed, creating a total ranking.
6. The first months of the ranking are the most representative of the multi-year series, while the last months are the least representative. For the composition of the TRY_{EN} , the most representative months are chosen, while for the ERY_{m1} and ERY_{m2} , the least representative months are selected. To avoid choosing the least representative months with lower air humidity ratio average values, a secondary selection of the months is performed by comparing the average humidity ratio values.

The selected months are assembled in a single year and the discontinuities between consecutive months are smoothed with a cubic interpolation of the last 8 hours and the first 8 hours of following month. As may be noted, the ERY_m procedure is similar to the TRY_{EN} procedure in EN ISO 15927-4:2005, except for point 6. The standard procedure produces a ranking which uses, as primary variables, dry-bulb air temperature, relative humidity and solar irradiance from the first (most representative) months of the ranking, and a secondary selection based on the wind speed is performed. The ERY_{m1} is obtained by considering the last (least representative) months of the ranking obtained using the dry-bulb air temperature and humidity ratio and the secondary selection is performed by comparing the mean of the humidity ratio values. The ERY_{m2} is obtained using a similar procedure, considering only the humidity ratio as a primary variable and not the dry-bulb air temperature.

2.2 Extreme Reference Year Evaluation

The proposed procedure attempts to generate weather files composed of actual measurements that respect the correlation between the weather varia-

bles and that should reproduce the extreme meteorological conditions that were registered in a location. In Pernigotto et al. (2019a), the reference years are designed to include warmer summers and colder winters while in Pernigotto et al. (2019b), extreme hot and cold reference years are suggested. In this work, the ERY_{m1} and ERY_{m2} are selected to obtain the highest humidity ratio values from the whole year. The success of the selection is first evaluated by a comparison of the monthly averages of the dry-bulb air temperature and of the air humidity ratio, then by the comparison between the results of moisture transfer simulations.

The resulting TRY_{EN} and ERY_m weather files were used as input for heat and moisture transfer simulations with the software Delphin 6 (Nicolai, 2007) in a moisture-related risk analysis of a set of three typical Italian walls, with two single-material walls used as a reference. The simulations were first performed without considering the rainfall intensity for four wall orientations (North, East, South and West). Subsequently, simulations with rainfall were performed, but only for Gemona del Friuli, due to the lack of availability of weather data for the other locations. The walls considered were (1) a well-insulated timber wall with a vapor barrier and an air gap, generally used to model X-LAM construction system, (2) an insulated hollow brick wall with two layers of hollow brick separated by an air gap and by the insulation, with a limited thermal resistance, and (3) a stone wall, with a layer of interior insulation and internal and external finishes. Two single-material walls were also simulated, in order to provide two simple results to be used as a reference. The two single layer walls were 20 cm thick, one made of concrete and the other of timber. The hygro-thermal properties of the walls are presented in Table 1.

In addition, two different indoor boundary conditions were considered in the simulation: the typical residential dwelling (normal moisture load according to WTA 6.2 guidelines, with the relative humidity values included between 20% and 60%) and a case characterized by larger indoor humidity generations (high moisture load according to WTA 6.2 guidelines, with the relative humidity values included between 40% and 70%). The results were expressed in terms of annual moisture content in the

walls and occurrences of interstitial moisture accumulation. The findings obtained with the typical year TRY_{EN} were compared to those with the extreme years, ERY_{m1} and ERY_{m2} . For Gemona del Friuli, the simulations carried out also considered rainfall.

Table 1 - Properties of the walls used in the simulations

Wall	d_{tot} (cm)	U_{tot} (W m ⁻² K ⁻¹)	$S_{d,tot}$ (m)
Timber wall (TW)	53	0.13	56
Hollow brick wall (HB)	51	0.36	8
Stone wall (SW)	34	0.19	4
Concrete layer (CONC)	20	10.50	15
Timber layer (TIMB)	20	1.75	4

3. Results

The results highlight how the choice of weather file is of primary importance in heat and mass transfer simulations, in particular when the goal is to assess the risks related to moisture condensation and accumulation across the opaque components and on their surfaces.

3.1 Weather File Comparison

The years ERY_{m1} and ERY_{m2} for the three locations under consideration were compared in terms of monthly average dry-bulb temperature values and monthly average air humidity ratio. The comparisons showed a general agreement with the month selection criteria:

- ERY_{m1} : extreme values dry-bulb air temperature (lower values) and humidity ratio (higher values);
- ERY_{m2} : extreme humidity ratio values (higher values);
- TRY_{EN} : representative values of temperature and relative humidity.

In Fig. 1a, the air temperatures for the three reference years of Legnaro are presented. The TRY_{EN} temperature values are generally lower than for the ERY_{m1} , while the ERY_{m2} temperatures are not constrained by the selection method. In Fig. 1b, the average monthly humidity ratio values for the three reference years for the same location show that the

in ERY_{m2} , the air humidity ratio is higher than in the TRY_{EN} , while the ERY_{m1} values are fall between the two, which is expected, as the selection procedure also involves the air temperature values.

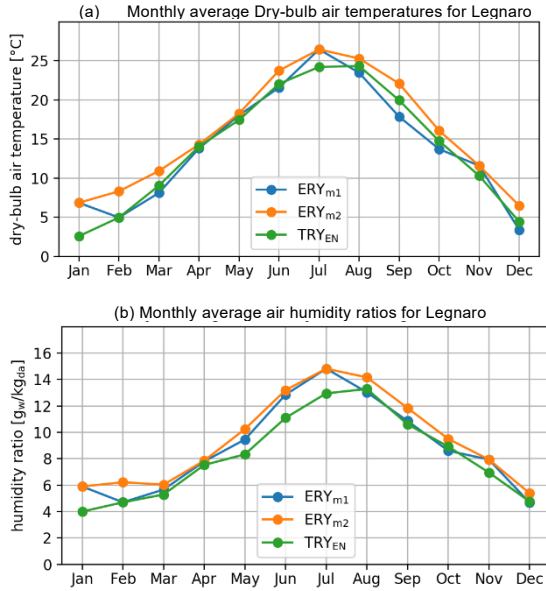


Fig. 1 – Monthly average dry-bulb air temperatures (a) and air humidity ratio monthly averages (b) for the reference years obtained for the location of Legnaro

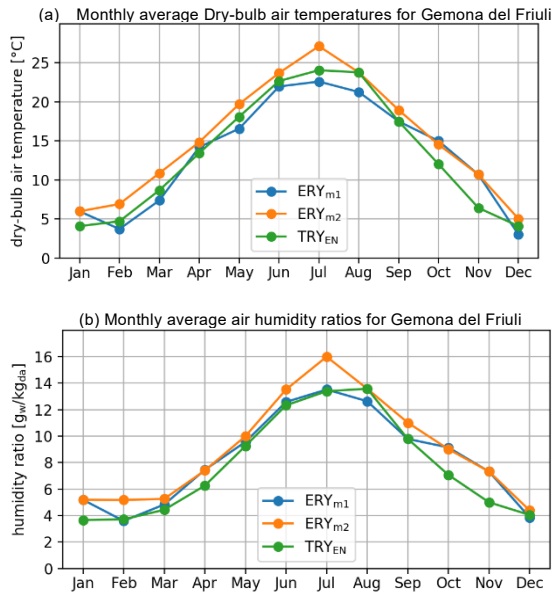


Fig. 2 – Monthly average dry-bulb air temperatures (a) and air humidity ratio monthly averages (b) for the reference years obtained for the location of Gemona del Friuli

Similar behaviors were found for Gemona del Friuli (Fig. 2), while for Trento the TRY_{EN} presented some extreme values during the year (Fig. 3). This is because some of the selected months in the reference

year included extreme weather events. This feature of the data was presented and discussed in Pernigotto et al., (2019a, 2019b). The effect of the selection on an annual base is presented in Fig. 4, in terms of the means of the air humidity ratio values. In each case, the air humidity ratio is lower for the TRY_{EN} and the ERY_{m1} values are lower than for the ERY_{m2} .

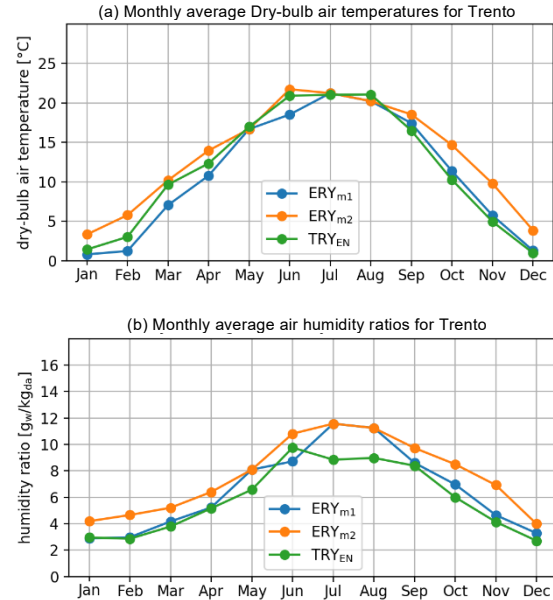


Fig. 3 – Monthly average dry-bulb air temperatures (a) and monthly average air humidity ratios (b) for the reference years obtained for Trento

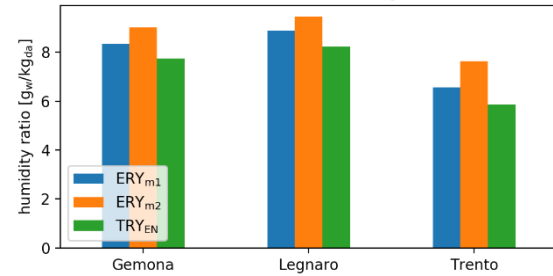


Fig. 4 – Annual mean air humidity ratio values for the reference years for the three considered locations

3.2 Simulation Results

Using the reference years to perform the heat and moisture transfer simulation of five wall build-ups made it possible to analyze the effect of the selection of the statistic on the moisture accumulation risk assessment. For each simulation, the presented results are those obtained after the dynamic equilibrium between the external conditions and the wall was reached (the initial conditions were similar to the moisture content distribution and the temperature

distribution of the last timestep of the reference year).

The simulations of the concrete and timber single layer walls showed, for all three locations, higher moisture content values for most days of the year, for the ERY_{m1} , and the lowest for the TRY_{EN} weather files. As an example, the moisture contents of the concrete single layer are shown in Fig. 5 for the case of Gemona del Friuli. The other walls under examination showed more complex behaviors (see, for instance, the hollow brick wall in Fig. 6), although the annual average moisture contents (presented in Fig. 7) confirm that the TRY_{EN} simulations have the lowest annual mean moisture contents.

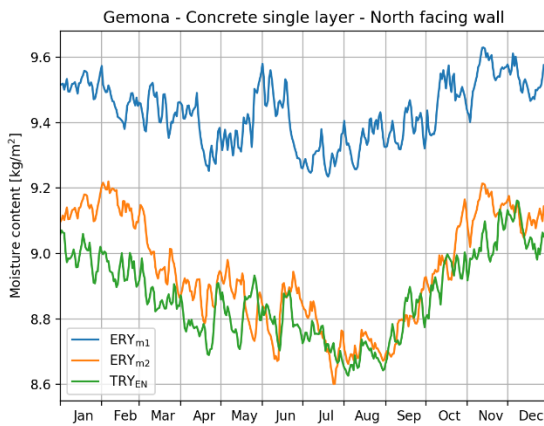


Fig. 5 – Daily average values of the moisture content of the concrete single layer facing North, for Gemona del Friuli

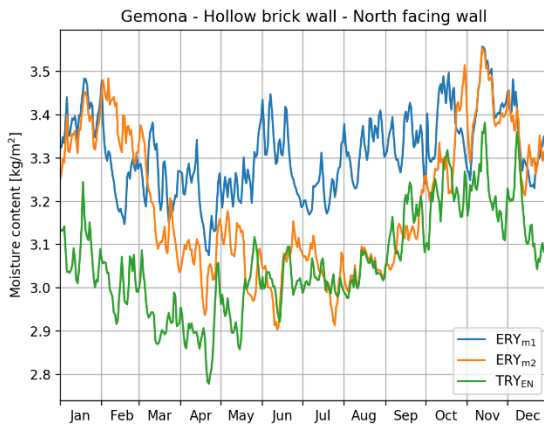


Fig. 6 – Daily average values of the moisture content of the hollow brick wall facing North, for Gemona del Friuli

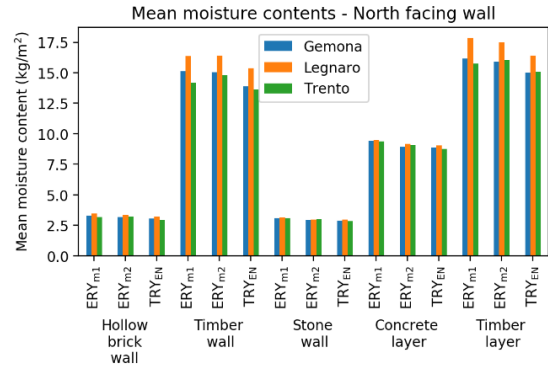


Fig. 7 – Annual mean total moisture contents of the five walls considered for the North orientation

Considering the wall build ups, the interstitial moisture accumulation risk was used as a parameter of comparison. For the sake of comparison, the interstitial moisture accumulation risk was calculated as the number of days in which the relative humidity was higher than the 80 % in the wall material, with the exception of the material layer exposed to the outside. Although Fig. 8 shows that the response of the walls to the external conditions was highly structure dependent, the ERY_{m1} and the ERY_{m2} provide higher risks than the TRY_{EN} . Similar results were obtained for the other orientations, with some exceptions such as the stone wall located in Gemona del Friuli. In this case, higher risks were found for the TRY_{EN} , even though the moisture content of the wall was lower than the ones obtained with ERY_{m1} and the ERY_{m2} . Potential differences in the behavior of different wall types should be expected, given that each wall has a different response to the same weather events and a weather event that is critical for the stone wall might not be critical for the hollow brick wall.

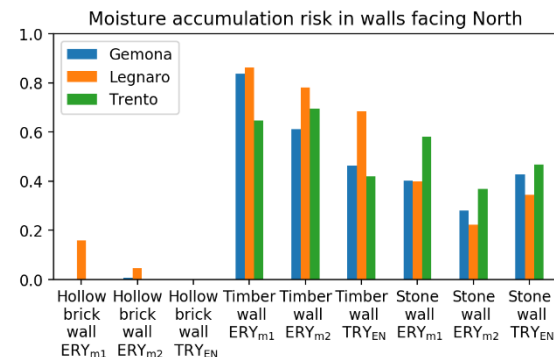


Fig. 8 – Moisture accumulation risk (fraction of days with relative humidity values over the 80 %) for the considered walls

Simulations were also performed to consider higher internal moisture loads. As shown in Fig. 9, the moisture contents were higher than in simulations with normal internal moisture loads and the relationship between the results of the three reference years was the same.

For Gemona del Friuli, the availability of the required weather data made it possible to run simulations which also included driving rain. In this case, the highest moisture contents were obtained using the ERY_{m2} (Fig. 10). A possible explanation for this effect could be that the months with extreme air humidity ratios are also the months with the highest rainfall intensity values and with the lowest drying potential.

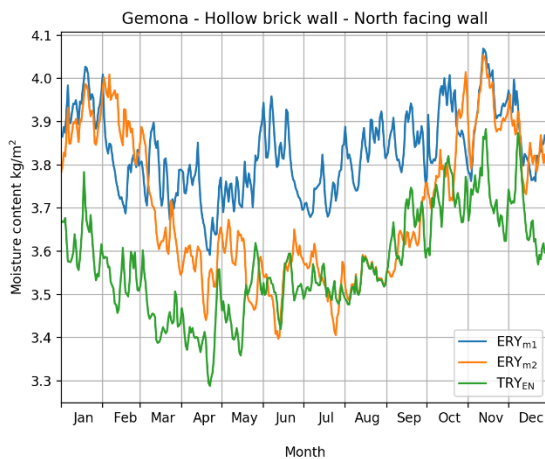


Fig. 9 – Moisture content of the hollow brick wall facing North, for Gemona del Friuli with high internal moisture loads

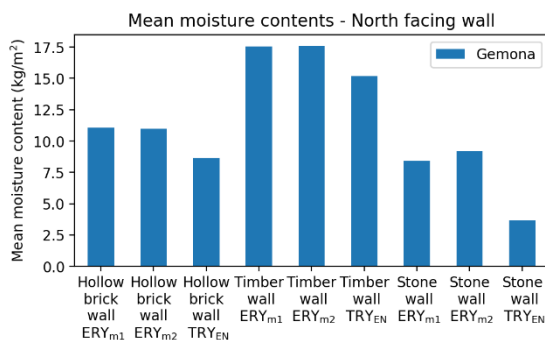


Fig. 10 – Annual mean moisture contents of the three considered walls facing North in Gemona del Friuli, considering driving rain

4. Conclusions

The comparison between typical and extreme weather files made it possible to confirm that the latter are more suitable for moisture accumulation risk analysis. This can be observed, in terms of larger moisture contents in the tested walls, and also in terms of risks of moisture accumulation. The use of extreme instead of typical conditions can allow for a more robust design of the opaque components and, consequently, longer durability and a higher thermal hygrometric performance. Nevertheless, even if the proposed approach represents an improvement on an approach based on EN ISO 15927-4:2005 reference years, some limitations remain and indicate opportunities for further advancements. In particular, further research is planned to combine rainfall and wind direction data to determine the risk of wet walls' surface and to evaluate the impact of such input in the extreme year definition and on the walls' thermal hygrometric performance.

In terms of further developments, for a safe application of risk analysis it is necessary to extend the evaluation of the extreme weather files to other building structures and materials.

Acknowledgement

The authors would like to thank ARPA Veneto, ARPA FVG (OSMER), and Fondazione Edmund Mach for supplying the raw weather data, and Bauklimatik Dresden Software GmbH for providing the software Delphin 6.

This research has been made possible thanks to PhD funding from the Provincia di Udine and has been partially funded by the project "Klimahouse and Energy Production" in the framework of the programmatic-financial agreement with the Autonomous Province of Bozen-Bolzano of Research Capacity Building.

Nomenclature

Symbols

p	General variable
m	Calendar month
y	Year of the Multi-year weather data record
i	Day of the year
\bar{p}	Daily mean of the values of the general variable p
$\Phi(p, m, i)$	Cumulative distribution function
$K(\bar{p}, m, i)$	Ranking of the i^{th} day of the month m
$F(p, y, m, i)$	Cumulative distribution function within the calendar month m of the year y
$J(i)$	Ranking of the i^{th} day of the month m of the year y
$F_s(p, y, m)$	Finkelstein-Shafer statistic
d_{tot}	Total thickness of a wall
$S_{d, \text{tot}}$	Total equivalent air thickness of a wall (vapor permeability)
U_{tot}	Total thermal transmittance of a wall

References

- Antonacci, G., and I. Todeschini. 2013. "Derivation of Meteorological Reference Year with Hourly Interval for Italy." *Building Simulation Applications* 2013: 49–57.
- CEN. 2005. *EN ISO 15927-4:2005 - Hygrothermal Performance of Buildings Calculation and Presentation of Climatic Data-Part 4: Hourly Data for Assessing the Annual Energy Use for Heating and Cooling*. European Committee for Standardization.
- CEN. 2007. *EN 15026:2007 - Hygrothermal performance of building components and building elements - Assessment of moisture transfer by numerical simulation*. European Committee for Standardization.
- CEN. 2012. *EN ISO 13788:2012 - Hygrothermal performance of building components and building elements — Internal surface temperature to avoid critical surface humidity and interstitial condensation — Calculation methods*. European Committee for Standardization.
- Finkelstein, J.M., and R.E. Schafer. 1971. "Improved Goodness-of-Fit Tests." *Biometrika*.
<https://doi.org/10.1093/biomet/58.3.641>
- Kalamees, T., and J. Vinha. 2004. "Estonian Climate Analysis for Selecting Moisture Reference Years for Hygrothermal Calculations." *Journal of Building Physics*.
<https://doi.org/10.1177/1097196304038839>
- Libralato, M., G. Murano, A. De Angelis, O. Saro, V. Corrado. 2018. "Hygrothermal Modelling of Building Enclosures: Reference Year Design for Moisture Accumulation and Condensation Risk Assessment." *7th International Building Physics Conference, IBPC2018*.
<https://doi.org/10.14305/ibpc.2018.ps19>
- Libralato, M., O. Saro, A. De Angelis, S. Spinazzè. 2019a. "Comparison between Glaser Method and Heat, Air and Moisture Transient Model for Moisture Migration in Building Envelopes." *Applied Mechanics and Materials* 887: 385–92.
<https://doi.org/10.4028/www.scientific.net/AMM.887.385>
- Libralato, M., G. Murano, A. De Angelis, O. Saro, V. Corrado. 2019b. "Generation of Moisture Reference Years for Interstitial Condensation Risk Assessment: Influence of the Meteorological Record Length Introduction." *Building Simulation 2019*.
- Murano, G., D. Dirutigliano, V. Corrado. 2018. "Improved Procedure for the Construction of a Typical Meteorological Year for Assessing the Energy Need of a Residential Building." *Journal of Building Performance Simulation*.
<https://doi.org/10.1080/19401493.2018.1479774>
- Nicolai, A. 2007. Modeling and Numerical Simulation of Salt Transport and Phase Transitions in Unsaturated Porous Building Materials. Ph.D. thesis, Syracuse University, NY, USA.
- Pernigotto, G., A. Prada, D. Cóstola, A. Gasparella, J.L.M. Hensen. 2014. "Multi-Year and Reference Year Weather Data for Building Energy Labelling in North Italy Climates." *Energy and Buildings* 72: 62–72.
<https://doi.org/10.1016/J.ENBUILD.2013.12.012>
- Pernigotto, G., A. Prada, A. Gasparella. 2019a. "Development of Extreme Reference Years for Building Energy Simulation Scenarios." *Applied*

- Mechanics and Materials* 887: 129–39.
<https://doi.org/10.4028/www.scientific.net/AMM.887.129>
- Pernigotto, G., A. Prada, A. Gasparella. 2019b. “Extreme reference years for building energy performance simulation.” *Journal of Building Performance Simulation*.
<https://doi.org/10.1080/19401493.2019.1585477>
- WMO. 2008. World Meteorological Organization. Guide to Meteorological Instruments and Methods of Observation.
<https://www.weather.gov/media/epz/mesonet/CWOP-WMO8.pdf>
- Zhou, X., D. Derome, J. Carmeliet. 2016. “Robust Moisture Reference Year Methodology for Hygrothermal Simulations.” *Building and Environment*.
<https://doi.org/10.1016/j.buildenv.2016.09.021>

Building Integrated Photovoltaic Thermal Collectors: Modelling and Experimental Investigation of Two Novel Cost-Effective Prototypes

Giovanni Barone – University of Naples Federico II, Italy – giovanni.barone@unina.it

Annamaria Buonomano – University of Naples Federico II, Italy / Concordia University, Canada – annamaria.buonomano@unina.it

Cesare Forzano – Free University of Bozen-Bolzano, Italy – cesare.forzano@natec.unibz.it

Adolfo Palombo – University of Naples Federico II, Italy – adolfo.palombo@unina.it

Abstract

This paper presents a comprehensive analysis of three different building-integrated solar systems. Specifically, two building-integrated photovoltaic thermal collector prototypes (alternatively water and air cooled) are investigated along with a building-integrated photovoltaic panel; these prototypes were fabricated and experimentally tested at University of Patras (Greece). Note that the active performance of such devices has already been investigated in other works. This chapter presents the analysis of the passive effects on a building's thermal behaviour caused by the integration of the devices. A suitable dynamic simulation tool, capable of assessing the whole device-building performance analysis, is outlined. A case study aimed at proving the potential of such code and showing the effects of the adoption of building integrated solar systems on a building's thermal behaviour is presented. The case study considers a simple dwelling unit in a multi-storey residential building, located in different weather zones and subject to diverse boundary conditions. The investigated collectors on the south facades of the building are integrated, and the associated passive effects are analysed. The analysis provides interesting outcomes from the point of view of energy and comfort.

1. Introduction

It is well known that the building sector is responsible for around 37% of the total primary energy consumption worldwide (European Council and Parliament); of this, 26% is due to residential and 11% to commercial buildings (Boermans et al., 2011; van de Bree et al., 2014). Several actions have been undertaken to overcome this problem and to reduce the impact of buildings (Buonomano et al.,

2019). Specifically, significant efforts have been made to i) enhance building performance through the use of opaque and transparent elements and phase-change materials (Forzano et al., 2019), and also to ii) increase the efficiency of systems such as HVAC, lightning, etc. (Barone et al., 2016). The integration of innovative technologies based on Renewable Energy Systems (RES) plays a crucial role in this effort (Lin and Zhu, 2019). The use of RES in small building-integrated installation is currently much more widespread than in larger centralized plants (Wang et al., 2018), leading to a “prosumer” conception of buildings. In this sense, the building is not just an energy consumer, but it also becomes the producer of its own consumed energy (Toffler, 1980). Such an approach, which is easily applicable to small detached houses, creates some issues when a high-rise building is considered, as renewable energy devices (solar thermal collectors, photovoltaic panels, photovoltaic thermal collectors, etc.) require a certain amount of space for their installation in order to satisfy building needs (and also normative requirements). Sufficient space is usually available in the case of detached houses or small buildings (which typically have a higher surface/volume ratio, more space near the building, etc.), but this is not true in the case of high-rise buildings. In the case of the latter, it is uncommon to have enough space near the building (as such buildings are usually located in cities) or on the roof (which is small in relation to the total floor area and, thus, in relation to the overall energy demand). This problem is even greater if we consider the increasing trend for city living, the ever-

increasing size of cities, and the consequent spread of high-rise living solutions.

1.1 BISS state-of-the-art

In this framework, one possible way to exploit distributed RES, despite the lack of space in the common high-rise metropolitan buildings, is to integrate solar devices into the building envelope (COST Action TU1205 (BISTS) 2015). For this reason, interest in Building Integrated Solar System (BISS) is constantly increasing (COST Action TU1205 (BISTS) 2015). In the literature, several works have investigated Building Integrated Solar Thermal Systems (BISTS) (Agathokleous et al., 2019; Forzano et al., 2019; Barone et al., 2019b), Building Integrated Photovoltaics (BIPV) (Barone et al., 2019a, 2019b), Building Integrated Photovoltaics/Thermal collectors (BIPVT) (Barone et al., 2019b), etc. However, despite the advantages of the adoption of a BISS, some issues can be identified, such as the architectural impact and the potentially high initial cost of the system (US Department of Energy, 2014). It should be noted that the economic cost (including of stand-alone solar devices) represents a significant obstacle for the diffusion of BISS (Maurer et al., 2017). Another issue, closely related to the question of building integration, is the variation of a building's thermal behaviour (Barone et al., 2019a; Maurer et al., 2017). The building envelope integration of RES devices affects the system thermal behaviour with desired (free heating) or undesired (overheating) passive effects. Building heating and cooling loads and demands are therefore modified with respect to those of traditional buildings without a BISS. An analysis of several papers available on BISS reveals a number of areas of misunderstanding or lack of knowledge, such as: i) the fact that the initial costs of BISS are usually too high to guarantee a good market diffusion is not considered; ii) few analyses are presented in literature about the passive effects of BISS; iii) the effects of the adoption of BISS on energy and comfort are usually neglected by most studies; iv) most studies investigate a device in a certain weather zone or in a certain season; v) there is a lack of suitably dynamic simulation models capable of assessing the whole building/BISS system behaviour. This lack of knowledge is much

more evident when BIPV and BIPVT are considered.

1.2 Aim of the work

In this framework context, the main aim of this work is to fill some of the gaps in knowledge outlined in the previous paragraph by investigating the passive effects of different BISS prototypes on a building's thermal behaviour. To this end, two innovative Building Integrated low-cost flat-plate Photovoltaic Thermal (BIPVT) collector prototypes (with water and air as working fluids), whose active performance had already been investigated in previous studies, were considered in order to assess their passive effects. These prototypes were developed with the aim of creating economically affordable collectors made of very cost-effective materials. By means of these hybrid collectors, both electricity and thermal energy can be obtained. Specifically, the two prototypes, which both contain a polycrystalline PV module, differ in terms of the adopted working fluid: air and water. The low-cost heat extraction systems are used to increase the electric efficiency of the PV module by lowering its working temperature. Simultaneously, the obtained hot fluids can be exploited for different building uses (the hot air can be adopted for direct free space heating or supplied to the evaporator of a heat pump system, whereas the hot water can be used for feeding a hydronic heating system or for producing DHW). In order to investigate the passive effects of these two BIPVT prototypes under different boundary and working conditions, a suitably dynamic simulation model for complete system analysis was developed in the MatLab environment. This simulation tool, capable of assessing the energy performance and environmental impact of the presented devices, is also able to accurately assess their passive effects. The hygrothermal comfort analysis can be carried out by considering the mean radiant temperatures obtained with and without the considered BISS devices. The model developed in-house was also validated by means of experimental data as presented in previous published work (Barone et al., 2019c) (here, a very good agreement between numerical results and experimental measurements

was achieved). Finally, in order to investigate the effects of the integration of the presented prototypes and to show the potentiality of the developed simulation tool, a suitable case study is discussed. Specifically, it refers to a single dwelling unit located in a multi-storey residential building, where the two BIPVT prototypes and a commercial BIPV panel) are alternatively integrated into the south-facing vertical façade (the BIPV is studied for the purposes of comparison). For the analysis, different European weather zones and boundary conditions were investigated. The results suggest that significant energy and economic savings can be achieved and useful design and operating criteria are outlined’.

2. Description of Prototypes

The developed BIPVT prototypes are briefly described in this section; more information can be found in Barone et al. (2019a, 2019b). Both PVT devices, built at the Renewable Energy Laboratory of University of Patras (Greece), were fabricated using the same PV panel (see Fig. 1). As is widely understood, the electrical efficiency of photovoltaic cells dramatically drops as the operating temperature rises. In order to improve the efficiency of photovoltaic cells by avoiding such overheating, two different heat extraction systems were created. Specifically, a cooling system was placed under the photovoltaic panel, composed of eleven PVC pipes (Fig. 2, left), and of two black galvanized steel sheets, shaped in such a way as to form seven air ducts (Fig. 2, right), for the water and air-based devices respectively.



Fig. 1 – Polycrystalline PV module



Fig. 2 – Water (left) and air (right) PVT heat extraction systems

Further information regarding the geometrical and thermophysical data, the collector performance, etc., can be found in the two previous papers (Barone et al., 2019a, 2019b).

3. Simulation Model

In order to investigate the performance under different boundary and working conditions of the prototypes presented, two mathematical models were developed (Barone et al., 2019a, 2019b) for the water-based and the air-based prototypes, respectively. Such models, based on the Hottel-Whillier equation set (Duffie and Beckman, 2013), suitably modified to consider the PV panel as an absorbing plate, were experimentally validated, proving their reliability. Very good agreement between the measured and experimental data was found, as reported in Barone et al. (2019a; 2019b), ensuring the reliability of the codes. Note that the BIPV mathematical model is derived by the BIPVT models by removing the part relating to heat extraction.

In order to assess the passive effects of the prototypes, the two prototype models are linked, in this paper, to a Building Energy Performance Software (BEPS) package developed in-house. The adopted BEPS, called DETECT, had been previously developed and validated (Buonomano and Palombo, 2014; Buonomano, 2016; Barone et al., 2019c). A detailed description of the building simulation tool can be found in Buonomano and Palombo (2014). In order to connect mathematical model of the prototypes to DETECT, the generalized equation of the overall thermal losses

for a Flat Plate Collector (FPC) (Duffie and Beckman, 2013), also adopted for PVT collectors, is:

$$\dot{Q}_{loss} = U_L \cdot A_C \cdot (T_p - T_a) \quad \text{with } U_L = (U_i + U_e + U_b) \quad (1)$$

Equation (3) is modified as follows for building integration:

$$\dot{Q}_{loss} = (U_i + U_e) \cdot A_C \cdot (T_p - T_a) + U_b^* \cdot A_C \cdot (T_p - T_{air}) \quad (2)$$

Here, U_L is the overall heat loss coefficient, which is the sum of top (U_t), back (U_b), and edges (U_e) loss coefficients, A_C is the collector aperture area. The back loss coefficient, U_b , is suitably modified in Eq. (2), U_b^* , to model the building integration. Specifically, it also considers thermophysical properties of the building, rather than only those of the collector, and connects the absorbing plate temperature (T_p) to that of indoor air (T_{air}) instead of outdoor ambient air (T_a). Consequently, when the collectors are integrated into the building envelope, the mathematical model is modified so that the collector back becomes the external layer of the wall and its back temperature is indirectly linked to building's indoor air temperature. More details are available in Agathokleous et al. (2019) and Barone et al. (2019a, 2019b)

4. Case Study

In order to show the capabilities of the developed dynamic simulation tool and analyse the passive effects on the building of the proposed integration of the prototypes, a suitable case study is here presented. Specifically, it refers to a dwelling unit located in a multi-storey residential building. A sketch of the reference building is shown in Fig. 3 (L. 4.7 m, H. 3.2 m, W. 3.5 m). Note that all the internal walls are adiabatic with the exception of the South facing wall, where a window is considered (L. 0.95 m, H. 1.6 m). The thermophysical properties of the building are presented in Table 1.

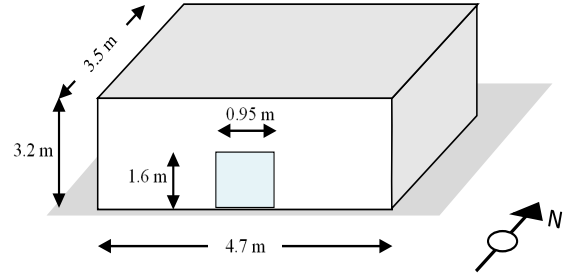


Fig. 3 – Reference building sketch

The reference building is enhanced by integrating in the South facing façade 9 water-based BIPVTs, 9 air-based BIPVTs, and 9 BIPVs, alternatively (see Fig. 4). The heat transfer fluid flow rates of the prototypes are equal to 0.0339 kg/s and 0.123 kg/s for water and air collectors, respectively. For the system based on the water-cooled device, a 360 l tank is considered.

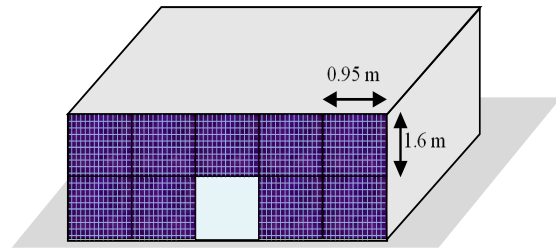


Fig. 4 – Proposed building sketch

To estimate the electricity consumption for space heating and cooling, a variable COP heat pump/chiller is modelled (Barone et al., 2016). To evaluate the system behaviour under different boundary conditions, three weather zones representing hot, temperate and cold European climates are investigated (Almeria, Naples and Milano, Table 2). In addition, three internal thermal loads (125, 150 and 500 W) and two ventilation flow rates (0.25 and 0.5 Vol/h) are simulated.

Table 1 – Building features

	Ext. wall	Int. wall	Window
Thickness [mm]	250	250	4/18/4
Thermal transmittance	1.2	-	4
Solar transmittance [-]	-	-	0.75

Table 2 – Considered climatic zone

Weather zone	HDD [Kd]	CDD [Kd]	ISR [kWh/m ² y]
Milano	2733	435	1188
Naples	1479	727	1529
Almeria	783	961	1724

5. Results and Discussion

In this section, the results of the analyses carried out are presented in detail. Note that only the passive effects results (from the point of view of temperature, energy and comfort) are presented.

5.1 Temperatures Analysis

The adoption of a BISS changes the thermophysical behaviour of the building wall in which the considered devices are integrated. This phenomenon can be observed in Figs 5 and 6 where the Reference vs. Proposed systems external wall temperatures are reported for three sample winter and summer days, respectively. In these figures, four different systems are considered: i) the reference building (blue lines); ii) the proposed system with the BIPV panel (black lines); iii) the proposed system with the water-based BIPVT collector (red lines), iv) the proposed system with the air-based BIPVT collector (green lines).

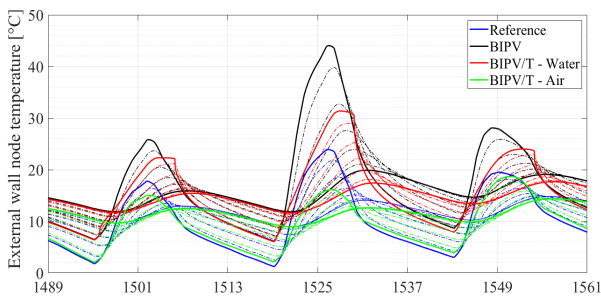


Fig. 5 – Reference vs. Proposed systems: external wall temperature time histories for three sample winter days (Naples, 250 W, 0.25 Vol/h)

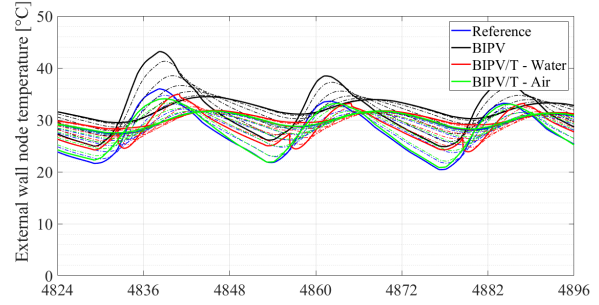


Fig. 6 – Reference vs. Proposed systems: external wall temperature time histories for three sample winter days (Naples, 250 W, 0.25 Vol/h)

For each wall, five temperature nodes are considered; two of these (continuous lines) refer to the superficial wall layers (not capacitive), while the other three (dotted lines) refer to the wall core thermal nodes (capacitive). By analysing the winter season (Fig. 5), several considerations can be made. The integration of BIPV (black lines) leads to a remarkable temperature increase with respect to the reference case (blue lines), this occurrence is due to the higher absorption coefficient of the PV sheet with respect of the standard building wall. A lower wall temperature peak with respect to the case of BIPV (but still higher than the reference case study wall) is reached when the water-cooled BIPV/T (red lines) is adopted. This is due to the cooling effect of the water flowing inside the collector. In addition, it is interesting to note that the wall temperature peak occurs at a later time, compared to the other solutions. This delay is due to the thermal capacity of the water inside the storage tank (the water-based device is the only one connected to a water loop including a hot-water storage tank). Finally, by considering the air-cooled BIPV/T (green lines), different behaviour is detected with respect to the other systems under consideration. Specifically, during the sunny hours, the air-cooled BIPV/T adoption returns a temperature wall decrease compared to the reference case study. This occurrence is due to the high cooling effect of the air flowing inside the collector (taken from the outdoor environment). Note that a different behaviour of the air-cooled BIPVT could be achievable by changing the operating conditions (e.g. if air was taken from the inside of the building and then exhausted). Trends similar to those detected for the

winter season can also be noticed for the summer season (Fig. 6), with the exception of the water-based BIPV/T (red lines), which corresponds to a remarkable drop in temperature, occurring during the early morning hours. This is due to the very low temperature of the water flowing inside the collector during these hours – the storage tank connected to the water-cooled BIPV/T collector is drained in the evening by the users for domestic purposes. The hot water is then replaced with cold tap water (15 °C). When the circulating pump of the system is activated the next morning, the water, still cold inside the storage tank, cools down the external wall surface, causing the striking temperature drop shown in Fig. 6.

The variation of the thermal behaviour of the wall, caused by the adoption of the BISS, also affects, in turn, the indoor air temperature. This effect is shown in Fig. 7 for the same three sample winter and summer days and for the same weather zone (Naples) considered for Figs 5 and 6.

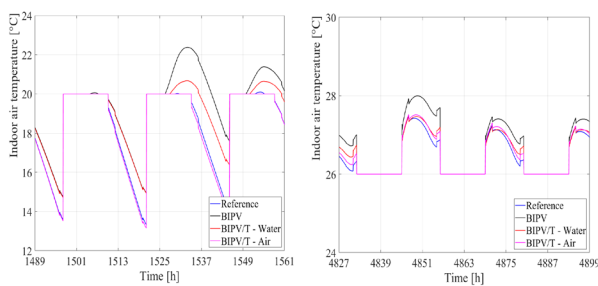


Fig. 7 – Reference vs. Proposed systems: indoor air temperature time histories for three sample winter and three sample summer days (Naples, 250 W, 0.25 Vol/h)

Starting from the winter season (Fig. 7, left), it can be noted that higher indoor air temperatures occur during the hours in which the HVAC system is switched off, by adopting the BIPV and the water-cooled BIPV/T solutions (black and red lines respectively). This is due, as mentioned previously, to the free-heating effects caused by the integration of these devices in the building. Note that this increase in indoor air temperature implies a higher indoor thermal comfort perception with respect to the reference building. In addition, an energy saving can also be achieved during the hours in which the HVAC is switched on (not detectable from Fig. 7 due to the thermostat temperature). Both comfort and energy demand variations are described in more detail in the energy and comfort analysis sec-

tions. Note that, in the case of the adoption of air-cooled BIPV/T (purple line), lower indoor air temperatures are detected with respect to the reference case study, as can be seen in Fig. 5. By considering the summer season (Fig. 7, right), higher indoor air temperatures, compared to the reference case study, are almost always obtained by taking into account the proposed systems. Higher energy consumption for space cooling and lower indoor thermal comfort levels are therefore expected during the summer season.

5.2 Thermal Power/Energy Analysis

The variations in indoor air temperature, shown in the previous section (Fig. 7), affect the required thermal power for space heating and space cooling. Fig. 8 shows the HVAC system thermal power time histories for the same three winter (left) and three summer (right) sample days previously considered.

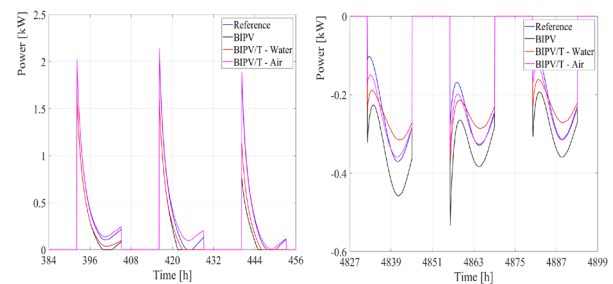


Fig. 8 – Reference vs. Proposed systems: thermal power time histories for three sample winter and three sample summer days (Naples, 250 W, 0.25 Vol/h)

Starting with the winter season (Fig. 8, left), several considerations can be made. The adoption of the BIPV and water-cooled BIPVT systems (black and red lines respectively) returns, as can be seen in Fig. 7, a lower thermal power demand for space heating with respect to the reference case study (blue line) due to the free heating effect of the BISS. It is interesting to note that in several hours the entire space heating need is covered by the BISS positive passive effect. By considering the air-cooled BIPVT prototype (purple line), the opposite effect can be detected: a higher thermal power demand for space heating with respect to the other solutions is obtained. This higher consumption, which is also seen in the temperature trends previously discussed (Fig. 7), is caused by the negative over-

cooling effect of the device due to the cold air flowing inside the collector. During the summer season (Fig. 8, right), the adoption of a BISS generally increases the thermal power demand for space cooling purposes due to the negative over-heating effect. As an example, the BIPV (black lines) returns a higher thermal power demand if compared to the reference case study (blue lines). A different situation is instead detected by considering the water and air-cooled BIPVT (blue and purple lines, respectively). Here, during the first hours of the day the adoption of these systems creates a lower thermal power demand for space cooling. By comparison, a higher demand is detected later in the day. This behaviour is in accordance with the temperature trends presented in Fig. 7.

From the results shown so far it is clear that the effect of the adoption of a BISS on the building thermal behaviour is strictly dependent on the season and on the hour of the day. This implies that the convenience linked to the building integration of such systems (from the point of view of passive effects) should be assessed on a seasonal/yearly basis. For this reason, the seasonal thermal energy demands are reported in Figs 9, 10 and 11, for Almeria, Naples and Milan, respectively. Note that in these figures the bar above and below the zero line represents the thermal energy demanded for space heating and space cooling, respectively. From the figures, it is possible to note that the adoption of a BISS generally returns lower energy consumption for space heating (positive free-heating effect) and higher energy consumption for space cooling (negative over-heating effect) with respect to the reference building (blue bars), as expected. By analysing the BIPV (black bars), it can be noted that this solution returns the highest effects magnitude (highest winter energy savings and highest summer energy demand increases) for all the considered case studies.

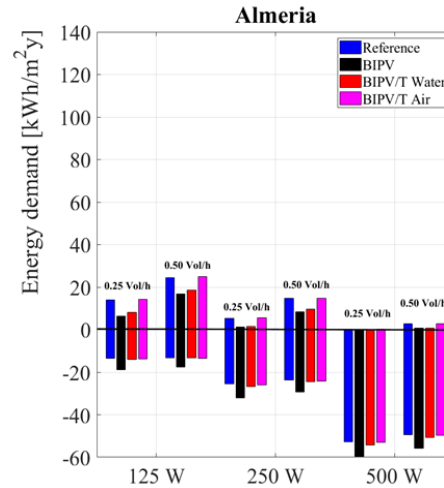


Fig. 9 – Reference vs. Proposed systems: thermal energy demands for space heating and space cooling (Almeria)

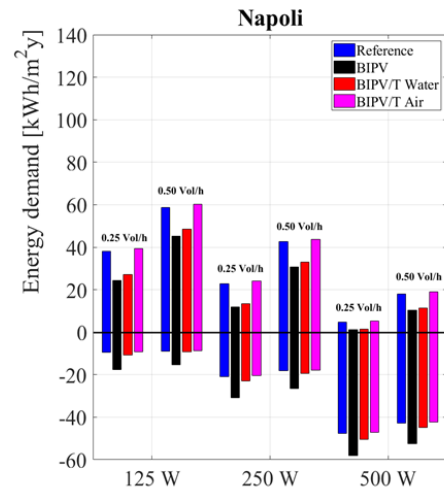


Fig. 10 – Reference vs. Proposed systems: thermal energy demands for space heating and space cooling (Naples)

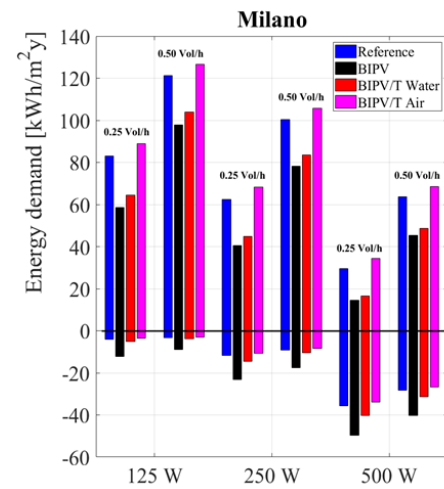


Fig. 11 – Reference vs. Proposed systems: thermal energy demands for space heating and space cooling (Milan)

A similar behaviour, but lower in magnitude, occurs by considering the water-cooled BIPVT (red bars). On the other hand, very low variations can be seen in Fig. 9 if the air-cooled BIPVT (purple bars) is considered. Small differences are detected only in case of the cold-dominated weather zone (Milan), especially for space heating purposes. The small variation in terms of demanded thermal energy, which is obtained by considering the air-cooled BIPVT, is in accordance with the very slight temperature variations returned by the technology and already shown in Figs. 5, 6 and 7 with respect to the reference building.

The seasonal results shown in Figs. 9, 10 and 11 imply the yearly results presented in Figs. 12, 13 and 14 in case of Almeria, Naples and Milan, respectively. Specifically, here the annual outcomes are reported in terms of yearly electricity savings with respect to the reference building for all the proposed case studies. Note that these results are a trade-off between the negative summer effects and the positive winter effects. From the figures, interesting considerations can be made. First, it is possible to note that the performance of BIPV and water-cooled BIPVT (black and red bars respectively) increases with the increase of the space heating demand (higher heating degree days (HDD), higher ventilation flow rate, lower internal loads). The opposite occurs for the air-cooled BIPVT (blue bars), for which the performance increases with the increase of the cooling loads (higher cooling degree days CDD, lower ventilation flow rate, higher internal loads). This discrepancy is due to the temperature behaviour shown in Figs. 5, 6 and 7. BIPV and water-cooled BIPVT, which return higher system temperatures with respect to the reference case study, perform better in weather zones where the effect of the winter season is greater than the summer season. Conversely, lower system temperatures are achieved for the air-cooled BIPVT.

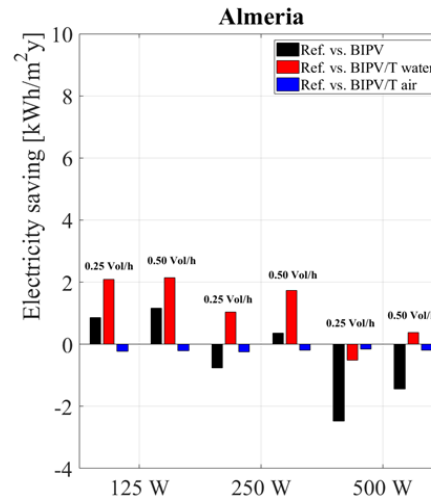


Fig. 12 – Reference vs. Proposed systems: yearly electricity savings (Almeria)

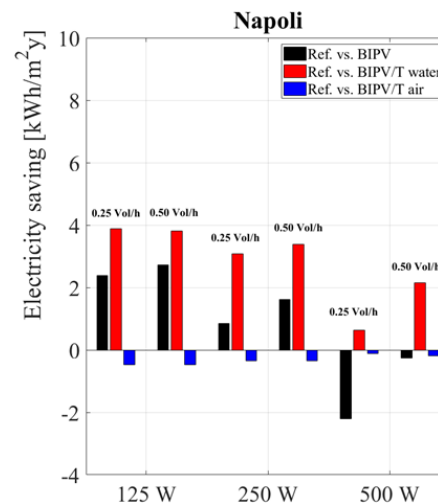


Fig. 13 – Reference vs. Proposed systems: yearly electricity savings (Naples)

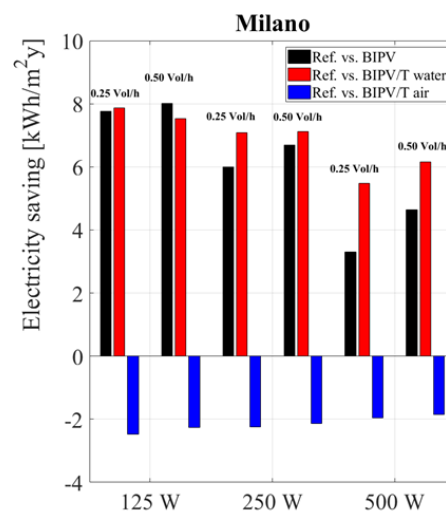


Fig. 14 – Reference vs. Proposed systems: yearly electricity savings (Milan)

By analysing each system singularly, it is possible to note that the adoption of water-cooled BIPVT (red bars) returns the highest savings for almost all the considered case studies. The only exception, where this system returns an energy increase, is in Almeria (internal gains set at 500 W, and ventilation flow rate equal to 0.5 Vol/h), where disadvantages in summer outweigh the benefits in winter.

Lower savings (i.e. higher energy demand) are detected by adopting the BIPV system (black bars). The higher system temperatures reached by the wall integrating this device with respect to the others (see Fig. 5, Fig. 6 and Fig. 7) imply a higher building heating demand for this system to be convenient. This is also demonstrated by the results for Milan (internal gains set at 125 W, and ventilation flow rate equal to 0.25 and 0.50 Vol/h). Here, the very high heating demand makes the adoption of BIPV more convenient than the water-cooled BIPVT.

The air-cooled BIPVT (blue bars), on the other hand, always return a worse performance with respect to the reference case study (negative primary energy saving), in accordance with the temperature time histories shown in Figs 7 and 8 and with the thermal energy one of Figs 9, 10 and 11. However, it should be noted that the adoption of this device in hot weather zones returns a negligible energy increase. By comparison, the lower PV panel temperature (reached thanks to the cooling air and the produced hot air itself) should be considered in the overall system convenience (together with the higher productivity and longer life). Note also that the air-cooled BIPVT behaviour is mainly due to the operating condition investigated in this paper; the considered prototype takes air from the outdoor environment instead of from the building indoor environment. This means that the temperature of the air entering the collector is always somewhat low, causing the subsequent overcooling effect previously described. Different results, and thus different performances could be achieved with different air intake strategies (e.g. if air is taken from the inside of the building and exhausted or adopted to enhance the heat pump COP during the winter).

5.3 Comfort analysis

The modifications to the thermal behaviour of a building due to adoption of the BISS also affects, in turn, the perception of indoor thermal comfort. This is due to the variation of both indoor air (see Fig. 7) and wall (see Fig. 5 and Fig. 6) temperatures affecting the indoor thermal comforts levels. In this section, an analysis of the thermal comfort when BISS are considered is presented. In order to conduct this investigation, the number of hours in which the indoor thermal comfort is satisfied was estimated. Following this, the variation of the number of comfort hours obtained in one year between the proposed and the reference case was assessed. Specifically, comfort conditions are considered when the Predicted Mean Vote (PMV) is included in the range of ± 0.5 . The results of such analysis are reported in Fig. 15 for all the considered case studies in terms of comfort hour variation.

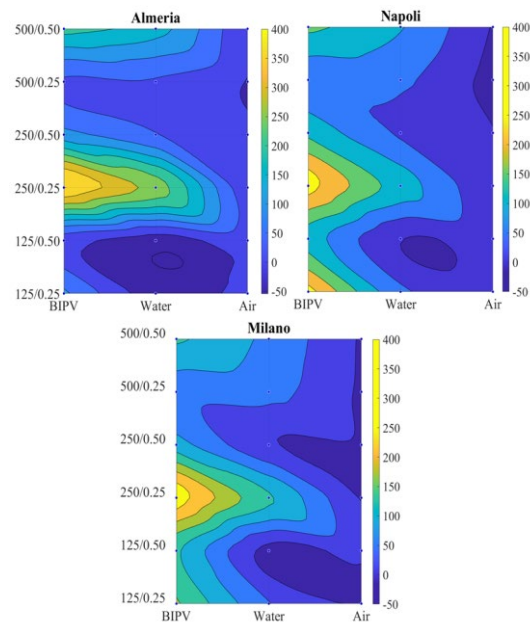


Fig. 15 – Reference vs. Proposed systems: yearly thermal comfort hour variation for all the considered case studies

By comparing Fig. 15 to Fig. 12, Fig. 13 and Fig. 14, it is possible to note that the best solutions, from the point of view of comfort and energy point do not always match. As an example, from Fig. 15 is possible to note that the application of the water-cooled BIPVT located in Naples (internal gains set at 125 W, and ventilation flow rate equal to 0.25

and 0.50 Vol/h) reports a decrease in comfort hours (~ -50 hours/year), although it represents the best solution from the point of view of energy (see the same case study results from Fig. 13). By comparison, in the case of the BIPV located in Almeria (internal gains set at 500 W, and ventilation flow rate equal to 0.25 and 0.50 Vol/h), a comfort increase is detected ($\sim +150/200$ hours/year), whereas the same case studies return a worse energy performance (see Fig. 12).

In general, it can be seen that the integration of BIPV is always the best solution from the point of view of comfort. Its convenience increases with an increase in HDD, due to the greater influence of the cooling season, which maximizes the benefits of the higher wall/indoor air temperature (see Fig. 5, Fig. 6 and Fig. 7). The convenience in adopting the water-cooled BIPVT, on the other hand, depends on the selected weather zone and boundary conditions. The application of this device leads to both an increase and decrease in comfort as a function of the considered case study (ranging from -50 to +150 hours/year). Finally, the worse comfort performance was achieved through the adoption of the air-cooled BIPVT (especially in case of the cold dominated weather zones – Milan). This is due to the over-cooling effect discussed above, and depends on operating conditions of the collectors (Fig. 5, Fig. 6 and Fig. 7).

6. Conclusions

This paper has discussed the effect of the building integration of several BISS devices. Specifically, two innovative low-cost BIPVT collectors (water and air cooled) prototypes were considered for this study, along with a BIPV panel. One of the main novelties of these prototypes is the low initial cost achieved by the adoption of cost-effective materials. The experimental campaigns, the mathematical models developed and the performance of these devices have been discussed in previous papers. In this paper, an analysis of the passive effects of the prototypes when integrated into the building envelope was presented. The prototypes were purposefully conceived to be integrated into the building envelope. Specifically, a dynamic simulation model,

capable of assessing the performance of the devices coupled to the building was presented. A suitable case study was presented, aimed at investigating the convenience of the presented prototypes from the point of view of their passive effects, and at showing the potentiality of the developed simulation tool. The case study referred to a single-family dwelling unit, located in a multi-storey residential building, where the two prototypes are integrated into the South vertical façade along with those of a BIPV panel. From the analysis, conducted for several weather zones and boundary conditions, a number of interesting outcomes are obtained, such as:

- i) non-negligible energy savings for space heating and cooling can be achieved by adopting the BIPV and the water-cooled BIPVT in cold and mild weather zones;
- ii) air-cooled BIPV can be a good solution, in summer dominated weather zones, to increase PV efficiency while producing hot air without affecting the energy consumption of a building (negligible passive effects);
- iii) in terms of the indoor comfort condition, the best performance is achieved with the BIPV; however interesting benefits are also obtained with the water-cooled BIPVT.

A further case-by-case analysis is required to analyse the convenience of these systems in different applications.

Nomenclature

Symbols

A	Area [m^2]
$BIPV$	Building Integrated Photovoltaic
$BIPVT$	Building Integrated Photovoltaic Thermal
$BISS$	Building Integrated Solar Systems
CDD	Cooling Degree Days
HDD	Heating Degree Days
$HVAC$	Heating Ventilation and Air Conditioning
PV	Photovoltaic
T	Temperature [K][$^{\circ}\text{C}$]
U	Heat loss coefficient [$\text{W}/\text{m}^2\text{K}$]

Subscripts/Superscripts

<i>a</i>	outdoor air
<i>b</i>	back
<i>c</i>	collector
<i>e</i>	edge
<i>air</i>	indoor air
<i>p</i>	absorbing plate

References

- Agathokleous, R., et al. 2019. "Building façade integrated solar thermal collectors for air heating: experimentation, modelling and applications." *Applied Energy* 239: 658-679.
- Barone, G., et al. 2016. "WLHP systems in commercial buildings: A case study analysis based on a dynamic simulation approach." *American Journal of Engineering and Applied Sciences* 9(3): 659-668.
- Barone, G., et al. 2019a. "Photovoltaic thermal collectors: Experimental analysis and simulation model of an innovative low-cost water-based prototype." *Energy* 179: 502-516.
- Barone, G., et al. 2019b. "Experimentation, modelling and applications of a novel low-cost air-based photovoltaic thermal collector prototype." *Energy Conversion and Management* 195: 1079-1097.
- Barone, G., et al. 2019c. "Building energy performance analysis: an experimental validation of an in-house dynamic simulation tool through a real test room." *Energies* 12(21): 4107.
- Boermans, T., et al. 2011. *BPIE - Principles for nearly-zero energy buildings. Paving the way for Effective Implementation of Policy Requirements*. Building Performance Institute Europe.
- Buonomano, A. 2016. "Code-to-Code Validation and Application of a Dynamic Simulation Tool for the Building Energy Performance Analysis." *Energies* 9(4): 301.
- Buonomano, A., et al. 2019. "Building-façade integrated solar thermal collectors: Energy-economic performance and indoor comfort simulation model of a water based prototype for heating, cooling, and DHW production." *Renewable Energy* 137: 20-36.
- Buonomano, A., and A. Palombo. 2014. "Building energy performance analysis by an in-house developed dynamic simulation code: An investigation for different case studies." *Applied Energy* 113: 788-807.
- COST Action TU1205 (BISTS). 2015. *Overview of BISTS state of the art, models and applications*.
- Duffie, J., and W. Beckman. 2013. *Solar engineering of thermal processes* Forth Edition.
- European Council and Parliament. "Directive 2012/27/EU on energy efficiency, amending Directives 2009/125/EC and 2010/30/EU and repealing Directives 2004/8/EC and 2006/32/EC." *Official Journal of the European Union*, Brussels.
- Forzano, C., et al. 2019. "Building integrating phase change materials: A dynamic hygrothermal simulation model for system analysis." *Journal of Sustainable Development of Energy, Water and Environment Systems* 7(2): 325-342.
- Kuznik, F., et al. 2008. "Optimization of a phase change material wallboard for building use." *Applied Thermal Engineering* 28(11-12): 1291-1298.
- Lin, B., and J. Zhu. 2019. "The role of renewable energy technological innovation on climate change: Empirical evidence from China." *Science of The Total Environment* 659: 1505-1512.
- Maurer, C., et al. 2017. "Progress in building-integrated solar thermal systems." *Solar Energy* 154: 158-186.
- Toffler, A. 1980. *The Third Wave*. Morrow.
- US Department of Energy. 2014. *Research & Development Needs for Building-Integrated Solar Technologies*.
energy.gov/sites/prod/files/2014/02/f7/BIST_TechnicalReport_January2014_0.pdf
- van de Bree, A., et al. 2014. *ECOFYS - Role of Building Automation related to Renewable Energy in nZEBs*. E. C. Institute. The Netherlands.
- Wang, X., et al. 2018. "Quantitative analysis of distributed and centralized development of renewable energy." *Global Energy Interconnection* 1(5): 576-584.

A Psycho-Acoustical Experiment Using a Stereo Dipole for Spatial Impression of Music Signals

Benedetto Nastasi – Delft University of Technology, The Netherlands – benedetto.nastasi@outlook.com

Massimiliano Manfren – University of Southampton, United Kingdom – m.manfren@soton.ac.uk

Francesca Merli – University of Bologna, Italy – francesca.merli8@unibo.it

Abstract

Acoustic performance of concert halls and opera houses is usually assessed by measuring the BIRs (Binaural Impulse Responses). Anechoic music convoluted with BIRs constitutes the virtual sound in the way it is played in the sound field, i.e. the room. From BIRs, the IACC (Inter-Aural Cross Correlation) can be computed. This parameter makes it possible to evaluate the spaciousness of the hall. However, the calculation of the IACC value is affected by the convolution technique used as well as the kind of musical motif. For example, in the same concert hall, the BIR provides three different IACC values in the case of three different motifs played in it. This study has conducted a psycho-acoustic experiment by using a virtual sound field representation produced by the stereo dipole technique in a listening room. In the experimental set-up there were two or four loudspeakers, corresponding to the single stereo-dipole or the dual stereo-dipole, respectively. By cancelling the cross-talk pathways (i.e. from left loudspeaker to right ear), the parallel sound presentation creates a 3D sound field for listeners sitting in the target point. The invert Kirkeby method was adopted to determine the inverse filters. Finally, the auralization technique with measured BIRs in theatres was utilized and the virtual sound field was generated in the Arlecchino listening room (Bologna, Italy), a low reverberation room equipped with an Ambisonic system. In the virtual sound field, the BIR was recorded again by the same dummy head used during the measurement in the theatres. The similarity between real and virtual sound fields was evaluated by comparing some acoustic parameters. The stereo-dipole technique demonstrates a good degree of accuracy of the sound field appearance. Moreover, the accuracy of the sound field appearance was analysed using two musical motifs and three musical instruments, comparing the values of the IACC calculated by echoic music with the virtual echoic music.

1. Introduction

In general, acoustical qualities of concert halls and opera houses are evaluated on the basis of BIRs (Binaural Impulse Responses) measured in them. The anechoic music convoluted with BIRs realizes the virtual sound as it was played in the sound field (Shimokura et al., 2011; Tronchin, 2012; Tronchin et al., 2020). The IACC (Interaural Cross Correlation) calculated from the BIRs represents one of the parameters to evaluate the spaciousness of halls. However, the value of the IACC is changed by the convolution technique according to the kind of musical motif used (Farina and Tronchin, 2000; Tronchin, 2013). For example, one BIR measured in the concert hall in Tsuyama (Japan) presents an IACC value of 0.16 whilst the IACC value of the symphony "Royal Pavane" (Orlando Gibbons) convoluted with that BIRs is 0.39 and the IACC value of the symphony "Symphonietta n14 the fourth movement" (Malcolm Arnold) convoluted with that BIR is 0.32. A proper evaluation of acoustic quality is also important for other purposes, such as retrofitting design (Caniato et al., 2019; Fabbri et al., 2014; Fabbri and Tronchin, 2015; Mancini et al., 2017; Tronchin et al., 2014, 2016 and 2018; Tronchin and Fabbri, 2017). The aim of this study is to conduct the psycho-acoustical experiment by using a virtual sound field representation by a stereo dipole technique in a listening room. The stereo-dipole technique is realized using two or four loudspeakers (corresponding to single stereo-dipole or dual stereo-dipole). The calculation of proper inverse filters, by means of the Kirkeby method, makes it possible to reproduce the virtual sound field by means of the (dual) stereo dipole method, avoiding cross-talk paths. In this study,

the psychoacoustic experiments were conducted using the stereo-dipole technique, considering measured BIRs in theatres, virtually reproduced in the Arlecchino listening room located at the University of Bologna, Italy. This listening room was previously redecorated and equipped with the Ambisonic reproducing system. After having calculated the inverse filters, the virtual sound field of the rooms was obtained and the BIRs were recorded again by the same dummy head used during the measurement in the theatres. The similarity between the real and the virtual sound fields was evaluated by comparing some acoustical parameters (SPL, EDT, IACC etc) calculated using real and virtual BIRs. These acoustical parameters were compared and the results suggest that the stereo-dipole has a good degree of accuracy of the sound field appearance (Farina and Tronchin, 2005 and 2013; Tronchin and Coli, 2015). In this further study, we examine the accuracy of the sound field appearance using some musical motifs, comparing the values of the IACC calculated by “echoic music” and “virtual echoic music”. The echoic music indicates the anechoic musical signal convoluted with a BIR measured in a hall, while the virtual echoic music indicates the recorded echoic musical signal by means of the single stereo-dipole. Using MIDI, the anechoic musical signals are composed by considering two different melodies and three kinds of musical instruments. The IACC of a long continuous music motif was calculated by sliding the fixed integration interval along time (Tronchin and Coli, 2015).

2. Materials and Methods

2.1 IACC (Interaural Cross Correlation)

When sound is propagated from a sound source, the signals received at the left and right ears of a listener are different. Interaural cross-correlation function (IACF) represents the interdependence between left (right) signal at the origin and the right (left) signal at a delay of 1ms. The IACC is one maximum value in the IACF. The IACC can be expressed by

$$IACC = \left| \frac{\int_{-T}^T p_l(t) p_r(t - \tau) dt}{\sqrt{\int_{-T}^T p_l^2(t) dt \int_{-T}^T p_r^2(t) dt}} \right|_{max} \quad (1)$$

where $2T$ is the integral interval, τ is the time delay, and $p_l(t)$ and $p_r(t)$ are signals obtained at left and right ears. In the case of evaluating a sound field, the $p_l(t)$ and $p_r(t)$ are corresponding to the impulse responses recorded at the left and right ear positions of a dummy head.

2.2 Acoustical Parameters Based on the IACC

In some research, the IACC has been modified based on the auditory nerve process or the acoustical characteristics of the musical performances in a hall.

Ando (1998) proposed that the IACF should be calculated with $p_l(t)$ and $p_r(t)$ which are obtained after passing through the A-weighting filter, which corresponds approximately to the sensitivity of the human ear (Tronchin, 2013). These calculative steps are based on the auditory-brain model for subjective responses. Unlike the spectral filtering, the $IACC_E$ is calculated in the limited integration time in 80 ms (Shimokura et al., 2011). The early part of the signal, such as EDT (Early Decay Time), is often evaluated to be important because most symphonic compositions include successive notes changing rapidly. The $IACC_{E3}$ is taken into account both for the spectral and temporal limitation. A signal is divided into one-octave spectral bands, and the values of the IACC are led from each band-passed signal limited to an integration time of 80 ms. The $IACC_{E3}$ is the IACC averaged with the results of the bands whose center frequencies are 0.5, 1, and 2 kHz because the spectral energy of a symphony distributes mainly around 0.5-2 kHz. To evaluate concert halls or musical instruments and opera houses acoustically, Farina utilized the $IACC_{E5}$, while Hidaka and Ando utilized the $IACC_{E3}$ (Ando, 1998; Farina, 2001; Farina et al., 1998). As a result, a correlation between $IACC_E$ and subjective evaluation of the halls was found by Farina. In another research, the $IACC_{E3}$ was found with a high correlation with a rank order of the halls' acoustical qualities by Hidaka et al. This controver-

sial results can be explained by several reasons (e.g. diverse assessments or subjects). However, it is noteworthy that the IACC values chosen by them were computed referring to the BIRs of different frequency ranges.

2.3 Acoustical Characteristic of a Signal

Ando proposed τ_1 and τ_e to determine temporal acoustical characteristics of musical performances and adopted them for virtual sound reconstructions (Ando, 1998; Tronchin and Knight, 2016). A normalized autocorrelation function (ACF) was used to extract τ_1 and τ_e as follows:

$$\phi(\tau) = \frac{\Phi(\tau)}{\Phi(0)} \quad (2)$$

Where

$$\Phi(\tau) = \frac{1}{2T} \int_{-T}^T p'(t)p'(t+\tau)dt \quad (3)$$

$2T$ is the integral interval, τ is the time delay, and $p'(t)$ is an original acoustical signal after passing through the A-weighting filter. τ_1 is a delay time of the first positive peak, and τ_e is an effective duration of the ACF, defined by the delay time where the envelope of the normalized ACF becomes and, then, remains smaller than 0.1 as depicted in Fig. 1. The value of τ_1 indicates the pitch of the signal, and the value of τ_e represents repetitive features, which corresponds to different kinds of musical instruments, tempo of the motif and the pattern of playing, such as legato or staccato. Generally, a fast tempo or a snap playing makes the τ_e shorter.

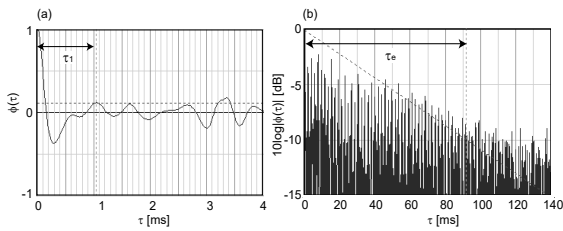


Fig. 1 – (a) Definition of τ_1 in normalized ACF; (b) Definition of τ_e in normalized ACF in logarithm scale

During a performance of music, the acoustic characteristics (e.g. pitch and tempo) varies as a function of time. For observing the fluctuation of acoustical characteristics, it is necessary to run the ACF. The running ACF is defined by:

$$\phi_p(\tau; t, T) = \frac{\Phi_p(\tau; t, T)}{[\Phi_p(0; t, T)\Phi_p(0; \tau + t, T)]^{1/2}} \quad (4)$$

Where

$$\Phi_p(\tau; t, T) = \frac{1}{2T} \int_{t-T}^{t+T} p'(s)p'(s+\tau)ds \quad (5)$$

After passing, the normalized ACF of $p'(t)$ was calculated in the range of integral interval $2T$ once passed through the A-weighting filter. $2T$ slides along the duration of the motif. The structure of the running ACF is reported in Fig. 2.

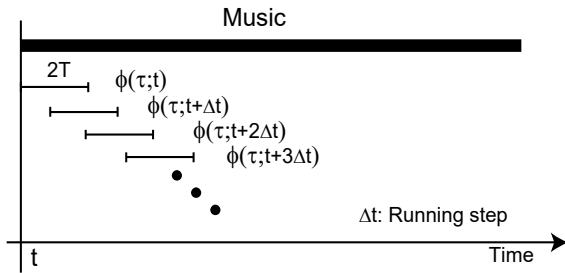


Fig. 2 – Running ACF of long musical motif

2.4 3D Sound Representation by Stereo-Dipole

2.4.1 BIR of the theatre

In this study, we utilize two kinds of BIR (“BIRn1” and “BIRn2”) measured in the traditional Italian opera house, Teatro Nuovo in Spoleto (Italy). In the acoustical measurement, the sound source and the receivers are an omnidirectional speaker (LookLine dodecahedral configuration) and a dummy head (Sennheiser), respectively. The loudspeaker was located in the two positions of the stage; one near (BIRn1) and another one far (BIRn2) from the frontal edge of the stage, and the dummy head was located in one position in the middle of the stalls. The values of the IACC of all-passed BIRn1 and BIRn2 are 0.39 and 0.26, and IACC_{E3} of the BIRs are 0.32 and 0.24, respectively.

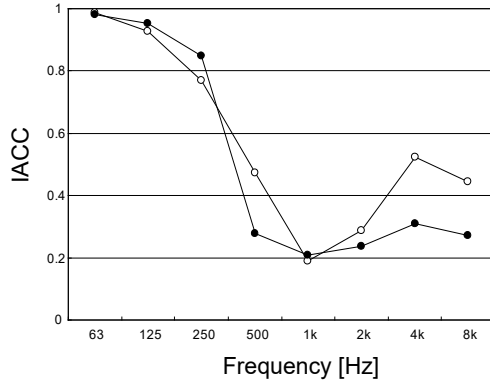


Fig. 3 – IACC of BIRn1 (○) and BIRn2 (●) as a function of frequency band

Fig. 3 shows the spectral characteristics of the IACC in these BIRs.

2.4.2 Anechoic musical motifs

Three kinds of anechoic musical motifs were used: “Melody A by trumpet”, “Melody A by piano”, and “Melody B by organ”. The scores of Melody A and Melody B are shown in Fig. 4. These anechoic musical motifs were generated by MIDI. The duration of the musical motifs is 30 s.



Fig. 4 – (a) Scores of Melody A (b) Scores of Melody B

To observe the acoustical characteristics of these anechoic musical signals, the running ACF calculation (see Equations (4) and (5)) was carried out along the signal duration. Fig. 5 shows the changes of τ_1 and τ_e in the early 5 s. The integral interval ($2T$) and the running step are 1 s and 0.1 s, respectively. Although the trends of “Melody B by piano” were included in Fig. 5 for comparison reasons, this musical motif is not employed in this stereo-dipole examination.

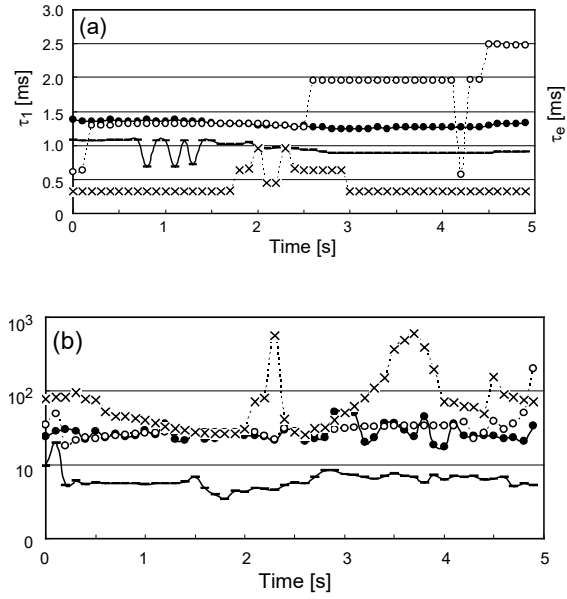


Fig. 5 – (Different symbols indicate different musical motifs: (-): Melody A by trumpet; (●): Melody A by piano; (x): Melody B by organ; (○): Melody B by piano. (a) Acoustical parameters for 5 s. τ_1 (b) Acoustical parameters for 5 s. τ_e

It has to be noticed that τ_1 is affected by the difference in musical instruments (trumpet, organ or piano) and τ_e is mainly affected by the difference in melody (Melody A or B).

Since both τ_1 and τ_e changes dynamically over time as shown in Fig. 5, it is not easy to determine a unique representative value to express distinctly the differences between these musical motifs. Particularly, the values of τ_e increase to a high value, so that the mean value of τ_e is meaningless. In this study, the 300 values obtained by the running ACF in a rate of 0.1 s along the duration of 30s are converted into the histogram, and the representative values are determined by the 50 % probability of cumulative frequency. These values are termed “ τ_1 (50%)” and “ τ_e (50%)”, and they are listed in Table 1.

Table 1 – Anechoic musical motifs and their τ_1 (50%) [ms] and τ_e (50%) [ms]

Musical motif	τ_1 (50%) [ms]	τ_e (50%) [ms]
Melody A by piano	1.33	246.5
Melody A by trumpet	0.88	54.9
Melody B by organ	0.46	526.7
Melody B by piano	1.94	308.8

2.5 Procedure of Dual Stereo-Dipole

2.5.1 Measurement in Arlecchino listening room

The single stereo-dipole representations were carried out in an Arlecchino listening room at University of Bologna (Italy). Two loudspeakers (Montarbo W400A) were located in front of a dummy head (Sennheiser) as reported in Fig. 6, whereas the other two loudspeakers (Montarbo W400A) were located to the rear of it. To obtain the BIRs in the listening room, a log swept-sine signal was generated by Adobe Audition and was presented by the two loudspeakers alternately.

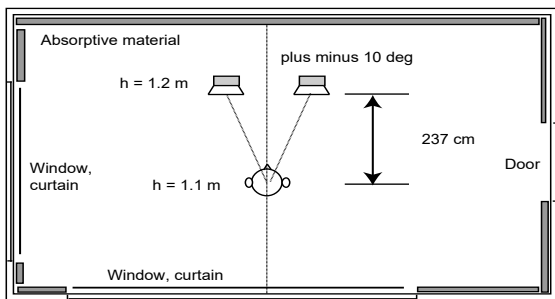


Fig. 6 – Arrangement of two loudspeakers and a dummy head in the Arlecchino listening room

After deconvolution of the signals recorded by the dummy head, the impulse response of the listening room can be obtained respectively for the left and right loudspeakers. The envelopes of impulse responses are smoothed in order to remove extra reflections and to leave only the direct sound.

2.5.2 Generation of cross-talk canceling filter

The smoothed impulse response was converted into cross-talk cancelling filter by using the plug-in of “Invert Kirkeby”¹ in Adobe Audition. Table 2

shows the calculation conditions of the Invert Kirkeby plug-in.

Table 2 – Properties of Invert Kirkeby plug-in

Filter length [sample]	2048
IN-band parameter	1
OUT-band parameter	10
Lower cut freq. [Hz]	80
High cut freq. [Hz]	16000
Width	0.33

2.5.3 Presentation

The “anechoic music” was convoluted with the impulse responses of the theatres. Conversely, the “echoic music” was convoluted again by the cross-talk cancelling filters based on the impulse response of the listening room. The resulted signals were presented by the two loudspeakers at the same time, and the sounds were recorded by the dummy head under almost the same conditions as when the impulse response of the Arlecchino listening room was measured. The recorded musical motifs are defined by “virtual echoic music”.

3. Results

During a musical performance, the IACC values vary as a function of time. The observation of the IACC fluctuation is helped by running IACF like the running ACF (Farina and Tronchin, 2013; Tronchin, 2013). Then, the IACF was computed in the range of integral interval $2T$ (1 s) that is sliding (step: 0.1 s) along the duration of the motif (30 s) after passing through the A-weighting filter. Fig. 7 compares the temporal fluctuation of the IACC produced by the running IACF in the cases of the echoic music (thick line) and the virtual echoic music (thin line). For *Melody A* by piano, the values of IACC are similar among the echoic and virtual echoic music, although it is difficult to observe the synchronous change.

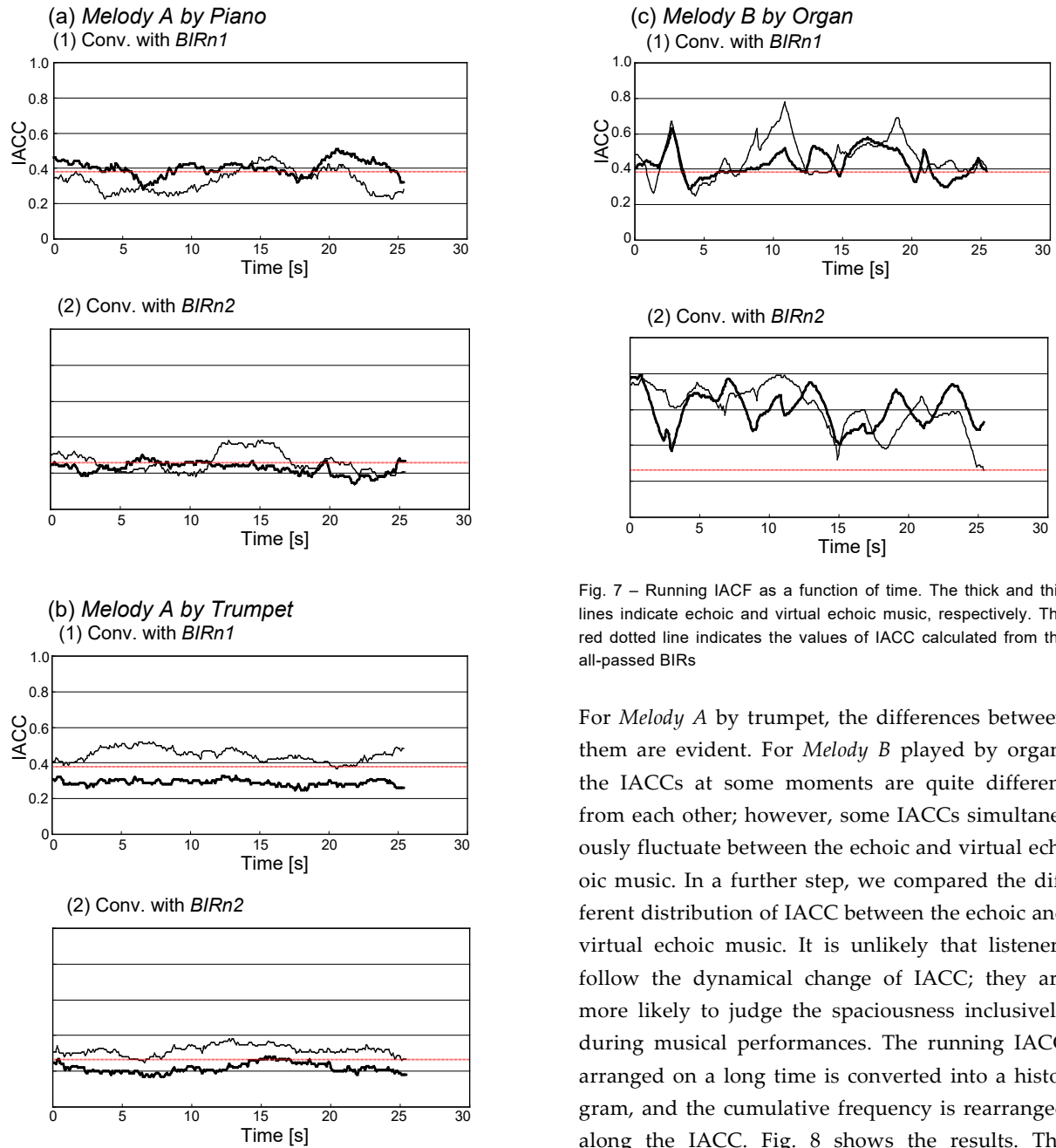


Fig. 7 – Running IACF as a function of time. The thick and thin lines indicate echoic and virtual echoic music, respectively. The red dotted line indicates the values of IACC calculated from the all-passed BIRs

For *Melody A* by trumpet, the differences between them are evident. For *Melody B* played by organ, the IACCs at some moments are quite different from each other; however, some IACCs simultaneously fluctuate between the echoic and virtual echoic music. In a further step, we compared the different distribution of IACC between the echoic and virtual echoic music. It is unlikely that listeners follow the dynamical change of IACC; they are more likely to judge the spaciousness inclusively during musical performances. The running IACC arranged on a long time is converted into a histogram, and the cumulative frequency is rearranged along the IACC. Fig. 8 shows the results. The distribution of IACC is close when the sound source is *Melody B* by organ. On the other hand, in the case of *Melody A* by trumpet, the distributions of IACC are more different from each other. Moreover, the results show that the case of *BIRn2* can represent the vertical echoic music more accurately than the case of *BIRn1*.

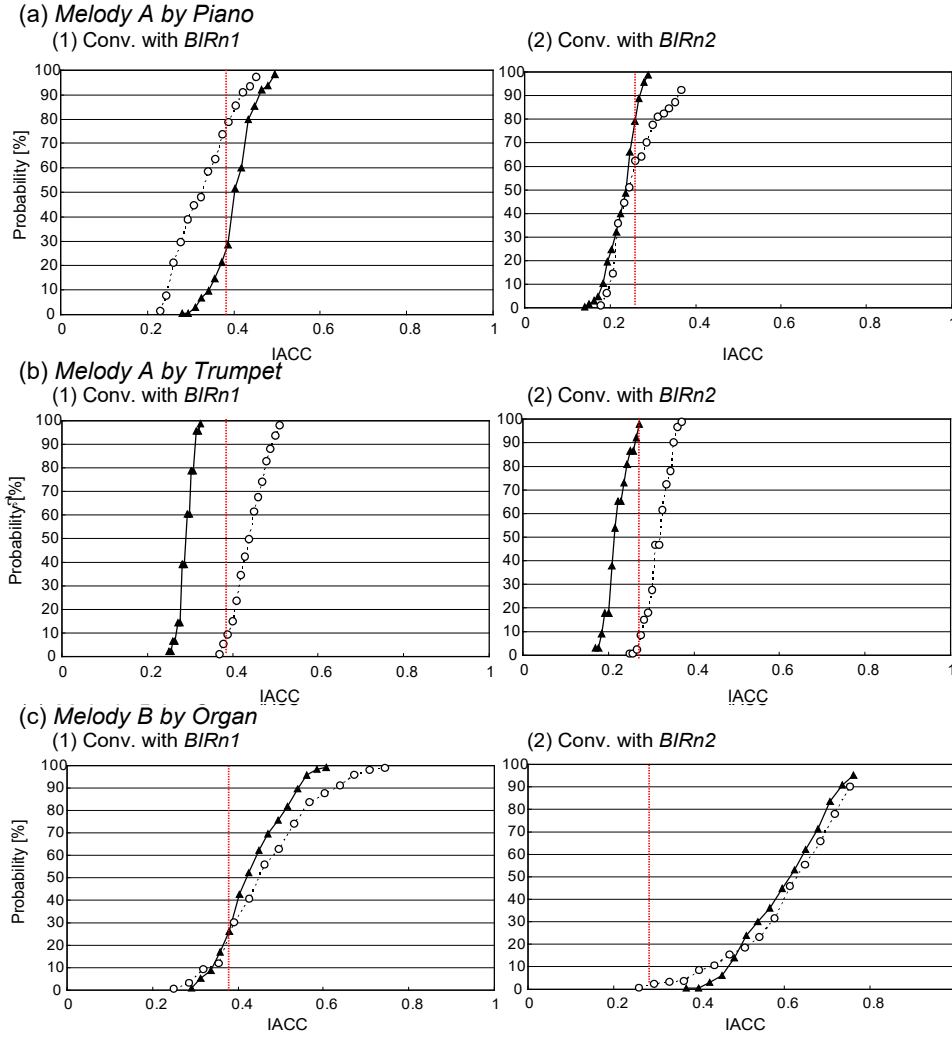


Fig. 7 Cumulative frequencies as a function of IACC of the echoic music (\blacktriangle) and the virtual echoic music (\circ). The red dotted line indicates the values of IACC calculated from the all-passed BIRs

In this study, the gap of IACC between the echoic and virtual echoic music was evaluated with

$$Error = \int_1^{100} |IACC_{echoic}(x) - IACC_{vecho}| \quad (6)$$

where $IACC_{echoic}(x)$ and $IACC_{vechoic}(x)$ are the values of the IACC calculated from the echoic music and the virtual echoic music in the probability x %. The errors can be seen in Table 3. It is important that the accuracy of the stereo-dipole is dependent not only on the kinds of BIRs, but also on the kinds of musical motifs. Although the kind of melody is the same, the errors in *Melody A* by piano and *Melody A* by trumpet are different. Although the kinds of motif are not enough to support the statistical sig-

nificance, the error values have a good correlation with τ_e (50%) extracted from anechoic musical motifs.

Table 3 – Errors of IACC arranged in terms of BIR and musical motif

Musical motif	BIRn1	BIRn2
Melody A by piano	0.07	0.03
Melody A by trumpet	0.16	0.10
Melody B by organ	0.04	0.03

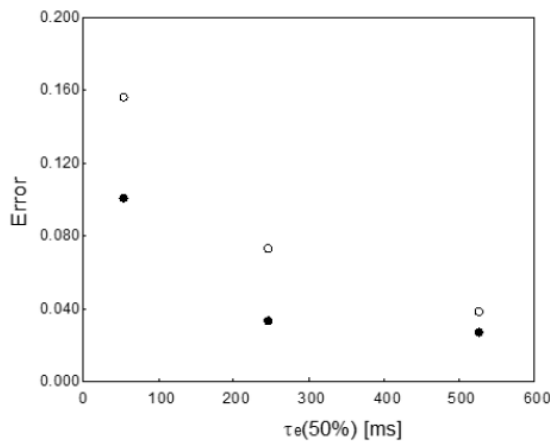


Fig. 8 – Errors of IACC as a function of $\tau_e(50\%)$ of anechoic musical motif

4. Conclusion

Ando developed a running ACF and IACF calculation of long continuous signal and proposed the effective duration, τ_e , extracted from the ACF of an anechoic musical signal to quantify the acoustical characteristics of it (Ando, 1998). These studies commonly emphasize the usefulness of τ_e in blending musical motif and sound field. In this study, three kinds of anechoic musical signals were employed to examine the accuracy of sound field representation by the stereo-dipole with a view to conducting the subjective experiment judging spatial impression of echoic musical motifs. The error of the IACC ranges from 0.03 to 0.16; this result seems to suggest that the stereo-dipole systemized in the listening room can reproduce the virtual sound field of the opera house, Teatro Nuovo di Spoleto, with a high correlation. The accuracy of results is dependent both on the kinds of BIR and on the kinds of the musical motif. It is interesting that the anechoic musical signal with longer τ_e improves the accuracy of stereo-dipole representation.

Acknowledgement

The authors wish to thank Ryota Shimokura and Lamberto Tronchin, for their collaboration during the experimental measurements

References

- Ando, Y. 1998. *Architectural Acoustics, Blending Sound Sources, Sound Fields, and Listeners*. AIP Press/Springer-Verlag, New York.
- Caniato, M., and A Gasparella. 2019. "Discriminating People's Attitude towards Building Physical Features in Sustainable and Conventional Buildings." *Energies* 12(8):1429. doi:10.3390/en12081429
- Fabbri, K., L. Tronchin and V. Tarabusi. 2014. "Energy retrofit and economic evaluation priorities applied at an Italian case study." *Energy Procedia* 45: 379-384. doi:10.1016/j.egypro.2014.01.041
- Fabbri, K., and L. Tronchin. 2015. "Indoor environmental quality in low energy buildings" *Energy Procedia* 78: 2778-2783. doi: 10.1016/j.egypro.2015.11.625
- Farina, A., A. Langhoff, and L. Tronchin. 1998. "Acoustic Characterisation of "virtual" Musical Instruments: Using MLS Technique on Ancient Violins." *Journal of New Music Research* 27(4): 359-379. doi:10.1080/09298219808570753
- Farina, A., and L. Tronchin. 2000. "On the "Virtual" Reconstruction of Sound Quality of Trumpets." *Acustica* 86(4): 737-745.
- Farina, A. 2001. "Acoustical quality of theatres: correlations between experimental measurements and subjective evaluations." *Applied Acoustics* 6: 889-916.
- Farina, A., and L. Tronchin 2005. "Measurements and reproduction of spatial sound characteristics of auditoria." *Acoustical Science and Technology* 26(2): 193-199. doi.org/10.1250/ast.26.193
- Farina, A., and L. Tronchin. 2013. "3D Sound Characterisation in Theatres Employing Microphone Arrays." *Acta Acustica United with Acustica* 99(1): 118-125. doi:10.3813/AAA.918595
- Mancini, F., C. Clemente, E. Carbonara, and S. Fraioli. 2017. "Energy and Environmental Retrofitting of the University Building of Orthopaedic." *Energy Procedia* 126: 195-202. doi: 10.1016/j.egypro.2017.08.140
- Shimokura, R., L. Tronchin, A. Cocchi, and Y. Soeta. 2011. "Subjective Diffuseness of Music Signals Convolved with Binaural Impulse

- Responses." *Journal of Sound and Vibration* 330(14): 3526-3537. doi:10.1016/j.jsv.2011.02.014
- Tronchin, L. 2012. "The Emulation of Nonlinear Time-Invariant Audio Systems with Memory by Means of Volterra Series." *AES: Journal of the Audio Engineering Society* 60(12): 984-886.
- Tronchin, L. 2013a. "On the Acoustic Efficiency of Road Barriers: The Reflection Index." *International Journal of Mechanics* 7(3): 318-326.
- Tronchin, L. 2013b. "Francesco Milizia (1725-1798) and the Acoustics of His Teatro Ideale (1773)." *Acta Acustica United with Acustica* 99(1): 91-97. doi:10.3813/AAA.918592
- Tronchin, L., M.C. Tommasino and K. Fabbri. 2014. "On the cost-optimal levels of energy-performance requirements for buildings: A case study with economic evaluation in Italy." *International Journal of Sustainable Energy Planning and Management* 3: 49-62. doi:10.5278/ijsepm.2014.3.5
- Tronchin, L., and V. L. Coli. 2015. "Further Investigations in the Emulation of Nonlinear Systems with Volterra Series." *AES: Journal of the Audio Engineering Society* 63(9): 671-683. doi:10.17743/jaes.2015.0065
- Tronchin, L., and D. J. Knight. 2016. "Revisiting Historic Buildings through the Senses Visualising Aural and Obscured Aspects of San Vitale, Ravenna." *International Journal of Historical Archaeology* 20(1): 127-145.
- Tronchin, L., M. Manfren and L C. Tagliabue. 2016. "Optimization of building energy performance by means of multi-scale analysis – Lessons learned from case studies" *Sustainable Cities and Society* 27:296-306. doi: 10.1016/j.scs.2015.11.003
- Tronchin, L., and K. Fabbri. 2017. "Energy and Microclimate Simulation in a Heritage Building: Further Studies on the Malatestiana Library." *Energies* 10(10). doi:10.3390/en10101621
- Tronchin, L., M. Manfren and P. A. James. 2018. "Linking design and operation performance analysis through model calibration: Parametric assessment on a Passive House building." *Energy* 165(A): 26-40. doi:10.1016/j.energy.2018.09.037
- Tronchin, L., M. Manfren, V. Vodola. 2020a. "The carabattola - vibroacoustical analysis and intensity of acoustic radiation (IAR)." *Applied Sciences* 10(2), 641.
- Tronchin, L., M. Manfren, V. Vodola. 2020b. "Sound characterization through intensity of acoustic radiation measurement: A study of persian musical instruments." *Applied Sciences* 10(2), 633.
- Tronchin, L., F. Merli, M. Manfren. B. Nastasi. 2020c. "The sound diffusion in Italian Opera Houses: Some examples." *Building Acoustics*, in press. doi:10.1177/1351010X20929216
- Tronchin, L., F. Merli, M. Manfren. B. Nastasi. 2020d. "Validation and application of three-dimensional auralisation during concert hall renovation." *Building Acoustics*, in press. doi:10.1177/1351010X20926791

On the Use of 3D Auralisation to Evaluate Room Acoustic Enhancement in Auditorium Restoration

Benedetto Nastasi – Delft University of Technology, The Netherlands – benedetto.nastasi@outlook.com

Massimiliano Manfren – University of Southampton, United Kingdom – m.manfren@soton.ac.uk

Francesca Merli – University of Bologna, Italy – francesca.merli8@unibo.it

Vincenzo Vodola – University of Bologna, Italy – vincenzo.vodola2@unibo.it

Abstract

The acoustic quality in auditorium and concert halls is normally evaluated by the measurements of Impulse responses (monaural, binaural or even MIMO). The subjective evaluation is often obtained by convolving anechoic music with the measured IRs. The psycho-acoustical experiment is achieved using a virtual sound field representation. At the University of Bologna, the listening room Arlecchino includes Ambisonics and stereo dipole techniques for playback. In this paper, two different Italian opera houses and two Japanese concert halls were analysed. They were the Teatro Nuovo in Spoleto (Italy), the Teatro Alighieri in Ravenna (Italy), the Kirishima International Musical Hall in Kagoshima (Japan), and the Tsuyama Musical Cultural Hall in Okayama (Japan). The similarity between real and virtual sound fields, obtained with stereo dipole technique, was evaluated by comparing different acoustic parameters calculated by real and virtual sound fields, in the four halls in different designed configurations. Finally, the stereo dipole technique was added to the ambisonic methodology to reproduce the sound fields for the psycho-acoustical experiment. The dual stereo-dipole technique using two kinds of cross-talk cancelling filters can be one of the solutions for improving the acoustical quality of home theatre.

1. Introduction

Refurbishing theatres, like other historical buildings, can be challenging environments for several reasons (Fabbri et al., 2014; Fabbri and Tronchin, 2015; Tronchin and Knight, 2016; Tronchin et al., 2018), even though the main use of theatre is for acoustic performances. In this

process, virtual sound fields can firstly help in the design process in order to reach the intended standards and secondly make it possible to test technological solutions. Two theatres are studied here with two concert halls.

1.1 Teatro Nuovo in Spoleto

The Teatro Nuovo in Spoleto opened in 1864 in spite of some discussion; the plan of the stalls is horseshoe shaped in the style of the classical Italian opera house, and the frontage of the four box rows or orders faces the stalls (Farina and Tronchin, 2005 and 2013; Tronchin, 2013). A loggia or a balcony crowned the last box order, and the ceiling is connected to it by a kind of coupling called “Vanvitelli” style or “Umbrella”, typical in that period. Stalls, boxes and loggia can contain a maximum of 800 people. Changes to the Teatro Nuovo have been carried out on different occasions; the most striking change was the reduction of the stage, which enlarged the orchestra place, in 1914. Such a modification has most likely damaged the good balance between the singer on the stage and the orchestra in the pit: Furthermore, some musical instruments, recently studied (Farina et al., 1998; Farina and Tronchin, 2000; Tronchin, 2012; Tronchin and Coli, 2015; Tronchin et al., 2020) now play under a flat reflecting surface, which means that some sound reaches the stalls more than 0.5 seconds later than the direct sound. In addition to these modifications, some other changes have been carried out. In 1933 all the original floors were renewed because of the new building safety regulations and consequently, the stage was dismantled to change its structure almost completely

by substituting steel for wood. In 1950, work started on the orchestra pit in order to extend its proper space in depth under the stage. More recently, the Regional Authorities have approved further restoration work in order to make some acoustical improvements in the theatre.



Fig. 1 – View of Teatro Nuovo in Spoleto, Italy

1.2 Teatro Alighieri in Ravenna

In 1838 the Municipality of Ravenna decided to build a new opera house, in order to replace the Teatro Comunitativo. The young Venetian architects Tomaso e Giovan Battista Meduna were commissioned to design the new opera house. They proposed a theatre not very different from the Venetian Teatro la Fenice, well known for its acoustics (Tronchin and Farina, 1997), which had opened just a couple of years earlier, after the burning of the first theatre designed by Selva (1795). However, the original design slightly changed a few years later, and in 1852 the Teatro Alighieri opened. The main hall contains many paintings of Venetian artists and golden stuccos. In 1929 the gallery replaced the balcony in the fourth order, and the stage was also remodelled, enlarging the stalls. The chandelier was added in 1960. One of the most relevant factors of the theatre is the cavity located below the orchestra pit. It is one of the few cavities not dismantled in other Italian styled opera houses during the 20th Century, and it was recognized as being responsible of some modification in strength and reverberation time during recent acoustic measurements in this theatre, which also involved other aspects (Caniato et al., 2015 and 2016; Tronchin, 2013).

1.3 Kirishima International Musical Hall

The Kirishima International Musical Hall was opened in 1994 in Kagoshima (Japan). The shape of stalls is based on the shoe-box style. However, the arrangements of the lateral walls are uneven like a natural leaf. The reflections which are returned from these lateral walls maintain the same angle of incidence when they arrive at listeners. This makes the value of the IACC (Inter Aural Cross Correlation) low. The audience area is covered by the ceiling: the shape of this ceiling is not unlike the inverted hull of a ship.



Fig. 2 – View of Teatro Alighieri in Ravenna, Italy

The enclosures realize the well-diffused sound field. There are 518 seats in the stalls and 252 seats in the gallery. The reverberation time is from 1.6 to 1.8 s.

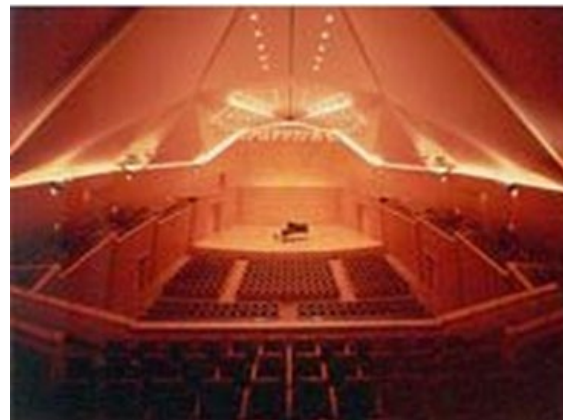


Fig. 3 – View of Kirishima International Musical Hall, Japan

1.4 Tsuyama Musical Cultural Hall

Tsuyama Musical Cultural Hall was opened in Okayama (Japan) in 1999. Following the concept of the “acoustics of the forest”, a large number of pillars are arranged in rows in front of the lateral walls. The diffused sounds would be similar to those which could be found in the forest. In the ceiling, the floating reflective boards are hung by wire ropes. There are 600 seats. The reverberation time is around 1.6 s.



Fig. 4 – View of Tsuyama Musical Cultural Hall, Japan

2. Materials and Methods

Acoustical measurements were taken by arranging source and receivers and the procedure of stereo-dipole was applied in 3 steps.

2.1 General Measurement Conditions

To obtain binaural and b-format impulse responses, a logarithmically sine-swept FM chirp was generated by a PC. The sine signal with exponential varied frequency was defined by a starting frequency 40 Hz, an ending frequency 20k Hz and a total duration ranging from 20 to 30 s, as normally measured in several acoustic applications (Caniato et al., 2016; Tronchin, 2013).

The sound source and the receiver were employed by an omnidirectional, pre-equalized loudspeaker (Look Line) and a dummy head (Neumann KU100). The waveforms were acquired by means of a multi-channel soundboard and stored at 96 kHz and 32 bits. The height of the source was 1.4 m when placed on the stage, and 1.2 m when placed in the orchestra pit. It was located 2 m from

the edge of the stage, whereas in the pit, it was 3.6 m from the pit fence. The height of the microphones was 1.1 m from the floor to ear. In the box, the microphones were brought near to the opening and chairs were moved close to the door. The direction the dummy head was facing was adjusted to the source position in each measurement.

2.2 The Layout of the Sources and Receivers

The measured impulse responses analysed in this paper are four for Teatro Nuovo, three for Teatro Alighieri, one for Kirishima musical hall, and one for Tsuyama musical hall. The arrangements of the sources and receivers and the names referred to in the following sections are shown in Table 1.

Table 1 – Kinds of measured impulse responses

Auditorium	Source	Receiver	Name
Teatro Nuovo di Spoleto	stage	stalls	SPO_ss
	pit	stalls	SPO_ps
	stage	box	SPO_sb
Teatro Alighieri di Ravenna	pit	box	SPO_pb
	stage	stalls	RAV_ss
	stage	box1	RAV_sb1
Kirishima musical hall	stage	box2	RAV_sb2
	stage	stalls	KIR_ss
Tsuyama musical hall	stage	stalls	TSU_ss

2.3 Stereo-Dipole 1: Measurement in Arlecchino Listening Room

The single and dual stereo-dipole representations were carried out in an Arlecchino listening room in Bologna (Italy), which has been developed to recreate other indoor environmental conditions (Caniato et al., 2019; Tronchin and Fabbri, 2017). The property of the swept-sine is shown in Table 2.

Table 2 – Properties of swept sine signal

Variable	Value
Start freq. [Hz]	50
End freq. [Hz]	18000
Duration [s]	30
Amplitude	8192
Sampling [Hz]	44100
Scale	32-bit

Two loudspeakers (Montarbo W400A) are located in front of a dummy head (Neumann) and the other two loudspeakers (Montarbo W400A) are located to the rear of it as shown in Figs 5 and 6.

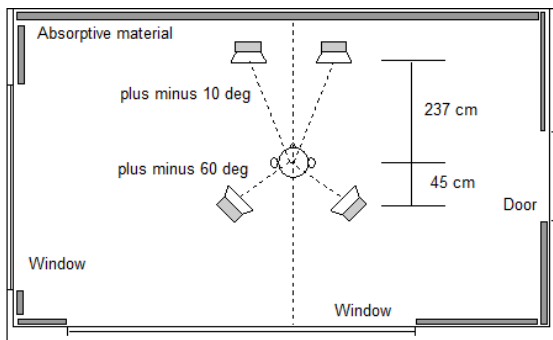


Fig. 5 – Plan of Arlecchino listening room

To obtain the BIR in the listening room, a log swept-sine signal is generated by Adobe Audition and is presented by the four loudspeakers alternately. After de-convolution of the signals recorded by the dummy head, the impulse response of the listening room can be obtained respectively for the front and rear loudspeakers. The envelopes of impulse responses are smoothed in order to cancel extra reflections and only the direct sound remains.

2.4 Stereo-Dipole 2: Generation of Cross-Talk Cancelling Filter

The smoothed impulse response is converted into cross-talk cancelling filter by using the plug-in of “Invert Kirkeby” in Adobe Audition. In this examination, the two kinds of cancelling filters are generated for the frontal loudspeakers and for the rear loudspeakers (Shimokura et al., 2011). Table 3 shows each calculation condition of the Invert Kirkeby plug-in.

Table 3 – Properties of Invert Kirkeby plug-in for Frontal and Rear cancelling filters

Variable	Value
Filter length [sample]	2048
Lower cut freq. [Hz]	80
IN-band parameter	1
High cut freq. [Hz]	16000
OUT-band parameter	10
Width	0.33

Fig. 7 shows the spectral characteristics of the two cancelling filters.

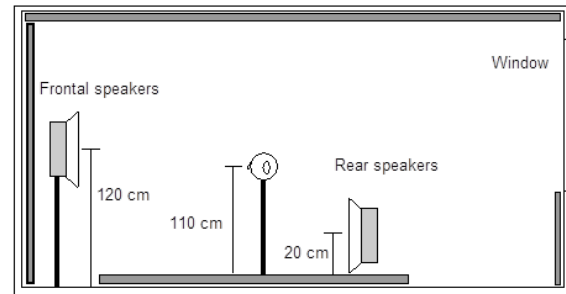


Fig. 6 – Section of Arlecchino listening room

Since the Arlecchino listening room is not a perfectly anechoic room, it is difficult to generate the cross-talk cancelling filters with linear spectral characteristics from the impulse responses in it. The two cancelling filters are calculated to lower the spectral gaps, as shown in Fig. 7.

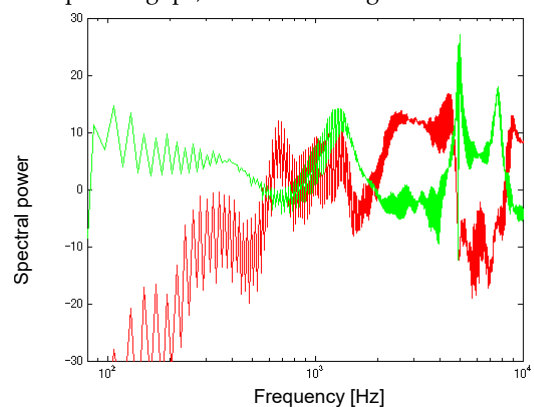


Fig. 7 – Spectral powers of front cancelling filter (red) and rear cancelling filter (green)

2.5 Stereo-Dipole 3: Presentation

The anechoic swept-sine signal was convoluted with the impulse responses of the theatres. The echoic swept-sine signals were convoluted again by the cancelling filters for the frontal and rear loudspeakers. The resulted signals were presented by the frontal and rear loudspeakers at the same time, and the sounds were recorded by the dummy head under similar conditions to those in the Arlecchino listening room when the impulse response was measured. Finally, by de-convoluting the recorded signal, an impulse response is generated. In this study, it is called “virtual IR” in order to distinguish the “real IR” that was measured in the theatres. A similar procedure was also applied for the Ambisonic playback system, but the results are not presented in this paper.

3. Results

To confirm the accuracy of the sound field representation by the stereo-dipole technique, in this paper the real IR and virtual IR were compared in terms of these acoustical parameters: SPL (Sound Pressure Level), EDT (Early Decay Time).

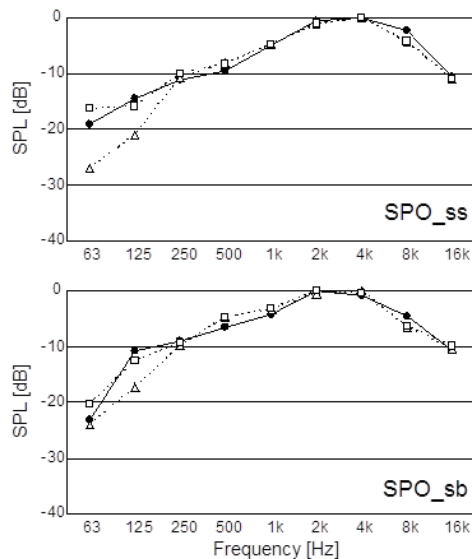


Fig. 8 – SPL: real IR (●), virtual IR by single stereo-dipole (Δ), virtual IR by dual stereo-dipole (◻): Spoleto 1/2

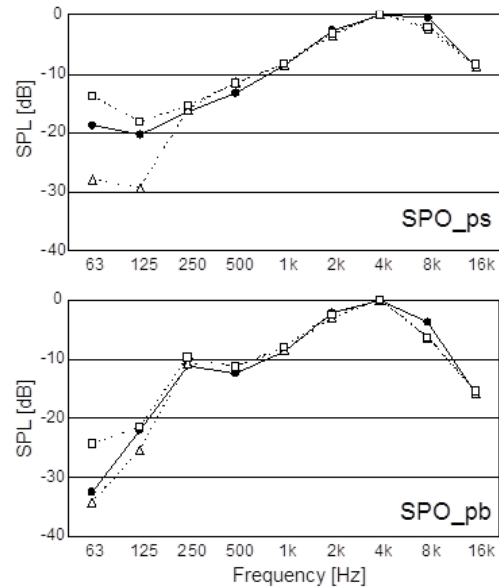


Fig. 9 – SPL as a function of band frequency: Spoleto 2/2

The values are the averaged SPL and EDT calculated from the left and right impulse responses. Only in the case of KIR_ss, is the data of the virtual IR by dual stereo-dipole a shortage. Figs 8 to 13 show the SPLs calculated from the real IR and the virtual IR by single and dual stereo-dipoles. The virtual IR by single stereo-dipole is obtained by using only the frontal loudspeakers.

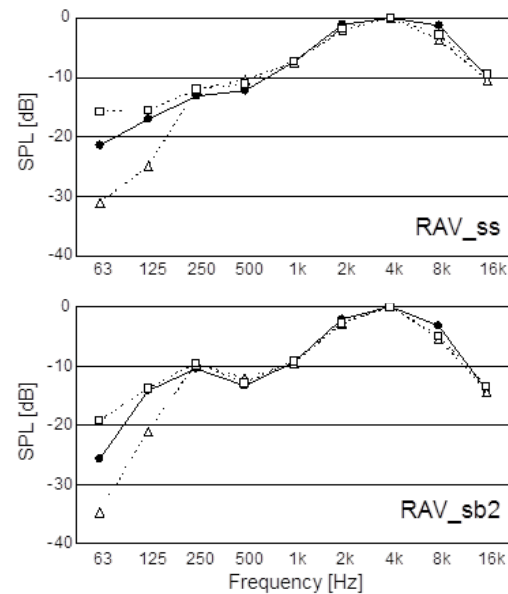


Fig. 10 – SPL as a function of band frequency: Ravenna 1/2

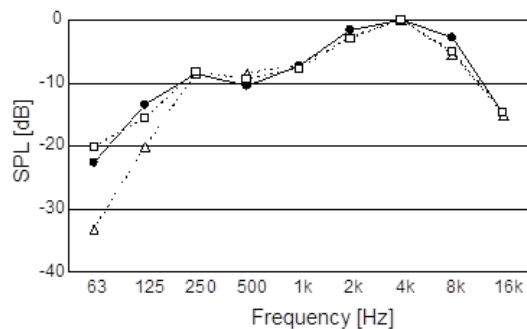


Fig. 11 – SPL as a function of band frequency: Ravenna 2/2

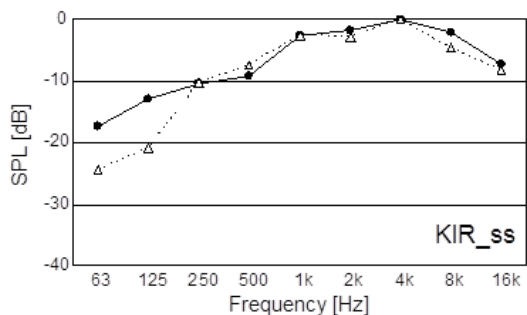


Fig. 12 – SPL as a function of band frequency: Kagoshima

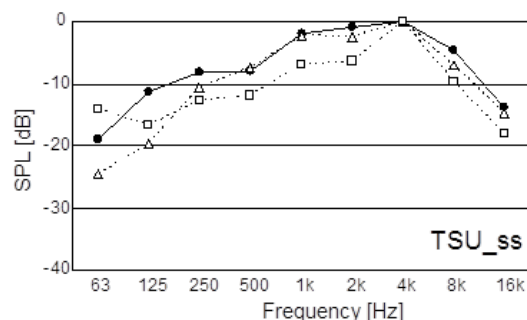


Fig. 13 – SPL as a function of band frequency: Okayama

In all cases, the SPL of the virtual IR is close to the SPL of the real IR. However, in the low-frequency range, the SPL of the virtual IR by single stereo-dipole tends to be lower than the SPL of real IR. The gap of SPL is improved by carrying out the dual stereo-dipole. For the concert hall, the single stereo-dipole shows better performances than the dual stereo-dipole. Figs 14 to 19 show the results of EDT. From these results, it can be seen that the stereo-dipole technique in the Arlecchino listening room works for the sound field representation with a high correlation. However, like the results of SPL, EDT of the real IR in the low-frequency range is difficult to be expressed by the single stereo-dipole.

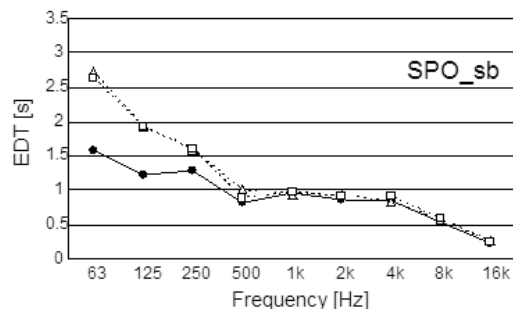
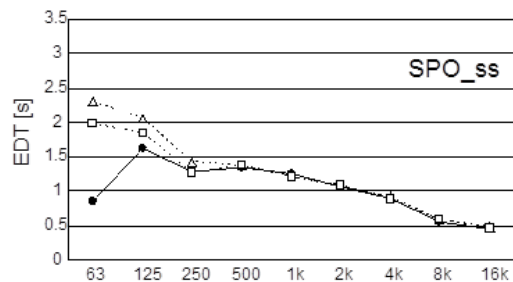


Fig. 14 – EDT: real IR (●), virtual IR by single stereo-dipole (Δ), and virtual IR by dual stereo-dipole (□): Spoleto 1/2

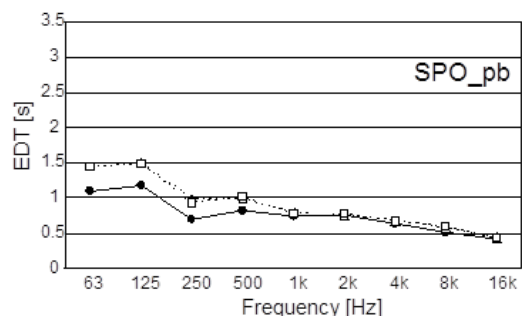
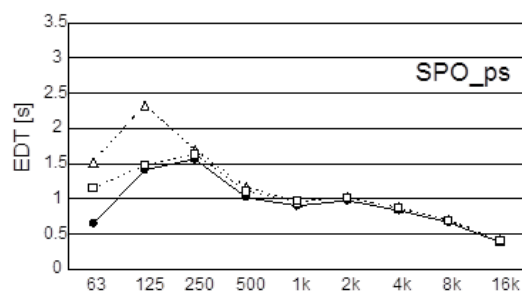


Fig. 15 – EDT as function of band frequency: Spoleto 2/2

The dual stereo-dipole contributes to covering the gap of EDT.

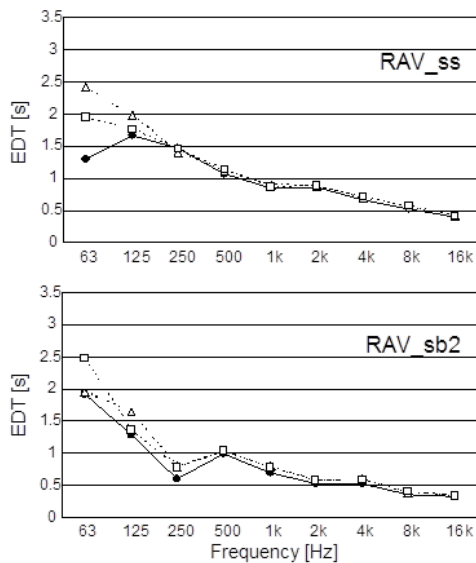


Fig. 16 – EDT as a function of band frequency: Ravenna 1/2

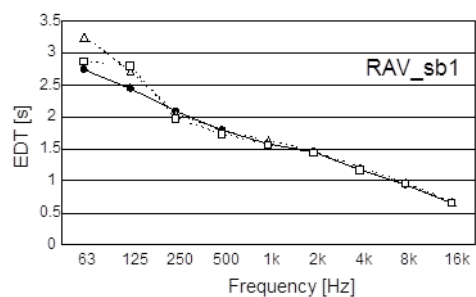


Fig. 17 – EDT as a function of band frequency: Ravenna 2/2

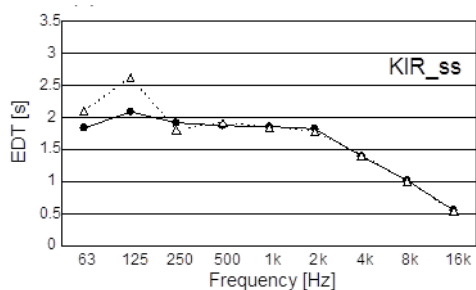


Fig. 18 – EDT as a function of band frequency: Kagoshima

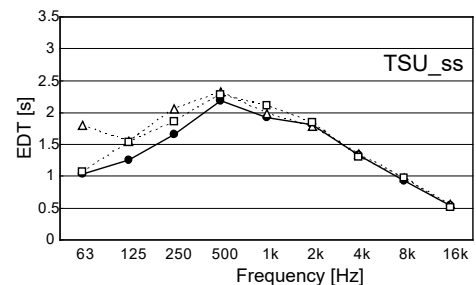


Fig. 19 – EDT as a function of band frequency: Okayama

4. Discussion

The Arlecchino listening room was redecorated by putting the absorptive material on the walls to perform the virtual sound field reproduction and listening tests. As a result, the reverberation in the high-frequency range (>500 Hz) was greatly removed while low-frequency reverberation (<250 Hz) remained again in the range shorter than 1s. In such a semi-anechoic condition, the generation of virtual sound fields by the stereo-dipole technique is not easy to carry out, because the cross-talk cancelling filter based on the impulse response with some reverberation is not flat spectrally. According to the parameters in the invert Kirkeby method, the cancelling filters have spectral peaks and dips as shown in Figs 14 to 19. However, the shortage of spectral power can be overcome by using two kinds of cancelling filters, which are presented by the dual-stereo dipole technique. Figs 8 to 13 and 14 to 19 show the advantages of dual stereo-dipole in terms of SPL and EDT. In general, the Ambisonic method, for reproducing virtual sound fields, showed a good enhancement at these frequencies. It is therefore likely that this limitation could be circumvented with the Ambisonic method.

5. Conclusion

The stereo-dipole technique has been developed to be applied to “home theatre”, which realizes the 3D sound for home use. Unlike the perfectly anechoic listening room in a laboratory, the room in a home has some reverberations unless absorptive materials are introduced in it. The dual stereo-dipole technique using two kinds of cross-talk cancelling filters can be one of the solutions to improve.

References

- Caniato, M., F. Bettarello, L. Marsich, A. Ferluga, O. Sbaizero and C. Schmid. 2015 “Time-depending performance of resilient layers under floating floors.” *Construction and Building Materials* 102(1). doi:10.1016/j.conbuildmat.2015.10.176

- Caniato, M., F. Bettarello, C. Schmid and P. Fausti. 2016 "Assessment criterion for indoor noise disturbance in the presence of low frequency sources." *Applied Acoustics* 113(1): 22–33.
- Caniato, M, F. Bettarello, C. Schmid, P. Fausti, 2019 "The use of numerical models on service equipment noise prediction in heavyweight and lightweight timber buildings." *Building Acoustics* 26(1): 35-55.
- Fabbri, K., L. Tronchin and V. Tarabusi. 2014 "Energy retrofit and economic evaluation priorities applied at an Italian case study." *Energy Procedia* 45: 379-384. doi:10.1016/j.egypro.2014.01.041
- Fabbri, K., and L. Tronchin. 2015. "Indoor environmental quality in low energy buildings." *Energy Procedia* 78: 2778–2783. doi: 10.1016/j.egypro.2015.11.625
- Farina, A., A. Langhoff, and L. Tronchin. 1998. "Acoustic Characterisation of "virtual" Musical Instruments: Using MLS Technique on Ancient Violins." *Journal of New Music Research* 27(4): 359-379. doi:10.1080/09298219808570753
- Farina, A., and L. Tronchin. 2000. "On the "Virtual" Reconstruction of Sound Quality of Trumpets." *Acustica* 86(4): 737-745.
- Farina, A., and L. Tronchin 2005. "Measurements and reproduction of spatial sound characteristics of auditoria." *Acoustical Science and Technology*, 26(2): 193-199. doi.org/10.1250/ast.26.193
- Farina, A., and L. Tronchin. 2013. "3D Sound Characterisation in Theatres Employing Microphone Arrays." *Acta Acustica United with Acustica* 99(1): 118-125. doi:10.3813/AAA.918595
- Shimokura, R., L. Tronchin, A. Cocchi, and Y. Soeta. 2011. "Subjective Diffuseness of Music Signals Convolved with Binaural Impulse Responses." *Journal of Sound and Vibration* 330(14): 3526-3537. doi:10.1016/j.jsv.2011.02.01
- Tronchin, L., and A. Farina. 1997."Acoustics of the former teatro "la fenice" in Venice." *AES: Journal of the Audio Eng. Society* 45(12): 1051-1062.
- Tronchin, L., and K. Fabbri. 2010. "A Round Robin Test for buildings energy performance in Italy." *Energy and Buildings*, 42(10): 1862-1877 doi:10.1016/j.enbuild.2010.05.022
- Tronchin, L. 2012. "The Emulation of Nonlinear Time-Invariant Audio Systems with Memory by Means of Volterra Series." *AES: Journal of the Audio Engineering Society* 60(12): 984-886.
- Tronchin, L. 2013a. "Francesco Milizia (1725-1798) and the Acoustics of His Teatro Ideale (1773)." *Acta Acustica United with Acustica* 99(1): 91-97. doi:10.3813/AAA.918592
- Tronchin, L. 2013b. "On the Acoustic Efficiency of Road Barriers: The Reflection Index." *International Journal of Mechanics* 7(3): 318-326.
- Tronchin, L., and V. L. Coli. 2015. "Further Investigations in the Emulation of Nonlinear Systems with Volterra Series." *AES: Journal of the Audio Engineering Society* 63(9): 671-683. doi:10.17743/jaes.2015.0065
- Tronchin, L., and D. J. Knight. 2016. "Revisiting Historic Buildings through the Senses Visualising Aural and Obscured Aspects of San Vitale, Ravenna." *International Journal of Historical Archaeology* 20(1): 127-145.
- Tronchin, L., and K. Fabbri. 2017. "Energy and Microclimate Simulation in a Heritage Building: Further Studies on the Malatestiana Library." *Energies* 10(10). doi:10.3390/en10101621
- Tronchin, L., M. Manfren and P. A. James. 2018. "Linking design and operation performance analysis through model calibration: Parametric assessment on a Passive House building." *Energy* 165(A): 26-40.
- Tronchin, L., M. Manfren, V. Vodola. 2020a. "The carabattola - vibroacoustical analysis and intensity of acoustic radiation (IAR)." *Applied Sciences* 10(2), 641.
- Tronchin, L., M. Manfren, V. Vodola. 2020b. "Sound characterization through intensity of acoustic radiation measurement: A study of persian musical instruments." *Applied Sciences* 10(2), 633.
- Tronchin, L., F. Merli, M. Manfren. B. Nastasi. 2020c. "The sound diffusion in Italian Opera Houses: Some examples." *Building Acoustics*, in press. doi:10.1177/1351010X20929216

Acoustic Comfort for Spaces Used by People with Cognitive Impairment: A Starting Point for the Application of Acoustic Event Detection and Sound Source Recognition Systems

Federica Bettarello – University of Trieste, Italy – fbettarello@units.it

Marco Caniato – Free University of Bozen-Bolzano, Italy – marco.caniato@unibz.it

Giuseppina Scavuzzo – University of Trieste, Italy – gscavuzzo@units.it

Andrea Gasparella – Free University of Bozen-Bolzano, Italy – andrea.gasparella@unibz.it

Abstract

The AED (Acoustic Event Detection) and SSR (Sound Source Recognition) systems are increasingly used in projects involving home automation, security, help for the visually impaired or for the elderly who want to pursue projects of independent living. The application of such technologies can also become a valid reference in the case of subjects suffering from cognitive, not just physical, deficits (Down syndrome, autism, etc.). In these cases remote assistance systems can represent a strong support both for the people who take care of them (parents, specialized personnel), and also for people with cognitive disabilities to pursue projects of independent living. Based on the study of the peculiarities that the internal spaces hosting activities for people with various cognitive deficits must have, criteria for acoustic comfort and internal design have been optimized for certain types of living, working and resting spaces. The aim of this work is to understand how the indoor sound field of dedicated rooms may affect boundary conditions for the installation of AED and SSR and how the specific interior design for special spaces may influence the speech intelligibility and clarity of these rooms.

1. Introduction

Acoustic Event Detection systems (AED) are designed to detect anomalous acoustic events and were developed to assist video surveillance systems (Pagin, 2016). They are based on the peculiarities of a sound signal that can be composed of very different time or spectral characteristics, different amplitude levels (consequently, different signal-to-noise ratio) and different duration. The detection

algorithms are based on pre-processing techniques necessary to detect potential alarm signals, such as the sensitivity of the detection algorithm (i.e. the ability to detect irregularities whose level is more or less close to the background noise) and the adaptability to sudden or slow changes in the signal (with respect to the variability of the background noise) (Dufaux, 2001; Tronchin, 2013). These systems are mainly used for "security" in outdoor environments or large environments (garages, airports, stations, etc.).

Sound Source Recognition systems (SSR) are more recent devices, which have allowed the passage from the request for help through a "button device" to the immediate sending of a distress call through the use of one's own voice or the recognition of a specific event. These technologies are becoming increasingly popular today, especially thanks to the development of home automation techniques within the Smarthome, i.e. those spaces that use a home controller to integrate the various home automation systems (Robles and Ki, 2010; Tronchin and Coli, 2015).

Sensors can provide information about a person's posture and movement or detect a fall. Smarthomes are therefore useful for measuring a person's activity or for helping people with, for example, cognitive or physical disabilities in their daily activities (Fleury et al., 2008).

There have been many projects on acoustic recognition algorithms over the years (Chang and Chang, 2013; Foster et al., 2015; Janvier et al., 2012; Lecouteux et al., 2018; Yong and Kean, 2014; Zhang et al., 2015). The systems involved use one

or more microphones, or are even embedded in robots that allow the subject to be followed very closely. As far as voice command is concerned, these systems are able to analyse and recognize many characteristics, including: intensity, timbre, rhythm, level. This makes it possible to distinguish whether the sending of an alarm may or may not be necessary.

Such systems therefore also allow non-autonomous people to maintain control of their environment and activities, their health, their well-being and their sense of dignity (Portet et al., 2011). Many of the studies presented so far see the elderly as the main stakeholders, in particular at that stage of their life when they are still able to look after themselves but need help to manage some difficult tasks or any situations of risk, danger and accident (Yoshioka et al., 2012).

The problems encountered during the implementation phases of this type of device are related to the background noise (Biagetti et al., 2011) and internal reverberation conditions of the environments (Piana et al., 2014; Yoshioka et al., 2012). It has been shown, for example, that recognition performance decreases significantly as soon as the microphone moves away from the user's mouth (e.g. when positioned on the ceiling) due to increased reverberation and the influence of background noise. The results under such conditions are optimal up to conditions of $T_R=0.5$ s and with the presence of speech and classical music in the background but not for the noise of technological systems or something similar (Lecouteux et al., 2011). Reverberation can be modelled as additive interference (Kinoshita et al., 2013).

The aim of this work is to understand how the indoor sound field in dedicated rooms may affect boundary conditions for the installation of AED and SSR and how the specific interior design for special spaces may influence the speech intelligibility and clarity of these rooms.

2. Materials and Methods

A case study was chosen in order to understand acoustic proprieties of buildings dedicated specifically to people with cognitive impairment. The

AUDI! Project had some stakeholders; one of them was Progettoautismo FVG Onlus, an association from the Friuli Venezia Giulia region (ITA) that supports people with autistic syndrome, Pervasive Developmental Disorders or Asperger's Syndrome and their families.

The selected rooms for possible application of the acoustic sensors were: (i) four different individual therapy rooms (speech therapy, psychomotricity, etc. Fig. 1), (ii) a soft room (multisensory room for the well-being of children and adults with autism, Fig. 2), (iii) an atelier (art workshop, Fig. 3) and (iv) a bedroom in the residential apartments (Fig. 4).



Fig. 1 – Box for individual therapy



Fig. 2 – Soft room

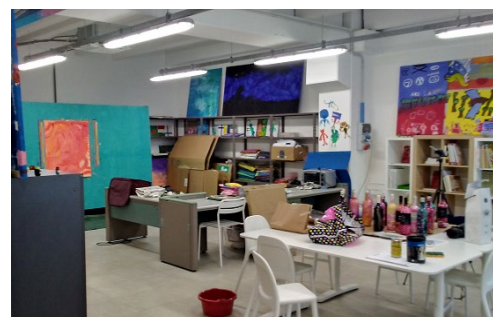


Fig. 3 – Atelier



Fig. 4 – Bedroom

The rooms for individual therapy are of different sizes, rectangular in shape, with an entrance door and no outdoor window, with very few interior furnishings (a table and two chairs, few toys and adhesive wall), with ceiling lights and sound absorbing panels. Some therapy rooms also have glass behind them so that relatives or other staff can attend the therapy session. They are made of a prefabricated structure consisting of pre-painted sheet metal/insulating material/pre-painted sheet metal type and are located in an area of the building which is particularly acoustic insulated from external noise and noise coming from inside the other parts of the building. These spaces have to be very quiet, because this is one of the particular needs for users. Here a single operator works with a single patient and it is of paramount importance that nothing may disturb the quiet relationship between operator and patient during the therapy. For this reason, the particular need for voice recognition devices is to recognize a help request from the operator, for example, through the recognition of a keyword, said without alteration of the voice (i.e. without screaming) and without making the patient understand the meaning of this request. The soft room is located inside the day-centre, equipped with impact resistant layering on the walls (up to about 2.10 m height), resilient flooring and soft cubes arranged in the space, useful both for playing and limiting patients in particular moments of venting and crisis. As for the use in the latter conditions, in which only the patient is left in the room while the operator monitors from outside through a window, the recognition device can recognize events (screams, blows) and activate a pro-

cess of help request, i.e. alert an additional operator and simultaneously trigger a process of audio-visual support inside the box.

The atelier (or art room) is a very large room, used for collective works, where inside you can find more guests and more operators. Here too, the particular need for voice recognition devices is to recognize a help request from the operator, for example, through the recognition of a keyword, said without altering the voice (i.e. without screaming) as described before.

A typical room in the residential apartments is 9 or 12 m² (hosting one or two patients) and has big outdoor windows and a private bathroom. Guests can spend the night alone, while the operator remains in a neighbouring room. The use of the acoustic recognition device becomes helpful to the operator in the next room as they can be instantly warned.

All simulations were performed using 3D acoustic simulators in order to obtain the indoor acoustic field distributions.

3. Results and Discussion

The applicability of a sound recognition device within a room is related to acoustic parameters such as reverberation time, clarity, definition and background noise. The performance of a speech recognition system in fact decreases significantly with the increase of the distance between the microphone and the source that emits the signal to be recognized, due to the increase in number of reflections and the influence of background noise.

Optimal conditions are represented by $T_R=0.5\pm0.7$ s, clarity $C_{50}>3$ dB and definition $D_{50}>70\%$ (Lecouteux et al., 2011; Farina and Tronchin, 2013; Kinoshita et al., 2013).

Reverberation has a dispersive effect on the characteristic sequence of speech. The energy ratio between the direct sound part and the first reflections and late reflections is represented by parameters C_{50} and D_{50} and is highly correlated to the performance of speech recognition.

In order to understand the real applicability of the sound recognition systems within the analysed spaces, a campaign of on-site acoustic measure-

ments and simulations with acoustic predicting software was performed. The on-site acoustic measurements were conducted with impulsive technique in accordance with standards (ISO 3382). The measurements made it possible to analyse the acoustic characteristics in terms of internal reverberation and were used for the calibration of the raytracing model. Fig. 5 shows the images of the rooms recreated for the acoustic simulation program and Fig. 6 shows the results in terms of reverberation time in octaves of frequency, which demonstrate a good agreement between the in situ and simulated results.

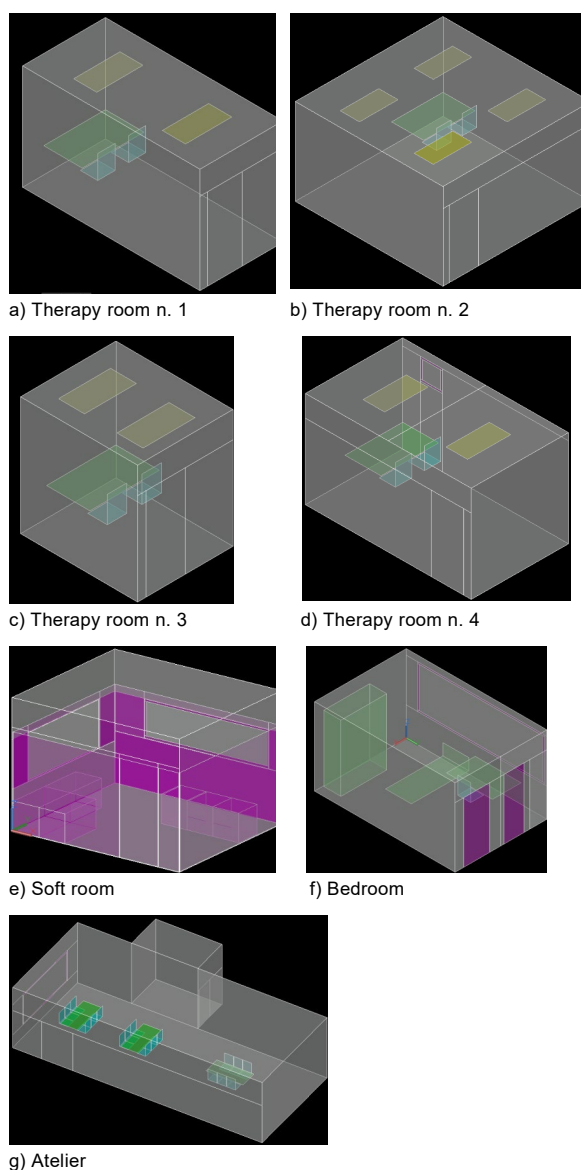


Fig. 5a–g – Images of the rooms recreated for the acoustic simulation program

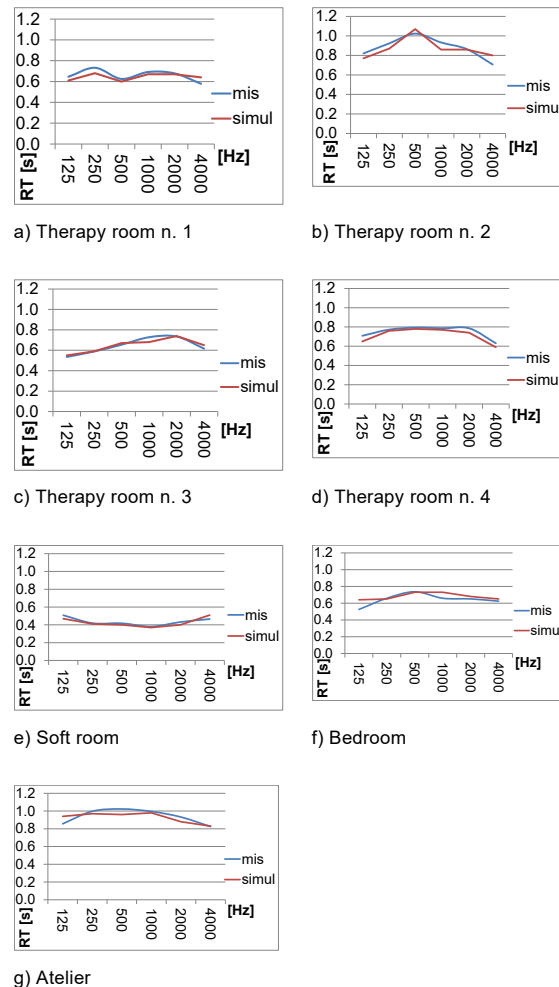


Fig. 6a–g – Reverberation time octaves frequency comparison: in situ results VS simulated once

The results obtained show that therapy rooms number 1 and 3 have optimal acoustic conditions for the use of speech recognition devices inside the rooms, while therapy rooms 2 and 4 (larger than the previous ones) need further sound absorbing treatment. The spatial distribution of the reverberation time parameter inside therapy room n. 2 (Fig. 7) shows how the corner positions of the room do not represent the optimal points of dislocation for the devices. It is therefore better to choose more central ceiling positions, setting the sensor suspended (not adjacent to the ceiling).

The spatial analysis by means of acoustic simulation of parameters C_{50} and D_{50} (Figs 8 and 9) also shows that the optimal spots for the acoustic recognition devices are a location as near as possible to the subject emitting the keywords. This means that two possibilities are imaginable: (i) defining the doctor-patient position inside the room and then

fixing the recognition device at a single point, or
(ii) installing several devices spatially covering most movements of the doctor and patient during therapy.

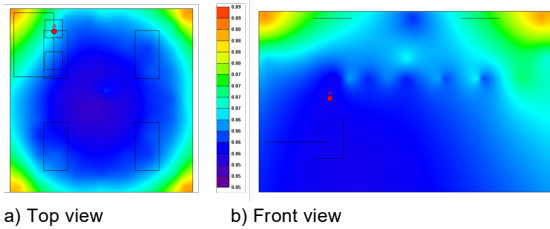


Fig. 7 – Simulated RT for therapy room n. 2: spatial distribution at 1000 Hz (graduation range from dark blue = 0.8 s to red = 0.9 s)

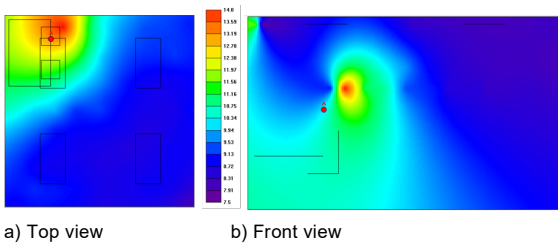


Fig. 8 – Simulated C_{50} for therapy room n. 2: spatial distribution at 1000 Hz (graduation range from dark blue = 7.5 to red = 14)

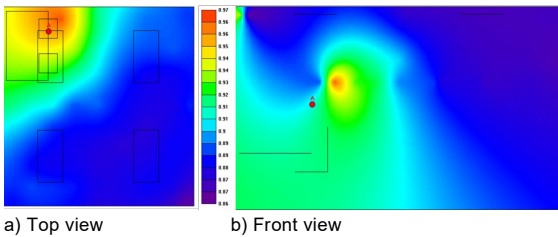


Fig. 9 – Simulated D_{50} for therapy room n. 2: spatial distribution at 1000 Hz (graduation range from dark blue = 0.85 to red = 1)

The same results obtained for therapy room n. 2 and 4 can be applied to the atelier: the larger dimensions of the room certainly require the application of several devices in order to reach and cover all the indoor space.

The soft room has low values of reverberation time (Fig. 10) because of the "soft" furniture intrinsically composed by sound-absorbing materials like polyurethane foams. Spatial distribution of Clarity and Definition (Fig. 11) are quiet good and it can be seen that a single sound suspended recognition device placed centrally on the ceiling can be sufficient for this type of room, and with the presence of one single user inside at a time.

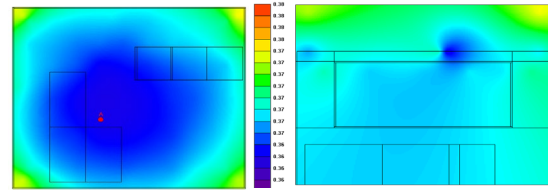


Fig. 10 – Simulated RT for soft room: spatial distribution at 1000 Hz (graduation range from dark blue = 0.3 s to red = 0.4 s)

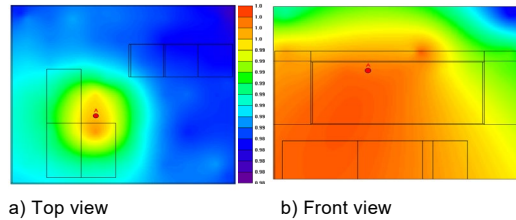


Fig. 11 – Simulated D_{50} for therapy room n. 2: spatial distribution at 1000 Hz (graduation range from dark blue = 0.9 to red = 1)

For the bedroom, the reverberation, clarity and definition are optimal for the application of sound recognition devices; at least one must be provided inside the bathroom and one should be provided inside the room. Positions of angle and proximity to the ceiling should be avoided. Obviously, however, the dimensions and the furnishings, optimized for the typical user, make the positioning of this device more "selective". For example, the presence of a wall fully equipped with windows, the location of the cabinets, the position of the bed and the presence of desks should be known in advance in order to choose the correct positioning of the devices.

4. Implementation

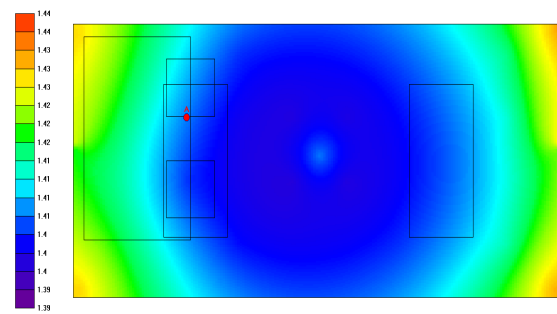
The procedural guidelines (Designing guidelines, 2008) for the design of spaces for people with cognitive disabilities such as autism, provide already optimal conditions for the introduction of assistive systems such as acoustic recognition devices. More important is the need to have simple and relaxing spaces: linear and well-proportioned geometries are positively evaluated, which guarantee good sound reverberation and good acoustics, without sources of noise that may cause distraction or discomfort (it is better to choose radiant heating systems on the ceiling or floor and natural or forced ventilation systems with acoustic attenuators).

People with autism are extremely sensitive to stimuli and because of the difficulty of filtering foreground and background information are often able to perceive details that normal people may not notice. The fundamental concept of "simplicity" for living spaces leads to a reduction to a minimum of the furnishing accessories in the rooms (Balisha, 2017; De Giovanni, 2015; Schrank and Ekici, 2017) and, above all, to the avoidance of the insertion of suspended soundproofing elements (buffers, curtains, etc.).

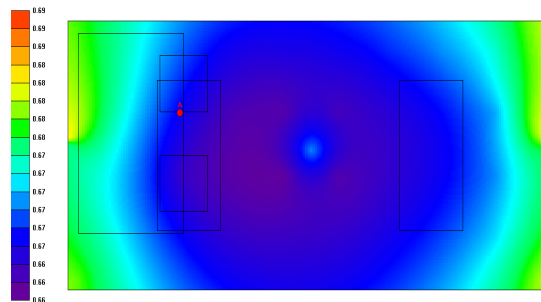
Rooms with long reverberation times, with acoustically highly reflective surfaces (i.e. those with large volumes and hard surfaces), are particularly unsuitable for many types of children's needs: some children with autism, for example, will find the room distressing. Children with hearing problems may also find the noise painful because it is amplified by their hearing aids.

All this means that the internal acoustic qualities of the room should be provided by the finishes of the walls, floors and ceilings. Moquette, for example, is soft and sound-absorbing, but difficult to clean. It is better to choose a linoleum flooring, perhaps choosing models with certified sound absorption coefficient values measured in accordance with the standard ISO 354. The walls can be covered with micro-perforated sound-absorbing panels, taking care not to alter the continuity of the wall itself. It is necessary to avoid creating elements that capture the eye and attention. Alternatively, furnishing accessories with sound absorbing elements on certain strategic points can be considered (the floor above the wardrobes or the lower part of the desk table, for example).

Fig. 12 shows some examples of the comparison results of the obtained acoustic simulations, starting from the studied rooms without furniture and sound absorbing elements, and then gradually implementing the necessary sound absorbing units in order to optimize the internal parameters of reverberation, definition and clarity. The procedure makes it possible to define in advance the installation positions of the necessary sound recognition devices, depending on the use that is made of the room and the operating needs required from time to time.



a) Without sound absorbing materials (graduation range: from dark purple 1.39 s – to red 1.44s)



b) With optimized sound absorbing materials

Fig. 12 – Comparison of simulated RT for therapy room n. 1: spatial distribution at 1000 Hz (graduation range: from dark purple 0.66 s – to red 0.69 s)

Specifically, for room therapy n. 1, the sound absorption measurements were performed using only sound absorbing panels on the ceiling in order not to alter the simple and clean look of the room and without the insertion of elements of possible distraction for the patient. Considering the possible positions in the space of the therapist and patient, the optimal positions for the sound recognition devices are along the longest sides of the room, at a height of about two meters from the ground.

For the bedroom, the sound absorption measurements were performed both through the insertion of sound absorbing panels on the ceiling/high part of the side walls and through the use of interior furnishings (Fig. 13). Here, considering the presence of large glass surfaces (for guests it is in fact better to choose as many sources of natural light as possible) and the need to insert furniture at full height (in order not to create discontinuity in the geometries, which can disturb the attention of the guest), it becomes advisable for the positioning of recognition devices to have a free wall on which to install one or two elements (depending on the size of the room) without obstacles that limit the scope of the operation (Fig. 14).

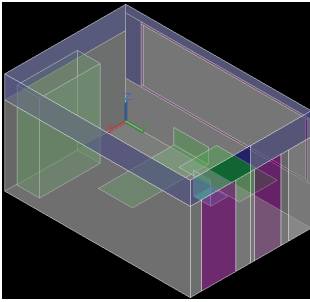


Fig. 13 – Example of optimized internal design for bedroom

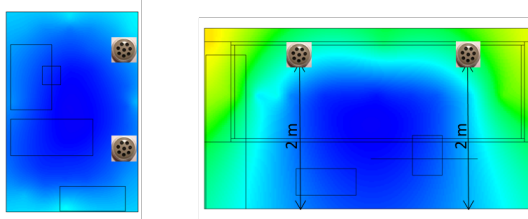


Fig. 14 – Example of optimized positions of recognition devices for bedroom (the room's internal colors represent the spatial distribution of the reverberation time parameter at 1000 Hz)

5. Conclusion

In this study, the results of the three-dimensional acoustic simulation of the spaces used by people with cognitive disabilities are presented, in order to understand the effective applicability of acoustic systems for remote voice monitoring and control.

It has been shown that interior design is very influential on acoustic fields and for this reason it may or may not allow the installation of AED and SSR technologies.

The inclusion of acoustic sensors, especially if combined with additional intelligent sensors monitoring and adjusting the environmental conditions (e.g. temperature, humidity, and acoustics) will allow a life as independent and autonomous as possible to people with cognitive disabilities, ensuring privacy and security. This technology will also make it possible to remotely deduce the state of people through centralized architectures by collecting data from a set of sensors deployed in their living environment.

Acknowledgement

The research was founded by University of Trieste in the framework of the ESF POR 2014-2020, Axis 3 of the Autonomous Region of Friuli Venezia Giulia, and ASTER system engineering smart technologies. The project is included in the Unit "HEaD Higher Education and Development" (CUP. FP1619892003). This research was also founded by EFRE 2014-2010 1095 E21@NOI CUP D56C18000180009.

Nomenclature

Symbols

AED	acoustic event detection
SSR	sound source recognition
TR	Reverberation time [s]
C ₅₀	Clarity (dB)
D ₅₀	Definition [%]

References

- AA.VV. 2008. *Designing for disabled children and children with special educational needs Guidance for mainstream and special schools*, BUILDING BULLETIN 102, England.
- Balisha, U. 2017. *Autism friendly design*. Didapress Dipartimento di Architettura, Florence University.
- Biagetti, G., P. Crippa, L. Falaschetti, S. Orcioni, C. Turchetti. 2018. *Speaker Identification in Noisy Conditions Using Short Sequences of Speech Frames* Springer.
- Chang, C., Y. Chang Y. 2013, "Application of Abnormal Sound Recognition System." *Proceedings of 9th International Conference on Information, Communications & Signal Processing (ICICS)*.
- De Giovanni, G. 2015. *Architecture for autism. Esempi Di Architettura* Vol. 2, N. 2 ed. Edizioni Scientifiche.
- Dufaux, A. 2001. *Detection and Recognition of Impulsive Sound Signals*. PhD thesis, Institute of Microtechnology University of Neuchatel Switzerland.

- Farina, A., L. Tronchin. 2013. "3D Sound Characterisation in Theatres Employing Microphone Arrays." *Acta Acustica United with Acustica* 99(1): 118-125. doi:10.3813/AAA.918595
- Fleury, A., N. Noury, M. Vacher, H. Glasson, J.-F. Serignat. 2008. "Sound and speech detection and classification in a Health smart home." *Proceedings of 30th Annual International Conference of the IEEE Engineering in Medicine and Biology Society*.
- Foster, P., S. Sigtia, S. Krstulovic, J. Barker, M. D. Plumbley. 2015 "Chime home: a dataset for sound source recognition in a domestic environment." *Proceeding of IEEE Workshop on Applications of Signal Processing to Audio and Acoustics*, October 18-21, New Paltz, NY.
- ISO. 2003. *ISO 354: Acoustics -- Measurement of sound absorption in a reverberation room*.
- ISO. 2009. *ISO 3382-1 Acoustics — Measurement of room acoustic parameters — Part 1: Performance spaces*.
- Janvier, M., X. Alameda-Pineda, L. Girin, R. Horaud. 2012 "Sound-Event Recognition with a Companion Humanoid." *Proceedings of 12th IEEE-RAS International Conference on Humanoid Robots*.
- Kinoshita, K., M. Delcroix, T. Yoshioka, T. Nakatani, et al. 2013. "The reverb challenge: a common evaluation framework for dereverberation and recognition of reverberant speech." *Proceedings of IEEE Workshop on Applications of Signal Processing to Audio and Acoustics*, New Paltz, NY, October 20-23.
- Lecouteux, B., M. Vacher, F. Portet. 2011. *Distant Speech Recognition for Home Automation: Preliminary Experimental Results in a Smart Home*. Laboratoire d'Informatique de Grenoble, GETALP Team.
- Lecouteux, B., M. Vacher, F. Portet. 2018. "Distant speech processing for smart home: comparison of ASR approaches in scattered microphone network for voice command." *International Journal of Speech Technology*.
<https://doi.org/10.1007/s10772-018-9520-y>
- Pagin, D. 2016. *Localization and recognition of sound events by means of microphone arrays*. Master's thesis in Computer Engineering, University of Padua Department of Information Engineering.
- Piana, E., P. Milani, N. Granzotto. 2014. "Simple method to determine the transmission loss of gypsum panels." *Proceedings of 21st International Congress on Sound and Vibration 2014, ICSV 2014*, vol. 5: 3700-3706; Beijing; China; July 13-17 2014.
- Portet, F., M. Vacher, C. Golanski, C. Roux, B. Meillon. 2011. *Design and evaluation of a smart home voice interface for the elderly: acceptability and objection aspects*. Springer, London.
- Robles, R. J., T. Ki. 2010. "Applications, Systems and Methods in Smart Home Technology: A Review." *International Journal of Advanced Science and Technology* 15.
- Schrank, S., D. Ekici. 2017. *Healing Spaces, Modern Architecture, and the Body*. Routledge.
- Tronchin, L. 2013. "On the Acoustic Efficiency of Road Barriers: The Reflection Index." *International Journal of Mechanics* 7(3): 318-326.
- Tronchin, L., V. L. Coli. 2015. "Further Investigations in the Emulation of Nonlinear Systems with Volterra Series." *AES: Journal of the Audio Engineering Society* 63(9): 671-683. doi:10.17743/jaes.2015.0065
- Yong, L., C. Kean. 2014 "Automatic classification of impact sounds based on time-frequency representation." *Proceedings of The 21st International Congress on Sound and Vibration*.
- Yoshioka, T., A. Sehr, M. Delcroix, K. Kinoshita, R. Maas, T. Nakatani, W. Kellermann. 2012. "Making Machines Understand Us in Reverberant Rooms [Robustness against reverberation for automatic speech recognition]." *Signal Processing Magazine, IEEE*: 114-126.
- Zhang, H., I. McLoughlin, Y. Song. 2015. "Robust sound event recognition using convolutional neural networks." *Proceedings of ICASSP 2015 - 2015 IEEE International Conference on Acoustics, Speech and Signal Processing (ICASSP)*.

Acoustics and Spatial Sound Distribution in the Theatre Comunale in Bologna, Italy

Massimiliano Manfren – University of Southampton, United Kingdom – m.manfren@soton.ac.uk

Benedetto Nastasi – Delft University of Technology, The Netherlands – benedetto.nastasi@outlook.com

Francesca Merli – University of Bologna, Italy – francesca.merli8@unibo.it

Vincenzo Vodola – University of Bologna, Italy – vincenzo.vodola2@unibo.it

Abstract

The acoustic quality of concert halls is extremely relevant for the modeling and simulation of the global music experience and for improving the acoustic design of music spaces. Furthermore, the acoustic characteristics of historical opera houses are considered to be one of the most important intangible elements of the cultural heritage of Italian history. An important Italian opera house is the theatre “Comunale” in Bologna (designed in the 18th Century by Galli Bibiena), and has a particular characteristic: the shape of the balconies and the materials with which they were constructed are different from those of a classical Italian opera house. This special feature of the balconies affects the listening conditions related to the position of sound sources on the stage and in the orchestra pit. This study investigates the acoustic properties of this important theatre in order to reproduce the sound properties by means of a 3D auralization. For describing the spatial sound characteristics of the hall, an experimental campaign was carried out. An omnidirectional, pre-equalized sound source was installed in the orchestra pit and on stage, and a dummy head was put in several listening positions on the balconies and in the stalls, accomplished with a B-format (soundfield) microphone. Moreover, the special features of the ACF (autocorrelation function) and the IACC (InterAural Cross Correlation) and other acoustic parameters were measured experimentally in order to reproduce them in the listening room “Arlecchino” at the laboratory of University of Bologna, by means of the Stereo Dipole and Ambisonics technique. The main results from the experiments are reported in this paper.

1. Introduction

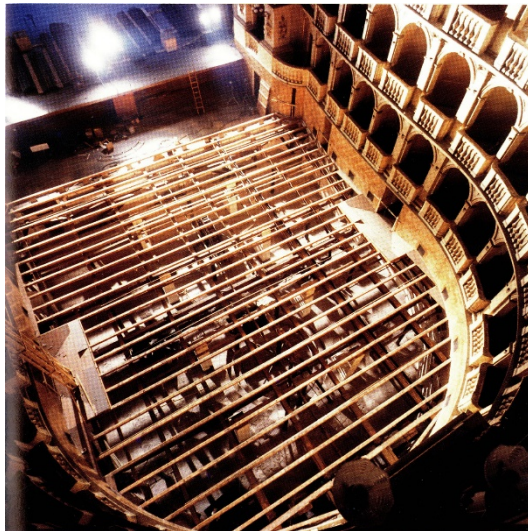
It is well known that the acoustic properties of opera houses and concert halls are extremely important for determining the global sensation that is experimented by listeners and musicians. Since the 1970s, with the work of Gerzon (1975) and subsequent research (Farina and Tronchin, 2005 and 2013; Tronchin, 2013; Tronchin and Coli, 2015), the sound properties of the special opera house have been considered to be of equal importance to ancient musical instruments (Tronchin et al., 2020). Therefore, cultural heritage is composed by their acoustical properties too apart from the architectural features. The theatre “Comunale” in Bologna is an important Italian opera house and has a particular characteristic: the shape of the balconies and the materials with which they were constructed are different from those of a classical Italian opera house. This special feature of the balconies affects the listening conditions related to the position of sound sources in the stage and in the orchestra pit. The aim of this paper is to investigate the acoustic properties of this important theatre with the purpose of reproducing its characteristics by means of a 3D auralization.

2. Materials and Methods

1.1 Historic Background of the Theatre

The Teatro *Comunale* in Bologna was designed by the architect Antonio Galli Bibiena, one of the most active architects for music venues in the 18th Century, and inaugurated in 1763. From the beginning

of the design process, Galli Bibiena considered a different shape of theatre to that of the typical horseshoe shape, namely a bell shape. Thus, the *Comunale* of Bologna was the first example of a special "phonic" shape conceived by Galli Bibiena, and was followed by the Teatro Scientifico in Mantova and the Four Horsemen Theatre in Pavia. At that time, however, this idea was not supported by other physicists and acousticians.



(a)



(b)

Fig. 1 – (a) The device below the floor of the stalls and (b) the hall

The *Comunale* also had other specific characteristics: the brick structure of the main hall was one of the most important innovations and was used instead of a wooden structure, in order to reduce the

risk of the theatre being damaged or destroyed in a fire. The theatre also had two major innovations in balconies and stalls. The balconies were designed to allow the owners to customize the walls, colour the walls, change the interiors, etc. The floor of the stalls was equipped with a special device: it could be lifted to the height of the stage by a special mechanism. There would have been a large cavity, with musicians and singers on the same level; Bibiena believed that the movement of the floor would enhance the intelligibility of the singers. This mechanism was active until 1820.

1.2 The Acoustic Measurements

A measurement campaign was undertaken in order to properly describe the spatial sound characteristics of the hall, with a special focus on the stage and orchestra pit and the relationship between the perception of the sound of the musical instruments and their characteristics in the stalls and balconies (Farina et al., 1998; Farina and Tronchin, 2000; Shimokura et al., 2011; Tronchin, 2012; Tronchin and Coli, 2015). Then, in a further step, the ACF (autocorrelation function) and IACC (InterAural Cross Correlation) and other acoustic parameters were calculated from the impulse responses thanks to the Stereo Dipole and Ambisonics techniques, in order to reproduce them in the listening room "Arlecchino" at the laboratory of University of Bologna.

The instruments used are::

- on the stage and in orchestra pit, an omnidirectional, frequency-equalized sound source (namely LookLine);
- at the receiver's positions (Neumann KU-100) to measure binaural impulse responses and parameters, a dummy head;
- in the theatre, similarly to the dummy head, a Soundfield microphone (MK V) probe. For calculating the monoaural and 3-dimensional parameters, a four-channel output was adopted.

An exponential, 30-second-long sine sweep (chirp) was played by the omnidirectional sound source and, to store the signals from the microphones, a 20-bit 96 kHz 8-channel sound board was utilized. The measurements were taken in 25 different positions, from stalls to balconies, as shown in Fig. 2.

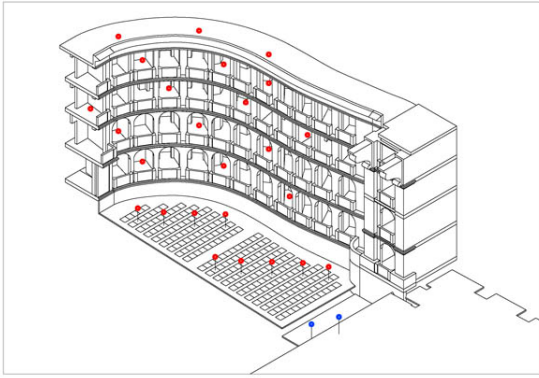


Fig. 2 – The points for measurements in red dots in the Comunale

Then, the authors used a numerical simulation model. On the stage the sound source was put and the measurements were repeatedly moved to the orchestra pit. To calculate the strength spatial maps at 1 m a reference position was added. Some additional measurements were carried out with the sound source to evaluate the different impulse responses during the 3D auralization process (Binaural and B-formats) including floor effects for sound insulation (Caniato et al., 2016 and 2018).

The mono-aural parameters, such as reverberation time, center time and clarity, were calculated considering the W channel from the Soundfield microphone, as well as spatial parameters, such as LE and LF and the B-format Impulse Response. The measurement of binaural parameters was taken by the dummy head, such as the IACC (Farina et al., 2013). In addition, the discovery of virtual acoustics in the theatre (Tronchin, 2013) was made possible by the B-format impulses obtained through the Soundfield and the bi-induction responses by the dummy head, crucial for retrofitting (Caniato et al., 2015 and 2019; Fabbri et al., 2014; Fabbri and Tronchin, 2015; Tronchin and Fabbri, 2017; Tronchin and Knight, 2016; Tronchin et al., 2014 and 2016).

3. Results

The results from the measurements are briefly reported in the following paragraphs. Various acoustic parameters were calculated from the measurements. Table 1 reports the average values of the acoustic parameters measured in the theatre. The results show that the position of the sound source from the stage and the orchestra pit modifies the parameters. As mentioned above, a sound source with a directivity pattern was also used during the measurements. For further analysing the influence of both the position of the sound source and its directional patterns, the results for a specific position in the stalls are shown in the graphs.

Table 1 – Values obtained in the Teatro Comunale of Bologna with reference to the positions of the sound source on the Stage

Frequency	C50 [dB]	C80 [dB]	D50 [%]	Ts [ms]	EDT [s]	T20 [s]	LF
63	-5.2	-1.7	26.2	179.9	2.1	2.3	0.94
125	-5.3	-1.5	25.0	154.2	1.8	2.0	0.81
250	-2.6	0.6	36.5	117.8	1.6	1.8	0.81
500	-2.4	0.6	37.6	111.3	1.6	1.7	0.78
1k	-2.8	0.2	35.3	114.7	1.6	1.6	0.78
2k	-3.1	0.2	34.1	113.1	1.6	1.6	0.68
4k	-2.4	1.2	37.4	94.9	1.3	1.3	0.58
8k	1.1	4.6	55.8	58.5	0.9	1.0	0.48

The *Teatro Comunale* gives an overall impression of the sound of typical Italian opera houses. The reverberation time at mid frequencies was approximately 1.4 s. The acoustics of the orchestra pit, however, differ significantly from the stage. These differences are particularly significant in the stalls rather than on the balconies. Variations in acoustic parameters could be seen specifically in the initial part of the impulse responses (less than 100 ms), as depicted in the graphics reporting the values of the acoustic parameters measured in one specific position not far from the orchestra pit. The energetic parameters (i.e. clarity) showed a significant difference from the stage with the orchestra pit whereas the position of the sound source, effected

by the fence, induces a diffuse sound field with no direct sound from the source to the receivers (which was clearly perceived by the receiver) and the orchestra pit. Including the reverberation times, the sound source from stage to pit was significantly different. The estimated Early Decay Time was affected more than the RT30, due to its longer decay time. In some cases, the variation of EDT also ranged from 0.5 s at mid-frequencies to 0.2 s in RT30.

Table 2 – Values obtained in the Teatro Comunale of Bologna with reference to the positions of the sound source on the Pit

Frequency	C50 [dB]	C80 [dB]	D50 [%]	Ts [ms]	EDT [s]	T20 [s]	LF
63	-0.2	3.5	49.1	112.4	1.0	2.1	0.8
125	-8.7	-0.8	17.7	148.5	1.7	2.0	0.7
250	-4.3	2.1	31.2	110.8	1.4	1.7	1.0
500	-4.2	1.3	32.0	108.2	1.4	1.6	1.1
1k	-3.4	0.8	34.5	110.9	1.6	1.6	1.0
2k	-3.0	1.0	35.3	104.1	1.5	1.5	0.8
4k	-1.7	2.2	41.1	86.7	1.2	1.3	0.6
8k	2.1	5.9	59.9	54.0	0.7	0.9	0.5

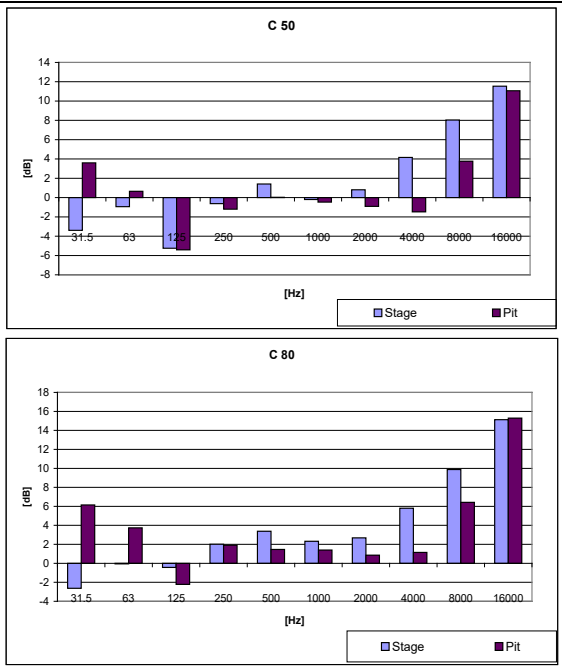


Fig. 3 – Values of Clarity measured in stalls (14F), in the Teatro Comunale of Bologna, Italy

Additional analysis consisted of a variety of sound source positions and directivity patterns. Some acoustic measured parameters in the hall are shown in Figs 6 to 8. There were remarkable variations in these parameters.

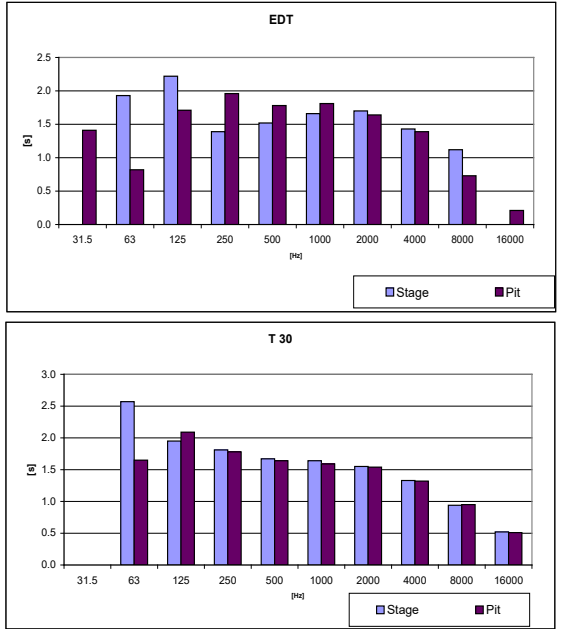


Fig. 4 – Values of Early Decay Time and Reverberation Time measured in stalls (14F), in the Teatro Comunale of Bologna, Italy

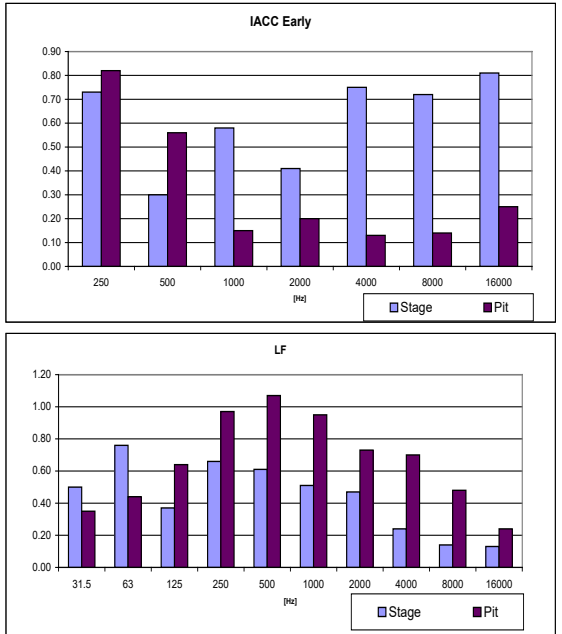


Fig. 5 – Values of InterAural Cross-Correlation and Lateral Fraction measured in stalls (14F), in the Teatro Comunale of Bologna, Italy

Even the *clarity* of the sound source changed considerably. Only the reverberation time with sound sources remained relatively stable. However, the analysis of the variation of the IACC led to the identification of differences of between 0.15 and 0.075 at the frequency of 2 kHz, depending on the sound source.

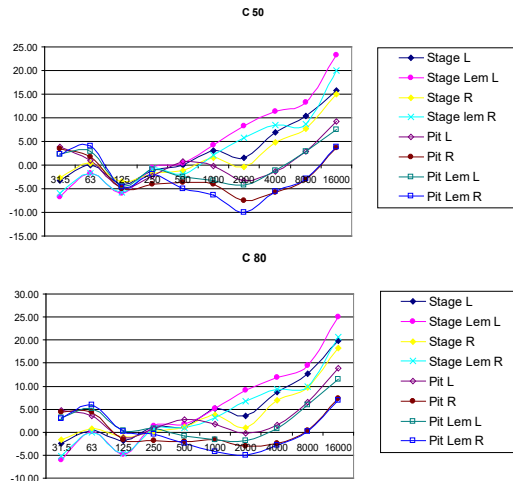


Fig. 6 – Values of Clarity measured in stalls (14F) with different sound sources and positions in the Teatro Comunale of Bologna

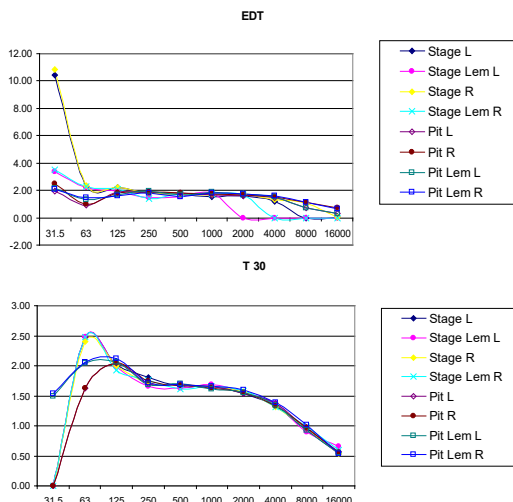


Fig. 7 – Values of Reverberation Time measured in stalls (14F) with different sound sources and positions in the Teatro Comunale of Bologna

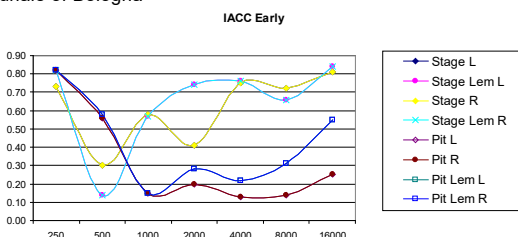


Fig. 8 – Values of IACC measured in stalls (14F) with different sound sources and positions in the Teatro Comunale of Bologna

This was not a surprise because the first 80 ms of the impulse response (IACC) were considered in the calculation, i.e. the component of the binaural impulse responses that was heavily dependent on the different characteristics of the sound sources and their positions.

4. Conclusion

In conclusion, based on the results discussed in this paper, it is possible to state that the Teatro Comunale presents the typical sound characteristics of Italian-style opera houses. Yet, the acoustics of the stage and the orchestra pit were found very different. This fact makes unique this opera house.

Acknowledgement

The authors acknowledge the help of Enrico Reatti and Lamberto Tronchin for their collaboration during the experimental measurements.

References

- Caniato, M., F. Bettarello, L. Marsich, A. Ferluga, O. Sbaizero and C. Schmid. 2015 "Time-depending performance of resilient layers under floating floors." *Construction and Building Materials* 102(1). doi: 10.1016/j.conbuildmat.2015.10.176
- Caniato, M., F. Bettarello, C. Schmid and P. Fausti. 2016 "Assessment criterion for indoor noise disturbance in the presence of low frequency sources." *Applied Acoustics* 113(1): 22–33.
- Caniato, M., S. Favretto, F. Bettarello, C. Schmid. 2018. "Acoustic Characterization of Resonance Wood." *Acta Acustica united with Acustica* 104(6) 1030–1040. doi: 10.3813/AAA.919269
- Caniato, M., F. Bettarello, C. Schmid, P. Fausti. 2019. "The use of numerical models on service equipment noise prediction in heavyweight and lightweight timber buildings." *Building Acoustics* 26(1): 35–55. doi:10.1177/1351010X18794523
- Fabbri, K., L. Tronchin and V. Tarabusi. 2014. "Energy retrofit and economic evaluation priorities applied at an Italian case study."

- Energy Procedia* 45: 379-384.
doi:10.1016/j.egypro.2014.01.041
- Fabbri, K., and L. Tronchin. 2015. "Indoor environmental quality in low energy buildings." *Energy Procedia* 78: 2778-2783. doi: 10.1016/j.egypro.2015.11.625
- Farina, A., A. Langhoff, and L. Tronchin. 1998. "Acoustic Characterisation of "virtual" Musical Instruments: Using MLS Technique on Ancient Violins." *Journal of New Music Research* 27(4): 359-379. doi:10.1080/09298219808570753
- Farina, A., and L. Tronchin. 2000. "On the "Virtual" Reconstruction of Sound Quality of Trumpets." *Acustica* 86(4): 737-745.
- Farina, A., and L. Tronchin 2005. "Measurements and reproduction of spatial sound characteristics of auditoria." *Acoustical Science and Technology* 26(2): 193-199. doi.org/10.1250/ast.26.193
- Farina, A., and L. Tronchin. 2013. "3D Sound Characterisation in Theatres Employing Microphone Arrays." *Acta Acustica United with Acustica* 99 (1): 118-125. doi:10.3813/AAA.918595
- Gerzon, M. 1975. "Recording Concert Hall Acoustics for Posterity." *Journal of Audio Engineering Society* 23(7): 569.
- Shimokura, R., L. Tronchin, A. Cocchi, and Y. Soeta. 2011. "Subjective Diffuseness of Music Signals Convolved with Binaural Impulse Responses." *Journal of Sound and Vibration* 330 (14): 3526-3537. doi:10.1016/j.jsv.2011.02.014
- Tronchin, L. 2012. "The Emulation of Nonlinear Time-Invariant Audio Systems with Memory by Means of Volterra Series." *AES: Journal of the Audio Engineering Society* 60(12): 984-886.
- Tronchin, L. 2013a. "Francesco Milizia (1725-1798) and the Acoustics of His Teatro Ideale (1773)." *Acta Acustica United with Acustica* 99(1): 91-97. doi:10.3813/AAA.918592
- Tronchin, L. 2013b. "On the Acoustic Efficiency of Road Barriers: The Reflection Index." *International Journal of Mechanics* 7(3): 318-326.
- Tronchin, L., M.C. Tommasino and K. Fabbri. 2014. "On the cost-optimal levels of energy-performance requirements for buildings: A case study with economic evaluation in Italy." *International Journal of Sustainable Energy Planning and Management* 3: 49-62. doi:10.5278/ijsepm.2014.3.5
- Tronchin, L., and V. L. Coli. 2015. "Further Investigations in the Emulation of Nonlinear Systems with Volterra Series." *AES: Journal of the Audio Engineering Society* 63(9): 671-683. doi:10.17743/jaes.2015.0065
- Tronchin, L., M. Manfren and L C. Tagliabue. 2016. "Optimization of building energy performance by means of multi-scale analysis – Lessons learned from case studies" *Sustainable Cities and Society* 27: 296-306. doi:10.1016/j.scs.2015.11.003
- Tronchin, L., and D. J. Knight. 2016. "Revisiting Historic Buildings through the Senses Visualising Aural and Obscured Aspects of San Vitale, Ravenna." *International Journal of Historical Archaeology* 20(1): 127-145.
- Tronchin, L., and K. Fabbri. 2017. "Energy and Microclimate Simulation in a Heritage Building: Further Studies on the Malatestiana Library." *Energies* 10(10). doi:10.3390/en10101621
- Tronchin, L., M. Manfren, V. Vodola. 2020a. "The carabattola - vibroacoustical analysis and intensity of acoustic radiation (IAR)." *Applied Sciences* 10(2), 641.
- Tronchin, L., M. Manfren, V. Vodola. 2020b. "Sound characterization through intensity of acoustic radiation measurement: A study of persian musical instruments." *Applied Sciences* 10(2), 633.
- Tronchin, L., M. Manfren, V. Vodola. 2020c. "Sound characterization through intensity of acoustic radiation measurement: A study of persian musical instruments." *Applied Sciences* 10(2), 633.
- Tronchin, L., F. Merli, M. Manfren. B. Nastasi. 2020d. "The sound diffusion in Italian Opera Houses: Some examples." *Building Acoustics*, in press. doi:10.1177/1351010X20929216

The Acoustic Simulation of Performing Area in the Auditorium: Some Examples in Italy

Vincenzo Vodola – University of Bologna, Italy – vincenzo.vodola2@unibo.it

Benedetto Nastasi – Delft University of Technology, The Netherlands – benedetto.nastasi@outlook.com

Massimiliano Manfredi – University of Southampton, United Kingdom – m.manfredi@soton.ac.uk

Francesca Merli – University of Bologna, Italy – francesca.merli8@unibo.it

Abstract

The design of auditoria and opera houses requires particular care for the stage area, where several different requirements should be achieved for the performers. Among these, the acoustic quality represents a fundamental aspect, and it differs from the listeners' perspective. Moreover, the performing area in concert halls is often an important area for non-acoustic reasons, since lighting, thermal plants, etc. are often placed in this special zone, and should be properly designed in order to guarantee a high level of global comfort. This paper presents some examples of how to design exhibition zones in opera houses and auditoriums that show both acoustic and technical improvements, both in theory and in architecture.

1. Introduction

The performance area is one of the most important aspects of acoustic design in the design of music spaces and in particular of opera houses. In addition, opera houses have two different spaces, the orchestra pit and the stage, and these are quite different in terms of their acoustics. However, even though in most cases both the singers (on stage) and the musicians (in the pit) cannot hear each other very well, the conductor (visible to both singers and musicians) is able to lead the performance because both the fence and the proscenium can receive direct sound and reflection. The design process should therefore consider many different aspects, ranging from acoustical requirements and flexibility.

In this paper, some example of the design of performing zones in opera houses and auditoria are

presented, showing both the theoretical and architectural requirements for acoustical and technical enhancements. Specifically, three main aspects of the design process are analysed: the design of the orchestra pit, the design of the diffusion in the stage, and the design of the acoustic chamber.

2. Materials and Methods

2.1 The Design of the Orchestra Pit

An orchestra pit holds all the musicians during the performance of an opera, which is the reason why this small area is very important when musicians and singers perform together. Since the stage and the pit are in different locations in opera halls, musicians have many difficulties during a performance. Moreover, in the event of a lack of balance between stage and orchestra pit, the acoustic quality of the theatre can be reduced. The acoustic design of the pit should aim to improve the balance between musicians and singers in order to solve these problems (Gade, 1989) and to improve the performance of singers moving across the stage during an opera.

The acoustic design should offer a very flexible variety of acoustics in the orchestra pit, while the fence must provide a satisfactory early reflection from the pit to the point and vice versa, in order to properly link the specific sound characteristics of each musical instrument (Farina et al., 1998; Farina and Tronchin, 2000; Tronchin 2012; Tronchin and Coli, 2015; Tronchin et al., 2020).

Final acoustic design was obtained for the Teatro Comunale in Treviso, simulating different pit configurations that could be moved up in height depending on the type of performance (opera, concert, drama) and the performance of the singers and instruments, as in other theatres (Tronchin, 2013; Tronchin and Knight, 2016).

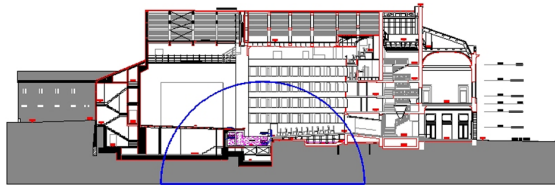


Fig. 1 – The theatre and the orchestra pit

A series of rotating acoustic boards, made of wood, were hung on the ceiling of the pit: one side of the panels is able to capture and tune at different frequencies, while the other side reflects the direct waveforms. The motion of the boards towards the stalls could generate a cavity below the stage, with a distinct volume and neck, and therefore tuned to different frequencies.

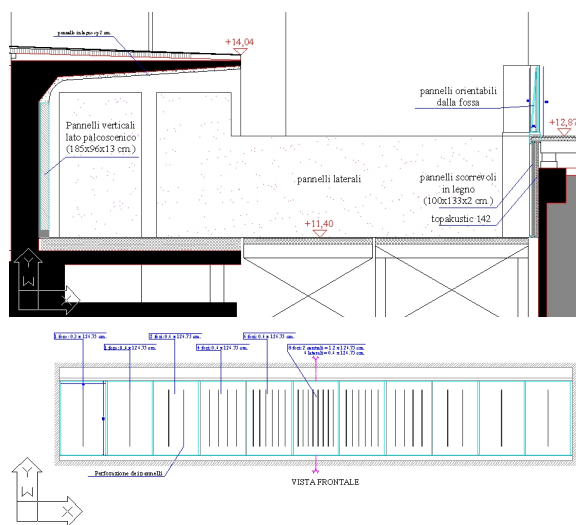


Fig. 2 – The orchestra pit: details

Particular attention was given to the aesthetics and acoustics of the fencing, which is located in front of the orchestra pit. The fence creates a strong early reflection of the sound from the pit to the stage, acting as a sound barrier from pit to stalls, based on its direction. For these reasons, its boundary can contribute to the diffusion of the sound in the room and significantly affects the balance between pit

and stage. The fence was therefore designed with different orientations, helping performers to perform better on the stage and in the pit.

2.2 The Design of Diffusion in the Stage

The stage in an opera is generally rectangular and the walls are made of concrete. This kind of shape, with two parallel side walls, does not provide the performers, particularly the musicians, with great acoustics throughout the stage. Furthermore, although a good acoustic chamber could solve these difficulties in orchestral configuration, some strong reflections cannot be avoided during a performance. To solve these issues, a series of diffusing panels were installed on the stage of the Teatro Vittorio Emanuele in Messina, Sicily, together with solutions for sound insulation (Caniato et al., 2015, 2016 and 2018).

The calculation followed the well-known number theory (Tronchin et al., 2020), and consequently diffractal boards were drawn up in accordance with the resulting frequencies. The stage dimensions permitted the design of modular, low frequency tuned panels, as shown in Fig. 4. A series of diffusing panels was also introduced to the orchestra pit, at the same theatre. A pyramid tracing software package, which could properly take diffusion into consideration, was used to detect the suitable position of panels both on stage and in the orchestra pit. The numerical model is shown in Fig. 3.

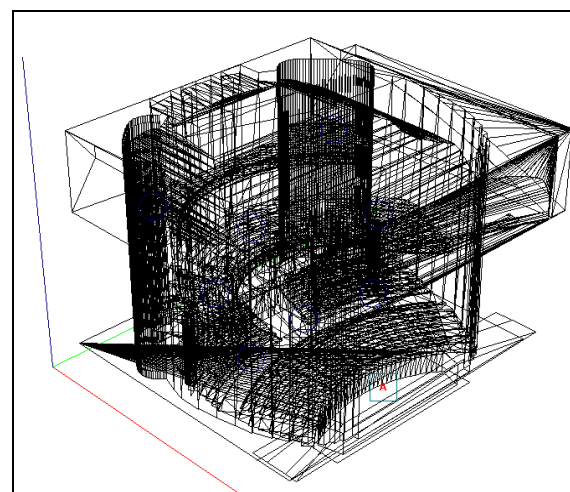


Fig. 3 – The model of the theatre Vittorio Emanuele in Messina

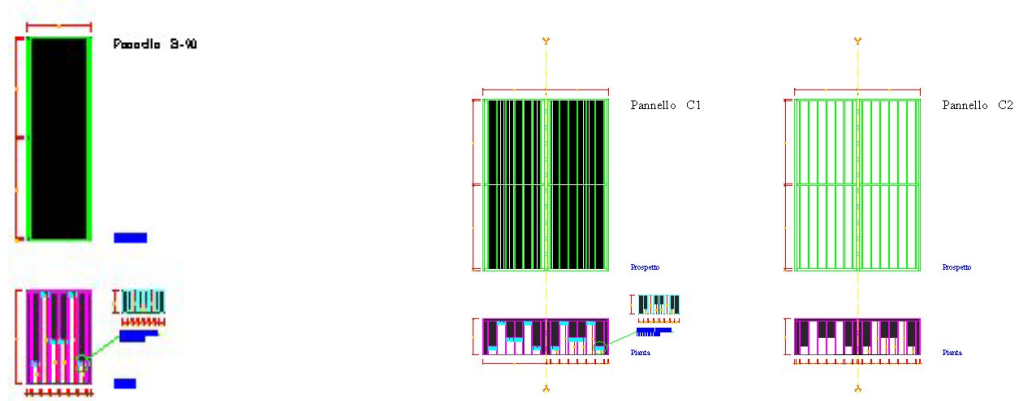


Fig. 4 – Diffusing panels in the orchestra pit (left) and in the stage (right)

Due to the energetic decay in the computed impulse responses, the optimal distribution of the diffusing surface was also calculated. In Figs 5–7, distinct feasible panel locations are shown, with the corresponding energy decay impulse responses achieved for each setup.

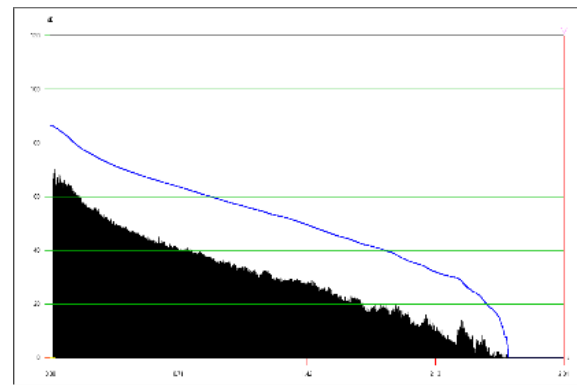
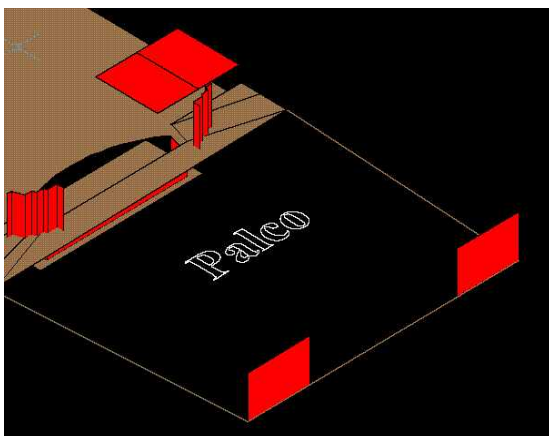


Fig. 5 –Solution A for the placement of the diffusing panels and their influence on the IRs

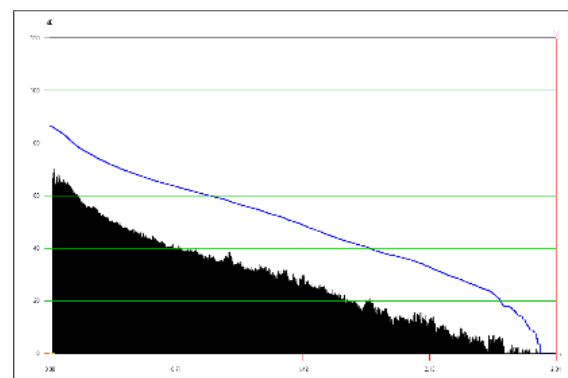
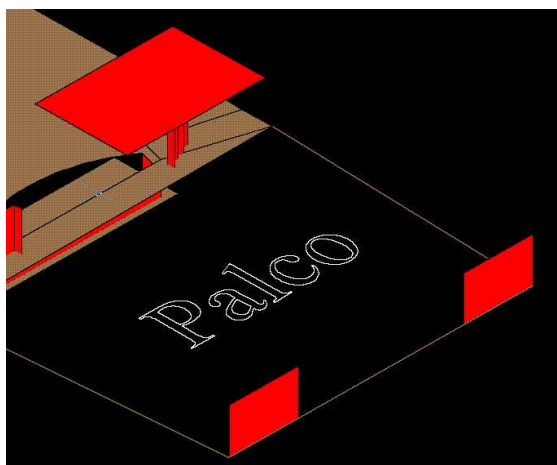


Fig. 6 – Solution B for the placement of the diffusing panels and their influence on the IRs

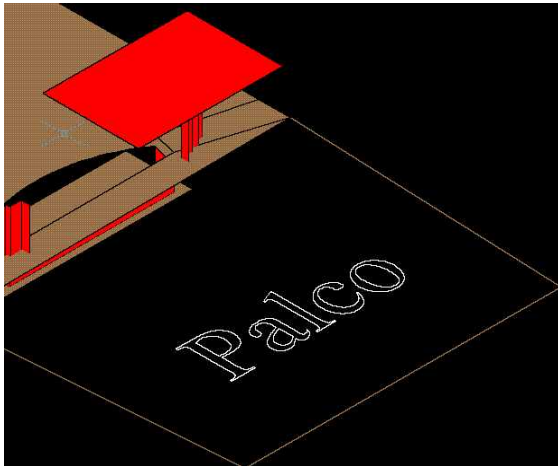
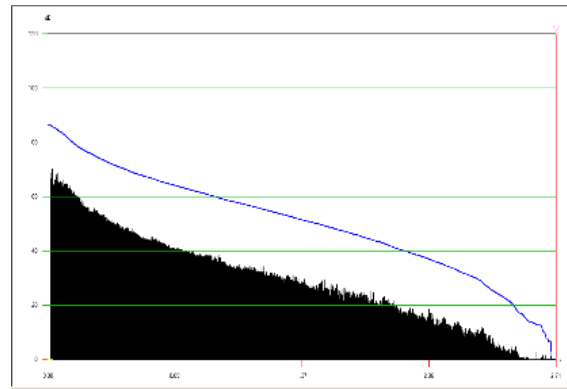


Fig. 7 – Solution C for the placement of the diffusing panels and their influence on the IRs



2.3 The Design of the Acoustic Chamber

Today, the acoustic design of the performing area in concert halls and especially in opera houses also includes the realization of the orchestra chamber, since an effective design of this can significantly improve the balance between all orchestral sections. However, the effectiveness of the chamber depends not only on its acoustic properties: it also depends on other variables such as simplicity, versatility and quickness of assembling and disassembling. In the Teatro Comunale in Treviso, the acoustic chamber was designed with three different configurations of the hall with reference to the position of the orchestra pit and, consequently, the type of performance. Considering a performance by a soloist, for example, the pit can be elevated to the stage level and cover the whole area of the acoustic chamber, which was specifically designed for this theatre. Support (ST1) and Early Ensemble Level (EEL), are among the most important acoustic parameters for the perception of music by the performer (Shimokura et al., 2011). With a triangular acoustic chamber, the optimum ST1 values of -11 to -13 dB were achieved. Furthermore, the strength and reverberation times in the receiver positions in stalls with a triangular shape were preferable.

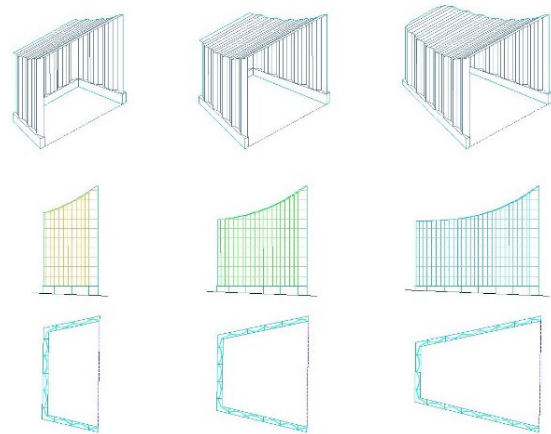


Fig. 8 – The three configurations of the acoustic chamber

3. Results

The results discussed in this paper emphasise the fact that the design process involves many different considerations, ranging from acoustic requirements to flexibility. What has been shown is that the systematic and detailed study of the various problems that can occur within a space dedicated to musical performance can lead to simple and effective solutions from the point of view of both the architecture and the quality of the acoustics. This is also replicable in infrastructures where prefabricated components are assembled and its modelling is crucial for performance (Caniato et al., 2019; Tronchin and Fabbri, 2017; Tronchin and Knight, 2018; Tronchin et al., 2018). Moreover, these solutions allow performers to perform their work in the best way, thus also guaranteeing better experience for end users.

4. Conclusion

In this paper, some examples of devices which can enhance the acoustic quality in opera houses were presented. However, the design process should not only consider acoustic performance but also many different aspects, including flexibility and costs. It is worth noting that in several cases, very valuable examples of acoustic devices (e.g. turning panels, etc.) are not normally used by the staff, i.e. technicians working in the theatre. In order to avoid this circumstance, the staff should be fully involved in the design process.

References

- Caniato, M., F. Bettarello, L. Marsich, A. Ferluga, O. Sbaizero and C. Schmid. 2015. "Time-depending performance of resilient layers under floating floors." *Construction and Building Materials* 102(1). doi: 10.1016/j.conbuildmat.2015.10.176
- Caniato, M., F. Bettarello, C. Schmid and P. Fausti. 2016. "Assessment criterion for indoor noise disturbance in the presence of low frequency sources." *Applied Acoustics* 113(1): 22–33.
- Caniato, M., S. Favretto, F. Bettarello, C. Schmid. 2018. "Acoustic Characterization of Resonance Wood." *Acta Acustica united with Acustica* 104(6) 1030–1040. doi: 10.3813/AAA.919269
- Caniato, M., F. Bettarello, C. Schmid, P. Fausti. 2019. "The use of numerical models on service equipment noise prediction in heavyweight and lightweight timber buildings." *Building Acoustics* 26(1): 35–55. <https://doi.org/10.1177/1351010X18794523>
- Farina, A., A. Langhoff and L. Tronchin. 1998. "Acoustic Characterisation of "virtual" Musical Instruments: Using MLS Technique on Ancient Violins." *Journal of New Music Research* 27(4): 359–379. doi:10.1080/09298219808570753
- Farina, A., and L. Tronchin. 2000. "On the "Virtual" Reconstruction of Sound Quality of Trumpets." *Acustica* 86(4): 737–745.
- Gade, A.C. 1989. "Investigation of musicians' room acoustics in concert halls: Part I and II." *Acustica* 69: 193–203.
- Shimokura, R., L. Tronchin, A. Cocchi and Y. Soeta. 2011. "Subjective Diffuseness of Music Signals Convolved with Binaural Impulse Responses." *Journal of Sound and Vibration* 330(14): 3526–3537. doi:10.1016/j.jsv.2011.02.014
- Tronchin, L. 2012. "The Emulation of Nonlinear Time-Invariant Audio Systems with Memory by Means of Volterra Series." *AES: Journal of the Audio Engineering Society* 60(12): 984–886.
- Tronchin, L. 2013a. "Francesco Milizia (1725–1798) and the Acoustics of His Teatro Ideale (1773)." *Acta Acustica united with Acustica* 99(1): 91–97. doi:10.3813/AAA.918592
- Tronchin, L. 2013b. "On the acoustic efficiency of road barriers: The reflection index" *International Journal of Mechanics* 7(3): 318–326.
- Tronchin, L., and V. L. Coli. 2015. "Further Investigations in the Emulation of Nonlinear Systems with Volterra Series." *AES: Journal of the Audio Engineering Society* 63(9): 671–683. doi:10.17743/jaes.2015.0065
- Tronchin, L., and D. J. Knight. 2016. "Revisiting Historic Buildings through the Senses Visualising Aural and Obscured Aspects of San Vitale, Ravenna." *International Journal of Historical Archaeology* 20(1): 127–145.
- Tronchin, L., and K. Fabbri. 2017. "Energy and Microclimate Simulation in a Heritage Building: Further Studies on the Malatestiana Library." *Energies* 10(10). doi:10.3390/en10101621
- Tronchin, L., and D.J. Knight. 2018. "Transmitting acoustic phenomena and aural illusions: Examples from Athanasius Kircher's *Phonosophia anacamptica*." *Building Acoustics* 25(2): 101–110. doi: 10.1177/1351010X18772709
- Tronchin, L., M. Manfren and P.A. James. 2018. "Linking design and operation performance analysis through model calibration: Parametric assessment on a Passive House building." *Energy* 165 (A): 26–40. doi:10.1016/j.energy.2018.09.037
- Tronchin, L., M. Manfren, V. Vodola. 2020a. "The carabattola - vibroacoustical analysis and intensity of acoustic radiation (IAR)." *Applied Sciences* 10(2), 641.
- Tronchin, L., M. Manfren, V. Vodola. 2020b. "Sound characterization through intensity of acoustic radiation measurement: A study of

persian musical instruments." *Applied Sciences* 10(2), 633.

Tronchin, L., F. Merli, M. Manfren, B. Nastasi. 2020c. "The sound diffusion in Italian Opera Houses: Some examples." *Building Acoustics*, in press. doi:10.1177/1351010X20929216

Tronchin, L., F. Merli, M. Manfren, B. Nastasi. 2020d. "Validation and application of three-dimensional auralisation during concert hall renovation." *Building Acoustics*, in press. doi:10.1177/1351010X20926791

Acoustic Refurbishment on a Temporary Auditorium: BIM Design and Interventions Influences

Marco Caniato – Free University of Bozen-Bolzano, Italy – marco.caniato@unibz.it

Federica Bettarello – University of Trieste, Italy – fbettarello@units.it

Matteo Bellè – Free University of Bozen-Bolzano, Italy – matteo.belle@unibz.it

Andrea Gasparella – Free University of Bozen-Bolzano, Italy – andrea.gasparella@unibz.it

Abstract

Building Information Modelling (BIM) is playing an increasingly greater role in the world of construction. BIM should combine as many stakeholders as possible during the design workflow and make it possible to manage the created object before its realization, as well as follow it during its entire lifetime. Holding together such a large number of functions is not an easy task; managing each of them in the best possible way is even more complex, especially if, as is happening today, the sectors involved in the construction of a building are becoming increasingly specialized. In order to verify (i) what the limits are that a BIM software can reach, (ii) what the most common difficulties are and (iii) in which sectors they usually appear, it is necessary to study a real project carried out in its entirety with the BIM method. For this reason, a complex case study has been chosen which would be useful in formulating a response to the previous key points. The critical aspects linked to the possible choices that should be made between the various software have been highlighted as well as the pros and cons of the possible paths that can be followed. Finally, the future scenarios of integrated software development are identified and the way in which they may be adopted to address the difficulties and weaknesses that BIM still presents, is discussed.

1. Introduction and Scope of Work

Moving from CAD (Computer Aided Design) to BIM (Building Information Modelling) includes the necessity to understand the difference between “drawing” and “modelling”, handling objects instead of geometrical elements and, moreover, “intelligent” objects, carrying with themselves a certain amount of information. Thus, it is evident that designed forms are

not only “shapes” anymore (Caputi et al., 2015).

BIM claim to be a unique cycle, which is able to treat in the same way most of the professional sectors involved in the design and the construction of a building, such as architectural design, load analysis, real time rendering etc. (Ciribini, 2013).

The main aim of the study is to assess and to give a clear image of how a BIM software operates in situations where it has to approach the most technical fields of buildings design, moving further than modelling as it was meant before, just virtually assembling different shapes together.

In order to develop this topic, a case study was carried out, namely the restyling of an auditorium. In this example the main goal was to link the existing edifice to the surroundings, providing a strong sound insulation system, no variations of the inner acoustics and a new lighting facility.

2. Materials and Methods

In order to better understand the importance of a comprehensive IT design, a case study was identified and studied. It consists of a real auditorium used often to host live events and located close to residential areas, in an Italian city (Fig. 1).

The primary function of the intervention included a covering body (Fig. 2), providing a solution to the problem of acoustic insulation with respect to the surrounding residential areas. The present temporary structure cannot limit the propagation of the noise, causing disturbances (Tronchin and Coli, 2015).

The existing structure is more similar to a temporary tensile composition made of steel beams supporting

a polymeric frame. This construction is typical of temporary edifices; however, it is not expected to be dismantled. It is actually considered one of the main suitable locations for concerts and similar events. The goal was the realisation of an external sound insulating covering; this whole process was carried out with the help of a Building Information Modelling software, which helped develop the entire plan, from the beginning to the end.



Fig. 1 – Project area, auditorium on the left, residential areas in the background

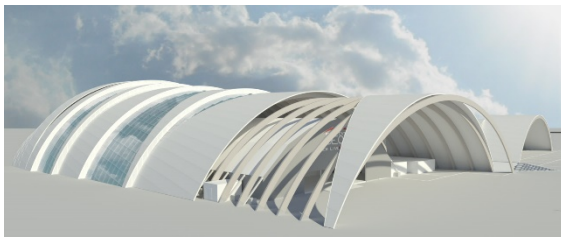


Fig. 2 – The covering roof structure

This kind of approach made it possible to separate and treat each of the working phases separately. This was the easiest and fastest way to understand in which stages of the process Building Information Modelling could actually be an advantage and, on the other hand, when adopting this alternative process could create some problems, and therefore not provide satisfying results.

In addition, an uncommon structure as the case study was chosen in order that unconventional architectural shapes could be used and particular volumes modelled. This was considered important because it was felt that all possible solutions which a BIM system provides to the user should be developed and investigated.

The different types of BIM software are similar but not equal even if they should all work in the same context (Wang et al., 2019). This is due to the fact

that over the last few years, a huge number of different companies have developed their own BIM software and, although the concept behind them is more or less the same, it is still possible to identify some significant differences. The first step is therefore choosing the right software for the specific need.

It is particularly important to discriminate between two main groups of programs; their leading distinction is the way they treat the elements, namely components of the building's model (Eastman et al., 2016).

The first sample (Fig. 3) works with single constructive elements, which means that each object is independent from the others: its features can be modified one by one without having an influence on anything else.



Fig. 3 – Functioning method of the first software sample

The second sample (Fig. 4) proposes a different approach: all the elements are assembled together in order to create the entire model; they are listed in categories, or “families” and “typologies”. This means that a single object belongs to a certain family and has a specific typology.



Fig. 4 – Functioning method of the second software sample

“Families” are groups of certain kinds of elements (furniture, constructive elements etc.), with the same standards. The “typologies” are the sections where slightly different objects of the same family are contained (Fig. 5) (Zhou et al., 2019); they are the same model, but with a couple of distinct features: dimensions for instance, materials or slightly different constructive characteristics (Gasteiger, 2015).

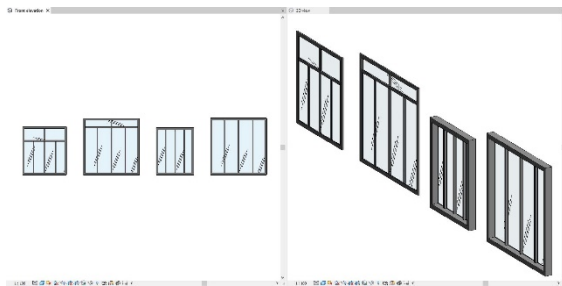


Fig. 5 – Example of more typologies of a window family

In this second kind of software, if a feature is modified, all the elements of the same type, which are already included in the file, are also adjusted too. If a customization is needed, a new typology or a new family must be created, so as to leave the other existing elements of that family unaltered (Hardin and McCool, 2015).

In this view, the first type of software could be advantageous for smaller projects, or at least when in a certain construction the number of elements is not too high. Therefore, they can still be managed without any particular difficulty by the user and, if necessary, updated one by one. In these cases, having the ability to interact with a single object, while leaving all the others unaltered, could make some processes faster to implement.

The second type is obviously the opposite, helping much more when numbers and values are increasing.

In this case, the chosen software belongs to the second group. This choice is dictated by the fact that a more in-depth parametric design could be implemented. In addition to the above-mentioned characteristics, this type of program is closer to an informatic approach and less to the world of architectural design. It means that the procedures adopted are mostly constructed following the operating mode of IT programming; thus, the software itself allows the user to access, organize and reassemble the information contained in a certain file. Parameters and data are available to the user who is able to manage an object from every point of view, not only in its external appearance. Choosing this type of software makes it possible therefore to reach the aim of the project from a more accurate perspective. Working with the first group could have possibly been faster in some steps, but, in this way, there is a wider range of aspects that are analyzed.

It is also important to point out the main differences in terms of planning between a BIM and a traditional CAD program. Building Information Modelling deals with the whole process involved in a construction, being able to follow all the different phases, from the design to the demolition or the relief and the renovation. This way of working is called “seven-dimensional planning” (Fig. 6), where each “dimension” indicates an extra field that is treated by these software, from the standard 3D spatial modelling to the 7th dimension that stays for “maintenance”.

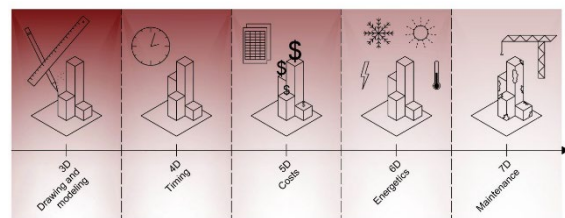


Fig. 6 – Representation of the “7D planning”

3. Results and Discussion

At this step, it can be stated that all the tasks related to the definition of the structure itself were simplified and completed more easily than if it had been carried out with other tools.

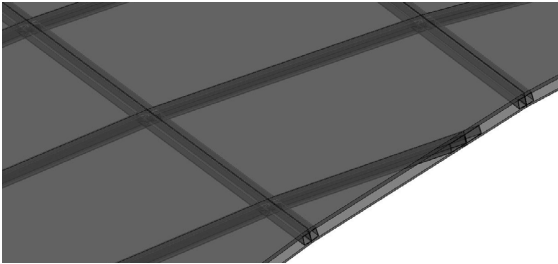


Fig. 7 – Detail of the constructive elements of the roof

The use of a parametric method is clearly advantageous (Mirshokraei et al., 2019). In this case, the designing of the external and internal shape could probably have been achieved with most computer aided modelling applications. Nevertheless, the adopted procedure seemed to be the best solution because the covering skin of the auditorium has a grid structure and is composed of individual construction elements (Fig. 7) and each of them must adapt to the required curvatures (Fig. 8).

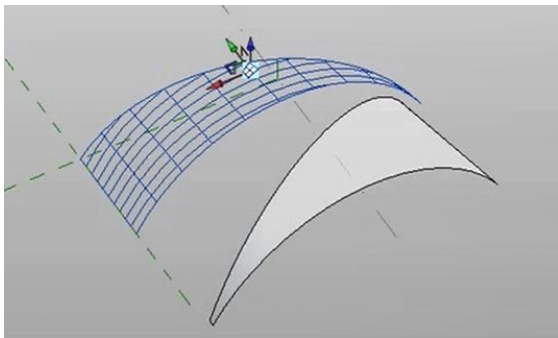


Fig. 8 – The grid adapted to the curvatures

On the one hand, the above-mentioned aspect is particularly evident in the change in size and characteristics (Fig. 9) of the frames and components: the way in which the latter adapt to the former is automatic, considerably faster and with less chance of making mistakes during the procedure.

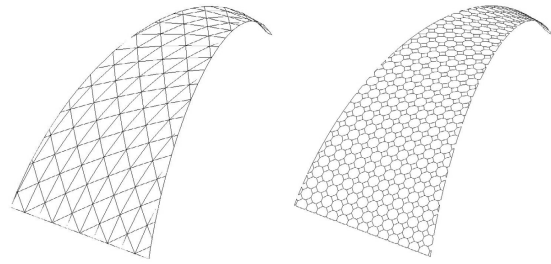


Fig. 9 – Comparison between two different frame systems, adapted to the same shape only by changing parameters

On the other hand, there is no specific section in the BIM language referring to acoustics or lighting technology. It is therefore important to understand which path to take to make it possible to solve the phases of design and subsequent assembly more easily and quickly.

It is also important to highlight that modelling in a BIM software does not always involve the same procedure. This means that the way an object is obtained depends greatly on its final function and how it will be positioned in the building and which cues and pointers it will have in its ultimate position. It is therefore very important for the user to be aware of the kind of construction element that has to be modelled and with which properties, at the very beginning of the process.

This creates the possibility of obtaining individual objects, frames, grids, modular systems and so on and each of them will adapt in the best possible way according to the function and role they play within the construction.

When analyzing the acoustic issue, the problems may be presented in a slightly different way. This includes many variables, which need to be predicted and analyzed in the best possible way (Farina and Tronchin, 2013; Ruggeri et al., 2015; Tronchin and Fabbri, 2017), even if realized using gypsum panels (Piana et al., 2014). It is not only necessary to consider the porosity or the surface impedance or airflow resistivity of the different materials (Fig. 10), but also the intensity and size of the different sound waves. These are not direct factors that can be included in a BIM software and some of them are impossible to manage to the last detail, especially because they may require a dynamic situation to be analyzed.

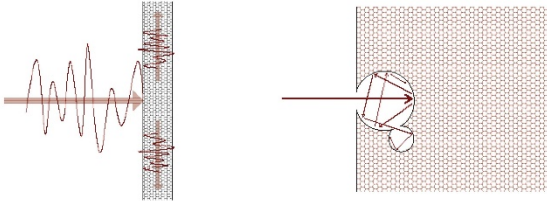


Fig. 10 – Sound-absorbing surface and soundwave interaction

In this way, another process must be adopted to simulate the diffusion of sound waves inside and outside the auditorium structure. In this case study, there were no other choices of importing the model into an external 3D ray-tracing acoustic software (Fig. 11), consequently losing all the included BIM-information.

Even if the procedure is not actually too long, the problem comes from the fact that for the first time in the design flow, other programs have to be involved, meaning that the model is leaving the BIM environment (Tanaka et al., 2019; Wu and Zhang, 2019). This causes the digital format to be changed. It is easily understandable that this kind of method could solve a task, but at the same time it would create a dead branch of the process as well. The exported and modified model would not be usable for other purposes except for the one it was created for (e.g. acoustic simulations).

This fact is exactly the opposite of what happens with BIM objects, involving the same model in as many sectors and professional areas as possible, without the necessity to export or to change any digital format, creating a two-way procedure.

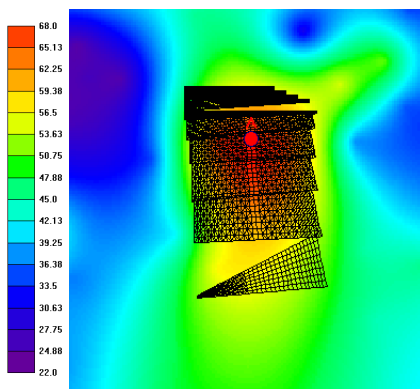


Fig. 11 – Sound insulation virtual simulation of sound pressure levels carried out without a BIM software. “A” indicates the noise source position

Further difficulties arise when analyzing the lighting tasks. This time the problem is not related to the model or its format. It is more about the way certain aspects are handled by the software: there is a lack of BIM tools that approach light as a dynamic aspect (Nawari, 2019).

This project involved the theme of light (Fig. 12) as a sign that makes it possible to understand from outside if the auditorium is hosting an event or not. This means that it becomes a variable, not only in the two directions “on or off” (what usually happens in an ordinary “day and night” situation), but in more cases. This implies the need to add a certain number of parameters more or less linked to each other, to be able to control these variations.

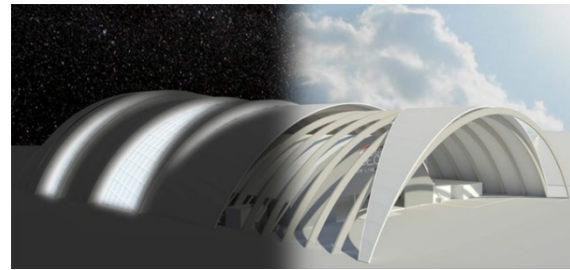


Fig. 12 – Day and night circumstances

BIM software include this possibility for a number of aspects, but have not been able to handle them during the flow of time so far.

It is not generally possible to create a dynamic model that can therefore help to understand how proper characteristics change over time (for example, distinction between day and night hours, or events presence). Even if the “time” variable is important in a BIM procedure, it is usually meant as a condition, not as a dynamic flow: the user can only modify the status of the project in the digital environment, in order to be able to predict how the real structure will react to wear. For these reasons, it was necessary to adopt a static solution (Fig. 12). It was therefore not possible to verify changes in the designed lighting during the different hours of the day, but several different static situations had to be created to distinguish how the structure would react to different lighting conditions (Fig. 13). In terms of final results, the quality was not lower, and it was still possible to analyze how the scenario would be in many different situations, but it was extremely time consuming.

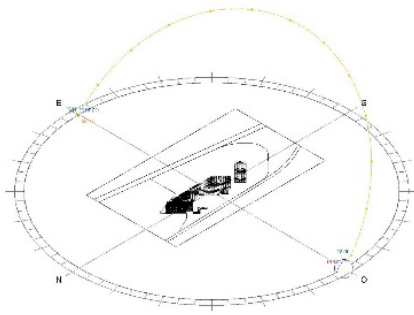


Fig. 13 – Solar light settings in a BIM software

In order to somehow include more aspects into BIM environments, software developers have adopted multiple and often different solutions. Most of the companies have included in their software the possibility to add external parts and sectors, which are useful to strengthen and to improve a certain aspect of the planning. These implementations belong to two main categories: tabs and plug-ins. Plug-ins are likely more complex and complete. They are extra software, based on and working with the main BIM program. On the other hand, tabs are often better connected and easier to use, because there is no need to leave the main software, since they are actually tools already integrated in the main software's environment.

Although BIM is not free of shortcomings and lacks, the whole issue must be seen in its entirety: this type of IT tool is still young and is probably in its main phase of development and growth. Furthermore, fields such as construction science and design have also been evolving very rapidly in recent decades. This fact therefore means that both sides most likely need time to adapt to each other.

The main goal then has to be to reach a complete "open BIM" situation: this term indicates a scenario in which all the different BIM software would be able to collaborate with each other without limitations, including output formats. This plan naturally requires a common digital standard, and for this reason the IFC (Industry Foundation Classes) format was created (Di Martino et al., 2020). This would be the way to connect all stakeholders who have to deal with a project together (Fig. 14), limiting the loss of time and of information between the different stages of its development. As the example shows, a good variety of tasks could be completed with the help of

an appropriate parametric setting; this is the best way to deal with aspects that may still present some interface difficulties, such as acoustics or lighting.

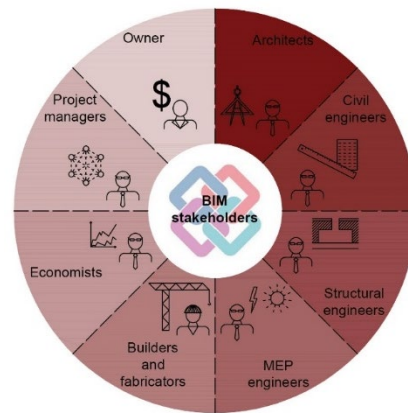


Fig. 14 – Possible stakeholders

Finally, in the authors' opinion, it is necessary to have a common framework, a standard format that can be used for the development of possible plug-ins of the main software. In this way, the different companies could have a common base to work on during the programming process. This fact could facilitate the interaction between the BIM software and its plug-ins and also highlight any areas not adequately covered by the various proposed tools.

4. Conclusions

In this paper, the problem of using the BIM method for complex structures involving acoustics and lighting properties has been addressed. The pros and cons of the various BIM modelling methodologies were analyzed and a complex case study was carried out to identify a possible way to implement these features, which are currently absent, in Building Information Modeling.

Finally, the possible improvements were highlighted, which are desirable in order to make the best use of this tool, which today still lacks many technical aspects related to building physics such as (i) the acoustic aspect of materials and components and (ii) the simulation of lighting in dynamic mode. A possible solution is represented by "open BIM", where the software can fully interact with other external programs and can be also implemented by

tools, able to resolve issues by taking full advantage of this type of virtual design.

References

- Caputi, M., P. Odorizzi and M. Stefani. 2015. *Il Building Information Modeling – BIM*. Santarcangelo di Romagna: Maggioli Editore.
- Ciribini, A. L. C. 2013. *L'information modeling e il settore delle costruzioni: IIM e BIM*. Segrate: Maggioli Editore.
- Di Martino, B., C. Mirarchi, S. Ciuffreda and A. Pavan. 2020. "Analysis of Existing Open Standard Framework and Ontologies in the Construction Sector for the Development of Inference Engines." *Advances in Intelligent Systems and Computing* 993: 837-846.
- Eastman, C., P. Teicholz, R. Sacks and K. Liston. 2016. *Il BIM*. Lavis: Hoepli.
- Farina, A., and L. Tronchin. 2013. "3D Sound Characterization in Theatres Employing Microphone Arrays." *Acta Acustica United with Acustica* 99(1): 118-125.
doi:10.3813/AAA.918595
- Gasteiger, A. 2015. *BIM in der Bauausführung*. Innsbruck: Innsbruck University Press.
- Hardin, B., and D. McCool. 2015. *BIM and construction management*. Indianapolis: Wiley.
- Mirshokraei, M., C.I. De Gaetani and F. Migliaccio. 2019. "A web-based BIM-AR quality management system for structural elements." *Applied Sciences* 9(19), 3984.
- Nawari, N.O. 2019. "BIM Data Exchange Standard for Hydro-Supported Structures." *Journal of Architectural Engineering* 25(3), 04019015.
- Piana, E., P. Milani and N. Granzotto. 2014. "Simple method to determine the transmission loss of gypsum panels." *21st International Congress on Sound and Vibration 2014, ICSV 2014*, Vol. 5: 3700-3706; Beijing; China; July 13th-17th 2014.
- Ruggeri, P., F. Peron, N. Granzotto and P. Bonfiglio. 2015. "A combined experimental and analytical approach for the simulation of the sound transmission loss of multilayer glazing systems." *Building Acoustics* 22(3-4): 177-192.
DOI: 10.1260/1351-010X.22.3-4.177
- Tanaka, F., M. Tsuchida, and M. Onosato. 2019. "Associating 2D sketch information with 3D CAD models for VR/AR viewing during bridge maintenance process." *International Journal of Automation Technology* 13(4): 482-489.
- Tronchin, L., and V. L. Coli. 2015. "Further Investigations in the Emulation of Nonlinear Systems with Volterra Series." *AES: Journal of the Audio Engineering Society* 63(9): 671-683.
doi:10.17743/jaes.2015.0065
- Tronchin, L., and K. Fabbri. 2017. "Energy and Microclimate Simulation in a Heritage Building: Further Studies on the Malatestiana Library." *Energies* 10(10). doi:10.3390/en10101621
- Wang, M., Y. B. Deng, J. Won and J. C. P. Cheng. 2019. "An integrated underground utility management and decision support based on BIM and GIS." *Automation in Construction* 107, 102931.
- Wu, J., and J. Zhang. 2019. "New Automated BIM Object Classification Method to Support BIM Interoperability." *Journal of Computing in Civil Engineering* 33(5), 04019033.
- Zhou, X., J. Zhao, J. Wang, X. Huang, X. Li, M. Guo and P. Xie. 2019. "Parallel computing-based online geometry triangulation for Building Information Modeling utilizing big data." *Automation in Construction* 107, 102942.

Control Strategies to Increase the Photovoltaic Self-Consumption for Air-Source Heat Pump Systems

Maria Pinamonti – Free University of Bozen-Bolzano, Italy – maria.pinamonti@natec.unibz.it

Alessandro Prada – University of Trento, Italy – alessandro.prada@unitn.it

Paolo Baggio – University of Trento, Italy – paolo.baggio@unitn.it

Abstract

Decreasing the use of fossil fuels for heating and cooling applications in buildings is one of the main concerns in reaching the energy reduction targets defined by the European Union countries. For this purpose, high efficiency heating and cooling systems are required, together with appropriate control strategies. The use of heat pumps (HP) in residential buildings is spreading, and the combination of these systems with the on-site production of photovoltaic (PV) energy can lead to high levels of renewable energy self-consumption. However, a poor design and a lack of control in the system can lead to a large amount of PV energy surplus, which has to be sold to the grid, or wasted. For this purpose, the use of energy storage and demand-side management strategies are crucial. This paper describes a control strategy for an air-source HP system combined with a PV plant for a residential building. The control strategy aims to maximize the self-consumption of PV power, varying the system behavior depending on the instantaneous PV production. When an overproduction of PV energy occurs, the HP operates to store the surplus of solar energy by exploiting the storage capacity and the building thermal capacitance. In this study, the heat pump was controlled by acting on the compressor rotational speed (i.e. the frequency of the supplied power). The compressor was controlled in order to operate at the maximum capacity level compatible with the power supplied by PV. The effectiveness of the control strategy was assessed over a whole year, considering both the heating and cooling season and domestic hot water (DHW) preparation. The simulations were performed using the TRNSYS simulation software, considering a double-story residential building in northern Italy. The results obtained with the proposed demand side management (DSM) strategy show a reduction of around 33% of the energy taken from the grid with respect to a similar system with a standard control strategy.

1. Introduction

In Europe, about 40% of the final energy consumption is related to building use (European Parliament and Council, 2012), and in particular the residential sector is responsible for about 25% of the total consumption (Eurostat, 2019).

Moreover, in 2017 Eurostat reported a share of renewable energy for heating and cooling in the residential sector of about 19.5% and about 30% for electricity production (Eurostat, 2018).

Decreasing the use of fossil fuels for heating and cooling applications in buildings is one of the main concerns in reaching the energy reduction targets defined by the European Union countries. A more efficient use of energy and a larger share of renewable energy sources are required solutions to decrease the impact of building energy use over the final European energy consumption. For this purpose, one of the most promising technologies, the use of which spreading in European countries, is the heat pump system coupled with photovoltaic panels (Battaglia et al., 2017). In Europe, the most common solution is the use of air-source heat pumps, which are able to provide heating, cooling and DHW simultaneously (Hardorn, 2015). These systems are driven mainly by electricity and can operate efficiently in combination with PV systems. Indeed, the heat pump can be directly connected to the photovoltaic panels and lead to direct consumption of the solar energy generated on-site. One of the main issues to optimize the self-consumption of these systems is the time gap between the peaks of the building loads and the PV power availability (Luthander et al. 2015). There are different solutions to improve the self-consumption rate, among which are the use of energy storage technologies and the

demand-side management (DSM) strategies for the building load shifting (Battaglia et al., 2017; Fischer and Madani, 2017). Different strategies for DSMs have already been de-fined, such as direct-load control, load limiters, de-mand bidding and smart metering and appliances (Strbac, 2008).

Several studies have analyzed different DSM controls and their impact on the overall energy consumption and performance of the system. In these studies, the use of modulating heat pumps is widespread to ensure a high level of PV self-consumption. Dentel and Betzold (2017) propose a control strategy which adapts the heat pump to the PV production, together with the use of thermal and electric storage, and reaches an increase of 21% in PV direct consumption. Bee et al. (2018) define a control strategy to store the energy within the thermal storage capacity of the system and the building thermal capacitance when the PV power is available. In this study, the self-consumption of the system increased from 7% to 65%.

The aim of this study is to define and analyze a DSM strategy to maximize the self-consumption rate for a modulating air-source heat pump system, considering a reference residential building in Bolzano, in the north of Italy.

2. Method

The study proposes and analyzes a control strategy for demand-side management, considering a modulating air-source heat pump for a residential building in northern Italy. The system provides space heating, space cooling and domestic hot water to the building over the whole year. The proposed DSM operates by varying the system's behavior according to the instantaneous PV power availability. The assessment of the system's performance and energy consumption was carried out by means of dynamic simulations with the TRNSYS software.

2.1 Test Case Building

The considered building proposed in the study is a small two-story building with 140 m² heated floor area and a heat dispersion surface vs a conditioned volume ratio S/V of 0.59. The building is divided

into four thermal zones, one in the north and one in the south part of each floor of the building. The envelope of the building has a high-insulation level, as shown in Table 1.

Table 1 – U-values of the building elements

Element	U-Value
Wall	0.18 Wm ⁻² K ⁻¹
Ground floor	0.18 Wm ⁻² K ⁻¹
Roof	0.17 Wm ⁻² K ⁻¹
Window	0.86 Wm ⁻² K ⁻¹
Ceiling	0.20 Wm ⁻² K ⁻¹

The heating and cooling loads of the building were calculated using the software TRNSYS and considering the test reference year for the climate of Bolzano. The building model was set up using the multi-zone building subroutine type 56 in TRNSYS. The DHW consumption was estimated around 186 l per day based on the Italian technical specification (UNI 2014) using the hourly demand profile determined by the European Standard (European Committee for Standardization-CEN 2016). The HVAC system includes a heat-recovery ventilation system and a dehumidification unit, which operates during the summer period to avoid the risk of condensation on the cooled floor. The air change rate is set to 0.5 vol/h during the heating season and 1.5 vol/h during the cooling season.

2.2 Building System

An air-source heat pump system was modelled in TRNSYS with a previously developed type (Bee et al., 2016). This type modelled a heat pump with a variable speed compressor, and evaluated the part load operation of the component by means of the performance map and the part-load performance function provided by the manufacturer. The heat pump provided the building with space heating (SH), space cooling (SC) and DHW production. The heat pump is connected to two tanks (type 60), one for DHW and the other one for SH and SC. The tank for SH and SC is connected to a radiant floor panel system, which has a pipe spacing of 0.12 m and diameter of 0.016 m. The radiant floor was modelled as an active layer within the floor in the building model. Four on-off thermostat controllers were connected to each thermal zone. The set-point for the

ambient temperature is equal to 20 °C for the heating mode and 26 °C for the cooling mode. The thermostats control the inlet flow of the radiant panels for each zone by switching on and off four single-speed pumps (Type 114). The SH tank temperature set-point is reset depending on the outdoor temperature. In the heating mode, such set-point varies from 40 to 20 °C. while in the cooling mode it goes from 26 to 18 °C. The inlet water temperature of the radiant panels varies accordingly.

A PV plant was modelled considering polycrystalline modules (Type 94) with a nominal power of 270 kWp. The panels have an array slope of 45° and a total area of about 20 m².

2.3 Control Strategy

The HP model was controlled by setting the compressor rotational speed. The input parameter is the frequency of the supplied power, which is controlled according to the difference between the set-point temperatures for SH and SC and the actual temperature of the outflow of the HP. In the DHW production mode, the compressor always runs at its maximum speed. The priority is given to the DHW production. The model calculates the heat pump power according to the inverter frequency (f), as the percentage of the total electric input ($Y_{el,\%}$) for the actual operating conditions. The relation between frequency and electric input was assessed for different sink and source temperatures based on manufacturer data, obtaining the curve shown in Fig. 1.

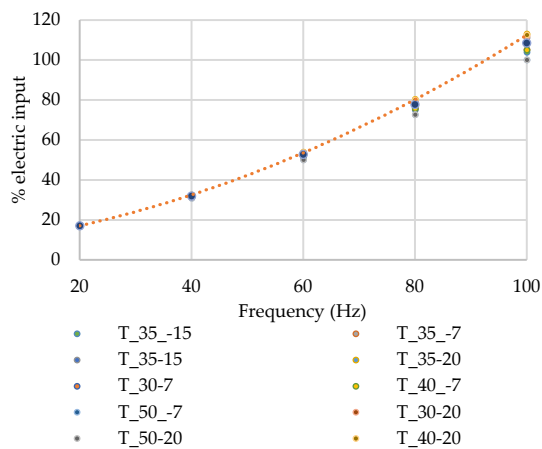


Fig. 1 – Inverter frequency and relative percentage of electric input for the heat pump at different operating conditions

Considering different operating temperatures, the results are similar at low frequency values, but they diverge (a little) at higher frequency levels. For the purpose of this study, the function used for the relation between frequency and electric power used by the heat pump is the one corresponding to the highest values of $Y_{el,\%}$. The trend can be fitted by the following quadratic function (Eq. 1):

$$Y_{el,\%} = 0.007 \cdot f^2 + 0.3522 \cdot f + 7.2073 \quad (1)$$

During each time step of the simulation, the software computed the power generated by the PV panels. The PV power covers directly the electric loads for ventilation, dehumidification, heat pump operation and hydronic system circulation pumps. In the base case, any PV overproduction is sent to the grid. The DSM proposed in this study aims to exploit the PV overproduction to maximize the self-consumption of the system and decrease the purchase of energy from the national grid. When a PV overproduction occurs, the DSM controls the compressor speed depending on the actual PV production, adapting the heat pump thermal output to the available PV power. Considering the operating conditions of the heat pump at the time-step where the overproduction is detected, the electric input (Y_{el}) is computed using a polynomial equation obtained from the manufacturer data of the heat pump power working at different sink and source temperatures. The equation (Eq. 2) contains four coefficients (b_n), the condenser outlet temperature ($\varphi_{cond,out}$) and the evaporator inlet temperature ($\varphi_{ev,in}$).

$$Y_{el} = b_0 + b_1 \cdot \varphi_{cond,out}^2 + b_2 \cdot \varphi_{ev,in} + b_3 \cdot \varphi_{ev,in}^2 \quad (2)$$

The available PV surplus power is then expressed as a percentage of the electric input Y_{el} and the frequency is calculated using Equation 1. This frequency is used as input to control the HP type. This frequency corresponds to the maximum capacity level of the HP compatible with the supplied PV power.

3. Simulations

The simulations were performed with the TRNSYS software, to assess the behavior of the building and the system during the whole year, using a time-step of 1 minute.

Five different cases were simulated to evaluate the efficiency of the proposed DSM.

In the first case, a standard HVAC control strategy was assessed without the integration of DSM. In this case, the PV power directly covered the electrical building loads, as defined in the previous chapter, and during the PV overproduction, the electricity was sent to the grid.

In the other cases, the DSM was applied with different strategies to store the excess thermal energy overproduced by the heat pump. The energy was stored by changing the set-point temperatures of the SH and SC tank to 65 °C for the heating mode and to 7 °C for the cooling mode. A diverting and mixing valve system controlled the return water from the radiant panels and mixed it with the hot water in the tank to maintain the inlet temperature of the water entering the panel at the set-point level. As described in the previous chapter, the set-point temperature varies depending on the outdoor air temperature. The overheating of the DHW tank brings the temperature up to 75 °C. Moreover, the possibility of exploiting the building thermal capacitance to store a larger amount of energy was evaluated. In this case, during the PV surplus periods, the set-point of the thermal zones of the building was modified by ± 2 °C. The four DSM strategies are defined as follows:

- DSM 1: in the case of PV overproduction, the priority was given to the overheating and overcooling of the SH-SC tank. When the maximum set-point was reached, the energy was stored in the DHW tank.
- DSM 2: the heat pump worked as in DSM 1, plus the set-points of the thermal zones were modified by ± 2 °C.
- DSM 3: the priority was given to the overheating of the DHW tank.
- DSM 4: the same as DSM 3, together with the change of the thermal zones' set-point.

4. Results and Discussion

The four DSM solutions were evaluated and compared with a standard HVAC control strategy to assess the potential reduction of energy use. The results are expressed as the amount of purchased energy from the grid. The monthly results for the 5 cases are shown in the graph (Fig. 2).

The results show that the DSM strategy reduced appreciably the amount of energy taken from grid with respect to the standard HVAC control strategy. Moreover, prioritizing the DHW tank overheating appeared to be favorable throughout the whole year. The difference between DSM 1 and DSM 3 consumption was larger during the summer season.

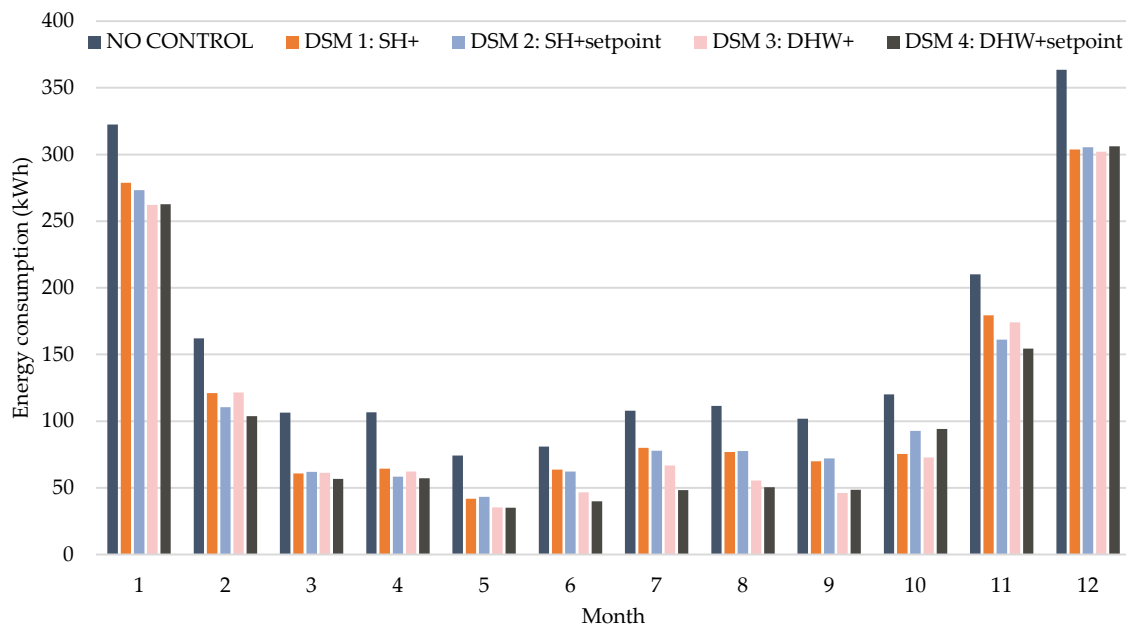


Fig. 1 – Grid consumption of the standard HVAC strategy and the different DSM solutions

The alteration of the thermal zones' set-point, evaluated in DSM 2 and DSM 4, was advantageous during most of the months. In the middle seasons, prioritizing the DHW or SH-SC led to similar results. Considering the annual energy consumption taken from the grid (Fig. 3), the results for the standard HVAC control strategy was around 13.30 kWh m⁻² y⁻¹. The annual grid consumption reduction achievable with the DSM strategies were 24%, 25%, 30% and 33% for the DSM 1, DSM 2, DSM 3 and DSM 4, respectively.

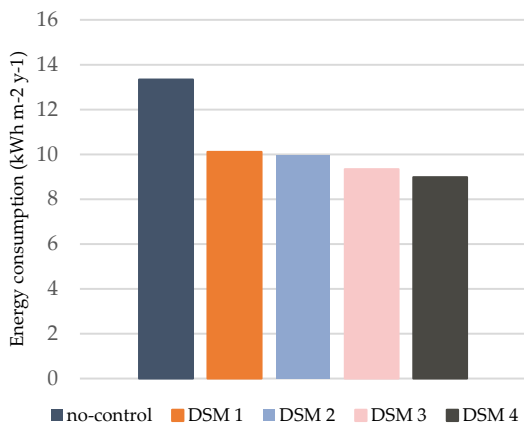


Fig. 3 – Total annual energy consumption from the grid for the standard HVAC strategy and the proposed DSM

Looking at the annual grid consumption, the DSM 4 seems to be the optimal solution.

A more detailed comparison has been carried out between the standard HVAC -control strategy and the DSM 4.

For these two cases, the total energy consumption is shown in the graphs in Figs 4 and 5, highlighting the different amounts of energy self-consumed by the system and purchased from the grid. For the DSM 4 case, the total amount of energy consumed by the system increased, but most of it was covered with the use of on-site solar energy production. In particular, the self-consumption rate reached values of around 85% during the summer period. For the no-control strategy, the maximum amount of self-consumption was around 55% during the summer.

In the same graphs, the COP and EER values show the average performance of the two systems for each month. Comparing the results for the two systems, the standard HVAC -control strategy presents higher levels of performance. The reason is due to

the overheating and overcooling of the tank in the DSM strategy, which lead the heat pump to work with a higher temperature difference and consequently, with lower performance. The only increase in EER value for the DSM 4 case is due to the fact that the systems worked during May for the overcooling of the tank, when the external temperatures were lower and the heat pump worked with higher performance, while in the standard HVAC control case the cooling was not required in that period.

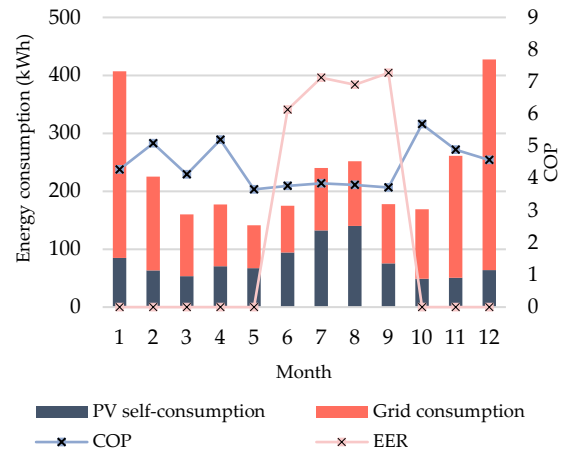


Fig. 4 – Total energy consumption of the system and performance indicators for the standard HVAC control

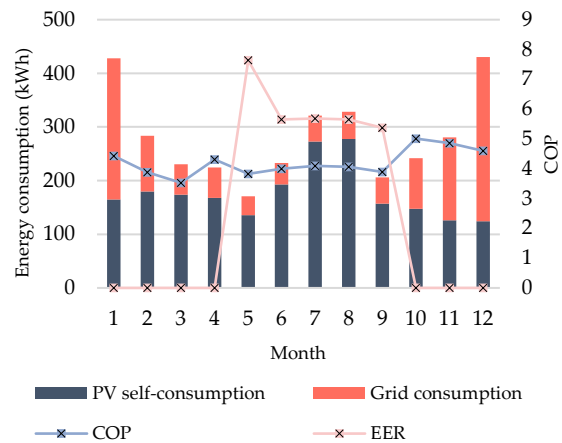


Fig. 5 – Total energy consumption of the system and performance indicators for the optimal solution DSM 4

In the following graphs, the PV power generation and the system's loads are shown for a few days of the heating season, the middle season and the cooling season for the two analyzed strategies. For the month of January (Fig.s 6 and 7), the PV production was almost half the production during the summer season, but the DSM shifted the system's load during the time when the PV was available, reducing

significantly the peaks due to the DHW production. During the middle season (Figs 8 and 9), the PV production was higher but the loads were lower, because no heating or cooling was required. In this case, the DSM shifted most of the load during the PV production period.

The same considerations are valid for the summer

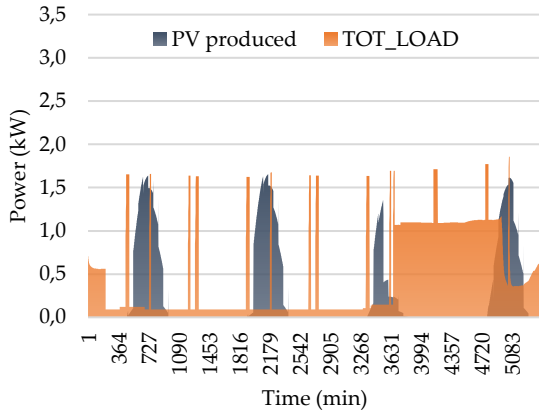


Fig. 6 – PV produced power and system's load for the standard HVAC strategy, from 15th to 19th of January

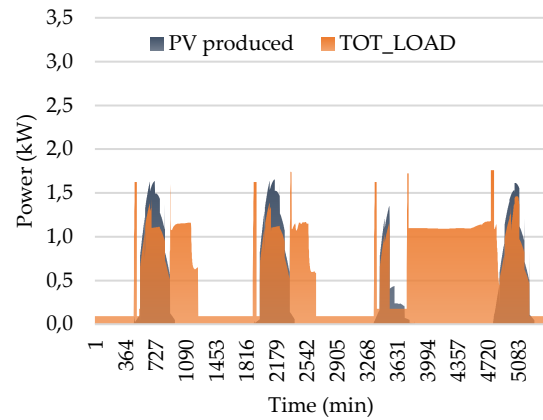


Fig. 7 – PV produced power and system's load for the DSM 4 strategy, from 15th to 19th of January

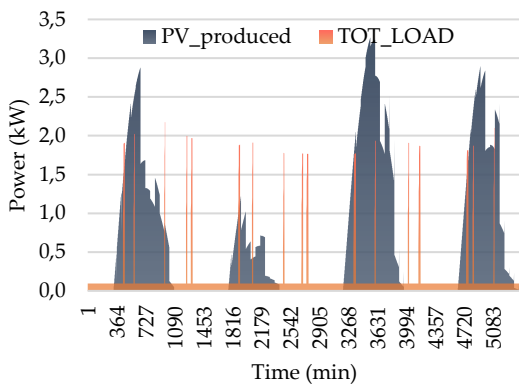


Fig. 8 – PV produced power and system's load for the standard HVAC strategy, from 15th to 19th of April

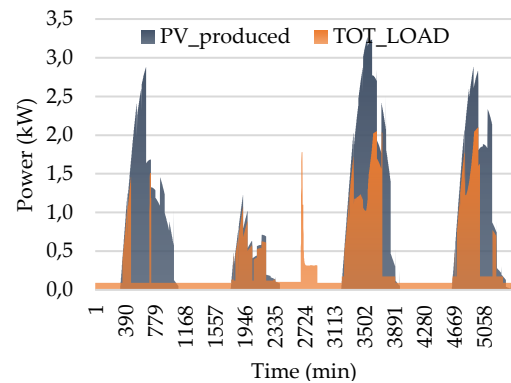


Fig. 9 – PV produced power and system's load for the DSM 4 strategy, from 15th to 19th of April

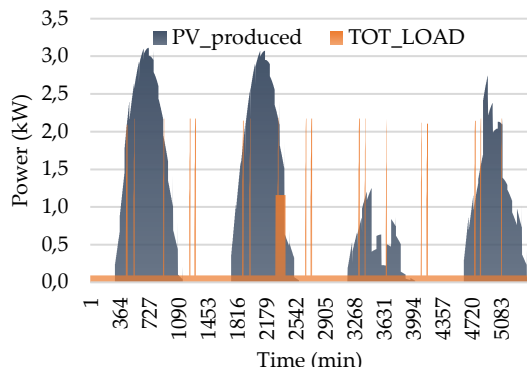


Fig. 10 – PV produced power and system's load for the standard HVAC strategy, from 15th to 19th of July

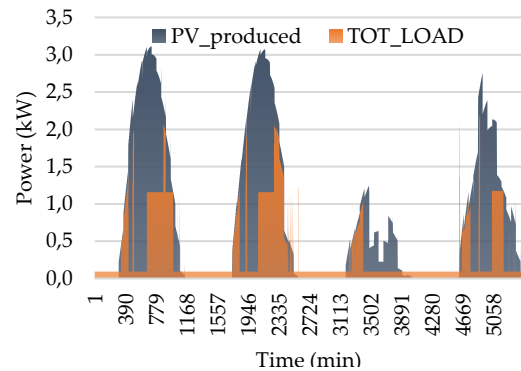


Fig. 11 – PV produced power and system's load for the DSM 4 strategy, from 15th to 19th of July

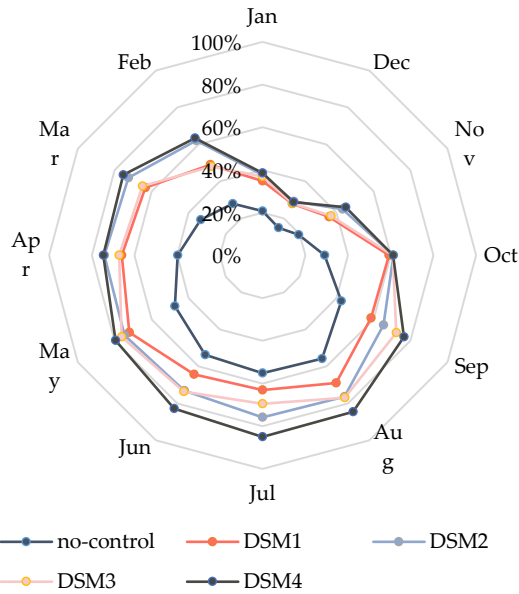


Fig. 12 – PV energy self-consumption during the whole year for the proposed DSM solutions

The figure shows the self-consumption for each month of the year, comparing the standard strategy with the proposed DSM. The comparison highlights how the amount of energy which is self-consumed by the system increases during the whole year for all the DSM strategies. In particular, the four DSM strategies have similar results during the winter period. The strategy where the thermal zone set-point is modified based on the PV overproduction, DSM 2 and DSM 4, shows the best performance during the middle seasons. Strategies DSM 3 and 4, where the DHW tank overheating is prioritized, increase their level of self-consumption during the summer season, in comparison to the other solutions. DSM 4 appears to be the best solution for most of the year, reaching levels of self-consumption of around 85%, and leading to the lowest energy withdrawal level from the grid. This result could likely be related to the high energy performance of the building envelope, which reduces the heating and cooling needs, leading to the DHW demand becoming more relevant. Different results are to be expected for less efficient buildings.

5. Conclusions

This paper has proposed different DSM strategies for an air-source heat pump coupled with a PV plant to increase the self-consumption rate of the system. Different solutions are evaluated by considering control strategies, which prioritize the space heating and cooling or the DHW production. Moreover, the exploitation of the thermal capacitance of the building to store energy is considered. The assessment of the DSM is carried out by means of dynamic simulations for the whole year, considering both the heating and cooling season.

The results of the study show that the DSM is effective in reducing the heating and cooling peak loads of the system and to reduce the grid energy consumption of the building. The maximum grid energy reduction achievable with the proposed DSM is 33%, compared to the energy consumption of a similar system with the standard HVAC control strategy. The increase in self-consumption is obtainable without the need for electric storage integration, therefore limiting the investment and the maintenance costs of the system.

Nomenclature

PV	Photovoltaic
DHW	Domestic Hot Water
DSM	Demand Side Management
SH	Space Heating
SC	Space Cooling
COP	Coefficient of Performance
EER	Energy Efficiency Ratio

Symbols

$Y_{el,\%}$	Percentage of electric input (-)
f	Frequency (Hz)
Y_{el}	Electric input (kW)

References

- Battaglia, M., R. Haberl, E. Bamberger, and M. Haller. 2017. "Increased Self-Consumption and Grid Flexibility of PV and Heat Pump Systems with Thermal and Electrical Storage." *Energy Procedia* 135: 358–66.
<https://doi.org/10.1016/j.egypro.2017.09.527>

- Bee, E., A. Prada, and P. Baggio. 2016. "Variable-Speed Air-to-Water Heat Pumps for Residential Buildings: Evaluation of the Performance in Northern Italian Climate." *Proceedings of CLIMA 2016*.
- Bee, E., A. Prada, and P. Baggio. 2018. "Demand-Side Management of Air-Source Heat Pump and Photovoltaic Systems for Heating Applications in the Italian Context." *Environments* 5(12): 132. <https://doi.org/10.3390/environments5120132>
- Dentel, A., and C. Betzold. 2017. "Control Strategies for Geothermal Heat Pump Systems in Combination with Thermal and Electrical Storage Units." *Proceedings of Building Simulation 2019*: 292–98. <https://doi.org/10.26868/25222708.2017.081>
- European Committee for Standardization-CEN. 2016. *EN 12381. Energy Performance of Buildings - Method for Calculation of Design Heat Load - Part 3: Domestic Hot Water Systems Heat Load and Characterisation of Needs, Module M8-2, M8-3*.
- European Parliament and Council. 2012. *Directive 2012/27/EU of 25 October 2012 on Energy Efficiency*.
- Eurostat. 2018. *Energy Statistics - Share of Energy from Renewable Energy Sources*.
- Eurostat. 2019. *Energy Statistics - Final Energy Consumption by Sector*.
- Fischer, D., and H. Madani. 2017. "On Heat Pumps in Smart Grids: A Review." *Renewable and Sustainable Energy Reviews* 70: 342–57. <https://doi.org/10.1016/j.rser.2016.11.182>
- Hardorn, J.-C., ed. 2015. *Solar and Heat Pump Systems for Residential Buildings*. <https://doi.org/10.1002/9783433604830>
- Luthander, R., J. Widén, D. Nilsson, and J. Palm. 2015. "Photovoltaic Self-Consumption in Buildings: A Review." *Applied Energy* 142: 80–94. <https://doi.org/10.1016/j.apenergy.2014.12.028>
- Strbac, G. 2008. "Demand Side Management: Benefits and Challenges." *Energy Policy* 36: 4419–26. <https://doi.org/10.1016/j.enpol.2008.09.030>.
- UNI. 2014. *UNI/TS 11300-2: Prestazioni Energetiche Degli Edifici - Parte 2*.

Sound Reduction Index of Clay Hollow Brick Walls

Nicola Granzotto – University of Brescia, Italy – nicola.granzotto@unibs.it

Edoardo A. Piana – University of Brescia, Italy – edoardo.piana@unibs.it

Antonino Di Bella – University of Padova, Italy – antonino.dibella@unipd.it

Abstract

This paper investigates the sound insulation properties of clay hollow brick walls with low void fraction, horizontal/vertical mortar joint and plaster finishing. Methods based on homogeneous walls (Sharp theory and ISO 12354 procedure) are evaluated. A reference curve obtained as the mean of normalised sound reduction index curves measured in laboratory on real brick walls is proposed and its suitability for sound insulation estimations is discussed.

1. Introduction

The use of clay hollow brick walls is widespread in the building construction sector, especially in southern Europe, due to the availability of raw material, consolidated production capacity and its high thermal and acoustic performance. Thanks to their large mass per unit area, such elements are particularly suitable for limiting low frequency noise, the importance of which has been pointed out by Caniato et al. (2015-2020).

There are different types of blocks on the market, the differences being related to composition, dimensions, geometry and void fraction, mass per unit area, and the fact that the blocks can be laid with or without a vertical mortar joint. In ISO 12354-1 (International Organization for Standardization, 2017), there are several semi-empirical correlations describing the sound insulation performances of some walls, but they are mostly dedicated to the derivation of the single weighted sound reduction index, R_w . In this standard, the sound reduction index R in one-third octave bands is defined only for homogeneous walls (ISO 12354-1 annex B). Nevertheless, a sound reduction index is

necessary when a detailed prediction model of the in-situ sound transmission according to the ISO 12354-1 standard is required.

The analysis of the sound reduction index in one-third octave bands could in principle be performed analytically, but this is not an easy task due to the difficulties in modelling the geometry of the block, the laying technique and the non-isotropic behaviour of the structure. All of these aspects may strongly influence the sound reduction index of the wall, as shown in the work of Fringuellino and Smith (1999). The types of blocks meant for a building envelope are developed so as to provide good thermal and acoustic properties, and their optimisation is a complex problem that cannot be solved by simple comparisons which aim to match the best values chosen among a selection of parameters based on the material properties (Di Bella et al., 2015). Di Bella et al. (2014) found that, in general, the increase in sound insulation is not directly dependent on the thermal insulation performance.

Several studies can be found in the literature on the sound reduction index of hollow brick walls. For example, Del Coz Díaz et al. (2010) investigated the insulation properties of a multilayer concrete hollow brick wall by Finite Element Method (FEM), while Jacus et al. (2010) showed how mass law does not properly represent the acoustic behaviour of the walls examined, and used a homogenisation technique to model the element as an orthotropic block with equivalent sound insulation properties.

Semi-empirical models based on vibrational tests can be used to obtain reliable predictions. Piana, Milani and Granzotto (2014) used a method based on the measurement of natural frequencies of beam samples to determine the sound insulation characteristics of gypsum panels; a similar technique was

applied by Fortini, Granzotto and Piana (2019) on multilayer panels for the shipbuilding industry featuring an innovative foam core; Piana, Granzotto and Di Bella (2017) compared the predictions obtained using a method based on the determination of the natural frequencies of a specimen with mobility measurements performed on drywall panels; finally, Ruggeri et al. (2015) determined the loss factor of multilayer glazing panels using the procedure outlined in ISO 6721-3 standard.

This paper investigates the sound insulation properties of different types of clay hollow brick walls. Methods based on Sharp's (1973) homogenous walls theory and ISO 12354-1 procedure are evaluated. The procedure proposed by Di Bella et al. (2016, 2018), who obtained reference curves of walls and floors made of cross laminated timber based on experimental measurements, is used to define a reference curve as the mean of normalised sound reduction index curves measured in laboratory on real brick walls. The applicability of this curve to actual sound insulation estimations is discussed.

2. Experimental Analysis

2.1 Sound Reduction Index

The transmission coefficient τ is defined as the ratio between the transmitted power and the incident power on a wall:

$$\tau = W_{\text{transmitted}} / W_{\text{incident}} \quad (1)$$

The sound reduction index, R , is defined as

$$R = 10 \log_{10} (1/\tau) \quad (2)$$

The sound reduction index R can be measured in the laboratory through a procedure requiring that a diffuse sound field is established in two adjacent rooms (Fig. 1). Through measurements of the sound pressure level and the sound absorption characteristics of the receiving room, the sound reduction index R can be determined as

$$R = L_1 - L_2 + 10 \log_{10} (S/A) \quad (3)$$

The equivalent absorption area A can be determined experimentally as

$$A = 0.16 (V/T) \quad (4)$$

with T reverberation time of the receiving room.

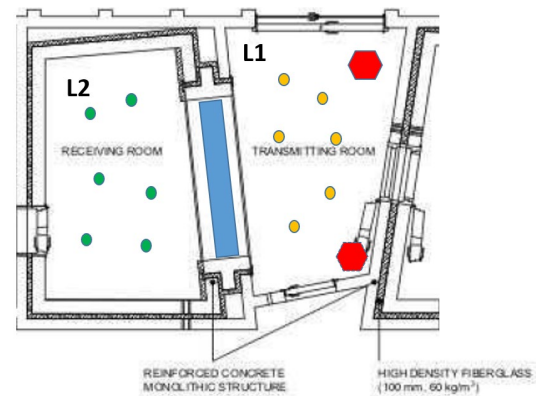


Fig. 1 – Acoustic laboratory at Padova University

2.2 Analysed Types of Hollow Brick Walls

The sound reduction index R_k of seven different types of clay hollow brick walls with vertical and horizontal mortar joints were investigated (subscript 'k' indicates the specific wall type). Sound insulation measurements were carried out in the laboratory, according to the ISO 10140 series (ISO, 2010a, 2010b, 2010c, 2016). The mass per unit area m' of the plastered walls was 305–377 kg/m², the thickness t was 206–330 mm and the void fraction was 37–55% (Table 1).

Table 1 – Characteristics of the walls

Type	Thickness [mm]	Mass per unit area [kg/m ²]	Void fraction [%]
A	280	330	44
B	206	321	37
C	240	305	53
D	280	343	55
E	270	359	45
F	280	327	45
G	330	377	45

An example of installation for a brick wall during the tests performed in sound transmission rooms is given in Fig. 2 and Fig. 3.



Fig. 2 – Clay hollow brick with horizontal and vertical mortal joints mounted in laboratory



Fig. 3 – Wall mounted in the laboratory

Young's modulus for the different walls, E , can be derived by applying the following equation (Italian Ministry of Infrastructure and Transport, 2018):

$$E = 1000 f_k \quad (5)$$

where the compressive strength of k -th type wall, f_k , is calculated with an M5 mortar type according to the declared compressive strength of the block, f_{bk} . Table 2 shows the values of the compressive strength and the resulting E modulus.

Fig. 4 gives the sound reduction index curves and the resulting weighted sound reduction index values R_w after the laboratory tests were computed according to ISO 717-1 standard (International Organization for Standardization, 2013). The resulting R_w values are in a range between 51 and 54 dB.

Table 2 – Compressive strength of the blocks, compressive strength of the wall and Young's modulus of the walls

Type	f_{bk} [MPa]	f_k [MPa]	E [GPa]
A	10.0	4.70	4.70
B	10.0	4.70	4.70
C	10.0	4.45	4.45
D	10.0	4.51	4.51
E	10.0	4.70	4.70
F	10.2	4.75	4.75
G	10.4	4.80	4.80

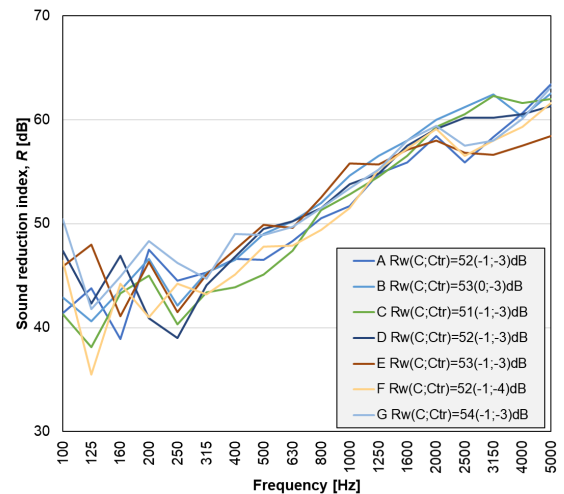


Fig. 4 – Sound reduction index laboratory measurements

The effect of the different sizes and thicknesses is evident for the low-frequency range (below 315 Hz), while the different behaviour for the high-frequency range (above 2000 Hz) may be caused by the boundary conditions (mounting) and inner brick geometry.

3. Prediction of Acoustic Insulation of Clay Hollow Brick Walls

Three procedures were evaluated to predict the acoustic behaviour of the measured walls:

- 1) a commercial software package based on Sharp's homogeneous wall theory (Sharp, 1973);
- 2) the analytical method indicated in ISO 12354-1: 2017 standard, annexes B and C;
- 3) a reference curve derived from the measured values.

In particular, the reference sound reduction index curve for hollow brick walls was obtained by aggregating the individual measured sound reduction index curves R_k with the following procedure. First, each R_k curve obtained from laboratory measurements was shifted so as to obtain a 'normalised' spectrum, $X_{0,k}$, with a weighted sound reduction index of $R_{w,k} = 0$ dB. The normalised value relative to the i -th one-third octave band is, for the k -th wall, $X_{0,i,k}$.

Subsequently, for each i -th one-third octave band ranging from 100 Hz to 5000 Hz, the arithmetic mean of the normalised values obtained for all the walls was calculated, in order to provide a mean value $X_{0,i}$ for the specific frequency band.

Fig. 5 shows the seven normalized curves, the mean value and the uncertainty limits ($U = 2.3 \sigma$).

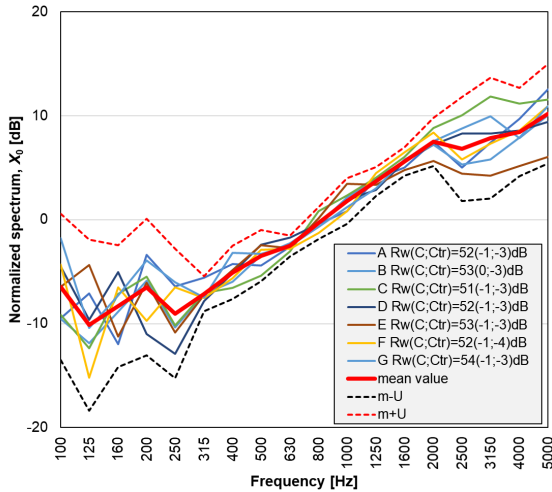


Fig. 5 – Normalized sound reduction indices and mean normalized sound reduction indices

Finally, the reference curve X_0 was shifted by a certain value R_0 in order to obtain the estimate of the sound reduction index for a given wall. A mass-dependent correlation for the parameter R_0 was derived by regression analysis of the data from the seven tested walls:

$$R_0(m') = 20.9 \log_{10}(m') \quad (4)$$

A shift was applied for each i -th one-third octave band according to the formula:

$$R_{0,i} = X_{0,i} + R_0(m') \quad (5)$$

The results were compared with the measurements of the sound reduction index performed in sound transmission suites.

The following graphs (Figs. 6–12) show the comparisons between the results of the application of the three procedures applied to different types of wall.

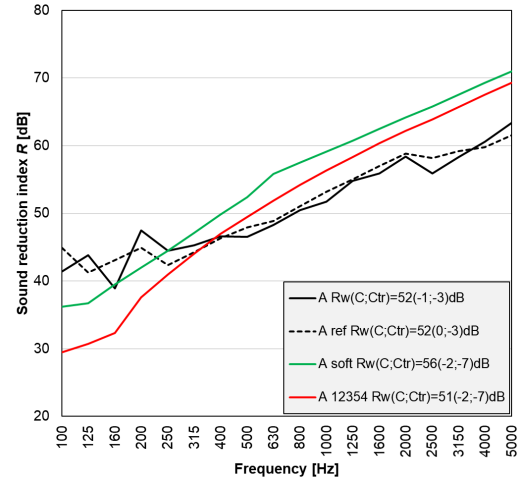


Fig. 6 – Comparison between method results for wall type A. Solid green: Sharp's theory; solid red: ISO 12354-1; dashed black: reference curve; solid black: measured data

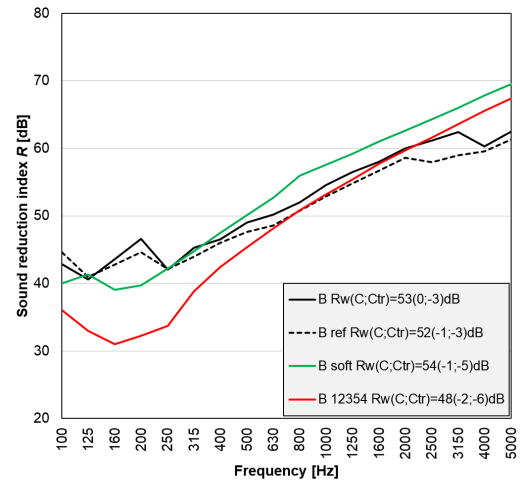


Fig. 7 – Comparison between method results for wall type B. Solid green: Sharp's theory; solid red: ISO 12354-1; dashed black: reference curve; solid black: measured data

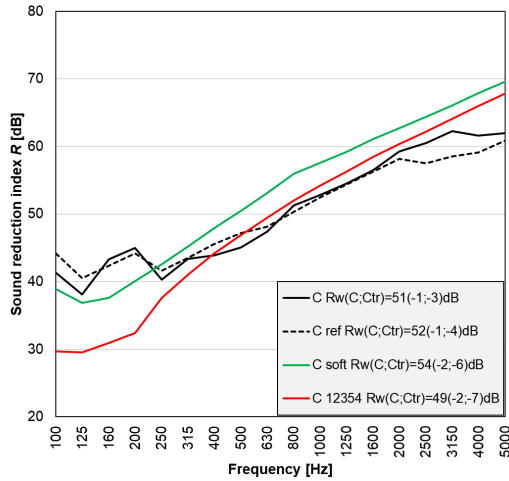


Fig. 8 – Comparison between method results for wall type C. Solid green: Sharp's theory; solid red: ISO 12354-1; dashed black: reference curve; solid black: measured data

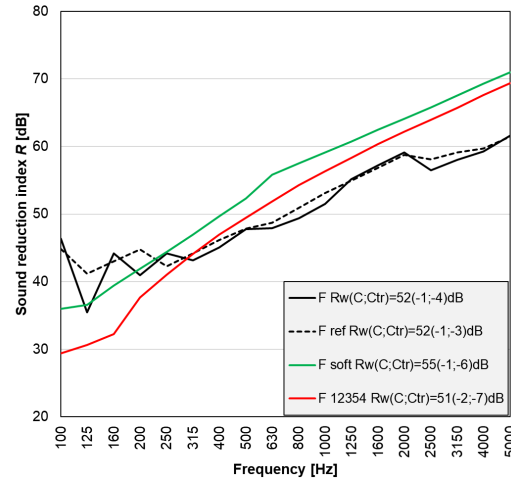


Fig. 11 – Comparison between method results for wall type F. Solid green: Sharp's theory; solid red: ISO 12354-1; dashed black: reference curve; solid black: measured data

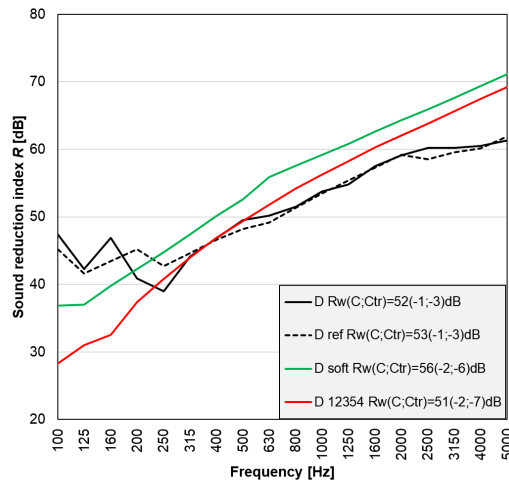


Fig. 9 – Comparison between method results for wall type D. Solid green: Sharp's theory; solid red: ISO 12354-1; dashed black: reference curve; solid black: measured data

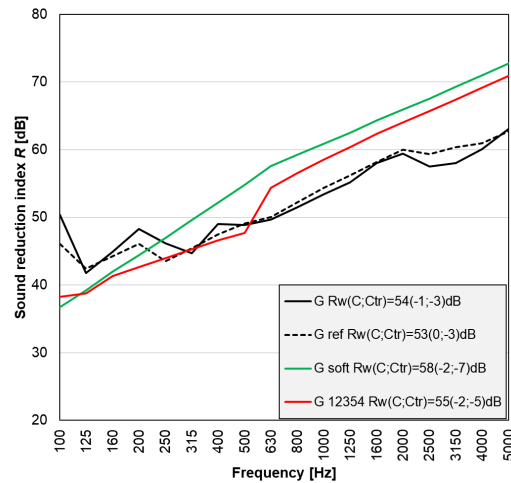


Fig. 12 – Comparison between method results for wall type G. Solid green: Sharp's theory; solid red: ISO 12354-1; dashed black: reference curve; solid black: measured data

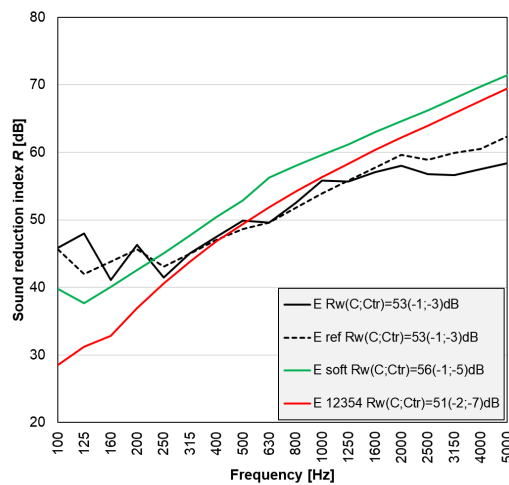


Fig. 10 – Comparison between method results for wall type E. Solid green: Sharp's theory; solid red: ISO 12354-1; dashed black: reference curve; solid black: measured data

Table 3 shows a comparison of the R_w values determined according to the three methods and the laboratory measurements.

Considering the wall as a homogeneous plate leads to an overestimation of the sound reduction index above the critical frequency and to an underestimation of the sound reduction index below the critical frequency. The software based on the Sharp's theory overestimates the R_w value from 1 to 4 dB while the analysis according to the ISO 12354-1 standard leads to differences from -5 to +1 dB. Similar differences can be observed if one-third octave band values are compared.

The use of the proposed reference curve leads to differences between -1 and +1 dB. These values can

be considered within the measurement uncertainty (International Organization for Standardization, 2014).

Table 3 – Weighted sound reduction indexes comparison (measured, reference curve, software, ISO 12354-1 method)

Type	R _w [dB]			
	Measured values	Sharp's theory	ISO 12354-1	Reference curve
A	52	56	51	52
B	53	54	48	52
C	51	54	49	52
D	52	56	51	53
E	53	56	51	53
F	52	55	51	52
G	54	58	55	53

4. Conclusion

This paper has focused on the acoustic insulation performances of clay hollow brick walls.

A reference curve for the family of plastered walls with mass per unit area 305-377 kg/m², thickness 206-330 mm, void fraction 37-55% and a mass-dependent shifting correlation based on experimental measurements was derived.

It was observed that the difference between experimental and estimated values never exceeds ±1 dB, indicating that the reference curve fairly represents the sound insulation behaviour of this family of brick walls.

Software based on Sharp's theory and ISO 12354-1 method (annex B), both developed for homogeneous thick walls, seems not to be suitable for reliably representing the acoustic behavior of hollow brick walls.

Nomenclature

Symbols

τ	sound transmission coefficient (-)
W	sound power (W)
R	sound reduction index (dB)
L	mean equivalent sound pressure level (dB)
S	surface of the specimen
A	equivalent absorption area of the receiving room (m ²)
V	volume of the receiving room (m ³)
T	mean reverberation time of the receiving room (s)
m'	mass per unit area (kg/m ²)
t	thickness of the wall (mm)
f_{bk}	compressive strength of the k -th type block (MPa)
f_k	compressive strength of the k -th type wall (MPa)
E	Young's modulus (GPa)
X	spectrum (dB)

Subscripts/Superscripts

1	transmitting room
2	receiving room
k	k -th type wall
i	i -th one-third octave band
w	weighted value
0	normalised quantity

References

- Caniato, M., F. Bettarello, L. Marsich, A. Ferluga, O. Sbaizero, C. Schmid. 2015. "Time-depending performance of resilient layers under floating floors." *Construction and Building Materials* 102. DOI: 10.1016/j.conbuildmat.2015.10.176
- Caniato, M., F. Bettarello, A. Ferluga, L. Marsich, C. Schmid, and P. Fausti. 2017. "Thermal and Acoustic Performance Expectations on Timber Buildings." *Building Acoustics* 24(4): 219–237. doi: 10.1177/1351010X17740477
- Caniato, M., G. Kyaw Oo D'Amore, J. Kaspar, A. Gasparella. 2020. "Sound absorption performance of sustainable foam materials: Applica-

- tion of analytical and numerical tools for the optimization of forecasting models." *Applied Acoustics* 161. <https://doi.org/10.1016/j.apacoust.2019.107166>.
- Caniato, M., A. Gasparella. 2019. "Discriminating People's Attitude towards Building Physical Features in Sustainable and Conventional Buildings." *Energies* 12(8): 1429. doi: 10.3390/en12081429
- Caniato, M., F. Bettarello, C. Schmid, P. Fausti. 2019. "The use of numerical models on service equipment noise prediction in heavyweight and lightweight timber buildings." *Building Acoustics* 26(1): 35-55. <https://doi.org/10.1177/1351010X18794523>
- Del Coz Díaz, J. J., F. P. Álvarez Rabanal, P. J. García Nieto, M. A. Serrano López. 2010. "Sound Transmission Loss Analysis through a Multilayer Lightweight Concrete Hollow Brick Wall by FEM and Experimental Validation." *Building and Environment* 45(11): 2373-2386. doi: 10.1016/j.buildenv.2010.04.013
- Di Bella, A., N. Granzotto, and C. Pavarin. 2014. "Comparative Analysis of Thermal and Acoustic Performance of Building Elements." *Proceedings of 7th Forum Acusticum*. Krakow, Poland, September 7th–12th 2014.
- Di Bella, A., N. Granzotto, H. Elarga, G. Semprini, L. Barbaresi, and C. Marinosci. 2015. "Balancing of Thermal and Acoustic Insulation Performances in Building Envelope Design." *44th International Congress and Exposition on Noise Control Engineering, INTER-NOISE 2015*. San Francisco, United States, August 9th–12th 2015.
- Di Bella, A., N. Granzotto, and L. Barbaresi. 2016. "Analysis of Acoustic Behavior of Bare CLT Floors for the Evaluation of Impact Sound Insulation Improvement." *Proceedings of Meetings on Acoustics*, 28(1), 015016. doi: 10.1121/2.0000420
- Di Bella, A., N. Granzotto, G. Quartaruolo, A. Speranza, and F. Morandi. 2018. "Analysis of Airborne Sound Reduction Index of Bare CLT Walls." *WCTE 2018 - World Conference on Timber Engineering*. Seoul, South Korea, August 20th–23rd 2018.
- Fortini, M., N. Granzotto, and E. A. Piana. 2019. "Vibro-acoustic Characterization of a Composite Structure Featuring an Innovative Phenolic Foam Core." *Applied Sciences* 9(7), 1276. doi: 10.3390/app9071276
- Fringuellini, M. A., and R. S. Smith. 1999. "Sound Transmission through Hollow Brick Walls." *Building Acoustics* 6(3): 211–224. doi: 10.1260/1351010991501419
- ISO (International Organization for Standardization). 2010a. *ISO 10140-2. Acoustics - Laboratory Measurement of Sound Insulation of Building Elements - Part 2: Measurement of Airborne Sound Insulation*. Geneva, Switzerland.
- ISO (International Organization for Standardization). 2010b. *ISO 10140-5. Acoustics - Laboratory Measurement of Sound Insulation of Building Elements - Part 5: Requirements for Test Facilities and Equipment*. Geneva, Switzerland.
- ISO (International Organization for Standardization). 2010c. *ISO 10140-4. Acoustics - Laboratory Measurement of Sound Insulation of Building Elements - Part 4: Measurement Procedures and Requirements*. Geneva, Switzerland.
- ISO (International Organization for Standardization). 2013. *ISO 717-1. Acoustics - Rating of Sound Insulation in Buildings and of Building Elements - Part 1: Airborne Sound Insulation*. Geneva, Switzerland.
- ISO (International Organization for Standardization). 2014. *ISO 12999-1. Acoustics - Determination and Application of Measurement Uncertainties in Building Acoustics Sound insulation*. Geneva, Switzerland.
- ISO (International Organization for Standardization). 2016. *ISO 10140-1. Acoustics - Laboratory Measurement of Sound Insulation of Building Elements - Part 1: Application Rules for Specific Products*. Geneva, Switzerland.
- ISO (International Organization for Standardization). 2017. *ISO 12354-1. Building acoustics - Estimation of Acoustic Performance of Buildings from the Performance of Elements - Part 1: Airborne Sound Insulation between Rooms*. Geneva, Switzerland.
- Italian Ministry of Infrastructures and Transport. 2018. "Decree 17 January 2018. Aggiornamento delle 'Norme Tecniche per le Costruzioni'." *Supplement to the Official Gazette of the Italian Republic*, 42 (in Italian).
- Jacqus, G., S. Berger, V. Gibiat, P. Jean, M. Villot,

- and S. Ciukaj. 2010. "Acoustic Properties of Hollow Brick Walls." *20th International Congress on Acoustics 2010, ICA 2010, Incorporating the 2010 Annual Conference of the Australian Acoustical Society*, 4: 2668–2673. Sydney, Australia, August 23rd–27th 2010.
- Piana, E. A., N. Granzotto, and A. Di Bella. 2017. "Sound Reduction index of Dry-wall Materials: Experimental Comparison of Model Predictions and Transmission Room Measurements." *24th International Congress on Sound and Vibration, ICSV 2017*. London, UK, July 23rd–27th 2017.
- Piana, E. A., P. Milani, and N. Granzotto. 2014. "Simple Method to Determine the Transmission Loss of Gypsum Panels." *21st International Congress on Sound and Vibration 2014, ICSV 2014*, 5: 3700–3706. Beijing, China, July 13th–17th 2014.
- Ruggeri, P., F. Peron, N. Granzotto, and P. Bonfiglio. 2015. "A Combined Experimental and Analytical Approach for the Simulation of the Sound Transmission Loss of Multilayer Glazing Systems." *Building Acoustics* 22(3–4): 177–192. doi: 10.1260/1351-010X.22.3-4.177
- Sharp, B. H. 1973. "A Study of Techniques to Increase the Sound Insulation of Building Elements." Wyle Laboratories Report, WR 73-5, Wyle Laboratories Research Staff, El Segundo, California. Distributed as PB-222 829, National Technical Information Service, US Department of Commerce, Springfield, Virginia.

Prediction of the Acoustic and Thermal Performance of a Multilayer Partition

Manuela Neri – University of Brescia, Italy – manuela.neri@unibs.it

Mariagrazia Pilotelli – University of Brescia, Italy – mariagrazia.pilotelli@unibs.it

Edoardo A. Piana – University of Brescia, Italy – edoardo.piana@unibs.it

Adriano M. Lezzi – University of Brescia, Italy – adriano.lezzi@unibs.it

Abstract

Multilayer partitions are often designed so that, because of their peculiar composition or structure, they exhibit characteristics that are not normally found in single layer panels. “Multifunctional” partitions are engineered to optimize different features at the same time. In this paper the authors try to deal with the problem of optimizing thermal and acoustic behavior by designing a thermo-acoustic insulation structure. From the thermal point of view, the material should combine good insulation properties, given by low thermal conductivity, and high delay of the thermal wave due to external conditions, given by low thermal diffusivity. From the acoustic point of view, the material should have good absorption characteristics, whenever possible, and primarily high transmission loss in order to respect the relevant law prescriptions. In this way the composite panel, used as a façade element, can improve the comfort conditions in buildings and reduce energy consumption for winter heating and summer cooling. The coupled thermo-acoustic element is made of different wooden and recycled material layers, chosen for their specific properties and sustainable characteristics. Thermal properties were estimated by means of a self-developed code based on the ISO 13786 standard. The acoustic properties of the individual layers, according to the ASTM E2611-09 standard procedure, were measured in a four-microphone impedance tube, and the transfer matrix method was used to estimate the overall acoustic behavior of the material. Particular attention was paid to the layer sequence, because of great importance for both thermal and acoustic performances. The preliminary combined study showed encouraging results.

1. Introduction

As stated by the European directive 2010/31/UE on the energy performance of buildings (European Parliament, 2010), buildings account for 40% of total energy consumption in the European Union. Therefore, the energy performance of buildings should be improved, taking into account outdoor climatic conditions and indoor climate requirements. According to the guideline, all the member States should take the necessary measures to ensure that minimum energy performance requirements are set for buildings and building units or building elements that constitute the building envelope and have a significant impact on its energy performance every time they are replaced or retrofitted. The limits should be set with the aim of achieving cost-optimal levels (Tronchin et al., 2014). The study of unconventional materials such as phase-change materials to fulfill winter and summer requirements (see for instance Neri et al., 2020) is also of broad and current interest.

The European directive 2010/31/UE came into force in Italy with the introduction of the Ministerial Decree (DM) of 26 June 2015 (Italian Ministry of Economic Development, 2015). This law classifies the types of building renovations, distinguishing between major first-level renovations, major second-level renovations and energy upgrading interventions. Major renovations are defined as those involving the elements of the building envelope with an incidence higher than 25% on the overall area. Major first-level renovations involve the building envelope with an incidence of more than 50% of its overall area and the renovation of the heating system and/or the cooling system of the entire building. In such cases the energy performance requirements

are applied to the entire building. Major second-level renovations involve the building envelope with an incidence of more than 25% of the overall area of the building and may affect the heating system and/or the cooling system. In such cases, the energy performance requirements relate to the thermo-physical characteristics of the portions and the dimensions of the elements and components of the building envelope involved in the energy renovation. Finally, energy upgrading interventions are all the other interventions with an impact on the energy performance of the building. These interventions therefore involve an area that is less than or equal to 25% of the overall area of the building, and/or involve the heating and/or cooling system. In such cases, the energy performance requirements apply only to the building components and installations involved. The DM 26 June 2015 also establishes the requirements for the different cases.

In terms of the envelope consisting of opaque vertical components of existing buildings undergoing renovation – which is the object of this work – in the case of major first-level renovations the value of the overall heat transfer transmission coefficient H_T have to fulfil the limit value of 0.73 W/m²K for the climatic zones A and B, 0.70 W/m²K for the climate zone C, 0.68 W/m²K for the climate zone D, 0.65 W/m²K for the climate zone E and 0.62 W/m²K for the climate zone F; moreover, for locations where the average monthly irradiance value on the horizontal plane in the month of maximum summer insolation is greater than or equal to 290 W/m², for all the opaque vertical walls with the exception of those included in the northwest / north / northeast quadrant, it is required that the value of the surface mass M_s is greater than 230 kg/m², or that the value of the periodic thermal transmittance Y_{ie} is lower than 0.10 W/m²K. In the case of major second-level renovations, the value of the overall heat transfer transmission coefficient H_T has to respect the limit values indicated above; moreover, the thermal transmittance U must comply with limit values, which will become stricter starting from 2021 (0.40 W/m²K for the climate zones A and B, 0.36 W/m²K for the climate zone C, 0.32 W/m²K for the climate zone D, 0.28 W/m²K for the climate zone E and 0.26 W/m²K for the climate zone F). In the case of energy upgrading interventions only the limit

values of the thermal transmittance U have to be respected.

Thermal coatings are frequently used to enhance the energy performance of existing buildings. They consist of an insulating layer applied to the outer surface of the wall and are more efficient than internal insulation systems because they significantly reduce the thermal bridges. Since a thermal coating is usually designed to improve thermal insulation, it can also improve summer thermal behavior if it makes it possible to significantly reduce and delay the transmission inside the building of the temperature peak reached on its outer surface during the central hours of the day. Therefore, in this work some solutions are proposed, taking into account both the effect of the transmittance U and of the periodic thermal transmittance Y_{ie} . For the thermal transmittance U the obtained values have been compared with those suggested in the cases of major second-level renovations and of energy upgrading interventions, whereas for the periodic thermal transmittance Y_{ie} the reference value is 0.10 W/m²K in the case of major first-level renovations.

For a multilayer partition, the thermal transmittance U depends upon the properties of the layers while the periodic thermal transmittance Y_{ie} depends also upon the sequence of the layers. The most influencing material properties are the thermal conductivity λ and the thermal capacity C . The thermal transmittance U represents the insulation of the building and can be determined by the electrical analogy in steady heat transfer conditions. The periodic thermal transmittance Y_{ie} refers to the dynamic behavior of the partition and is especially relevant for summer performances. The dynamic thermal characteristics of a building component describe its thermal behavior when it is subject to variable boundary conditions, such as a variable heat flow rate or a variable temperature. The ISO 13786 standard (ISO, 2017a) considers only time-dependent sinusoidal boundary conditions and makes it possible to define the periodic thermal conductance, which is a complex number relating cyclic heat flow rate to cyclic temperature variations. In the case of one dimensional heat flow, valid for walls consisting of flat homogeneous layers, it is possible to define the thermal admittance, relating specific heat flow rate to temperature variations on the same side of the com-

ponent, and the periodic thermal transmittances, relating specific heat flow rate to temperature variations on the two sides of the component. In particular, the internal thermal admittance is defined as $Y_{ii} = q''_i/T_i$, where T_i is a sinusoidal function and T_e is constant, the external thermal admittance is defined as $Y_{ee} = q''_e/T_e$, where T_e is a sinusoidal function and T_i is constant, and the periodic thermal transmittance is defined as $Y_{ie} = -q''_i/T_e$, where T_e is a sinusoidal function and T_i is constant. As prescribed by the ISO 13786 standard, the value of Y_{ii} , Y_{ee} and Y_{ie} can be determined from the elements of the heat transfer matrix $Z_{ee} = Z_{se} \cdot Z \cdot Z_{si}$ where Z_{se} and Z_{si} are the heat transfer matrices of the boundary layers and Z is the transfer matrix of a multi-layer component from surface to surface:

$$\begin{bmatrix} T_e \\ q''_e \end{bmatrix} = \begin{bmatrix} Z_{ee11} & Z_{ee12} \\ Z_{ee21} & Z_{ee22} \end{bmatrix} \begin{bmatrix} T_i \\ q''_i \end{bmatrix} \quad (1)$$

The elements of Z_{si} and Z_{se} depend on the surface resistance of the boundary layer, including convection and radiation, and should be determined in accordance with the ISO 6946 standard (ISO, 2017b):

$$Z_s = \begin{bmatrix} 1 & -R_s \\ 0 & 1 \end{bmatrix} \quad (2)$$

Z is obtained by multiplying the heat transfer matrices of the N layers of the component $Z = Z_N \cdot Z_{N-1} \cdot \dots \cdot Z_3 \cdot Z_2 \cdot Z_1$ where, as a convention, layer 1 is the innermost layer. The elements of Z_1 , Z_2 , ..., Z_N depend on the thickness, the thermal conductivity and the thermal capacity of the layers by means of the expressions listed in the ISO 13786 standard. For each layer,

$$Z = \begin{bmatrix} Z_{11} & Z_{12} \\ Z_{21} & Z_{22} \end{bmatrix} \quad (3)$$

where

$$Z_{11} = Z_{22} = \cosh\left(\frac{d}{\delta}\right) \cos\left(\frac{d}{\delta}\right) + j \sinh\left(\frac{d}{\delta}\right) \sin\left(\frac{d}{\delta}\right) \quad (4)$$

$$Z_{12} = -\frac{\delta}{2\lambda} \left\{ \sinh\left(\frac{d}{\delta}\right) \cos\left(\frac{d}{\delta}\right) + \cosh\left(\frac{d}{\delta}\right) \sin\left(\frac{d}{\delta}\right) + j \left[\cosh\left(\frac{d}{\delta}\right) \sin\left(\frac{d}{\delta}\right) - \sinh\left(\frac{d}{\delta}\right) \cos\left(\frac{d}{\delta}\right) \right] \right\} \quad (5)$$

$$Z_{21} = -\frac{\lambda}{\delta} \left\{ \sinh\left(\frac{d}{\delta}\right) \cos\left(\frac{d}{\delta}\right) - \cosh\left(\frac{d}{\delta}\right) \sin\left(\frac{d}{\delta}\right) + j \left[\sinh\left(\frac{d}{\delta}\right) \cos\left(\frac{d}{\delta}\right) + \cosh\left(\frac{d}{\delta}\right) \sin\left(\frac{d}{\delta}\right) \right] \right\} \quad (6)$$

Here, d is the thickness of the layer, λ is its thermal conductivity and δ is its periodic penetration depth computed as $\delta = [86400 \times \lambda / (\pi \times C)]^{1/2}$ for a period of 24 h.

This method allows the evaluation of thermal transmittance U and periodic thermal transmittance Y_{ie} for building components consisting of homogeneous layers. Standards ISO 6946 and ISO 13786 describe how to estimate U and periodic thermal conductances L_{ie} and L_{ei} for components made of inhomogeneous layers, where inhomogeneities act as thermal bridges. Analytical and neural methods to determine the strength of such thermal bridges have been proposed by several authors (Benedetti et al., 2019; Luscietti et al., 2014; Tenpierik et al., 2008).

When dealing with comfort in buildings, acoustic quality must also be taken into account. In particular, there are two main properties which need to be considered: the attitude of the material to dissipate sound energy, expressed through the sound absorption coefficient α , and the sound insulation capability, represented by the sound transmission loss TL , which is related to the sound transmission coefficient τ through the formula $TL = 10 \log_{10}(1/\tau)$. Different types of tests, such as reverberation room and standing wave tube, make it possible to obtain these parameters. The impedance tube is a double standing wave tube equipped with four microphones. It can be used to estimate only the normal incidence parameters, but it has the advantage of requiring the use of a small sample of material and of simultaneously providing further valuable information, such as the propagation wavenumber, the characteristic impedance and the speed of sound in the tested specimen. Moreover, the impedance tube, combined with the transfer matrix method, can establish the correlation between the state variables on the two sides of the sample,

$$\begin{bmatrix} p_0 \\ u_0 \end{bmatrix} = \begin{bmatrix} \Theta_{11} & \Theta_{11} \\ \Theta_{11} & \Theta_{11} \end{bmatrix} \begin{bmatrix} p_d \\ u_d \end{bmatrix} = \Theta \begin{bmatrix} p_d \\ u_d \end{bmatrix} \quad (7)$$

where p is the sound pressure and u the particle velocity, 0 and d subscripts indicate, respectively, the front and back surfaces of the sample, referring to the direction of the incident sound wave, and Θ_{ij} are the elements of the transfer matrix. This method is particularly convenient for the acoustic characterization and optimization of complex layered struc-

tures, whose total transfer matrix, and, consequently, acoustic properties, can be obtained as the product of the individual transfer matrices in the correct sequence (Lee and Xu, 2009):

$$\Theta_{\text{total}} = \Theta_1 \cdot \Theta_2 \cdot \dots \cdot \Theta_N \quad (8)$$

When using the impedance tube to estimate the transmission loss, one must consider that the resulting TL can be assumed to be independent of boundary conditions only for materials which are considered as an equivalent fluid, that is their shear modulus is negligible (Feng, 2013). In the case of rigid panels, the transfer matrix can be written as

$$\Theta_p = \begin{bmatrix} 1 & Z_p \\ 0 & 1 \end{bmatrix} \quad (9)$$

so that the actual boundary conditions are taken into account through direct measurements and gathered in the acoustic impedance of the material, Z_p . The latter parameter can be calculated as $Z_p = j\omega M_s \times [1 - (1 + j\eta) \times (f/f_c) \times \sin^2 \vartheta]$, where M_s is the mass per unit area of the panel, η is the loss factor, f_c is the critical frequency, that is defined for a homogeneous plate as $f_c = c^2 \times (2\pi)^{-1} \times (M_s/D_p)^{1/2}$, with D_p bending stiffness per unit width.

2. Materials and Methods

In accordance with the ISO 6946 standard, the thermal transmittance U of the multilayer partition was determined as

$$U = (R_{S1} + R_1 + R_2 + \dots + R_N + R_{S2})^{-1} \quad (10)$$

where R_1, R_2, \dots, R_N are the thermal conductive resistances of the individual layers obtained by the ratio between the thickness and the thermal

conductivity of each layer, whereas R_{S1}, R_{S2} are the surface resistances of the boundary layer, including convection and radiation.

In accordance with the ISO 13786 standard, the periodic thermal transmittance Y_{ie} was determined from the elements of the heat transfer matrix from environment to environment Z_{ee} as

$$Y_{ie} = -\frac{1}{Z_{ee12}} \quad (11)$$

The ASTM E2611 standard procedure (ASTM, 2017) establishes the use of a four-microphone impedance tube (Fig. 1). At one endpoint of the tube a loudspeaker is installed and generates a wide-band white noise test signal. The specimen is located in a test sample holder in the central section of the tube, between two microphone pairs. The second end of the tube can be equipped with either anechoic or reflecting termination.

With reference to Fig. 1, by comparing signals from four microphones it is possible to decompose the resulting sound wave field into forward and backward travelling waves on either side of the specimen. The incident and reflected fractions, denoted as A, B, C, D in Fig. 1, are used to compute the elements of the transfer matrix according to the expressions provided by standard ASTM E2611. Finally, the absorption coefficient α (hard-backed) is obtained as

$$\alpha = 1 - \left| \frac{\Theta_{11} - \rho c \Theta_{21}}{\Theta_{11} + \rho c \Theta_{21}} \right|^2 \quad (12)$$

and the sound transmission loss TL (anechoic-backed) can be expressed as:

$$TL = 20 \log_{10} \left| \frac{\Theta_{11} + \left(\frac{\Theta_{12}}{\rho c}\right) + \Theta_{21} \rho c + \Theta_{22}}{2 \times \exp(jkd)} \right| \quad (13)$$

where ρ is the air density, c is the speed of sound and k is the wavenumber in air.

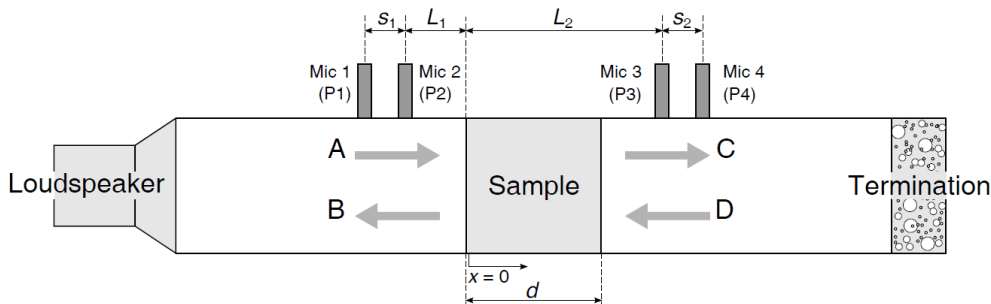


Fig. 1 – Schematic drawing of a four-microphone impedance tube

The custom-made impedance tube is made of two segments of length 1200 mm and internal diameter 45 mm. With such a cross-section, the plane-wave assumption is valid up to about 3800 Hz. The source endpoint holds a loudspeaker of 100 mm enclosed in a sealed and isolated volume, while the second endpoint is shut by a rigid reflective termination or

an anechoic termination. For high-frequency measurements the microphone ports are spaced 45 mm apart, while for low-frequency measurements are spaced 500 mm. The sample is located in a separate segment of tube of appropriate length, installed between the two measurement sections described above. The model of the tube is shown in Fig. 2.

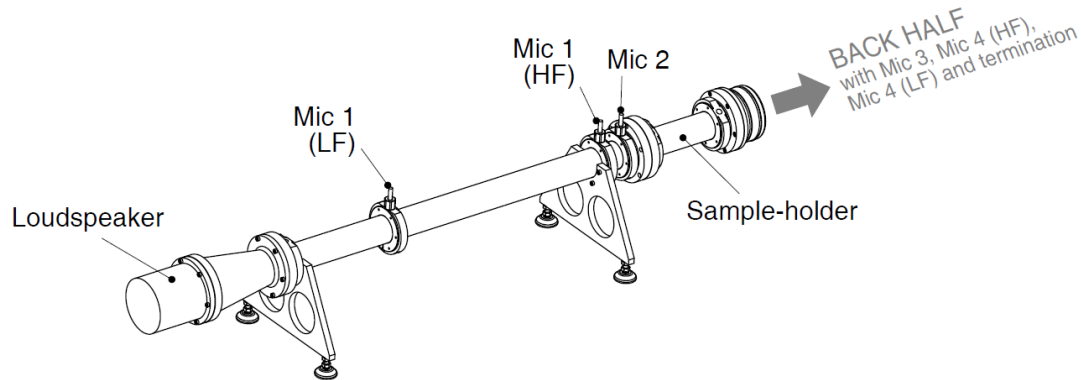


Fig. 2 – Portion of the tube including the loudspeaker. LF = low frequency; HF = high frequency

Four microphones are housed in o-ring-equipped ports and connected to a multichannel analyzer generating the test signal. A pistonphone was used to calibrate the microphones. The measured transfer functions were saved and post-processed by means of a self-built code based on the ASTM E2611 standard procedure. The script provides the acoustic parameters of the specimen, such as the sound absorption coefficient, the sound transmission loss, the propagation wavenumber, the speed of sound in the material and the characteristic acoustic impedance. Three multilayer partitions were thermally analyzed (see Table 1). They can be considered representative of thermal coatings applied to a hollow

brick wall of thickness 200 mm – P200 in Table 1 – which, alone, is characterized by poor thermal performances. The first solution, labeled P-200+WF140-80, consisted of a thermal coating of wood fiber (density 140 kg/m³, thickness 80 mm). The second solution, labeled P-200+WF110-80+WF265-40, consisted of a thermal coating made of two layers of wood fiber (respectively density 110 kg/m³, thickness 80 mm and density 265 kg/m³, thickness 40 mm). The third solution, labeled P-200+A-50, consisted of a thermal coating of aerogel (density 180 kg/m³, thickness 50 mm). All three solutions need only a layer of external plaster to be completed.

Table 1 – Thermal transmittance and periodic thermal transmittance of the analyzed multilayer partitions

Test case	Layers	λ [W/mK]	ρ [kg/m ³]	c [J/kg·K]	d [m]	d_{tot} [m]	U [W/m ² K]	Y_{ie} [W/m ² K]
P-200	Hollow bricks	0.252	817	840	0.200	0.200	1.038	0.643
P-200+WF140-80	Hollow bricks	0.252	817	840	0.200	0.280	0.337	0.0747
	Wood fiber	0.040	140	2100	0.080			
P-200+WF110-80 +WF265-40	Hollow bricks	0.252	817	840	0.200	0.320	0.256	0.0423
	Wood fiber	0.038	110	2100	0.080			
	Wood fiber	0.048	265	2100	0.040			
P-200+A-50	Hollow bricks	0.252	817	840	0.200	0.250	0.245	0.0554
	Aerogel	0.016	180	1030	0.050			

The aerogel panels are obtained through nanotechnological processes combining amorphous silica aerogel and high density reinforcing mineral fibers. Therefore, they can be considered metamaterials providing tunable thermal performance and easy to use. Other authors have used aerogel to obtain a compact soft acoustic metamaterial (Guild et al., 2016).

The thermal optimization was carried out first, then the acoustic properties of the thermally optimized structures were predicted through the transfer matrix method.

3. Results

The thermal performances of the three multilayer partitions are summarized in the Table 1.

All the proposed structures can significantly enhance the thermal performances, and consequently improve the comfort conditions inside the building, both in winter and in summer conditions. The transmittance values fulfil the limit values prescribed in Italy by the DM 26 June 2015 for vertical walls involved in building renovation. In particular, considering the more severe limit values valid by the year 2021, partition P-200+WF140-80 fulfils the limit

value of $0.36 \text{ W/m}^2\text{K}$ for the thermal zone C and could be used in the thermal zones A, B and C, whereas the partitions P-200+WF110-80+WF265-40 and P-200+A-50 fulfil the limit value of $0.26 \text{ W/m}^2\text{K}$ for the thermal zone F and could be used in all the Italian thermal zones. Moreover, all the partitions have good values of periodic thermal transmittance, less than the limit value of $0.1 \text{ W/m}^2\text{K}$. The partition P-200+A-50 is preferred since it makes it possible to obtain very good results with a small thickness.

Based on the thermal analysis, a 50 mm multilayer aerogel sample was tested in the impedance tube, while the hollow brick sound transmission loss data was derived from the sound transmission suites measurement. The acoustic performances of layered partitions featuring these two materials were predicted with the transfer matrix method (see for instance the results obtained for P-200+A-50 configuration in Fig. 3).

The addition of the aerogel layer slightly improved the sound insulation in the low frequency range, whereas the improvement was considerable above 2 kHz due to the multilayered nature of the aerogel package. The weighted single number sound reduction index for the considered façade increased from an initial performance $R_w = 51 \text{ dB}$ to an improved performance $R_w = 52 \text{ dB}$.

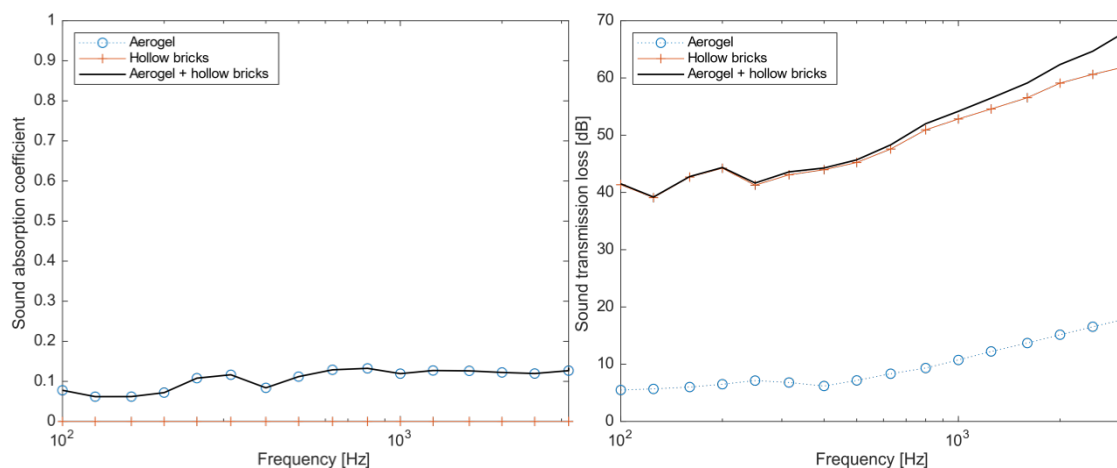


Fig. 3 – Sound absorption coefficient and sound transmission loss of aerogel and hollow brick wall (measured) and predicted properties for composite wall

4. Conclusions

In this work, the preliminary acoustic and thermal evaluation of layered structures designed for im-

proving the performances of a façade has been proposed.

The thermal performance of different walls was simulated in accordance with ISO 13786, which

made it possible to identify the preferred structure in terms of transmittance and reduced thickness as a combination of standard hollow bricks and aerogel layers.

The acoustic analysis has been performed by the transfer matrix method with a four-microphone impedance tube, which made it possible to experimentally characterize the aerogel and to predict the behavior of the whole structure by combining the transfer matrices of the individual layers together.

Acknowledgement

The authors would like to thank Ecofine S.r.l. for providing the Aerogel samples used in the tests. The research was developed for the project SISMACOMF in the framework of the University of Brescia strategic plan Health & Wealth 2015.

Nomenclature

Symbols

c	speed of sound (m/s)
C	thermal capacity (J/ m ³ K)
d	thickness of the layer (m)
D_p	bending stiffness per unit width (Nm)
f	frequency (Hz)
f_c	critical frequency (Hz)
H'_T	overall heat transfer transmission coefficient (W/m ² K)
k	wavenumber in air (m ⁻¹)
M_s	surface mass (kg/m ²)
L_{ie}, L_{ei}	periodic thermal conductances (W/K)
N	layers of the multi-layer component
p	sound pressure (Pa)
R	thermal resistance (m ² K/W)
R_w	weighted single number sound reduction index (dB)
T	temperature (°C, K)
TL	sound transmission loss
u	particle velocity (m/s)
U	thermal transmittance (W/m ² K)
Y_{ee}	external thermal admittance (W/m ² K)

Y_{ie}	periodic thermal transmittance (W/m ² K)
Y_{ii}	internal thermal admittance (W/m ² K)
Z	heat transfer matrix (W/m ² K)

Greek symbols

α	sound absorption coefficient
δ	periodic penetration depth (m)
η	loss factor
λ	thermal conductivity (W/mK)
ϑ	angle of incidence
Θ	acoustic transfer matrix element
τ	sound transmission coefficient
ω	angular frequency (rad/s)

Subscripts/Superscripts

0	front surface
1,2,...,N	number of the layer
d	back surface
e	external
i	internal
p	panel
si	internal surface
se	external surface

References

- ASTM (American Society for Testing and Materials). 2017. *ASTM E2611. Standard Test Method for Normal Incidence Determination of Porous Material Acoustical Properties Based on the Transfer Matrix Method*. West Conshohocken, Pennsylvania, US.
- Benedetti, M., P. Gervasio, D. Luscietti, Mariagrazia Pilotelli and A. M. Lezzi 2019. "Point Thermal Transmittance of Rib Intersections in Concrete Sandwich Wall Panels." *Heat Transfer Engineering* 40(13–14): 1075–1084. doi: 10.1080/01457632.2018.1457208
- European Parliament. 2010. "2010/31/EU. Directive of the European Parliament and of the Council on the Energy Performance of Buildings (EPBD Recast)."
- Feng, L. 2013. "Modified impedance tube measurements and energy dissipation inside absorptive materials." *Applied Acoustics* 74(12): 1480–1485. doi: 10.1016/j.apacoust.2013.06.013

- Guild, M. D., V. M. García-Chocano, J. Sánchez-Dehesa, T. P. Martin, D. C. Calvo and G. J. Orris. 2016. "Aerogel as a Soft Acoustic Metamaterial for Airborne Sound." *Physical Review Applied* 5, 034012. doi: 10.1103/PhysRevApplied.5.034012
- ISO (International Organization for Standardization). 2017a. *ISO 13786. Thermal Performance of Building Components - Dynamic Thermal Characteristics - Calculation Methods*. Geneva, Switzerland.
- ISO (International Organization for Standardization). 2017b. *ISO 6946. Building Components and Building elements - Thermal Resistance and Thermal Transmittance - Calculation Methods*. Geneva, Switzerland.
- Italian Ministry of Economic Development. 2015. "DM 26 giugno 2015. Applicazione delle Metodologie di Calcolo delle Prestazioni Energetiche e Definizione delle Prescrizioni e dei Requisiti Minimi degli Edifici." *Supplement to the Official Gazette of the Italian Republic*, 162. In Italian.
- Lee, C.-M., and Y. Xu. 2009. "A modified Transfer Matrix Method for Prediction of Transmission Loss of Multilayer Acoustic Materials." *Journal of Sound and Vibration* 326(1–2): 290–301. doi: 10.1016/j.jsv.2009.04.037
- Luscietti, D., P. Gervasio, and A. M. Lezzi. 2014. "Computation of linear transmittance of thermal bridges in precast concrete sandwich panels." *Journal of Physics: Conference Series* 547(1), 012014. doi: 10.1088/1742-6596/547/1/012014
- Neri, M., P. Ferrari, D. Luscietti and M. Pilotelli. 2020. "Computational Analysis of the Influence of PCMs on Building Performance in Summer." *Advances in Intelligent Systems and Computing* 982: 3–15. doi: 10.1007/978-3-030-19756-8_1
- Tenpierik, M., W. van Der Spoel and H. Cauberg. 2008. "An Analytical Model for Calculating Thermal Bridge Effects in High Performance Building Enclosure". *Journal of Building Physics* 31(4): 361–387. doi: 10.1177/1744259107088008
- Tronchin, L., K. Fabbri and M. C. Tommasino. 2014. "On the Cost-Optimal Levels of Energy-Performance Requirements for Buildings: A Case Study with Economic Evaluation in Italy." *International Journal of Sustainable Energy Planning and Management* 3: 49–62. doi: 10.5278/ijsepm.2014.3.5

Implementing the Sustainable Energy (and Climate) Action Plans: Quasi-Steady State or Dynamic Modeling Approach

Concettina Marino – University “Mediterranea” of Reggio Calabria, Italy – concettina.marino@unirc.it

Antonino Nucara – University “Mediterranea” of Reggio Calabria, Italy – antonino.nucara@unirc.it

Giorgia Peri – Università degli Studi di Palermo, Italy – giorgia.peri@unipa.it

Matilde Pietrafesa – University “Mediterranea” of Reggio Calabria, Italy – matilde.pietrafesa@unirc.it

Gianfranco Rizzo – Università degli Studi di Palermo, Italy – gianfranco.rizzo@unipa.it

Gianluca Scaccianoce – Università degli Studi di Palermo, Italy/National Research Council of Italy – gianluca.scaccianoce@unipa.it

Abstract

Actions contemplated in Sustainable Energy (and Climate) Action Plans (SEAPs), which municipalities adhering to the EU initiative called “The Covenant of Mayors” are required to prepare, regard many sectors, among which are buildings. To implement such plans, it is necessary to make use of methods for predicting energy use in buildings. Technicians involved in this tend to adopt easy-to-use simulation models because of the common mid-level expertise of the offices involved. However, such simplified methods could result in a less accurate evaluation of the energy demand of buildings. In this paper the suitability of the quasi-steady state and the dynamic approach, in the frame of these new urban energy planning tools, is assessed. Specifically, a comparison between the two methods reported in the EN ISO 52016-1 Standard (namely the quasi-steady state monthly method and the dynamic hourly method), used here as representative of the two cited classes of models, is drawn. Despite some limitations of the quasi-steady state model found in the analysis, the possibility to still use both modelling approaches to implement SEAPs is argued in the paper. Moreover, a tentative procedural scheme is proposed, which technicians working on SEAPs can usefully follow in order to choose the most appropriate modelling approach that can be used depending on the specific situation to address.

1. Introduction

In 2008 the European Commission launched an important initiative entitled the “Covenant of Mayors” (<https://www.covenantofmayors.eu/en/>), which intends to gather local and regional authorities voluntarily committed to achieving the greenhouse gas emissions reduction targets indicated in the EU “2030 climate and energy framework” (<https://eur-lex.europa.eu/legal-content/EN>). Signatories are required to develop and submit two plans, namely a Sustainable Energy Action Plan (SEAP) and a Sustainable Energy and Climate Action Plan (SECAP). Planned actions within both SEAPs and SECAPs should regard several sectors such as transport, energy, lighting, and buildings. The latter is certainly one of the most relevant sectors, due to the effect on both life of citizens and the energy consumption of a whole city (Giaccone et al., 2017).

In order to implement the cited plans, and particularly to define the above-cited energy efficiency actions for the building sector of a given territory, it becomes necessary to use methods aimed at the evaluation of the building energy performances. In this regard, technicians and experts have at their disposal two different categories of methods: quasi-steady state methods based on either a monthly or a seasonal balance, and detailed dynamic hourly methods.

Generally, technicians tend to exploit ease to use models (Peri and Rizzo, 2012) because of the commonly mid-level of expertise of the involved offices.

Generally, technicians tend to exploit ease to use models (Peri and Rizzo, 2012) because of the commonly mid-level of expertise of the involved offices.

Consequently, quasi-steady state simulation models would seem the most attractive (instead of dynamic detailed models) for technicians, due to their intrinsic simplicity and for the fact that they require effortlessly available input data. Nonetheless, such simplified methods could result in a less accurate evaluation of the energy demand of buildings.

On the other hand, the high level of detail characterizing the dynamic modelling approach is not always necessary for the level of accurateness required by the type of analysis suited to a SEAP.

To clarify this aspect, it is worth noting that energy efficiency actions on buildings, planned within a SEAPs and SECAPs, may regard single buildings and/or building stocks. In both circumstances, the interventions may consist in the design, and/or in the energy rehabilitation (Marino et al., 2019). Specifically, the rehabilitation of a building stock may be conducted either on each single building of the stock (“detailed” rehabilitation of the stock) or may regard the stock in its entirety (“general” rehabilitation). Therefore, as depicted in Fig. 1, if the

intervention consists in the design or in a “general” rehabilitation of a building stock, then using a dynamic modelling approach, which requires considerable amount of input data and shows a greater complexity of use, might turn out unnecessary. Indeed, in this case, buildings characterized by “standardized” performances (“virtual” sample buildings that can be assumed as representative of the considered stock) will have to be modelled and to do this, a detailed definition of the building envelopes, HVAC, orientations, etc. is not needed. Therefore, in such circumstances, despite its limits, choosing the quasi-static method would be preferable.

Conversely, if the action consists in designing or rehabilitating single buildings, the quasi-steady state approach would not be compatible with the accuracy required for the analysis. In this case, a model for predicting the energy use that is able to reproduce the specific building envelope, HVAC system, usage profile, and that is able to capture the dynamic behaviour of the given building should be used.

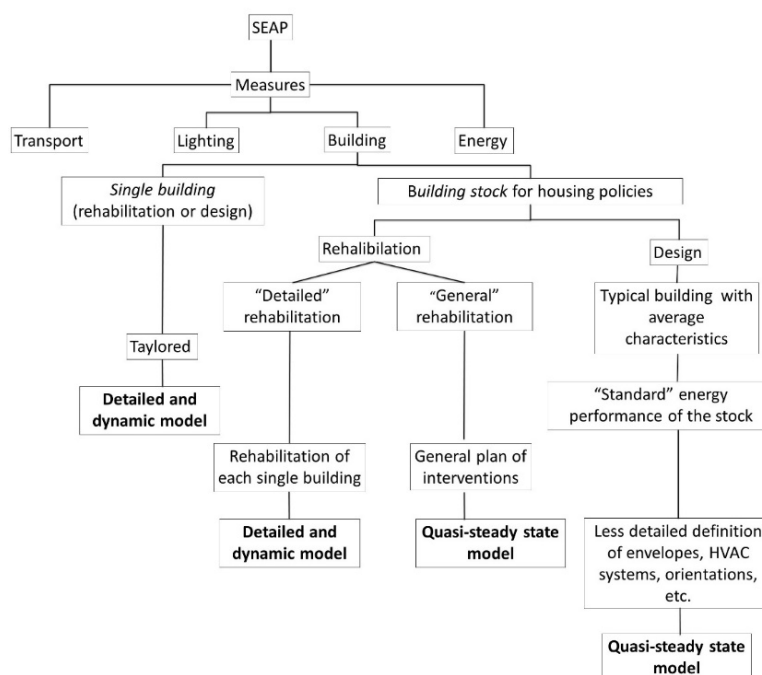


Fig. 1 – Tentative approach for the selection of the most suitable type of energy simulation model

Starting from these considerations, this paper further discusses the practicability of the quasi-steady state and dynamic modelling approaches, as tools that can be used within the decision-making process leading to selection and implementation of energy

efficiency measures in various climate configurations by urban planners.

To accomplish this task, as representative of both cited different approaches, two simulation models have been selected, i.e. the quasi-steady state

monthly method and the dynamic hourly method, both devised by the recently issued EN ISO 52016-1 standard. Specifically, for a plain sample building, located in sites characterized by different weather configurations (Athens, Messina, and Rome), the results obtained using these two methods were compared to the outcome yielded by the well-known building dynamic simulation code, that is Energy Plus (used as a reference).

Based on the analysis performed, some further criticisms of these two modelling approaches have arisen with reference to their use in the frame of the above cited energy planning tools for sustainable and resilient cities.

2. Materials and Methods

2.1 The Analysis Approach

To fulfil the aim of this work, we have selected two simulation models, used here as representative of the two previously cited classes of approaches thanks to their large popularity among technicians and researchers. These are the monthly and the hourly models devised by the recently issued EN ISO 52016-1 standard (CEN, 2017) that replaces the EN ISO 13790 (CEN, 2008); the standard constitutes a reference to the energy performance certification of buildings at national or regional levels. The models were implemented in Excel™ spreadsheet and Visual Basic™ functions were also used.

A plain sample building was considered and its monthly energy consumption was calculated using both the quasi-steady state monthly model and the hourly dynamic model.

Clearly, to properly carry out comparisons among different calculation procedures, univocal climate data are needed; therefore, a database which is suitable for all the procedures must be selected. After a careful analysis, the database of the Energy Plus simulation software (U.S. Department of Energy, 2017) was identified as complete and suited to this purpose. Data concerning outside temperature and solar radiation were obtained.

The results gained through the two EN ISO 52016-1 standard methods were compared with the outcomes of dynamic simulations performed by means

of the Energy Plus code (Crawley et al., 2001). The analysis was repeated in three different cities, namely Messina, Rome and Athens, considered here as representative of weather conditions typical of the Mediterranean climate.

In this context, proper attention was paid to input data such as envelope data, building use data and climatic data, because their uncertainties may produce an important variation in the assessed energy performance and label (Corrado and Mechri, 2009). In order to reduce this type of uncertainty, univocal databases were used in spite of the fact that the three considered calculation methods often require different typologies of input data (e.g. monthly or hourly average air temperatures).

The building module and the climate characteristics of the selected sites are described in the following sections.

2.2 Building Module Characteristics

With a view to executing the described comparison, the building module reported in Fig. 2 was studied. Its dimensions are 5.00 m x 5.00 m x 2.70 m. The vertical structures and the roof are non-adiabatic and facing outdoor, so that their outside boundary condition consists of the outdoor environment, whereas the floor, which is also non-adiabatic, has soil as the outside boundary condition. On the South wall, a glazed surface is installed and its dimensions are 1.20 m x 1.40 m (Fig. 2).

It is worth underlining that the shape described would not be considered as representative of any building practice. It has been selected in order to verify the compliance of simulation codes with the purposes of a SEAP (or SECAP) application. In other words, the analysis aims at providing information able to lead administrators in the choice of steady-state or dynamic approaches in their building energy evaluations. Because of this, a generic shape has been adopted for the building module. The South-facing window allows the solar radiation to be taken into account. However, since among the selected sites warm climates are involved, the window area was reduced in order to avoid the overheating phenomena that could occur in warmer climates.

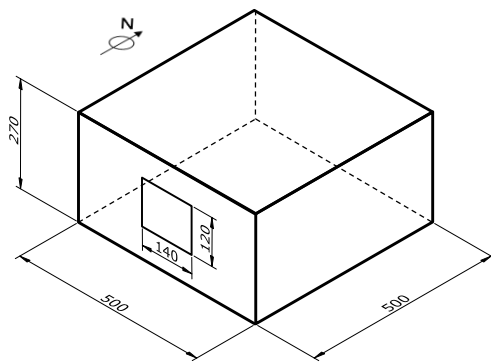


Fig. 2 – Description of the building module used for simulations

The thermal transmittance values of the envelope structures are: $1.70 \text{ W/m}^2\text{K}$ for the glazed surface, $0.85 \text{ W/m}^2\text{K}$ for external walls, $0.80 \text{ W/m}^2\text{K}$ for the floor, $0.36 \text{ W/m}^2\text{K}$ for the roof. Heat capacity per area is: $432 \text{ kJ/m}^2\text{K}$ for walls, $402 \text{ W/m}^2\text{K}$ for the floor and $501 \text{ W/m}^2\text{K}$ for the roof. These values have been adopted here as representative of the more recent (constructed after 1990) Italian building stock (<http://www.building-typology.eu>; Corgnati et al., 2013) with improvements due to renovations typical of the last few years (Bertini et al., 2018).

In more detail, in the case of glazed surfaces, whose values are traditionally higher than $3 \text{ W/m}^2\text{K}$, we decided to push values towards those typical of an advanced refurbishment since these components are the ones that can more easily be modified compared to the opaque parts of the envelope and therefore are usually subject to the first energy refurbishment actions, especially considering the technical improvement they are currently undergoing (Piccolo et al., 2018). On the other hand, the substitution of these envelope components also induces acoustical benefits to the building occupants: this is another reason why building owners often tend to modify them. These values were also preliminarily assumed valid for Athens.

As regards the typology, the edifice is an office building, the thermostat control strategy was assumed as continuous with a constant temperature set-point of 20°C . The infiltration rate was set to 0.5 air change/h continuously (24 hours per day for the full year). No ventilation system is present (CEN, 2017). The internal heat gains were evaluated with a constant value of 6 W/m^2 (UNI, 2014). No shading devices are present and the effect of obstructions was not taken into account.

2.3 Climate Characteristics of the Selected Sites

As stated earlier, the energy simulations were carried out considering the building module located in three different cities in the Mediterranean area: Athens ($37^\circ 54'$ North Latitude, $23^\circ 43'$ Est Longitude; 1112°C HDD , 2966°C CDD); Messina ($38^\circ 12'$ North Latitude, $15^\circ 33'$ Est Longitude; 758°C HDD , 3261°C CDD); Rome ($41^\circ 47'$ North Latitude, $12^\circ 13'$ Est Longitude; 1444°C HDD , 2333°C CDD),

With regard to the ASHRAE climatic classification system, based on the heating and cooling degree days (ASHRAE, 2010), the selected cities are located in two different climatic zones, that is: warm (Messina and Rome) and mixed (Athens).

3. Results

For the case study described in the previous section, the heating and cooling monthly energy demand were calculated. These results were further exploited to assess the energy needs on a seasonal basis.

For the sake of simplicity, and without prejudice for the generality, the simulations were conducted with a constant set-point of 20°C for the internal air temperature for every month of the year: this avoids the problem of the preliminary identification of different heating and cooling periods for each considered location.

For each of the three selected cities, the energy needs for heating and cooling, were calculated for the 12 months of the year, thereby obtaining 72 output data for each of the adopted calculation methods (steady state and dynamic).

Aggregated results are shown in Fig. 3, where the monthly values of energy demand obtained by means of both the monthly and hourly methods are reported versus the Energy Plus output (EP) which was adopted as a reference.

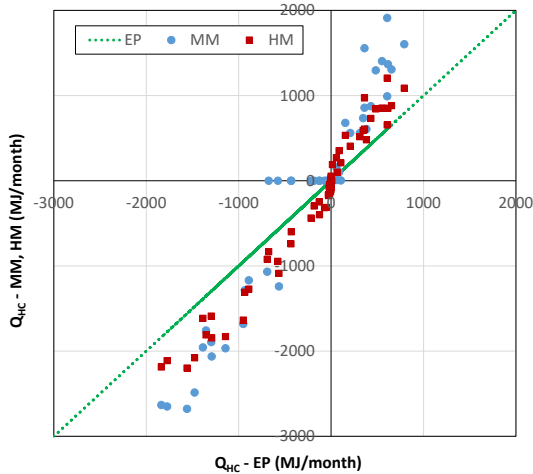


Fig. 3 – Comparison of the monthly energy needs for heating (positive values) and cooling (negative values), obtained with both the monthly (MM) and the hourly (HM) methods with those obtained with EnergyPlus (EP) for all the considered cities

The diagram of Fig. 3 shows that, assuming Energy Plus output as a reference, the monthly method (MM) significantly ($R^2 = 0.925$ for MM and $R^2 = 0.966$ for the HM) overestimates the monthly demand, during both heating and cooling periods. Furthermore, the higher the value of the energy demand, the larger the difference between the two methods. This phenomenon is barely evident for the results of the hourly method (HM), its outcome being very close to the Energy Plus output (EP).

As regards the seasonal energy demand, Fig. 4 reports the yearly cooling and heating energy needs for each of the analysed cities.

It can be noted that even on an annual basis, in comparison to Energy Plus, the monthly method overestimates the heating energy needs more than the hourly one. This behaviour does not regard the cooling needs; indeed, in this case, the results of the monthly method are lower than the values calculated by means of the hourly method. The reasons behind this behaviour are more easily inferable from Fig. 5, which reports, for the site of Rome, the monthly needs for heating and cooling at each site. Specifically, graphs show six different profiles: three in the upper part of the diagram pertinent to MM, HM, and EP, extended over 12 months and referring to space heating (clearly, in the months when heating is not required, the methods provide a value of zero energy), and three in the lower part of the diagram pertinent to MM, HM, and EP, extended over 12 months and referring to cooling (clearly, in

the months when cooling is not required, the methods provide a value of zero energy).

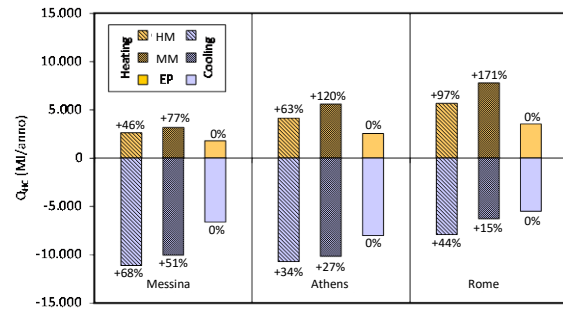


Fig. 4 – Seasonal energy demand for heating and cooling purposes: monthly method (MM), hourly method (HM), EnergyPlus (EP)

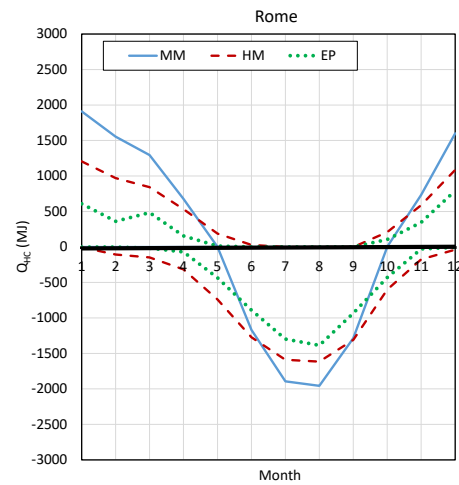


Fig. 5 – Monthly needs for heating (positive values) and cooling (negative values) purposes

It is shown that although the monthly method yields generally the greatest values of energy demand during the hottest months, it returns the smallest values (equal to zero) during spring/autumn.

The combined effects of these two occurrences make the yearly cooling demand assessed through the monthly method smaller than the one calculated by means of the hourly method. This occurs because of the intrinsic structure of the monthly method that, using the monthly average values of the outdoor air temperature as input data, does not allow simultaneous calculation of possible occurrences of heating and cooling for the same month, which is the case in spring/fall periods. In other words, at least one of the two terms is zero for the intrinsic structure of the monthly method.

By contrast, both the hourly method and the Energy Plus code use hourly values of the outdoor air temperature as input data and, hence, they allow the contemporary assessment of both heating and cooling daily loads when they occur

To sum up, as can be observed from Fig. 4, the hourly method always overestimates the cooling energy needs compared to the base case (and more than the monthly method, which overestimates them as well). In terms of the space heating, the hourly method overestimates the energy needs with respect to the base case but less than the monthly method.

4. Discussion

As earlier stated, the purpose of the proposed analysis is not the assessment of the accuracy and reliability of the quasi-steady state and dynamic methods in predicting the building energy performances, but rather the evaluation of their suitability in sight of their utilization within the process leading to selection and implementation of energy efficiency measures in Mediterranean climate configurations by urban planners and building technicians who work on SEAPs. In other words, the aim of the analysis is to possibly identify the most appropriate model that can be used in each of the situations depicted in Fig. 1.

Results shown in the previous section outline the different behaviour of the two modelling approaches depending on the type of assessment, whether monthly or seasonal. The results show that on one hand, the quasi-steady state approach permits an easy assessment of the seasonal energy demand of buildings both for its intrinsic simplicity and for the fact that it requires effortlessly available input data (features that render this approach particularly attractive for technicians). On the other hand, it is affected by some relevant limitations as it significantly overestimates the monthly demand, during both heating and cooling periods, and concerning the seasonal demand, it overestimates the heating energy needs more than HM with respect to Energy Plus.

Results of HM and Energy Plus, both of which are based on transient regime thermal balances, were instead found comparable, and compliant with the climate time variability characterizing the sites, allowing more reliable analysis when coexistence of heating and cooling loads is highly possible.

Some considerations can therefore be provided concerning the level of suitability of the quasi-steady state method (MM) and the hourly dynamic method (HM) in the frame of SEAPs (or SECAPs).

Among the main features of the MM there is the simplicity of the model structure and the requirement of easily available input data. Both these two features render the MM suitable for the development of a SEAP, because the first one matches the mid-level expertise of the committed offices, while the second one matches a common circumstance of the committed offices, i.e. the set of data (definition of envelope, HVAC features, etc.) needed for detailed analyses is generally not completely available.

Another characteristic of the MM is that no greatly detailed building/HVAC modelling is required. Because of this, the suitability of the MM approach depends on the required level of accuracy of the analysis to be performed, whether high, low, etc. Therefore, in the context of SEAPs, the MM turns out to be more appropriate in the case of the design and “general rehabilitation” of a building stock (Fig. 1). In this case, buildings characterized by “standardized” performances (“virtual” sample buildings that can be assumed as representative of the considered stock) will need to be modelled and to do this, a detailed definition of the building envelopes, HVAC, etc. is not required.

Results of our analysis also signal that when using the MM, a possible overrating of the monthly energy demand (both in heating and cooling seasons), and the annual heating energy demand could occur. Such a characteristic renders the MM suitable for the development of a SEAP although some misinterpretations could occur. Consequently, the MM turns out to be more appropriate for reliable estimations of the cooling energy demand and for rough estimations of monthly energy savings deriving from a planned set of measures, for instance, for the “general rehabilitation” of a building stock, and in the

case of rough estimations of yearly energy savings for space heating.

Furthermore, outcomes of our analysis indicate that a possible miscalculation of the energy demand in mild climate or mild months (spring/fall), when both heating and cooling needs might coexist, could occur due to its dual intrinsic structure. This feature makes the MM suitable for the development of a SEAP even if some concerns arise. Because of this, the MM turns out to be more appropriate in the case that the analysis regards the energy demand for well-characterized seasons (heating and cooling) which are clearly separated. If shorter periods need to be investigated (for instance because the edifices are used for a limited period during the whole year), more detailed methods should be exploited, instead.

Among the main features of the MM there is the complexity of the model structure and the requirement of a considerable amount of not easily available input data. Because of these factors, the HM is suitable for the development of a SEAP but only in those cases when a detailed analysis is required and when the amount and type of needed data is at the disposal of the offices responsible for the action planning.

Another characteristic of the HM is that it requires a high level of detail due to, for instance, the consideration of the hourly variation of the weather conditions as input data. Because of this, the suitability of the HM depends on the required level of accuracy of the analysis to be performed (high, low, etc.). Therefore, in the context of SEAPs, the HM turns out to be more appropriate in the case of the design or the rehabilitation of single buildings, and in the case of a “detailed rehabilitation” of a given building stock (Fig. 1).

Results of the analysis also signal that a possible overestimation of the annual cooling demand could occur. Such a characteristic renders the HM suitable for the development of a SEAP although some misinterpretations could occur. Consequently, the HM turns out to be more appropriate for accurate estimations of heating and in the case of rough estimations of cooling energy saving deriving from planned set of measures, for instance, on a single building for its rehabilitation.

Furthermore, outcomes of the analysis signal that coexistence of both heating and cooling needs is

suitably taken into account by the HM. This feature renders the HM suitable for the development of a SEAP because it makes it possible to have a more realistic image of the energy consumption of the single building or of the given building stock. Because of this feature, this method turns out to be more appropriate in the case of accurate estimations of the energy saving even in the mild months.

5. Conclusions

The purpose of the proposed analysis is not the assessment of the accuracy and reliability of the quasi steady-state and dynamic methods in predicting the building energy performances, but rather the evaluation of their suitability in sight of their utilization within the process leading to selection and implementation of energy efficiency measures by urban planners and building technicians who work on SEAPs, particularly in Mediterranean climate configurations. In other words, the aim of the analysis is to possibly identify the most appropriate model - whether it exists - which can be used in each of the situations depicted in Fig. 1.

The results have outlined the different behaviour of the two modelling approaches, whether monthly or hourly. These results show that on one hand, the quasi-steady state (monthly) approach permits an easy assessment of the seasonal energy demand of buildings both for its intrinsic simplicity and for the fact that it requires effortlessly available input data (features that render this approach particularly attractive for technicians). On the other hand, it is affected by some relevant limitations, that is: it is not able to properly evaluate the monthly demand during spring/fall periods when heating and cooling needs may coexist and overestimates the heating energy needs more than the hourly method with respect to Energy Plus; however, it performs with greater accordance to Energy Plus as far as the yearly cooling demand is concerned.

Results of the hourly method and Energy Plus, both of which are based on transient regime thermal balances, were instead found comparable on a monthly basis and compliant with the climate time variability characterizing the sites.

Based on these considerations and criticisms, further analyses are needed particularly referring to other climatic situations of different sites. Additionally, the present analysis should be properly extended to other building typologies and thermophysical envelope characteristics. Meanwhile, technicians working on SEAPs can usefully follow the tentative procedural scheme presented in the Introduction and discussed in Section 4, in order to choose the most appropriate modelling approach suited to the specific situation to be addressed in SEAP design. Until further research findings become available, such a scheme as presented in this paper, represents a precautionary approach that can be followed, being based on reasonable considerations concerning the compliance between the kind of method adopted for the simulation and the level of the results required.

References

- ASHRAE. 2010. *ANSI / ASHRAE / IESNA Standard 90.1 - 2010. Energy Standard for Buildings Except Low-Rise Residential Buildings*. Atlanta, GA: American Society of Heating, Refrigerating and Air-Conditioning Engineers, Inc. Atlanta, GA.
- Bertini, I., A. Federici, D. Prisinzano, E. Allegrini, G. Azzolini, and A. Martelli. 2018. *Detrazioni Fiscali*. In Italian. Roma: ENEA - Agenzia Nazionale Efficienza Energetica.
- CEN. 2008. *EN ISO 13790 - Energy Performance of Buildings - Calculation of Energy Use for Space Heating and Cooling*. Bruxelles: European Committee for Standardization.
- CEN. 2017. *EN ISO 52016-1: Energy Performance of Buildings - Energy Needs for Heating and Cooling, Internal Temperatures and Sensible and Latent Heat Loads - Part 1: Calculation Procedures*. Brussels: European Committee for Standardization.
- Corgnati, S. P., E. Fabrizio, M. Filippi, and V. Monetti. 2013. "Reference Buildings for Cost Optimal Analysis: Method of Definition and Application." *Applied Energy* 102: 983–93. <https://doi.org/10.1016/j.apenergy.2012.06.001>
- Corrado, V., and H. E. Mechri. 2009. "Uncertainty and Sensitivity Analysis for Building Energy Rating." *Journal of Building Physics* 33(2): 125–56. <https://doi.org/10.1177/1744259109104884>
- Crawley, D. B, L. K Lawrie, C. O Pedersen, R. K. Strand, R. J. Liesen, F. C. Winkelmann, W. F. Buhl, et al. 2001. "EnergyPlus: Creating a New-Generation Building Energy Simulation Program." *Energy and Buildings* 33(4): 331–39.
- Giaccone, A., G. Lascari, G. Peri, and G. Rizzo. 2017. "An Ex Post Criticism, Based on Stakeholders' Preferences, of a Residential Sector's Energy Master Plan: The Case Study of the Sicilian Region." *Energy Efficiency* 10(1): 129–49. <https://doi.org/10.1007/s12053-016-9444-9>
- Marino, C, A Nucara, M F Panzera, and M Pietrafesa. 2019. "Towards the Nearly Zero and the plus Energy Building: Primary Energy Balances and Economic Evaluations." *Thermal Science and Engineering Progress* 13, 100400. <https://doi.org/10.1016/j.tsep.2019.100400>
- Peri, G., and G. Rizzo. 2012. "The Overall Classification of Residential Buildings: Possible Role of Tourist EU Ecolabel Award Scheme." *Building and Environment* 56: 151–61. <https://doi.org/10.1016/j.buildenv.2012.03.003>
- Piccolo, A., C. Marino, A. Nucara, and M. Pietrafesa. 2018. "Energy Performance of an Electrochromic Switchable Glazing: Experimental and Computational Assessments." *Energy and Buildings*. <https://doi.org/10.1016/j.enbuild.2017.12.049>
- U.S. Department of Energy. 2017. "Energy Plus Weather Data." 2017. https://energyplus.net/weather-region/europe_wmo_region_6/DEU
- UNI. 2014. *UNI/TS 11300-1 - Energy Performance of Buildings - Part 1: Evaluation of Energy Need for Space Heating and Cooling*. UNI - Ente Nazionale Italiano di Unificazione -Milano.

Comparison Between the EN ISO 52016-1 Hourly Calculation Method and a Fully Detailed Dynamic Simulation

Giovanna De Luca – Politecnico di Torino, Italy – giovanna.deluca@polito.it

Mamak P.Tootkaboni – Politecnico di Torino, Italy – mamak.ptootkaboni@polito.it

Ilaria Ballarini – Politecnico di Torino, Italy – ilaria.ballarini@polito.it

Vincenzo Corrado – Politecnico di Torino, Italy – vincenzo.corrado@polito.it

Abstract

The present research proposes a preliminary investigation of the new hourly method for the assessment of building energy needs for heating and cooling introduced by the EN ISO 52016-1 standard. It was applied to a case study and compared with a fully detailed dynamic model (EnergyPlus). The comparison was performed considering two building operation modes: in a free-floating condition, the hourly differences between the indoor operative temperatures were analysed considering the different contributions to the heat balance; in an ideal heating and cooling system operation, the heating and cooling energy needs were compared on a monthly basis. The discrepancies between the calculation methods, both in the indoor operative temperature and in the thermal energy needs, were investigated and the causes of the deviations were identified.

1. Introduction

As indicated in the recast of European directive 2010/31/EU (European Commission, 2010), buildings are responsible for approximately 40% of overall energy consumption in the European Union. Energy efficiency of buildings plays a crucial role in reducing global energy consumption. To this purpose, it is vital to assess energy performance accurately (Wang et al., 2012). The past decade has seen the rapid development of standards for the assessment of the overall energy performance of buildings (EPB). However, different calculation methods do not provide the same level of details, transparency, reproducibility, etc. The use of simplified models is preferable for verifying the EPB requirements since detailed dynamic simulations introduce a large

number of choices, details and complexities that reduce the reproducibility and transparency of the model (van Dijk, 2018). Thus, the accuracy of simplified models as compared to detailed dynamic models should be investigated and increased.

The new EN ISO 52016-1 standard (European Committee for Standardization, 2017) specifies a new Simplified Hourly Calculation Method (SHCM) for the calculation of the (sensible) energy need for heating and cooling and the (latent) energy need for (de)humidification, the internal temperatures and the heating and cooling loads. The SHCM takes time variations into account by considering hourly time intervals and daily alterations such as changing weather conditions are therefore not neglected. Furthermore, the amount of required input data for this method does not significantly exceed that required for the monthly method. The use of the new EN ISO 52016-1 hourly method, which replaced the simple hourly method of EN ISO 13790 (European Committee for Standardization, 2008), has not yet been investigated sufficiently in literature. Siva Kamaraj (2018) compared the new standard with the TRN-SYS model for six BESTEST cases, using the weather file of Milan (Italy), Palermo (Italy), Denver (USA), and Colorado (USA). Results showed a range of difference between 10% to 30% in the heating needs, and between 25% to 40% in cooling needs for various cases (heavyweight, lightweight, etc.). A similar study was carried out for Croatian reference buildings for a wide range of building uses, envelope properties, climates, and heating/cooling needs (Zakula et al., 2019). The study concluded that the new standard results are acceptable in some cases, although there is a certain level of inconsistency between the two calculation methods in other cases.

Recently, Ballarini et al. (2019) investigated the hourly model of EN ISO 52016-1 by comparing it to the simplified hourly model of EN ISO 13790 and the detailed dynamic model of EnergyPlus. All methods were applied to a two-story single-family house in order to calculate the heating and cooling needs. It was found that the results generated using the new method were more similar to the results obtained using EnergyPlus than those using the simplified model of EN ISO 13790. However, this conclusion is reliable for the assessment of simple case studies and there is a need for further study with more complex buildings.

The literature reveals the need to broaden current knowledge of the newly proposed standard EN ISO 52016-1. This study sets out to assess the accuracy of the new method in predicting the building thermal behaviour. The present study attempts to validate the new hourly method by comparing it with a detailed dynamic simulation applied in the framework of the energy audit of an existing building located in Turin (northern Italy). Both calculation methods were implemented by means of two software applications: Open Studio platform, which implements the EnergyPlus modelling engine, and an Italian commercial tool, which implements the new hourly calculation model, in compliance with the EN ISO 52016-1 standard. The analysis was carried out through the comparison and discussion of the operative temperature and heating and cooling energy needs. In addition, this study also investigates the building model calibration procedure performed through the simplified hourly calculation model.

2. Methodology

2.1 Steps of Analysis

A case-study approach was used to facilitate the achievement of the research goals. The procedure applied is based on a first phase, consisting of the case-study energy model calibration, and a second phase in which the calculation model comparison was performed. As regards the first phase, initial data processing was performed to extrapolate the

heating energy needs from the overall energy consumption (for heating and domestic hot water production). The energy model calibration was performed by means of the new EN ISO 52016-1 hourly calculation model, implemented using an Italian commercial tool. In the second phase, the calibrated energy model was then modelled with EnergyPlus to perform the model comparison. A set of consistency options was applied to both models to make their results comparable. The comparison was performed based on the hourly profile of the indoor operative temperature (in a free-floating condition), and the thermal needs of the building for heating and cooling.

2.2 Case Study

The analysed case study is one of the eighteen existing building blocks (named "Pavilion I") of the military base "Riberi" sited in Turin (northern Italy). It was built between 1903 and 1913 and a major restoration of the building was performed in 2006 with the aim of accommodating more than a thousand journalists during the Turin 2006 Winter Olympics. It is currently used as a military guest house.

The pavilion is a three-story building (a representative story plan is shown in Fig. 1) with a gross conditioned volume of 10 261 m³, a net conditioned floor area of 1 633 m² and a compactness factor of 0.29 m⁻¹.

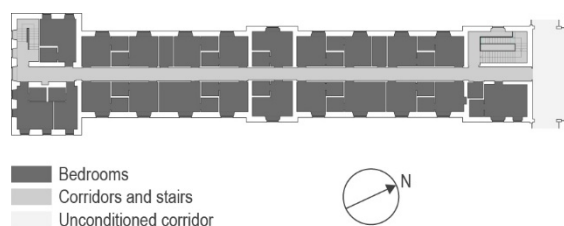


Fig. 1 – Representative building story and thermal zoning

The building envelope is characterized by uninsulated load-bearing brick exterior walls (finished with a layer of plaster), reinforced concrete slabs and double-glazed windows with wooden frames and roller shutters (used only at night-time from 8 p.m. to 8 a.m.), while no solar shading devices are installed in the building. The windows are mainly South-East and North-West oriented. The bottom floor borders on a ventilated crawl space (built on

the existing floor), while the upper floor adjoins an unconditioned attic. Table 1 shows the thermal properties of the envelope. Standard values, derived from the UNI/TR 11522 technical report abacus (Ente Italiano di Normazione, 2014), were adopted for the opaque building envelope due to the lack of reliable information, while actual construction data were considered for the transparent envelope.

Table 1 – Building envelope thermal properties

Envelope component	U -value [W m ⁻² K ⁻¹]
External walls	1.04
Windows	1.86
Bottom floor (vs. ground)	0.62
Upper floor (vs. unconditioned attic)	0.48

Standardized user behaviour, related to occupancy, heat gains, natural ventilation and lighting, was considered. The internal gain values and hourly schedules were derived from the ISO 18523-1 technical standard (International Organization for Standardization, 2016). An additional heat gain due to the presence of an indoor hot water storage was taken into account and calculated according to UNI/TS 11300-2 (Ente Nazionale di Normazione, 2019). Considering all the internal heat sources, the daily average value of internal gains was assumed to be equal to 9.5 W m⁻². In the first-stage simulation, a constant ventilation rate (0.25 h⁻¹) was adopted. All the pavilions are supplied by district heating, which provides thermal energy both for space heating and domestic hot water. The heat exchange substation that serves the eighteen pavilions is composed of four single heat exchangers with a total power of 3 600 kW. The distribution system is characterized by uninsulated underground water pipes. Each room is equipped with a fan-coil, with no heating control systems. Due to the lack of data and the high indoor temperatures encountered during the site inspections, a 22 °C heating set-point was assumed in the first-stage simulations.

3. Energy Model Calibration

3.1 Energy Consumption Data Processing

The actual energy consumptions for space heating and domestic hot water production were analysed in order to extrapolate the energy needs for space heating. In this way, the heating needs can be compared with the outcomes of the hourly calculation method provided by the EN ISO 52016-1 technical standard. The extrapolation was performed through an energy signature based on the actual energy consumption of three heating seasons (monitored on a one-week basis starting from May 2017) and the actual average outdoor temperature in the same period, provided by the Regional Agency for the Protection of the Environment of Piedmont (ARPA Piemonte). The sequence below was followed:

1. Pattern recognition for domestic hot water energy consumption (black dots in Fig. 2);
2. Identification of an energy consumption benchmark, related to the heating system heat losses;
3. Final computation of the energy needs for space heating by subtracting the energy consumption identified in the previous phases from the heating energy consumptions (grey dots in Fig. 2).

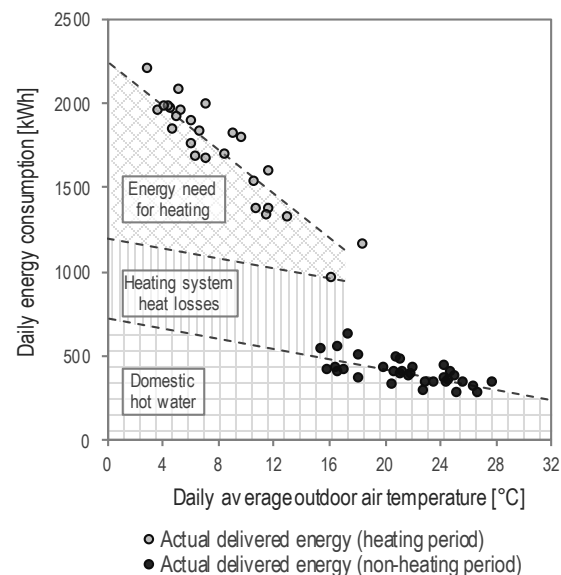


Fig. 2 – Extrapolation of the energy needs of the building for heating from overall energy consumption

3.2 Model Calibration Results

The calibration of the model was performed by means of a graphical comparison technique (Fig. 3): the grey dots in Fig. 2 represent the actual energy need; the black dots, by comparison, refer to the results of the simulation with the EN ISO 52016-1 hourly method and relate to the calibrated model. The first-stage simulation was characterized by an overestimation of the calculated heating energy needs with respect to actual needs, and a larger slope in the line representing the simulated energy needs. To correct the slope, the parameters affected by the outdoor–indoor air temperature difference were calibrated. As mentioned above, due to the lack of reliable information, it was not possible, in calibrating the model, to consider the thermal properties of the opaque building envelope. Thus, the ventilation air changes were reduced during the unoccupied hours (0.12 h^{-1}) so as to accurately represent the actual opening of the windows while ensuring the infiltration air flow rate. Moreover, due to the fact that the opaque building envelope was un-insulated, only the thermal bridge between the external walls and the windows was considered. On the other hand, due to the uncertainty related to the absence of heating control systems, the heating set point was lowered to 20°C (with a continuous operation) to reduce the gap between the actual and simulated lines.

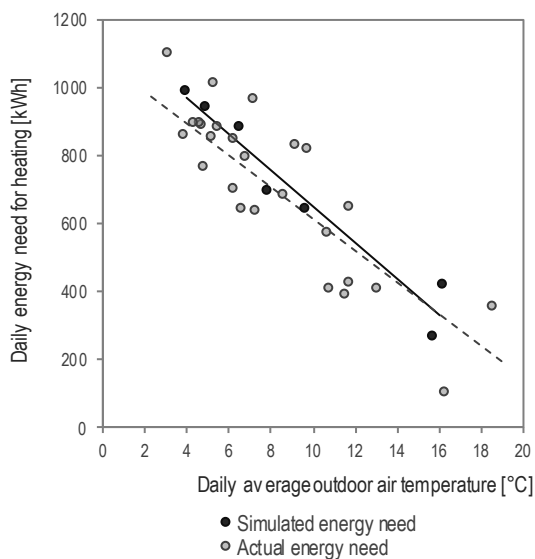


Fig. 3 – Results of the calibration procedure

4. Comparison of the Calculation Models

4.1 Consistency Options

The investigation of the reliability of the new hourly calculation method in predicting the indoor temperatures and the heating and cooling needs was based on its comparison with the detailed dynamic model. The comparison was developed using two different analyses, as outlined above, considering indoor operative temperatures and both the heating and cooling needs. Some consistency options were applied to the two models to make their results comparable. The options, applied to the calibrated model (and in addition to the boundary conditions, geometrical data and thermal properties of the building envelope, and the user behaviour parameters) are as follows:

1. Ground temperature. A constant ground surface temperature of 18°C was assumed;
2. Heating and cooling set-point temperatures. The set-points referred to the operative temperatures, and were set at 20°C and 26°C for heating and cooling operation respectively;
3. Convective and radiative fractions of internal heat sources. The heat flow was assumed to be 40% convective and 60% radiative;
4. Fully convective heating and cooling systems. In both models, the heat supplied by the heating and cooling systems was assumed to be completely convective;
5. Furniture heat capacity applied to the air node. The standard value indicated in the EN ISO 52016-1 ($10\,000 \text{ J m}^{-2} \text{ K}^{-1}$) was modelled in the EnergyPlus tool by means of the “zone sensible heat capacity multiplier parameter”.

Standard hourly weather data (test reference year for the city of Turin) were provided by the Italian Thermo-technical Committee and used in the comparison between the two calculation models.

Regarding solar heat gains, the convective fraction of the solar radiation was assumed to be equal to 0.1 in the simplified model, and a “FullExterior” algorithm for the solar distribution was adopted in the EnergyPlus simulations.

As far as thermal capacity assessment of the building is concerned, the finite difference heat conduction model was applied to the EnergyPlus model. In the EN ISO 52016-1, the heat capacity of envelope components was applied to the external surface node or assumed to be equally distributed (external walls).

4.2 Internal Operative Temperature

The operative temperature comparison was performed on an annual basis, considering a free-floating condition (the heating and cooling systems were assumed to be switched off), by applying the principle of superposition of effects. This principle was applied to investigate the reason for the discrepancy between the models, based on the deviation of the resulting internal temperature profile. Thus, the effects of each driving force on the air heat balance in the indoor environment were identified. To this purpose, the considered driving forces were added in four different simulations (identified by a simulation-ID), as follows:

1. In the first simulation (ID: EnvTr), ventilation (both natural ventilation and infiltrations), solar radiation and internal heat sources were removed, so that the only driving force considered was the heat transmission through the building envelope components due to the outdoor air temperature;
2. In the second simulation (ID: VenTr), the effect of ventilation due to the outdoor air temperature was added by considering the correct values for the air change rates;
3. In the third simulation (ID: IntG), the effects of the internal heat sources were considered, by introducing the correct values for the internal heat gains;
4. Finally, the fourth simulation (ID: SolG) was a complete simulation, in which the effect of the solar radiation was considered by adding the contribution of the solar radiation incident on the opaque and transparent envelope.

For each of the aforementioned simulations, the analysis was performed by considering the hourly difference between the indoor operative temperatures calculated through the EN ISO 52016-1 and the EnergyPlus methods, as described in equation (1), for a typical winter and summer week.

$$\Delta\theta_i = \theta_{\text{EN ISO 52016-1},i} - \theta_{\text{EnergyPlus},i} \quad (1)$$

where $\theta_{\text{EN ISO 52016-1},i}$ and $\theta_{\text{EnergyPlus},i}$ are the indoor operative temperatures from EN ISO 52016-1 and EnergyPlus respectively, at time step i . The results of the indoor operative temperature comparison are presented in Fig. 4 for two representative thermal zones, the bedrooms on the ground floor (GF) and on the second floor (SF) respectively. In Fig. 4, a negative difference means an overestimation in the calculation of the operative temperatures in the detailed dynamic tool, while a positive difference means an underestimation. The results are presented for one typical winter week (from January 17th to 23rd) and one summer week (from June 12nd to 18th).

The main result that can be seen in Fig. 4 is the strong influence of solar radiation compared to the other driving forces, which results in an underestimation of the prediction of the internal temperature by the EN ISO 52016-1 model, compared to the prediction obtained using the EnergyPlus model. Considering the first three simulations and their relative driving forces, the temperature trends are consistent between the two models, mainly in the typical summer week, with temperature differences lower than ± 1 °C. If the simplified hourly method gives consistent results in terms of free-floating operative temperatures for the second-floor thermal zone both in cold and hot weeks, a negative influence of the heat transfer through the ground on the energy behaviour of the ground floor is registered in the winter week. The EN ISO 52016-1 model calculates higher temperatures than EnergyPlus, even though the ground temperature was made consistent between the two models. The difference is therefore strictly related to the ground heat transfer solving models. On the other hand, a negligible deviation between the two models is reported during the typical summer week, as can be seen in the chart on the top right of Fig. 4.

The introduction of the contribution of the solar radiation on the opaque and transparent envelope affects the amplitude of the temperature difference, both in the winter and the summer season. On the ground floor, solar radiation leads to an increase in the predicted temperature in the detailed dynamic simulation (of around 2 and 4 °C), even though the

ground floor is only slightly influenced by solar radiation due to the shading of the surrounding buildings. The wide exposure of the 2nd floor to solar radiation, the orientation of the windows and the absence of any solar shading devices lead to significant discrepancies in the free-floating operative temperatures: a difference of 2 °C is registered in the winter week, while the operative temperature rises by 6 °C in the summer week. However, the lack of outputs in the commercial tool did not allow for the reasons for this deviation to be investigated in more depth.

This analysis was performed, as previously mentioned, for two typical winter and summer weeks. However, the identified trends were also demonstrated in the numerical evaluation of the reliability of the models in predicting the operative temperatures, conducted by means of the Root Mean Square Error (*RMSE*) calculation on an annual basis, as follows:

$$RMSE = \sqrt{\frac{\sum_{i=1}^{N_i} (\theta_{\text{EN ISO 52016-1},i} - \theta_{\text{EnergyPlus},i})^2}{N_i}} \quad (2)$$

where $\theta_{\text{EN ISO 52016-1},i}$ and $\theta_{\text{EnergyPlus},i}$ is the indoor operative temperature from the EN ISO 52016-1 and EnergyPlus respectively, at time step i , and N_i is the number of the considered time steps (8 760 time steps). Table 2 summarizes the annual *RMSE* values for the four simulations; for the first three steps, the *RMSE* values remain within acceptable values (1 °C). The introduction of solar radiation (fourth simulation, ID: SolG) causes the *RMSE* to rise by 2.35 and 4.19 °C for the ground and the second floor bedroom thermal zones respectively.

Table 2 – Annual *RMSE* [°C] related to each driving force

Thermal zone	EnvTr	VenTr	IntG	SolG
Bedrooms GF	1.01	0.94	0.79	2.35
Bedrooms SF	0.80	0.81	0.97	4.19

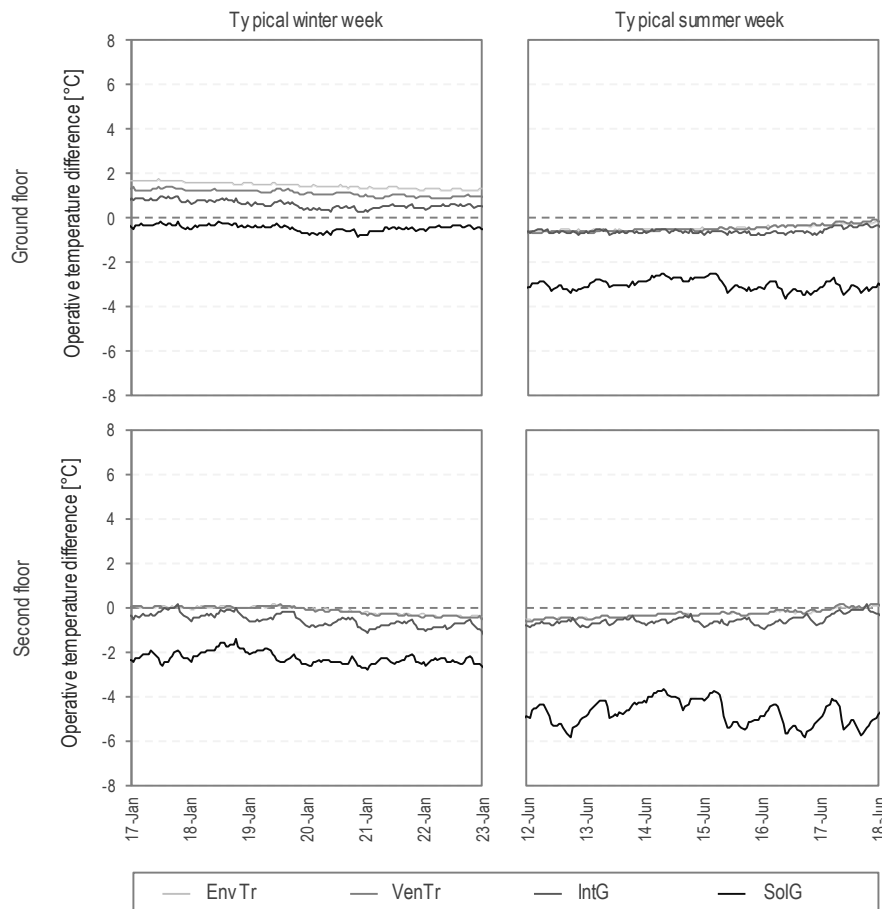


Fig. 4 – Operative temperature comparison for two thermal zones (ground and second floor bedrooms) for typical winter and summer weeks

4.3 Building Thermal Needs

The operative temperature comparison made it possible to better understand the results of the comparison between the thermal needs of the building predicted by the two considered calculation models. In the present analysis, the EN ISO 52016-1 “basic” heating/cooling energy need calculation and the EnergyPlus “ideal load” system were assumed. For both calculation models, a continuous operation and no power restriction for the heating/cooling system were assumed, as well as a purely convective emission. The monthly thermal energy needs for the whole building are shown in Fig. 5.

Interesting results, which confirm the results previously discussed, can be derived from this analysis. Generally, the hourly method introduced by the new EN ISO 52016-1 tends to slightly overestimate the heating energy needs with respect to the detailed dynamic calculation model. Despite the overestimation, the discrepancy between the two models does not exceed 5% on a monthly basis. On the other

hand, in ‘mid-season’ months (e.g. March, April and October), the prediction of heating energy needs shows significant discrepancies (e.g. the EN ISO 52016-1 model overestimates the heating energy needs in March by 21.5%). As highlighted in the analysis previously presented, the influence of the solar radiation driving force may be the reason for such differences. However, it should be noted that the EnergyPlus model produces a remarkable underestimation of energy needs for heating in mid-season months (specifically in April and October) for an uninsulated building sited in a heating dominated climatic context.

The critical discrepancy in the operative temperatures due to the solar radiation driving force presented in the previous analysis translates into large differences in the calculation of the cooling energy needs. In this instance, the EnergyPlus model calculates cooling energy needs consistently higher than the EN ISO 52016-1 model (the discrepancy ranges from 52.9 to 74.3%).

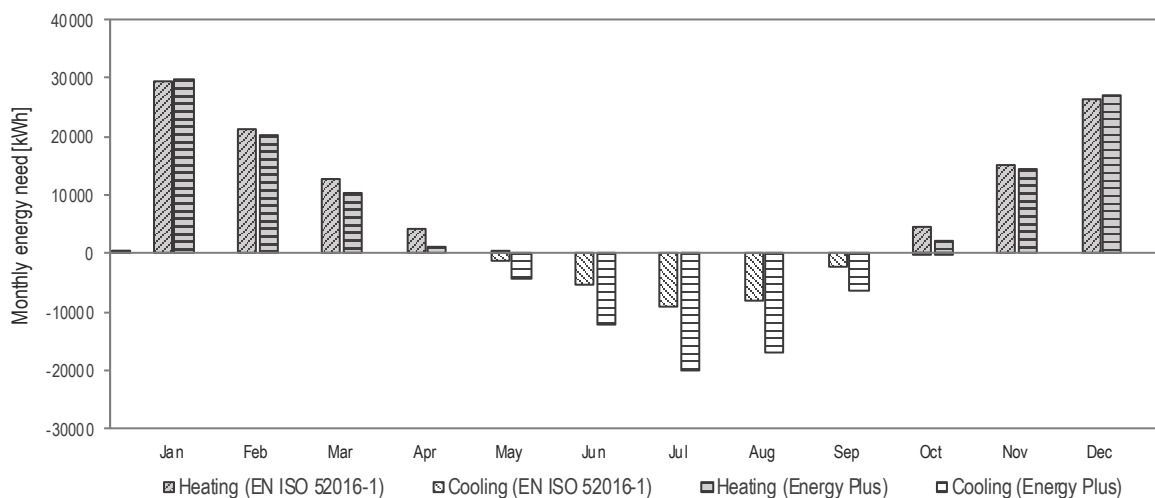


Fig. 5 – Comparison between the monthly heating and cooling energy need

5. Discussion and Conclusion

A number of conclusions can be drawn from the analysis presented in this paper. Firstly, the extrapolation of the heating energy need made it possible to calibrate a model independently from the modelling of the technical building system. However, the lack of reliable information on building use, user behaviour and, particularly on the building enve-

lope – considering that the building is uninsulated – made it impossible to reach a more acceptable model calibration. Nevertheless, the new hourly method introduced by EN ISO 52016-1 proved to be a suitable tool for the calibration of the energy models for the building.

As regards the investigation of the accuracy of the new hourly method in comparison with a detailed dynamic one, two different behaviours can be

pointed out. First, negligible deviations between temperatures and thermal energy needs were registered in the winter months. Second, the results of the performed analysis showed a remarkable deviation in mid-season and summer months. Deriving from the evaluation of the effect of the different driving forces on the air heat balance, solar radiation was identified as the main cause of the highlighted discrepancy. However, the explanation should not be limited to the different modelling of the solar gains through windows, as it is also related to the modelling of the thermal capacity of the building in the new simplified hourly method.

The results in this study cannot be generalized, since they are related to a heavyweight case study building. Moreover, the present work was affected by the lack of transparency of the commercial tool implementing the EN ISO 52016-1 hourly calculation model. Due to the limited inputs and outputs of the tool (temperatures and thermal needs), it was not possible to investigate the deviation between the two models in depth.

Future research is planned to focus on a larger number of case studies and on the investigation of the deviation caused by the solar heat gains and building heat capacity modelling.

References

- Ballarini, I., A. Costantino, E. Fabrizio. and V. Corrado. 2019. "The Dynamic Model of EN ISO 52016-1 for the Energy Assessment of Buildings Compared to Simplified and Detailed Simulation Methods." *Proceedings of Building Simulation 2019: 16th Conference of IBPSA*, Rome, Italy, September 1st-4th 2019.
- EC700. EdilClima Engineering & Software. Accessed October 11. <https://www.edilclima.it/software-termotecnica/prog-termotecnica-energetica/scheda/700> (in Italian)
- EnergyPlus. Accessed October 11. <https://energyplus.net/>
- Ente Italiano di Normazione (UNI). 2014. *UNI TR 11552: Opaque envelope components of buildings – Thermo-physical parameters* (in Italian).
- Ente Italiano di Normazione (UNI). 2019. *UNI/TS 11300-2: Energy performance of buildings – Part 2: Evaluation of primary energy need and of system efficiencies for space heating, domestic hot water production, ventilation and lighting for non-residential buildings* (in Italian).
- European Commission. 2010. *Directive 2010/31/EU of 19 May 2010 on the energy performance of buildings (recast)*.
- European Committee for Standardization (CEN). 2008. *EN ISO 13790: Energy performance of buildings - Calculation of energy use for space heating and cooling*. CEN: Brussels, Belgium.
- European Committee for Standardization (CEN). 2017. *EN ISO 52016-1: Energy Performance of Buildings – Energy Needs for Heating and Cooling, Internal Temperature and Sensible and Latent Heat Loads. Part 1: Calculation procedures*. CEN: Brussels, Belgium.
- International Organization for Standardization (ISO). 2016. *ISO 18523-1: Energy performance of buildings – Schedule and condition of building, zone and space usage for energy calculation Non-residential buildings*.
- OpenStudio. Accessed October 11. <https://www.openstudio.net/>
- Siva Kamaraj, V. 2018. "Dynamic building modelling using an extensive RC network according to ISO 52016: numerical implementation and testing." Ph.D. thesis, Politecnico di Milano.
- van Dijk, D. 2018. "EPB standards: Why choose hourly calculation procedures?" *REHVA Journal*: 6-12.
- Wang, S., Y. Chengchu, and X. Fu. 2012. "Quantitative energy performance assessment methods for existing buildings." *Energy and buildings* 55: 873-888. doi: 10.1016/j.enbuild.2012.08.037
- Zakula, T., M. Bagaric, N. Ferdelji, B. Milovanovic, S. Mudrinic, and K. Ritosa. 2019. "Comparison of dynamic simulations and the ISO 52016 standard for the assessment of building energy performance." *Applied Energy* 254: 113553. doi: 10.1016/j.apenergy.2019.113553

On the Thermophysical Performance Optimization of Italian Schools of the 60s: A Case Study in Ostia (RM)

Francesco Asdrubali – Roma Tre University, Italy – francesco.asdrubali@uniroma3.it

Luca Evangelisti – Roma Tre University, Italy – luca.evangelisti@uniroma3.it

Lucia Fontana – Roma Tre University, Italy – lucia.fontana@uniroma3.it

Claudia Guattari – Roma Tre University, Italy – claudia.guattari@uniroma3.it

Ilaria Montella – Roma Tre University, Italy – ilaria.montella@uniroma3.it

Pietro Prestininzi – Roma Tre University, Italy – pietro.prestininzi@uniroma3.it

Ginevra Salerno – Roma Tre University, Italy – ginevra.salerno@uniroma3.it

Chiara Tonelli – Roma Tre University, Italy – chiara.tonelli@uniroma3.it

Valeria Vitale – Roma Tre University, Italy – valeria.vitale@uniroma3.it

Abstract

In recent years, energy efficiency and energy saving issues have dominated the field of buildings research. Since new constructions are characterized by an efficient design, the real challenge is to define accurate and effective retrofit interventions for existing buildings. In order to understand the energy behavior of buildings and identify the best viable retrofit solutions, accurate analyses, carried out by means of dynamic simulations and in-situ measurement campaigns, are needed. Furthermore, in Italy compliance of the effects of the proposed interventions with standards is necessary. In this paper, a school built in the 1960s was considered as a case study and its energy performance was investigated. An in-situ measurement campaign was conducted with a thermal imaging camera, a heat flow meter and air temperature probes. Following this, a dynamic model of the school was implemented by means of TRN-SYS dynamic code and different retrofit scenarios were evaluated and compared. The aim of this analysis was to quantify the effectiveness of the chosen refurbishment strategies on the energy demands of the investigated school.

1. Introduction

In recent years, there has been a significant increase in energy consumption due, in part, to the economic growth of developing countries. This has led to a greater exploitation of fossil fuels, with a consequent increase in CO₂ emissions and other greenhouse gases.

The reduction of the overall energy demand of buildings is an important environmental objective. The aim to be pursued is to make public and private buildings consistent with the principles of energy efficiency and environmental sustainability (Marrone et al., 2018; Stabile et al., 2019). The importance of defining strategies to increase energy efficiency and reduce energy consumption and greenhouse gas emissions is a priority to which it is necessary to give precise and certain answers. Technical solutions have evolved over the years and for this reason, it is important to understand the energy behavior of buildings through accurate energy analyses (Dalla Mora et al., 2017; Evangelisti et al., 2017; Gori et al., 2016).

The construction sector clearly has a significant role in terms of energy consumption. Encouraging research and promoting retrofit interventions on buildings could act as an engine for the entire sector and contribute to achieving the objectives defined by the European Union. For this reason, effective policies and strict controls must be promoted to guarantee the expected results.

This work is part of the "Sustainability of Schools - SoS" project: an interdisciplinary project funded by Roma Tre University, which involves the Departments of Architecture and Engineering at Roma Tre University, together with the Departments of Economics, Mathematics and Physics, and Sciences. The final goal of the whole project, which involves different disciplinary fields, is to develop and validate

predictive models of energy efficiency, comfort and health of existing school buildings, with the aim of proposing best practices and procedures for users (Marrone et al., 2018).

The aim of this paper is to study a selected category of educational building and define retrofit interventions in order to reduce energy consumption, support better internal environmental conditions and suggest more sustainable solutions. Preliminary experimental results and simulations are presented in the present paper.

1.1 The Selected Case Study

Prefabrication – introduced in Italy in the 1960s – took advantage of a considerably reduced construction time compared to traditional systems. Due to the economic boom and increase in birth rates in this period, many buildings were constructed, often by assembly of “large panel” prefabricated systems.

Due to the need to respond to the strong demographic growth, Law No. 17 of January 26 1962 allocated funding for developing prefabricated school buildings. Furthermore, the Ministry of Education provided funding for the construction of approximately 340 schools in 35 Italian provinces. This happened before the implementation of the Technical Standards for School Construction (Ministerial Decree of May 18, 1975), the Norms for Fire Prevention in School Buildings (Ministerial Decree of August 26, 1992) and the provisions on energy saving (Law No. 10 of January 9, 1991). Consequently, the selected case study, along with all the other buildings built in the same period, do not comply with the important laws in all the aforementioned areas.

The strong and frequent impact of thermal bridges, performance losses, condensation phenomena and structural inadequacy of the external prefabricated large-panel walls has become an issue over time. This has led to the need to focus on stratigraphy, joints and technological solutions, in order to ascertain whether it is possible to improve the envelope behavior, in order to reach the performance level currently required.

As can be seen in Fig. 1, the investigated case study

is characterized by a modular structure, with encapsulated asbestos cement panels that imply the presence of several thermal bridges. The windows, with a single glass sheet of 4 mm, are relatively old and the in-situ survey revealed that the frames do not close perfectly.



Fig. 1 – External view of the school

2. Methodology

The methodology used consisted of an experimental and numerical framework aimed at both supporting strategies and best practices for an efficient use of an educational building in the Lazio region and evaluating the effectiveness of possible retrofit interventions.

A prefabricated building was selected as case study: a school (see Figs. 1 and 2), in Ostia, near Rome (climatic zone D), representative of a high number of educational facilities built in Italy during the 1960s.

The stratigraphy was established starting from information provided by the technical staff of the school and in-situ surveys. The stratigraphy and the theoretical transmittance value are reported in Table 1. The total thickness of the external walls is about 21 cm (Fig. 3).

Given the impossibility of intervention with destructive diagnostic techniques in order to investigate the actual stratigraphy, it was necessary to move to non-destructive diagnostic investigations. In particular, infrared thermography and the heat-flow meter method were employed.

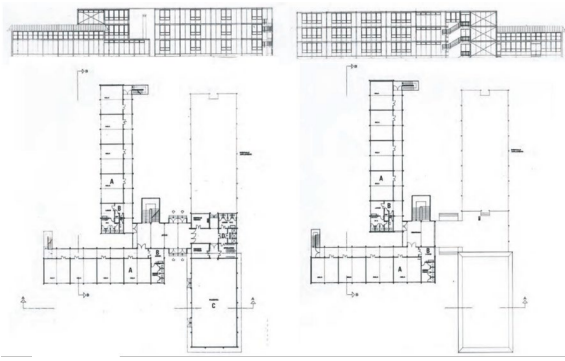


Fig. 2 – School layout and facades

Table 1 – Stratigraphy of the wall

Layer	Thick ness [m]	Thermal conductivity [W/mK]	Thermal resistance [m²K/W]
1) int.	-		0.13
plasterboard	0.015	0.200	0.075
2) fiber cement panels	0.008	0.500	0.016
3) Polystyrene granulate and cement	0.040	0.070	0.571
4) Cement- Asbestos	0.100	0.700	0.143
5) Polystyrene granulate and cement	0.040	0.070	0.571
6) fiber cement panels	0.008	0.500	0.016
ext.	-		0.04
Wall thermal resistance			1.563 m²K/W
Wall thermal transmittance			0.640 W/m²K

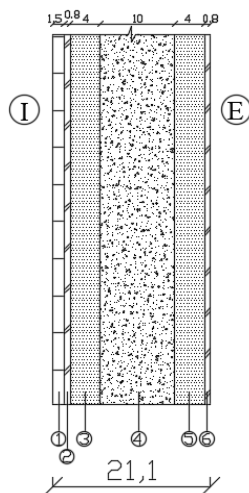


Fig. 3 – Stratigraphy of the wall

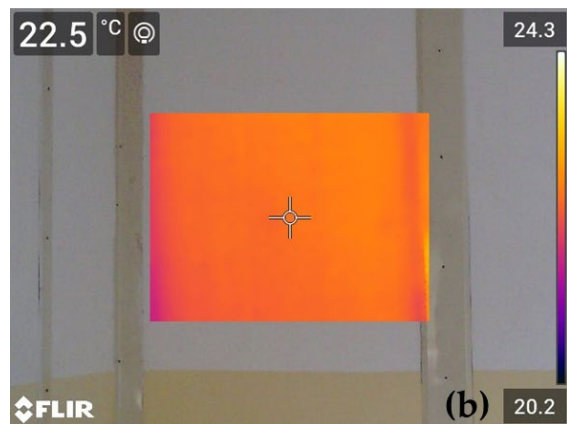


Fig. 4 – External (a) and internal (b) infrared thermography survey

The measurement campaign was conducted in April 2019 by means of a heat-flow meter through which heat fluxes, and indoor and outdoor temperatures were acquired. In addition, a thermographic survey was conducted in order to identify both thermal bridges in the structure and for the proper installation of the heat-flux sensor (see Fig. 4).

Thermal transmittance values were measured by following the ISO 9869-1 (2014). In accordance with this Standard, measurements were carried out for 8 days, with an acquisition time step equal to 10 min.

The heat-flow meter was applied to a north-west facing wall, in order to avoid direct solar radiation as much as possible.

A calibrated dynamic model was created by means of the TRNSYS simulation code. The geometrical characteristics of the building were reproduced through TRNSYS-build (Type 56) and a thermal transmittance measurement was used to generate a correct wall model.

Physical environmental phenomena were set in TRNSYS-studio, reproducing the outdoor environmental conditions by using Type 54, inside which actual average air temperatures, relative humidity and wind velocity were introduced in order to generate realistic climatic data. Solar radiation measurements were not performed, and data were obtained by Type 109. The heating energy demand was increased by 20% in order to consider the influence of thermal bridges. Regarding internal boundary conditions, internal gains were represented by people, characterized by sensible heat of 65 W and latent heat of 55 W; an infiltration rate for each thermal zone equal to 0.6 1/h was set.

In order to attempt to provide effective retrofit solutions, external thermal coats made of XPS and characterized by different thicknesses were tested. In addition, windows with a higher thermal performance (thermal transmittance value equal to 1.300 W/m²K and g-value equal to 29.8%) were tested in the simulation.

The calibration procedure, based on a comparison between simulated and actual indoor air temperatures, was achieved by calculating the Mean Bias Error (*MBE*) and the Coefficient of Variation of Root Mean Square Error (*CV(RMSE)*).

The retrofit intervention mentioned above was tested in order to verify the reductions in monthly heating energy needs.

3. Results and Discussion

From the results obtained through the heat-flow meter measurement campaign, it was assessed that the building envelope is characterized by a thermal transmittance value equal to 0.522 W/m²K. As shown in Fig. 1, the building facades are characterized by panels joined together, creating a discontinuous structure characterized by many thermal bridges. Moreover, the windows are quite old, and do not ensure high thermal insulation levels. Due to these problems, energy refurbishment measures are needed in order to enhance the thermal behavior and the indoor thermal comfort.

Comparing the experimental thermal transmittance (equal to 0.522 W/m²K) with the theoretical transmittance (equal to 0.640 W/m²K), it is possible to

observe a percentage difference equal to -18.43%, matching the ISO9869-1 criterion (Evangelisti et al., 2019).

Starting from the experimental data, a dynamic simulation, through the well-known dynamic code TRNSYS (2018), was carried out in order to verify the effectiveness of different retrofit scenarios.

Due to the intended use of the building, simulations aimed at assessing the energy needs of the building were performed only during the winter. A comparison between energy needs for heating after the retrofit interventions with those related to the current conditions was considered. Attention was also paid to the spring months, in which indoor temperatures become higher than the winter ones, due to the poor inertial properties of the building. In particular, the analysis focused on two periods: from 15th of April to the end of June; and from September to October. During these months, the heating system is switched off.

3.1 Retrofit Scenarios

Two retrofit scenarios were simulated: an external insulation improvement (using XPS) and the replacement of the windows, using solar control glass.

As mentioned above, the building is characterized by a light structure, with high internal thermal gains represented by students in the classrooms. Consequently, the first test involved the addition of an insulation layer on the external side of the walls. During this analysis, three different thicknesses of XPS were tested (5 cm, 10 cm and 16 cm). This approach led to reduced heating energy needs but with an average reduction value of less than 8%. Detailed results are listed in Table 2.

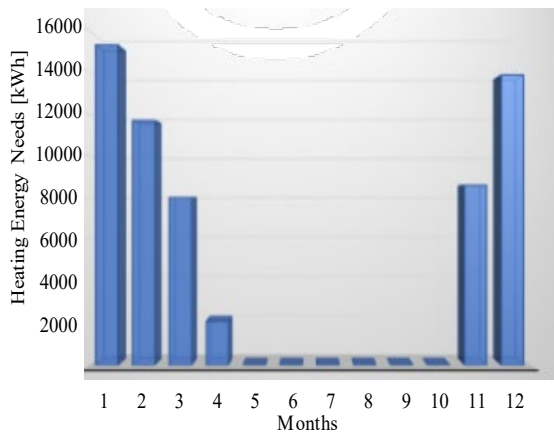


Fig. 4 – Heating energy needs of the actual conditions

Table 2 – Monthly heating energy needs and average percentage differences obtained by applying XPS

Month	Actual conditions [kWh]	XPS 5cm [kWh]	XPS 10cm [kWh]	XPS 16cm [kWh]	Average percentage difference [%]
J	15293	14702	14505	14391	-4.97%
F	11685	11202	11043	10952	-5.30%
M	8009	7624	7496	7424	-6.17%
A	2095	1967	1925	1902	-7.81%
M	0	0	0	0	-
J	0	0	0	0	-
J	0	0	0	0	-
A	0	0	0	0	-
S	0	0	0	0	-
O	0	0	0	0	-
N	8597	8205	8079	8008	-5.81%
D	13859	13306	13118	13011	-5.15%

The results indicate that this type of intervention cannot be considered as particularly effective.

The second test involved the installation of windows with solar control glass, characterized by a thermal transmittance value equal to $1.300 \text{ W/m}^2\text{K}$ and a solar factor (g-value) equal to 29.8%. The corresponding results are reported in Table 3.

Observing the data listed in Table 3, it is possible to ascertain that the replacement of the windows is very effective, reducing the annual energy need for heating by approximately 77%, on average.

During the retrofit phase, attention was paid to two aspects. Firstly, an additional external insulation layer results in higher indoor air temperatures during the winter, causing lower heating requirements. However, such higher indoor temperatures during spring and autumn can significantly compromise the comfort of users. This can cause 'incorrect' user behaviour, from the point of view of energy use, for example, the opening of windows even though the heating systems are switched on. The thickness of the external XPS layer should therefore be limited, which implies lower costs and better conditions during the warmer months, when the effects of solar radiation start to become significant.

Table 3 – Monthly heating energy needs and average percentage differences obtained by replacing windows

Month	Actual conditions [kWh]	Solar control windows [kWh]	Percentage difference [%]
J	15293	4157	-72.82%
F	11685	2848	-75.63%
M	8009	1512	-81.12%
A	2095	214	-89.79%
M	0	0	-
J	0	0	-
J	0	0	-
A	0	0	-
S	0	0	-
O	0	0	-
N	8597	1629	-81.05%
D	13859	3610	-73.95%

Thermal insulation should not be the only method considered to improve the energy performance of this category of building: the existing walls are characterized by low thermal transmittance and an improvement of the thermal resistance of the envelope is not the only viable and effective solution.

The building is negatively affected by the influence of solar radiation because it is characterized by a light structure, with a not-significant thermal inertia. External environmental conditions are not filtered by the envelope, which is distinguished by low attenuation and phase shift characteristics. This causes incorrect user behaviour, affecting, in turn, the energy consumption of the building.

4. Conclusion

An Italian school built in the 1960s was investigated, from the point of view of energy need, by using an experimental and simulative approach. Dynamic performance was analysed by means of a calibrated model and some retrofit interventions were tested. In particular, an external insulation improvement (using XPS) and the replacement of the windows, using solar control glasses, were considered.

Using XPS, the monthly energy needs for heating did not vary significantly. The average percentage reduction ranges from -7.81% (during April) to -4.97% (during January). In comparison, by substituting the windows a percentage difference ranging from -89.79% (during April) to -72.82 (during January) was achieved. These results suggest that replacement of the windows is the most cost effective intervention to reduce annual energy demand. However, thermal insulation improvements should not be the method considered to enhance the energy performance of this kind of building, at this latitude. Light structures are affected by poor dynamic thermal performance, and are negatively affected by the influence of solar radiation, with consequent overheating. Subsequently, improving the thermal insulation of the envelope does not represent the most effective solution because it makes it possible to only slightly reduce the energy needs of the building, and implies an increase in internal air temperature values. As a consequence,

incorrect user behavior can occur, for example, the opening of windows when heating systems are switched on, affecting, in turn, the energy consumption of the building.

Further measurements will be performed during the winter season and more comprehensive simulations and retrofit scenarios will be studied. Following the preliminary results reported here, movable solar shading devices will be the first additional retrofit solution to be considered. This kind of device may be an effective energy efficiency measure for this building, which is particularly affected by the influence of solar radiation due to its structural characteristics. Shading devices may also affect the indoor lighting, and their installation and the assessment of daylighting will be carefully considered in the next step of the research.

Acknowledgement

This research was carried out as part of the "Sustainability of Schools - SoS" Research Project, funded by Roma Tre University. The full name of project is "SoS - Sustainability of Schools. Definizione di tecnologie, metodologie e protocolli d'uso per salubrità, benessere e risparmio energetico nei luoghi di formazione" ("SoS - Sustainability of Schools. Definition of technologies, methodologies and protocols of use for health, well-being and energy saving in training places"), published in the 'Extraordinary research development plan, Action 4, for experimental funding action for innovative and interdisciplinary research projects', and recipient of a research grant of 64,000 €.

References

- Dalla Mora, T., A. Righi, F. Peron and P. Romagnoni. 2017. "Cost-Optimal measures for renovation of existing school buildings towards nZEB." *Energy Procedia* 140: 288-302.
- Evangelisti, L., C. Guattari, P. Gori and F. Bianchi. 2017. "Heat transfer study of external convective and radiative coefficients for building applications." *Energy and Buildings* 151: 429-438.

- Evangelisti, L., C. Guattari and F. Asdrubali. 2019. "Comparison between heat-flow meter and Air Surface Temperature Ratio techniques for assembled panels thermal characterization." *Energy and Buildings* 203, 109441.
- Gori, P., C. Guattari, L. Evangelisti and F. Asdrubali. 2016. "Design criteria for improving insulation effectiveness of multilayer walls." *International Journal on Heat and Mass Transfer* 103: 349-359.
- ISO. 2014. *ISO 9869-1 - Thermal Insulation—Building Elements—In-Situ Measurement of Thermal Resistance and Thermal Transmittance*. ISO: Geneva, Switzerland.
- Marrone, P., P. Gori, F. Asdrubali, L. Evangelisti, L. Calcagnini and G. Grazieschi. 2018. "Energy Benchmarking in Educational Buildings through Cluster Analysis of Energy Retrofitting". *Energies* 11(3), 649-669.
- Stabile, L., G. Buonanno, A. Frattolillo and M. Dell'Isola. 2019. "The effect of the ventilation retrofit in a school on CO₂, airborne particles, and energy consumptions." *Building and Environment* 156, 1-11.
- TRNSYS. A Transient Systems Simulation Program. 2018.

On the Parasitic Heat Transfer Between Dwellings in the Case of Individual Heating: First Results by Simulation Across the EU

Viola Iaria – Tor Vergata University of Rome, Italy – viola.iaria@uniroma2.it

Carlo Mazzenga – Tor Vergata University of Rome, Italy – carlo.mazzenga@uniroma2.it

Vincenzo A. Spena – Sapienza University of Rome, Italy – vincenzo.spena@uniroma1.it

Abstract

In residential applications with individual thermostat controls, a major problem arises as a consequence of heat transfer between conterminous dwellings when at least one is unconditioned or under-conditioned. Any absence of people, or under-heating by any tenant, can significantly falsify the accounting of heat flows, particularly in the case of highly performing building envelopes. In this paper, the effects of this kind of “parasitic” heat transfer across the apartments of a residential building is simulated, using, as a preliminary approach, a simplified proprietary calculation code, which considers different set-points of thermostats assumed by different tenants, and internal gains as occupancy-related. Results show that there is a real need for thermal insulation of interior partitions and, especially for existing buildings, diseconomies as much high as the climate is mild. These results reveal the intrinsic heat accounting iniquity as a result of parasitic heat transfer through conterminous dwellings.

1. Introduction

In the wide parameter space involved in the correct assessment of the thermal performance of a building, the basic role played by the occupant’s behavior appears not to have yet been deeply explored. The European Directive 2012/27/EU on energy efficiency – the ‘EED’ (European Parliament, 2012) – suggests that individual heat metering in multi-apartment buildings is a remarkable driver of energy savings. Nevertheless, EU member States intend to implement the EED quite differently. Some countries, such as Germany or Austria, make very few exceptions to the commitment; while in other countries, such as France or Sweden, the duty appears less severely enforced. In countries like Italy, where resi-

dential multi-storey buildings have always been conceived as merely isothermal inside (Hensen and Lamberts, 2011; Shiel et al., 2018), with and interior partitions (interfloor slabs and walls) hence designed to be uninsulated, economical suitability (Celenza et al., 2016) of the EED appears conflicting. The advent of individual heat metering and accounting made – unexpectedly as well as inappropriately (Spena, 2017) – a huge amount of interior partitions highly heat dissipating, because it is unable to prevent heat exchanges (Pessenlehner and Mahdavi, 2003). On this matter, no relevant improvements were added by the recent European Directive 2018/844/EU (European Parliament, 2018), except for the use of Smart Readiness Indicators (SRI); by comparison, imbalances in room temperature levels were incautiously promoted.

2. Simulation

As an initial approach to examine this issue, a suitable SW code, already used (Spena et al., 2017) by some of the authors, was implemented to simulate the effects of different behaviors by tenants on energy consumption and metering.

2.1 The Source Code Structure

Weather data, set-point temperature levels, building envelope and fabric properties are described partly by deterministic, partly by stochastic models using algorithms and source code routines. In the present application one reference day per each month, hourly simulation time-steps, two selected typical surface exposures (NE and SW), together with a 13 h per day (7.00 am–20.00) heat metering

and accounting range at the coils, are assumed in iterative procedures.

2.1.1 The climatic model

The model is extensively described elsewhere (Spena et al., 2010). Solar radiation on the building envelope is simulated through the atmosphere model provided by Ashrae (ASHRAE, 2017). To explore to what extent the implementation of the EED can differ across the EU, two locations representing respectively a continental (Berlin, lat. 52.3°N) and a Mediterranean (Rome, lat. 41.5°N) climate condition of a nearly equal longitude (12.3° vs 13.2°) are compared. Cloudiness is also considered, by means of the Monte Carlo-based algorithm discussed in Spena et al. (1997). Thermal flows through walls are obtained from Fourier's general equation, also taking into account the inward flowing fraction of absorbed solar radiation by means of the so-called sol-air temperature (ASHRAE, 2017). A generally stabilized periodic regime is simulated (Spena, 1984; Tabunshchikov, 1993) as follows:

$$q(t) = U * (\overline{Tsa} - Ti) + U * \sigma * (Tsa(t - \varphi) - \overline{Tsa}) \quad (1)$$

where:

- t = time (hrs)
- U = overall heat transfer coefficient ($\frac{W}{m^2 \cdot K}$)
- Tsa = sol-air temperature (°C)
- Ti = indoor air temperature (°C)
- σ = heat flow damping (dimensionless)
- φ = phase-lag (hrs).

Heat flow damping and phase-lag are estimated according to the Alford, Ryan and Urban model (Alford, 1939). Corrective factors are introduced in (1) to properly consider the effects of solar radiation on walls. The sol-air temperature effect is neglected in the case of transparent components as it involves an increase in the overall heat gain of no more than 1%.

Outdoor weather data are taken from reference years described elsewhere (Spena, 2017; <http://www.eurometeo.com>); one representative day per month, namely the 15th of each month, is considered.

2.1.2 The building model

A dynamic simulation was carried out on the base portion of a residential multi-apartment building shown in Fig. 1, with a rectangular-prism geometry. Two exterior walls are assumed (black bold lines), one facing NE, the other SW. Interior walls (blue lines) are assumed (see § 2.2) as adiabatic. The total floor area (of about 160 m²) is divided equally between the two apartments. To evaluate internal gains from occupancy, a presence of 0.025 persons per square meter, with a simultaneity factor of 0.5 (Jian, 2018; Mahdavi, 2011) is assumed. The glazing area is assumed to be 15% of the exterior surface.

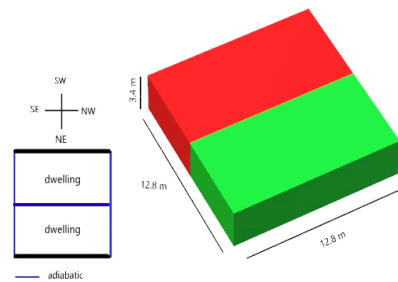


Fig. 1 – Sketch of the dwellings

Two levels of insulation of the envelope are considered: high (HI), and low (LI) insulation. U-values are as follows (Table 1):

Table 1 – Overall heat transfer coefficients for the envelope

Insulation	U_{wall} ($\frac{W}{m^2 \cdot K}$)	U_{window} ($\frac{W}{m^2 \cdot K}$)	U_{roof} ($\frac{W}{m^2 \cdot K}$)
HI	0.30	1.51	0.28
LI	0.93	4.07	0.81

Correspondingly, two values of the global solar heat gain coefficient SHGC are considered: 0.150 (HI) and 0.187 (LI). Values also include shading and framing effects.

2.1.3 The facilities model

Because of the capabilities of the model, the following assumptions are made. A centralized (or district) hot water system feeds room heating coils. According to the EED, individual heat metering and accounting by means of cost allocators is shared by all tenants. In accordance with the Italian UNI 10339 standard, an average continuous infiltration rate of 0.25 ACR (air change rates, i.e. volumes per hours)

is supposed. This is consistent with the above occupancy simultaneity factor of 0.5. As far as visual comfort for occupants is concerned, lighting conditions refer (CEN, 2017) to standard EN 15193-1. Daylighting and/or artificial lighting always ensure an average level of 125 lx. Over time, the contribution of daylighting is evaluated through the mean daylight factor FDL as follows:

$$FDLm = \frac{\sum_i \tau_i * S_i * \psi_i * \varepsilon_i}{(1 - rm) * Stot} \quad (2)$$

where:

- i = i th glazing surface
- τ = glazing solar transmittance
- S = glazing area
- ψ = rear positioning factor (with respect to the facade)
- ε = shape factor
- rm = glazing mean light reflectivity
- $Stot$ = overall room interior surface.

For each room space, FDLm is the ratio between the interior and exterior illuminance, measured on a horizontal plane viewing the entire sky in overcast conditions (the amount of available light is therefore independent of exposure). Once daylighting levels, standard requirements (Fontoynt, 1999; Hunt, 1979), and lighting efficiency (we suppose the use of fluorescent lamps with 50 lm/W) are given, the FDL factor enables us to estimate hourly the internal gains resulting from complementary artificial lighting.

2.2 The Cases Studied

The simulation was applied to the described base portion of the building, considering different situations. The period of year studied was the winter season, from November to March, when the most severe weather conditions are experienced by both locations. Energy balances take into account the two opposite building facades (NE and SW); hence, in addition to heat flows through walls and windows, differences in heat demand are due to solar radiation-related loads. Internal gains result from artificial lighting – which is zeroed in the case of unoccupied dwellings – and from occupancy of the dwelling.

To start with, the most significant case of parasitic heat flow – that which occurs through interfloor slabs, rather than through vertical partitions – will be considered.

heat flow through interfloor slabs also took into account a realistic air temperature stratification: a gap of + 0.5 °C and of – 0.5 °C from the mean dwelling temperatures was assumed in the ceiling and on the floor of each room respectively. Moreover, slightly different values of the combined (radiative plus convective) interior surface coefficients were used, according to the different free convective motions (Fisher and Pedersen, 1997; Tabunshikov, 1993), leading to the following U-values for the horizontal walls: $U_{downward} = 1.58 \frac{W}{m^2 * ^\circ C}$; $U_{upwards} = 1.51 \frac{W}{m^2 * ^\circ C}$.

The thermal inertia of the walls was not considered for the interfloor slabs, for the following reasons:

- i) their thermal mass together with surface temperature oscillations are one order of magnitude lower than those on the external walls; ii) there is no solar radiation contribution (which might increase imbalances).

The calculations in relation to heating demand (namely, of thermal energy end-uses demand) were made regardless of the type of heating or HVAC equipment.

2.2.1 Basic heat demand

A preliminary study (base cases) was carried out to determine the basic heating demand with all apartments occupied and kept at the same standard temperature (20 °C). Four cases were obtained by combining the two different envelopes of Table 1 with the two EU locations, namely Berlin and Rome. Following this, the simulated cases of unbalance were as follows.

2.2.2 Apartment occupied, kept at a lower temperature

The apartment above the reference apartment (20 °C) is kept, by the tenant, at a temperature from 1 to 5 °C (namely at set points from 15 to 19 °C) lower.

2.2.3 Apartments left unoccupied, heating turned off

This scenario contains two relevant sub-cases:

1. an unoccupied apartment between two apartments kept each at a standard temperature
2. an occupied apartment kept at a standard temperature, placed in between two unoccupied apartments, with the upper apartment being on

the top floor, and the lower apartment on the ground floor.

All other conditions being equal, infiltration thermal loads will depend on both outdoor and indoor temperatures. It was also assumed that in the case of overheating (an excess in heat gains), no cooling is provided, with the exception of free cooling by opening the windows.

3. Results

3.1 The Cases of Balanced Dwellings: Basic Heat Demand

With a standard average indoor temperature of 20 °C for all apartments, and under steady interior conditions, only small thermal flows occur, as a consequence of stratification, from bottom to top. Apart from border apartments such as those on the top-floor or ground-floor (IEA, 2014), the vertical thermal balance is zeroed for each intermediate dwelling; its hourly heating demand is merely given by the algebraic sum of exterior surface-related thermal loads.

As an example, Fig. 2 shows the hourly energy loads of a December reference day of one of the apartments facing NE. The case is that of a low-insulated building located in Rome. In Fig. 2 the hourly trend of heat flow through windows is specular to the one of outdoor temperature while the trend of the heat flow through the walls is damped and time-shifted by their thermal mass. At the considered exposure, solar gains occur in the first part of the day, while artificial lighting occurs in the early morning and in the evening.

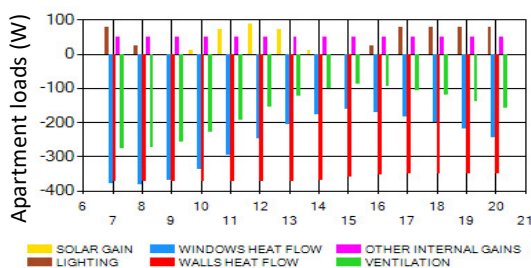


Fig. 2 – Rome, December, LI case, NE exposure. Energy demand over the reference day

As an insight into the effects of orientation, Fig. 3 reports the different percentages of total heating de-

mand – for the coldest month and the winter season overall – corresponding to the different exposures. In the considered reference year, the coldest month for Berlin and Rome is respectively January, and December. As expected (Brouns et al., 2016), apartments facing NE always require more heat than those facing SW because of the lower total (direct plus diffuse) solar radiation; the more the solar radiation-related thermal loads increase, the more this gap widens (as for high insulation and high solar radiation, at a given percentage of fenestration).

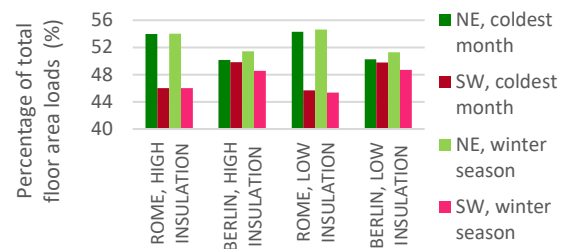


Fig. 3 – Percentages of total heating demand

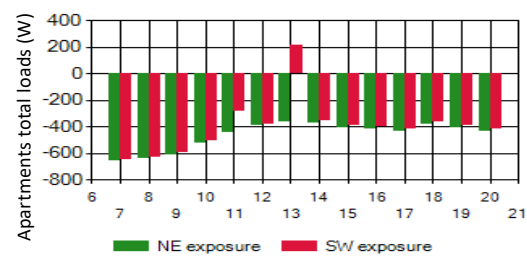


Fig. 4 – Berlin, March, HI case. Energy demand over the reference day

As a matter of interest, Fig. 4 shows, for the northern location (Berlin), overheating (solar and other gains exceeding heat dissipation through walls and windows) of SW side-spaces around midday. Even though with different intensities, simulations show that, from a qualitative point of view, this phenomenon recurs often throughout the whole winter season.

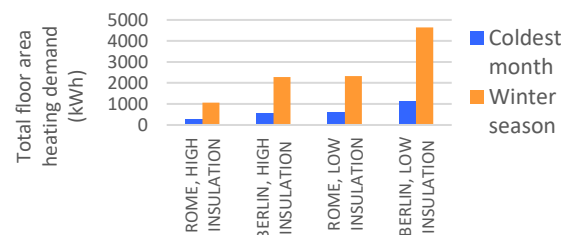


Fig. 5 – Dwellings overall basic heating demand

Finally, in Fig. 5 the overall basic heat demands of the dwellings are reported. As expected (Pedrini et al., 2002), they increase in case of low outdoor temperatures (i.e. at higher latitudes) and of poor building envelope insulation.

3.2 The Case of Unbalanced Dwellings

3.2.1 Upper apartment at a lower temperature

In this example, the upper apartment temperature is kept from 1 °C to 5 °C below the standard level (see Fig. 6). From this point onwards, green graphs will refer to NE exposure, and red graphs to SW exposure.

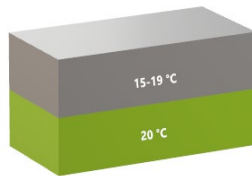


Fig. 6 – Two-apartments case sketch

Since now on, as an indicator of the relevance of the problem posed by the present paper, the ratio R between the “parasitic” heat loss to other neighboring apartments, and the basic heat demand of a considered apartment kept at a standard temperature, will be adopted. The results are summarized in Figs 7 and 8 as a function of the temperature gap (°C) which is the driving cause of the effect.

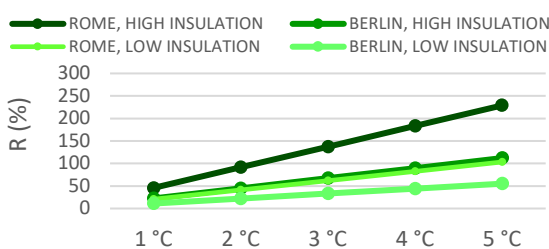


Fig. 7 – NE exposure. Relative increase on heating demand

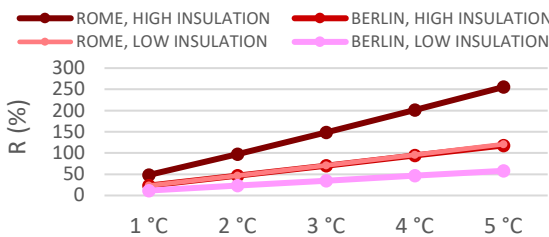


Fig.8 – SW exposure. Relative increase on heating demand

At any temperature difference, all apartments facing SW show relative parasitic increases in heating demand R that are slightly higher than for NE facing apartments, according to their lower overall basic heating need. More specifically, at the given conditions, whatever the climate, a temperature difference of 2 °C in case of high insulation has the same effect as a temperature difference of 4 °C with low insulation; inversely, with an equal temperature difference, departures are halved. It is clear that relevant parasitic heat transfer occurs (with R values up to a factor 2.5) not only in Northern climates (such as Berlin) with high insulation, but also in Southern climates (such as Rome) with low insulation, particularly in apartments with SW exposures. On the other hand, with high latitudes (such as Berlin) and weak insulation, parasitic heat flow across interfloor slabs remains lower than heat flow towards the outside, at least until the temperature difference between the apartments remains below 4÷4.5 °C.

3.2.2 Unoccupied border-lying apartments

In this scenario, two main situations are considered: Case 1, shown in Fig. 9, is an unoccupied apartment lying between two occupied apartments both kept at a standard temperature (20 °C); and Case 2, shown in Fig. 10, is an occupied apartment kept at a standard temperature, located between two unoccupied apartments, the upper apartment being on the top floor, and the lower apartment on the ground floor. For each situation, both NE and SW exposures were studied.

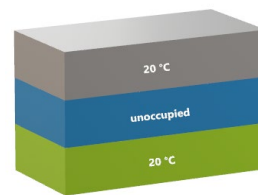


Fig. 9 – Unoccupied border-lying apartments. Case 1

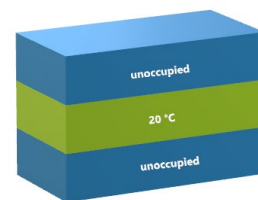


Fig. 10 – Unoccupied border-lying apartments. Case 2

It was assumed that in the unoccupied apartments all the coils were switched-off. Thus, in both cases, in the unoccupied apartment the lower the insulation and the lower the outdoor temperatures, the greater the decrease in the indoor average temperature. The results of the simulations indicated that low insulation leads to average temperatures in the unoccupied apartments as follows:

- from a minimum of 10.6 °C (Case 2, in January) to a maximum of 17.8 °C (Case 1, in March) for the Northern (Berlin) location
- from a minimum of 14.0 °C (Case 2, in December) to a maximum of 18.9 °C (Case 1, in March) for the Southern (Rome) location.

Correspondingly, high insulation led to average temperatures of the unoccupied apartments as follows:

- from a minimum of 15.6 °C (Case 2, in January) to a maximum of 19.1 °C (Case 1, in March) for the Northern (Berlin) location
- from a minimum of 16.3 °C (Case 2, in December) to a maximum of 19.6 °C (Case 1, in March) for the Southern (Rome) location.

It may be observed that with high insulation, the coldest space is always the ground floor; by comparison, with low insulation the coldest space is always the top floor. In Figs 11 and 12, the relative parasitic increase in heating demand R through the interfloor slabs for the apartment occupied and kept at 20 °C is reported, for both the considered exposures.



Fig.11– NE exposure. Relative increase on heating demand



Fig. 12 - SW exposure. Relative increase on heating demand

These results appear qualitatively similar to those previously obtained: the greatest seasonal relative increase in R always corresponds to Case 2, while the apartment facing SW remains more sensitive to the parasitic effect. More importantly, the effects of parasitic heat flows in Mediterranean climates (such as Rome) appear to be greater, even with low insulation (and particularly with SW exposures), than in continental climates (such as Berlin), even with high insulation. The difference between R values for Case 2 and Case 1, while decreasing as both insulation and climate warmth diminish, remains high, ranging from a factor of 5 (low insulation) to 8 (high insulation).

4. Discussion

Figs 13–16 summarize and compare the results in terms of homogeneous configurations in order to better understand what has been discussed and presented thus far.

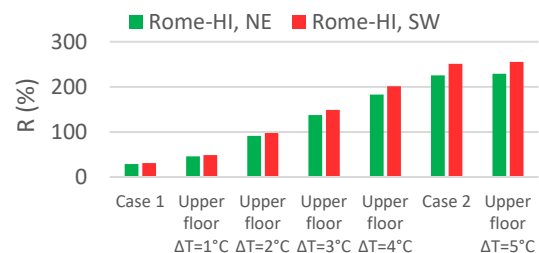


Fig. 13 – Rome-HI. Comparison of the results

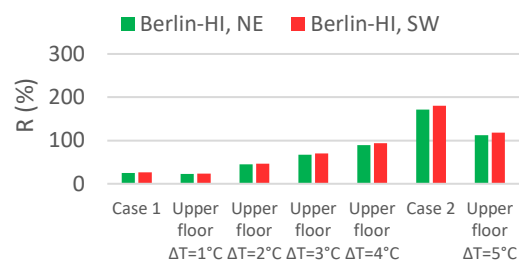


Fig. 14 – Berlin-HI. Comparison of the results

As previously observed, the NE facing apartments present values of R that are again slightly lower than for the SW facing apartments. This is due to the fact that the parasitic additional heat flow - being equal for both exposures - has a greater impact when basic heat demand is lower (solar and other gains are zeroed for unoccupied apartments in this con-

figuration). For both locations, greater R values are shown with high envelope insulation and with SW exposure.

For Rome, low external envelope overall heat transfer coefficients cause greater R values for an apartment kept at 20 °C and lying in contact with an unoccupied apartment (for the whole winter season), whilst high external overall heat transfer coefficients tend to reduce the drops in temperature in the unoccupied apartments. In the latter case, the worst scenario is that in which the upper apartment is constantly kept at the minimum considered temperature (15 °C).

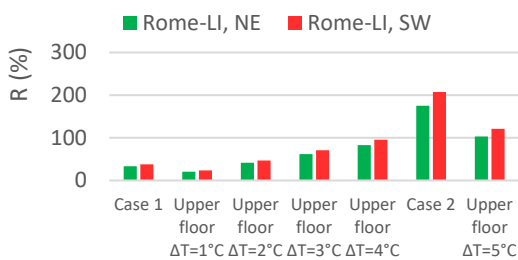


Fig. 15 – Rome-LI. Comparison of the results

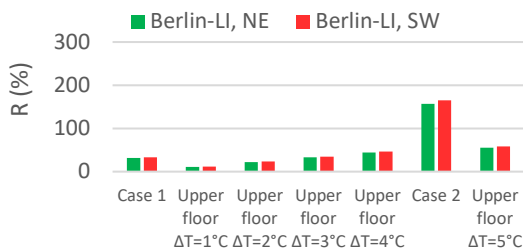


Fig. 16 – Berlin-LI. Comparison of the results

For Berlin, given that weather conditions are generally more severe, Case 2 is always the worst, regardless of the insulation level of the building envelope. The order of criticality is almost the same for the case of an apartment in Rome with low insulation and an apartment in Berlin with high insulation; in mild climates a lower level of building envelope insulation has the same effect as a higher envelope insulation level in severe climates.

As far as uncertainties are concerned, it's worth to remember that any limitation in the level of details allowed by a model, as well as any simplifying assumption made in the calculations, unavoidably can affect the results. As an example, this is the case of having neglected heat flow through vertical partitions, or of having selected a specific accounting

time. Nevertheless, and especially in terms of comparisons, the importance of the problem identified in this paper remains clear.

5. Conclusions and Further Insights

The study has highlighted how individual heating in an existing multi-storey residential building, especially in mild climates, can lead to an involuntary (as well as unavoidable) increase in individual cumulated heat consumption up to a factor of 3 or 4 over its basic voluntary heat demand.

Owing to the complexity of the topic, the initial results reported in this paper were obtained by using a set of simplified assumptions, and thus require further investigation. Nevertheless, from a qualitative point of view, the results clearly show that the differing use of individual heat metering and accounting for the buildings considered implies: i) a self-evident heat accounting iniquity in terms of parasitic heat transfer between conterminous dwellings; ii) a strong need for thermal insulation of interior partitions (especially of interfloor slabs), which is even more urgent than that for exterior walls; iii) the necessity to explore any potential for mitigation of the problem by means of advanced domotics; iv) the need for more detailed audits and sensitivity analyses, particularly for Mediterranean weather conditions; v) the need for further research on tailored calibrations and accuracy evaluations, in addition to improved predictions and modelling of the behavior of occupants.

In any case, not only do improvements in regulatory frameworks appear necessary, but also changes in the design criteria for new buildings. In the meantime, the need for retrofits of existing buildings by means of interior partition insulation and – most of all – for urgent mitigations in heat accounting rules, appears to be self-evident.

References

- Alford, J. S., J. E. Ryan, P. O. Urban. 1939. "Effect of heat storage and variation in outdoor temperature and solar intensity on heat transfer through walls." *Ashve Transaction* 45, 369.

- ANSI/ASHRAE. 2017. *Standard 140-2017, Standard Method of Test for the Evaluation of Building Energy Analysis Computer Programs*. American Society of Heating, Refrigerating and Air-Conditioning Engineers, Atlanta, GA.
- ASHRAE. 2017. *ASHRAE Handbook of Fundamentals*. ASHRAE. Atlanta (U.S.A).
- Brouns, J., A. Nassiopoulos, F. Bourquin, K. Limam. 2016. "Dynamic building performance assessment using calibrated simulation." *Energy and Buildings* 122: 160-174.
- Celenza, L., M. Dell'Isola, G. Ficco, M. Greco, M. Grimaldi. 2016. "Economical and technical feasibility of metering and sub-metering systems for heat accounting." *International Journal of Energy Economics and Policy* 6(3): 581-587.
- CEN - European Committee for Standardization 2017. *Energy performance of buildings - Energy requirements for lighting - Part 2: Explanation and justification of EN 15193-1, Module M9*. (UNI CEN/TR 15193-2:2017).
- Eurometeo website (<http://www.eurometeo.com>).
- European Parliament. 2018. *Directive 2018/844/EU*.
- European Parliament. 2012. *Directive 2012/27/EU*.
- Fisher, D. E., C. O. Pedersen. 1997. "Convective Heat Transfer in Building Energy and Thermal Load Calculation." *ASHRAE Transactions* 103(2): 137-148.
- Fontoyront, M. (edited by). 1999. *Daylight Performance of Buildings*. Routledge. London, U.K.
- Hensen, J.L.M., R. Lamberts (edited by). 2011. *Building Performance Simulation for Design and Operation*. Routledge. London, U.K.
- Hunt, D. 1979. "The use of artificial lighting in relation to daylight levels and occupancy." *Building and Environment* 14: 21-33.
- IEA - International Energy Agency. 2014. *Building Energy Simulation Test and Diagnostic Method (IEA BESTEST)*. *In-Depth Diagnostic Cases for Ground Coupled Heat Transfer Related to Slab-on-Grade Construction*. Approved by ASHRAE as an Addendum to Standard 140-2011.
- Italian Thermotechnical Committee (CTI). 1994. *UNI 10339 - Impianti aeraulici a fini di benessere. Generalità, classificazione e requisiti. Regole per la richiesta d'offerta, l'offerta, l'ordine e la fornitura*.
- Jian, Y. 2018. "Modelling and simulating occupant behaviour on air conditioning in residential buildings." *Energy and Buildings* 175: 1-10.
- Mahdavi, A. 2011. *People in Building Performance Simulation*. In Hensen, J.L.M., Lamberts R. *Building Performance Simulation for Design and Operation*. Routledge. London, U.K.
- Pedrini, A., F. S. Westphal, R. Lamberts. 2002. "A methodology for building energy modeling and calibration in warm climates." *Building and Environment* 37(8-9): 903-912.
- Pessenlehner, W., A. Mahdavi. 2003. "Building morphology, transparence, and energy performance." *Eighth International IBPSA Conference*. Eindhoven, the Netherlands, August 11th - 14th 2003.
- Shiel, P., S. Tarantino, M. Fischer. 2018. "Parametric analysis of design stage building energy performance simulation models." *Energy and Buildings* 172: 78-93.
- Spena, A. 1984. "Studio comparativo, mediante simulazione, della produzione combinata di energia elettrica, calore e freddo per la copertura dei fabbisogni di un comprensorio edilizio per attività terziarie." *Proceeding of XXXII ATI National Congress*. L'Aquila, Italy.
- Spena, A., A. Vitaliti, F. Cardarelli. 1997. "Primi risultati di un metodo per la generazione di congruenti valori orari della componente della radiazione solare al suolo." *Proceeding of LII ATI National Congress*, Cernobbio, Italy.
- Spena, A., C. Strati, G. D'Angiolini. 2010. "First Correlations for a Mediterranean Cloud Cover Model." *Proceeding of SPIE Solar Energy Plus Technology*. San Diego, U.S.A.
- Spena, A. 2017. "Efficienza energetica. Governare la complessità delle opzioni più avanzate." *La Termotecnica*, 11.
- Spena, A., V. Iaria, C. Mazzenga. 2017. "Dynamic Simulation of the Influence of Fenestration on Buildings Energy Consumption. A Comparison Between Northern and Southern Europe." *Proceedings of BSA 2017: Building Simulation Applications Conference*. Bolzano, Italy, February 8th - 10th 2017.
- Tabunshikov, Y.A. 1993. *Mathematical Models of Thermal Conditions in Buildings*. CRC Press. Boca Raton, U.S.A.

Analysis of the Surroundings Impact on the Building Energy Performance by Means of a BIM Analytical Model Coupled with Dynamic Simulation

Alessia Maiolatesi – University of Trento, Italy – alessia.maiolatesi@unitn.it

Alessandro Prada – University of Trento, Italy – alessandro.prada@unitn.it

Fabio Luce – University of Trento, Italy – fabio.luce@unitn.it

Giovanna Massari – University of Trento, Italy – giovanna.massari@unitn.it

Paolo Baggio – University of Trento, Italy – paolo.baggio@unitn.it

Abstract

Building design often does not result in an actual limitation of energy consumption during the building occupation phase since a performance gap emerges. This gap is often related to occupant behaviour, but other factors, such as uncertainties and errors occurring during the design, construction and management phases, may also have an impact. Because of this, the correct evaluation of the interactions between the building and the context is an important consideration, but is often not correctly incorporated into energy analyses. The correct modelling of neighbouring buildings can be an expensive activity due to the difficulty in gathering data.

The research reported here describes a methodology to develop a simulation model of an existing building and its surroundings by using a drone survey. With reference to a point cloud created from a drone survey, a geometric description of an existing building is developed in the BIM environment (Building Information Modelling). Following this, the BIM model is converted into a dynamic simulation model and the impact of neglecting the building's surroundings is quantified. The aim of this complete and complex approach is to propose a working methodology and a process that integrates geometric-architectural and energy disciplines. The results suggest that it is possible to develop an innovative operating methodology for intervention in existing built heritage.

1. Introduction

The coming into force of the EU Directive 2010/31/EU led to the need to reduce energy demand and carbon emissions in the European building stock. Retrofitting the existing building stock is a key strategy for reducing greenhouse gas emissions and mitigate climate change, as the effectively designed renovation of existing buildings can provide high energy savings. The importance of the refurbishment of the existing building stock, with a strong focus on energy saving, has become a key theme both in the literature and also in practice. (Li et al., 2017, Vilches et al., 2017).

Although building performance simulations (BPS) can provide a valuable support in the design of effective energy efficiency measures, the effort needed to create a complete and accurate model can hinder its application in practice. The development of an energy simulation model is an error-prone activity that relies on manual and time-consuming input activity (Lobos-Calquin, 2017). Furthermore, this step requires the energy modeller to replicate the 3D geometric model definition already prepared by the architect. Designers often adopt building information modelling software (BIM) in order to support the building design and lifecycle management as it contains a great deal of rich geometry and information.

Another important aspect of the design of energy efficiency interventions is that it may fail to achieve the expected performance. A building design often does not result in an actual limitation of energy

consumption during the building occupation phase and a performance gap emerges. This gap is often related to the occupant's behaviour but many other factors may impact on it. In this regard, the correct evaluation of the interactions between the building and the local context is an important consideration, but is very often not correctly incorporated into energy analyses because of the difficulty in gathering the data required to model neighbouring buildings.

The automated generation of simulation models based on the interoperability of building information modelling (BIM) and building performance simulation software (BPS) offers a promising solution to these problems (Bres et al., 2017). To achieve the main objective of an effective reduction of energy consumption, an integration between the existing building heritage and energy efficiency measures is tested in this study, making use of innovative digital technologies. Parametric digitalization operations of an existing building and the development of three-dimensional model in the Building Information Modelling tool were performed (Fig. 1).

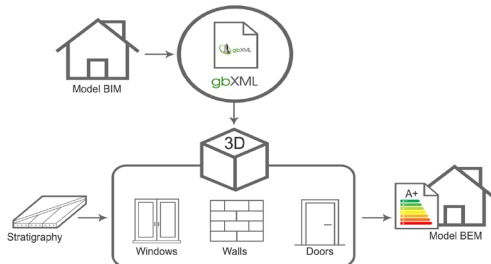


Fig. 1 – Evolution from the BIM model to the BEM model

The proposed approach is based on a model developed in a BIM (Building Information Modelling) environment, which acts as a coordination tool for the modelling, design, implementation and management phase of the chosen case study. The BIM to BEM interoperability is tested and the energy saving measures are evaluated by evaluating different energy saving scenarios.

2. Methods

2.1 Research Objectives

This research aimed to ascertain whether it is possible to integrate BIM and BEM modelling to evaluate different energy saving solutions for an existing building. One of the research goals was to define a workflow to develop a building energy model starting from a geometric survey. Furthermore, the research aimed to investigate the extent to which the surrounding buildings affect the building performance simulation. It was decided that an effective and efficient survey strategy would be to use a drone in order to represent the building's surroundings. The objectives of the proposed workflow are to:

- determine how the context affects the energy consumption of the building;
- propose an example of an enhanced geometrical survey for the definition of the BEM of an existing building;
- compare the results obtained from the model with those of the model including the surrounding buildings.

2.2 Test Case

The test case is an existing social housing block located in the province of Trento (Italy) in a neighbourhood with other social housing (Fig. 2). The test case is a poorly insulated five-floor building with 32 apartments built in the 1970s.

Table 1 – Actual energy consumption of the test case

Period	Consumption [kWh m ⁻²]	Degree Days [K day ⁻¹]
2006/2007	158.0	2344
2007/2008	149.5	2759
2008/2009	161.1	2767
2009/2010	159.3	2776
2010/2011	162.0	2605
2011/2012	146.1	2617
2012/2013	165.5	2776
2013/2014	147.0	2409
2014/2015	160.2	2252
2015/2016	170.8	2539

The heating system of the building uses a centralized boiler and the terminal units are radiators fed with a single pipe loop for each apartment.

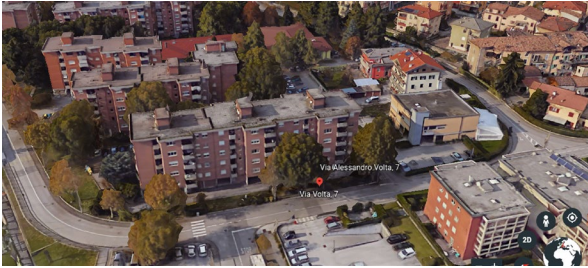


Fig. 2 – Framework of the context in which the case study is located

The building has high energy consumption for heating since it predates the first Italian energy law (enforced in 1976); details of the energy consumption are shown in Table 1.

2.3 Proposed Workflow

A good knowledge of the existing building is essential for designing effective retrofit measures. For this reason, the development of an accurate energy model was considered key. The study took five steps, as follows:

- the analysis of the as-built building and its surroundings
- the development of a three-dimensional model in a BIM environment (Building Information Model),
- data transfer from the BIM to BEM (Building Energy Model) (Fig 3) in order to create an energy analysis model (EAM),
- refinement of the EAM model in the energy simulation software,
- running of the simulation and post-processing of the results.

The first step involved the detailed analysis of the artefact chosen as a case study, the conformation of the orography and the building's surroundings. The analysis of the building's surroundings is key, as it effects the amount of solar radiation and, consequently, may have a significant impact on actual energy needs.

An analysis of a building's surroundings is often neglected in the energy analysis, as it is an expensive and time consuming activity, and involves difficult data collection. However, it is

something that can, to a certain extent, impact on a building's performance and can also become one of the causes of the performance gap.

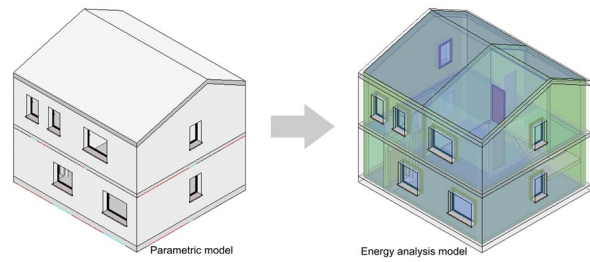


Fig. 3 – From the parametric model (BIM) to the energy analysis model (EAM)

In this study, the evaluation of the building's geometry and surroundings was carried out by exploiting advanced survey techniques.

The internal geometry of the apartments was detected through the use of a 3D laser scanner. This technique speeds up the survey and makes it possible to collect the internal dimensions. The procedure therefore allows the development of a BIM model that is more accurate than one based only on available original design documentation. Similarly, an enhanced analysis of the urban context was carried out by using pictures taken by a drone (Fig. 4). A point cloud was obtained from the overlap of the different pictures taken by the drone through the use of post-processing software. The point cloud represents the size of the building and of the neighboring buildings. This cloud was subsequently imported into the BIM software (Fig. 5) and converted into a parametric three-dimensional model of the building (Fig 6). The three-dimensional model of the existing building and its surroundings is the first phase of the adopted methodological process.

The operational approach typical of Building Information Modeling, allows the organization of complex and structured three-dimensional models based on energy, architectural, structural and thermal data. Furthermore, a BIM model contains a systematized database, which can be used both for integrated building design and for the management of the building throughout its life cycle.

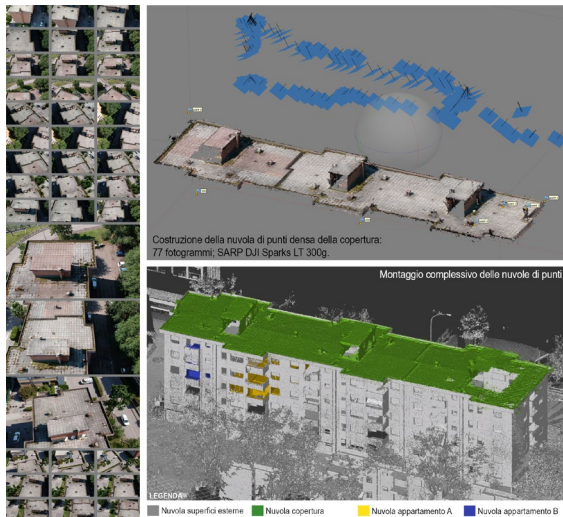


Fig. 4 – Point cloud acquisition through drone survey

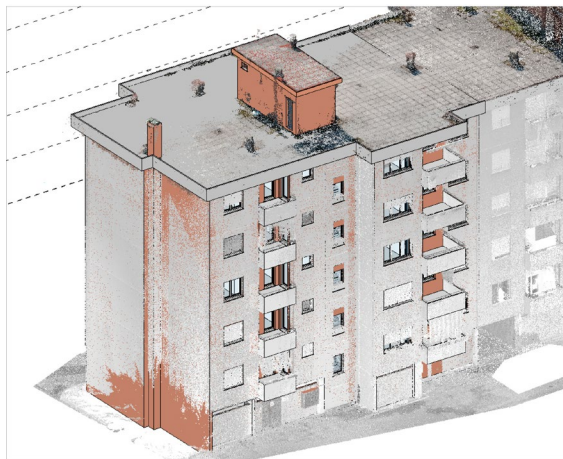


Fig. 5 – Parametric modeling based on the acquired point cloud



Fig. 6 – Importing the north block modeled into the context in Autodesk Revit 2019

The BIM to BEM interchange was divided into three distinct operational phases.

- **Analytical model.** According to the software definition, an analytical model is a simplified 3D representation of a structural physical model (Fig. 6). The analytical model consists of those structural elements, geometry, material properties, and loads, that together form the

building. Autodesk Revit 2019 software was used for the development of the three-dimensional model in a BIM environment.

- **File interchange format.** The BIM software converts the analytical model in the gbXML (Green Building XML) export file (Fig. 7). This is one of the common interchange formats between BIM and BEM software (Fig. 9). The gbXML file includes all of the information about the building and HVAC systems. Fig. 9 identifies the surfaces that delimit the air volume of each thermal zone. This is the control volume on which the dynamic simulation software performs energy balances. Furthermore, information regarding wall layers, wall exposures and wall adjacency are connected to these surfaces, while air conditioning systems, internal gains etc. are linked to the volumes.
- **Import of the gbXML model** into the chosen energy simulation software. In this research, we used the Design Builder GUI to set up the Energy Plus model, run the simulation and to post-process the results;

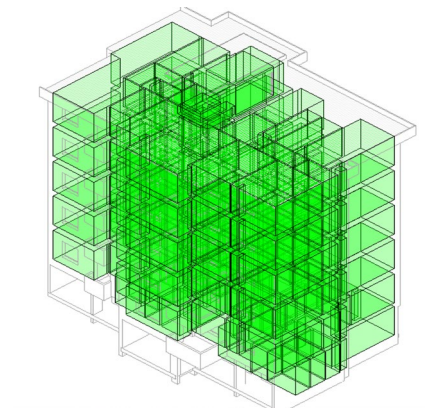


Fig. 7 – Export procedure using the gbXML format

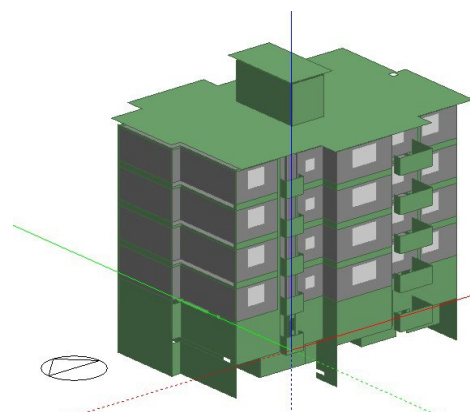


Fig. 8 – Importing the BIM model into Design Builder GUI

Two different exports of the interchange file were carried out in order to assess the influence of surrounding buildings on the energy performance of the test case. For this reason, in the first model, only the test case building was converted to BEM, while the neighbouring buildings were converted into shading elements only in the second model (Fig. 9).

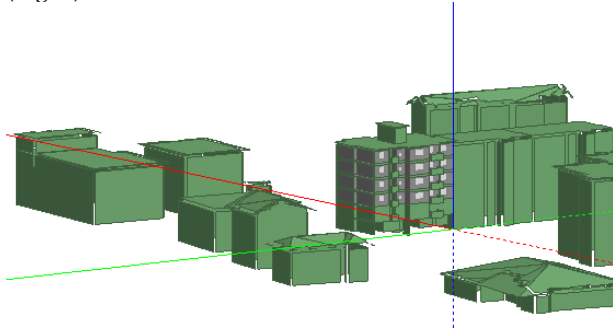


Fig. 9 – Importation of the context modeled within Design Builder

For both models, the simulations were performed by using a sub hourly time step, according to the Energy Plus references.

Internal heat gains were defined using a time dependent function, according to the utilization profiles specified in the Italian technical specification UNI/TS 11300-1 for different zones. The maximum gains were equal to $20 \text{ W}\cdot\text{m}^{-2}$ for the kitchen and living room, and $6 \text{ W}\cdot\text{m}^{-2}$ for the other conditioned zones. The natural ventilation rate (including infiltration effects) was assumed to be equal to 0.5 ACH (air changes per hour) according to std. UNI/TS 11300-1.

2.4 Retrofit Design

After a careful comparison of the results describing the building's performance, both with and without the surrounding buildings, the research turned to the analysis of possible energy saving measures. In this first phase, we focused on possible interventions to improve the building envelope. As suggested by the European Commission, the application of mature and off-the-shelf technologies can lead to a reduction of one third of total energy consumption. Insulation of the envelope and the replacement of windows are two common solutions.

One important issue can be the high initial investment cost of the energy saving measures on the

façade, if the owner of a building has a low income. For this reason, an integrated and prefabricated façade solution was designed in order to limit the initial costs by reducing the amount of work required on site and the use of scaffolding. A second skin, made of timber panel, was anchored to the existing structure. The new windows were integrated into the prefabricated panels.

Through the dynamic simulation model, the optimal characteristics of the new wall were evaluated in order to limit energy consumption while taking into account construction constraints. A parametric evaluation of different insulation levels was performed by coupling a custom Matlab code to the Energy Plus simulation engine.

3. Results

3.1 Impact of Surrounding Buildings

The first results are those from the comparison between the performances predicted by the model, depending on whether the shading brought by the surrounding buildings is considered or not. Fig. 10 shows how the adjacent buildings cast shadows on the windowed surfaces of the case study building during some hours of the day. This aspect obviously affects energy performance and the peak power required by the cooling system. The graph in Fig. 11 shows the simulation outcomes when the interactions between the building and its context are neglected. The results show how the net energy required is mainly used for heating, with 103.8 kWh m^{-2} per year; energy use for cooling, by comparison, is 10.66 kWh m^{-2} . These figures are quite compatible with the data in Table 1, taking into account that the data in Table 1 relate to primary energy consumption, which also includes HVAC efficiency and the domestic hot water demand.

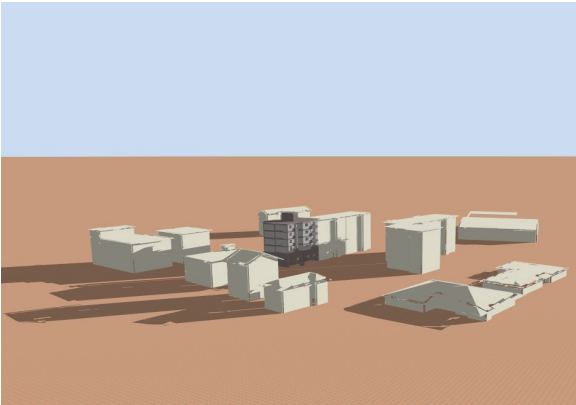


Fig. 10 – Shadows cast by surrounding buildings

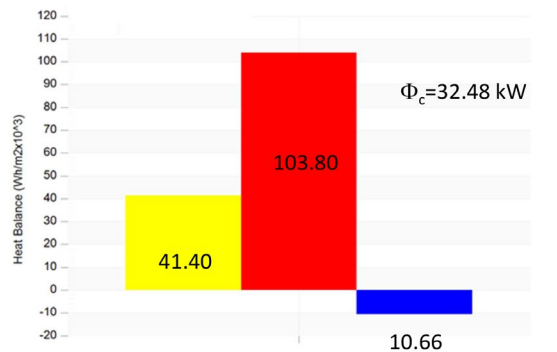


Fig. 11 – Solar gains (yellow bar) heating (red bar) and cooling demand (blue bar) predicted by the model which does not consider building surroundings

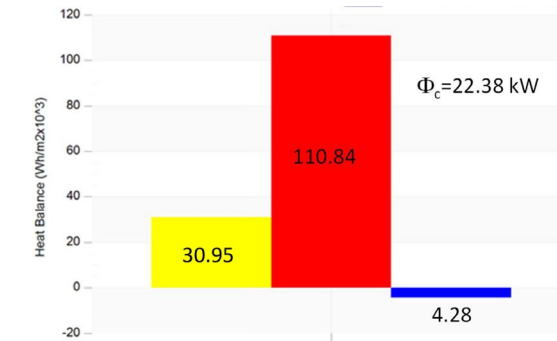


Fig. 12 – Solar gains (yellow bar) heating (red bar) and cooling demand (blue bar) predicted by the model which considers building surroundings

The graph also shows annual solar gains of 41.4 kWh m^{-2} and peak cooling power of 32.48 kW . Fig. 12, in comparison, shows a similar graph with the performances calculated using the detailed model which considers the shadows cast by the neighboring buildings. As can be seen, solar inputs are reduced by almost 25% during the entire year, which causes a 7% increase in heating demand and a 60% reduction in cooling demand. The more detailed model estimates a 31% reduction of the

peak power required for the cooling system. These appreciable variations were obtained considering a passive use of the building. That is, variations in internal gains related to lighting fixtures or the activation of external screens by occupants were not considered. These aspects are closely connected to the urban context that the building is situated in: the illuminance distribution is affected by the shadows cast by the surrounding buildings. For example, Figs. 13 and 14 show the different illuminance distribution on the third floor in the mid-afternoon on a winter's day.

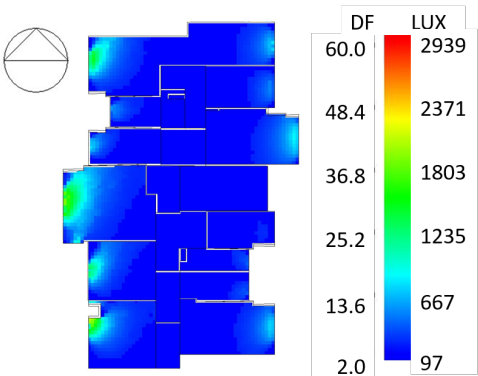


Fig. 13 – Illuminance and Daylighting Factor on the third floor on January 15 at 3 PM without surrounding buildings in the model

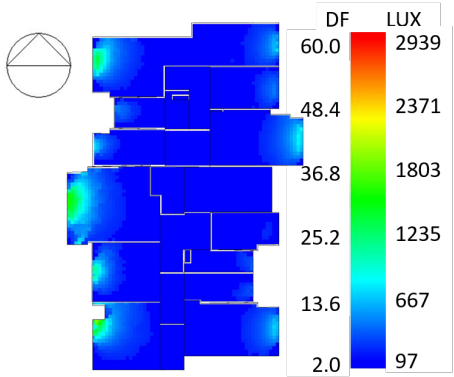


Fig. 14 – Illuminance and Daylighting Factor on the third floor on January 15 at 3 PM with surrounding buildings in the model

Although it is possible to note a different percentage of space in which the illumination level reaches the minimum threshold, this comparison still remains punctual and tied to the particular time of day. The daylighting autonomy (sDA) was therefore evaluated in order to obtain a metric that was more accurate in terms of lighting consumption, and therefore to internal gains. The sDA quantifies how often a minimum work plane illuminance of

300 lux can be maintained by daylight alone. It is defined as the percentage of occupied hours in a year when a minimum work plane illuminance threshold of 300 lux can be maintained by daylight alone.

An appreciable variation in the percentage of hours of the year in which the minimum lighting level is guaranteed by daylighting can be seen by comparing the results in Fig. 15 to those in Fig. 16. These variations may have further impacts on energy requirements.

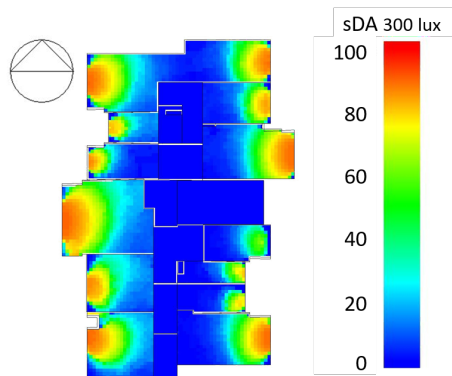


Fig. 15 – Spatial daylight autonomy with a 300 lux level on the third floor without surrounding buildings in the model

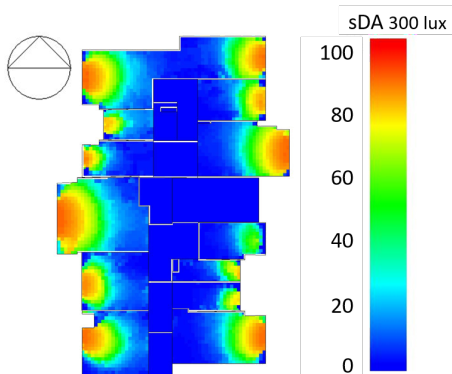


Fig. 16 – Spatial daylight autonomy with a 300 lux level on the third floor without surrounding buildings in the model

3.2 Retrofit Design

After the analysis on the impact of the shadows on heating requirements, a parametric analysis was conducted on the optimal thickness of the insulation to be installed on the external walls. Multiple EnergyPlus simulations were carried out by means of a custom Matlab script with the purpose of evaluating the extent to which insulation thickness affects energy use for heating the entire building (Fig. 17).

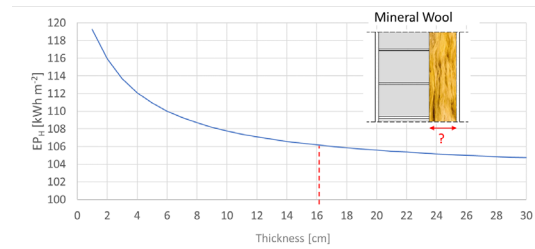


Fig. 17 – Results of the parametric analysis on the optimal insulation thickness

The graph in Fig. 17 shows a negligible energy performance increase for an insulation thickness greater than 16 cm. Furthermore, there are higher construction costs of the façade for a thickness greater than 16 cm, since this also requires a greater depth in the timber pillars. For this reason, during the design phase this insulation thickness was selected.

4. Conclusions

This paper has proposed a methodology to develop a simulation model of an existing building and its surroundings, using a drone survey and a BIM approach.

BIM and aerial drone mapping are suitable for building a context model. This method highlighted the importance of the correct modelling of the urban context even with simplified simulation input and despite the external obstructions not being particularly intrusive. Significant variations emerged in the building's heating and cooling needs. The biggest impact was on the cooling performance because of the key role of solar radiation. However, high performance buildings may also be more sensitive in the heating period. Furthermore, the detailed modelling of the shadows cast by the surrounding buildings made it possible to evaluate the proper peak power for cooling. Neglecting the urban context leads to a 31% increase in peak power for the test case and, consequently, to the system being oversized, with a consequent reduction in operating performance.

Proper modelling of the urban context makes it possible to achieve a better characterization of the initial state of the existing building and therefore to design more effective energy performance solutions. In this work, for example, the detailed simulation model was used to evaluate the optimal insulation thickness to be installed on vertical walls.

Acknowledgement

This study was funded by Caritro Foundation in the framework of the project “BIM Methodologies for a new industrialization of the energy requalification interventions of the existing building heritage”.

References

- Bres, A., F. Judex, G. Suter, P. de Wilde. 2017. “A Method for Automated Generation of HVAC Distribution Subsystems for Building Performance Simulation.” *Proceeding of BS2017 15th Building Simulation Conference 2017*, edited by IBPSA, 1548 -1557. San Francisco (USA).
- Li, J., S. T. Nga, M. Skitmore. 2017. “Review of low-carbon refurbishment solutions for residential buildings with particular reference to multi-story buildings in Hong Kong.” *Renewable and Sustainable Energy Reviews* 73: 393–407. doi: 10.1016/j.rser.2017.01.105
- Lobos Calquin, D. A. 2017. “Automated Building Data Exchange between BIM and BPS Supporting Building Environmental Assessment Methods (BEAM).” *Proceeding of BS2017 15th Building Simulation Conference*, edited by IBPSA, 1329-1333. San Francisco (USA).
- Vilches, A., A. Garcia-Martinez, B. Sanchez-Montañes. 2017. “Life cycle assessment (LCA) of building refurbishment: A literature review.” *Energy and Buildings* 135: 286-301. doi: 10.1016/j.enbuild.2016.11.042

Calibration of a UMI Simulation Model for a Neighborhood in Bolzano, Italy

Federico Battini – Free University of Bozen-Bolzano, Italy – federico.battini@natec.unibz.it

Giovanni Pernigotto – Free University of Bozen-Bolzano, Italy – giovanni.pernigotto@unibz.it

Andrea Gasparella – Free University of Bozen-Bolzano – andrea.gasparella@unibz.it

Abstract

In recent decades, public authorities have focused their attention on the building sector, since it is responsible for a large share of the total energy consumption and, thus, should be involved in the development of sustainable energy policies. In this context, Urban Building Energy Models UBEM can play a significant role as they make it possible to study the behaviour of whole cities, as well as the potential of different building retrofitting strategies. In this contribution, the UBEM tool *umi* is used to study a neighbourhood in Bolzano, Italy, to contrast its capabilities and test the potential of a *k*-fold approach as preliminary calibration of the model, based on energy certificates and annual energy consumption data.

1. Introduction

The continuous growth of the world's population, combined with the phenomena of urbanization, will lead to an additional 2.5 billion people living in urban areas by 2050 (UN Department of Economic and Social Affairs, 2018). In this scenario, the building sector, which is already responsible for 40% of total energy consumption (European Parliament, 2010), will be crucial in ensuring sustainable development. Specifically, not only should new buildings be designed in a way that respects high efficiency criteria but also a thorough renovation of the existing building stock should be planned. To do so, it is necessary to: (1) identify those buildings responsible for the largest energy consumptions, and (2) define and optimize the impact of energy retrofitting programs.

Building Energy Models BEM, such as DOE-2 (Birdsall et al., 1990), TRNSYS (Klein, 1988) and En-

ergyPlus (U.S. Department of Energy, 2019), are widely employed to analyse the energy behaviour of single buildings. Furthermore, some studies in the literature have extended their range of application by evaluating the energy demand of groups of buildings (Huber and Nytsch-Geusen, 2012; Huang and Brodrick, 2000; Salom, 2002). However, the large amount of information needed as input and the required computational time make the BEM approach unsuitable for large scale applications.

As an alternative, urban scale simulations often rely on Urban Building Energy Models UBEM, which implement physical models of heat and mass flows in and around buildings to predict operational energy use, as well as indoor and outdoor environmental conditions (Reinhart and Davila, 2015). Examples of developed and validated UBEM software are CityBES (Chen et al., 2017), CitySim (Robinson et al., 2009), HUES (Bollinger and Dorer, 2016), SimStadt (Monsalvete et al., 2015), TEASER (Remmen et al., 2017), and the Urban Modeling Interface *umi* by MIT Sustainable Design Lab (Reinhart et al., 2013). Despite the variety of alternative models, a common issue faced by researchers is the availability of the whole set of required inputs and the need for model calibration.

In this work, *umi* was adopted to simulate the energy performance of a small neighbourhood served by a district heating network in the city of Bolzano, Italy, with the aim of discussing its capabilities and the impact of its modelling assumptions. After the preparation of the model, a *k*-fold cross calibration and validation procedure was run, using actual annual heating and domestic hot water energy demands as reference.

2. Methodology

2.1 Case Study

A residential neighbourhood located in the western part of Bolzano, Italy, was chosen to develop the urban model. The area is composed of 95 residential buildings, built at the beginning of the 1990s and served by the local district heating network. Specifically, the space heating and domestic hot water (DHW) demands in the selected neighbourhood are supplied by 14 substations. Annual energy consumption is available for each substation for four years (2012, 2013, 2014, 2015). Since the substations serve different purposes (i.e. space heating demands, DHW demands, or both), for the sake of simplicity and consistency they were merged into 11 groups, each satisfying both heating and DHW demands for each cluster of the 95 buildings. Available annual space heating and DHW demands are distinguished for half of the buildings in the sample while for the remaining half, the DHW share of the global demand was considered for calibration.

2.2 Model Development

Building an urban energy model requires different steps, such as: model characterization, calibration and validation of the obtained results.

2.2.1 Geometry input data

As a first step, geometrical shape and height data for the buildings were collected. For this case study, the buildings' footprints were imported into Rhinoceros (McNeel, 2012) through a GIS file with the aid of the Grasshopper plug-in Meerkat (Lowe, 2015). To evaluate the heights of the buildings, the difference between a Digital Surface Model DSM and a Digital Terrain Model DTM were calculated for every building. Assuming a floor height equal to 3 m, the number of floors was first computed and then checked with Google Maps (Google, 2019). For those buildings characterized by a complex shape, different polysurfaces were prepared in order to obtain geometries representative of the case-study.

Since detailed data on the area of distribution of windows were not available, a glazing area per floor equal to 1/8 of the floor area was assumed, as prescribed by Italian law. To perform the glazing area calculation, floors were approximated as rectangular shapes, and a matrix with total floor areas and side lengths ranging from 1 to 60 m was prepared. All floor areas in the matrix were divided first by 8 and then by the number of externally exposed sides of each building, obtaining 4 different matrices. Finally, a division by each façade area (i.e. by 3 times the side length, as floor height was assumed to be 3 m) was performed. Using this process (shown in Fig. 1), it was possible to obtain the total glazing area for each side of every building, as well as the window to wall ratio, and these were used in the model.

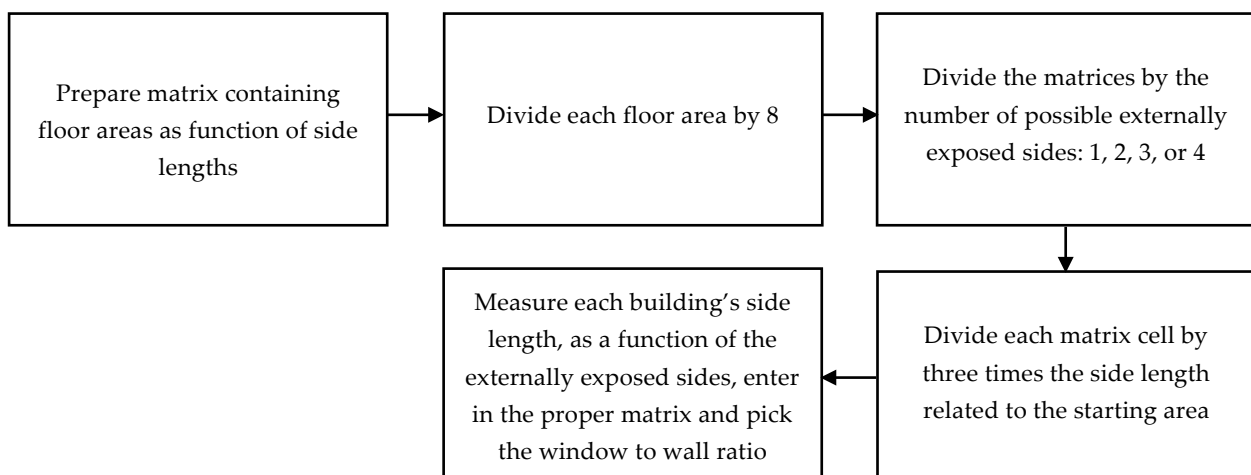


Fig. 1 – Window to wall ratio evaluation flowchart

After evaluating the window to wall ratio for every building, a model geometry inclusive of the surroundings, generated for shading purposes, was created, as shown in Fig. 2.

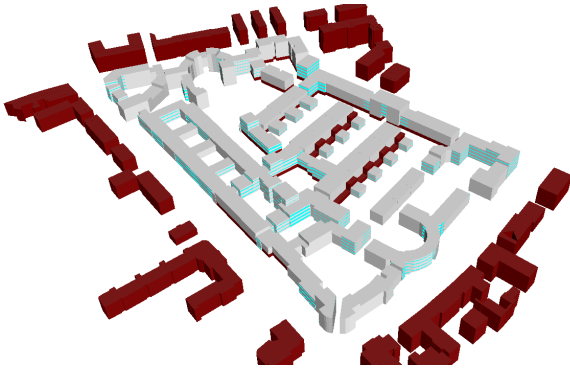


Fig. 2 – Model geometry and surroundings

2.2.2 Non-geometric properties

Non-geometric properties of the buildings in the sample, e.g. wall material layers, were obtained by consulting the 60 available energy certificates. Material properties and thermal transmittances of the different envelope components were used to generate 3 archetypes (Fig. 3). Buildings whose energy certificates were not available were assigned to Archetype 1, since they share similarities with this archetype when it comes to the period of construction and are mainly surrounded by buildings of this group.



Fig. 3 – Definition of archetypes

Operation schedules and simulation parameters have been kept the same for each archetype and set according to Italian regulations and technical standards.

2.2.3 Sensitivity analysis

Once the model was created, a sensitivity analysis was carried out on schedule and simulation parameters. The weather conditions for 2012 were chosen as a test year and a variation of $\pm 20\%$ was applied to the base values of ventilation rates and HVAC system efficiency, equal to 0.5 ACH and 0.87 respectively.

2.3 Model Calibration

2.3.1 Target energy consumption data

As mentioned above, actual annual energy consumptions are available for the 11 clusters of buildings from 2012 to 2015, although separate space heating and DHW demand data were provided for only half of the groups. From the available data, it was observed that the DHW share is typically between 25 % and 30 % of the total consumptions (Fig. 4).

2.3.2 Calibration and k -fold validation

The most significant variables resulting from the sensitivity analysis, as well as the DHW flow demand, were involved in a parametric calibration performed according to a k -fold cross validation approach. The k -fold cross validation is a statistical method which divides the available data into k segments (or folds), and performs k iterations of training and validation, each time selecting a different fold for validation and the remaining $k-1$ folds for training.

In this case-study, the root mean square difference RMSD was adopted in order to compare the simulated annual results to the actual ones in the k -fold validation process. Specifically, for each group of buildings, the RMSD was computed over three years and the set of values with the lowest RMSD was checked for the fourth year, analyzing all possible combinations. The most frequent values for calibrated variables were selected for each group of buildings.

3. Results

Preliminary results were obtained from the sensitivity analysis using 2012 weather data to run the simulation. As regards the impact of ventilation rates and *HVAC* system efficiency, a -20 % variation causes, respectively, a reduction of 52 % and an increase of 135 % in heating demand. By comparison, a variation of +20 % leads to, respectively, an increase of 60 % and a reduction of 86 %. As a consequence, both variables were included in the calibration process, using the following ranges:

- between 0.82 and 0.87 with a 0.01 step for *HVAC* system efficiency;
- between 0.4 and 0.6 ACH with a 0.05 ACH step for the ventilation rate;
- between 0.001395 and 0.001845 $\text{m}^3 \text{m}^{-2} \text{h}^{-1}$ with a step of 0.000035 $\text{m}^3 \text{m}^{-2} \text{h}^{-1}$ for the water flow rate (i.e., a usage per capita between 55.8 l/person and 73.8 l/person per day).

The chosen combination for each group of buildings is reported in Table 1 and results for the year 2014 are found in Table 2. As can also be seen in Fig. 5, after the calibration the deviation from actual consumption is within 5 % in the majority of cases.

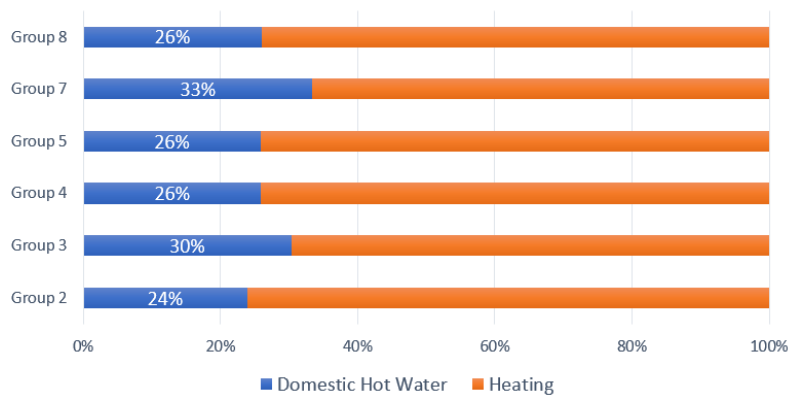


Fig. 4 – DHW share for group of buildings with subdivision

Table 1 – Chosen combinations after calibration results

Building group	<i>HVAC</i> efficiency	Ventilation rate [ACH]	Water consumption [$\text{m}^3 \text{m}^{-2} \text{h}^{-1}$]	DHW share	Mean heating RMSD [%]	Mean DHW RMSD [%]
Group 1	0.83	0.55	0.001535	30 %	11.2	4.9
Group 2	0.82	0.60	0.001430	-	17.9	4.1
Group 3	0.84	0.50	0.001845	-	1.4	12.8
Group 4	0.84	0.55	0.001430	-	4.2	1.1
Group 5	0.84	0.55	0.001500	-	15.1	5.3
Group 6	0.83	0.60	0.001395	25 %	23.1	9.7
Group 7	0.85	0.55	0.001810	-	26.0	4.5
Group 8	0.83	0.60	0.001600	-	25.2	2.7
Group 9	0.83	0.60	0.001430	25 %	10.1	5.0
Group 10	0.87	0.55	0.001635	30 %	8.5	6.6
Group 11	0.85	0.40	0.001500	25 %	8.7	13.2

Table 2 Obtained results for 2014 and comparison with first simulation with base parameters

Building group	2014 heating demand [MWh]	2014 initial simulation [MWh]	2014 calibrated results [MWh]	DHW share	Initial simulation deviation	Calibrated simulation deviation
Group 1	292.3	264.3	288.0	30 %	-9.6 %	-1.4 %
Group 2	474.3	434.8	491.1	-	-8.3 %	3.5 %
Group 3	155.2	152.5	154.6	-	-1.7 %	-0.4 %
Group 4	129.6	121.6	124.7	-	-6.2 %	-3.8 %
Group 5	449.5	440.0	466.6	-	-2.1 %	3.8 %
Group 6	586.5	511.5	567.9	25 %	-12.8 %	-3.2 %
Group 7	820.6	819.9	855.9	-	-0.1 %	4.3 %
Group 8	294.4	260.5	293.6	-	-11.5 %	-0.3 %
Group 9	376.1	316.9	362.1	25 %	-15.7 %	-3.7 %
Group 10	349.8	334.0	341.4	30 %	-4.5 %	-2.4 %
Group 11	308.2	334.3	300.4	25 %	8.5 %	-2.5 %

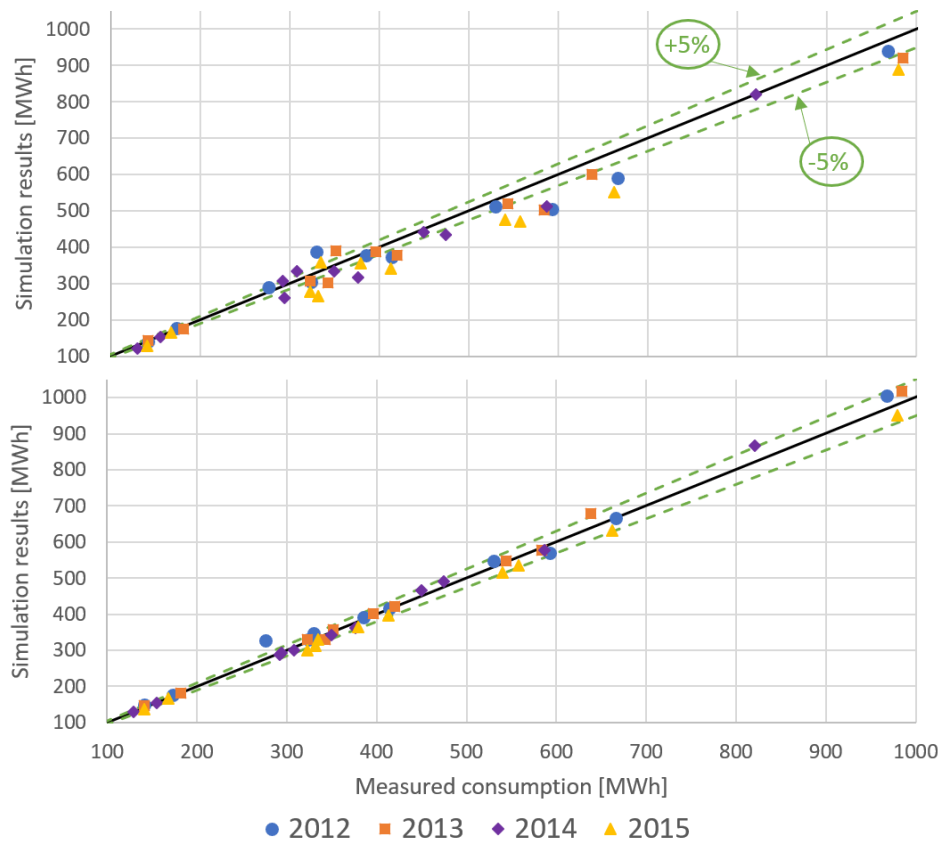


Fig. 5 – Heating demand results prior and after calibration

4. Discussion and Conclusion

In this work, the Urban Modeling Interface *umi* was used to develop and calibrate a model for a neighbourhood in Bolzano, referring to energy certificates and annual energy consumptions for space heating and domestic hot water. After creating the geometrical model and identifying the non-geometrical properties of the buildings, a sensitivity analysis and a calibration through the *k*-fold validation approach were performed. After calibration, it was shown that the *umi* model was able to provide representative results for space heating and domestic hot water demands for the considered case-study district. Moreover, the adopted *k*-fold approach demonstrated the effectiveness and potential for the calibration of urban models in these contexts; this can be seen in the presented case-study, in which the available data for model training and validation was limited and provided only on annual scale.

With a reliable model available, further developments can be now considered. These include comparisons with different approaches, and the assessment of the impact of several different conditions pertaining to the urban environment, as well as the non-energy performance of buildings in the district, such as occupant comfort. In particular, both energy and non-energy performances can be the object of further multi-objective optimization studies aimed at identifying the most effective energy efficiency measures based on indoor environmental quality, in addition to energy and cost efficiency.

Acknowledgement

This study has been funded by the project “Klimahouse and Energy Production” in the framework of the programmatic-financial agreement with the Autonomous Province of Bozen-Bolzano of Research Capacity Building.

The Authors would also like to thank the Klimahaus Agency for providing access to the building energy certificates and to the Municipality of Bozen-Bolzano for the building energy consumption data.

References

- Birdsall, B., W. F. Buhl, K. L. Ellington, A. E. Erdem, and F. C. Winklemann. 1990. *Overview of the DOE-2 building energy analysis program, Version 2. 1D*. United States: Lawrence Berkley Lab.
- Bollinger, A. L., and V. Dorer. 2016. "A Simulation Platform to Facilitate the Design of Distributed Energy Systems for Buildings and Districts." 19. *Status-Seminar Forschen für den Bau im Kontext von Energie und Umwelt*.
- Chen, Y., T. Hong, and M. A. Piette. 2017. "Automatic generation and simulation of urban building energy models based on city datasets for city-scale building retrofit analysis." *Applied Energy* 323-335.
- European Parliament, Council of the European Union. 2010. "Directive 2010/31/EU of the European Parliament and of the Council on the energy performance of buildings." May 19.
- Google. 2019. *Google Maps*. Accessed May 2019. <https://www.google.it/maps>
- Huang, Y. J., and J. Brodrick. 2000. "A Bottom-Up Engineering Estimate of the Aggregate Heating and Cooling Loads of the Entire U.S. Building Stock." 2000 *ACEEE Summer Study on Energy Efficiency in Buildings*. Pacific Grove.
- Huber, J., and C. Nytsch-Geusen. 2012. "Development of modeling and simulation strategies for large-scale urban districts." *Proceedings of Building Simulation 2011: 12th Conference of International Building Performance Simulation Association*. Sydney.
- Klein, S. A. 1988. "TRNSYS - A transient system simulation program." *University of Wisconsin-Madison, Engineering Experiment Station* 12-38.
- Lowe, N. 2015. *Meerkat GIS*. Accessed October 2018. <https://www.food4rhino.com/app/meerkat-gis>.
- McNeel. 2012. *Rhinoceros version 5.0*. Accessed September 2018. <https://www.rhino3d.com/>
- Monsalvete, P., D. Robinson, and U. Eicker. 2015. "Dynamic Simulation Methodologies for Urban Energy Demand." 6th *International Building Physics Conference, IBPC 2015*.
- Reinhart, C. F., and C. Cerezo Davila. 2015. "Urban building energy modeling - A review of a nascent field." Boston, December 2.

- Reinhart, C. F., T. Dogan, J. A. Jakubiec, T. Rahka, and A. Sang. 2013. "Umi - an Urban Simulation Environment for Building Energy Use, Daylighting and Walkability." *Proceedings of the 13th Conference of International Building Performance Simulation Association*, Chambéry, France, August 2013.
- Remmen, P., M. Lauster, M. Mans, M. Fuchs, T. Osterhage, and D. Müller. 2017. "TEASER: an open tool for urban energy modelling of building stocks." *Journal of Building Performance Simulation* 84-98.
- Robinson, D., F. Haldi, P. Leroux, and A. Rasheed. 2009. "CITYSIM: Comprehensive Micro-Simulation of Resource Flows for Sustainable Urban Planning." *Building Simulation 2009: Eleventh International IBPSA Conference*. Glasgow, Scotland.
- Salom, J. 2002. "Study of the Residential Building Sector in the Plan for Energy Improvement of Barcelona." *Proceedings EuroSun2002-Congress*. Bologna, Italy.
- U.S. Department of Energy. 2019. *EnergyPlus*. Accessed May 2019, 28. <https://energyplus.net/>
- UN Department of Economic and Social Affairs, Population Division. 2018. "United Nations: World Urbanization Prospects: the 2018 Revision." New York NY.